Yoshiro Kakehashi

# Modern Theory of Magnetism in Metals and Alloys



# Springer Series in

# **SOLID-STATE SCIENCES**

Series Editors:

M. Cardona P. Fulde K. von Klitzing R. Merlin H.-J. Queisser H. Störmer

The Springer Series in Solid-State Sciences consists of fundamental scientific books prepared by leading researchers in the field. They strive to communicate, in a systematic and comprehensive way, the basic principles as well as new developments in theoretical and experimental solid-state physics.

Please view available titles in *Springer Series in Solid-State Sciences* on series homepage http://www.springer.com/series/682

# Yoshiro Kakehashi

Modern Theory of Magnetism in Metals and Alloys



Yoshiro Kakehashi Faculty of Science, Department of Physics University of the Ryukyus Nishihara, Japan

Series Editors:

Professor Dr., Dres. h. c. Manuel Cardona Professor Dr., Dres. h. c. Peter Fulde\* Professor Dr., Dres. h. c. Klaus von Klitzing Professor Dr., Dres. h. c. Hans-Joachim Queisser

Max-Planck-Institut für Festkörperforschung, Heisenbergstrasse 1, 70569 Stuttgart, Germany

\*Max-Planck-Institut für Physik komplexer Systeme, Nöthnitzer Strasse 38

01187 Dresden, Germany

Professor Dr. Roberto Merlin Department of Physics, University of Michigan 450 Church Street, Ann Arbor, MI 48109-1040, USA

Professor Dr. Horst Störmer

Dept. Phys. and Dept. Appl. Physics, Columbia University, New York, NY 10027, USA and Bell Labs., Lucent Technologies, Murray Hill, NJ 07974, USA

ISSN 0171-1873 Springer Series in Solid-State Sciences
ISBN 978-3-642-33400-9 ISBN 978-3-642-33401-6 (eBook)
DOI 10.1007/978-3-642-33401-6
Springer Heidelberg New York Dordrecht London

Library of Congress Control Number: 2012954262

### © Springer-Verlag Berlin Heidelberg 2012

This work is subject to copyright. All rights are reserved by the Publisher, whether the whole or part of the material is concerned, specifically the rights of translation, reprinting, reuse of illustrations, recitation, broadcasting, reproduction on microfilms or in any other physical way, and transmission or information storage and retrieval, electronic adaptation, computer software, or by similar or dissimilar methodology now known or hereafter developed. Exempted from this legal reservation are brief excerpts in connection with reviews or scholarly analysis or material supplied specifically for the purpose of being entered and executed on a computer system, for exclusive use by the purchaser of the work. Duplication of this publication or parts thereof is permitted only under the provisions of the Copyright Law of the Publisher's location, in its current version, and permission for use must always be obtained from Springer. Permissions for use may be obtained through RightsLink at the Copyright Clearance Center. Violations are liable to prosecution under the respective Copyright Law.

The use of general descriptive names, registered names, trademarks, service marks, etc. in this publication does not imply, even in the absence of a specific statement, that such names are exempt from the relevant protective laws and regulations and therefore free for general use.

While the advice and information in this book are believed to be true and accurate at the date of publication, neither the authors nor the editors nor the publisher can accept any legal responsibility for any errors or omissions that may be made. The publisher makes no warranty, express or implied, with respect to the material contained herein.

Printed on acid-free paper

Springer is part of Springer Science+Business Media (www.springer.com)

### **Preface**

Metallic magnetism has a long history because there have been continuous discoveries of many intriguing phenomena and difficulties in their theoretical description. One of the long-standing problems has been known as the itinerant vs localized behavior of the magnetism. The ground-state properties of Fe, Co, and Ni such as magnetization and the T-linear specific heat at low temperatures, for example, are explained by the band model, while their finite temperature properties such as the paramagnetic susceptibility and the large specific heat anomaly at the Curie temperature are explained well by the localized model.

The dual property of metallic magnetism led to two paths in theoretical investigations. One is to develop the band theory at the ground state taking into account correlation effects on the one electron potential for electrons. There the density functional theory (DFT) has played an important role. Theoretical improvement of metallic magnetism at the ground state has been achieved as a part of the developments of the DFT in the electronic structure calculations.

Another direction of the development has been to take into account the spin fluctuations in order to describe local-moment behaviors of metallic magnetism at finite temperatures. Theoretical results in this direction until 1980 are summarized in the book by Moriya (*Spin Fluctuations in Itinerant Electron Magnetism* (Springer, Berlin, 1985)). Although spin fluctuation theories have succeeded in describing the local moment behavior at finite temperatures in metallic magnetism, the underlying electronic structure related to the magnetism of a certain individual material seems to be oversimplified. A book which unifies the two paths on the same footing would be valuable for readers to understand the metallic magnetism.

This book aims to describe the theories of metallic magnetism from both view-points, namely spin fluctuations and the electronic structure. It attempts to clarify the magnetism from metals to disordered alloys to amorphous alloys.

The book covers most of the traditional topics of metallic magnetism such as electron correlation effects on the ferromagnetism, magnetic excitations, as well as the stability of antiferromagnetism and spin density waves. But it also includes topics which have been developed in the past three decades. The first is the development of the dynamical CPA (coherent potential approximation), which describes

vi Preface

the dynamical spin and charge fluctuations on the basis of the microscopic electronic structure within the single-site approximation. In particular, the first-principles dynamical CPA has reduced the gap between the spin fluctuation theory and the band theoretical approach to a large extent, thus allowing the investigation of the relationship between metallic magnetism and electronic structure. We elucidate this theory in Chap. 3. We also point out in the same chapter that the dynamical CPA is equivalent to the dynamical mean-field theory (DMFT) in the metal-insulator transition.

The second topic is the theory of local environment effects (LEE) in disordered alloys, which goes beyond the single-site CPA theory of magnetism. In Chap. 8, we describe the theory and clarify the magnetic behavior in the vicinity of the magnetic instability of Fe–Ni, Ni–Mn, and Ni–Cu alloys. This chapter also includes the molecular dynamics approach, which automatically determines the complex magnetic structure in metals and alloys. The third topic is the theoretical development of magnetism in amorphous metals and alloys. The finite-temperature theory sheds light on the amorphous magnetism from the viewpoint of spin fluctuations and the LEE, and clarifies how structural disorder drastically changes the magnetic properties of metals and alloys. This development is discussed in Chap. 9. Chapter 1 presents an introduction for the readers who are not familiar with the magnetism.

The frustrated system with heavy effective mass (e.g.,  $YMn_2$  and  $LiV_2O_4$ ) is not described in this book, because it is still under development. Recent topics on the spintronics are also omitted for the same reason. Non-local theory of dynamical spin fluctuations which goes beyond the dynamical CPA is left as a problem of future concern.

I would like to express my sincere thanks to Professor Peter Fulde, Professor Matin C. Gutzwiller, and Professor Hiroshi Miwa for their continuous support and encouragement over 30 years. I would like to thank Professor Takashi Uchida and Professor Ming Yu for their critical reading of the manuscript as well as their valuable comments; Professor Shi-Yu Wu and Professor Sung G. Chung for their valuable suggestions for improvement; and Professor Takeo Fujiwara and Professor Mojmir Sob for their kind comments. Dr. M.A.R. Patoary kindly prepared useful figures to whom I am most indebted. Thanks are also given to Mr. K. Chung for his help in proofreading the manuscript. Finally, I am grateful to Dr. C. Ascheron, Publishing Editor of Springer Verlag for his support towards the publication of this book.

Okinawa July 2012 Y. Kakehashi

# **Contents**

1	Intr	oduction to Magnetism									
	1.1	Magnetic Moments									
	1.2	Basic Hamiltonian									
	1.3	Formation of Atomic Moments									
	1.4	Metal and Insulator in Solids									
	1.5	Quenching of Orbital Magnetic Moments									
	1.6	Heisenberg Model									
	1.7	Magnetic Structure									
2	Met	allic Magnetism at the Ground State									
	2.1	Band Theory of Ferromagnetism									
	2.2	Electron Correlations on Magnetism									
		2.2.1 Stoner Condition in the Correlated Electron System 36									
		2.2.2 Stability of Ferromagnetism in the Low Density Limit 37									
		2.2.3 Gutzwiller Theory of Electron Correlations									
	2.3	Density Functional Approach									
		2.3.1 Slater's Band Theory									
		2.3.2 Density Functional Theory 48									
		2.3.3 Tight-Binding Linear Muffin-Tin Orbitals 53									
		2.3.4 Ferromagnetism in Transition Metals									
3	Met	allic Magnetism at Finite Temperatures									
	3.1										
	3.2	Functional Integral Method									
	3.3	58 5 5 5 5 5 7 7-									
	3.4	Dynamical CPA Theory									
	3.5	Dynamical CPA with Harmonic Approximation									
	3.6	Dynamical CPA and Dynamical Mean-Field Theory 95									
		3.6.1 The Many-Body CPA and Its Equivalence									
		to the Dynamical CPA									
		3.6.2 The DMFT and Its Equivalence to the Dynamical CPA 96									

viii Contents

		of Relations	102
	3.7	First-Principles Dynamical CPA and Metallic Magnetism	
4	Mag	gnetic Excitations	. 115
	4.1	Spin Waves in the Local Moment System	
	4.2	Spin Waves in Itinerant Ferromagnets	
	4.3	Dynamical Susceptibility	
	4.4	Dynamical Susceptibility in the RPA and Spin Wave Excitations	
5	Spir	n Fluctuation Theory in Weak Ferromagnets	. 135
	5.1	Free-Energy Formulation of the Stoner Theory	
	5.2	Self-Consistent Renormalization Theory	. 140
6	Anti	iferromagnetism and Spin Density Waves	. 149
	6.1	Antiferromagnetism in Metals	. 149
	6.2	Generalized Static Susceptibility and Antiferromagnetism	. 157
	6.3	Molecular Dynamics Theory for Complex Magnetic Structures	. 162
	6.4	Phenomenological Theory of Magnetic Structure	
		6.4.1 Multiple SDW with Commensurate Wave Vectors	
		6.4.2 Multiple SDW with Incommensurate Wave Vectors	. 177
7	Mag	gnetism in Dilute Alloys	. 181
	7.1	Magnetic Interactions and Spin Glasses in Dilute Alloys	. 181
	7.2	Magnetic Impurity in Noble Metals	. 193
8	Mag	gnetism of Disordered Alloys	203
	8.1	Slater–Pauling Curves	. 203
	8.2	Single-Site Theory of Disordered Alloys	. 206
	8.3	Theory of Local Environment Effects in Magnetic Alloys	. 217
	8.4	Computer Simulations for Disordered Magnetic Alloys	. 242
9	Mag	gnetism of Amorphous Metals and Alloys	
	9.1	Introduction to the Amorphous Metallic Magnetism	
	9.2	Amorphous Structure and Electronic Structure	
	9.3	Theory of Amorphous Metallic Magnetism	
	9.4	Magnetism of Amorphous Transition Metals	
		9.4.1 General Survey	
		9.4.2 Magnetism of Amorphous Fe, Co, and Ni	
		9.4.3 Degree of Structural Disorder and Nonunique Magnetism .	
	9.5	Theory of Magnetism in Amorphous Alloys	. 280
	9.6	Magnetism of Amorphous Transition Metal Alloys	
		9.6.1 TM–TM Amorphous Alloys	
		9.6.2 The Other TM Alloys	. 295
Apj	pendi	x A Equivalence of the CPA Equations (3.83), (3.85),	
	and	(3.89)	. 301
App	pendi	x B Dynamical CPA Based on the Multiple Scattering Theory	305

Contents ix

	<b>Derivation of the Single-Site Spin Fluctuation Theory Dynamical CPA</b>
Appendix D	Expansion of $D_{\nu\sigma}$ with Respect to Dynamical Potential 313
Appendix E	Linear Response Theory
	Isothermal Molecular Dynamics and Canonical tion
Appendix G	<b>Recursion Method for Electronic Structure Calculations</b> . 325
Appendix H	An Integral in the RKKY Interaction
References .	
Index	

# **Chapter 1 Introduction to Magnetism**

Magnetic properties originate in the spin degrees of freedom of electrons and their associated motion in solids. We first describe the microscopic magnetic moments of electrons, and the formation of atomic magnetic moments due to strong Coulomb interactions in an atom with unfilled shell. Atomic magnetic moments change their nature when the atoms form a solid. The key to understanding the behavior of magnetic moments in solids is the degree of electron localization. We briefly introduce the concept of the metal and the insulator (i.e., the Mott insulator). Electrons in the latter are localized on each atom, so that their magnetic properties are described by the atomic magnetic moments and the magnetic interactions between them. We present in this chapter only a minimal discussion on the magnetism in insulators. On the other hand, electrons move from site to site over the entire crystal in metals, so that the magnetic properties are connected to the whole degrees of freedom of correlated electrons. Needless to say, the main theme of this book is the magnetism of metals and alloys. In the last section, we elucidate various magnetic structures in solids to provide a basic knowledge on magnetism.

### 1.1 Magnetic Moments

Magnetic moment M in the electromagnetics is defined by the torque N on a magnet under the magnetic field H as

$$N \equiv M \times H. \tag{1.1}$$

It originates in electrons in the magnet. According to the classical electromagnetics, the coil-type local current i(r) due to electron motion causes a magnetic moment. It is given in the CGS-Gauss unit as [1]

$$\mathbf{M}_L = \frac{1}{2c} \int \mathbf{r} \times \mathbf{i}(\mathbf{r}) d^3 x. \tag{1.2}$$

1

Y. Kakehashi, *Modern Theory of Magnetism in Metals and Alloys*, Springer Series in Solid-State Sciences 175, DOI 10.1007/978-3-642-33401-6\_1, © Springer-Verlag Berlin Heidelberg 2012 Here c is the speed of light. i(r) is the current density of electrons, given by  $i(r) = -\sum_i e v_i \delta(r - r_i)$  with  $v_i$  being the velocity of the electron and -e the charge of the electron at  $r_i$ . Substituting the expressions into (1.2), we obtain

$$M_L = -\sum_i \frac{e}{2m_e c} l_i. \tag{1.3}$$

Here  $m_e$  is the mass of an electron and  $l_i$  denotes the angular momentum of electron i. Equation (1.3) indicates that an electron with angular momentum l generates a magnetic moment,

$$\mathbf{m}_l = -\frac{e}{2m_e c} \mathbf{l}.\tag{1.4}$$

This is called the orbital magnetic moment for an electron.

According to the quantum mechanics, an electron has its own magnetic moment called the spin magnetic moment [2]. It is given by

$$\boldsymbol{m}_{s} = -g_{e} \frac{e}{2m_{e}c} s. \tag{1.5}$$

Here s is the spin angular momentum of an electron with spin s = 1/2. The constant  $g_e = 2.0023$  is referred as the g-value of electron. The deviation from 2 is caused by the interaction with electro-magnetic fields. The spin magnetic moment was found first experimentally by Stern and Gerlach in 1922, and was established theoretically in 1928 by Dirac in his relativistic theory of electrons [3]. In the following we assume that  $g_e = 2$  for simplicity.

As seen from (1.5), the spin of an electron leads to the magnetic moment

$$\mu_{\rm B} = \frac{e\hbar}{2m_{\rm e}c} = 0.9274 \times 10^{-20} \,\text{emu}.$$
 (1.6)

Here  $\hbar$  is the Planck constant divided by  $2\pi$ . The magnetic moment  $\mu_B$  denotes the Bohr magneton, and is often used as a unit of the magnetic moment in atomic scale.

Equations (1.4) and (1.5) indicate that an electron has the following magnetic moment in the atomic scale.

$$m = m_l + m_s = -(l + 2s)\mu_B,$$
 (1.7)

and the total magnetic moment is given by

$$\mathbf{M} = -\left\langle \sum_{i} (\mathbf{I}_i + 2\mathbf{s}_i) \mu_{\mathbf{B}} \right\rangle. \tag{1.8}$$

1.2 Basic Hamiltonian 3

Here the angular momenta l and s are measured in units of  $\hbar = 1$ . The  $l_i$  and  $s_i$  at the right-hand-side (r.h.s.) of the above equation should be regarded as quantum mechanical operators, and  $\langle \sim \rangle$  means a quantum mechanical expectation value. In the following, we omit the minus sign at the r.h.s. of (1.8) for convenience bearing in mind that the real magnetic moments are opposite in direction.

It should be noted that the nuclei in the magnet also have magnetic moments because they have their own spins. The size of their magnetic moments is however characterized by the nuclear magneton  $\mu_N$ , which is defined by

$$\mu_{\rm N} = \frac{e\hbar}{2m_{\rm p}c}.\tag{1.9}$$

Here  $m_{\rm p}$  denotes the mass of proton. The nuclear magneton  $\mu_{\rm N}$  is only 1/1800 of the Bohr magneton  $\mu_{\rm B}$  because  $\mu_{\rm N}/\mu_{\rm B}=m_{\rm e}/m_{\rm p}$ . Therefore the magnetism in solids is dominated by the magnetic moments of electrons. In the following equations, we adopt a unit of  $\mu_{\rm B}=1$  for simplicity.

### 1.2 Basic Hamiltonian

Magnetic moments and magnetic properties are governed by the Hamiltonian of the system. The basic Hamiltonian of electrons in solids is given as follows in the second quantization.

$$H = \int \psi^{\dagger}(\mathbf{r}) \left( -\frac{1}{2} \nabla^{2} + v_{N}(\mathbf{r}) \right) \psi(\mathbf{r}) d\mathbf{r}$$

$$+ \frac{1}{2} \int \psi^{\dagger}(\mathbf{r}) \psi^{\dagger}(\mathbf{r}') \frac{1}{|\mathbf{r} - \mathbf{r}'|} \psi(\mathbf{r}') \psi(\mathbf{r}) d\mathbf{r} d\mathbf{r}'$$

$$+ \int \psi^{\dagger}(\mathbf{r}) \left[ \frac{1}{2} \nabla v_{N}(\mathbf{r}) \times (-i \nabla) \cdot \frac{1}{2} \sigma \right] \psi(\mathbf{r}) d\mathbf{r}$$

$$- \int \psi^{\dagger}(\mathbf{r}) (\mathbf{l} + 2s) \psi(\mathbf{r}) d\mathbf{r} \cdot \mathbf{H}. \tag{1.10}$$

Here we have adopted the units  $m_e = 1$ ,  $\hbar = 1$ , and e = 1 for simplicity.  $\psi(\mathbf{r}) = (\psi_{\uparrow}(\mathbf{r}), \psi_{\downarrow}(\mathbf{r}))$  is the electron field operator.  $v_{\rm N}(\mathbf{r})$  is the one electron potential energy due to nuclei, and is given by  $v_{\rm N}(\mathbf{r}) = -\sum_i Z_i/|\mathbf{r} - \mathbf{R}_i|$ .  $Z_i$  is the atomic number of the atom at position  $\mathbf{R}_i$ .  $\mathbf{H}$  denotes the magnetic field, and  $\sigma = (\sigma_x, \sigma_y, \sigma_z)$  denote the Pauli spin matrices given by

$$\sigma_x = \begin{pmatrix} 0 & 1 \\ 1 & 0 \end{pmatrix}, \qquad \sigma_y = \begin{pmatrix} 0 & -i \\ i & 0 \end{pmatrix}, \qquad \sigma_z = \begin{pmatrix} 1 & 0 \\ 0 & -1 \end{pmatrix}.$$
 (1.11)

The first term in the Hamiltonian (1.10) consists of the kinetic energy and the attractive potential due to nuclei, and describes the independent motion of electrons.

The second term denotes the electron–electron interaction, the third term denotes the spin–orbit interaction, and the last term is the Zeeman interaction due to magnetic field. Note that in the above expression we have omitted the diamagnetic term which is proportional to the square of the magnetic field [2], because we do not consider the diamagnetism in this book.

In solids, we may express the field operators by means of a basis set of wavefunctions  $\{\varphi_i(\mathbf{r})\}$  as follows.

$$\psi_{\sigma}(\mathbf{r}) = \sum_{i} a_{i\sigma} \varphi_{i}(\mathbf{r}). \tag{1.12}$$

Here  $\varphi_i(r)$  are orthonormal basis functions. The suffix i stands for a set of the atomic position i (quantum number n) and orbital L (momentum k) when we adopt atomic orbitals (one-electron eigen functions in solids) as the basis functions.

Using the orthonormal basis set, we can express the Hamiltonian (1.10) as follows.

$$H = \sum_{ij\sigma} \varepsilon_{ij} a_{i\sigma}^{\dagger} a_{j\sigma} + \frac{1}{2} \sum_{ijkl\sigma\sigma'} V_{ijkl} a_{i\sigma}^{\dagger} a_{j\sigma'}^{\dagger} a_{k\sigma'} a_{l\sigma} + H_{SO} + H_{Zeeman}.$$
(1.13)

Here  $\varepsilon_{ij}$  ( $V_{ijkl}$ ) are the matrix elements for the independent electron (the Coulomb interaction) part of the Hamiltonian (1.10). They are given by

$$\varepsilon_{ij} = \int d\mathbf{r} \, \varphi_i^*(\mathbf{r}) \left( -\frac{1}{2} \nabla^2 + v_{\rm N}(\mathbf{r}) \right) \varphi_j(\mathbf{r}), \tag{1.14}$$

$$V_{ijkl} = \int d\mathbf{r} \, d\mathbf{r}' \, \frac{\varphi_i^*(\mathbf{r}) \varphi_j^*(\mathbf{r}') \varphi_k(\mathbf{r}') \varphi_l(\mathbf{r})}{|\mathbf{r} - \mathbf{r}'|}. \tag{1.15}$$

The third and last terms at the r.h.s. of (1.13) are the spin-orbit interaction term and the Zeeman term, respectively.

$$H_{SO} = \sum_{i\alpha i\gamma} \zeta_{i\alpha j\gamma} a_{i\alpha}^{\dagger} a_{j\gamma}, \qquad (1.16)$$

$$H_{\text{Zeeman}} = -\sum_{i\alpha j\gamma} (l + 2s)_{i\alpha j\gamma} a_{i\alpha}^{\dagger} a_{j\gamma} \cdot \boldsymbol{H}. \tag{1.17}$$

Here the spin-orbit interaction matrix elements  $\zeta_{i\alpha j\gamma}$  are given by

$$\zeta_{i\alpha j\gamma} = \int d\mathbf{r} \, \varphi_i^*(\mathbf{r}) \left[ \frac{1}{2} \nabla v(\mathbf{r}) \times (-i\nabla) \right] \varphi_j(\mathbf{r}) \cdot (\mathbf{s})_{\alpha\gamma}. \tag{1.18}$$

In molecules and solids, atomic orbitals are often useful as the basis functions.

$$\varphi_i^{(\text{atom})}(\mathbf{r}) = \phi_{inl}(|\mathbf{r} - \mathbf{R}_i|)Y_{lm}(\mathbf{r} - \mathbf{R}_i). \tag{1.19}$$

Here  $\phi_{inl}(|\mathbf{r} - \mathbf{R}_i|)$  is a radial wave function for an atom located at  $\mathbf{R}_i$ , the subscripts n and l denote the principal quantum number and the azimuthal quantum number,

.2 Basic Hamiltonian 5

respectively.  $Y_{lm}(\mathbf{r} - \mathbf{R}_i)$  is the spherical harmonics located at atom  $\mathbf{R}_i$ , and m denotes the magnetic quantum number.

In the application to solids, it is convenient to make use of real functions  $\{P_{l\nu}\}$  instead of complex basis functions  $\{Y_{lm}\}$ . The former called the cubic harmonics are constructed by linear combinations of spherical harmonics. Defining the orbital  $L = (l, \nu)$ , the atomic functions for solids are written as follows.

$$\varphi_{inL}(\mathbf{r}) = \phi_{inl}(|\mathbf{r} - \mathbf{R}_i|) P_{l\nu}(\mathbf{r} - \mathbf{R}_i). \tag{1.20}$$

The cubic harmonics are constructed to yield the irreducible representation for the cubic symmetry of the point group in crystal. The s (l=0) function belonging to the  $A_{lg}$  representation for the cubic point symmetry is a constant function.

$$P_{a_{1g}}(\mathbf{r}) = Y_{00} = \frac{1}{\sqrt{4\pi}}. (1.21)$$

The p (l = 1) functions belonging to the  $T_{1u}$  representation are defined as follows.

$$P_{t_{1u}\alpha}(\mathbf{r}) = \frac{1}{\sqrt{2}}(-Y_{11} + Y_{1,-1}) = \sqrt{\frac{3}{4\pi}} \frac{x}{r},$$
(1.22)

$$P_{t_{1u}\beta}(\mathbf{r}) = \frac{i}{\sqrt{2}}(Y_{11} + Y_{1,-1}) = \sqrt{\frac{3}{4\pi}} \frac{y}{r},$$
(1.23)

$$P_{t_{1u}\gamma}(\mathbf{r}) = Y_{10} = \sqrt{\frac{3}{4\pi}} \frac{z}{r}.$$
 (1.24)

The d (l=2) orbitals form the  $E_{\rm g}$   $(d\gamma)$  and  $T_{\rm 2g}$   $(d\varepsilon)$  representations. The d functions belonging to the  $E_{\rm g}$  representation are given by

$$P_{e_{gu}}(\mathbf{r}) = Y_{20} = \sqrt{\frac{5}{4\pi}} \frac{1}{2} \frac{3z^2 - r^2}{r^2},$$
(1.25)

$$P_{e_{gv}}(\mathbf{r}) = \frac{1}{\sqrt{2}}(Y_{22} + Y_{2,-2}) = \sqrt{\frac{5}{4\pi}} \frac{\sqrt{3}}{2} \frac{x^2 - y^2}{r^2}.$$
 (1.26)

The remaining d (l = 2) functions belonging to the  $T_{2g}$  representation are given by

$$P_{t_{2g\xi}}(\mathbf{r}) = \frac{i}{\sqrt{2}}(Y_{21} + Y_{2,-1}) = \sqrt{\frac{5}{4\pi}}\sqrt{3}\frac{yz}{r^2},\tag{1.27}$$

$$P_{t_{2g\eta}}(\mathbf{r}) = \frac{1}{\sqrt{2}}(-Y_{21} + Y_{2,-1}) = \sqrt{\frac{5}{4\pi}}\sqrt{3}\frac{zx}{r^2},\tag{1.28}$$

$$P_{t_{2g\zeta}}(\mathbf{r}) = \frac{i}{\sqrt{2}}(-Y_{22} + Y_{2,-2}) = \sqrt{\frac{5}{4\pi}}\sqrt{3}\frac{xy}{r^2}.$$
 (1.29)

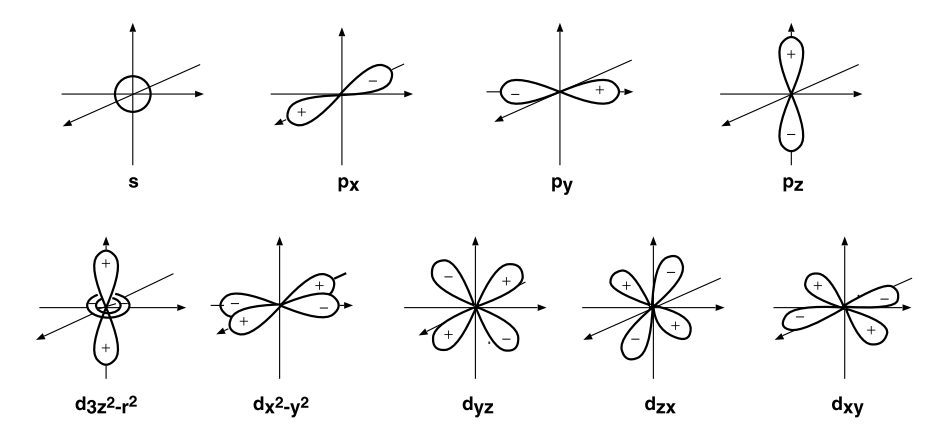


Fig. 1.1 Atomic orbitals from s to d symmetry. The sign of wave functions is shown by + and - in the figure

The angular dependence of the cubic harmonics is shown in Fig. 1.1. The spatial distribution of the atomic wave functions governs the electron hoppings in solids, thus determining the electronic and magnetic properties of solids.

### 1.3 Formation of Atomic Moments

The electronic structure and related properties of an atom may be understood by an independent-electron picture. The spin—orbit interaction in the Hamiltonian (1.13) is smaller than the Coulomb interaction in the 'light' elements such as the 3d transition metals. We first neglect the former, and treat the latter by means of the following approximation.

$$a_{i\sigma}^{\dagger} a_{j\sigma'}^{\dagger} a_{k\sigma'} a_{l\sigma} = \langle a_{i\sigma}^{\dagger} a_{l\sigma} \rangle a_{j\sigma'}^{\dagger} a_{k\sigma'} + a_{i\sigma}^{\dagger} a_{l\sigma} \langle a_{j\sigma'}^{\dagger} a_{k\sigma'} \rangle$$
$$- \langle a_{i\sigma}^{\dagger} a_{k\sigma'} \rangle a_{j\sigma'}^{\dagger} a_{l\sigma} - a_{i\sigma}^{\dagger} a_{k\sigma'} \langle a_{j\sigma'}^{\dagger} a_{l\sigma} \rangle$$
$$- \langle a_{i\sigma}^{\dagger} a_{i\sigma'}^{\dagger} a_{k\sigma'} a_{l\sigma} \rangle. \tag{1.30}$$

Here the average  $\langle \ \rangle$  is taken with respect to an independent particle system which will be chosen later. Note that the two particle operator has been decoupled so that (1.30) exactly holds true when we take the average. This is called the Hartree–Fock approximation.

In the Hartree–Fock approximation, the Hamiltonian (1.13) is reduced to

$$H = \sum_{ij\sigma} h_{ij\sigma} a_{i\sigma}^{\dagger} a_{j\sigma} - \frac{1}{2} \sum_{ijkl\sigma\sigma'} (V_{ijkl} - V_{ijlk} \delta_{\sigma\sigma'}) \langle a_{i\sigma}^{\dagger} a_{l\sigma} \rangle \langle a_{j\sigma'}^{\dagger} a_{k\sigma'} \rangle.$$
(1.31)

Here  $h_{ij\sigma}$  is given as follows.

$$h_{ij\sigma} = \int \varphi_{i\sigma}^{\dagger}(\mathbf{r}) \left( -\frac{1}{2} \nabla^{2} + v_{N}(\mathbf{r}) + \int d\mathbf{r}' \frac{\langle n(\mathbf{r}') \rangle}{|\mathbf{r} - \mathbf{r}'|} \right) \varphi_{j\sigma}(\mathbf{r})$$
$$- \int d\mathbf{r} d\mathbf{r}' \varphi_{i\sigma}^{\dagger}(\mathbf{r}) \frac{\langle \psi_{\sigma}^{\dagger}(\mathbf{r}') \psi_{\sigma}(\mathbf{r}) \rangle}{|\mathbf{r} - \mathbf{r}'|} \varphi_{j\sigma}(\mathbf{r}'). \tag{1.32}$$

The Hartree–Fock one-electron wave functions  $\{\varphi_{i\sigma}(\mathbf{r})\}$  are determined by solving the following self-consistent equations.

$$\left(-\frac{1}{2}\nabla^{2} + v_{N}(\mathbf{r}) + \int d\mathbf{r}' \frac{\langle n(\mathbf{r}')\rangle}{|\mathbf{r} - \mathbf{r}'|}\right) \varphi_{i\sigma}(\mathbf{r}) 
- \sum_{i} \langle n_{j\sigma} \rangle \int d\mathbf{r}' \frac{\varphi_{j\sigma}^{*}(\mathbf{r}')\varphi_{i\sigma}(\mathbf{r}')}{|\mathbf{r} - \mathbf{r}'|} \varphi_{j\sigma}(\mathbf{r}) = \varepsilon_{i\sigma}\varphi_{i\sigma}(\mathbf{r}).$$
(1.33)

Here  $\varepsilon_{i\sigma}$  is the Hartree–Fock energy eigen value. When we apply the Hartree–Fock independent particle Hamiltonian in the average  $\langle \ \rangle$ ,  $\langle n_{j\sigma} \rangle$  is given by the Fermi distribution function  $f(\varepsilon_{j\sigma})$  and  $\langle n(r) \rangle = \sum_{j\sigma} f(\varepsilon_{j\sigma}) \varphi_{j\sigma}^*(r) \varphi_{j\sigma}(r)$  denotes a charge density in the Hartree–Fock approximation. The third term at the l.h.s. of (1.33) gives the electrostatic potential due to electrons. The last term also originates in the Coulomb interaction, but the wave functions have been exchanged due to the anti-symmetric property of the Slater determinant. It is referred as the exchange potential. The Hartree–Fock wave function is the best Slater determinant at the ground state according to the variational principle [4].

Taking the Hartree–Fock wavefunctions as the basis functions, one can express the Hartree–Fock Hamiltonian (1.31) as follows.

$$H = \sum_{i\sigma} \varepsilon_{i\sigma} n_{i\sigma} - \frac{1}{2} \sum_{ij\sigma\sigma'} (V_{ijji} - V_{ijij} \delta_{\sigma\sigma'}) \langle n_{i\sigma} \rangle \langle n_{j\sigma'} \rangle.$$
 (1.34)

Here  $V_{ijji}$  ( $V_{ijij}$ ) is known as the Coulomb integral (exchange integral). (Note that  $V_{ijkl}$  should more precisely be  $V_{i\sigma j\sigma'k\sigma'l\sigma}$ .) The second term at the r.h.s. is to eliminate the double counting of Coulomb interaction in the Hartree–Fock one-electron energy.

The exchange potential in the Hartree–Fock equation (1.33) is nonlocal. Slater proposed an approximate local exchange potential, using the free-electron wave functions. It is given as follows [4].

$$v_{\text{ex}\sigma}(\mathbf{r}) = -3\left(\frac{3}{4\pi}\right)^{1/3} n_{\sigma}(\mathbf{r})^{1/3},$$
 (1.35)

where  $n_{\sigma}(\mathbf{r})$  is the electron density with spin  $\sigma$ .

The effective potential in the Hartree–Fock self-consistent equation is spherical in the atomic system when we apply the potential (1.35). We can express the atomic

wave function for an electron as

$$\varphi_{nlm\sigma}(\mathbf{r}) = \phi_{nl\sigma}(r) Y_{lm}(\hat{\mathbf{r}}). \tag{1.36}$$

Here  $\phi_{nl\sigma}(r)$  is the radial wave function, and  $Y_{lm}(\hat{r})$  is the spherical harmonics. n, l, and m denote the principal quantum number, the azimuthal quantum number, and the magnetic quantum number, respectively. Orbitals  $l=0,1,2,3,\ldots$  are called s, p, d, f, ..., respectively. The nl shells are therefore written as ns, np, nd, nf, etc. In each shell, there are 2l+1 degenerate orbitals.

With the use of the Hartree–Fock atomic orbitals, a many electron state of an atom is expressed in the form of the Slater determinant. The ground-state electronic structure of an atom is constructed according to the Pauli principle. For example, in the case of Ar, we have the ground state  $1s^22s^22p^63s^23p^6$ . Since the outermost electron shell of Ar is closed, the magnetic moment of Ar vanishes.

For an atom with an unfilled shell, the magnetic moment may appear. Since the total number of electrons (N), the total spin (S), and the total orbital moment (L) of an atom commute with the Hamiltonian, the eigen function  $\Psi$  should be specified by the set  $(NLMSM_s)$ :  $\Psi(NLMSM_s)$ , where L(S) and  $M(M_s)$  denote the magnitude and z component of orbital moment L (spin S), respectively. The eigen energy, on the other hand, should depend only on N, L, and S because of the rotational symmetry:  $E_A(NLS)$ .

The ground state of electrons in an atom should be obtained by minimizing the Coulomb energy. The Coulomb interaction of the Hamiltonian for the unfilled shell is written as follows according to (1.13).

$$H_{\text{Coulomb}} = \sum_{\nu} U_{\nu\nu} n_{\nu\uparrow} n_{\nu\downarrow} + \sum_{\nu>\nu'} \left( U_{\nu\nu'} - \frac{1}{2} J_{\nu\nu'} \right) n_{\nu} n_{\nu'} - 2 \sum_{\nu>\nu'} J_{\nu\nu'} s_{\nu} \cdot s_{\nu'}.$$
(1.37)

Here  $\nu$  denotes an orbital lm ( $m=-l\dots l$ ).  $n_{\nu}$  ( $s_{\nu}$ ) denotes the charge (spin) density operator for electrons in the orbital  $\nu$ . We have taken into account the Hartree–Fock Coulomb and exchange interactions,  $U_{\nu\nu'}=V_{\nu\nu'\nu'\nu}$  and  $J_{\nu\nu'}=V_{\nu\nu'\nu\nu'}$ , and omitted the other types of interactions. The first term at the r.h.s. of (1.37) denotes the intraorbital Coulomb interaction, the second term expresses the inter-orbital interaction, and the third term the exchange interaction between the spins on different orbitals. Note that  $U_{\nu\nu} > U_{\nu\nu'}(\nu \neq \nu') > J_{\nu\nu'} > 0$ . Typical values of Coulomb interactions are  $U_{\nu\nu} \approx 20$  eV,  $U_{\nu\nu} - U_{\nu\nu'} \approx 2$  eV, and  $U_{\nu\nu} \approx 0.9$  eV for 3d transition-metal elements [5]. Note that  $U_{\nu\nu} = U_{\nu\nu'} \approx 0.9$  eV for 3d transition-metal shell when the Hamiltonian (1.37) is applied.

The intra-orbital Coulomb interaction (i.e., the first term at the r.h.s. of (1.37)) acts to reduce the doubly occupied states on the same orbital so that it creates active spins on the orbitals of an unfilled shell. The third term in (1.37) aligns the active spins on the orbitals because  $J_{\nu\nu'} > 0$ . These effects suggest that the magnitude of the total spin S is maximized at the ground state. This is known as Hund's first rule, and therefore  $J_{\nu\nu'}$  are often called the Hund-rule couplings. On the other hand, the

second term in (1.37) is the energy associated with the configuration of electrons on different orbitals. One might expect that such an interaction energy is reduced when electrons move around the nucleus in the same direction avoiding each other. Thus we expect that the magnitude of the total angular momentum L should be maximized at the ground state under the maximum magnitude of total spin. This is referred as Hund's second rule. The first and second Hund rules are verified by the full Hartree–Fock numerical calculations.

The maximum S and L at the ground state are obtained by using the Pauli principle and the Hund rule, especially from the conditions  $S = M_s(\text{Max})$  and L = M(Max) under the maximum S that corresponds to the state  $\Psi(NLLSS)$ :

$$S = \begin{cases} \frac{N}{2} & \text{for } N \le 2l + 1, \\ \frac{4l + 2 - N}{2} & \text{for } N > 2l + 1, \end{cases}$$
 (1.38)

$$L = \begin{cases} \frac{1}{2}N(2l+1-N) & \text{for } N \le 2l+1, \\ \frac{1}{2}(N-2l-1)(4l+2-N) & \text{for } N > 2l+1. \end{cases}$$
 (1.39)

The ground state  $\Psi(NLMSM_{\rm S})$  is (2L+1)(2S+1)-fold degenerate. The multiplet is written as  $^{2S+1}L_J$  where L takes S, P, D, F, G, H,... according to  $L=0,1,2,3,4,5,\ldots$ , and J (=  $|L\pm S|$ ) is the total angular momentum. These properties are summarized in Fig. 1.2 for 3d transition metal atoms.

The value of J at the ground state is determined by the spin-orbit interaction. The spin-orbit interaction (1.16) in the atomic system can be written as

$$H_{SO} = \sum_{\nu\alpha\nu'\gamma} \zeta_{nl} (\mathbf{l})_{\nu\nu'} \cdot (\mathbf{s})_{\alpha\gamma} a_{\nu\alpha}^{\dagger} a_{\nu'\gamma}. \tag{1.40}$$

Here

$$\zeta_{nl} = \frac{1}{2} \int_0^\infty \left| \phi_{nl}(r) \right|^2 \frac{dV}{dr} r \, dr > 0. \tag{1.41}$$

Assume that the ground state is determined by the Hund rule, and the temperature is such that the corresponding thermal energy is much lower than that of the first excited state of the Coulomb interaction, i.e., the Hund-rule coupling  $J_{\rm H}$ :  $k_{\rm B}T\ll J_{\rm H}$ . Here  $J_{\rm H}$  is an average value of  $\{J_{\nu\nu'}\}$ , and  $k_{\rm B}$  denotes Boltzmann's constant. Moreover the spin-orbit interaction energy is much smaller than  $J_{\rm H}$  in 3d transition metals. In this case, we can neglect all the excited state of the Coulomb interactions, and limit the states to the (2L+1)(2S+1) dimensional Hund-rule subspace:  $\{\Psi(NLMSM_{\rm S})\}$ . We can then verify the following relation in the subspace.

$$\langle \Psi(NLMSM_{s}) | H_{SO} | \Psi(NLM'SM'_{s}) \rangle$$

$$= \lambda(NLS) \langle \Psi(NLMSM_{s}) | L \cdot S | \Psi(NLM'SM'_{s}) \rangle. \tag{1.42}$$

m <sub>Z</sub> N	1	2	3	4	5	6	7	8	9	10
2	+	+	+	+	<b>†</b>	<b>+</b>	<b>+</b>	<b>+</b>	<b>+</b>	<b>†</b> ‡
1		+	+	+	+	+	##	<b>‡</b> ‡	<b>+</b>	<b>+</b>
0			+	+	+	+	+	##-	-‡∳-	<b>†</b> ‡
-1				+	+	+	+	+	<b>+</b>	<b>†</b>
-2					+	+	+	+	+	<b>†</b> ‡
S	1/2	1	3/2	2	5/2	2	3/2	1	1/2	0
L	2	3	3	2	0	2	3	3	2	0
J=IL7SI	3/2	2	3/2	0	5/2	4	9/2	4	5/2	0
G S	<sup>2</sup> D <sub>3/2</sub>	<sup>3</sup> F <sub>2</sub>	<sup>4</sup> F <sub>3/2</sub>	<sup>5</sup> <b>D</b> <sub>0</sub>	<sup>6</sup> S <sub>5/2</sub>	<sup>5</sup> <b>D</b> <sub>4</sub>	<sup>4</sup> F <sub>9/2</sub>	<sup>3</sup> F <sub>4</sub>	<sup>2</sup> D <sub>5/2</sub>	¹S <sub>0</sub>
λ (eV)	0.014	0.013	0.011	0.007	0.00	-0.012	-0.022	-0.042	-0.105	0.00
Ions	Sc <sup>2+</sup> Ti <sup>3+</sup>	Ti <sup>2+</sup> V <sup>3+</sup>	V <sup>2+</sup> Cr <sup>3+</sup>		Mn <sup>2+</sup> Fe <sup>3+</sup>	Fe <sup>2+</sup> Co <sup>3+</sup>	Co <sup>2+</sup>	Ni <sup>2+</sup>	Cu <sup>2+</sup>	Zn <sup>2+</sup>
	V <sup>4+</sup>	Cr <sup>4+</sup>	Mn <sup>4+</sup>							

Fig. 1.2 The ground state of atoms with 3d unfilled shell. N and  $m_z$  denote the d electron number and the orbital magnetic quantum number, respectively. Electron configuration for each N in the upper row of the figure shows the state  $\Psi(NLLSS)$  leading to the total spin S and the orbital angular momentum L at the ground state. J denotes the total angular momentum. The ground state multiplets (GS) are expressed as  ${}^{2S+1}L_J$ . The experimental values of the spin–orbit coupling constant  $\lambda$  are given. Examples of the 3d transition metal ions are also given in the bottom row

Thus we have an effective Hamiltonian for the spin-orbit interaction in the Hundrule subspace as follows.

$$H_{SO} = \lambda(NLS)\boldsymbol{L} \cdot \boldsymbol{S}. \tag{1.43}$$

The coefficient  $\lambda(NLS)$  is obtained by comparing the diagonal matrix element of  $H_{SO}$  for the state  $\Psi(NLLSS)$  obtained from (1.40) with that of the r.h.s. of (1.43).

$$\lambda(NLS) = \begin{cases} \frac{\zeta_{nl}}{N} & \text{for } N \le 2l + 1, \\ -\frac{\zeta_{nl}}{4l + 2 - N} & \text{for } N > 2l + 1. \end{cases}$$
 (1.44)

Because  $\zeta_{nl} > 0$ ,  $\lambda(NLS) > 0$  for  $N \le 2l+1$  and  $\lambda(NLS) < 0$  for N > 2l+1. Thus, J = |L-S| is realized for  $N \le 2l+1$ , and J = |L+S| for N > 2l+1 at the ground state among possible states J = |L+S|, |L+S-1|, ..., |L-S|. Therefore J = |L-S| is the ground-state in the light transition-metal elements and the light

rare-earth elements, and J = |L + S| is the ground state in the heavy transition-metal elements and the heavy rare-earth elements. Note that the typical value of the spin-orbit coupling is only one tenth of the Hund rule coupling ( $J_{\rm H} \sim 1$  eV) in the case of 3d transition metal ions as shown in Fig. 1.2. When the spin-orbit coupling is significant as in the rare-earth atoms, the ground-state should be (2J + 1)-fold degenerate instead of (2S + 1)(2L + 1) fold.

Ions such as  $Ti^{2+}$ ,  $V^{3+}$ , and  $Cr^{4+}$ , for example, have two electrons in the d shell (see the N=2 column in Fig. 1.2). The Hund rule tells us that the total spin and orbital angular momenta at the ground state are S=1 and L=3, respectively. Because the spin–orbit coupling  $\lambda>0$  in the light atoms, the total angular momentum at the ground state is given by J=3-1. Thus we have the ground-state multiplet  ${}^3F_2$  according to the notation  ${}^{2S+1}L_J$ . In the same way, the ion  $Co^{2+}$  has 7 electrons in the d shell. According to the Hund rule, we find the ground-state spin and orbital momenta S=3/2 and L=3, respectively. Because the spin–orbit coupling  $\lambda<0$  in the heavy atoms, the total angular momentum is given by J=9/2. Thus we obtain the ground-state multiplet  ${}^4F_{9/2}$  for  $Co^{2+}$  ion.

When the external magnetic field H is applied to the atoms, the energy due to the magnetic field is given by  $-g_J\mu_BJ_zH$ . Here  $g_J$  is Landé's g factor and is given by  $g_J = 3/2 + [S(S+1) - L(L+1)]/2J(J+1)$ . The susceptibility which is defined by the induced magnetization divided by H is then given by

$$\chi = \frac{g_J^2 \mu_{\rm B}^2 J(J+1)}{3k_{\rm B}T}.$$
 (1.45)

The above temperature dependence is referred as the Curie law, and  $C \equiv g_J^2 \mu_{\rm B}^2 J(J+1)/3k_{\rm B}$  is called the Curie constant. The observation of the Curie law in the susceptibility measurement is regarded as an indication of the existence of local magnetic moments.

### 1.4 Metal and Insulator in Solids

When atoms form a solid, electrons in the outermost shell of atoms start to hop from atom to atom via overlap between atomic orbitals. The question then is whether electrons tend to remain in each atom or to itinerate in the solid. In the case of the former, atomic magnetic moments are well defined in solids and their properties are expected to be explained from the atomic point of view. In the case of the latter, magnetic properties may be quite different from those expected from atomic ones and one has to start from the itinerant limit in order to explain their magnetism.

Whether electrons in solids are movable or not is governed by the detailed balance between the energy gain due to electron hopping and the loss of Coulomb interaction. The simplest example may be the case of the hydrogen molecule  $H_2$ . According to the molecular orbital picture, the 1s atomic orbitals split into the bonding state with energy  $\varepsilon_0 - |t|$  and the anti-bonding state with energy  $\varepsilon_0 + |t|$  when hydrogen atoms form a molecule. Here  $\varepsilon_0$  denotes the atomic ground state, and t is the

electron hopping integral which is defined by atomic potential v(r) and wave function  $\varphi(r)$  as  $t = \int \varphi(r - R)v(r - R)\varphi(r) dr$ . The bonding orbital is occupied by two electrons according to the Pauli principle. It leads to the total energy gain 2|t|. This is the covalent bond in the hydrogen molecule. In this state, electrons hop from one atom to another, and thus they are movable. The covalent bond is stabilized by the kinetic energy gain of independent electrons. It consists of the polarized state in which the 1s orbital of an atom is doubly occupied and the orbital of another atom is unoccupied, and the neutral state in which each atomic orbital is occupied by an electron.

When the Coulomb interaction between electrons are taken into account, the covalent bonding state is not necessarily stable because it contains the polarization state with double occupancy on an atomic orbital. Assume that the loss of the intraatomic Coulomb interaction energy in the covalent bonding state is given by U, and consider the neutral-atom state as the state in which each electron is localized on an atom. The total energy in the covalent bonding state is given by  $E(\text{covalent}) = 2\varepsilon_0 - 2|t| + U$ , while the energy in the neutral atom state is given by  $E(\text{neutral}) = 2\varepsilon_0$ . Thus, the neutral atom state is realized when the following condition is satisfied.

$$2|t| < U. \tag{1.46}$$

This condition is satisfied when the interatomic distance goes to infinity because |t| goes to zero. Thus the neutral atom state in which electrons are localized on each atom and each atom has a well defined local magnetic moment s = 1/2 is realized in the atomic limit.

In solids, we expect the same behavior as found in the hydrogen molecule. Let us consider the behavior of electrons when atoms form a solid. Electrons in solids move in a potential obtained by a superposition of the atomic potentials  $\sum_i v(\mathbf{r} - \mathbf{R}_i)$ . Here  $v(\mathbf{r} - \mathbf{R}_i)$  denotes the atomic potential on site i. When we adopt the atomic orbitals  $\{\varphi_{iv}(\mathbf{r} - \mathbf{R}_i)\}$  as the basis functions and assume the orthogonality between the orbitals, the Hamiltonian for electrons on the outermost shells in solids may be obtained from (1.13) as

$$H = H_0 + H_{\text{Coulomb}}, \tag{1.47}$$

$$H_0 = \sum_{i\nu} \varepsilon_{i\nu} n_{i\nu} + \sum_{i\nu j\nu'} t_{i\nu j\nu'} a^{\dagger}_{i\nu\sigma} a_{j\nu'\sigma}, \qquad (1.48)$$

$$H_{\text{Coulomb}} = \sum_{i\nu} U_{i\nu\nu} n_{i\nu\uparrow} n_{i\nu\downarrow} + \sum_{i} \sum_{\nu>\nu'} \left( U_{i\nu\nu'} - \frac{1}{2} J_{i\nu\nu'} \right) n_{i\nu} n_{i\nu'}$$
$$-2 \sum_{i} \sum_{\nu>\nu'} J_{i\nu\nu'} s_{i\nu} \cdot s_{i\nu'}. \tag{1.49}$$

Here  $\varepsilon_{i\nu}$  is the atomic level for the orbital  $\nu$  of site i, and  $t_{i\nu j\nu'}$  the transfer integral between the orbital  $\nu$  at site i and the orbital  $\nu'$  at site j. The latter is expressed in

the two-center approximation as

$$t_{i\nu j\nu'} = \int \varphi_{i\nu}^*(\mathbf{r} - \mathbf{R}_i) v(\mathbf{r} - \mathbf{R}_i) \varphi_{i\nu'}(\mathbf{r} - \mathbf{R}_j) d\mathbf{r}.$$
 (1.50)

Note that we have taken into account in  $H_{\text{Coulomb}}$  only the intra-atomic Coulomb interactions and omitted the inter-site Coulomb interaction contributions for simplicity.

It is not easy to treat the electrons in solids described by the Hamiltonian (1.47) because both the electron hoppings and the Coulomb repulsions have to be taken into consideration. In order to discuss both the itinerant and localized behaviors of electrons in solids, we can consider a simpler Hamiltonian consisting of one orbital per site as follows.

$$H = \sum_{i\sigma} \varepsilon_0 n_{i\sigma} + \sum_{ij\sigma} t_{ij} a_{i\sigma}^{\dagger} a_{j\sigma} + \sum_i U n_{i\uparrow} n_{i\downarrow}. \tag{1.51}$$

Here  $\varepsilon_0$ ,  $t_{ij}$ , and U denote the atomic level, the transfer integral between sites i and j, and the intra-atomic Coulomb interaction energy, respectively. The Hamiltonian (1.51) is known as the Hubbard model, and was proposed by Gutzwiller and Hubbard independently [6–10].

The Hubbard model (1.51) is the simplest Hamiltonian which describes the motion of interacting electrons in solids. Nevertheless it describes the localization of electrons as well as their itinerant behavior in solids. Let us consider the atomic limit of the model. For an atom, we have 4 atomic states: the empty state  $(n_{\uparrow}=0,n_{\downarrow}=0)$ , the single electron states  $(n_{\uparrow}=1,n_{\downarrow}=0)$  and  $(n_{\uparrow}=0,n_{\downarrow}=1)$ , and the doubly occupied state  $(n_{\uparrow}=1,n_{\downarrow}=1)$ . Associated energies are given as 0,  $\varepsilon_0$ ,  $\varepsilon_0$ , and  $2\varepsilon_0+U$ , respectively. An unfilled shell with spin S=1/2 appears only for the n=1 state. Note that there is no Hund's rule arrangement for spin in this case.

In the atomic limit for a solid where  $t_{ij}=0$ , electron number  $n_i$  on each atom is no longer constant, though the total number of electrons N is given;  $N=\sum_{i\sigma}n_{i\sigma}$ . The eigenstates are given by  $|\Psi\rangle=|\{n_{i\sigma}\}\rangle$ , i.e., a set of the electron numbers with spin  $\sigma$  on site i. The eigenenergy for the state is given by

$$E(\{n_{i\sigma}\}) = \sum_{i} (\varepsilon_0 n_i + U n_{i\uparrow} n_{i\downarrow}). \tag{1.52}$$

It should be noted that the energy of the system increases by U when the number of doubly occupied states D is increased by one. The ground-state energy  $E_0$  of the atomic limit is obtained by minimizing the energy with respect to the number of double occupancy in solid. Assume that the number of lattice points is given by L. When N < L, the ground-state energy is obtained as  $E_0 = \varepsilon_0 N$  by choosing D = 0. Magnetic moments on the sites with an electron are active in this case as shown in Fig. 1.3. Because there are L!/N!(L-N)! electron configurations on the L lattice points, the ground state is  $[2^N L!/N!(L-N)!]$ -fold degenerate.

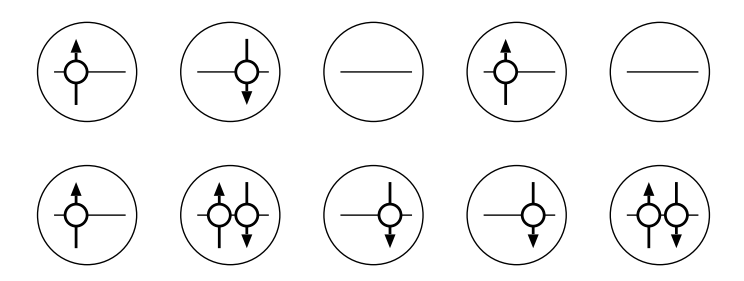


Fig. 1.3 Electron configurations for less than half filling (*upper figure*) and for more than half filling (*lower figure*) in the atomic limit

At half filling, all the atoms are occupied by an electron so that spin degrees of freedom by  $2^N$  remain; the degenerated wave functions are given by  $|1s_{1z}1s_{2z}1s_{3z}...\rangle$  when the wave function  $|\{n_{i\sigma}\}\rangle$  is written as  $|n_1s_{1z}n_2s_{2z}n_3s_{3z}...\rangle$  by using the charge  $n_i = n_{i\uparrow} + n_{i\downarrow}$  and the spin  $s_{iz} = (n_{i\uparrow} - n_{i\downarrow})/2$ .

When the electron number N is larger than L, it is no longer possible to keep D=0; the minimum value of D is given by D=N-L. The ground state energy is then given by  $E_0=\varepsilon_0N+U(N-L)$ . The ground state is  $[2^{2L-N}L!/(2L-N)!(N-L)!]$ -fold degenerate because there are L!/(2L-N)!(N-L)! configurations for choosing 2L-N(< L) sites with the single electron from L lattice sites and there are  $2^{2L-N}$  spin degrees of freedom for each configuration. Note that the spins on 2L-N sites are active in this case.

Let us consider the case that electron hopping  $t_{ij}$  is small but finite. When  $N \neq L$ , electrons are mobile at T=0 because electrons can move from site to site without increasing the double occupation number D. Thus the system is a metal. However, at half-filling, electron hopping creates a doubly occupied state, thus creating a finite excitation energy by the amount of Coulomb interaction energy U. Therefore electrons cannot move under the infinitesimal electric field. We have then an insulator with local magnetic moments at each site in this case.

When there is no Coulomb interaction (U=0), on the other hand, electrons are generally itinerant. The Hamiltonian is given as

$$H = \sum_{ij\sigma} (\boldsymbol{H}_0)_{ij} a_{i\sigma}^{\dagger} a_{j\sigma}. \tag{1.53}$$

Here  $(\boldsymbol{H}_0)_{ij} = \varepsilon_0 \delta_{ij} + t_{ij} (1 - \delta_{ij})$ . The noninteracting Hamiltonian is diagonalized by a unitary transformation  $a_{i\sigma} = \sum_k a_{k\sigma} \langle i|k \rangle \; (a_{i\sigma}^\dagger = \sum_k a_{k\sigma}^\dagger \langle i|k \rangle^*)$  so that

$$H = \sum_{k\sigma} \varepsilon_k n_{k\sigma},\tag{1.54}$$

where  $\varepsilon_k = \sum_{ij} \langle k|i \rangle (\boldsymbol{H}_0)_{ij} \langle j|k \rangle$  is an eigen value for the tight-binding one-electron Hamiltonian matrix  $\boldsymbol{H}_0$ , and the set  $\{\langle j|k \rangle\}$   $(j=1,\ldots,L)$  is the eigen vector for  $\varepsilon_k$ .

The eigen states for noninteracting Hamiltonian H are given by  $|\Psi\rangle = |\{n_{k\sigma}\}\rangle$ , i.e., a set of electrons with momentum k and spin  $\sigma$ . The eigenenergy is given by

$$E(\{n_{k\sigma}\}) = \sum_{k\sigma} \varepsilon_k n_{k\sigma}, \qquad (1.55)$$

where the c-number  $n_{k\sigma}$  takes on the value of 0 or 1. The ground state is obtained by putting electrons on the energy levels from the bottom to the Fermi level  $\varepsilon_F$  according to the Pauli principle,

$$|\phi_0\rangle = \left[\prod_{k\sigma}^{\varepsilon_k < \varepsilon_F} a_{k\sigma}^{\dagger}\right]|0\rangle, \tag{1.56}$$

so that the ground-state energy is given by

$$E_0(\{n_{k\sigma}\}) = \sum_{k\sigma}^{\varepsilon_k < \varepsilon_F} \varepsilon_k. \tag{1.57}$$

Alternatively, defining the density of states per atom per spin as

$$\rho(\varepsilon) = \frac{1}{L} \sum_{k} \delta(\varepsilon - \varepsilon_k), \tag{1.58}$$

we can express the ground-state energy per atom as

$$E_0 = 2 \int_{-\infty}^{\varepsilon_{\rm F}} \varepsilon \rho(\varepsilon) \, d\varepsilon. \tag{1.59}$$

A non-interacting electron system is in general metallic unless the electrons in the atom form a closed shell. The electrons in such systems are mobile. This is because one can add an electron at the energy level just above the Fermi level by applying infinitesimal electric field. Note that spins of itinerant electrons are also mobile. We may expect that there is a transition from metal to insulator at half filling when the intra-atomic Coulomb interaction is increased. Assume that there is a band for a non-interacting system whose band width is W. The center of the gravity of the noninteracting band is assumed to be located at  $\varepsilon_0$ . When the Coulomb interaction U is increased, each atom tends to be occupied by one electron, and electron hopping to neighboring sites tends to be suppressed in order to reduce the on-site Coulomb interaction energy. In the strongly correlated region, an electron should have a potential  $\varepsilon_0 + U$  on a site having an opposite-spin electron because of the increment of the Coulomb interaction energy due to double occupation, while an electron has a potential  $\varepsilon_0$  on an empty site. We then expect one more band with the band width of order of W around  $\varepsilon_0 + U$ . The density of states as excitation spectrum is expected to split into two bands at  $U_c \sim W$  (see Fig. 1.4). The formation

**Fig. 1.4** The upper and lower Hubbard bands created by on-site Coulomb interaction *U* 

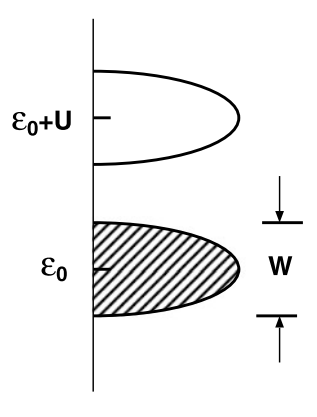
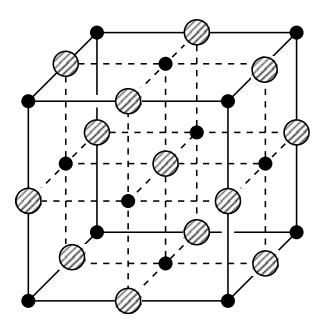


**Fig. 1.5** NaCl type structure in NiO



of a gap at the Fermi level implies the existence of an insulator. The insulating state therefore may be realized by the electron correlations when

$$U > W. \tag{1.60}$$

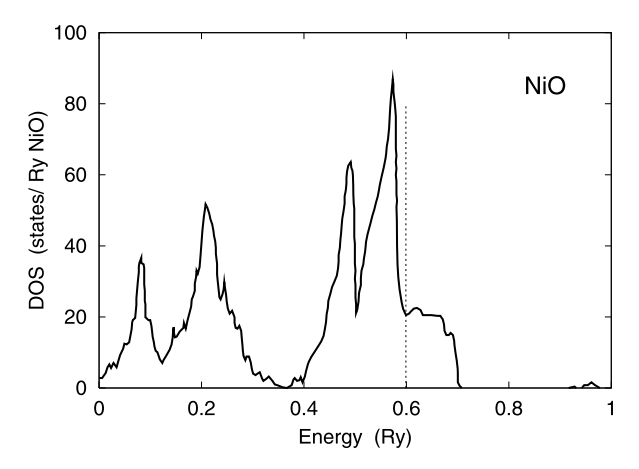
This is Hubbard's alloy analogy picture to the metal–insulator transition [9, 10]. The metal–insulator transition due to electron correlations as mentioned above is commonly known as the Mott transition. The split bands are named the upper and lower Hubbard bands, respectively. The insulator caused by the electron correlations is referred as the Mott insulator.

The concept of the Mott insulator was first proposed by Mott [11]. He considered the case of NiO. NiO has the NaCl structure in which Ni–O chain network is formed along [100] direction (see Fig. 1.5). The electronic configuration of the Ni<sup>28</sup> (O<sup>8</sup>) atom is given by 1s<sup>2</sup>2s<sup>2</sup>2p<sup>6</sup>3s<sup>2</sup>3p<sup>6</sup>3d<sup>8</sup>4s<sup>2</sup> (1s<sup>2</sup>2s<sup>2</sup>2p<sup>4</sup>). The oxygen atoms are considered to form a closed shell in the compound taking electrons from Ni atoms, so that we have

$$Ni^{2+} \colon \quad 1s^2 2s^2 2p^6 3s^2 3p^6 3d^8 \qquad O^{2-} \colon \quad 1s^2 2s^2 2p^6.$$

In this case, the Fermi level should be on the d bands in the crystalline system, and we can expect a metal because the 5-fold d bands overlap each other in general (see Fig. 1.6).

Fig. 1.6 Density of states for NiO in the paramagnetic state obtained by the band calculation [12]. The *vertical dashed line* shows the Fermi level



Experimental results however indicate that NiO is an insulator. To clarify the insulating behavior, Mott considered the electron hopping on the NiO network. Let us estimate an excitation energy  $\Delta E_g$  when an electron moves to the neighboring Ni<sup>2+</sup> site. This process is similar to an excitation of the H<sub>2</sub> molecule to a polarized state.

$$(Ni^{2+}O^{2-})_2 \longrightarrow Ni^{3+}O^{2-} + Ni^+O^{2-}.$$

Assume that the intra-atomic Coulomb interaction is given by  $\sum_i \sum_{(\nu\sigma,\nu'\sigma')} U \cdot n_{i\nu\sigma} n_{i\nu'\sigma'}$  for simplicity. There an electron is coupled to the remaining 7 electrons via the on-site Coulomb interaction. After the hopping, the electron is coupled to 8 electrons at the neighboring site, so that the Coulomb interaction is increased by U. On the other hand, the kinetic energy gain due to electron hopping at Ni<sup>3+</sup> and Ni<sup>2+</sup> sites may be given by

$$2z|t| \sim W. \tag{1.61}$$

because electrons in surrounding Ni sites can enter into the Ni<sup>3+</sup> ions and the electrons in Ni<sup>2+</sup> ions can jump to the surrounding Ni sites. Here z is the number of Ni nearest neighbors, and t is an effective electron hopping between Ni atoms. Note that |t| corresponds to an energy gain for the formation of the bonding state due to electron hopping in the H<sub>2</sub> molecule, while U corresponds to the Coulomb energy loss in the polarized state. The excitation energy of an electron hopping is therefore given by

$$\Delta E_{\rm g} \sim U - W. \tag{1.62}$$

Thus, we again have the same criterion for the formation of the Mott insulator (1.60) from the condition  $\Delta E_g > 0$ .

The magnetic materials in the insulator are considered to be the Mott-type insulator in which the atomic magnetic moments are built up in the unfilled shell. CrO<sub>2</sub> and CrBr<sub>2</sub> are typical ferromagnetic insulators, while MnO, FeO, CoO, and NiO

are known as antiferromagnetic insulators in which the atomic magnetic moments change their direction alternatively from site to site.

On the other hand, there are many magnetic metals where the polarized electrons are mobile. These materials are referred as the metallic magnets or itinerant electron magnets. The magnetic properties of these systems are known as the metallic magnetism or itinerant magnetism. Fe, Co, and Ni are typical examples of the metallic ferromagnet, while Cr and Mn alloys show the antiferromagnetism. We describe in this book the itinerant magnetism of metals and alloys.

### 1.5 Quenching of Orbital Magnetic Moments

The expectation value of the total orbital magnetic moment  $\langle M_L \rangle = \langle L \rangle$  is usually quenched in the crystalline system due to the crystalline potential of electrons. Let us consider the case where the spin-orbit interactions are negligible as in the 3d transition metals, and that the magnetic field is not applied. Moreover we may assume in solids that the ground state is nondegenerate. One can then choose the ground-state wave function to be real;  $\Psi^* = \Psi$ .

The angular momentum  $\langle L \rangle$  is real because it is a physical quantity:

$$\langle L \rangle = \langle L \rangle^*. \tag{1.63}$$

Using the relation  $\Psi^* = \Psi$ , the r.h.s. of the above equation is written as

$$\langle L \rangle^* = -\langle \Psi | L | \Psi \rangle. \tag{1.64}$$

Therefore (1.63) indicates that

$$\langle L \rangle = \mathbf{0}.\tag{1.65}$$

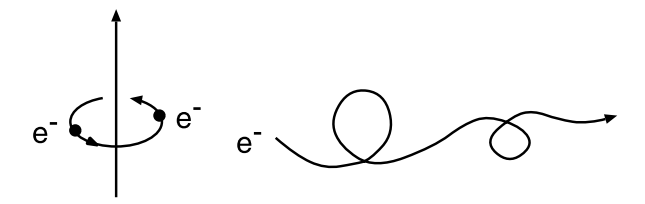
Thus, one can expect in metals with sufficiently small spin-orbit interactions that only spin magnetic moments contribute to the magnetization.

$$\langle \mathbf{M} \rangle = \langle 2\mathbf{S} \rangle. \tag{1.66}$$

This is referred as the quenching of orbital magnetic moments.

In the atomic system, electrons are bound by the nuclei, and the orbital angular momentum is finite in general according to Hund's second rule. In the crystalline system, the Coulomb energy gain leading to Hund's second rule is not expected because electrons can hop to the neighboring sites to reduce the Coulomb energy, and electrons can move turning around to right and left (see Fig. 1.7). It may lead to  $\langle L \rangle = 0$ . This is a physical reason for the quenching of orbital moments in solids. In the 3d transition metals and alloys which we will discuss, the orbital magnetic moments are usually quenched. In the system with a large spin–orbit coupling such as the rare-earth metals or the system with a strong magnetic field, the orbital moments remain.

Fig. 1.7 Concept of orbital magnetic moments in atom  $(L \neq 0: left)$  and solids (L = 0: right)



### 1.6 Heisenberg Model

In the insulator, magnetic behaviors are often described by a simple Hamiltonian known as the Heisenberg model. We briefly discuss the Hamiltonian and related properties of the insulator magnetism in this section.

Let us consider the hydrogen molecule. We assume one orbital for each hydrogen atom,  $\varphi_1$  for atom 1 and  $\varphi_2$  for atom 2, and neglect the overlap integrals for simplicity, i.e.,  $\langle \varphi_1 | \varphi_2 \rangle = 0$ . The Hamiltonian for the hydrogen molecule is obtained from (1.13) as we derived (1.47).

$$H = \sum_{i\sigma} \varepsilon_0 n_{i\sigma} + \sum_{ij\sigma} t_{ij} a_{i\sigma}^{\dagger} a_{j\sigma} + \sum_i U n_{i\uparrow} n_{i\downarrow} + \left(K - \frac{1}{2}J\right) n_1 n_2 - 2J s_1 \cdot s_2.$$

$$\tag{1.67}$$

Here K and J denote the intersite Coulomb and exchange integrals given by

$$K = \int d\mathbf{r} \, d\mathbf{r}' \, \frac{\varphi_1^*(\mathbf{r}) \varphi_2^*(\mathbf{r}') \varphi_2(\mathbf{r}') \varphi_1(\mathbf{r})}{|\mathbf{r} - \mathbf{r}'|},\tag{1.68}$$

$$J = \int d\mathbf{r} \, d\mathbf{r}' \, \frac{\varphi_1^*(\mathbf{r}) \varphi_2^*(\mathbf{r}') \varphi_1(\mathbf{r}') \varphi_2(\mathbf{r})}{|\mathbf{r} - \mathbf{r}'|}.$$
 (1.69)

In the atomic subspace where  $n_1 = n_2 = 1$  and the electron hopping is suppressed, the Hamiltonian (1.67) reduces as follows.

$$H = 2\varepsilon_0 + K - \frac{1}{2}J - 2Js_1 \cdot s_2. \tag{1.70}$$

It is diagonalized with the use of the total spin S (in the representation of S and  $S_z$ ) as

$$H = 2\varepsilon_0 + K - J[S(S+1) - 1].$$
 (1.71)

Therefore the hydrogen molecule has the energy  $2\varepsilon_0 + K - J$  for the triplet state and  $2\varepsilon_0 + K + J$  for the singlet state when the inter-site atomic distance is large. This is the Heitler-London theory for the hydrogen molecule.

The last term in (1.70) denotes an interaction between the atomic spins  $s_1$  and  $s_2$ . In general, the following Hamiltonian showing the interactions between atomic

spins  $\{S_i\}$  is known as the Heisenberg model.

$$H = -\sum_{(i,j)} J_{ij} S_1 \cdot S_2. \tag{1.72}$$

The interaction  $J_{ij} = 2J$  in the Heitler–London theory is the inter-site exchange integral due to the Coulomb interaction. This coupling in the Heisenberg model is referred as the direct exchange interaction. The direct exchange interaction is generally positive in sign (i.e., ferromagnetic).

Another type of the Heisenberg model with effective exchange coupling is possible in the insulator. In order to derive the effective Hamiltonian, we first derive the perturbative effective Hamiltonian from a more general point of view [13]. The effective Hamiltonian is constructed such that it yields the same energy eigen values in a subspace as in the original Hamiltonian acting on the full Hilbert space.

Let us consider a subspace  $\mathscr{P}$  spanned by a set of states  $\{|s\rangle\}$ , and introduce a projection operator  $P = \sum_{s} |s\rangle\langle s|$  which projects any state onto subspace  $\mathscr{P}$ . The projection operator which chooses the complementary subspace  $\mathscr{Q}$  is defined by Q = 1 - P. Note that  $P^2 = P$ ,  $Q^2 = Q$ , and PQ = QP = 0.

The eigen value problem of the original Hamiltonian H is written as

$$(H - E)\psi = 0. \tag{1.73}$$

Inserting the identity 1 = P + Q into the above equation as  $(P + Q)(H - E)(P + Q)\psi = 0$  and multiplying P from the l.h.s. of the equation, we obtain

$$[(PHP - E)P + PHQ]\psi = 0. \tag{1.74}$$

In the same way, we can derive the following equation

$$[QHP + (QHQ - E)Q]\psi = 0. \tag{1.75}$$

In (1.74) and (1.75), the wave function  $\psi$  is separated into two components belonging to different subspaces,  $P\psi$  and  $Q\psi$ . From both equations, one can eliminate the wave function  $Q\psi$  that leads to the eigenvalue equation in subspace  $\mathcal{P}$ , namely,

$$[PHP - PHQ(QHQ - E)^{-1}QHP]P\psi = EP\psi.$$
 (1.76)

The above equation indicates that the following Hamiltonian  $H_p(E)$  acting on the wave function  $P\psi$  in the subspace  $\mathscr P$  is regarded as an effective Hamiltonian which yields the same eigen value E as in the original Hamiltonian H, where

$$H_{\rm p}(E) = PHP - PHQ(QHQ - E)^{-1}QHP.$$
 (1.77)

The effective Hamiltonian depends on the energy which should be obtained selfconsistently. Taking the subspace spanned by a subset of the eigenfunctions of an unperturbed Hamiltonian, one can derive the effective Hamiltonian which is correct up to the second order of the interaction Hamiltonian. Assume that the Hamiltonian consists of a noninteracting part  $H_0$  and an interaction part  $H_I$  such that  $H = H_0 + H_I$ . The eigenvalues  $\{E_k^0\}$  and eigenfunctions  $\{\phi_k\}$  for  $H_0$  are assumed to be known. We define the subspace  $\mathscr P$  spanned by a part of  $\{|\phi_k\rangle\}$ . The projection operator is then defined by  $P = \sum_{\mu}^{\mathscr P} |\phi_{\mu}\rangle\langle\phi_{\mu}|$ . We have the relation  $QHP = QH_IP$ , and thus obtain the effective Hamiltonian which is correct up to the second order in interaction, after having replaced the Hamiltonian H and the energy E in the denominator of (1.77) with the zeroth-order ones,  $H_0$  and  $E_k^0$ , i.e.,

$$H_{\rm p} = PHP - PH_{\rm I}Q(QH_0Q - E_k^0)^{-1}QH_{\rm I}P. \tag{1.78}$$

The effective Hamiltonian depends on the eigen state k explicitly. Therefore we rewrite the second term as follows.

$$(QH_0Q - E_k^0)^{-1}QH_1P\phi_k = \sum_{\mu}^{\mathscr{P}} \sum_{\nu}^{\mathscr{Q}} (E_{\nu}^0 - E_{\mu}^0)^{-1} |\phi_{\nu}\rangle\langle\phi_{\nu}|H_1|\phi_{\mu}\rangle\langle\phi_{\mu}|\phi_k\rangle.$$
(1.79)

Thus the perturbative Hamiltonian (1.78) is expressed as follows.

$$H_{\rm p} = PHP - PH_{\rm I}Q(E_Q^0 - E_P^0)^{-1}QH_{\rm I}P.$$
 (1.80)

Here  $E_P^0$  ( $E_Q^0$ ) denotes the eigenvalues belonging to subspace  $\mathscr{P}$  ( $\mathscr{Q}$ ). The eigen value equation for the perturbative effective Hamiltonian is then given by

$$H_{\mathbf{p}}P\psi_k = E_k P\psi_k. \tag{1.81}$$

We can derive the effective Heisenberg model in the strong Coulomb interaction regime at half-filling using the formula (1.80). Let us consider the Hubbard model (1.51). As found in Sect. 1.4, the ground state of the atomic limit at half-filling is specified by  $\{n_i = 1\}$  states. The ground state is  $2^L$ -fold degenerate, L being the number of sites. We start from the ground state in the atomic limit at half filling, i.e., the  $\{n_i = 1\}$  states, and define the subspace  $\mathscr P$  from them. The complementary subspace  $\mathscr Q$  consists of the subspace containing empty states and the subspace containing the doubly occupied states. In the strongly correlated region, the electron hopping rate  $|t_{ij}|$  is much smaller than the Coulomb interaction strength U, so that the Hamiltonian H is separated into the atomic state  $H_0 = \sum_{ij\sigma} \varepsilon_0 n_{i\sigma} + \sum_i U n_i \uparrow n_i \downarrow$  and the 'interaction' term  $H_1 = \sum_{ij\sigma} t_{ij\sigma} a_{i\sigma}^\dagger a_{j\sigma}$ . The first term at the r.h.s. of (1.80) is given by  $PL\varepsilon_0 P$ . In the calculations of the second term, we have  $QH_1P = \sum_{ij\sigma} t_{ij} a_{i\sigma}^\dagger a_{j\sigma} P$  because  $a_{i\sigma}^\dagger a_{j\sigma} P$  belong to the space  $\mathscr Q$ . Moreover,  $E_Q^0 - E_P^0 = U$  when it is operated on the single doubly-occupied state  $QH_1P$ . Thus we obtain the expression for the second term at the r.h.s.

of (1.80) as follows.

$$PH_{\rm I}Q(E_Q^0 - E_P^0)^{-1}QH_{\rm I}P = \sum_{ijkl\sigma\sigma'} \frac{t_{lk}t_{ij}}{U} P a_{l\sigma'}^{\dagger} a_{k\sigma'} a_{i\sigma}^{\dagger} a_{j\sigma} P.$$
 (1.82)

Among the summation at the r.h.s. of (1.82) only the k = i and l = j terms remain. Rearranging the creation and annihilation operators, we obtain the relation.

$$\sum_{\sigma\sigma'} a_{j\sigma'}^{\dagger} a_{i\sigma'} a_{i\sigma}^{\dagger} a_{j\sigma} = n_j - \frac{1}{2} n_i n_j - 2s_i \cdot s_j. \tag{1.83}$$

Substituting the above relation into (1.82), we obtain the following effective Hamiltonian.

$$H_{p} = P \left[ L \left( \varepsilon_{0} - \frac{1}{2} \sum_{j} \frac{|t_{ij}|^{2}}{U} \right) + \sum_{(i,j)} \frac{4|t_{ij}|^{2}}{U} s_{i} \cdot s_{j} \right] P.$$
 (1.84)

Apart from the constant term, we arrive at the following effective Heisenberg model in the strong Coulomb interaction regime at half filling, which operates on the subspace  $\mathcal{P}$ .

$$H = -\sum_{(i,j)} J_{ij} s_1 \cdot s_2. \tag{1.85}$$

Here

$$J_{ij} = -\frac{4|t_{ij}|^2}{U}. (1.86)$$

The effective exchange integral (1.86) is known as the super exchange interaction because it is caused by a virtual exchange of electrons belonging to different atoms via transfer integrals. The super exchange interaction is antiferromagnetic, while the direct exchange interaction (1.69) is ferromagnetic. Note that the subspace on which the Hamiltonian (1.85) acts is given by  $\{P|n_1s_{1z}, n_2s_{2z}, \ldots\} = \{|1s_{1z}, 1s_{2z}, \ldots\} \}$ . This can be simplified as  $\{|s_{1z}, s_{2z}, \ldots\} \}$ . In many magnetic insulators, anions are often located between the magnetic ions. In such a case, the super exchange interaction becomes dominant. The Heisenberg model (1.85) is not justified in the metallic system where the band width  $W \sim U$ . Nevertheless, we often find the same type of the intersite magnetic interactions, which are useful for qualitative understanding of the magnetism (see Sects. 6.4 and 8.3 for examples).

### 1.7 Magnetic Structure

Magnetic materials have their microscopic structure for arrangement of atomic magnetic moments. This is called the magnetic structure. The structure characterizes the

magnetic property as well as the electronic structure. In this section, we introduce the Fourier representation of the magnetic structure and explain briefly the magnetic structures in solids.

The magnetic structure is characterized by the magnetic moment density which is given by

$$\mathbf{M}(\mathbf{r}) = \langle \psi^{\dagger}(\mathbf{r}) \mathbf{m} \psi(\mathbf{r}) \rangle. \tag{1.87}$$

Here  $\psi(\mathbf{r}) = (\psi_{\uparrow}(\mathbf{r}), \psi_{\downarrow}(\mathbf{r}))$  is the field operator of electrons.  $\mathbf{m}$  denotes the magnetic moment for an electron as given by (1.7).

In a crystalline system, we may divide the space into the Wigner–Seitz cells for each atom. Then we can define a magnetic moment of atom i as follows.

$$\boldsymbol{m}_i = \int_i \boldsymbol{M}(\boldsymbol{r}) \, d^3 x. \tag{1.88}$$

Here the integration is over the Wigner–Seitz cell belonging to atom *i*. In a non-crystalline system we may adopt the Voronoi polyhedra instead of the Wigner–Seitz cells.

In the case of the crystalline system, the atomic position  $R_l$  is expressed by using the primitive translational vectors a, b, c as

$$\mathbf{R}_{l} = l_{1}\mathbf{a} + l_{2}\mathbf{b} + l_{3}\mathbf{c}. \tag{1.89}$$

The atomic magnetic moment is expanded with use of the Fourier lattice series as follows.

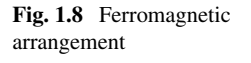
$$\mathbf{m}_l = \sum_{\mathbf{q}} \mathbf{m}(\mathbf{q}) e^{i\mathbf{q} \cdot \mathbf{R}_l}. \tag{1.90}$$

Here q is the wave vector in the first Brillouin zone. The Fourier components of the magnetic moments are given as

$$\boldsymbol{m}(\boldsymbol{q}) = \frac{1}{L} \sum_{l} \boldsymbol{m}_{l} e^{-i\boldsymbol{q} \cdot \boldsymbol{R}_{l}}, \qquad (1.91)$$

L being the number of lattice points. Note that  $m(-q) = m(q)^*$  because  $m_l$  are real. Moreover we assumed that there is only one atom per unit cell. When there are more than one atom per unit cell, we have to add the atomic position in a unit cell  $\eta_{\lambda}$  to (1.89). Accordingly, the magnetic moments (1.90) and (1.91) are specified by the type of atom  $\lambda$  as  $m_l^{(\lambda)}(m^{(\lambda)}(q))$ . Hereafter we consider the crystalline system with one magnetic atom per unit cell.

The microscopic magnetic structure of magnetic materials is specified by a set of  $\{m_l\}$  or  $\{m(q)\}$ . The simplest structure is that all of the atomic magnetic moments have the same direction. It is realized when all the Fourier components vanish except m(q=0)=m, and is known as the ferromagnetic structure (see Fig. 1.8). Typical transition metals such as Fe, Co, and Ni exhibit the ferromagnetism.



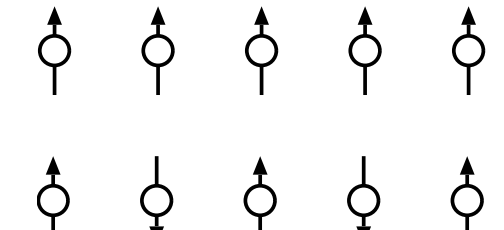


**Fig. 1.9** Antiferromagnetic arrangement

The antiferromagnetic structure (AF) is defined by alternative arrangement of the atomic magnetic moments along a direction, e.g., the z direction (see Fig. 1.9). It is specified by a set,  $m(\pm Q) = mk \exp(\pm i\alpha)$  and  $m(q \neq \pm Q) = 0$ , where Q consists of half a reciprocal lattice vectors, and k denotes a unit vector along the z axis, and  $\alpha$  denotes a phase of the structure. In the case  $\alpha = 0$ , we have

$$\boldsymbol{m}_l = m\boldsymbol{k}\cos(\boldsymbol{Q} \cdot \boldsymbol{R}_l). \tag{1.92}$$

When the position  $R_l$  moves along Q vector,  $Q \cdot R_l$  changes by  $\pi$ . Accordingly, the magnetic moment  $m_l$  changes its sign.

The AF structure on the simple cubic lattice as shown in Fig. 1.10(a) is expressed by the wave vector  $\mathbf{Q} = (\mathbf{K}_1 + \mathbf{K}_2 + \mathbf{K}_3)/2 = (1, 1, 1)\pi/a$ , a being the lattice constant. The AF structure on the body-centered cubic lattice as shown in Fig. 1.10(b) is expressed by the wave vector  $\mathbf{Q} = (-\mathbf{K}_1 + \mathbf{K}_2 + \mathbf{K}_3)/2 = (0, 0, 1)2\pi/a$ . In the case of the face-centered cubic lattice (fcc) structure, two kinds of AF structures are known. The AF structure of the first-kind as shown in Fig. 1.10(c) is described by a wave vector  $\mathbf{Q} = (\mathbf{K}_2 + \mathbf{K}_3)/2 = (0, 0, 1)2\pi/a$ . The atomic moment alternatively changes the direction with a translation by (0, 0, 1)a/2. It is also possible to change direction alternatively along  $\langle 1 \ 1 \ 1 \rangle$  axis. This is referred as the AF structure of the second-kind, and is characterized by  $\mathbf{Q} = (\mathbf{K}_1 + \mathbf{K}_2 + \mathbf{K}_3)/2 = (1, 1, 1)\pi/a$  (see Fig. 1.11). Cr with 1 at% Mn on the bcc lattice shows the AF structure, and  $\gamma$ -Mn on the fcc lattice shows the AF structure of the first-kind according to the neutron diffraction experiments.

It should be noted that the network consisting of the up-spin atoms (or the down-spin atoms) forms a lattice referred as the sublattice. There are two sublattices in the antiferromagnetic structures shown in Fig. 1.10. Each sublattice forms the fcc lattice with the lattice constant 2a in the case of the sc structure (Fig. 1.10(a)), the sc lattice with the lattice constant a in the case of the bcc structure (Fig. 1.10(b)), and the simple tetragonal structure with the lattice constants  $a/\sqrt{2}$  and a in the case of the fcc structure (Fig. 1.10(c)), respectively.

The sinusoidal spin density wave (SDW) structure is expressed by

$$\mathbf{m}_l = m\mathbf{k}\sin(\mathbf{Q} \cdot \mathbf{R}_l + \alpha),\tag{1.93}$$

where Q vector is neither equal to  $\mathbf{0}$  nor to the AF wave vectors. The magnetic moment sinusoidally changes with a period  $\lambda = 2\pi/|Q|$  along the Q direction (see

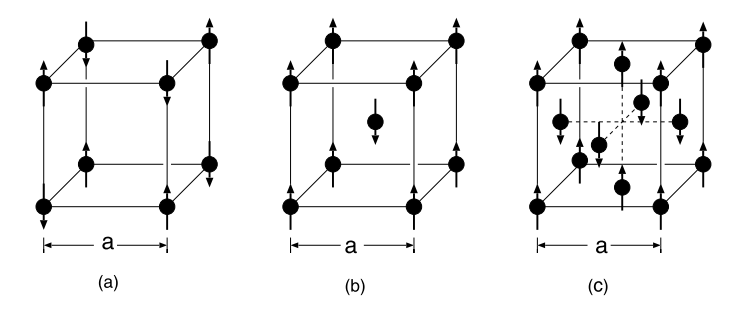
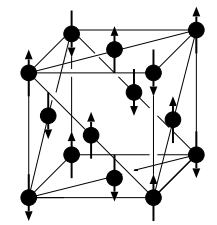


Fig. 1.10 Antiferromagnetic arrangements on the simple cubic lattice ( $\mathbf{a}$ ), body-centered cubic lattice ( $\mathbf{b}$ ), and face-centered cubic lattice ( $\mathbf{c}$ ). The lattice constants are shown by a

Fig. 1.11 The antiferromagnetic structure of the second-kind on the face-centered cubic lattice



**Fig. 1.12** Spin density wave structure

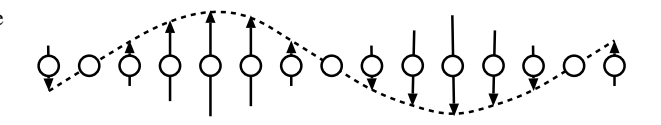


Fig. 1.12). Note that the period is not necessarily commensurate with the lattice spacing in general. Cr is a well-known example of the SDW.

It is also possible that the magnetic moment rotates with a translation (see Fig. 1.13). This is known as the helical structure, and is expressed as

$$\mathbf{m}_{l} = m [\mathbf{e}_{1} \cos(\mathbf{Q} \cdot \mathbf{R}_{l} + \alpha) + \mathbf{e}_{2} \sin(\mathbf{Q} \cdot \mathbf{R}_{l} + \alpha)]. \tag{1.94}$$

Here  $e_1$  and  $e_2$  are the unit vectors being orthogonal to each other. The magnetic moment with amplitude m rotates on the  $e_1-e_2$  plane with the translation along the Q vector.

The above expression (1.94) can also be written as

$$\mathbf{m}_{l} = \mathbf{m}(\mathbf{Q})e^{i\mathbf{Q}\cdot\mathbf{R}_{l}} + \mathbf{m}(\mathbf{Q})^{*}e^{-i\mathbf{Q}\cdot\mathbf{R}_{l}}, \tag{1.95}$$

with

$$m(Q) = \frac{m}{2}(e_1 - ie_2)e^{i\alpha}.$$
 (1.96)

It indicates that the helical structure is specified by the Q vector and the condition

$$\boldsymbol{m}(\boldsymbol{Q})^2 = 0. \tag{1.97}$$

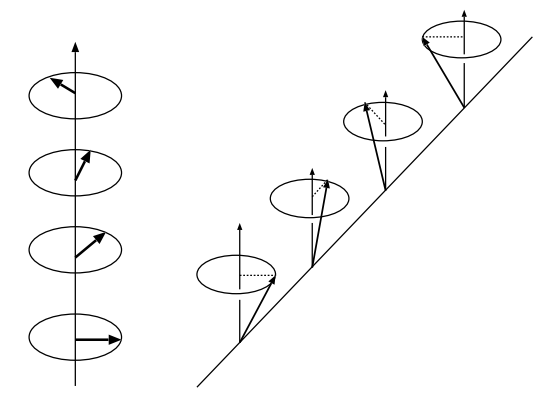
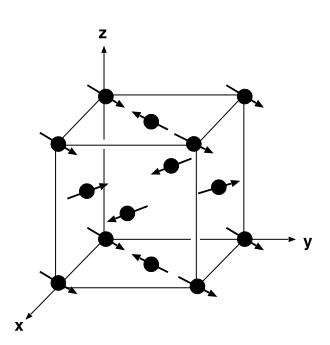


**Fig. 1.13** Helical structure (*left*) and conical structure (*right*)

**Fig. 1.14** 2 *Q* multiplespin-density wave structure



It is known from the neutron experiments that Au<sub>2</sub>Mn, MnO<sub>2</sub>, CrO<sub>2</sub>, Eu, Tb, Dy, Ho etc. show the helical structure.

So far the magnetic structures are characterized by only one Q vector. One can also consider the helical type structure with the bulk magnetization as follows.

$$\mathbf{m}_{l} = m_{z}\mathbf{k} + m(\mathbf{i}\cos(\mathbf{Q} \cdot \mathbf{R}_{l} + \alpha) + \mathbf{j}\sin(\mathbf{Q} \cdot \mathbf{R}_{l} + \alpha)). \tag{1.98}$$

The above expression is alternatively written as

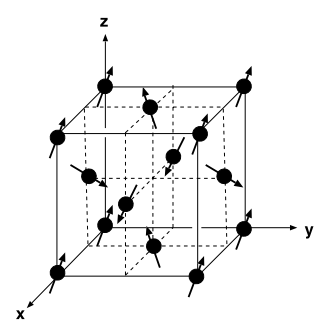
$$\boldsymbol{m}_{l} = m_{z}\boldsymbol{k} + \boldsymbol{m}(\boldsymbol{Q})e^{i\boldsymbol{Q}\cdot\boldsymbol{R}_{l}} + \boldsymbol{m}(\boldsymbol{Q})^{*}e^{-i\boldsymbol{Q}\cdot\boldsymbol{R}_{l}}, \tag{1.99}$$

with

$$m(Q)^2 = 0. (1.100)$$

This is referred as the conical magnetic structure (see Fig. 1.13). The magnetic moment rotates for example on the x-y plane when the moment translates along the direction of Q.

**Fig. 1.15** 3 *Q* multiplespin-density wave structure



One can also consider a magnetic structure consisting of two wave vectors,  $Q_1$  and  $Q_2$ . For example, we can consider a structure such as

$$\boldsymbol{m}_{l} = \boldsymbol{m}(\boldsymbol{Q}_{1})e^{i\boldsymbol{Q}_{1}\cdot\boldsymbol{R}_{l}} + \boldsymbol{m}(\boldsymbol{Q}_{2})e^{i\boldsymbol{Q}_{2}\cdot\boldsymbol{R}_{l}} + \text{c.c.}$$
(1.101)

Assuming that  $m(Q_1) = m_x i/2$  and  $m(Q_2) = m_x j/2$ , we have

$$\mathbf{m}_{l} = m_{x} \mathbf{i} \cos(\mathbf{Q}_{1} \cdot \mathbf{R}_{l}) + m_{y} \mathbf{j} \cos(\mathbf{Q}_{2} \cdot \mathbf{R}_{l}). \tag{1.102}$$

This is known as a double Q multiple SDW (2Q-MSDW) (see Fig. 1.14). In the case of the fcc lattice, we may consider the wave vectors  $Q_1 = (1, 0, 0)2\pi/a$  and  $Q_2 = (0, 1, 0)2\pi/a$ . Then the x(y) component changes the sign with a translation  $R_l = (1, 0, 0)a/2$  ( $R_2 = (0, 1, 0)a/2$ ) as shown in Fig. 1.14.

We can also consider the magnetic structure consisting of three wave vectors  $Q_1$ ,  $Q_2$  and  $Q_3$ , which is the so-called triple Q multiple SDW (3 Q-MSDW). For example, we have a 3 Q-MSDW such that

$$\mathbf{m}_{l} = m_{x} \mathbf{i} \cos(\mathbf{Q}_{1} \cdot \mathbf{R}_{l}) + m_{y} \mathbf{j} \cos(\mathbf{Q}_{2} \cdot \mathbf{R}_{l}) + m_{z} \mathbf{k} \cos(\mathbf{Q}_{3} \cdot \mathbf{R}_{l}), \quad (1.103)$$

with  $Q_1 = (1, 0, 0)2\pi/a$ ,  $Q_2 = (0, 1, 0)2\pi/a$ , and  $Q_3 = (0, 0, 1)2\pi/a$ . Each component changes sign after the translation by a/2 along the same direction as shown in Fig. 1.15.

In the substitutional disordered alloys, we have more complicated structures which cannot be described by a small number of wave vectors. When we take a configurational average of the atomic magnetic moments, we can define the average magnetization  $[m_l]_c$ . Here  $[\sim]_c$  denotes the configurational average. In some

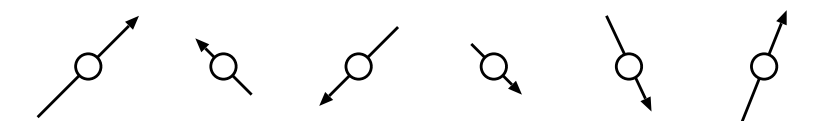


Fig. 1.16 Spin glass arrangement

cases, an ordered state with randomly oriented magnetic moments referred as the spin glass (SG) appears (see Fig. 1.16). The SG is considered to be characterized by the condition such that

$$[\mathbf{m}_l]_c = \mathbf{0}$$
 and  $[\mathbf{m}_l^2]_c = 0.$  (1.104)

The disordered dilute alloys such as  $Cu_{1-x}Mn_x$  ( $x \le 0.1$ ) and  $Au_{1-x}Fe_x$  ( $x \le 0.1$ ) are known to show a SG at low temperatures (see Sect. 7.1).

Experimentally most magnetic structures of crystalline systems are determined by the neutron elastic scattering experiments. The readers who are interested in the experimental determination of the magnetic structure are recommended to refer to the books by Marshall and Lovesey [14, 15].

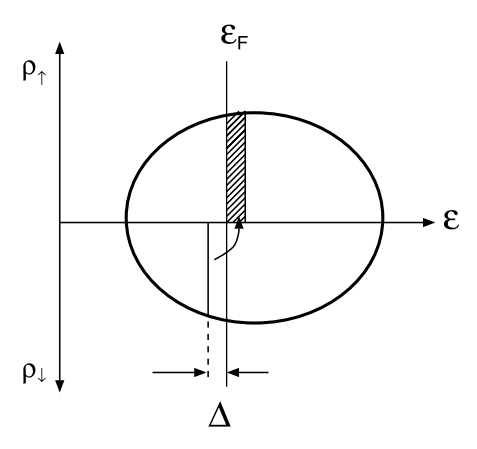
# **Chapter 2 Metallic Magnetism at the Ground State**

We deal with the ferromagnetism in metals at the ground state in this chapter. The stability of ferromagnetism is one of the fundamental problems in magnetism. Since the spin polarization is carried out by itinerant electrons in metals, we start from the band model to consider the stability. The Hartree–Fock approximation overestimates the magnetic energy gain due to spin polarization. We clarify the effects of electron correlations on the ferromagnetic instability by using the low density approximation and the Gutzwiller variational theory. These theories lead to the notion of an effective Coulomb interaction. The density functional theory (DFT) provides us with a quantitative description of the ground-state magnetism in metals. We present the band theory of ferromagnetism based on the DFT in the second half of the chapter, and discuss quantitative aspects of the ferromagnetism of 3d transition metals at the ground state.

## 2.1 Band Theory of Ferromagnetism

When atoms form a solid, most of the elements on the periodic table lose the atomic magnetic moments and show a simple paramagnetism. Only a few metals such as Fe, Co, and Ni in 3d transition metal series and heavy rare earth metals from Gd to Tm show the ferromagnetism. In the case of the rare-earth system, the 4f orbitals are well localized so that the atomic magnetic moment on each atom remains. The ferromagnetism of rare-earth metals is realized by the ferromagnetic couplings between these atomic magnetic moments [16]. On the other hand, in the 3d metal system, electrons in the 3d unfilled shell are considered to be itinerant and to form bands near the Fermi level. In fact, the atomic moment model does not explain the experimental observations that the ground-state magnetizations of Fe, Co, and Ni show the non-integer values of 2.2, 1.7, and 0.6  $\mu_{\rm B}$  per atom, respectively. The Sommerfeld coefficients of specific heat show large values of 5–7 mJ/K<sup>2</sup> mol in these ferromagnets, indicating the formation of narrow d bands. The ferromagnetism in 3d transition metals is therefore considered to be caused by the 3d itinerant electrons.

**Fig. 2.1** Spin polarization in bands



A way to clarify the origin of the itinerant magnetism at the ground state is to start from the band limit and to take into account the electron–electron interactions. Let us consider the ferromagnetism in metals, and assume that the itinerant band electrons are polarized. The polarization gives the magnetization per atom as  $\langle m \rangle = \langle n_{\uparrow} \rangle - \langle n_{\downarrow} \rangle$ . Here  $\langle n_{\sigma} \rangle$  denotes the average number of electrons with spin  $\sigma$  per atom. The spontaneous spin polarization cannot be explained without the Coulomb interaction. Let us assume that the down-spin electrons in a small energy range  $[\varepsilon_{\rm F} - \Delta, \varepsilon_{\rm F}]$  just below the Fermi level  $\varepsilon_{\rm F}$  move to the up-spin band on the Fermi level as shown in Fig. 2.1. The number of moved electrons  $\delta N$  is given by  $\delta N = \Delta \cdot L \rho(0)$ , where  $\rho(0)$  is the density of states (DOS) per atom and per spin at the Fermi level in the paramagnetic state. L denotes the number of lattice points. Therefore, we have the energy width  $\Delta$  as  $\Delta = \delta N/L \rho(0)$ . The change of the band energy  $\Delta E_1$  is given by

$$\Delta E_1 = \Delta \cdot \delta N = \frac{(\delta N)^2}{L\rho(0)} > 0. \tag{2.1}$$

Thus the ferromagnetic spin polarization in the noninteracting system always increases the energy irrespective of details of the band structure.

One needs the intraatomic Coulomb interaction U to stabilize the ferromagnetism. In order to understand the mechanism, we consider the energy change  $\Delta E_2$  of Coulomb interactions due to small polarization  $2\delta N$ . Consider the single band model with the intra-atomic Coulomb interaction U. In a mean-field approximation, the intra-atomic Coulomb interaction energy may be given by

$$L U \langle n_{\uparrow} n_{\downarrow} \rangle \sim L U \langle n_{\uparrow} \rangle \langle n_{\downarrow} \rangle. \tag{2.2}$$

Then, the Coulomb energy change is given by

$$\Delta E_2 \sim -L U \left(\frac{\delta N}{L}\right)^2 < 0. \tag{2.3}$$

The total energy change  $\Delta E = \Delta E_1 + \Delta E_2$  is given by

$$\Delta E \sim \left(\frac{1}{\rho(0)} - U\right) \frac{(\delta N)^2}{L}.$$
 (2.4)

Therefore the ferromagnetism is stabilized when  $\Delta E < 0$ , i.e.,

$$\rho(0) U > 1. \tag{2.5}$$

The above condition for the appearance of the ferromagnetism is called the Stoner condition. The ferromagnetism is stabilized when the energy gain of the Coulomb interaction due to small spin polarization overcomes the band energy loss. In the case of the single band model, the spin polarized state can be stabilized by reducing the double occupancy  $\langle n_{\uparrow}n_{\downarrow}\rangle$ .

The Stoner criterion and the magnetization are obtained by the Hartree–Fock approximation more clearly. Let us consider first the single band for a qualitative argument, and adopt the Hubbard model (1.51). In the Hartree–Fock approximation, the interaction term is decoupled as

$$Un_{\uparrow}n_{\downarrow} \approx U(n_{\uparrow}\langle n_{\downarrow}\rangle + \langle n_{\uparrow}\rangle n_{\downarrow} - \langle n_{\uparrow}\rangle \langle n_{\downarrow}\rangle). \tag{2.6}$$

The approximation neglects the fluctuation term  $U\delta n_{\uparrow}\delta n_{\downarrow}$ . Here  $\delta n_{\sigma}=n_{\sigma}-\langle n_{\sigma}\rangle$ . Using the approximation, we obtain the Hartree–Fock Hamiltonian as follows.

$$\tilde{H} = \sum_{i\sigma} (\varepsilon_0 + U \langle n_{i-\sigma} \rangle) n_{i\sigma} + \sum_{ij\sigma} t_{ij} a_{i\sigma}^{\dagger} a_{j\sigma} - \sum_i U \langle n_{i\uparrow} \rangle \langle n_{i\downarrow} \rangle.$$
 (2.7)

Here  $U\langle n_{i-\sigma}\rangle$  is the Hartree–Fock potential for an electron with spin  $\sigma$ . The total energy in the Hartree–Fock approximation is given by

$$E = \sum_{i} \varepsilon_{0} \langle n_{i} \rangle + \left\langle \sum_{ij\sigma} t_{ij} a_{i\sigma}^{\dagger} a_{j\sigma} \right\rangle + \sum_{i} U \langle n_{i\uparrow} \rangle \langle n_{i\downarrow} \rangle. \tag{2.8}$$

At the ground state, the energy is written as

$$E = \sum_{k} \varepsilon_{k} \langle n_{k\sigma} \rangle + L U \langle n_{\uparrow} \rangle \langle n_{\downarrow} \rangle. \tag{2.9}$$

Here  $\varepsilon_k$  is the band energy obtained by diagonalizing the noninteracting Hamiltonian matrix  $(\boldsymbol{H}_0)_{ij} = \varepsilon_0 \delta_{ij} + t_{ij} (1 - \delta_{ij})$ .  $n_{k\sigma}$  is the electron occupation number for an electron with momentum k and spin  $\sigma$ , and  $\langle n_{\sigma} \rangle = \sum_{k\sigma} \langle n_{k\sigma} \rangle / L$ . The first (second) term at the r.h.s. of (2.9) is the kinetic energy  $E_1$  (interaction energy  $E_2$ ) discussed in (2.1) and (2.3).

When the potential is spatially uniform, one can obtain a self-consistent equation for the average electron number using the Hartree–Fock Hamiltonian (2.7) as follows.

$$\langle n_{i\sigma} \rangle = \int d\omega f(\omega) \rho^0 (\omega - U \langle n_{i-\sigma} \rangle + \mu).$$
 (2.10)

Here  $f(\omega)=1/(\mathrm{e}^{\beta\omega}+1)$  is the Fermi distribution function,  $\beta$  being the inverse temperature.  $\rho^0(\omega)$  is the DOS per atom per spin for the noninteracting Hamiltonian, and  $\mu$  denotes the Fermi level.

The above equations are expressed by the local charge  $\langle n \rangle = \sum_{\sigma} \langle n_{i\sigma} \rangle$  and magnetization  $\langle m \rangle = \sum_{\sigma} \sigma \langle n_{i\sigma} \rangle$  as follows.

$$\langle n \rangle = \sum_{\sigma} \int d\omega f(\omega) \rho^{0} \left( \omega - \frac{1}{2} U \langle n \rangle + \frac{1}{2} U \langle m \rangle \sigma + \mu \right), \tag{2.11}$$

$$\langle m \rangle = \sum_{\sigma} \sigma \int d\omega \, f(\omega) \rho^0 \left( \omega - \frac{1}{2} U \langle n \rangle + \frac{1}{2} U \langle m \rangle \sigma + \mu \right). \tag{2.12}$$

The first equation determines the Fermi level  $\mu$  when the electron number n is given, while the second one determines the magnetization  $\langle m \rangle$  self-consistently.

In the same way one can also express the Hartree–Fock energy per atom as follows.

$$E/L = \mu \langle n \rangle + \int d\omega f(\omega) \omega \sum_{\sigma} \rho^{0} \left( \omega - \frac{1}{2} U \langle n \rangle + \frac{1}{2} U \langle m \rangle \sigma + \mu \right)$$
$$- \frac{1}{4} U \left( \langle n \rangle^{2} - \langle m \rangle^{2} \right). \tag{2.13}$$

Here we omitted the site suffix for simplicity assuming uniform charge and spin polarization.

Appearance of the ferromagnetism may be characterized by an instability of the paramagnetic state. The latter is obtained from the uniform susceptibility. Let us apply an infinitesimal magnetic field h. We then have additional potential  $-h\sigma$  in the Hartree–Fock self-consistent equations. The uniform paramagnetic spin susceptibility  $\chi$  is given by  $\chi = [\partial \langle m \rangle / \partial h]_{h=0}$ . Using (2.12) with additional potential  $-h\sigma$ , we obtain the Hartree–Fock susceptibility at the ground state as follows.

$$\chi = \frac{2\rho(0)}{1 - \rho(0)U}. (2.14)$$

Here  $\rho(0)$  is the DOS per atom per spin at the Fermi level in the nonmagnetic state. When  $\rho(0)U=1$ , the susceptibility diverges, and we again obtain the Stoner condition (2.5).

In order to obtain the magnetization we have to solve the self-consistent equations (2.11) and (2.12). There are two types of the ferromagnetism in general. When the Coulomb interaction strength is large enough, we can expect that the up-spin band is below the Fermi level so that the magnetization is not changed by the magnetic field. Another case is that holes remain in the up-spin band so that both the up and down bands are laid on the Fermi level as shown in Fig. 2.2. The former is called the complete ferromagnetism or the strong ferromagnetism, while the latter is called the incomplete ferromagnetism or the weak ferromagnetism.

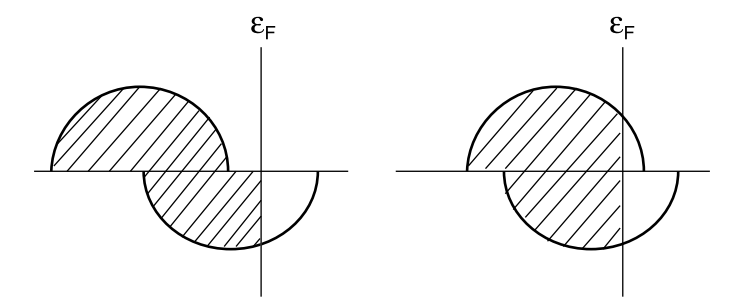


Fig. 2.2 The strong (*left*) and weak (*right*) ferromagnets

To describe the ferromagnetism in 3d transition metals in more detail, we have to take into account five d orbitals. The Hartree–Fock approximation to the degenerate-band Hamiltonian (1.47) yields the following effective Hamiltonian (see (1.34)).

$$\tilde{H} = \sum_{iL\sigma} \varepsilon_{iL\sigma} n_{iL\sigma} + \sum_{iLjL'} t_{iLjL'} a_{iL\sigma}^{\dagger} a_{jL'\sigma} - \langle H_1 \rangle, \qquad (2.15)$$

$$\langle H_1 \rangle = \sum_{i} \left[ \frac{1}{4} \sum_{m} U_{mm} \langle n_{iL} \rangle^2 + \frac{1}{2} \sum_{mm'} \left( U_{mm'} - \frac{1}{2} J_{mm'} \right) \langle n_{iL} \rangle \langle n_{iL'} \rangle \right.$$

$$\left. - \frac{1}{4} \sum_{mm} U_{mm} \langle m_{iL} \rangle^2 - \frac{1}{4} \sum_{mm'} \langle m_{iL} \rangle \langle m_{iL'} \rangle \right]. \qquad (2.16)$$

Here L(L') denotes the atomic orbital lm(lm') with l = 2.  $\varepsilon_{iL\sigma}$  is the atomic level with the Hartree–Fock potential, and is given by

$$\varepsilon_{iL\sigma} = \varepsilon_{iL} - \frac{1}{2} \left( U_{mm} \langle m_{iL} \rangle + \sum_{m' \neq m} J_{mm'} \langle m_{iL'} \rangle \right) \sigma, \tag{2.17}$$

$$\varepsilon_{iL} = \varepsilon_L^0 - \mu + \frac{1}{2} U_{mm} \langle n_{iL} \rangle + \sum_{m' \neq m} \left( U_{mm'} - \frac{1}{2} J_{mm'} \right) \langle n_{iL'} \rangle. \tag{2.18}$$

Note that  $\varepsilon_L^0$  is the atomic level and we have introduced the chemical potential for convenience.

The local charge and magnetization for orbital L are given by

$$\langle n_L \rangle = \sum_{\sigma} \langle n_{L\sigma} \rangle,$$
 (2.19)

$$\langle m_L \rangle = \sum_{\sigma} \sigma \langle n_{L\sigma} \rangle,$$
 (2.20)

and

$$\langle n_{L\sigma} \rangle = \int d\omega f(\omega) \rho_{L\sigma}(\omega).$$
 (2.21)

We have omitted the site indices i in the above expressions for simplicity.  $\rho_{L\sigma}(\omega)$  is the Hartree–Fock DOS for orbital L and spin  $\sigma$ .

$$\rho_{L\sigma}(\omega) = \sum_{k} \left| \langle iL|k \rangle \right|^{2} \delta(\omega - \tilde{\varepsilon}_{k\sigma}). \tag{2.22}$$

Here  $\tilde{\varepsilon}_{k\sigma}$  is the eigen value for the Hamiltonian matrix  $(\tilde{\boldsymbol{H}}_0)_{iLjL'} = \varepsilon_{L\sigma}\delta_{ij}\delta_{LL'} + t_{iLjL'}$ , and  $\langle iL|k\rangle$  is the overlap integral between the local orbital iL and the one-electron eigen state k.

For simplicity, we neglect in the following the orbital dependence of the Coulomb and exchange integrals as

$$U_{mm'} = U_0 \delta_{mm'} + U_1 (1 - \delta_{mm'}), \tag{2.23}$$

$$J_{mm'} = J(1 - \delta_{mm'}). \tag{2.24}$$

Here  $U_0$  ( $U_1$ ) is the average intraorbital (interorbital) Coulomb interaction and J is the average exchange interaction. Moreover we assume that the orbitals form a basis set of the irreducible representation of point symmetry. We have then

$$\varepsilon_{iL\sigma} = \varepsilon_L - \frac{1}{2} \left[ U_0 \langle m_\Gamma \rangle + J \left( \langle m \rangle - \langle m_\Gamma \rangle \right) \right] \sigma, \tag{2.25}$$

$$\varepsilon_L = \varepsilon_L^0 - \mu + \frac{1}{2} U_0 \langle n_\Gamma \rangle + \left( U_1 - \frac{1}{2} J \right) \left( \langle n \rangle - \langle n_\Gamma \rangle \right). \tag{2.26}$$

Here  $\langle n_{\Gamma} \rangle$  ( $\langle m_{\Gamma} \rangle$ ) denotes the average electron number of orbital L, i.e.,  $\langle n_{L} \rangle$  (magnetic moment  $\langle m_{L} \rangle$ ) belonging to the point symmetry representation  $\Gamma$ . Moreover,  $\langle n \rangle = \sum_{\Gamma} d_{\Gamma} \langle n_{\Gamma} \rangle$  ( $\langle m \rangle = \sum_{\Gamma} d_{\Gamma} \langle m_{\Gamma} \rangle$ ) denotes the total charge (magnetization) on a site, and  $d_{\Gamma}$  is the number of orbitals belonging to the point symmetry  $\Gamma$ .

When all the magnetic moments on each orbital are assumed to make the same contribution, we have  $\langle m_{\Gamma} \rangle = \langle m \rangle / D$ , with  $D = \sum_{\Gamma} d_{\Gamma}$  being the number of orbital degeneracy. In this case, the atomic level is given by

$$\varepsilon_{L\sigma} = \varepsilon_L - \frac{1}{2}\tilde{J}\langle m\rangle\sigma - h\sigma,$$
 (2.27)

and

$$\tilde{J} = \frac{1}{D}U_0 + \left(1 - \frac{1}{D}\right)J.$$
 (2.28)

We added the magnetic field h for convenience. The average electron number is then given by

$$\langle n_{L\sigma} \rangle = \int d\omega f(\omega) \rho_L \left( \omega + \frac{1}{2} \tilde{J} \langle m \rangle \sigma + h\sigma \right).$$
 (2.29)

Here  $\rho_L(\omega)$  is the DOS for orbital L per spin in the nonmagnetic state. Taking the same step as in the single band case, we obtain the uniform susceptibility as

$$\chi = \frac{2\rho(0)}{1 - \rho(0)\tilde{J}}. (2.30)$$

Here  $\rho(0) = \sum_{\Gamma} d_{\Gamma} \rho_{\Gamma}(0)$  is the DOS per atom per spin, and  $\tilde{J}$  is the effective exchange interaction given by (2.28).

When there is only one symmetry band  $\Gamma$  on the Fermi level and the other bands are below it, we have the atomic level (2.27) in which the effective exchange interaction  $\tilde{J}$  has been replaced by

$$\tilde{J} = \frac{1}{d_{\Gamma}} U_0 + \left(1 - \frac{1}{d_{\Gamma}}\right) J. \tag{2.31}$$

Therefore we have again the same form of susceptibility (2.30).

The susceptibility (2.30) indicates that the Stoner condition to the degenerateband system is given by

$$\rho(0)\,\tilde{J} > 1. \tag{2.32}$$

As seen from (2.28) and (2.31), the intraorbital Coulomb interaction  $U_0$  which is much larger than J remains in the effective exchange interaction J even in the degenerate bands system in the Hartree-Fock approximation. According to the Hartree-Fock atomic calculations, the intra- and inter-orbital Coulomb interactions in Fe are  $U_0 = 25$  eV and J = 0.9 eV, respectively [5]. Using (2.28), we obtain J = 5.8 eV. The band width of Fe is estimated from a band calculation as  $W \approx 5$  eV [17], and consequently we expect  $\rho(0) \sim 1$  assuming a rectangular DOS. Therefore we expect that  $\rho(0)\tilde{J} \sim 6$ , and the Stoner condition (2.32) explains the ferromagnetism of Fe. The same arguments are also possible for Ni. There we have  $U_0 = 28$  eV and J = 1.0 eV, respectively. Using (2.31) in this case, we obtain J=10 eV. The band width of Ni is estimated to be  $W\approx 4$  eV, and thus  $\rho(0)\sim 0.75$ assuming a rectangular DOS consisting of the  $t_{2g}$  bands at the Fermi level. We have then  $\rho(0)\tilde{J}\sim 10$ , which is consistent with the ferromagnetism in Ni. However the Stoner condition in the Hartree–Fock approximation (2.32) also predicts the ferromagnetism for the nonmagnetic transition metals. For example, in the case of Ti we have  $U_0 = 18$  eV and J = 0.6 eV, and thus we obtain  $\tilde{J} = 10$  eV using (2.28). The band width of Ti is estimated to be  $W \approx 5.5$  eV, and thus  $\rho(0) \sim 0.9$ . We have then  $\rho(0)\tilde{J} \sim 4$  for Ti, which satisfies again the Stoner condition (2.32). The inconsistency suggests strong electron correlations in transition metals, which are not described by the Hartree–Fock approximation.

#### 2.2 Electron Correlations on Magnetism

#### 2.2.1 Stoner Condition in the Correlated Electron System

The Hartree–Fock approximation used in the last section for explaining the ferromagnetism takes into account the effects of electron–electron interactions only via the Hartree–Fock potential. The fluctuations neglected in the approximation in general tend to destroy the ordered state realized by the mean-field approximation. The effects of correlated motion of electrons leading to quantum fluctuations, which are not described by the Hartree–Fock approximation, are called electron correlations.

As mentioned before in the physics of metal-insulator transition (see Sect. 1.4), electron correlations suppress electron hopping when the on-site Coulomb interaction U is large. In a simple approximation, the electron hopping energy might be renormalized as follows.

$$\left\langle \sum_{ij\sigma} t_{ij} a_{i\sigma}^{\dagger} a_{j\sigma} \right\rangle = q \left\langle \sum_{ij\sigma} t_{ij} a_{i\sigma}^{\dagger} a_{j\sigma} \right\rangle_{0}. \tag{2.33}$$

Here q is a phenomenological band-narrowing factor (<1), and  $\langle \sim \rangle_0$  denotes the Hartree–Fock average. Moreover, electron correlations reduce the double occupation number  $\langle n_\uparrow n_\perp \rangle$  on each site. We may express it as

$$\langle n_{\uparrow} n_{\downarrow} \rangle = r \langle n_{\uparrow} n_{\downarrow} \rangle_{0}. \tag{2.34}$$

Here r is a phenomenological reduction factor (<1). The total energy is then expressed as

$$E = \sum_{i} \varepsilon_{0} \langle n_{i} \rangle + q \left\langle \sum_{ij\sigma} t_{ij} a_{i\sigma}^{\dagger} a_{j\sigma} \right\rangle_{0} + r \sum_{i} U \langle n_{i\uparrow} n_{i\downarrow} \rangle_{0}.$$
 (2.35)

One can examine the stability of the ferromagnetism taking the same steps as in the Hartree–Fock approximation (see (2.1-2.5)). When there is an infinitesimal spin polarization on the Fermi level, the change in the kinetic energy  $\Delta E_1$  is given by

$$\Delta E_1 = q \frac{(\delta N)^2}{L\rho(0)} > 0. \tag{2.36}$$

On the other hand, the change in the interaction energy is given as

$$\Delta E_2 = -rLU \left(\frac{\delta N}{L}\right)^2 < 0. \tag{2.37}$$

Thus the condition (2.5) for the spin polarization ( $\Delta E = \Delta E_1 + \Delta E_2 < 0$ ) is modified as

$$\rho(0) U_{\text{eff}} > 1.$$
 (2.38)

Here  $U_{\text{eff}}$  denotes an effective Coulomb interaction defined by

$$U_{\text{eff}} = \frac{rU}{q}.\tag{2.39}$$

Needless to say, it is not possible to conclude whether or not electron correlations stabilize the ferromagnetism, without knowing the band narrowing factor q and the reduction rate of the double occupancy r. In the following subsections we introduce two types of theories of electron correlations at the ground state which provide us with the correlation factors q and r.

#### 2.2.2 Stability of Ferromagnetism in the Low Density Limit

In the low density limit, electron correlations between two particles become dominant. In this subsection, we consider the correlation energy in the two electron system, and derive the effective Coulomb interaction in the low density limit [18].

Let us adopt the single-band Hubbard model (1.51) on a lattice.

$$H = H_0 + H_{\rm I}. {(2.40)}$$

The noninteracting Hamiltonian  $H_0$  and the on-site Coulomb interaction  $H_1$  are expressed in the momentum representation as follows.

$$H_0 = \sum_{k\sigma} \varepsilon_k n_{k\sigma}, \qquad (2.41)$$

$$H_{\rm I} = \frac{U}{2L} \sum_{kk'q\sigma} a^{\dagger}_{k+q\sigma} a^{\dagger}_{k'-q-\sigma} a_{k'-\sigma} a_{k\sigma}. \tag{2.42}$$

Here  $\varepsilon_k$  is the one electron energy eigen value for the noninteracting Hamiltonian matrix  $(\boldsymbol{H}_0)_{ij} = \varepsilon_0 \delta_{ij} + t_{ij} (1 - \delta_{ij})$ , and  $n_{k\sigma}$  is the electron occupation number operator for an electron with momentum  $\boldsymbol{k}$  and spin  $\sigma$ . The creation (annihilation) operator in the momentum representation are defined by  $a_{k\sigma}^{\dagger} = \sum_i a_{i\sigma}^{\dagger} \langle k|i\rangle^* (a_{k\sigma} = \sum_i a_{i\sigma} \langle k|i\rangle)$ , where  $\langle k|i\rangle = \exp(i\boldsymbol{k} \cdot \boldsymbol{R}_i)/\sqrt{L}$ .

We now consider the two-electron state  $|k_1\sigma_1k_2\sigma_2\rangle$  in a solid such that

$$|k_1\sigma_1k_2\sigma_2\rangle = a^{\dagger}_{k_1\sigma_1}a^{\dagger}_{k_2\sigma_2}|0\rangle. \tag{2.43}$$

Note that the creation operator at the r.h.s. of the equation is ordered so that the two electron states are orthogonal to each other;  $\langle k_1 \sigma_1 k_2 \sigma_2 | k_1' \sigma_1 k_2' \sigma_2 \rangle = \delta_{k_1 k_1'} \delta_{\sigma_1 \sigma_1'} \delta_{k_2 k_2'} \delta_{\sigma_2 \sigma_2'}$ . Applying the Hamiltonian (2.40) to the two electron state, we find

$$H|k_1\sigma_1 k_2\sigma_2\rangle = (\varepsilon_{k_1} + \varepsilon_{k_2})|k_1\sigma_1 k_2\sigma_2\rangle + \frac{U}{L}\delta_{\sigma_1-\sigma_2} \sum_{q} |k_1 + q \sigma_1 k_2 - q \sigma_2\rangle.$$
 (2.44)

When  $\sigma_1 = \sigma_2$ , we have  $H_1|k_1\sigma_1 k_2\sigma_1\rangle = 0$ . Thus  $|k_1\sigma_1 k_2\sigma_1\rangle$  becomes the eigen state with no correlations.

$$H|k_1\sigma_1 k_2\sigma_1\rangle = (\varepsilon_{k_1} + \varepsilon_{k_2})|k_1\sigma_1 k_2\sigma_1\rangle. \tag{2.45}$$

The result is based on the Pauli principle that two electrons with the same spin cannot occupy the same site, so that there is no on-site Coulomb repulsion energy.

When  $\sigma_1 = -\sigma_2$ , the interaction term in (2.44) remains. In this case, we introduce the triplet and singlet states defined by

$$|k_1 k_2\rangle = \frac{1}{\sqrt{2}} (|k_1 \uparrow k_2 \downarrow\rangle \pm |k_1 \downarrow k_2 \uparrow\rangle). \tag{2.46}$$

Note that  $\{|k_1 k_2\rangle\}$  are orthogonal to each other;  $\langle k_1 k_2 | k_1' k_2' \rangle = \delta_{k_1 k_1'} \delta_{k_2 k_2'}$ . Applying the Hamiltonian (2.40) onto the state  $\{|k_1 k_2\rangle\}$  and adopting (2.44), we obtain

$$H|k_1 k_2\rangle = (\varepsilon_{k_1} + \varepsilon_{k_2})|k_1 k_2\rangle + \frac{U}{L} \sum_{q} |k_1 + q k_2 - q\rangle. \tag{2.47}$$

The above equation indicates that the singlet (triplet) state  $|k_1 k_2\rangle$  is scattered into  $\{|k_1 + q k_2 - q\rangle\}$ .

In order to solve the energy eigen value equation, we assume that the eigen state is given as

$$|\Psi\rangle = \sum_{k_1 k_2} \Gamma(k_1 k_2) |k_1 k_2\rangle.$$
 (2.48)

The eigen states are classified by the total spin states. The triplet states correspond to the ferromagnetic state, while the singlet state corresponds to the nonmagnetic state. Note that  $|k_2 k_1\rangle = \mp |k_1 k_2\rangle$ . Thus one can verify that  $\Gamma(k_2 k_1) = -\Gamma(k_1 k_2)$  for the triplet state and  $\Gamma(k_2 k_1) = \Gamma(k_1 k_2)$  for the singlet state. Substituting the wave function (2.48) into the eigen value equation

$$H|\Psi\rangle = E|\Psi\rangle,\tag{2.49}$$

we obtain

$$(\varepsilon_{k_1} + \varepsilon_{k_2} - E)\Gamma(k_1k_2) + \frac{U}{L} \sum_{q} \Gamma(k_1 + q \ k_2 - q) = 0.$$
 (2.50)

In the case of the triplet state, we can verify that  $\sum_q \Gamma(k_1+q\,k_2-q)=0$  using the relation  $\Gamma(k_2k_1)=-\Gamma(k_1k_2)$ . Thus there is no Coulomb energy contribution to the triplet state.

$$E(k_1k_2: \text{triplet}) = \varepsilon_{k_1} + \varepsilon_{k_2}. \tag{2.51}$$

Next we consider the solution for the singlet state. Starting from the singlet state  $|k_1 k_2\rangle$ , we take into account the scatterings due to Coulomb interactions. Putting  $\Gamma(k_1 k_2) = 1$  and defining the Coulomb energy contribution as

$$\Delta E(k_1 k_2) = E - \varepsilon_{k_1} - \varepsilon_{k_2}, \tag{2.52}$$

we obtain from (2.50) the following energy.

$$\Delta E(k_1 k_2) = \frac{U}{L} \left( 1 + \sum_{q}' \Gamma(k_1 + q k_2 - q) \right). \tag{2.53}$$

The equation for  $\Gamma(k_1 + q k_2 - q)$  at the r.h.s. of the above equation is obtained from (2.50) as

$$(\varepsilon_{k_1+q} + \varepsilon_{k_2-q} - E)\Gamma(k_1 + q \, k_2 - q) + \frac{U}{L} \left( 1 + \sum_{k'' \neq 0} \Gamma(k_1 + k'' \, k_2 - k'') \right) = 0.$$
(2.54)

Dividing the above equation by  $(\varepsilon_{k_1+q} + \varepsilon_{k_2-q} - E)$  and taking summation with respect to q, we obtain

$$\sum_{q}' \Gamma(k_1 + qk_2 - q) = -\frac{UG(k_1k_2)}{1 + UG(k_1k_2)},$$
(2.55)

where

$$G(k_1 k_2) = \frac{1}{L} \sum_{q} \frac{1}{\varepsilon_{k_1 + q} + \varepsilon_{k_2 - q} - \varepsilon_{k_1} - \varepsilon_{k_2} - \Delta E(k_1 k_2)}.$$
 (2.56)

Substituting (2.55) into (2.53), we obtain the interaction energy as follows.

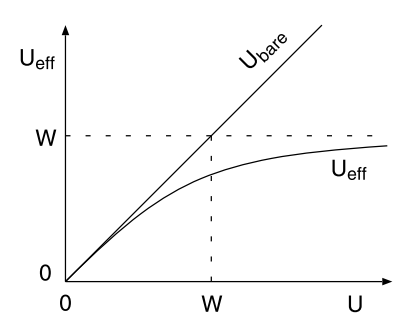
$$\Delta E(k_1 k_2) = \frac{U}{L} \frac{1}{1 + UG(k_1 k_2)}.$$
 (2.57)

Alternatively,

$$E = \varepsilon_{k_1} + \varepsilon_{k_2} + \frac{U}{L} \frac{1}{1 + UG(k_1 k_2)}.$$
 (2.58)

The above result indicates that the Coulomb interaction U has been renormalized by the electron–electron scatterings as  $U/(1+UG(k_1k_2))$ , since the Hartree–Fock energy in the singlet state is given by  $\varepsilon_{k_1} + \varepsilon_{k_2} + U/L$ . We then find the band narrowing factor q=1 and the renormalization factor of Coulomb energy  $r=1/(1+UG(k_1k_2))$ . Note that there is no band narrowing in the low density limit because there is no electron on the surrounding sites which interrupts the motion of an electron. In conclusion, multiple scatterings of two electrons yield the

Fig. 2.3 Effective Coulomb interaction  $U_{\rm eff} = U/(1+U/W)$  as a function of U, where W is the band width.  $U_{\rm bare}$  is defined by the Hartree–Fock value  $U_{\rm bare} = U$ 



following effective Coulomb interaction U.

$$U_{\text{eff}} = \frac{U}{1 + UG(k_1 k_2)}. (2.59)$$

In the quantity  $G(k_1k_2)$ , we may omit  $\Delta E(k_1k_2)$  in the denominator because  $\Delta E \sim O(1/L)$ . Moreover  $\varepsilon_{k_1+q} + \varepsilon_{k_2-q} - \varepsilon_{k_1} - \varepsilon_{k_2}$  is of order of the band width W. Thus we obtain

$$U_{\text{eff}} \approx \frac{U}{1 + \frac{U}{W}}.\tag{2.60}$$

Since  $\partial U_{\rm eff}/\partial U=1/(1+U/W)^2>0$ , the effective Coulomb interaction  $U_{\rm eff}$  monotonically increases with increasing U, but it is saturated to W as shown in Fig. 2.3. Consequently, the effective Coulomb interaction cannot exceed the band width, and the Stoner condition (2.38) is not satisfied irrespective of U for a moderate band with the band width W because  $\rho(0) \sim W$ .

$$\rho(0) U_{\text{eff}} \lesssim \frac{1}{W} \cdot W = 1. \tag{2.61}$$

The result indicates that the ferromagnetism is suppressed by electron correlations. Only for the system with large DOS at the Fermi level  $\rho(0)$ , the ferromagnetism is possible.

Nickel which has about 9 d-electrons per atom is regarded as a low density system according to the hole picture. The ferromagnetism of Ni is considered to be stabilized by this mechanism because of the high density of states at the Fermi level (see Fig. 2.6).

## 2.2.3 Gutzwiller Theory of Electron Correlations

When electron number is increased, one cannot apply the low density approximation. In this subsection, we introduce the Gutzwiller variational method for electron correlations at the ground state [6–8], which is useful for any electron density.

The Hartree-Fock ground state is expressed by an independent particle state as follows.

$$|\phi\rangle = \left(\prod_{k}^{N_{\uparrow}} a_{k\uparrow}^{\dagger}\right) \left(\prod_{k}^{N_{\downarrow}} a_{k\downarrow}^{\dagger}\right) |0\rangle. \tag{2.62}$$

Here  $N_{\sigma}$  denotes the total electron number for spin  $\sigma$ . Making use of a unitary transformation such as  $a_{k\sigma}^{\dagger} = \sum_{i} a_{i\sigma}^{\dagger} \mathrm{e}^{ikR_{i}}/\sqrt{L}$ , we obtain the wavefunction in the real space representation as follows.

$$|\phi\rangle = \sum_{C(N_{\uparrow}, N_{\downarrow})} \det\left(\frac{1}{\sqrt{L}} e^{i\mathbf{k}_{i} \cdot \mathbf{R}_{l(j)}}\right) \det\left(\frac{1}{\sqrt{L}} e^{i\mathbf{k}_{i} \cdot \mathbf{R}_{m(j)}}\right) \left(\prod_{i}^{N_{\uparrow}} a_{l(i)\uparrow}^{\dagger}\right) \left(\prod_{i}^{N_{\downarrow}} a_{m(i)\downarrow}^{\dagger}\right) |0\rangle.$$
(2.63)

Here L denotes the number of lattice.  $k_i$  is a momentum of the i-th electron below the Fermi level. A set of sites  $(l(1), l(2), \ldots, l(N_{\uparrow}))$   $((m(1), m(2), \ldots, m(N_{\downarrow})))$  denote a configuration of electrons with up (down) spin on the lattice, and  $(R_{l(1)}, R_{l(2)}, \ldots, R_{l(N_{\uparrow})})$  denote the positions of the sites. The determinants are defined for the matrices whose (i, j) element is given by  $(1/\sqrt{L}) \exp(ik_i \cdot R_{l(j)})$  and  $(1/\sqrt{L}) \exp(ik_i \cdot R_{m(j)})$ , respectively. Furthermore,  $\sum_{C(N_{\uparrow}, N_{\downarrow})}$  means the sum over all the configurations of electrons on a lattice when electron numbers of up and down spins are given. It should be noted that the  $\{l(i)\}$   $(\{m(i)\})$  are ordered as  $l(1) < l(2) < \cdots < l(N_{\uparrow})$   $(m(1) < m(2) < \cdots < m(N_{\uparrow}))$  in the Fock space.

In the Hartree–Fock wavefunction, doubly occupied sites appear irrespective of the Coulomb interaction strength U in various electron configurations on a lattice. Such a state with doubly occupied sites causes a loss of Coulomb interaction energy. In the correlated electron system, the probability amplitudes of doubly occupied states must be reduced to decrease the total energy. In order to describe the on-site electron correlations, Gutzwiller introduced a correlated wavefunction as follows.

$$|\Psi\rangle = \left[\prod_{i}^{L} \left(1 - (1 - g)n_{i\uparrow}n_{i\downarrow}\right)\right] |\phi\rangle. \tag{2.64}$$

Here  $n_{i\uparrow}n_{i\downarrow}$  is a projection operator that chooses the doubly occupied state on site i, and g is a variational parameter controlling the amplitudes of doubly occupied states in the Hartree–Fock wavefunction. Note that the g=1 state corresponds to an uncorrelated state, and the g=0 state corresponds to the atomic state in which all the doubly occupied states have been removed.

Substituting (2.63) into the Gutzwiller wave function (2.64), we obtain the real-space representation as follows.

$$|\Psi\rangle = \sum_{D} g^{D} \sum_{C(D, N_{\uparrow}, N_{\downarrow})} \det\left(\frac{1}{\sqrt{L}} e^{i\mathbf{k}_{i} \cdot \mathbf{R}_{l(j)}}\right) \det\left(\frac{1}{\sqrt{L}} e^{i\mathbf{k}_{i} \cdot \mathbf{R}_{m(j)}}\right) \left(\prod_{i}^{N_{\uparrow}} a_{l(i)\uparrow}^{\dagger}\right) \times \left(\prod_{i}^{N_{\downarrow}} a_{m(i)\downarrow}^{\dagger}\right) |0\rangle.$$
(2.65)

Here D is the number of doubly occupied sites, and  $C(D, N_{\uparrow}, N_{\downarrow})$  denotes the electron configurations on a lattice when  $D, N_{\uparrow}$ , and  $N_{\downarrow}$  are given.

The energy for the Hubbard Hamiltonian (1.51) with  $\varepsilon_0 = 0$  is then given as follows.

$$E(g) = \frac{\sum_{ij\sigma} t_{ij} \langle \Psi | a_{i\sigma}^{\dagger} a_{j\sigma} | \Psi \rangle + U \langle \Psi | \sum_{i} n_{i\uparrow} n_{i\downarrow} | \Psi \rangle}{\langle \Psi | \Psi \rangle}.$$
 (2.66)

Each term at the r.h.s. is given as follows.

$$\langle \Psi | \Psi \rangle = \sum_{D} g^{2D} \sum_{C(D, N_{\uparrow}, N_{\downarrow})} \left( w_{\uparrow} (R - R') \begin{vmatrix} R_{l(1)} & R_{l(2)} & \cdots & R_{l(N_{\uparrow})} \\ R_{l(1)} & R_{l(2)} & \cdots & R_{l(N_{\uparrow})} \end{vmatrix} \right) \\
\times \left( w_{\downarrow} (R - R') \begin{vmatrix} R_{m(1)} & R_{m(2)} & \cdots & R_{m(N_{\downarrow})} \\ R_{m(1)} & R_{m(2)} & \cdots & R_{m(N_{\downarrow})} \end{vmatrix} \right), \qquad (2.67)$$

$$\left\langle \Psi \middle| \sum_{i} n_{i\uparrow} n_{i\downarrow} \middle| \Psi \middle\rangle \\
= \sum_{D} D g^{2D} \sum_{C(D, N_{\uparrow}, N_{\downarrow})} \left( w_{\uparrow} (R - R') \middle| R_{l(1)} & R_{l(2)} & \cdots & R_{l(N_{\uparrow})} \\ R_{l(1)} & R_{l(2)} & \cdots & R_{l(N_{\uparrow})} \end{pmatrix} \right) \\
\times \left( w_{\downarrow} (R - R') \middle| R_{m(1)} & R_{m(2)} & \cdots & R_{m(N_{\downarrow})} \\ R_{m(1)} & R_{m(2)} & \cdots & R_{m(N_{\downarrow})} \right). \qquad (2.68)$$

Here the function  $w_{\sigma}(R - R')$  is defined by

$$w_{\sigma}(R - R') = \frac{1}{L} \sum_{k}^{N_{\sigma}} e^{ik_{n} \cdot (R - R')}.$$
 (2.69)

The Gutzwiller overlap function with  $w_{\sigma}(R-R')$  in (2.67) and (2.68) is defined by

$$\begin{pmatrix} f(x,y) \middle| x_1 & x_2 & \cdots & x_n \\ y_1 & y_2 & \cdots & y_n \end{pmatrix} = \begin{vmatrix} f(x_1,y_1) & f(x_1,y_2) & \cdots & f(x_1,y_n) \\ f(x_2,y_1) & f(x_2,y_2) & \cdots & f(x_2,y_n) \\ \cdots & \cdots & \cdots & \cdots \\ f(x_n,y_1) & f(x_n,y_2) & \cdots & f(x_n,y_n) \end{vmatrix} .$$
(2.70)

In order to calculate the electron hopping term in the numerator of (2.66), we classify the configuration  $C(D, N_{\uparrow}, N_{\downarrow})$  into 4 parts according to the 4 electron

configurations on sites i and j;  $C(D, N_{\uparrow}, N_{\downarrow}, i \uparrow = j \uparrow = 0)$ ,  $C(D, N_{\uparrow}, N_{\downarrow}, i \uparrow = 0, j \uparrow = 1)$ ,  $C(D, N_{\uparrow}, N_{\downarrow}, i \uparrow = 1, j \uparrow = 0)$ , and  $C(D, N_{\uparrow}, N_{\downarrow}, i \uparrow = j \uparrow = 1)$ . When the electron hopping operator  $a^{\dagger}_{i \uparrow} a_{j \uparrow}$  is applied to  $\Psi$ , the configuration  $C(D, N_{\uparrow}, N_{\downarrow}, i \uparrow = 0, j \uparrow = 1)$  remains among 4 types of configurations. The number of doubly occupied states in each configuration of  $a^{\dagger}_{i \uparrow} a_{j \uparrow} | \Psi \rangle$  can changes from D according to the configuration of the down spin electrons on sites i and j. When we express the configuration as  $(i, j) = \binom{i \uparrow}{i \downarrow} j \downarrow$ , the number of the doubly occupied states of  $a^{\dagger}_{i \uparrow} a_{j \uparrow} | \Psi \rangle$  is given by D for  $(i, j) = \binom{0 \ 1}{0 \ 0}$ , D - 1 for  $(i, j) = \binom{0 \ 1}{0 \ 1}$ , D + 1 for  $(i, j) = \binom{0 \ 1}{1 \ 0}$ , and D for  $(i, j) = \binom{0 \ 1}{1 \ 1}$ . We therefore obtain

$$\begin{aligned}
\langle \Psi | a_{i\uparrow}^{\dagger} a_{j\uparrow} | \Psi \rangle \\
&= \left[ \sum_{D} g^{2D} \sum_{C(D, N_{\uparrow}, N_{\downarrow}, (i,j) = \begin{pmatrix} 0 & 1 \\ 0 & 0 \end{pmatrix})} + \sum_{D} g^{2D-1} \sum_{C(D, N_{\uparrow}, N_{\downarrow}, (i,j) = \begin{pmatrix} 0 & 1 \\ 0 & 1 \end{pmatrix})} \right. \\
&+ \sum_{D} g^{2D+1} \sum_{C(D, N_{\uparrow}, N_{\downarrow}, (i,j) = \begin{pmatrix} 0 & 1 \\ 1 & 0 \end{pmatrix})} + \sum_{D} g^{2D} \sum_{C(D, N_{\uparrow}, N_{\downarrow}, (i,j) = \begin{pmatrix} 0 & 1 \\ 1 & 1 \end{pmatrix})} \right] \\
&\times \left( w_{\uparrow} (R - R') \middle| R_{i} R_{l(1)} \cdots R_{l(N_{\uparrow})} \right. \\
&\times \left. \left( w_{\downarrow} (R - R') \middle| R_{m(1)} R_{m(2)} \cdots R_{m(N_{\downarrow})} \right) \right. \\
&\times \left( w_{\downarrow} (R - R') \middle| R_{m(1)} R_{m(2)} \cdots R_{m(N_{\downarrow})} \right). 
\end{aligned} (2.71)$$

The configuration in the above expression (2.71), for example,  $C(D, N_{\uparrow}, N_{\downarrow}, (i, j)) = \binom{0}{0} \binom{0}{0}$  means the electron configuration when  $D, N_{\uparrow}$ , and  $N_{\downarrow}$  are given, and there is no electron on site i, but site j is occupied by an up-spin electron.

The difficulty in the Gutzwiller variational method is how to take the sums with respect to the electron configurations in each term of the energy containing the overlap functions of  $w_{\sigma}(R-R')$ . Gutzwiller replaced these overlap functions with their average values. This is called the Gutzwiller approximation. For example, in the calculation of the norm  $\langle \Psi | \Psi \rangle$ , we make the following approximation.

$$\langle \Psi | \Psi \rangle \approx \sum_{D} g^{2D} \sum_{C(D,N_{\uparrow},N_{\downarrow})} \left[ \frac{1}{(\sum_{D} \sum_{C(D,N_{\uparrow},N_{\downarrow})})} \sum_{D} \sum_{C(D,N_{\uparrow},N_{\downarrow})} \right] \times \left( w_{\uparrow} (R - R') \begin{vmatrix} R_{l(1)} & R_{l(2)} & \cdots & R_{l(N_{\uparrow})} \\ R_{l(1)} & R_{l(2)} & \cdots & R_{l(N_{\uparrow})} \end{pmatrix} \right) \times \left( w_{\downarrow} (R - R') \begin{vmatrix} R_{m(1)} & R_{m(2)} & \cdots & R_{m(N_{\downarrow})} \\ R_{m(1)} & R_{m(2)} & \cdots & R_{m(N_{\downarrow})} \end{pmatrix} \right).$$
 (2.72)

We then obtain

$$\langle \Psi | \Psi \rangle \approx \frac{W_0(g)}{W_0(1)} \langle \phi | \phi \rangle.$$
 (2.73)

Here  $\langle \phi | \phi \rangle = 1$ .  $W_0(g)$  is a sum over all configurations of correlation weight  $g^{2D}$  for double occupation number. It is defined by

$$W_0(g) = \sum_{D} \sum_{C(D, N_{\uparrow}, N_{\downarrow})} g^{2D}.$$
 (2.74)

In the same way, we obtain

$$\langle \Psi | a_{i\uparrow}^{\dagger} a_{j\uparrow} | \Psi \rangle \approx \frac{W_{1\uparrow}(g)}{W_{1\uparrow}(1)} \langle \phi | a_{i\uparrow}^{\dagger} a_{j\uparrow} | \phi \rangle,$$
 (2.75)

$$\langle \Psi | n_{i\uparrow} n_{i\downarrow} | \Psi \rangle \approx \frac{W_{2\uparrow}(g)}{W_{2\uparrow}(1)} \langle \phi | n_{i\uparrow} n_{i\downarrow} | \phi \rangle.$$
 (2.76)

Here

$$W_{1\uparrow}(g) = \sum_{D} \sum_{C(D, N_{\uparrow}, N_{\downarrow}, (i, j) = \binom{0}{0} \binom{1}{0})} g^{2D} + \sum_{D} \sum_{C(D, N_{\uparrow}, N_{\downarrow}, (i, j) = \binom{0}{0} \binom{1}{1})} g^{2D-1} + \sum_{D} \sum_{C(D, N_{\uparrow}, N_{\downarrow}, (i, j) = \binom{0}{0} \binom{1}{1})} g^{2D},$$

$$(2.77)$$

$$W_2(g) = \sum_{D} \sum_{C(D, N_{\uparrow}, N_{\downarrow})} D g^{2D}.$$
 (2.78)

The weighting functions  $W_0(g)$ ,  $W_1(g)$ , and  $W_2(g)$  are expressed by the following type of the hypergeometric functions.

$$F(\alpha - N_{\uparrow}, \beta - N_{\downarrow}, L - N + \gamma; g^{2})$$

$$= \sum_{D=0}^{\infty} \frac{(L - N + \gamma - 1)!(\alpha - N_{\uparrow} + D - 1)!(\beta - N_{\downarrow} + D - 1)!g^{2D}}{D!(L - N + \gamma + D - 1)!(\alpha - N_{\uparrow} - 1)!(\beta - N_{\downarrow} - 1)!}. (2.79)$$

Here N is the total number of electrons.  $\alpha$ ,  $\beta$ , and  $\gamma$  are integers of order of 1. In the evaluation of the sums over D in these functions, we can adopt the maximum term approximation because D is a macroscopic variable. The weights for each D term is proportional to

$$\frac{(\alpha - N_{\uparrow} + D - 1)!(\beta - N_{\downarrow} + D - 1)!g^{2D}}{D!(L - N + \nu + D - 1)!}.$$
 (2.80)

The representative value of D that maximizes the above factor is given by

$$g^{2} = \frac{D(L - N_{\uparrow} + D)}{(N_{\uparrow} - D)(N_{\downarrow} - D)}.$$
 (2.81)

By making use of the representative value D, we can express the total energy as follows.

$$E(g) = \sum_{\sigma} q_{\sigma} \left( \sum_{k}^{N_{\sigma}} \varepsilon_{k} \right) + UD. \tag{2.82}$$

Here the band narrowing factor  $q_{\sigma}$  is given as

$$q_{\sigma} = \frac{\left(\sqrt{(N_{\sigma} - D)(L - N + D)} + \sqrt{D(N_{-\sigma} - D)}\right)^{2}}{N_{\sigma}(L - N_{\sigma})}.$$
 (2.83)

In the nonmagnetic state at half-filling (N = L), the energy per site is simplified as follows.

$$\varepsilon(g) = -q|\varepsilon_{\mathbf{b}}| + Ud. \tag{2.84}$$

Here

$$q = 16\left(\frac{1}{2} - d\right)d,\tag{2.85}$$

$$g = \frac{d}{\frac{1}{2} - d},\tag{2.86}$$

and d=D/L denotes the double occupation number per site.  $\varepsilon_b$  is the band energy per site, and is given by the noninteracting density of states per atom and per spin  $\rho(\varepsilon) = L^{-1} \sum_k \delta(\varepsilon - \varepsilon_k)$  as follows.

$$\varepsilon_{\rm b} = 2 \int_{-\infty}^{0} \varepsilon \rho(\varepsilon) \, d\varepsilon. \tag{2.87}$$

Minimizing the energy (2.84) with respect to g (i.e., d), we obtain

$$q = 1 - \frac{U^2}{U_c^2},\tag{2.88}$$

$$d = \frac{1}{4} \left( 1 - \frac{U}{U_{\rm c}} \right),\tag{2.89}$$

and

$$g = \frac{1 - \frac{U}{U_{\rm c}}}{1 + \frac{U}{U_{\rm c}}}. (2.90)$$

Here  $U_c = 8|\varepsilon_b|$  is a critical Coulomb interaction at which q and d vanish. The ground-state energy is given by

$$\varepsilon(g) = -\frac{1}{8}U_{\rm c}\left(1 - \frac{U}{U_{\rm c}}\right)^2. \tag{2.91}$$

When  $U > U_c$ , there is another solution: g = 0 or d = 0 which yields the minimum energy  $\varepsilon(g) = 0$ . Note that electrons are completely localized at  $U = U_c$ ; q = d = 0. This implies that the metal-insulator transition occurs at  $U = U_c$ .

Equation (2.89) means that the rate of double occupation  $r = d/(\langle n_{\uparrow} \rangle_0 \langle n_{\downarrow} \rangle_0)$  is given by

$$r = 1 - \frac{U}{U_c}. (2.92)$$

By making use of (2.88) and (2.92), we obtain the effective Coulomb interaction for the ferromagnetic instability which is defined by (2.39), i.e.,  $U_{\text{eff}} = rU/q$ .

$$U_{\text{eff}} = \frac{U}{1 + \frac{U}{U_c}}.\tag{2.93}$$

Since  $U_c = 2W$  for the rectangular DOS with the band width W, the expression above is essentially the same as the effective Coulomb interaction (2.60) in the low density approximation. We therefore again find that the electron correlations suppress the ferromagnetism in the case of usual electron density as well.

In the above analysis, we omitted the polarization via  $q_{\sigma}$  and r. More detailed calculations of spin susceptibility yield [19]

$$\chi = \frac{2\rho(0)\frac{m^*}{m_e}}{1 - \rho(0)\tilde{U}_{\text{eff}}}.$$
 (2.94)

Here  $m^*/m_e = q^{-1}$  is the effective mass of electrons and  $\tilde{U}_{\rm eff}$  is defined by

$$\tilde{U}_{\text{eff}} = \frac{U\left(1 + \frac{U}{2U_{c}}\right)}{\left(1 + \frac{U}{U_{c}}\right)^{2}} \approx \frac{U}{1 + \frac{U}{U_{c}}}.$$
(2.95)

Note that the susceptibility diverges at the metal-insulator point  $U = U_c$  via effective mass due to the formation of the atomic state with spin s = 1/2 in the Gutzwiller approximation. The effective Coulomb interaction  $\tilde{U}_{\rm eff}$  is associated with the formation of the ferromagnetism via the denominator in (2.94), and is essentially the same as  $U_{\rm eff}$  given by (2.93).

The theory mentioned above is based on the single band model. More realistic calculations on the stability of the ferromagnetism have been made on the basis of the five d band model and the local ansatz variational method; the latter takes into account the on-site Hund's rule correlations as well as the density correlations [20]. The degeneracy of the bands in general increases the channel of electron hopping, so that the correlation effects tend to be reduced. The effective Coulomb interac-

tions for the stability of the ferromagnetism are typically reduced by 30–40 % as compared with the bare values in the case of 3d transition metals. One of the important results of the theory is that the energy difference between the ferromagnetic state and the nonmagnetic state is much reduced by electron correlations. In case of Fe, for example, the difference is 0.56 eV per atom in the Hartree–Fock theory, reduced to 0.22 eV when the density correlations are taken into account, and reduced even further to 0.15 eV when both density and spin correlations are taken into account [21].

#### 2.3 Density Functional Approach

#### 2.3.1 Slater's Band Theory

Towards a realistic description of magnetic properties in metals and alloys, it is desirable to calculate one electron state in solids quantitatively. A reasonable one electron state may be the Hartree–Fock wave function. As we have mentioned in Sect. 1.3, the wavefunctions are determined by the following Hartree–Fock self-consistent equation at the ground state.

$$\left(-\frac{1}{2}\nabla^{2} + v_{N}(\mathbf{r}) + \int d\mathbf{r}' \frac{n(\mathbf{r}')}{|\mathbf{r} - \mathbf{r}'|}\right) \varphi_{i\sigma}(\mathbf{r}) 
- \sum_{i}^{\text{occ}} \int d\mathbf{r}' \frac{\varphi_{j\sigma}^{*}(\mathbf{r}')\varphi_{i\sigma}(\mathbf{r}')}{|\mathbf{r} - \mathbf{r}'|} \varphi_{j\sigma}(\mathbf{r}) = \varepsilon_{i\sigma}\varphi_{i\sigma}(\mathbf{r}).$$
(2.96)

Here  $\varepsilon_{i\sigma}$  is the Hartree–Fock one-electron energy eigen value.  $\sum_{j}^{\text{occ}}$  denotes a summation over occupied Hartree–Fock orbital  $\{j\}$ , and  $n(\mathbf{r}) = \sum_{j\sigma}^{\text{occ}} \varphi_{j\sigma}^*(\mathbf{r}) \varphi_{j\sigma}(\mathbf{r})$  denotes a charge density in the Hartree–Fock approximation. The third term at the l.h.s. expresses the electrostatic potential due to electrons. The last term called the exchange potential originates in the Coulomb interaction and the anti-symmetric property of the Slater determinant. The Hartree–Fock total energy is given by

$$\langle H_{\rm HF} \rangle = \sum_{i\sigma}^{\rm occ} \varepsilon_{i\sigma} - \frac{1}{2} \sum_{ij\sigma\sigma'} (V_{ijji} - V_{ijij} \delta_{\sigma\sigma'}) \langle n_{i\sigma} \rangle \langle n_{j\sigma'} \rangle. \tag{2.97}$$

Here  $V_{iji}$  ( $V_{iji}$ ) is the Coulomb (exchange) energy integral.

Because of the exchange potential, the self-consistent equation is non-linear, so that it is not easy to solve the equation in solids. In order to simplify the exchange term, Slater rewrote it as

$$-\sum_{j}^{\text{occ}} \int d\mathbf{r}' \frac{\varphi_{j\sigma}^{*}(\mathbf{r}')\varphi_{i\sigma}(\mathbf{r}')}{|\mathbf{r} - \mathbf{r}'|} \varphi_{j\sigma}(\mathbf{r})$$

$$= -\left[\sum_{i}^{\text{occ}} \int d\mathbf{r}' \frac{\varphi_{j\sigma}^{*}(\mathbf{r}')\varphi_{i\sigma}(\mathbf{r}')\varphi_{i\sigma}^{*}(\mathbf{r})\varphi_{j\sigma}(\mathbf{r})}{\varphi_{i\sigma}^{*}(\mathbf{r})\varphi_{i\sigma}(\mathbf{r})|\mathbf{r} - \mathbf{r}'|}\right] \varphi_{i\sigma}(\mathbf{r}). \tag{2.98}$$

The term [ $\sim$ ] at the r.h.s. of the above equation is regarded as an effective potential. Slater [4] took an average of the effective potential with respect to the orbital i with a weight  $\varphi_{i\sigma}^*(\mathbf{r})\varphi_{i\sigma}(\mathbf{r})/(\sum_{l}^{\text{occ}}\varphi_{l\sigma}^*(\mathbf{r})\varphi_{l\sigma}(\mathbf{r}))$ , so that the exchange term is written as

$$-\sum_{i}^{\text{occ}} \int d\mathbf{r}' \frac{\varphi_{j\sigma}^{*}(\mathbf{r}')\varphi_{i\sigma}(\mathbf{r}')}{|\mathbf{r} - \mathbf{r}'|} \varphi_{j\sigma}(\mathbf{r}) \approx -\int d\mathbf{r}' \frac{\tilde{n}_{\text{ex}\sigma}(\mathbf{r}, \mathbf{r}')}{|\mathbf{r} - \mathbf{r}'|} \varphi_{i\sigma}(\mathbf{r}), \qquad (2.99)$$

$$\tilde{n}_{\text{ex}\,\sigma}(\mathbf{r},\mathbf{r}') = \frac{\sum_{i}^{\text{occ}} \sum_{j}^{\text{occ}} \varphi_{i\sigma}^{*}(\mathbf{r}') \varphi_{j\sigma}(\mathbf{r}') \varphi_{j\sigma}^{*}(\mathbf{r}) \varphi_{i\sigma}(\mathbf{r})}{\sum_{j}^{\text{occ}} \varphi_{i\sigma}^{*}(\mathbf{r}) \varphi_{j\sigma}(\mathbf{r})}.$$
(2.100)

The Hartree-Fock equation is then reduced to a linear equation as follows.

$$\left(-\frac{1}{2}\nabla^{2}+v_{N}(\mathbf{r})+\int d\mathbf{r}'\frac{\langle n(\mathbf{r}')\rangle}{|\mathbf{r}-\mathbf{r}'|}+v_{\mathrm{ex}\,\sigma}^{(\mathrm{HFS})}(\mathbf{r})\right)\varphi_{i\sigma}(\mathbf{r})=\varepsilon_{i\sigma}\varphi_{i\sigma}(\mathbf{r}). (2.101)$$

Here  $v_{\mathrm{ex}\,\sigma}^{\mathrm{(HFS)}}(\mathbf{r})$  is the Hartree–Fock–Slater exchange potential defined by

$$v_{\text{ex}\,\sigma}^{\text{(HFS)}}(\mathbf{r}) = -\int d\mathbf{r}' \frac{\tilde{n}_{\text{ex}\,\sigma}(\mathbf{r},\mathbf{r}')}{|\mathbf{r}-\mathbf{r}'|}.$$
 (2.102)

Slater simplified further the potential by using the free electron wave functions as follows [4].

$$v_{\text{ex}\,\sigma}(\mathbf{r}) = -3\left(\frac{3}{4\pi}\right)^{1/3} n_{\sigma}(\mathbf{r})^{1/3},$$
 (2.103)

where  $n_{\sigma}(\mathbf{r})$  is the electron density for spin  $\sigma$ . For more practical use, Slater proposed the following potential with an adjustable parameter  $\alpha$ .

$$v_{\mathbf{X}\alpha\,\sigma}(\mathbf{r}) = -3\alpha \left(\frac{3}{4\pi}\right)^{1/3} n_{\sigma}(\mathbf{r})^{1/3}.\tag{2.104}$$

This is known as the  $X\alpha$  potential. Numerical calculations suggest that  $\alpha = 1/2-2/3$  is suitable for explaining various experiments.

## 2.3.2 Density Functional Theory

As discussed before, the orthodox approach to the electronic structure and magnetism in solids may be to first apply the Hartree–Fock theory leading to the best one electron wavefunction at the ground state, and then taking into account the correlation corrections. This scheme however seems to be inconvenient for quantitative calculations, firstly because the Hartree–Fock equation is too complicated due to nonlinear exchange potentials, secondly because the Hartree–Fock approximation

is not necessarily a good starting point to describe the magnetism as mentioned before in Sect. 2.2.

We have discussed a simplified Hartree–Fock–Slater potential for practical use of the Hartree–Fock approach in the last subsection. Kohn, Sham, and Hohenberg proposed the density functional theory (DFT) which justifies Slater's idea for the exchange potential [22–25]. The theory allows us to include electron correlations in solids in a simple manner.

The DFT is based on the Hohenberg–Kohn theorem [22, 24]. It states that the ground state energy  $E_0$  is given by the minimization of a density functional E[n]:

$$E_0 \leqslant E[n],\tag{2.105}$$

$$E[n] = F[n] + \int v_{\text{ext}}(\mathbf{r})n(\mathbf{r}) d\mathbf{r}, \qquad (2.106)$$

$$F[n] = \langle \Psi_n^{\min} | (\hat{T} + \hat{V}_{ee}) | \Psi_n^{\min} \rangle, \tag{2.107}$$

$$v_{\text{ext}}(\mathbf{r}) = -\sum_{l} \frac{Z_l}{|\mathbf{r} - \mathbf{R}_l|}.$$
 (2.108)

Here  $n(\mathbf{r})$  is an electron density.  $\hat{T}$  ( $\hat{V}_{\text{ee}}$ ) is the kinetic energy (electron-electron interactions).  $\Psi_n^{\min}$  is the wave function that minimizes the energy under a given density  $n(\mathbf{r})$ , and  $v_{\text{ext}}(\mathbf{r})$  is the electron-nuclear interaction as an external field. Note that the energy of the electron system F[n] is a universal functional which does not depend on  $v_{\text{ext}}(\mathbf{r})$ .

In order to verify the inequality in (2.105), let us express the ground state energy as

$$E_0 = \operatorname{Min}_{\{\Psi\}} \left( \left\langle \Psi \left| (\hat{T} + \hat{V}_{ee}) \right| \Psi \right\rangle + \int v_{ext}(\boldsymbol{r}) n(\boldsymbol{r}) d\boldsymbol{r} \right). \tag{2.109}$$

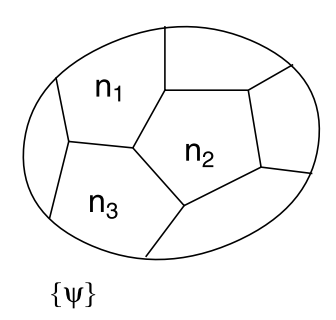
Here  $\operatorname{Min}_{\{\Psi\}}$  means to choose from possible Fermion wave functions  $\{\Psi\}$ , the ground-state wavefunction that minimizes the total energy. When the N electron Hilbert space is partitioned by the wave functions with the same density n, the above expression is written as follows (see Fig. 2.4).

$$E_0 = \operatorname{Min}_{\{n\}} \left( \operatorname{Min}_{\{\Psi \mid n\}} \langle \Psi \mid (\hat{T} + \hat{V}_{ee}) \mid \Psi \rangle + \int v_{\text{ext}}(\mathbf{r}) n(\mathbf{r}) d\mathbf{r} \right). \quad (2.110)$$

The notation  $\min_{\{\Psi|n\}}$  means to minimize the following term by choosing a wavefunction among those which yield the same density n. The first term at the r.h.s. of (2.110) is given by F[n], which is defined by (2.107), thus the above equation leads to the inequality (2.105).

Kohn and Sham [23] assumed that the many-body electron density is reproduced by the density of noninteracting electrons with an effective potential v(r), and wrote

**Fig. 2.4** The *N* electron Hilbert space is partitioned by the wave functions with the same density *n* 



the energy F[n] as follows.

$$F[n] = T_s[n] + \frac{1}{2} \int \frac{n(\mathbf{r})n(\mathbf{r}')}{|\mathbf{r} - \mathbf{r}'|} d\mathbf{r} d\mathbf{r}' + E_{XC}[n].$$
 (2.111)

The first term  $T_s[n]$  at the r.h.s. is a kinetic energy for a noninteracting system

$$T_s[n] = \sum_{i}^{\text{occ}} \left\langle \psi_i \left| \left( -\frac{1}{2} \nabla^2 \right) \right| \psi_i \right\rangle = \sum_{i}^{\text{occ}} \varepsilon_i - \int v(\mathbf{r}) n(\mathbf{r}) \, d\mathbf{r}.$$
 (2.112)

Here  $n(\mathbf{r}) = \sum_{i}^{\text{occ}} |\psi_i(\mathbf{r})|^2$  is a density of noninteracting electrons, and  $\psi_i(\mathbf{r})$  is a one-electron eigen function for the eigen value  $\varepsilon_i$ .

$$\left(-\frac{1}{2}\nabla^2 + v(\mathbf{r})\right)\psi_i(\mathbf{r}) = \varepsilon_i\psi_i(\mathbf{r}). \tag{2.113}$$

It should be noted that the kinetic energy  $T_s[n]$  is not identical with  $T[n] = \langle \Psi | \hat{T} | \Psi \rangle$ ;  $T_s[n] - T[n]$  has been included in the exchange correlation energy  $E_{\rm XC}[n]$ . The electron number is given by

$$\int n(\mathbf{r}) d\mathbf{r} = N. \tag{2.114}$$

When the universal functional  $E_{XC}[n]$  is assumed to be known, one can determine the effective potential v(r) from the variational principle.

$$\delta(E[n] - \mu N) = 0, \tag{2.115}$$

where  $\mu$  is the chemical potential. Substituting (2.106) and (2.111) into the above equation and taking the variation, we obtain

$$v(r) = v_{\text{ext}}(r) + \int \frac{n(r') dr}{|r - r'|} + v_{\text{xc}}(r) - \mu,$$
 (2.116)

and the exchange-correlation potential  $v_{xc}(\mathbf{r})$  is defined by

$$v_{\rm xc}(\mathbf{r}) = \frac{\delta E_{\rm XC}}{\delta n(\mathbf{r})}.$$
 (2.117)

Equations (2.113) and (2.116) are referred as the Kohn–Sham equations. Using (2.116), the total energy is given by

$$E[n] = \sum_{i}^{\text{occ}} \varepsilon_{i} - \frac{1}{2} \int \frac{n(\mathbf{r})n(\mathbf{r}')}{|\mathbf{r} - \mathbf{r}'|} d\mathbf{r} d\mathbf{r}' + E_{\text{XC}}[n] - \int v_{\text{xc}}(\mathbf{r})n(\mathbf{r}) d\mathbf{r} + \mu N.$$
(2.118)

The Kohn–Sham theory provides us with a method to calculate the density and the total energy of correlated electron system by solving one-electron Schrödinger equation once we know a universal exchange-correlation energy  $E_{\rm XC}[n]$ .

The Hohenberg-Kohn-Sham method can be extended to the spin polarized case. In this case, we introduce a magnetic field H(r) coupled to the spin density m(r). The energy becomes a functional of the charge and spin densities: E[n, m], and

$$E_0 \leqslant E[n, \mathbf{m}],\tag{2.119}$$

$$E[n, \mathbf{m}] = F[n, \mathbf{m}] + \int (v_{\text{ext}}(\mathbf{r})n(\mathbf{r}) - \mathbf{m}(\mathbf{r}) \cdot \mathbf{H}(\mathbf{r})) d\mathbf{r}.$$
 (2.120)

The universal functional F[n, m] in the Kohn–Sham method is expressed as

$$F[n, m] = T_s[n, m] + \frac{1}{2} \int \frac{n(r)n(r')}{|r - r'|} dr dr' + E_{XC}[n, m].$$
 (2.121)

Introducing the wave function  $\psi_k(r) = (\psi_{k\uparrow}(r), \psi_{k\downarrow}(r))$  and the spin dependent potential  $\Delta(r) = (\Delta_x(r), \Delta_y(r), \Delta_z(r))$ , the Kohn–Sham one-electron eigen value equation is given by

$$\left(-\frac{1}{2}\nabla^2 + v(\mathbf{r}) - \mathbf{\Delta}(\mathbf{r}) \cdot \mathbf{\sigma}\right) \psi_k(\mathbf{r}) = \varepsilon_k \psi_k(\mathbf{r}). \tag{2.122}$$

The charge and spin densities are obtained by  $n(\mathbf{r}) = \sum_{k\sigma}^{\text{occ}} |\psi_{k\sigma}(\mathbf{r})|^2$  and  $\mathbf{m}(\mathbf{r}) = \sum_{k\sigma\sigma'}^{\text{occ}} \psi_{k\sigma}^*(\mathbf{r})(\sigma)_{\sigma\sigma'}\psi_{k\sigma'}(\mathbf{r})$ , respectively. The potentials obtained by the variational principles are given by (2.116) and

$$\Delta(r) = \Delta_{xc}(r) + H(r). \tag{2.123}$$

The exchange correlation potentials  $v_{xc}(\mathbf{r})$  and  $\boldsymbol{\Delta}_{xc}(\mathbf{r})$  are defined by

$$v_{\rm xc}(\mathbf{r}) = \frac{\delta E_{\rm XC}[n, \mathbf{m}]}{\delta n(\mathbf{r})}, \qquad \mathbf{\Delta}_{\rm xc}(\mathbf{r}) = \frac{\delta E_{\rm XC}[n, \mathbf{m}]}{\delta \mathbf{m}(\mathbf{r})}. \tag{2.124}$$

The ground-state energy in the Kohn–Sham scheme is then given by

$$E[n, \mathbf{m}] = \sum_{k}^{\text{occ}} \varepsilon_{k} - \frac{1}{2} \int \frac{n(\mathbf{r})n(\mathbf{r}')}{|\mathbf{r} - \mathbf{r}'|} d\mathbf{r} d\mathbf{r}' + E_{\text{XC}}[n, \mathbf{m}]$$
$$- \int \left(v_{\text{xc}}(\mathbf{r})n(\mathbf{r}) - \mathbf{\Delta}_{\text{xc}}(\mathbf{r}) \cdot \mathbf{m}(\mathbf{r})\right) d\mathbf{r} + \mu N. \tag{2.125}$$

Actual expressions of the exchange correlation potentials have been obtained by many investigators. The simplest way is to assume that the exchange correlation energy is a function of the electron densities and adopt an approximate form obtained from the homogeneous electron gas system.

$$E_{\rm XC}[n] = \int n(\mathbf{r}) \varepsilon_{\rm xc}(n(\mathbf{r})). \tag{2.126}$$

Here  $\varepsilon_{xc}(n(r))$  is the exchange correlation energy per electron for a homogeneous electron gas. This is called the Local Density Approximation (LDA). The LDA is referred as the Local Spin Density Approximation (LSDA) when spin polarization is taken into account.

The exchange-correlation energy  $\varepsilon_{xc}(n)$  consists of the exchange energy part  $\varepsilon_{x}(n)$  and the correlation part  $\varepsilon_{c}(n)$ ;  $\varepsilon_{xc}(n) = \varepsilon_{x}(n) + \varepsilon_{c}(n)$ . The exchange energy in the electron gas is given by

$$\varepsilon_{\rm x}(n) = -\frac{3}{4} \left(\frac{3n}{\pi}\right)^{1/3}.$$
 (2.127)

This yields the exchange potential in the paramagnetic state.

$$v_{\rm x}^{\rm P}(n) = -\left(\frac{3n}{\pi}\right)^{1/3} = -\frac{0.611}{r_{\rm s}}$$
 [a.u.]. (2.128)

where  $r_{\rm s}$  denotes a radius for the sphere with the volume per electron, i.e.,  $r_{\rm s} = (4\pi n/3)^{-1/3}$ . When the correlation term is neglected, the potential reduces to the Slater exchange potential (2.103) with the difference by a factor  $\alpha = 2/3$ .

Barth and Hedin [26] proposed the exchange correlation potential with use of the result of the random phase approximation for electron gas. Assuming the ferromagnetic spin polarization, the potential  $v_{\sigma}^{\rm xc}(\mathbf{r}) = v_{\rm xc}(\mathbf{r}) - \Delta_z(\mathbf{r})\sigma$  is given as follows.

$$v_{\sigma}^{\mathrm{xc}}(\mathbf{r}) = v_{\sigma}^{\mathrm{x}}(\mathbf{r}) + v_{\sigma}^{\mathrm{c}}(\mathbf{r}). \tag{2.129}$$

The exchange part is given by

$$v_{\sigma}^{\mathbf{x}}(\mathbf{r}) = v_{\mathbf{x}}^{\mathbf{P}} + \left(v_{\mathbf{x}}^{\mathbf{F}} - v_{\mathbf{x}}^{\mathbf{P}}\right) f\left(\frac{n_{\sigma}}{n}\right). \tag{2.130}$$

Here  $v_x^{\rm F} = -0.770/r_{\rm s}$  is the exchange potential for the complete polarization state  $(n_{\uparrow} = n)$  and the function f(x) is defined by

$$f(x) = \frac{1}{1 - 2^{-1/3}} \left[ x^{4/3} + (1 - x)^{4/3} - 2^{-1/3} \right]. \tag{2.131}$$

Note that f(1/2) = 0 in the paramagnetic state and f(0) = 1 in the complete ferromagnetic state.

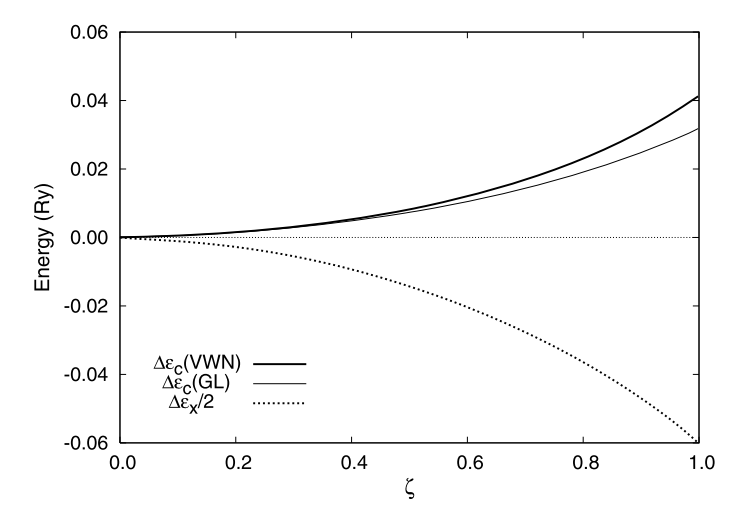


Fig. 2.5 Exchange and correlation energies  $(\Delta \varepsilon_{\rm X} = \varepsilon_{\rm X} - \varepsilon_{\rm X}^{\rm P} \text{ and } \Delta \varepsilon_{\rm C} = \varepsilon_{\rm C} - \varepsilon_{\rm C}^{\rm P})$  per electron as a function of spin polarization  $\zeta = (n_{\uparrow} - n_{\downarrow})/n$  (case of  $r_{\rm S} = 2$ ) [27]. VWN:  $\Delta \varepsilon_{\rm C}$  by Vosko et al., GL:  $\Delta \varepsilon_{\rm C}$  by Gunnarsson et al.

The correlation potential  $v_{\sigma}^{c}(\mathbf{r})$  is expressed as

$$v_{\sigma}^{c}(\mathbf{r}) = v_{c}^{P} + \left(v_{c}^{F} - v_{c}^{P}\right) f\left(\frac{n_{\sigma}}{n}\right). \tag{2.132}$$

The correlation potentials in the paramagnetic and ferromagnetic states are defined by

$$v_{\rm c}^{\rm P} = -\frac{0.0504}{2} \ln\left(1 + \frac{30}{r_{\rm s}}\right), \qquad v_{\rm c}^{\rm F} = -\frac{0.0254}{2} \ln\left(1 + \frac{75}{r_{\rm s}}\right).$$
 (2.133)

Figure 2.5 shows the energy gain of correlation energy per electron as a function of spin polarization  $\zeta = (n_{\uparrow} - n_{\downarrow})/n$ . As expected from our discussions in the previous sections, the spin polarization is caused by the exchange energy gain, but the correlation energy acts to suppress polarization. This is the same physics as discussed in the last subsection. It should be noted that in the local orbital representation the on-site Coulomb interaction was very large ( $\sim$ 20 eV). In the LSDA based on the homogeneous electron gas the contribution from the Coulomb integral on the same orbital is negligible because the wave functions for electron gas are extended over the crystal.

## 2.3.3 Tight-Binding Linear Muffin-Tin Orbitals

In the LDA scheme, calculations of the ground-state properties in solids are reduced to an eigen-value problem for one electron Hamiltonian  $H = -\nabla^2/2 + v(\mathbf{r})$  as given

by (2.113):

$$H\psi_i(\mathbf{r}) = \varepsilon_i \psi_i(\mathbf{r}). \tag{2.134}$$

Among various methods to solve the eigen value equation in solids, the Tight-Binding Linear Muffin-Tin Orbital (TB-LMTO) method [28–30] is compatible with the tight-binding model which has been used in the previous sections, and allows us the first-principles calculations of the Hamiltonian matrix elements in real space. In this subsection, we describe the TB-LMTO method for electronic structure calculations.

The basic idea of the TB-LMTO method is found in the one electron eigen value problem of a hydrogen molecule. The eigen states are approximately given by a linear combination of atomic orbitals  $\varphi(r)$  at the origin and  $\varphi(r-R)$  at another position of hydrogen atom R.

$$\varphi_{\mathbf{B}}(\mathbf{r}) = \varphi(\mathbf{r}) + \varphi(\mathbf{r} - \mathbf{R}), \tag{2.135}$$

$$\varphi_{\mathbf{A}}(\mathbf{r}) = \varphi(\mathbf{r}) - \varphi(\mathbf{r} - \mathbf{R}). \tag{2.136}$$

Here  $\varphi_B(\mathbf{r})$  ( $\varphi_A(\mathbf{r})$ ) is the bonding (antibonding) orbital of the hydrogen molecule leading to the eigen value  $E_B$  ( $E_A$ ). Solving the above equations with respect to  $\varphi(\mathbf{r})$  and  $\varphi(\mathbf{r} - \mathbf{R})$ , we can express the atomic orbitals as

$$\varphi(\mathbf{r}) = \frac{1}{2} (\varphi_{\mathbf{B}}(\mathbf{r}) + \varphi_{\mathbf{A}}(\mathbf{r})), \qquad (2.137)$$

$$\varphi(\mathbf{r} - \mathbf{R}) = \frac{1}{2} (\varphi_{\mathbf{B}}(\mathbf{r}) - \varphi_{\mathbf{A}}(\mathbf{r})). \tag{2.138}$$

We introduce here an energy-dependent wave function for the hydrogen molecule  $\varphi_E(\mathbf{r})$  such that  $H\varphi_E(\mathbf{r}) = E\varphi_E(\mathbf{r})$  where H is the one-electron Hamiltonian of the molecule, and rewrite the above equations as

$$\varphi(\mathbf{r}) \simeq \varphi_{E_0}(\mathbf{r}) + c_1 \dot{\varphi}_{E_0}(\mathbf{r}), \tag{2.139}$$

$$\varphi(\mathbf{r} - \mathbf{R}) \simeq c_2 \dot{\varphi}_{E_0}(\mathbf{r}). \tag{2.140}$$

Here  $E_0$  is an energy such that  $E_B \le E_0 \le E_A$ , and  $\dot{\varphi}_{E_0}(\mathbf{r}) = \partial \varphi_{E_0}(\mathbf{r})/\partial E$ . The above expressions of atomic orbitals suggest that the atomic orbitals as the basis functions for solids can be expressed by a linear combination of the energy dependent wave functions  $\varphi_{E_0}(\mathbf{r})$  and their derivatives  $\dot{\varphi}_{E_0}(\mathbf{r})$ .

Let us assume that the crystalline potential consists of the spherical potentials centered at each nucleus and the flat potential in the interstitial region. The former potentials are called the muffin-tin (MT) potentials. We then define the following atomic orbital on site i and orbital L = (l, m) as a basis function of solid.

$$\chi_{iL}^{\alpha}(\mathbf{r} - \mathbf{R}_i) = \varphi_{iL}(\mathbf{r} - \mathbf{R}_i) + \chi_{iL}^{i}(\mathbf{r} - \mathbf{R}_i) + \sum_{jL'} \dot{\varphi}_{jL'}^{\alpha}(\mathbf{r} - \mathbf{R}_j) h_{jL'iL}^{\alpha}, \quad (2.141)$$

$$\dot{\varphi}_{iL}^{\alpha}(\mathbf{r} - \mathbf{R}_i) = \dot{\varphi}_{iL}(\mathbf{r} - \mathbf{R}_i) + \varphi_{iL}(\mathbf{r} - \mathbf{R}_i)o_{iL}^{\alpha}. \tag{2.142}$$

The wave functions  $\chi_{iL}^{\alpha}(\mathbf{r} - \mathbf{R}_i)$  are called the LMTO. Here the spin part has been omitted for simplicity. The atomic wave function  $\varphi_{iL}(\mathbf{r} - \mathbf{R}_i)$  is defined to satisfy the Schrödinger equation with an energy  $E_{viL}$  inside the MT sphere i with radius  $s_{iR}$ ;  $(H - E_{viL})\varphi_{iL}(\mathbf{r} - \mathbf{R}_i) = 0$ , and vanishes outside the sphere i. Because of the spherical potential inside the MT sphere, it is written as  $\varphi_{iL}(\mathbf{r}) = \varphi_{iL}(E_{viL}, \mathbf{r})Y_L(\hat{\mathbf{r}})$  using the cubic harmonics  $Y_L(\hat{\mathbf{r}})$ .  $\varphi_{iL}(E, r)$  is determined by the radial Schrödinger equation with energy E. The energy  $E_{viL}$  is usually chosen to be the center of the gravity of energy eigen values below the Fermi level for each orbital. Note that  $\varphi_{iL}$ 's are normalized in the MT sphere as  $\langle \varphi_{iL} | \varphi_{iL'} \rangle = \delta_{ij} \delta_{LL'}$ .

The second term at the r.h.s. of (2.141), i.e.,  $\chi_{iL}^i(r-R_i)$  is an atomic wave function for the interstitial region that satisfies the Schrödinger equation in the interstitial region;  $(\nabla^2 + k^2)\chi_{iL}^i = 0$  with k = 0, so that the function is expressed by the irregular solution of the Laplace equation as follows.

$$\chi_{iL}^{i}(\mathbf{r} - \mathbf{R}_{i}) = K_{iL}(\mathbf{r} - \mathbf{R}_{i}) = \left(\frac{|\mathbf{r} - \mathbf{R}_{i}|}{s_{iR}}\right)^{-l-1} Y_{L}(\widehat{\mathbf{r} - \mathbf{R}_{i}}). \tag{2.143}$$

The wave function  $\chi_{iL}^i(\mathbf{r} - \mathbf{R}_i)$  inside the MT spheres is defined to be zero.

Inside each MT sphere  $(j \neq i)$ , the basis wave function is described by the third term at the r.h.s. of (2.141) where  $\dot{\varphi}_{iL}^{\alpha}(r - R_i)$  is defined by (2.142).  $\dot{\varphi}_{iL}(r - R_i)$  is the energy derivative of  $\varphi_{iL}(r - R_i)$  at  $E_{vil}$ ;  $\dot{\varphi}_{iL}(r - R_i) = [\partial \varphi_{iL}(r - R_i)] / \partial E_{E=E_{viL}}$ , and  $\langle \varphi_{iL} | \dot{\varphi}_{jL'} \rangle = 0$ . Note that the wave function  $\dot{\varphi}_{iL}^{\alpha}(r - R_i)$  describing the tails of the LMTO contains an arbitrary parameters  $o_{iL}^{\alpha}$  which allows us to control the localization of the basis function.

The coefficients  $h_{jL'iL}^{\alpha}$  in the tail part of (2.141) are determined so that the wave function  $\chi_{iL}^{i}(r-R_i)$  in the interstitial region is smoothly connected to those inside the MT spheres. This can be performed by using an envelope function

$$K_{iL}^{\infty}(\mathbf{r} - \mathbf{R}_i) = K_{iL}(\mathbf{r} - \mathbf{R}_i) - \sum_{jL'} J_{jL'}^{\alpha}(\mathbf{r} - \mathbf{R}_j) S_{jL'iL}^{\alpha}, \qquad (2.144)$$

which smoothly connects the interstitial wave function  $\chi_{iL}^i(\mathbf{r} - \mathbf{R}_i)$  inside all the MT spheres.  $J_{iL}^{\alpha}$  is a linear combination of the regular solution  $J_{iL}$  and the irregular solution  $K_{iL}$  of the Laplace equation being defined by

$$J_{iL}^{\alpha}(\mathbf{r} - \mathbf{R}_i) = J_{iL}(\mathbf{r} - \mathbf{R}_i) - K_{iL}(\mathbf{r} - \mathbf{R}_i)\alpha_{iL}. \tag{2.145}$$

The matrix  $S_{iLjL'}^{\alpha}$  in (2.144) is the so-called screened structure constant which is expressed by the canonical structure constant  $S_{iLjL'}$  as

$$S_{iLiL'}^{\alpha} = \left[ S(1 - \alpha S)^{-1} \right]_{iLiL'}.$$
 (2.146)

Here  $S_{iLiL'}$  is given by

$$S_{jL'iL} = \sqrt{4\pi} g_{l'm'lm} \left( \frac{|\mathbf{r} - \mathbf{R}_j|}{s_w} \right)^{-l-l'-1} Y_{l+l'm'-m}^* (\widehat{\mathbf{R}_i - \mathbf{R}_j}),$$

$$g_{l'm'lm} = (-)^{l+1} \sqrt{4\pi} \frac{2(2l''-1)!!}{(2l-1)!!(2l'-1)!!} C_{lml'm'l'm''}, \qquad (2.147)$$

 $C_{lm\,l'm'\,l''m''}$  being the Gaunt coefficient, and  $s_w$  is an arbitrary length such as the average Wigner–Seitz radius of the lattice.

The parameters  $\alpha_{iL}$  screen the structure constant  $S^{\alpha}_{jL'iL}$  as seen from (2.146). With the use of the matching condition on each muffin-tin sphere, we obtain the relation between  $\alpha_{iL}$  and  $o^{\alpha}_{iL}$  via  $\dot{\varphi}^{\alpha}_{iL}$  as

$$\alpha_{iL} = \frac{(s_{iR}/s_w)^{2l+1}}{2(2l+1)} \frac{D\{\dot{\varphi}^{\alpha}\} - l}{D\{\dot{\varphi}^{\alpha}\} + l + 1}.$$
 (2.148)

Alternatively  $o_{iL}^{\alpha}$  is expressed by  $\alpha_{iL}$  as

$$o_{iL}^{\alpha} = -\frac{w_{iL}\{J, \dot{\varphi}\} - w_{iL}\{K, \dot{\varphi}\}\alpha_{iL}}{w_{iL}\{J, \dot{\varphi}\} - w_{iL}\{K, \varphi\}\alpha_{iL}}.$$
(2.149)

Here  $w_{iL}\{a,b\}$  is the Wronskian defined by

$$w_{iL}\{a,b\} = s_{iR}a_{iL}(s_{iR})b_{iL}(s_{iR})[D\{b_{iL}\} - D\{a_{iL}\}],$$
  

$$D\{a\} = s_{iR}a'(s_{iR})/a(s_{iR}).$$
(2.150)

Finally the tail function  $h_{iLjL'}^{\alpha}$  is obtained from the global matching between  $\chi_{iL}^{\alpha}$  and  $K_{iL}^{\infty}$  on the muffin-tin spheres.

$$h_{iLjL'}^{\alpha} = -\frac{w_{iL}\{K,\varphi\}}{w_{iL}\{K,\varphi^{\alpha}\}} \delta_{ij} \delta_{LL'} + \sqrt{\frac{2}{s_w}} w_{iL} \{J^{\alpha},\varphi\} S_{iLjL'}^{\alpha} w_{jL'} \{J^{\alpha},\varphi\} \sqrt{\frac{2}{s_w}}.$$
(2.151)

According to (2.148), the choice  $o_{iL}^{\alpha} = 0$  corresponds to the choice of  $\alpha_{iL} = \gamma_{iL}$  such that

$$\gamma_{iL} = \frac{(s_{iR}/s_w)^{2l+1}}{2(2l+1)} \frac{D\{\dot{\varphi}\} - l}{D\{\dot{\varphi}\} + l + 1}.$$
 (2.152)

The choice of  $\alpha_{iL} = \gamma_{iL}$  is called the nearly orthogonal representation (or  $\gamma$ -representation) because in this case the MTO's become orthogonal to each other up to the second order in  $h_{iLjL'}^{\gamma}$ . Andersen et al. [28] showed that the following choice of  $\alpha_{iL}$  yields well localized basis set  $\{\chi_{iL}^{\alpha}(\mathbf{r} - \mathbf{R}_i)\}$ ;  $\alpha_{is} = 0.34850$ ,  $\alpha_{ip} = 0.05303$ ,  $\alpha_{id} = 0.010714$ , and  $\alpha_{il(\geqslant 3)} = 0.0$ . The MTO's with such a set of  $\{\alpha_{iL}\}$  are called the TB-LMTO.

In the atomic sphere approximation (ASA) in which the Wigner–Seitz cells are replaced by the atomic spheres with the same volume, the interstitial region disappear, so that the basis function reduces to

$$\chi_{iL}^{\alpha}(\mathbf{r} - \mathbf{R}_i) = \varphi_{iL}(\mathbf{r} - \mathbf{R}_i) + \sum_{jL'} \dot{\varphi}_{jL'}^{\alpha}(\mathbf{r} - \mathbf{R}_j) h_{jL'iL}^{\alpha}. \tag{2.153}$$

In the  $\gamma$  representation, we have

$$\chi_{iL}^{\gamma}(\mathbf{r} - \mathbf{R}_i) = \varphi_{iL}(\mathbf{r} - \mathbf{R}_i) + \sum_{iL'} \dot{\varphi}_{jL'}(\mathbf{r} - \mathbf{R}_j) h_{jL'iL}^{\gamma}. \tag{2.154}$$

The coefficients  $h_{iLjL'}^{\alpha}$  and  $o_{iL}^{\alpha}$  are parameterized by the position potential parameter  $c_{iL}^{\alpha}$  defined by  $c_{iL}^{\alpha}=\langle\chi_{iL}^{\alpha}|H|\chi_{iL}^{\alpha}\rangle$ , and the parameter  $\Delta_{iL}^{\alpha}=-(2/s_w)^{1/2}w_{iL}\{J^{\alpha},\varphi\}$  as follows.

$$h_{iLjL'}^{\alpha} = (c_{iL}^{\alpha} - E_{viL})\delta_{ij}\delta_{LL'} + (\Delta_{iL}^{\alpha})^{1/2}S_{iLjL'}^{\alpha}(\Delta_{jL'}^{\alpha})^{1/2}, \qquad (2.155)$$

$$o_{iL}^{\alpha} = -\frac{\gamma_{iL} - \alpha_{iL}}{\Delta_{iL}^{\alpha} + (\gamma_{iL} - \alpha_{iL})(c_{iL}^{\alpha} - E_{\nu iL})}.$$
(2.156)

In the next step, we construct the Hamiltonian matrix. Using the basis set of  $\gamma$  representation (2.154), we obtain the matrix elements of the Hamiltonian  $H_{iLjL'}$  and overlap integral  $O_{iLjL'}$  as follows.

$$H_{iLjL'}^{\gamma} = \langle \chi_{iL}^{\gamma} | H | \chi_{jL'}^{\gamma} \rangle = h_{iLjL'}^{\gamma} + E_{viL} \delta_{ij} \delta_{LL'} + \sum_{kL''} h_{iLkL''}^{\gamma} E_{vkL''} p_{kL''}^{\gamma} h_{kL''jL'}^{\gamma},$$
(2.157)

$$O_{iLjL'}^{\gamma} = \left\langle \chi_{iL}^{\gamma} \middle| \chi_{jL'}^{\gamma} \right\rangle = \delta_{ij} \delta_{LL'} + \sum_{kL''} h_{iLkL''}^{\gamma} p_{kL''}^{\gamma} h_{kL''jL'}^{\gamma}. \tag{2.158}$$

Here  $p_{iL}^{\gamma} = \langle \dot{\varphi}_{iL}^2 \rangle \equiv \langle \dot{\varphi}_{iL} | \dot{\varphi}_{iL} \rangle$ . In the matrix form, they are written as

$$\boldsymbol{H}^{\gamma} = \boldsymbol{h}^{\gamma} + \boldsymbol{E}_{\nu} + \boldsymbol{h}^{\gamma} \boldsymbol{E}_{\nu} \boldsymbol{p}^{\gamma} \boldsymbol{h}^{\gamma}, \tag{2.159}$$

$$\mathbf{O}^{\gamma} = \mathbf{I} + \mathbf{h}^{\gamma} \, \mathbf{p}^{\gamma} \, \mathbf{h}^{\gamma}. \tag{2.160}$$

Similarly, the matrix elements of the Hamiltonian  $H_{iLjL'}$  and overlap integral  $O_{iLjL'}$  in the  $\alpha$  representation are given as follows.

$$\boldsymbol{H}^{\alpha} = (\boldsymbol{I} + \boldsymbol{h}^{\alpha} \boldsymbol{o}^{\alpha}) \boldsymbol{h}^{\alpha} + (\boldsymbol{I} + \boldsymbol{h}^{\alpha} \boldsymbol{o}^{\alpha}) \boldsymbol{E}_{\nu} (\boldsymbol{I} + \boldsymbol{o}^{\alpha} \boldsymbol{h}^{\alpha}) + \boldsymbol{h}^{\alpha} \boldsymbol{E}_{\nu} \boldsymbol{p}^{\alpha} \boldsymbol{h}^{\alpha}, (2.161)$$

$$O^{\alpha} = (I + h^{\alpha} o^{\alpha})(I + o^{\alpha} h^{\alpha}) + h^{\alpha} p^{\alpha} h^{\alpha}.$$
 (2.162)

Note that we can switch the basis set  $\{\chi^{\alpha}\}$  into the set  $\{\chi^{\gamma}\}$  via the following relations,

$$\chi_{iL}^{\gamma} = \sum_{jL'} \chi_{jL'}^{\alpha} \left[ \left( \boldsymbol{I} + \boldsymbol{o}^{\alpha} \boldsymbol{h}^{\alpha} \right)^{-1} \right]_{jL'iL}, \tag{2.163}$$

and

$$\boldsymbol{h}^{\gamma} = \boldsymbol{h}^{\alpha} (\boldsymbol{I} + \boldsymbol{o}^{\alpha} \boldsymbol{h}^{\alpha})^{-1} = \boldsymbol{h}^{\alpha} - \boldsymbol{h}^{\alpha} \boldsymbol{o}^{\alpha} \boldsymbol{h}^{\alpha} + \cdots$$
 (2.164)

Using the above expressions, the Hamiltonian in the completely orthogonal representation is given by

$$H = O^{\gamma - 1/2} H^{\gamma} O^{\gamma - 1/2} = O^{\alpha - 1/2} H^{\alpha} O^{\alpha - 1/2}.$$
 (2.165)

The Hamiltonian matrix element in this representation is given as follows to the second order in  $E - E_{vil}$ .

$$H_{iLjL'} = E_{viL}\delta_{ij}\delta_{LL'} + h_{iLjL'}^{\gamma} = E_{viL}\delta_{ij}\delta_{LL'} + h_{iLjL'}^{\alpha} - (\boldsymbol{h}^{\alpha}\boldsymbol{o}^{\alpha}\boldsymbol{h}^{\alpha})_{iLjL'}.$$
(2.166)

Thus, the Hamiltonian in the nearly orthogonal basis set has the same form as Slater's two-center tight-binding Hamiltonian [31].

$$H_{iLjL'} = \varepsilon_{iL}\delta_{ij}\delta_{LL'} + t_{iLjL'}(1 - \delta_{ij}\delta_{LL'}). \tag{2.167}$$

Here  $\varepsilon_{iL} = E_{\nu iL} + h_{iLiL}^{\gamma}$  and  $t_{iLjL'} = h_{iLjL'}^{\gamma} = h_{iLjL'}^{\alpha} - (\boldsymbol{h}^{\alpha} \boldsymbol{o}^{\alpha} \boldsymbol{h}^{\alpha})_{iLjL'}$ . This is the first-principles TB-LMTO Hamiltonian.

In the actual band calculations, we solve the eigen value equation in the  $\alpha$  representation.

$$\sum_{jL'} H_{iLjL'}^{\alpha} u_{jL'}(\mathbf{k}) = \varepsilon_n(\mathbf{k}) \sum_{jL'} O_{iLjL'}^{\alpha} u_{jL'}(\mathbf{k}). \tag{2.168}$$

Here  $\varepsilon_n(\mathbf{k})$  is the energy eigen value for the momentum  $\mathbf{k}$  and the quantum number n.  $u_{iL}(\mathbf{k})$  is the eigen vector in the  $\alpha$  representation. The self-consistent calculations of potential are also possible by recalculating the charge (as well as spin) density within the atomic sphere after we obtain eigen values and the wave functions in the atomic sphere.

## 2.3.4 Ferromagnetism in Transition Metals

Using the TB-LMTO and ASA, one can obtain the effective exchange energy parameter called the Stoner parameter. Let us assume that one-electron energy eigen values for spin  $\sigma$  are given by  $\varepsilon_{n\sigma}(\mathbf{k})$ . The exchange splitting for the electron with quantum number  $(n, \mathbf{k})$  is given by  $\Delta \varepsilon_{n\sigma}(\mathbf{k}) = \varepsilon_{n\downarrow}(\mathbf{k}) - \varepsilon_{n\uparrow}(\mathbf{k})$ . The average exchange splitting near the Fermi level is therefore given by

$$\Delta \varepsilon = \frac{1}{N\rho(\varepsilon_{\rm F})\Delta} \sum_{nk}^{\varepsilon_{\rm F} \le \varepsilon_{n\sigma}(k) \le \varepsilon_{\rm F} + \Delta} \Delta \varepsilon_{n\sigma}(\mathbf{k}). \tag{2.169}$$

Here N is the number of atoms.  $\rho(\varepsilon_F)$  is the total DOS per atom per spin at the Fermi level, and  $\Delta$  is an infinitesimal width of energy at the Fermi level.

The exchange splitting is caused by the exchange correlation potential  $v_{\sigma}^{\rm xc}(\mathbf{r}) = \delta E_{\rm XC}/\delta n_{\sigma}(\mathbf{r})$ . In the LDA, the exchange correlation potential has the form  $E_{\rm XC} = \int_{\mathcal{S}_P} n\varepsilon_{\rm XC}(n,m)\,d\mathbf{r}$ . Defining G(n,m) by

$$G(n,m) = n\varepsilon_{xc}(n,m), \tag{2.170}$$

the exchange correlation potential is given as follows for a small polarization m(r).

$$v_{\sigma}^{\text{xc}}(\mathbf{r}) = G_n'(n,0) + G_m''(n,0)m\sigma. \tag{2.171}$$

Here  $G'_n(n,m) = \partial G/\partial n$  and  $G''_m(n,m) = \partial^2 G/\partial m^2$ . Then we obtain the splitting  $\Delta \varepsilon_{n\sigma}(\mathbf{k})$  as

$$\Delta \varepsilon_{n\sigma}(\mathbf{k}) = -2\langle \psi_n(\mathbf{k}) | G_m''(n,0)m(\mathbf{r}) | \psi_n(\mathbf{k}) \rangle. \tag{2.172}$$

Substituting  $\Delta \varepsilon_{n\sigma}(k)$  from (2.172) into (2.169) and using the ASA, we obtain

$$\Delta \varepsilon = \frac{1}{N} \sum_{il} I_{il} \, m_i \, \frac{\rho_{il}(\varepsilon_{\rm F})}{\rho(\varepsilon_{\rm F})}, \tag{2.173}$$

$$I_{il} = -\int_0^{s_R} 2G''_m(n,0) \frac{m_i(r)}{m_i} \phi_{il}(\varepsilon_F, r)^2 r^2 dr.$$
 (2.174)

Here  $m_i(m_i(r))$  is the magnetic moment (the spin density) on site i.  $\rho_{il}(\varepsilon_F)$  is the partial DOS for the orbital l per spin in the nonmagnetic state, and is defined by  $\rho_{il}(\varepsilon_F) = \sum_m \sum_{nk} \langle \chi_{iL} | \psi_n(\mathbf{k}) \rangle \delta(\varepsilon - \varepsilon_n(\mathbf{k})) \langle \psi_n(\mathbf{k}) | \chi_{iL} \rangle$ . The Stoner parameter  $I_i$  on site i may be defined by

$$\Delta \varepsilon = \frac{1}{N} \sum_{i} I_i m_i. \tag{2.175}$$

Comparing (2.175) with (2.173), we find

$$I_{i} = \sum_{l} I_{il} \frac{\rho_{il}(\varepsilon_{\rm F})}{\rho(\varepsilon_{\rm F})}.$$
 (2.176)

This is the exchange energy parameter derived from the DFT-LDA theory, i.e., the Stoner parameter.

The spin density  $m_i(r)$  on site i in (2.174) is given by  $m_i(r) = n_{i\uparrow}(r) - n_{i\downarrow}(r)$ , and each  $n_{i\sigma}(r)$  is given by

$$n_{i\sigma}(r) = \frac{1}{4\pi} \int^{\varepsilon_{\rm F}} d\varepsilon \sum_{l} \phi_{il\sigma}(\varepsilon, r)^2 \rho_{il\sigma}(\varepsilon). \tag{2.177}$$

For small polarization, we have a polarized wave function  $\phi_{il\sigma}(\varepsilon, r) = \phi_{il}(\varepsilon + \Delta\varepsilon\sigma/2, r)$  and the polarized DOS  $\rho_{il\sigma}(\varepsilon) = \rho_{il}(\varepsilon + \Delta\varepsilon\sigma/2)$  according to the

**Table 2.1** Stoner parameters and Stoner criterions in transition metals [32]

Metal	V	Fe	Co	Ni	Pd	Pt
I (eV)	0.80	0.92	0.99	1.01	0.70	0.63
$\rho(\varepsilon_{\rm F})I$	0.9	1.6	1.7	2.1	0.8	0.5

Schrödinger equation with constant exchange splitting  $\Delta \varepsilon$ . We therefore obtain the magnetization  $m_i(r) = n_{i\uparrow}(r) - n_{i\downarrow}(r)$  from (2.177) as follows.

$$\frac{m_i(r)}{m_i} = \frac{1}{4\pi} \sum_{l} \phi_{il}(\varepsilon_{\rm F}, r)^2 \frac{\rho_{il}(\varepsilon_{\rm F})}{\rho_i(\varepsilon_{\rm F})}.$$
 (2.178)

Here  $\rho_i(\varepsilon)$  is the local DOS per spin on site *i*.

Substituting (2.178) into (2.174), we obtain

$$I_{il} = \sum_{l'} \left[ \int_0^{s_{iR}} \frac{1}{4\pi} \left( -2G_m''(n,0) \right) \phi_{il'}(\varepsilon_{\rm F}, r)^2 \phi_{il}(\varepsilon_{\rm F}, r)^2 r^2 dr \right] \frac{\rho_{il'}(\varepsilon_{\rm F})}{\rho_i(\varepsilon_{\rm F})}. \quad (2.179)$$

In transition metals, the d component is dominant in the total DOS at the Fermi level, so that we obtain

$$I = -\frac{1}{2\pi} \int_0^{s_R} G_m''(n,0)\phi_{il}(\varepsilon_F, r)^4 r^2 dr.$$
 (2.180)

The Stoner condition for the ferromagnetism in the LDA-DFT is therefore given by

$$\rho(\varepsilon_{\rm F})I > 1. \tag{2.181}$$

Here  $\rho(\varepsilon_F)$  is the total DOS per atom per spin.

Gunnarsson calculated the Stoner parameters of transition metals [32]. The results are presented in Table 2.1. Calculated Stoner parameters for Fe, Co, and Ni are 0.92, 0.99, and 1.01 eV, respectively. These values are close to the exchange energy parameters in atoms obtained by the Hatree–Fock calculations: 0.88, 0.94, and 0.99 eV, but they are much smaller than the effective exchange energy parameters in the Hatree–Fock approximation  $\tilde{J} = U_0/5 + 4J/5$  (see (2.28)): 5.7, 6.0, and 6.4 eV, respectively, according to the Hatree–Fock atomic calculations. The discrepancy is due to a large intra-atomic Coulomb interaction energy between the same orbitals ( $U_0 \sim 20$  eV). The Hartree–Fock approximation is not a good starting point for such a condition. The electron correlations reduce this to  $U_{\rm eff} \sim W$  as discussed in Sect. 2.2, so that one can expect that the effective  $\tilde{J}$  becomes comparable to those obtained from the DFT-LDA. It should be noted that the intra-orbital Coulomb interactions are negligible in the free electron gas, so that the large  $U_0$  term as found in the atomic calculations does not appear in the DFT-LDA scheme.

The densities of states (DOS) in the paramagnetic state of 3d transition metals are presented in Fig. 2.6. The bcc DOS is characterized by a two-peak structure and a deep valley between the main peaks. The Fermi level of V is near the top of

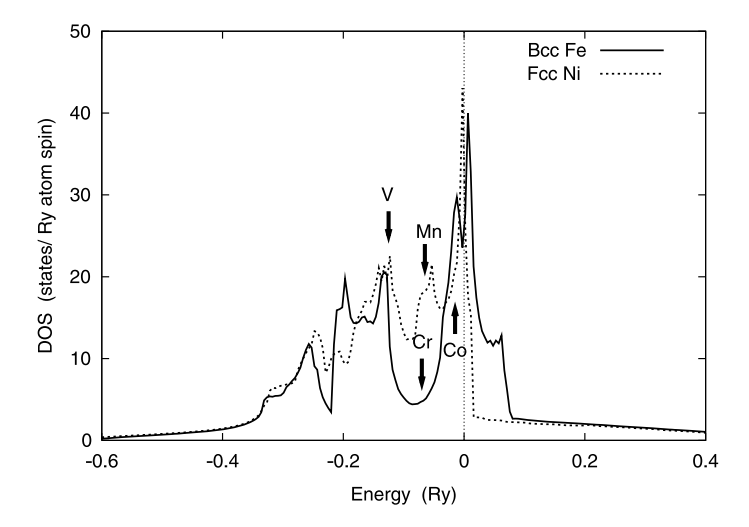


**Fig. 2.6** Densities of states of bcc Fe (*solid curve*) and fcc Ni (*dotted curve*). The Fermi levels of bcc V, bcc Cr, fcc Mn, and fcc Co are shown by the *arrows* 

**Table 2.2** Theory vs. experiment of the ground-state magnetizations M for Fe, Co, and Ni [34]. Theoretical results are the spin contribution to the magnetizations calculated at the experimental lattice constant. The values in the parentheses in the experimental data denote the spin contribution

$M(\mu_{ m B})$	Fe	Co	Ni
LDA	2.15	1.51	0.59
Expt.	2.22 (2.12)	1.74 (1.71)	0.62 (0.60)

the second peak. The Fermi level of Cr is near the bottom of the valley. The Fermi level of the bcc Fe is located on the main peak, so that bcc Fe is favorable to the ferromagnetism. The fcc DOS is characterized by a high DOS in the main peak, which is caused by the  $t_{2g}$  d bands. The Fermi level of the fcc Ni is on the peak, and thus it is favorable for the strong ferromagnetism.

The Stoner parameters as well as the DOS at the Fermi level obtained by the LSDA explain the ferromagnetism in bcc Fe, Co, and Ni, and the paramagnetism in V, Pd, and Pt as shown in Table 2.1. Janak [33] performed the spin susceptibility calculations for 32 metallic elements from Li to In on the basis of the DFT-LDA, and demonstrated that the other elements do not satisfy the Stoner criterion as they should.

Moruzzi et al. [34] calculated the ground-state magnetization of transition-metal ferromagnets. As shown in Table 2.2, the LDA quantitatively explains the ground-state magnetization in Fe, Co, and Ni. The LDA, however, does not explain the crystal structure of Fe correctly; the nonmagnetic fcc structure is stabilized for Fe in the LDA. Perdew et al. [35–37] developed a method which self-consistently takes into

account the gradient terms of the spin and charge densities being neglected in the LDA. The method called the generalized gradient approximation (GGA) improves the structural properties of solids. The GGA yields the ground-state magnetizations 2.17  $\mu_B$  for bcc Fe, 1.66  $\mu_B$  for fcc Co, and 0.66  $\mu_B$  for Ni at calculated lattice constants [38]. The ground-state magnetization in Ni is somewhat overestimated. In general the GGA enhances the magnetization as compared with the LDA.

# **Chapter 3 Metallic Magnetism at Finite Temperatures**

When temperature is elevated, various excited states of electrons appear in the ensemble average of magnetic moments. In this chapter, we present the theories of metallic ferromagnetism at finite temperatures. We first deal with the finitetemperature ferromagnetism by means of the Hartree-Fock approximation called the Stoner theory, and point out that the theory overestimates the Curie temperature due to the lack of spin fluctuations. The single-site spin fluctuation theory (SSF) describes thermal spin fluctuations, and significantly improves the Stoner theory. We introduce in Sect. 3.2 the functional integral method (FIM) which describes spin fluctuations at finite temperatures with use of the auxiliary exchange fields, and derive the SSF in Sect. 3.3 on the basis of the FIM. The SSF yields the Curie-Weiss susceptibility, and explains various properties of metallic magnetism at finite temperatures qualitatively. But dynamical spin and charge fluctuations are not taken into account in the theory because it is based on the high temperature approximation called the static approximation. We present the dynamical CPA in Sects. 3.4 and 3.5, which completely takes into account the dynamical spin as well as charge fluctuations at finite temperatures within the single-site approximation. We discuss the dynamical effects on the metallic magnetism. The dynamical CPA is an extension of the SSF to the dynamical case, and equivalent to the dynamical mean field theory in the metal-insulator transition. This equivalence is discussed in Sect. 3.6. In the last section, we extend the theory to the first-principles dynamical CPA and discuss the quantitative aspects of the finite-temperature magnetism in Fe, Co, and Ni.

# 3.1 Stoner Theory

The Hartree–Fock–Stoner theory is useful to understand the origin of the ferromagnetism at the ground state in itinerant-electron system. The Stoner condition (2.5) shows that the ferromagnetism is caused by a balance between the energy gain due to Coulomb interaction and the band energy loss of electrons via the Fermi level, though electron correlations play a significant role in its stabilization. We will dis-

cuss in this section the Stoner theory at finite temperatures to understand the nature of the mean-field theory of magnetism.

Finite-temperature properties of the Stoner theory are obtained from the self-consistent equations (2.11) for average charge n per atom and (2.12) for magnetization m per atom.

$$n = \sum_{\sigma} \int d\omega f(\omega) \rho(\omega + \Delta \cdot \sigma + \Delta \mu), \tag{3.1}$$

$$m = \sum_{\sigma} \sigma \int d\omega f(\omega) \rho(\omega + \Delta \cdot \sigma + \Delta \mu). \tag{3.2}$$

Here we introduced the Hartree–Fock density of states (DOS) in the nonmagnetic state as  $\rho(\omega) = \rho^0(\omega - Un/2 + \varepsilon_F)$ , the exchange potential  $\Delta = Um/2 + h$ , and the change of chemical potential  $\Delta\mu$  due to spin polarization.  $\varepsilon_F$  and h denote the Fermi level in the nonmagnetic state and the uniform magnetic field, respectively. Note that the DOS  $\rho(\omega)$  satisfies the following relation by definition.

$$n = \int d\omega f(\omega) \sum_{\alpha} \rho(\omega). \tag{3.3}$$

In the weak ferromagnetic limit ( $\Delta \ll 1$ ), we can obtain the explicit expressions of magnetization and susceptibility in the Stoner theory as follows. Let us take the difference between (3.1) and (3.3) to obtain  $\Delta \mu$ .

$$\int d\omega f(\omega) \sum_{\sigma} [\rho(\omega + \Delta \cdot \sigma + \Delta \mu) - \rho(\omega)] = 0.$$
 (3.4)

Expanding the above equation with respect to small  $\Delta$ , we obtain  $\Delta\mu$  as follows.

$$\Delta \mu = a\Delta^2 \left[ 1 + \left( a^2 + 3b + \frac{c}{a} \right) \Delta^2 + \cdots \right]. \tag{3.5}$$

The coefficients a, b, and c are defined as

$$a = -\frac{1}{2a_0} \int d\omega f(\omega) \rho^{(2)}(\omega), \qquad b = -\frac{1}{6a_0} \int d\omega f(\omega) \rho^{(3)}(\omega),$$

$$c = -\frac{1}{24a_0} \int d\omega f(\omega) \rho^{(4)}(\omega).$$
(3.6)

Here  $\rho^{(n)}(\omega)$  means that  $\rho^{(n)}(\omega) = \frac{\partial^n \rho(\omega)}{\partial \omega^n}$ , and the coefficient  $a_0$  is defined by

$$a_0 = \int d\omega f(\omega) \rho^{(1)}(\omega). \tag{3.7}$$

3.1 Stoner Theory 65

In the same way, (3.2) is expressed as

$$m = \int d\omega f(\omega) \sum_{\sigma} \sigma \left[ \rho(\omega + \Delta \cdot \sigma + \Delta \mu) - \rho(\omega) \right]. \tag{3.8}$$

Expanding the r.h.s. of the above equation with respect to small  $\Delta$  and  $\Delta\mu$ , and substituting the relation (3.5) into the equation, we obtain

$$m = 2a_0 \Delta [1 - (2a^2 + b)\Delta^2 + \cdots].$$
 (3.9)

At T=0, we have  $a_0=\rho$ ,  $a=-\rho^{(1)}/2\rho$ , and  $b=-\rho^{(2)}/6\rho$ , where  $\rho$ ,  $\rho^{(1)}$ , and  $\rho^{(2)}$  stand for  $\rho(0)$ ,  $\rho^{(1)}(0)$ , and  $\rho^{(2)}(0)$  at T=0, respectively. When h=0 and T=0, (3.9) yields the ground state magnetization,

$$m(0) = \sqrt{\frac{8(\rho U - 1)}{\rho U F_1 U^2}}. (3.10)$$

Here  $F_1 = (\rho^{(1)}/\rho)^2 - \rho^{(2)}/3\rho$ .

The paramagnetic susceptibility is obtained by taking the linear term in  $\Delta$  at the r.h.s. of (3.9).

$$\chi(T) = \frac{2a_0(T)}{1 - a_0(T)U}. (3.11)$$

At T = 0, we have  $a_0 = \rho$ , thus (3.11) reduces to (2.14), the susceptibility in the Hartree–Fock approximation at the ground state.

At finite temperatures, we may adopt the low temperature expansion for the Fermi distribution function because here we are considering very weak ferromagnetism. Furthermore it should be noted that  $\rho(\omega)$ , the DOS in the nonmagnetic state, depends on temperature T via  $\Delta \varepsilon_F$ , the change of  $\varepsilon_F$  due to temperature. Here we express its temperature dependence explicitly as  $\rho(\omega, T)$ . The change  $\Delta \varepsilon_F$  and  $\rho(\omega, T)$  are determined by (3.3) as

$$\Delta \varepsilon_{\rm F} = -\frac{\pi^2}{6} T^2 \frac{\rho^{(1)}}{\rho},\tag{3.12}$$

$$\rho(\omega, T) = \rho(\omega, 0) - \rho^{(1)}(\omega, 0) \frac{\pi^2}{6} T^2 \frac{\rho^{(1)}}{\rho} + \cdots$$
 (3.13)

Then  $a_0(T)$  defined by (3.7) is expanded as

$$a_0(T) = \int d\omega \left( -\frac{\partial f(\omega)}{\partial \omega} \right) \rho(\omega, T) = \rho \left[ 1 - \frac{\pi^2}{6} R T^2 + \dots \right]. \tag{3.14}$$

Here

$$R = \left(\frac{\rho^{(1)}}{\rho}\right)^2 - \frac{\rho^{(2)}}{\rho}.\tag{3.15}$$

The Curie temperature is obtained from the condition that the denominator in (3.11) vanishes,  $a_0(T_C)U = 1$ . With use of (3.14), it is given as

$$T_{\rm C} = \sqrt{\frac{6(\rho U - 1)}{\pi^2 R \rho U}}.$$
 (3.16)

Note that  $0 < \rho U - 1 \ll 1$  because we are considering the very weak ferromagnetism. Therefore, we may replace  $\rho U$  in the denominator of the above expression by one. Substituting (3.14) into (3.11) and using the expression of  $T_{\rm C}$ , we obtain

$$\chi(T)^{-1} = \frac{\pi^2 R(\rho U)^2}{12\rho} (T^2 - T_{\rm C}^2). \tag{3.17}$$

The inverse susceptibility in the Stoner theory is proportional to  $T-T_{\rm C}$  near  $T_{\rm C}$ , i.e., the susceptibility follows the Curie–Weiss law. But it deviates from it at higher temperatures.

The magnetization at finite temperatures is obtained from (3.9):

$$m(A + 2Bm^2 + \cdots) = 0,$$
 (3.18)

with

$$A = \frac{1 - a_0 U}{4a_0} = \frac{1}{2\chi},\tag{3.19}$$

$$B = \frac{1}{32} (2a^2 + b) U^3. \tag{3.20}$$

Solving (3.18), we obtain

$$m(T) = \sqrt{-\frac{A(T)}{2B(T)}}.$$
 (3.21)

Substituting (3.17) of  $\chi(T)$  into A(T) and replacing B(T) with B(0) in the above expression, we reach

$$m(T) = m(0)\sqrt{1 - \left(\frac{T}{T_C}\right)^2}$$
 (3.22)

Here m(0) is given by (3.10).

The temperature dependence of magnetization and susceptibility in the very weak ferromagnet, which is based on the Stoner theory is summarized in (3.22) and (3.17), respectively. The change of the magnetization  $\Delta m(T) = m(T) - m(0)$  follows the  $T^2$  law at low temperatures. In the actual transition metals, we have an additional term being proportional to  $T^{3/2}$ . This is explained by the spin wave excitations as will be discussed in Sect. 4.2. Near  $T_C$ , the magnetization vanishes as

**Table 3.1** The LDA+Stoner theory vs. experiment of the Curie temperatures for Fe, Co, and Ni [39, 40]

Metal	Fe	Co	Ni
$LDA+Stoner T_C (K)$	6000	4000	2900
Expt. $T_{\rm C}$ (K)	1040	1390	630

 $(T_{\rm C}-T)^{1/2}$ . This is characteristic of the mean-field theory (see also the Ginzburg–Landau theory in Sect. 6.4). However the  $T^2$  dependence of the inverse susceptibility in (3.17) seems to be inconsistent with the experimental data of weak ferromagnets which indicate the Curie–Weiss law in a wide range of temperature. It suggests that one has to take into account the spin fluctuations neglected in the Stoner theory.

In the above analysis, we assumed a very weak ferromagnetism where  $0 < \rho U - 1$ ,  $m \ll 1$ . When the magnetization is large, we have to solve (3.1) and (3.2) self-consistently. In the realistic calculations, one can adopt the tight-binding LMTO Hamiltonian (2.167) and the first-principles Stoner parameter I (2.180) obtained by the DFT-LDA theory in Sect. 2.3.4. The Stoner model is then described by the following Hamiltonian.

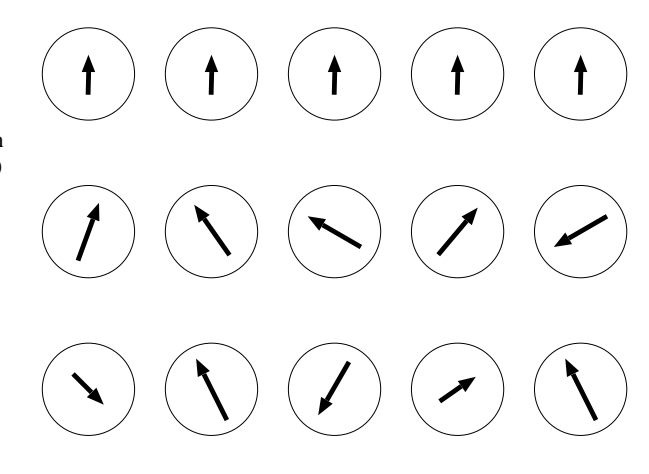
$$H = \sum_{iL\sigma} \left( \varepsilon_{iL} - \frac{1}{2} Im \cdot \sigma \delta_{ld} \right) n_{iL\sigma} + \sum_{iLjL'\sigma} t_{iLjL'} a^{\dagger}_{iL\sigma} a_{jL'\sigma} + \frac{1}{4} Im^2.$$
 (3.23)

Gunnarsson et al. [39, 40] calculated the Curie temperatures of Fe, Co, and Ni on the basis of the Stoner theory and the DFT-LDA Stoner parameters. The results are presented in Table 3.1. Calculated values are overestimated by a factor of 3–6 as compared with the experimental result. This is because the Stoner theory does not take into account the spin fluctuations at finite temperatures. The spin fluctuations reduce the magnetic energy and produce the magnetic entropy at finite temperatures. We will present the theory at finite temperatures in the following sections.

# 3.2 Functional Integral Method

We have discussed that the Hartree–Fock type independent-particle approximation overestimates magnetic energy and underestimates magnetic entropy because it neglects charge and spin fluctuations. The approximation therefore overestimates the Curie temperatures as well as the magnetic order. Figure 3.1 shows various pictures of spin fluctuations in metallic magnetism. In the Hartree–Fock–Stoner theory (top panel), the magnetic moments on each site show no spin fluctuations with increasing temperature. The moments uniformly decrease only via Fermi distribution function due to single-particle excitations of independent electrons with exchange splitting. In the local moment system (middle panel), the amplitudes of local moments on each site are well defined, but the transverse spin fluctuations take place with increasing temperatures. In the metallic systems, in general, one can expect fluctuations in both the amplitude and the direction as shown in the bottom panel of Fig. 3.1. One

Fig. 3.1 The Hartree– Fock–Stoner picture (top), local-moment picture (middle), and the spin-fluctuations expected in the metallic system (bottom)



has to explicitly take into account the spin fluctuations mentioned above to reduce the magnetic energy and to describe the magnetic entropy. The functional integral method is a suitable technique for this purpose, because auxiliary exchange fields introduced in the method can describe spin fluctuations in a simple way [41, 42].

In the functional integral method we transform the two-body interactions into a time-dependent random potential using the Hubbard–Stratonovich transformation.

$$e^{A\hat{O}^2} = \sqrt{\frac{A}{\pi}} \int d\xi \, e^{-A\xi^2 + 2A\hat{O}\xi}.$$
 (3.24)

Here  $\hat{O}$  is an operator, and A denotes an interaction strength.

Let us consider the Hubbard model (1.51) for simplicity. We divide the Hamiltonian into two parts, the noninteracting Hamiltonian  $H_0$  and the interaction part  $H_1$ , as follows.

$$H = H_0 + H_1, (3.25)$$

$$H_0 = \sum_{i,j,\sigma} t_{ij} a_{i\sigma}^{\dagger} a_{j\sigma}, \qquad (3.26)$$

$$H_{\rm I} = \sum_{i,\sigma} (\varepsilon_0 - \mu) n_{i\sigma} + \sum_i U n_{i\uparrow} n_{i\downarrow}. \tag{3.27}$$

Here  $\varepsilon_0$  and  $t_{ij}$  are the atomic level and the transfer integrals between sites i and j, respectively. U denotes the intraatomic Coulomb interaction energy parameter on each site. The chemical potential  $\mu$  has been inserted for convenience.

It should be noted that there are various representations of the interaction part because of the Pauli principle  $n_{i\sigma}^2 = n_{i\sigma}$ . For example,

$$n_{i\uparrow}n_{i\downarrow} = \frac{1}{4}(n_i^2 - m_i^2),$$
 (3.28)

$$n_{i\uparrow}n_{i\downarrow} = \frac{1}{2}n_i - \frac{1}{2}m_i^2,$$
 (3.29)

or using the relation  $s_x^2 = s_y^2 = s_z^2$ , we have

$$n_{i\uparrow}n_{i\downarrow} = \frac{1}{2}n_i - \frac{1}{6}m_i^2. \tag{3.30}$$

Here  $m_i = 2s_i$  is the spin magnetic moment on site i, and  $m_i = m_{iz}$ . Among various forms of interactions, we adopt the form (3.28) in the following, because in this case the simplest approximation to the functional integral method, which is called the static approximation, yields the Hatree–Fock approximation at the ground state.

The free energy  $\mathscr{F}$  is expressed in the interaction representation as follows [43].

$$e^{-\beta\mathscr{F}} = \text{Tr}\bigg(e^{-\beta H_0}\mathscr{T}\exp\bigg(-\int_0^\beta H_{\rm I}(\tau)\,d\tau\bigg)\bigg). \tag{3.31}$$

Here  $\beta$  denotes the inverse temperature (i.e.,  $1/k_BT$ ,  $k_B$  being the Boltzmann constant),  $\mathscr{T}$  denotes the time-ordered product (T product), and  $H_I$  is the interaction (3.27). Note that the interactions  $H_I(\tau_n)$  and  $H_I(\tau_{n'})$  between different times commute each other under  $\mathscr{T}$  product, because they are the Bose type operators consisting of the even products of creation and annihilation operators. Discretizing the integral with respect to time  $\tau$ , we have the following relation under  $\mathscr{T}$  product.

$$\exp\left(-\int_{0}^{\beta} H_{I}(\tau) d\tau\right) = \exp\left[-\frac{\beta}{N'} \sum_{n=1}^{N'} \sum_{i=1}^{N} (\varepsilon_{0} - \mu) n_{i\sigma}(\tau_{n})\right]$$

$$\times \prod_{n=1}^{N'} \prod_{i=1}^{N} \exp\left[-\frac{\pi \beta U}{4\pi N'} n_{i}^{2}(\tau_{n}) + \frac{\pi \beta U}{4\pi N'} m_{i}^{2}(\tau_{n})\right]. \quad (3.32)$$

Here N' is the number of segments of time interval  $[0, \beta]$ .

Applying the Hubbard–Stratonivich transformation (3.24) to the above interaction terms of  $n_i^2(\tau_n)$  ( $m_i^2(\tau_n)$ ) at each time  $\tau_n$ , we reach

$$e^{-\beta \mathscr{F}} = \int \left[ \prod_{i=1}^{N} \delta \xi_i(\tau) \delta \eta_i(\tau) \right] Z^0[\xi, \eta]$$

$$\times \exp \left[ -\frac{1}{4} U \sum_{i=1}^{N} \int_0^\beta d\tau \left\{ \eta_i^2(\tau) + \xi_i^2(\tau) \right\} \right]. \tag{3.33}$$

Here the functional integral  $\int \delta \xi(\tau)$  for the auxiliary field  $\xi(\tau)$  is defined by

$$\int \delta \xi(\tau) \equiv \int \left[ \prod_{n=1}^{N'} \sqrt{\frac{\beta U}{4\pi}} \frac{d\xi(\tau_n)}{\sqrt{N'}} \right] \quad (N' \to \infty), \tag{3.34}$$

and  $Z^0[\xi,\eta]$  is the partition function for noninteracting electrons under time-dependent random fields  $\xi(\tau)$  and  $\eta(\tau)$ .

$$Z^{0}[\xi,\eta] = \text{Tr}\bigg(\mathscr{T}\exp\bigg[-\int_{0}^{\beta}d\tau\,H\big(\tau,\xi(\tau),\eta(\tau)\big)\bigg]\bigg). \tag{3.35}$$

Note that  $H(\tau, \xi(\tau), \eta(\tau))$  denotes the one-electron Hamiltonian in the random charge and exchange fields, which is defined by

$$H(\tau, \xi(\tau), \eta(\tau)) = \sum_{i,\sigma} v_{i\sigma}(\xi_i(\tau), \eta_i(\tau)) n_{i\sigma}(\tau) + \sum_{i,j,\sigma} t_{ij} a_{i\sigma}^{\dagger}(\tau) a_{j\sigma}(\tau), \quad (3.36)$$

where the time-dependent potential  $v_{i\sigma}(\xi_i(\tau), \eta_i(\tau))$  is defined by

$$v_{i\sigma}(\xi_i(\tau), \eta_i(\tau)) = \varepsilon_0 - \mu \mp i \frac{1}{2} U \eta_i(\tau) - \frac{1}{2} U \xi_i(\tau) \sigma.$$
 (3.37)

Defining the energy functional  $E[\xi, \eta]$  by

$$E[\xi,\eta] = -\frac{1}{\beta} \ln Z^{0}[\xi,\eta] + \sum_{i} \frac{U}{4\beta} \int_{0}^{\beta} d\tau \left\{ \eta_{i}^{2}(\tau) + \xi_{i}^{2}(\tau) \right\}, \tag{3.38}$$

the free energy  $\mathscr{F}$  given by (3.33) is expressed as follows.

$$\mathscr{F} = -\frac{1}{\beta} \ln \int \left[ \prod_{i} \delta \xi_{i} \delta \eta_{i} \right] e^{-\beta E[\xi, \eta]}. \tag{3.39}$$

In order to obtain a more explicit form of the partition function  $Z^0[\xi, \eta]$ , we separate the time-dependent Hamiltonian (3.36) as follows.

$$H_{\lambda}(\tau, \xi, \eta) = H_0(\tau) + \lambda H_1(\tau, \xi, \eta). \tag{3.40}$$

Here we defined  $H_0(\tau)$  by the second term at the r.h.s. of (3.36), and defined  $H_1(\tau, \xi, \eta)$  by the first term. We introduced arbitrary interaction strength parameter  $\lambda$  for convenience. Then the logarithmic derivative of the partition function is expressed by a Green function  $G_{ij\sigma}^{\lambda}(\tau, \tau')$  as follows.

$$\frac{\partial \ln Z_{\lambda}^{0}}{\partial \lambda} = -\sum_{j,\sigma} \int_{0}^{\beta} d\tau \, v_{j\sigma}(\tau) G_{jj\sigma}^{\lambda}(\tau, \tau^{+}), \tag{3.41}$$

where  $\tau^+$  means  $\tau$  plus an infinitesimal positive number. The Green function for the time-dependent potentials  $v_{i\sigma}(\tau)$  is defined by

$$G_{ij\sigma}^{\lambda}(\tau,\tau') \equiv -\frac{\operatorname{Tr}(\mathcal{T}a_{i\sigma}(\tau)a_{j\sigma}^{\dagger}(\tau')e^{-\int_{0}^{\beta}H_{\lambda}(\tau'')d\tau''})}{\operatorname{Tr}(\mathcal{T}e^{-\int_{0}^{\beta}H_{\lambda}(\tau'')d\tau''})}.$$
 (3.42)

The Green function is obtained by solving the following Dyson equation [43, 44].

$$G_{ij\sigma}^{\lambda}(\tau,\tau') = g_{ij\sigma}(\tau-\tau') + \int_{0}^{\beta} d\tau'' \sum_{k} g_{ik\sigma}(\tau-\tau'') \lambda v_{k\sigma}(\tau'') G_{kj\sigma}(\tau'',\tau'). \quad (3.43)$$

Here  $g_{ij\sigma}(\tau - \tau')$  is the Green function for noninteracting Hamiltonian  $H_0$ . The Dyson equation is solved in the matrix form as follows.

$$G^{\lambda} = (g^{-1} - \lambda v)^{-1}, \tag{3.44}$$

where  $(G^{\lambda})_{i\tau\sigma j\tau'\sigma'} = G^{\lambda}_{ij\sigma}(\tau,\tau')\delta_{\sigma\sigma'}$ . Substituting the expression into (3.41) and integrating it with respect to  $\lambda$  from 0 to 1, we obtain

$$\ln Z^0 = \ln Z_0^0 + \operatorname{Sp} \ln(1 - vg). \tag{3.45}$$

Here  $Z_0^0$  is the partition function for the noninteracting system  $H_0$ , and Sp means a trace over site, time, and spin. Substituting (3.45) into (3.38), we obtain

$$E[\xi, \eta] = -\frac{1}{\beta} \left( \ln Z_0^0 + \operatorname{Sp} \ln g + \operatorname{Sp} \ln (g^{-1} - v) \right) + \sum_i \frac{U}{4\beta} \int_0^\beta d\tau \left\{ \eta_i^2(\tau) + \xi_i^2(\tau) \right\}.$$
(3.46)

Equations (3.39) and (3.46) indicate that the statistical mechanics of two-body interaction have been transformed into those of classical integrals of determinants with infinite dimensions.

Note that the Green function (3.42) for the time-dependent dynamical potentials  $v_{i\sigma}(\tau)$  differs from the temperature Green function for the interacting Hamiltonian (3.25). The latter is defined by

$$\mathscr{G}_{i\sigma j\sigma'}(\tau - \tau') = -\langle \mathscr{T}a_{\mathrm{H}i\sigma}(\tau)a_{\mathrm{H}i\sigma'}^{\dagger}(\tau') \rangle. \tag{3.47}$$

Here  $a_{\mathrm{H}i\sigma}(\tau)$  ( $a_{\mathrm{H}i\sigma}^{\dagger}(\tau)$ ) is the Heisenberg representation of the annihilation (creation) operator of an electron on site i with spin  $\sigma$ ;  $a_{\mathrm{H}i\sigma}(\tau) = \mathrm{e}^{\tau K} a_{i\sigma} \mathrm{e}^{-\tau K}$  ( $a_{\mathrm{H}i\sigma}^{\dagger}(\tau) = \mathrm{e}^{\tau K} a_{i\sigma}^{\dagger} \mathrm{e}^{-\tau K}$ ), where  $K = H - \mu N$ ,  $\mu$  being the chemical potential. We can prove that the temperature Green function is given by the Green function (3.42) as

$$\mathscr{G}_{i\sigma j\sigma'}(\tau - \tau') = \langle G_{i\sigma j\sigma'}(\tau, \tau') \rangle = \frac{\int \left[ \prod_{i} \delta \xi_{i} \delta \eta_{i} \right] G_{i\sigma j\sigma'}(\tau, \tau') e^{-\beta E[\xi, \eta]}}{\int \left[ \prod_{i} \delta \xi_{i} \delta \eta_{i} \right] e^{-\beta E[\xi, \eta]}}. \quad (3.48)$$

To prove the above relation, we express the temperature Green function (3.47) with use of the interaction representation as follows.

$$e^{-\beta \mathscr{F}} \mathscr{G}_{i\sigma j\sigma'} (\tau - \tau') = -\operatorname{Tr} \left( \mathscr{T} a_{i\sigma}(\tau) a_{j\sigma'}^{\dagger} (\tau') e^{-\int_0^{\beta} H_{\rm I}(\tau'') d\tau''} \right). \tag{3.49}$$

Since terms with different times in the integral of  $H_I(\tau'')$  at the r.h.s. commute each other under  $\mathscr{T}$  product, we can apply the Hubbard–Stratonovich transformation (3.24) discretizing the integral as (3.32), so that we obtain the formula (3.48).

The charge and magnetic moment on site i are obtained by taking the derivatives of (3.39) with respect to the atomic level  $\varepsilon_i^0$  and the local magnetic field  $h_i$  on site i as  $\partial \mathcal{F}/\partial \varepsilon_i^0$  and  $-\partial \mathcal{F}/\partial h_i$ .

$$\langle n_i \rangle = \sum_{\sigma} \left\langle \frac{1}{\beta} \int_0^{\beta} d\tau \, G_{ii\sigma}(\tau, \tau^+) \right\rangle,$$
 (3.50)

$$\langle m_i \rangle = \sum_{\sigma} \sigma \left\langle \frac{1}{\beta} \int_0^{\beta} d\tau \, G_{ii\sigma}(\tau, \tau^+) \right\rangle.$$
 (3.51)

The average  $\langle \sim \rangle$  at the r.h.s. of (3.50) and (3.51) is defined by a thermal average with respect of the energy functional  $E[\xi, \eta]$ .

$$\langle \sim \rangle \equiv \frac{\int \left[ \prod_{i} \delta \xi_{i} \delta \eta_{i} \right] (\sim) e^{-\beta E[\xi, \eta]}}{\int \left[ \prod_{i} \delta \xi_{i} \delta \eta_{i} \right] e^{-\beta E[\xi, \eta]}}.$$
 (3.52)

We can obtain alternative expressions with use of the auxiliary fields. To derive the expressions, we write the local charge as  $\langle n_i \rangle = \langle \partial E[\xi, \eta]/\partial \varepsilon_i^0 \rangle$ . Since  $\varepsilon_i^0$  appears in the energy  $E[\xi, \eta]$  via the time-dependent energy  $\varepsilon_i(\tau) \equiv \varepsilon_i^0 - \mu \mp Ui\eta_i(\tau)/2$  according to (3.38), we take the derivative for every time segment  $\tau_n$  as

$$\langle n_i \rangle = \sum_{n} \left\langle \frac{\partial}{\partial \varepsilon_i(\tau_n)} E[\xi, \eta] \right\rangle.$$
 (3.53)

We can rewrite  $\partial E/\partial \varepsilon_i(\tau_n)$  in the above equation using  $\partial E/\partial \eta_i(\tau_n)$  via the relation  $\partial E/\partial \eta_i(\tau_n) = \mp i(U/2)\partial E/\partial \varepsilon_i(\tau_n) + (\Delta \tau/2\beta)U\eta_i(\tau_n)$ . By integration by parts, we obtain an alternative expression as follows.

$$\langle n_i \rangle = \langle \pm i \, \eta_i \rangle. \tag{3.54}$$

For the local magnetic moment, we make use of the time-dependent magnetic field  $h_i(\tau_n) \equiv U\xi_i(\tau_n)/2 + h_i$  instead of the time-dependent energy  $\varepsilon_i(\tau_n)$ . Taking the same steps, we obtain the following formula.

$$\langle m_i \rangle = \langle \xi_i \rangle. \tag{3.55}$$

Here  $\xi_i$  and  $\eta_i$  are the time-averaged static field variables defined by

$$\xi_i = \frac{1}{\beta} \int_0^\beta \xi_i(\tau) d\tau, \qquad \eta_i = \frac{1}{\beta} \int_0^\beta \eta_i(\tau) d\tau. \tag{3.56}$$

The results (3.54) and (3.55) indicate that the averages of the zero frequency components of the charge and exchange fields determine local charge and magnetization on the same site. In particular, (3.55) suggests that a 'magnetic moment'  $\xi_i$  on site *i* thermally fluctuates as shown in the bottom panel of Fig. 3.1.

In the functional integral method, one has to evaluate the energy functional  $E[\xi, \eta]$  (i.e., (3.46)) first, and then perform the functional integrals as found in (3.39) and (3.52). In order to obtain the free energy describing spin fluctuations, we make use of the time-averaged static variables (3.56). Using the identity

$$1 = \int d\xi_{i} \,\delta\left(\xi_{i} - \frac{1}{\beta} \int_{0}^{\beta} \xi_{i}(\tau) \,d\tau\right)$$
$$= \int \sqrt{\frac{\beta U}{4\pi}} \,d\xi_{i} \int dx_{i} \exp\left[-2\pi i x_{i} \sqrt{\frac{\beta U}{4\pi}} \left(\xi_{i} - \frac{1}{\beta} \int_{0}^{\beta} \xi_{i}(\tau) \,d\tau\right)\right], (3.57)$$

one can express the free energy (3.32) by means of the static variables  $\xi_i$  and  $\eta_i$  as follows.

$$e^{-\beta\mathscr{F}} = \int \left[ \prod_{i=1}^{N} \frac{\beta U}{4\pi} d\xi_{i} d\eta_{i} \right] \int \left[ \prod_{i=1}^{N} \delta \xi_{i}(\tau) \delta \eta_{i}(\tau) dx_{i} dy_{i} \right] Z^{0}[\xi, \eta]$$

$$\times \exp \left[ \sum_{i=1}^{N} \left( -\frac{1}{4} U \int_{0}^{\beta} \xi_{i}(\tau)^{2} d\tau + i x_{i} \frac{\sqrt{\beta \pi U}}{\beta} \int_{0}^{\beta} \left( \xi_{i}(\tau) - \xi_{i} \right) d\tau \right) \right]$$

$$\times \exp \left[ \sum_{i=1}^{N} \left( -\frac{1}{4} U \int_{0}^{\beta} \eta_{i}(\tau)^{2} d\tau + i y_{i} \frac{\sqrt{\beta \pi U}}{\beta} \int_{0}^{\beta} \left( \eta_{i}(\tau) - \eta_{i} \right) d\tau \right) \right]. \tag{3.58}$$

The simplest approximation is to replace the time-dependent fields  $\xi_i(\tau)$  and  $\eta_i(\tau)$  in the Hamiltonian of  $Z^0[\xi,\eta]$  with the static ones, i.e.,  $\xi_i$  and  $\eta_i$ , as  $H(\tau,\xi(\tau),\eta(\tau)) \to H(\tau,\xi,\eta)$ . This is called the static approximation. The partition function (3.35) then reduces to the following form.

$$Z_{\rm st}^{0}(\xi,\eta) = \text{Tr}(\exp[-\beta H_{\rm st}(\xi,\eta)]), \tag{3.59}$$

and

$$H_{\rm st}(\xi,\eta) = \sum_{i} v_{i\sigma}(\xi_i,\eta_i) n_{i\sigma} + \sum_{i,j,\sigma} t_{ij} a_{i\sigma}^{\dagger} a_{j\sigma}. \tag{3.60}$$

Here  $v_{i\sigma}(\xi_i, \eta_i)$  is a random static potential (3.37) in which the dynamical-field variables  $\xi_i(\tau)$  and  $\eta_i(\tau)$  have been replaced by the static ones.

$$v_{i\sigma}(\xi_i, \eta_i) = \varepsilon_0 - \mu \mp \frac{1}{2} i U \eta_i - \frac{1}{2} U \xi_i \sigma. \tag{3.61}$$

The remaining functional integrals can be performed with use of the Gaussian integrals, and we obtain the following expression for the free energy  $\mathscr{F}_{st}$  in the

static approximation.

$$e^{-\beta \mathscr{F}_{st}} = \int \left[ \prod_{i=1}^{N} \sqrt{\frac{\beta U}{4\pi}} \, d\xi_i \sqrt{\frac{\beta U}{4\pi}} \, d\eta_i \right] Z_{st}^0(\xi, \eta) \exp \left[ -\frac{1}{4} \beta U \sum_{i=1}^{N} (\eta_i^2 + \xi_i^2) \right].$$
(3.62)

Here  $Z_{\rm st}^0(\xi,\eta)$  is the partition function (3.59) for the Hamiltonian  $H_{\rm st}$  with the random static potential  $v_{i\sigma}(\xi_i,\eta_i)$ . The free energy (3.62) is also written as follows.

$$\mathscr{F}_{st} = -\frac{1}{\beta} \ln \int \left[ \prod_{i} \sqrt{\frac{\beta U}{4\pi}} d\xi_{i} \sqrt{\frac{\beta U}{4\pi}} d\eta_{i} \right] e^{-\beta E_{st}(\xi, \eta)}, \qquad (3.63)$$

$$E_{\rm st}(\xi,\eta) = -\beta^{-1} \ln \text{Tr} \left( e^{-\beta H_{\rm st}(\xi,\eta)} \right) + \frac{1}{4} U \sum_{i=1}^{N} (\eta_i^2 + \xi_i^2). \tag{3.64}$$

Needless to say, the static approximation is exact in the noninteracting limit. It is also exact in the atomic limit because the Hamiltonian  $H_0$  commutes with the interaction  $H_1$  there, so that the replacement  $H(\tau, \xi(\tau), \eta(\tau)) \to H(\tau, \xi, \eta)$  is justified. Also, the approximation becomes exact in the high temperature limit where the time interval  $[0, \beta]$  becomes zero. At T = 0, on the other hand, one can take the saddle point of  $E_{\rm st}(\xi, \eta)$  to calculate the free energy. The ground state energy is then given by

$$\langle H \rangle = \mu N + \langle H_{\rm st}(\xi^*, \eta^*) \rangle_0 + \frac{1}{4} U \sum_i (\eta_i^{*2} + \xi_i^{*2}).$$
 (3.65)

Here  $\langle (\sim) \rangle_0$  means the average with respect to the Hamiltonian  $H_{\rm st}(\xi^*,\eta^*)$  at T=0. The saddle point values  $\xi_i^*$  and  $\eta_i^*$  are determined from the conditions,  $\partial E_{\rm st}/\partial \xi_i=0$  and  $\partial E_{\rm st}/\partial \eta_i=0$ , i.e.,

$$\xi_i^* = \langle m_i \rangle_0 (\xi^*, \eta^*), \qquad \mp i \eta_i^* = \langle n_i \rangle_0 (\xi^*, \eta^*). \tag{3.66}$$

These coupled equations for  $\xi_i^*$  and  $\eta_i^*$  are nothing but the Hartree–Fock equations, and the potential  $v_{i\sigma}(\xi^*, \eta^*)$  reduces to the Hartree–Fock one,  $\varepsilon_0 - \mu + U \langle n_i \rangle_0 / 2 - U \langle m_i \rangle_0 \sigma / 2$ . Therefore, the energy (3.65) is identical with the Hartree–Fock energy at the ground state.

# 3.3 Single-Site Theory in the Static Approximation

The static approximation to the functional integral method yields a physical picture of spin fluctuations as indicated in Fig. 3.1, though it is a rather crude approximation at low temperatures. In this section we present a single-site theory of spin

fluctuations based on the static approximation, which is known as the single-site spin fluctuation theory (SSF) [45–49].

We adopt here the saddle point approximation to the charge fields,  $\zeta_i \equiv \mp i \eta_i^* = \langle n_i \rangle_0(\xi, \pm i \zeta)$ , and express the free energy (3.63) and the energy potential (3.64) as follows.

$$\mathscr{F}_{st} = -\frac{1}{\beta} \ln \int \left[ \prod_{i} \sqrt{\frac{\beta U}{4\pi}} \, d\xi_{i} \right] e^{-\beta E_{st}(\xi)}, \tag{3.67}$$

$$E_{\rm st}(\xi) = \int d\omega \, f(\omega) \frac{1}{\pi} \, \text{Im} \, \text{Tr} \Big[ \ln(z - H_{\rm st}) \Big] + \frac{1}{4} U \sum_{i} (\xi_i^2 - \zeta_i^2). \tag{3.68}$$

Here  $z = \omega + i\delta$ ,  $\delta$  being the infinitesimal positive number.  $H_{\rm st}$  is the one-electron Hamiltonian matrix defined by

$$(H_{\rm st})_{i\sigma j\sigma'} = \left[ v_{i\sigma}(\xi)\delta_{ij} + t_{ij}(1 - \delta_{ij}) \right] \delta_{\sigma\sigma'}. \tag{3.69}$$

The random static potential is now given by

$$v_{i\sigma}(\xi) = \varepsilon_0 - \mu + \frac{1}{2}U\zeta_i(\xi) - \frac{1}{2}U\xi_i\sigma, \tag{3.70}$$

and  $\zeta_i(\xi) = \langle n_i \rangle_0(\xi)$  denotes the Hartree–Fock charge on site *i* when the random exchange fields  $\{\xi_i\}$  are given.

The Hamiltonian matrix  $H_{\rm st}$  in (3.68) consists of the random potential  $(v)_{i\sigma j\sigma'} = v_{i\sigma}\delta_{ij}\delta_{\sigma\sigma'}$  and the transfer integral matrix  $(t)_{i\sigma j\sigma'} = t_{ij}\delta_{\sigma\sigma'}$ ;  $H_{\rm st} = v + t$ . In order to reduce the number of integrations in the free energy (3.67), we introduce an energy-dependent complex potential called the coherent potential  $\Sigma_{\sigma}(z)$  into the potential part as  $H_{\rm st} = \Sigma + t + \delta v$ .  $\delta v$  denotes a scattering potential from a medium  $\Sigma$ ;  $\delta v = v - \Sigma$ .

The energy (3.68) is then expressed as follows.

$$E_{\rm st}(\xi) = \tilde{\mathscr{F}} + \int d\omega f(\omega) \frac{1}{\pi} \operatorname{Im} \operatorname{Tr} \left[ \ln(1 - \delta v \tilde{G}) \right] + \frac{1}{4} U \sum_{i} \left( \xi_i^2 - \zeta_i^2 \right). \tag{3.71}$$

Here  $\tilde{\mathscr{F}}$  is the coherent part of the free energy given by

$$\tilde{\mathscr{F}} = \int d\omega \, f(\omega) \frac{1}{\pi} \operatorname{Im} \operatorname{Tr} \left[ \ln(z - \Sigma - t) \right]. \tag{3.72}$$

The second term at the r.h.s. of (3.71) is a contribution from the scattering potential  $\delta v$ . The coherent Green function  $\tilde{G}$  is defined by

$$(\tilde{G})_{i\sigma j\sigma'} = \left[ (z - \Sigma - t)^{-1} \right]_{i\sigma j\sigma} \delta_{ij} \delta_{\sigma\sigma'}. \tag{3.73}$$

The last term of the r.h.s. of (3.71) is the Gaussian contribution to the free energy. In order to expand the second term in (3.71) with respect to sites, we divide the Green function  $\tilde{G}$  into the diagonal part F and the off-diagonal F' as follows.

$$\tilde{G} = F + F', \tag{3.74}$$

where

$$(F)_{i\sigma j\sigma'} = F_{i\sigma}(z)\delta_{ij}\delta_{\sigma\sigma'} = \left[ (z - \Sigma - t)^{-1} \right]_{i\sigma i\sigma}\delta_{ij}\delta_{\sigma\sigma'}, \tag{3.75}$$

$$(F')_{i\sigma j\sigma'} = (\tilde{G})_{i\sigma j\sigma} (1 - \delta_{ij}) \delta_{\sigma\sigma'}. \tag{3.76}$$

We can then expand the energy (3.71) with respect to the site as follows.

$$E(\xi) = \tilde{\mathscr{F}} + \sum_{i} E_i(\xi_i) + \Delta E(\xi). \tag{3.77}$$

The second term at the r.h.s. of (3.77) consists of the single-site energies on each site.

$$E_i(\xi_i) = \int d\omega f(\omega) \frac{1}{\pi} \operatorname{Im} \sum_{\sigma} \ln(1 - \delta v_{i\sigma}(z, \xi) F_{i\sigma}(z)) + \frac{1}{4} U(\xi_i^2 - \zeta_i^2). \quad (3.78)$$

Here

$$\delta v_{i\sigma}(z,\xi) = v_{i\sigma}(\xi) - \Sigma_{\sigma}(z). \tag{3.79}$$

The last term in (3.77) describes the inter-site interaction.

$$\Delta E(\xi) = \int d\omega f(\omega) \frac{1}{\pi} \operatorname{Im} \operatorname{Tr} \left[ \ln \left( 1 - \tilde{t} F' \right) \right]. \tag{3.80}$$

Here  $\tilde{t}$  is the single-site t matrix for the scattering  $\delta v$ .

$$\tilde{t} = (1 - \delta v F)^{-1} \delta v. \tag{3.81}$$

In the single-site approximation (SSA), we neglect the last term in (3.77), and obtain the free energy as follows.

$$\mathscr{F}_{SSA} = \tilde{\mathscr{F}} - \beta^{-1} \sum_{i} \ln \int \sqrt{\frac{\beta U}{4\pi}} \, d\xi_i \, e^{-\beta E_i(\xi_i)}. \tag{3.82}$$

The coherent potential  $\Sigma_{\sigma}(z)$  is determined so that the contribution from the inter-site corrections (3.80) becomes as small as possible. This implies that

$$\langle \tilde{t}_{i\sigma} \rangle = \left\langle \frac{\delta v_{i\sigma}}{1 - \delta v_{i\sigma} F_{i\sigma}} \right\rangle = 0.$$
 (3.83)

Here the average  $\langle \sim \rangle$  means a classical average with respect to the impurity energy  $E_i(\xi_i)$ .

$$\langle \sim \rangle = \frac{\int \sqrt{\frac{\beta U}{4\pi}} \, d\xi_i \, (\sim) e^{-\beta E_i(\xi_i)}}{\int \sqrt{\frac{\beta U}{4\pi}} \, d\xi_i \, e^{-\beta E_i(\xi_i)}}.$$
 (3.84)

Equation (3.83) is equivalent to the following condition (see Appendix A).

$$\langle G_{i\sigma}^{(i)}(z,\xi)\rangle = F_{i\sigma}(z). \tag{3.85}$$

Here

$$G_{i\sigma}^{(i)}(z,\xi) = \frac{1}{F_{i\sigma}(z)^{-1} - \delta v_{i\sigma}(z,\xi)}.$$
 (3.86)

The function  $G_{i\sigma}^{(i)}(z,\xi)$  is an on-site Green function for a system with an impurity potential  $v_{i\sigma}$  embedded in an effective medium  $\Sigma_{\sigma}(z)$ , whose Hamiltonian is given by

$$(H^{(i)}(z))_{il\sigma} = [v_{i\sigma}(z,\xi)\delta_{ij} + \Sigma_{\sigma}(z)(1-\delta_{ij})]\delta_{jl} + t_{jl}(1-\delta_{jl}).$$
(3.87)

The coherent Green function  $F_{i\sigma}(z)$  is defined by (3.75), and expressed by the density of states  $\rho(\varepsilon)$  for the noninteracting Hamiltonian  $t_{ij}$  as

$$F_{i\sigma}(z) = \int \frac{\rho(\varepsilon) d\varepsilon}{z - \Sigma_{\sigma}(z) - \varepsilon}.$$
 (3.88)

The form is known as the Lehmann representation of the Green function.

The single-site approximation with use of a site-diagonal effective potential  $\Sigma_{\sigma}(z)$  is known as the coherent potential approximation (CPA), and (3.83) and (3.85) are called the CPA equation. These equations are also verified to be equivalent to the stationary condition of the free energy (3.82) with respect to the coherent potential (see Appendix A).

$$\frac{\delta \mathscr{F}_{\text{SSA}}}{\delta \Sigma_{\sigma}(z)} = 0. \tag{3.89}$$

The CPA was first introduced as a method to treat the electronic structure of disordered alloys [50, 51], which will be discussed in more detail in Sect. 8.2. The schematic picture of the CPA equation is given in Fig. 3.2. We have replaced the random potentials  $\{v_{j\sigma}\}$  of the one-electron Hamiltonian  $H_{\rm st}$  (i.e., (3.69)) with the coherent potential  $\Sigma_{\sigma}(z)$  at the surrounding sites in order to reduce the number of field variables. We then have an impurity system described by an effective Hamiltonian (3.87), and obtain the impurity Green function (3.86). The l.h.s. in Fig. 3.2 shows the thermal average of such a system. On the other hand, we can consider a coherent system in which all the random potentials are replaced by the coherent

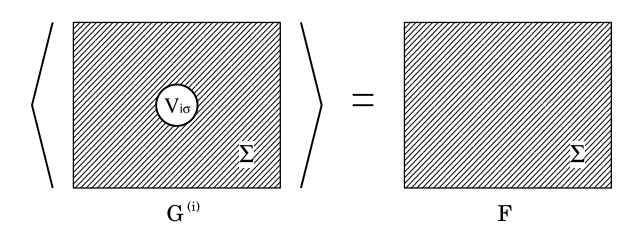


Fig. 3.2 Physical picture for the coherent potential approximation (CPA). The *left-hand side* (l.h.s.) shows an impurity system with a random potential  $v_{i\sigma}$  on site i, which is embedded in the effective potential  $\Sigma_{\sigma}$ . The *right-hand side* shows a uniform system with the effective potential only. When the average is taken at the l.h.s. with respect to a random potential  $v_{i\sigma}$ , it should be identical with the r.h.s

ones, as shown at the r.h.s. in Fig. 3.2. We then obtain the coherent Green function (3.88). The CPA equation (3.85) indicates that these states should be identical when the effective medium is chosen to be best.

One can rederive the formula (3.54) of local charge on site i from the single-site free energy (3.82) by using the stationary conditions (3.89) and  $\partial E_i(\xi_i)/\partial \zeta_i = 0$ , as well as the relations  $\langle n_i \rangle = \partial \mathscr{F}_{SSA}/\partial \varepsilon_i^0$ .

$$\langle n_i \rangle = \langle \zeta_i(\xi) \rangle, \tag{3.90}$$

$$\zeta_i(\xi) = \int d\omega f(\omega) \sum_{\sigma} \rho_{i\sigma}(\omega, \xi). \tag{3.91}$$

Here  $\rho_{i\sigma}(\omega,\xi)$  is the single-site density of states (DOS) given by

$$\rho_{i\sigma}(\omega,\xi) = -\frac{1}{\pi} \operatorname{Im} G_{i\sigma}^{(i)}(z,\xi). \tag{3.92}$$

In the same way, we can rederive the formula (3.55) of the local magnetic moment on site *i* using the relation  $\langle m_i \rangle = -\partial \mathscr{F}_{SSA}/\partial h_i$ .

$$\langle m_i \rangle = \langle \xi_i \rangle. \tag{3.93}$$

The average at the r.h.s. is now taken with respect to the single-site energy  $E_i(\xi_i)$  (see (3.84)). Equation (3.93) indicates that the magnetic moment at finite temperatures is determined by a thermal average of a flexible local moment  $\xi_i$  with respect to the energy potential  $E_i(\xi)$ .

The amplitude of local moment is obtained from the relations  $\langle m_i^2 \rangle = \langle n_i \rangle - 2 \langle n_i \uparrow n_{i \downarrow} \rangle$  and  $\langle n_i \uparrow n_{i \downarrow} \rangle = \partial \mathscr{F}_{SSA} / \partial U_i$  [52].

$$\langle m_i^2 \rangle = \langle n_i \rangle - \frac{1}{2} \left( \langle \zeta_i^2(\xi) \rangle - \langle \xi_i^2 \rangle + \frac{2}{\beta U} \right).$$
 (3.94)

The second term at the r.h.s. of the equation shows that the amplitude of local moment is flexible and can vary with elevated temperature.

The entropy S per atom is also obtained from the relation  $S = -\partial \mathscr{F}_{SSA}/\partial T/L$ , where L denotes the number of atoms [52].

$$S = -\int d\omega \,\tilde{\rho}(\omega) \left[ \left( 1 - f(\omega) \right) \ln \left( 1 - f(\omega) \right) + f(\omega) \ln f(\omega) \right]$$

$$+ \ln \int \sqrt{\frac{\beta U}{4\pi}} \, d\xi \, e^{-\beta (E_i(\xi) - \langle E_i(\xi) \rangle)} - \frac{1}{2}.$$
(3.95)

Here  $\tilde{\rho}(\omega)$  is the DOS per atom for the coherent state, which is given by  $\tilde{\rho}(\omega) = -\pi^{-1} \operatorname{Im} \sum_{\sigma} F_{i\sigma}(z)$ . The first term expresses an entropy for the independent particle system. This is essentially the same as in the Stoner theory. The second term causes a magnetic entropy associated with the local magnetic moment  $\xi$ . The last term is a constant which originates in the prefactor  $\sqrt{\beta U/4\pi}$  of the integral. The energy per atom in the SSA is obtained from the relation  $\langle H - \mu N \rangle = \mathscr{F}_{\text{SSA}} + \beta^{-1} S$  as

$$\langle H \rangle = \mu n + \int d\omega f(\omega) \omega \tilde{\rho}(\omega) - \frac{1}{4} U \left( \langle \zeta_i^2(\xi) \rangle - \langle \xi_i^2 \rangle + \frac{2}{\beta U} \right). \tag{3.96}$$

Here n is the electron number per atom. The energy in the static approximation has the same form as the Hartree–Fock one (2.13), though the DOS  $\tilde{\rho}(\omega)$  and the amplitude  $\langle \xi_i^2 \rangle$  shows a strong temperature dependence.

It should be noted that the coherent potential  $\Sigma_{\sigma}(z)$  and the chemical potential  $\mu$  are self-consistently determined in the single-site theory of spin fluctuations by means of the CPA equation (3.85) and the condition (3.90) for a given charge n. The noninteracting DOS  $\rho(\varepsilon)$  for the Hamiltonian matrix  $t_{ij}$  is assumed to be given in the theory. We first assume  $\Sigma_{\sigma}$  and  $\mu$ , and calculate the coherent Green function (3.88). Then we obtain the Hartree–Fock charge  $\zeta_i(\xi)$  for each  $\xi$  solving the self-consistent equations (3.70) and (3.91). Using these solutions, we can calculate the energy potential  $E_i(\xi)$  according to (3.78), therefore the l.h.s. of the CPA equation (3.85) taking the thermal average with respect to  $E_i(\xi)$ . When the CPA equation (3.85) is not satisfied, we may renew the coherent potential, for example, using the following equation.

$$\Sigma_{\sigma}^{(\text{new})}(z) = \Sigma_{\sigma}^{(\text{old})}(z) - \left[ \frac{\langle G_{i\sigma}^{(i)}(z,\xi) \rangle - F_{i\sigma}(z)}{\langle G_{i\sigma}^{(i)}(z,\xi) \rangle F_{i\sigma}(z)} \right]_{\text{old}}.$$
 (3.97)

The above equation was found in the averaged t-matrix approximation to the CPA [51] (see also Appendix B). The renewed potential  $\Sigma_{\sigma}^{(\text{new})}(z)$  improves the self-consistency, and after several iterations we may find the CPA solution  $\Sigma_{\sigma}(z)$  for each z. Next we calculate the average charge according to (3.90). When the obtained charge is not consistent with the given charge n, we can renew the chemical potential  $\mu$ , for example, by using Newton's method, and return to the beginning of

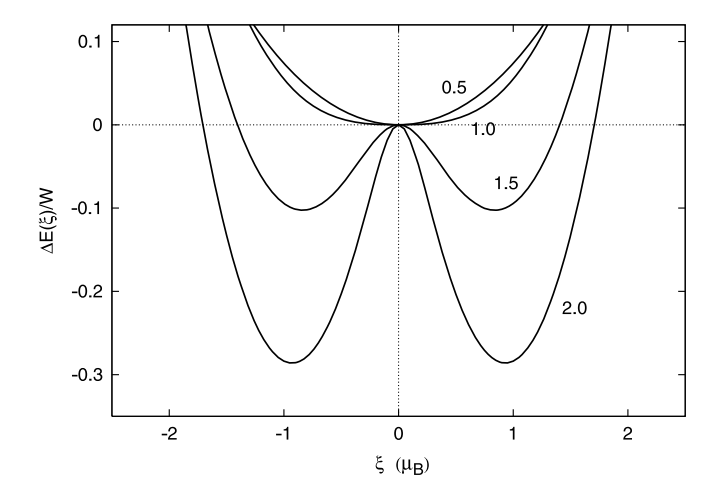


Fig. 3.3 Energy potential curves  $\Delta E_i(\xi) = E_i(\xi) - E_i(0)$  calculated at half-filling for U/W = 0.5, 1.0, 1.5, 2.0 in the paramagnetic state at T/W = 0.06 [53], where W denotes a half the band width. Semi-elliptical model density of states  $\rho(\varepsilon) = 2\sqrt{W^2 - \varepsilon^2}/\pi W^2$  is assumed for noninteracting electrons

the procedure mentioned above. When the self-consistency for both  $\Sigma_{\sigma}(z)$  and  $\mu$  is achieved, we can calculate various physical quantities.

The basic behavior of local magnetic moments is determined by the single-site energy  $E_i(\xi)$  (see (3.78)). Let us consider the paramagnetic state at half-filling, where  $\zeta_i(\xi)=1$  irrespective of  $\xi$ . When  $\xi$  is small, we have  $E_i(\xi)=E_i(0)+A\xi^2/2$ . For small U, the Gaussian term in  $E_i(\xi)$  (i.e., the second term at the r.h.s. of (3.78)) is dominant because it is proportional to U, so that A>0, while A<0 for large U because the kinetic energy term (i.e., the first term at the r.h.s. of (3.78)) decreases as  $\xi$  increases and its magnitude is proportional to  $U^2$ . When  $\xi$  is large, the Gaussian part again becomes dominant. Therefore  $E_i(\xi)$  shows a single minimum structure for small U, while it shows a double-minimum structure for large U as shown in Fig. 3.3.

When the system shows a single minimum structure in energy potential  $E_i(\xi)$  (see the curve for U/W=0.5 in Fig. 3.3), the magnetic moment  $\xi$  vanishes at T=0. In this case, it may appear with the polarization of the effective medium. The magnetic moment fluctuates around the minimum point with elevating temperature. When the system shows a double-minimum structure (see the curves for U/W=1.5 and U/W=2.0 in Fig. 3.3), the magnetic moment given by the condition  $\partial E_i(\xi_i)/\partial \xi_i=0$  appears at T=0, and thermally fluctuates between the two minima. In this case, large spin fluctuations which changes their direction are possible. Accordingly, the magnetic entropy of  $\ln 2$  occurs. We call such a system the local moment system.

Various model calculations for the ferromagnetism have been performed with use of the single-site theory in the static approximation. In the single-site theory, the ferromagnetism is defined as a polarized state of the effective medium;

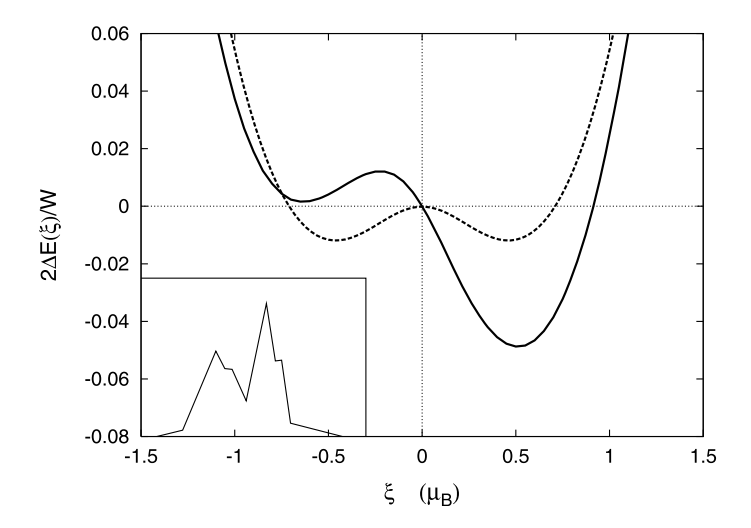


**Fig. 3.4** Energy potential curves  $\Delta E_i(\xi) = E_i(\xi) - E_i(0)$  calculated at a temperature below (*solid curve*) and above (*dashed curve*) the Curie temperature for n = 1.44 and 2U/W = 2.29 ('bcc Fe') [54], W being a width of the model band shown in the *inset* 

 $\Sigma_{\uparrow}(z) \neq \Sigma_{\downarrow}(z)$ . The ferromagnetic solution is usually found in the system with non-half-filled bands and a large Coulomb interaction. Figure 3.4 shows a numerical example for electron number n=1.44 which corresponds to bcc Fe when electron number n is multiplied by 5 (number of d orbitals) [54]. In the paramagnetic state, we have double minima in energy curve  $E_i(\xi)$ . Below the Curie temperature  $T_{\rm C}$ , we have an energy-dependent molecular field  $\Sigma_{\uparrow}(z) - \Sigma_{\downarrow}(z)$ , consequently the energy potential curve becomes asymmetric as shown by the solid curve in the figure, and the ferromagnetism with the magnetization at the minimum is stabilized.

Figure 3.5 shows another example of the energy potential curves for a system with n = 1.8 on the fcc lattice, which might correspond to fcc Ni. In this case, we find the single minimum structure both above and below  $T_{\rm C}$ . With the appearance of the energy-dependent molecular field  $\Sigma_{\uparrow}(z) - \Sigma_{\downarrow}(z)$ , the minimum point shifts to the positive region of  $\xi$ , and the ferromagnetism is realized.

Temperature dependence of calculated magnetic moments is presented in Fig. 3.6. In the case of n=1.44 and 2U/W=2.29 ('bcc Fe'), the ground-state magnetization is  $m_0=0.511$  (= 2.56/5)  $\mu_{\rm B}$ . With increasing temperature the magnetization decreases and vanishes at  $T_{\rm C}/W=0.0253$  ( $T_{\rm C}=900$  K for W=0.45 Ry). In the case of n=1.80 and 2U/W=3.43 ('fcc Ni'), we obtain the ground-state magnetization  $m_0=0.146$  (= 0.73/5)  $\mu_{\rm B}$  and the Curie temperature  $T_{\rm C}/W=0.0192$  ( $T_{\rm C}=530$  K for W=0.35 Ry). In both cases, we find the paramagnetic susceptibilities which follow the Curie–Weiss law,  $\chi=(m_{\rm eff}^2/3)/(T-T_{\rm C})$ . Here the effective Bohr magneton numbers are obtained as  $m_{\rm eff}=1.75m_0$  for 'bcc Fe' and  $m_{\rm eff}=3.20m_0$  for 'fcc Ni', respectively, while the experimental data indicate that

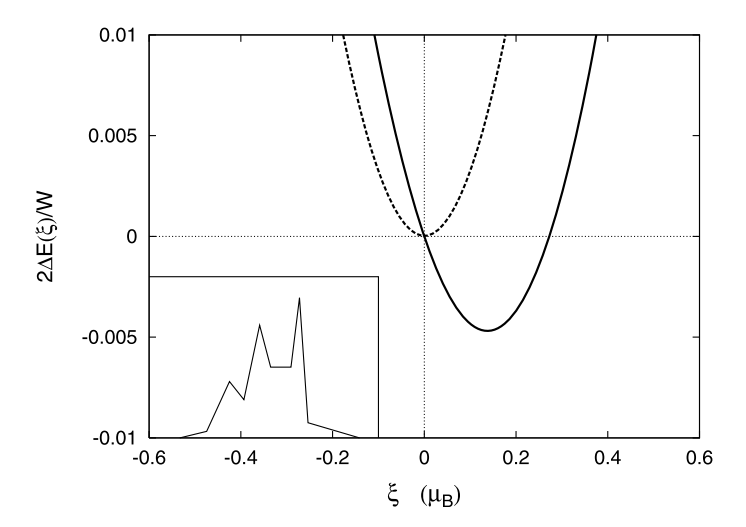
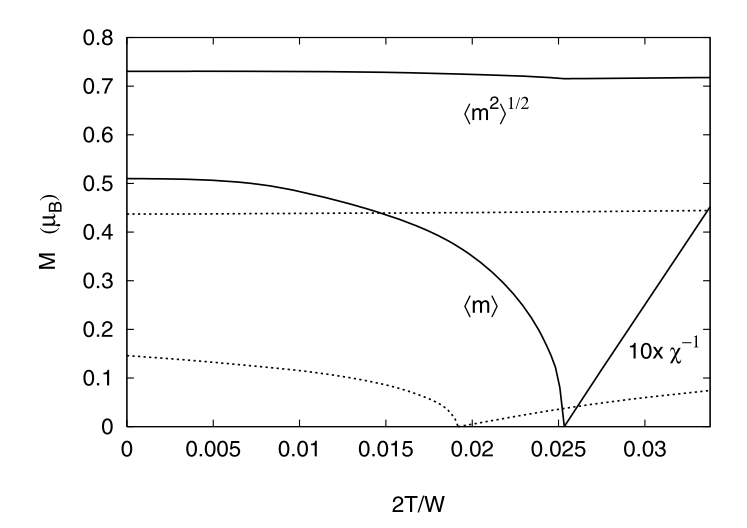


Fig. 3.5 Energy potential curves  $\Delta E_i(\xi)$  calculated below (solid curve) and above (dashed curve) the Curie temperature for n=1.80 and 2U/W=3.43 ('fcc Ni') [54]. The inset shows the model density of states for fcc Ni



**Fig. 3.6** Magnetization vs. temperature curves, inverse susceptibilities, amplitudes of local moments for 'bcc Fe': n = 1.44, 2U/W = 2.29 (*solid curves*), and for 'fcc Ni': n = 1.80, 2U/W = 3.43 (*dotted curves*) [54]

 $m_{\rm eff} = 1.44 m_0$  for bcc Fe and  $m_{\rm eff} = 2.68 m_0$  for fcc Ni. These results show that the SSF qualitatively explains the metallic ferromagnetism, and significantly improve the Hartree–Fock results.

#### 3.4 Dynamical CPA Theory

The single-site theory of spin fluctuations (SSF) discussed in the last section is based on the static approximation, i.e., the high-temperature approximation. The theory reduces to the Hartree–Fock approximation at the ground state and thus it does not take into account electron correlations at zero temperature. More important is that it does not describe the Fermi liquid state as found in metals and alloys at low temperatures. It is also expected that the dynamical spin fluctuations which are not taken into account further reduce the magnetization and the Curie temperature. In order to overcome these difficulties, we extend here the theory to the dynamical case [54–57]. The theory is called the dynamical coherent-potential approximation (CPA).

We introduced the energy dependent effective medium  $\Sigma_{\sigma}(z)$  to the static energy potential (3.68) in the SSF. In the dynamical CPA, we introduce a time-dependent effective medium  $\Sigma$  defined by

$$(\Sigma)_{i\tau\sigma j\tau'\sigma'} \equiv \Sigma_{i\sigma} (\tau - \tau') \delta_{ij} \delta_{\sigma\sigma'}, \tag{3.98}$$

and insert it into the potential part of the energy functional (3.46) as follows.

$$\operatorname{Sp}\ln(g^{-1} - v) = \operatorname{Sp}\ln(g^{-1} - \Sigma - \delta v) = \operatorname{Sp}\ln(\tilde{G}^{-1} + \operatorname{Sp}\ln(1 - \delta v\tilde{G})). \quad (3.99)$$

Here  $\delta v = v - \Sigma$ , and the coherent Green function is defined by

$$(\tilde{G})_{i\tau\sigma j\tau'\sigma'} = \left[ \left( g^{-1} - \Sigma \right)^{-1} \right]_{i\tau\sigma j\tau'\sigma} \delta_{\sigma\sigma'}. \tag{3.100}$$

The energy functional  $E[\xi, \eta]$  (see (3.46)) is then divided into the coherent part and the remaining correction term as

$$E[\xi, \eta] = -\frac{1}{\beta} \left[ \ln \tilde{Z}_0 + \operatorname{Sp} \ln(1 - \delta v \tilde{G}) \right]$$

$$+ \sum_i \frac{U}{4\beta} \int_0^\beta d\tau \left( \eta_i^2(\tau) + \xi_i^2(\tau) \right).$$
(3.101)

The partition function  $\tilde{Z}_0$  is defined by  $\ln \tilde{Z}_0 = \ln Z_0^0 + \operatorname{Sp} \ln(1 - \Sigma g)$ . Defining the diagonal coherent Green function F and the off-diagonal F' as

$$\tilde{G} = F + F', \tag{3.102}$$

$$(F)_{i\tau\sigma j\tau'\sigma'} = \left[ \left( g^{-1} - \Sigma \right)^{-1} \right]_{i\tau\sigma i\tau'\sigma'} = (\tilde{G})_{i\tau\sigma i\tau'\sigma} \delta_{ij} \delta_{\sigma\sigma'}, \tag{3.103}$$

$$(F')_{i\tau\sigma i\tau'\sigma'} = (\tilde{G})_{i\tau\sigma j\tau'\sigma} (1 - \delta_{ij})\delta_{\sigma\sigma'}, \tag{3.104}$$

one can expand the scattering potential  $\delta v$  in the energy functional with respect to sites as follows.

$$E[\xi, \eta] = \tilde{\mathscr{F}}[\Sigma] + \sum_{i} E_{i}[\xi_{i}, \eta_{i}] + \Delta E[\xi, \eta]. \tag{3.105}$$

Here the first term at the r.h.s. of the above equation is the coherent part of the free energy defined by

$$\tilde{\mathscr{F}}[\Sigma] = -\beta^{-1} \ln \tilde{Z}_0 = -\beta^{-1} \ln Z_0^0 - \beta^{-1} \operatorname{Sp} \ln(1 - \Sigma g). \tag{3.106}$$

The impurity contribution to the energy functional is given by

$$E_i[\xi_i, \eta_i] = -\beta^{-1} \operatorname{tr} \ln(1 - \delta v_i F_i) + \frac{U}{4\beta} \int_0^\beta d\tau \left( \eta_i^2(\tau) + \xi_i^2(\tau) \right), \quad (3.107)$$

where tr means a trace over time and spin, and we used the notation  $(F_i)_{\tau\sigma\tau'\sigma'} \equiv (F)_{i\tau\sigma i\tau'\sigma'}$  is used. The last term in (3.105) is the off-diagonal contribution to the energy functional, which is given by

$$\Delta E[\xi, \eta] = -\beta^{-1} \operatorname{Sp} \ln(1 - \tilde{t}F').$$
 (3.108)

Here  $\tilde{t}$  is the single-site t matrix defined by

$$\tilde{t} = (1 - \delta v F)^{-1} \delta v. \tag{3.109}$$

Substituting (3.105) into (3.39), we obtain the following expression of the free energy.

$$\mathscr{F} = \widetilde{\mathscr{F}}[\Sigma] - \sum_{i} \frac{1}{\beta} \ln \int \delta \xi_{i} \delta \eta_{i} e^{-\beta E_{i}[\xi_{i}, \eta_{i}]} - \frac{1}{\beta} \ln \langle e^{-\beta \Delta E} \rangle_{0}.$$
 (3.110)

Here  $\langle \sim \rangle_0$  means the single-site average with respect to its energy functionals.

$$\langle \sim \rangle_0 \equiv \frac{\int \left[ \prod_i \delta \xi_i \delta \eta_i \right] (\sim) e^{-\beta \sum_i E_i [\xi_i, \eta_i]}}{\int \left[ \prod_i \delta \xi_i \delta \eta_i \right] e^{-\beta \sum_i E_i [\xi_i, \eta_i]}}.$$
 (3.111)

The single-site approximation (SSA) is to neglect the inter-site term (the last term) in the free energy expansion (3.110). We choose the effective medium so that the corrections from the last term becomes minimum. As expected from (3.108), the condition is given by  $\langle \tilde{t}_i \rangle_0 = 0$ ; that is,

$$\langle \tilde{t}_i \rangle = 0. \tag{3.112}$$

Here  $\langle \sim \rangle$  stands for the single-site average as

$$\langle \sim \rangle = \frac{\int \delta \xi_i \delta \eta_i(\sim) e^{-\beta E_i[\xi_i, \eta_i]}}{\int \delta \xi_i \delta \eta_i e^{-\beta E_i[\xi_i, \eta_i]}}.$$
 (3.113)

The matrix  $\tilde{t}_i$  in (3.112) denotes the single-site t matrix due to a local potential  $\delta v_i$ .

$$\tilde{t}_i = (1 - \delta v_i F_i)^{-1} \delta v_i,$$
(3.114)

and

$$(\delta v_i)_{\tau \sigma \tau' \sigma'} = \Delta \tau \delta v_{i\sigma} (\tau, \tau') \Delta \tau \delta_{\sigma \sigma'}$$
  
=  $\Delta \tau (v_{i\sigma}(\tau) \delta(\tau - \tau') - \Sigma_{i\sigma}(\tau - \tau')) \Delta \tau \delta_{\sigma \sigma'}.$  (3.115)

Here  $\Delta \tau = \beta/N$ , N being the number of mesh in the time interval  $[0, \beta]$ . Equation (3.112) means that the single-site t matrix due to the scattering potential from the effective medium should vanishes in average.

One can rewrite the condition (3.112) as

$$\langle (F_i^{-1} - \delta v_i)^{-1} \rangle = F_i.$$
 (3.116)

Equations (3.112) and (3.116) are referred as the dynamical CPA equation. The r.h.s. of (3.116) is the diagonal part of the coherent Green function, i.e., (3.103). The l.h.s. is an impurity Green function for the system with impurity potential  $v_i$  embedded in the effective medium  $\Sigma$ . One can verify the fact as follows. The Hamiltonian in the interaction representation is given by

$$H^{(i)}(\tau) = \tilde{H}(\tau) + \sum_{\sigma} \int_{0}^{\beta} d\tau' \, a_{i\sigma}^{\dagger}(\tau) \{ v_{i\sigma}(\tau) \delta(\tau - \tau') - \Sigma_{i\sigma}(\tau - \tau') \} a_{i\sigma}(\tau').$$
(3.117)

Here  $\tilde{H}(\tau)$  is the time-dependent Hamiltonian for the coherent potential.

$$\tilde{H}(\tau) = H_0(\tau) + \sum_{i\sigma} \int_0^\beta d\tau' \, a_{i\sigma}^\dagger(\tau) \, \Sigma_{i\sigma} (\tau - \tau') a_{i\sigma}(\tau'). \tag{3.118}$$

The impurity Green function for the Hamiltonian  $H^{(i)}(\tau)$  is defined as follows (see (3.42)).

$$G_{jl\sigma}^{(i)}(\tau,\tau') \equiv -\frac{\text{Tr}(\mathcal{T}a_{j\sigma}(\tau)a_{l\sigma}^{\dagger}(\tau')e^{-\int_{0}^{\beta}H^{(i)}(\tau'')d\tau''})}{\text{Tr}(\mathcal{T}e^{-\int_{0}^{\beta}H^{(i)}(\tau'')d\tau''})}.$$
 (3.119)

The Dyson equation for the Green function  $G_{jl\sigma}^{(i)}(\tau,\tau')$  is given by [43, 44]

$$G_{jl\sigma}^{(i)}(\tau,\tau') = g_{jl\sigma}(\tau - \tau') + \int_0^\beta d\tau_1 d\tau_2 \sum_k g_{jk\sigma}(\tau - \tau_1)$$

$$\times \{ \Sigma_{k\sigma}(\tau_1 - \tau_2) + \delta v_{i\sigma}(\tau_1,\tau_2) \delta_{ik} \} G_{kl\sigma}^{(i)}(\tau_2,\tau'). \quad (3.120)$$

The above equation yields the following solution in the matrix representation.

$$G^{(i)} = (F_i^{-1} - \delta v_i)^{-1}. (3.121)$$

This is identical with the inside of the average at the l.h.s. of (3.116). Therefore the CPA equation (3.116) is expressed as

$$\langle G^{(i)} \rangle = F_i. \tag{3.122}$$

The dynamical CPA equations (3.112) and (3.122) have the same form as (3.83) and (3.85) in the static approximation. Thus the physical picture of the dynamical CPA equation is the same as given in Fig. 3.2. We have replaced the dynamical potentials  $\{v_{j\sigma}\}$  with dynamical coherent potential  $\Sigma$  at the surrounding sites in order to reduce the number of field variables. We have then an impurity system described by an effective Hamiltonian (3.117), thereby obtaining the impurity Green function (3.121). The l.h.s. in Fig. 3.2 shows such a system. On the other hand, we can consider a coherent system in which all dynamical potentials have been replaced by coherent ones as shown at the r.h.s. in Fig. 3.2. Corresponding Green function is the coherent Green function (3.103). The CPA equation (3.122) indicates that these states should be identical when the effective medium is chosen to be best.

The free energy in the dynamical CPA is obtained from (3.110) as follows.

$$\mathscr{F}_{\text{CPA}} = \tilde{\mathscr{F}}[\Sigma] - \sum_{i} \frac{1}{\beta} \ln \int \delta \xi_{i} \delta \eta_{i} e^{-\beta E_{i}[\xi_{i}, \eta_{i}]}.$$
 (3.123)

One can verify that the dynamical CPA equations (3.112) and (3.122) are also equivalent to the following stationary condition for the CPA free energy.

$$\frac{\delta \mathscr{F}_{\text{CPA}}}{\delta \Sigma_{i\sigma}(\tau - \tau')} = 0. \tag{3.124}$$

In order to verify the above relation, we express the functional derivative of  $\delta \mathscr{F}_{\text{CPA}}/\delta \Sigma_{n\sigma}(\tau-\tau')$  as

$$\frac{\delta \mathscr{F}_{\text{CPA}}}{\delta \Sigma_{n\sigma}(\tau - \tau')} = \left\langle \frac{\delta}{\delta \Sigma_{n\sigma}(\tau - \tau')} \left( \tilde{\mathscr{F}} + \sum_{i} E_{i}[\xi_{i}, \eta_{i}] \right) \right\rangle. \tag{3.125}$$

Substituting (3.106) and (3.107) into (3.125), we obtain

$$\frac{\delta \mathscr{F}_{\text{CPA}}}{\delta \Sigma_{n\sigma}(\tau - \tau')} = -\beta^{-1} \left\langle -(F_n)_{\tau'\tau\sigma} + \left[ F_n (1 - \delta v_n F_n)^{-1} \right]_{\tau'\tau\sigma} - \sum_{i} \text{tr} \left[ (1 - \delta v_i F_i)^{-1} \delta v_i \frac{\delta F_i}{\delta \Sigma_{n\sigma}(\tau - \tau')} \right] \right\rangle. \quad (3.126)$$

Here tr means taking the trace over time and spin. The first and the second terms at the r.h.s. of the above equation are written by the single-site t-matrix on site n, so that we obtain

$$\frac{\delta \mathscr{F}_{\text{CPA}}}{\delta \Sigma_{n\sigma}(\tau - \tau')} = \left[ F_n \langle \tilde{t}_n \rangle F_n \right]_{\tau'\tau\sigma} - \sum_i \text{tr} \left[ \langle \tilde{t}_i \rangle \frac{\delta F_i}{\delta \Sigma_{n\sigma}(\tau - \tau')} \right]. \quad (3.127)$$

Using the CPA condition (3.112), we reach (3.124).

The formulae (3.50), (3.51), (3.54), and (3.55) of the local charge and magnetic moment on site i can be rederived by taking the derivatives  $\partial \mathscr{F}_{\text{CPA}}/\partial \varepsilon_i^0$  and  $-\partial \mathscr{F}_{\text{CPA}}/\partial h_i$ , after having introduced a site-dependent atomic level  $\varepsilon_i^0$  and a magnetic field  $h_i$  acting on site i. The Green function  $G_{ii\sigma}(\tau, \tau^+)$  in (3.50) and (3.51), however, should be replaced by the coherent  $F_{ii\sigma}(\tau, \tau^+)$ .

$$\langle n_i \rangle = \sum_{\sigma} \frac{1}{\beta} \int_0^{\beta} d\tau \, F_{ii\sigma} (\tau, \tau^+), \qquad (3.128)$$

$$\langle m_i \rangle = \sum_{\sigma} \sigma \frac{1}{\beta} \int_0^{\beta} d\tau \, F_{ii\sigma}(\tau, \tau^+).$$
 (3.129)

In actual calculations of physical quantities, the Fourier representation is more convenient. The Green function for noninteracting Hamiltonian  $H_0$  is expressed as

$$g_{ij\sigma}(\tau - \tau') = \frac{1}{\beta} \sum_{l} g_{ij\sigma}(i\omega_l) e^{-i\omega_l(\tau - \tau')}.$$
 (3.130)

Here  $\omega_l$  is the Matsubara frequency for the anti-periodic function,  $\omega_l = (2l+1)\pi/\beta$ . The Fourier transform  $g_{ij\sigma}(i\omega_l)$  is obtained as

$$g_{ij\sigma}(i\omega_l) = \sum_{k} \frac{\langle i|k\rangle\langle k|j\rangle}{i\omega_l - \varepsilon_k}.$$
 (3.131)

In the same way, the Fourier representations of the coherent Green function and the coherent potential are given as follows.

$$F_{i\sigma}(\tau - \tau') = \frac{1}{\beta} \sum_{l} F_{i\sigma}(i\omega_{l}) e^{-i\omega_{l}(\tau - \tau')}, \qquad (3.132)$$

$$\Sigma_{i\sigma}(\tau - \tau') = \frac{1}{\beta} \sum_{l} \Sigma_{i\sigma}(i\omega_{l}) e^{-i\omega_{l}(\tau - \tau')}.$$
 (3.133)

Here  $F_{i\sigma}(i\omega_l)$  is given by (3.88) with  $z = i\omega_l$  and  $\Sigma_{i\sigma}(i\omega_l)$  should be determined by the dynamical CPA equation.

For the field variables associated with the dynamical potential, it is suitable to adopt the Fourier transform as the periodic function (i.e.,  $v(\tau < 0) = v(\tau + \beta)$ ).

$$\xi_i(\tau) = \sum_{l} \xi_i(i\omega_l) e^{-i\omega_l \tau}, \qquad (3.134)$$

where  $\omega_l = 2l\pi/\beta$ . The dynamical potential is therefore expressed as

$$v_i(\tau) = \sum_{l} v_i(i\omega_l) e^{-i\omega_l \tau}.$$
 (3.135)

Here the Fourier representation of the potential is given by

$$v_{j\sigma}(i\omega_l) = (\varepsilon_0 - \mu)\delta_{l0} - \frac{1}{2}U\{\pm i\eta_j(i\omega_l) + \xi_j(i\omega_l)\sigma\}. \tag{3.136}$$

The free energy in the Fourier representation has the same form as (3.123):

$$\mathscr{F}_{\text{CPA}} = \tilde{\mathscr{F}}[\Sigma] - \sum_{i} \frac{1}{\beta} \ln \int \delta \xi_{i} \delta \eta_{i} e^{-\beta E_{i}[\xi_{i}, \eta_{i}]}.$$
 (3.137)

The coherent part  $\tilde{\mathscr{F}}[\Sigma]$  defined by (3.106) is now given by

$$\widetilde{\mathscr{F}}[\Sigma] = -\frac{1}{\beta} \ln \operatorname{tr}(e^{-\beta H_0}) - \frac{1}{\beta} \operatorname{Sp} \ln(1 - \Sigma g)$$

$$= -\frac{1}{\beta} \sum_{k,l,\sigma} \ln \{i\omega_l - \varepsilon_k - \Sigma_{\sigma}(i\omega_l)\}.$$
(3.138)

Here Sp stands for a trace over site, frequency, and spin. The functional integral in (3.137) is given by

$$\int \delta \xi = \int \sqrt{\frac{\beta U}{4\pi}} \, d\xi(0) \left[ \prod_{l=1}^{\infty} \frac{\beta U}{2\pi} \, d^2 \xi(i\omega_l) \right], \tag{3.139}$$

where  $d^2\xi(i\omega_l) = d\operatorname{Re}\xi(i\omega_l) d\operatorname{Im}\xi(i\omega_l)$ .

The energy functional defined by (3.107) is expressed in the frequency representation as follows.

$$E_{i}[\xi_{i}, \eta_{i}] = -\frac{1}{\beta} \operatorname{tr} \ln(1 - \delta v_{i} F_{i}) + \frac{1}{4} U \sum_{l} \{ \left| \eta_{i}(i\omega_{l}) \right|^{2} + \left| \xi_{i}(i\omega_{l}) \right|^{2} \}.$$
 (3.140)

Here tr stands for a trace over frequency and spin. It should be noted that  $\delta v_i$  is not diagonal in the frequency representation because it contains the Fourier transform of the time dependent potential.

$$(\delta v_i)_{il\sigma jm\sigma'} = \delta v_{i\sigma}(i\omega_l, i\omega_m)\delta_{ij}\delta_{\sigma\sigma'}, \tag{3.141}$$

$$\delta v_{i\sigma}(i\omega_l, i\omega_m) = v_{i\sigma}(i\omega_l - i\omega_m) - \Sigma_{i\sigma}(i\omega_l)\delta_{lm}. \tag{3.142}$$

The Fourier transform of the dynamical CPA equation (3.122) is given by

$$\langle G_{i\sigma}^{(i)}(i\omega_l, i\omega_l)\rangle = F_{i\sigma}(i\omega_l), \qquad (3.143)$$

$$G_{i\sigma}^{(i)}(i\omega_l, i\omega_l) = \left[ \left( F_i^{-1} - \delta v_i \right)^{-1} \right]_{l\sigma l\sigma}. \tag{3.144}$$

The stationary condition (3.124), which is equivalent to the dynamical CPA equation, is expressed in the frequency representation as follows.

$$\frac{\delta \mathscr{F}_{\text{CPA}}}{\delta \Sigma_{i\sigma}(i\omega_l)} = 0. \tag{3.145}$$

The dynamical CPA is also obtained from the Dyson equation (3.43) for a time-dependent Green function by making use of the multiple scattering theory (see Appendix B). The dynamical CPA completely takes into account the single-site spin and charge fluctuations. Thus the theory is the best single-site approximation. As will be shown in Sect. 3.6, the dynamical CPA is equivalent to the many-body CPA in the disordered alloys [61], the dynamical mean-field theory (DMFT) in the metal-insulator transition [62, 63], and the projection operator method CPA in the excitation problem [64].

When we approximate the dynamical potential with the static one:  $v_{i\sigma}(i\omega_l - i\omega_m) \approx v_{i\sigma}(0)\delta_{lm}$ , we can perform the integration with respect to the dynamical variables  $\{\xi(i\omega_l), \eta(i\omega_l)\}(l \neq 0)$  using the Gaussian integrals. The free energy (3.137) then reduces to

$$\mathscr{F}_{\text{CPA}} = \tilde{\mathscr{F}}[\Sigma] - \beta^{-1} \sum_{i} \ln \int \sqrt{\frac{\beta U}{4\pi}} \, d\xi_i \sqrt{\frac{\beta U}{4\pi}} \, d\eta_i \, e^{-\beta E_i(\xi_i, \eta_i)}, \quad (3.146)$$

and

$$E_i(\xi_i, \eta_i) = -\beta^{-1} \operatorname{tr} \ln(1 - \delta v_i(0) F_i) + \frac{1}{4} U(\xi_i^2 + \eta_i^2).$$
 (3.147)

Here  $(\delta v_i(0))_{l\sigma m\sigma'} = (v_{i\sigma}(0) - \Sigma_{\sigma}(i\omega_l))\delta_{lm}\delta_{\sigma\sigma'}$ .  $\xi_i = \xi_i(0)$  and  $\eta_i = \eta_i(0)$  are the static field variables defined by (3.56).

When all the sites are equivalent to each other one can omit the subscript i. Making use of the saddle-point approximation to the charge field  $(\partial E_i/\partial \eta_i = 0)$ , we obtain the free energy per atom in the static approximation as follows.

$$\mathscr{F}_{\text{CPA}} = \tilde{\mathscr{F}}[\Sigma] - \beta^{-1} \ln \int \sqrt{\frac{\beta U}{4\pi}} d\xi \, e^{-\beta E_i(\xi)}. \tag{3.148}$$

Here  $\mathscr{F}_{CPA}$  ( $\tilde{\mathscr{F}}$ ) now denotes the free energy (coherent free energy) per site, and the static energy potential is expressed as follows.

$$E_{i}(\xi) = -\beta^{-1} \sum_{l\sigma} \ln(1 - \delta v_{\sigma}(i\omega_{l}, \xi) F_{\sigma}(i\omega_{l})) + \frac{1}{4} U(\xi^{2} - \zeta^{2}(\xi)).$$
(3.149)

Here  $\delta v_{\sigma}(i\omega_l, \xi)$  is defined by (3.79), and

$$\zeta(\xi) = \frac{1}{\beta} \sum_{l\sigma} G_{i\sigma}^{(i)}(i\omega_l, \xi). \tag{3.150}$$

The static Green function  $G_{i\sigma}^{(i)}(z,\xi)$  is defined by (3.86). In the same approximation, the dynamical CPA equation (3.143) reduces to the static one as

$$\langle G_{i\sigma}^{(i)}(i\omega_l, \xi) \rangle = F_{i\sigma}(i\omega_l). \tag{3.151}$$

The frequency sums in (3.149) and (3.150) can be transformed into the integrals on the real axis of the complex z plane, so that one can verify that the free energy (3.148), the energy potential (3.149), the self-consistent equation for the charge field (3.150) and the CPA equation (3.151) are identical with those obtained in the single-site spin fluctuation theory (SSF) presented in the last section (see (3.82), (3.78), (3.91), and (3.85)). That is, the dynamical CPA reduces to the SSF when the static approximation is made. The derivation is given in Appendix C.

#### 3.5 Dynamical CPA with Harmonic Approximation

We have seen in Sect. 3.3 that the single-site theory based on the static approximation (i.e., SSF) describes well the high temperature properties of metallic magnetism. Thus it is reasonable to take into account the dynamical corrections starting from the static limit, i.e., from the high temperature limit. In this section we present such an approach based on the harmonic approximation [54].

We assume that all the sites are equivalent, and express the free energy (3.137) as follows.

$$\mathscr{F}_{\text{CPA}} = \tilde{\mathscr{F}} - \beta^{-1} \ln \int \sqrt{\frac{\beta U}{4\pi}} d\xi \, e^{-\beta E_{\text{eff}}(\xi)}. \tag{3.152}$$

Here we omitted the site indices for simplicity.  $\mathscr{F}_{CPA}$  ( $\widetilde{\mathscr{F}}$ ) denotes the free energy (coherent part of the free energy) per site. The effective potential  $E_{eff}(\xi)$  projected onto the static field variable  $\xi$  is defined by

$$e^{-\beta E_{\text{eff}}(\xi)} = \int \left[ \prod_{l=1}^{\infty} \frac{\beta U}{2\pi} d^2 \xi(i\omega_l) \frac{\beta U}{2\pi} d^2 \eta(i\omega_l) \right] e^{-\beta E[\xi,\eta]}. \tag{3.153}$$

Note that we have taken the saddle point  $\eta^*$  for static charge field  $\eta = \eta(0)$  for simplicity.

In order to start from the static limit, we divide the dynamical potential (3.136) into the static part  $v_0$  and the dynamical part  $\tilde{v}$  as  $v = v_0 + \tilde{v}$ , where

$$(v_0)_{l\sigma m\sigma'} \equiv v_{i\sigma}(0)\delta_{lm}\delta_{\sigma\sigma'},\tag{3.154}$$

$$(\tilde{v})_{l\sigma m\sigma'} \equiv \left(v_{i\sigma}(i\omega_l - i\omega_m) - v_{i\sigma}(0)\delta_{lm}\right)\delta_{\sigma\sigma'}.$$
 (3.155)

Accordingly, the first term in the single-site energy functional (3.140) can be divided into two parts as follows.

$$\operatorname{tr}\ln(1-\delta vF) = \operatorname{tr}\ln(1-\delta v_0F) + \operatorname{tr}\ln(1-\tilde{v}\tilde{g}). \tag{3.156}$$

Here  $\delta v_0 = v_0 - \Sigma$ , and the static Green function  $\tilde{g}$  is defined by

$$(\tilde{g})_{l\sigma m\sigma'} \equiv \left[ \left( g^{-1} - v_0 \right)^{-1} \right]_{l\sigma m\sigma'} = \tilde{g}_{\sigma}(i\omega_l)\delta_{lm}\delta_{\sigma\sigma'}, \tag{3.157}$$

$$\tilde{g}_{\sigma}(i\omega_l) = \left(F_{\sigma}(i\omega_l)^{-1} - \delta v_{\sigma}(i\omega_l, \xi)\right)^{-1}.$$
(3.158)

Here  $\delta v_{\sigma}(i\omega_l, \xi)$  is defined by (3.79). Note that the diagonal part  $\tilde{g}_{\sigma}(i\omega_l)$  is identical with (3.86) with  $z = i\omega_l$ .

Substituting the single-site energy functional (3.140) with the relation (3.156) into (3.153), we can divide the effective potential into two parts as follows.

$$E_{\text{eff}}(\xi) = E_{\text{st}}(\xi) + E_{\text{dyn}}(\xi).$$
 (3.159)

The first term  $E_{\rm st}(\xi)$  is the static energy potential given by (3.149). The second term is the dynamical contribution  $E_{\rm dyn}(\xi)$  given by

$$e^{-\beta E_{\text{dyn}}(\xi)} = \int \left[ \prod_{l=1}^{\infty} \frac{\beta U}{2\pi} d^2 \xi(i\omega_l) \frac{\beta U}{2\pi} d^2 \eta(i\omega_l) \right] D_{\uparrow} D_{\downarrow}$$

$$-\frac{\beta U}{2} \sum_{l=1}^{\infty} (|\xi(i\omega_l)|^2 + \eta(i\omega_l)|^2)$$

$$\times e \qquad (3.160)$$

Here we used the relation  $\operatorname{tr} \ln(1 - \tilde{v}\tilde{g}) = \ln \det(1 - \tilde{v}\tilde{g})$ . The determinant  $D_{\sigma}$  is defined by

$$D_{\sigma} = \det \left[ \delta_{lm} - \tilde{v}_{\sigma} (i\omega_{l} - i\omega_{m}) \tilde{g}_{\sigma} (i\omega_{m}) \right]. \tag{3.161}$$

The r.h.s. of (3.160) is a Gaussian average of  $D_{\uparrow}D_{\downarrow}$  with respect to the dynamical variables  $\{\xi(i\omega_l), \eta(i\omega_l)\}$ . Thus we express the dynamical contribution as

$$e^{-\beta E_{\rm dyn}(\xi)} = \overline{D_{\uparrow} D_{\downarrow}}. \tag{3.162}$$

Here the upper bar denotes the Gaussian average.

It should be noted that the dynamical CPA equation (3.143) is obtained from the stationary condition (3.145) and the free energy (3.152). Making use of the stationary condition, we find that the dynamical Green function (3.144) is obtained from the dynamical part of the effective potential as follows.

$$\langle G_{\sigma}^{(i)}(i\omega_{l}, i\omega_{l})\rangle = \left\langle \tilde{g}_{\sigma}(i\omega_{l}) - \beta \frac{\delta E_{\rm dyn}(\xi)}{\kappa_{\sigma}(i\omega_{l})\delta \Sigma_{\sigma}(i\omega_{l})} \right\rangle_{\rm eff}.$$
 (3.163)

Here  $\kappa_{\sigma}(i\omega_l) = 1 - F_{\sigma}(i\omega_l)^{-2} \delta F_{\sigma}(i\omega_l) / \delta \Sigma_{\sigma}(i\omega_l)$  and the average  $\langle \sim \rangle_{\rm eff}$  at the r.h.s. denotes a classical average with respect to the effective potential  $E_{\rm eff}(\xi)$ .

In this reformulation of the dynamical CPA with the use of the effective potential, the problem reduces to how to obtain the dynamical contribution  $E_{\rm dyn}(\xi)$  in (3.162) and (3.163). In order to calculate the dynamical contribution, we expand here the determinant with respect to the frequency modes of the dynamical potential  $\tilde{v}_{\sigma}(i\omega_{\nu})$  as follows.

$$D_{\sigma} = 1 + \sum_{\nu} (D_{\nu\sigma} - 1) + \sum_{(\nu,\nu')} (D_{\nu\nu'\sigma} - D_{\nu\sigma} - D_{\nu'\sigma} + 1) + \cdots, \quad (3.164)$$

$$D_{\nu\sigma} = \det[\delta_{lm} - (\tilde{v}_{\sigma}(i\omega_{\nu})\delta_{l-m,\nu} + \tilde{v}_{\sigma}(i\omega_{-\nu})\delta_{l-m,-\nu})\tilde{g}_{\sigma}(i\omega_{m})], \qquad (3.165)$$

$$D_{\nu\nu'\sigma} = \det[\delta_{lm} - (\tilde{v}_{\sigma}(i\omega_{\nu})\delta_{l-m,\nu} + \tilde{v}_{\sigma}(i\omega_{-\nu})\delta_{l-m,-\nu})\tilde{g}_{\sigma}(i\omega_{m}) - (\tilde{v}_{\sigma}(i\omega_{\nu'})\delta_{l-m,\nu'} + \tilde{v}_{\sigma}(i\omega_{-\nu'})\delta_{l-m,-\nu'})\tilde{g}_{\sigma}(i\omega_{m})]. \qquad (3.166)$$

The first term in (3.164) corresponds to the zeroth approximation (i.e. the static approximation), the second term expresses the independent scattering due to each dynamical potential  $v_{\sigma}(i\omega_{\nu})$ , and the higher order terms express the mode-mode couplings. We neglect here the mode-mode coupling terms and only take into account the independent frequency terms. This is known as the harmonic approximation (HA) [58, 59].

The approximation is exact up to the second order of U in the weak Coulomb interaction region. Numerical studies also indicate that it describes well the strong Coulomb interaction limit [60]. The approximation is independent of the Coulomb interaction strength, so that the HA is considered to be suitable for description of the intermediate region.

The determinant  $D_{\nu\sigma}$  can be expanded with respect to the dynamical potential as

$$D_{\nu\sigma} = \sum_{n=0}^{\infty} \frac{1}{n!} \left( 4\beta \tilde{v}_{\sigma}(\nu) \tilde{v}_{\sigma}(-\nu) \right)^{n} \left( \frac{i}{8\pi \nu} \right)^{n} B_{\nu\sigma}^{(n)}. \tag{3.167}$$

Here we adopted a simplified notation  $\tilde{v}_{\sigma}(v) = v_{\sigma}(i\omega_{v})$ .  $B_{v\sigma}^{(n)}$  consists of a linear combination of 2n products of the static Green function (see Appendix D).

Because  $\overline{D}_{\nu\sigma} = 1$  and  $\overline{D}_{\nu\sigma}D_{\nu'\sigma'} = \overline{D}_{\nu\sigma}\overline{D}_{\nu'\sigma'} = 1$  for  $\nu' \neq \nu$ , we obtain from (3.162) the dynamical part of effective potential in the harmonic approximation as

$$E_{\rm dyn}(\xi,\eta) = -\frac{1}{\beta} \ln \left[ 1 + \sum_{\nu=1}^{\infty} (\overline{D_{\nu\uparrow} D_{\nu\downarrow}} - 1) \right]. \tag{3.168}$$

Here  $\overline{D_{\nu\uparrow}D_{\nu\downarrow}}$  is calculated by using the Gaussian integrals as follows.

$$\overline{D_{\nu\uparrow}D_{\nu\downarrow}} = \sum_{l=0}^{\infty} U^{2l} \left(\frac{i}{2\pi\nu}\right)^{2l} B_{\nu\uparrow}^{(l)} B_{\nu\downarrow}^{(l)}. \tag{3.169}$$

Substituting (3.168) into (3.163), we obtain the impurity Green function as

$$\left\langle G_{\sigma}^{(i)}(i\omega_{l}, i\omega_{l}) \right\rangle = \left\langle \tilde{g}_{\sigma}(i\omega_{l}) + \frac{\sum_{\nu=1}^{\infty} \frac{\delta(\overline{D_{\nu\uparrow}D_{\nu\downarrow}})}{\kappa_{\sigma}(i\omega_{l})\delta\Sigma_{\sigma}(i\omega_{l})}}{1 + \sum_{\nu=1}^{\infty} (\overline{D_{\nu\uparrow}D_{\nu\downarrow}} - 1)} \right\rangle_{\text{eff}}.$$
 (3.170)

In the actual calculations of  $\overline{D_{\nu\uparrow}D_{\nu\downarrow}}$ , we make use of the exact expression up to 2l-th order. For higher orders, we adopt an asymptotic approximation, which is

exact in the high frequency limit [54].

$$\overline{D_{\nu\uparrow}D_{\nu\downarrow}} = \sum_{n=0}^{l} U^{2n} \left(\frac{i}{2\pi\nu}\right)^{2n} B_{\nu\uparrow}^{(n)} B_{\nu\downarrow}^{(n)} + \sum_{n=l+1}^{\infty} U^{2n} \left(\frac{i}{2\pi\nu}\right)^{2n} \tilde{B}_{\nu\uparrow}^{(n)} \tilde{B}_{\nu\downarrow}^{(n)}. \quad (3.171)$$

Here  $ilde{B}_{v\sigma}^{(n)}$  denotes the coefficient  $B_{v\sigma}^{(n)}$  in the asymptotic approximation.

The local charge and moment in the harmonic approximation are derived from the free energy (3.152) as

$$\langle n \rangle = \langle \zeta(\xi) \rangle_{\text{eff}},$$
 (3.172)

$$\langle m \rangle = \langle \xi \rangle_{\text{eff}}.$$
 (3.173)

The above expressions are consistent with the general formula, (3.54) and (3.55). Note that  $\zeta(\xi)$ , the electron number under static exchange field  $\xi$ , is not defined by (3.150) now. Instead it is given by the impurity Green function for the dynamical potential (3.170) as

$$\zeta(\xi) = \frac{1}{\beta} \sum_{l\sigma} G_{\sigma}^{(i)}(i\omega_l, i\omega_l). \tag{3.174}$$

The expression of the amplitude of local moment is obtained with use of the relation  $\langle n_{i\uparrow} n_{i\downarrow} \rangle = \partial \mathscr{F}_{\text{CPA}} / \partial U$ .

$$\langle m^2 \rangle = \langle n \rangle - \frac{1}{2} \langle \zeta(\xi)^2 \rangle_{\text{eff}} + \frac{1}{2} \left( \langle \xi^2 \rangle_{\text{eff}} - \frac{2}{\beta U} \right) - 2 \left\langle \left[ \frac{\partial E_{\text{dyn}}(\xi)}{\partial U} \right]_{v} \right\rangle_{\text{eff}}.$$
 (3.175)

Here  $[\sim]_v$  means to take the derivative fixing the static potential  $v_{\sigma}(0)$ .

The harmonic approximation (HA) takes into account the dynamical contributions successively starting from the high temperature limit (i.e., the static limit). Figure 3.7 shows examples of effective potentials in the paramagnetic 'bcc Fe', which are calculated by means of the dynamical CPA + HA and the same model DOS as in the static case (see Fig. 3.4). The potential curve in the static approximation shows a double-minimum structure, and hardly depends on the temperature. The dynamical corrections are small at high temperatures (see the dot-dashed curve), so that the effective potential is close to the static one. The dynamical corrections increase with decreasing temperature, and become significant near the Curie temperature  $T_{\rm C}$  as shown by dotted curve, so that the effective potential shows a single minimum at  $\xi = 0$ , indicating a disappearance of 'local moment'. The same feature is obtained below  $T_{\rm C}$ . This indicates that the thermodynamics of the metallic ferromagnets in the intermediate region of the Coulomb interaction are dominated by the quantum fluctuations rather than the thermal spin fluctuations, though the orbital degeneracy plays an important role in the real system as will be discussed in Sect. 3.7.

The dynamical effects strongly influence the magnetic properties. Figure 3.8 shows the result of model calculations for temperature variation of magnetic moments and susceptibility for 'bcc Fe'. Both the static and dynamical CPA lead to the

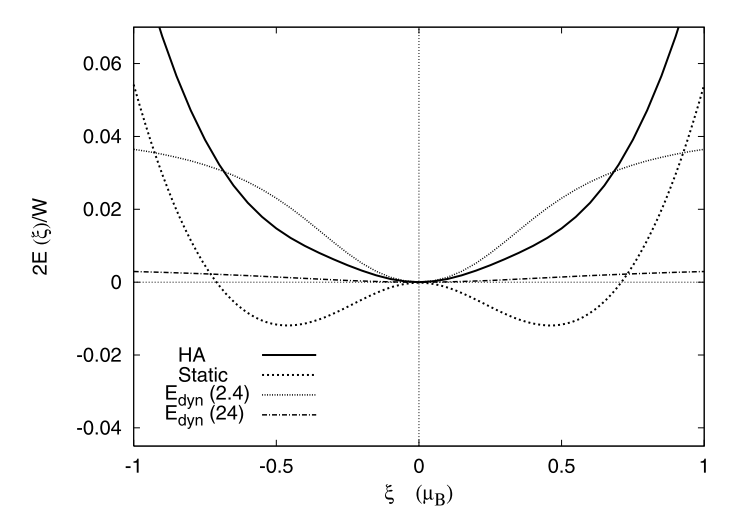
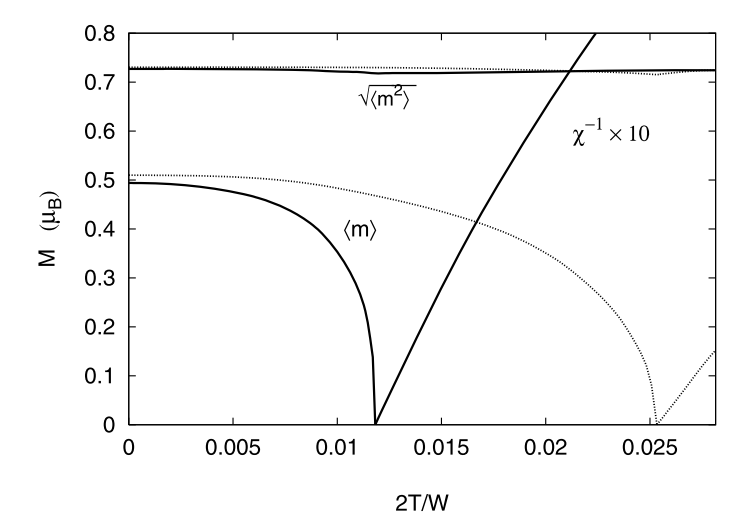


Fig. 3.7 Effective potentials of the paramagnetic 'bcc Fe' calculated with use of the dynamical CPA + HA and the model DOS given in Fig. 3.4 [54]. W denotes the d band width for noninteracting system. The static contribution (*dotted curve*) has double minima. The dynamical correction is small at  $T/T_C = 24$  (*dot-dashed curve*), while it is significant at  $T/T_C = 2.4$  (*thin dotted curve*), so that the total effective potential (*solid curve*) shows a single minimum structure



**Fig. 3.8** Magnetization vs. temperature curves, inverse susceptibility curves, and the amplitude of local moment of 'bcc Fe' calculated with use of the model DOS given in Fig. 3.4 [54]. *Solid curves* (*dotted curves*): the results obtained by the dynamical CPA + HA (the static approximation)

Curie–Weiss susceptibility. The Curie temperature, however, is reduced by a factor of two due to dynamical spin and charge fluctuations.

#### 3.6 Dynamical CPA and Dynamical Mean-Field Theory

The dynamical CPA presented in Sects. 3.4 and 3.5 is equivalent to some single-site theories of electron correlations. We clarify in this section the basic ideas of these theories, i.e., the many-body CPA (MB-CPA) in the disordered alloys [61], the dynamical mean-field theory (DMFT) in the metal–insulator transition [62, 63], and the projection operator method CPA (PM-CPA) in the excitation problem [64], and verify that the dynamical CPA is equivalent to these theories.

# 3.6.1 The Many-Body CPA and Its Equivalence to the Dynamical CPA

The many-body CPA (MB-CPA) is an extension of the CPA in disordered alloys to the correlated electron system. The theory has been applied to the Ni-based alloys to elucidate the electron-correlation effects on magnetism [61]. To clarify the relation of the MB-CPA to the dynamical CPA, we consider here a pure metal and adopt the Hubbard model with an intra-atomic Coulomb interaction. The theory starts from the temperature Green function in the interaction representation as

$$\mathscr{G}_{i\sigma}(\tau - \tau') = -Z^{-1} \operatorname{Tr} \left[ \mathscr{T} a_{i\sigma}(\tau) a_{i\sigma}^{\dagger}(\tau') e^{-\int_{0}^{\beta} H(\tau'') d\tau''} \right]. \tag{3.176}$$

Here Z denotes the partition function of the system.

The Hamiltonian  $H(\tau)$  in the interaction representation is approximated by an effective Hamiltonian  $\tilde{H}(\tau)$ , i.e., (3.118) with the time-dependent coherent potential  $\Sigma_{i\sigma}(\tau - \tau')$ :

$$\tilde{H}(\tau) = H_0(\tau) + \sum_{i\sigma} \int_0^\beta d\tau' \, a_{i\sigma}^{\dagger}(\tau) \, \Sigma_{i\sigma} \left(\tau - \tau'\right) a_{i\sigma}(\tau'). \tag{3.177}$$

Note that we defined here the noninteracting Hamiltonian as  $H_0 = \sum_{i\sigma} \varepsilon_{\sigma}^0 n_{i\sigma} + \sum_{ij\sigma} t_{ij} a_{i\sigma}^{\dagger} a_{j\sigma}$ , and  $\varepsilon_{\sigma}^0 = \varepsilon^0 - \mu$ , so that the interaction is given by  $H_{\rm I} = \sum_i U n_i \uparrow n_i \downarrow$ . The diagonal Green function  $F_{i\sigma}(\tau - \tau')$  for  $\tilde{H}(\tau)$  is given as follows according to the Dyson equation.

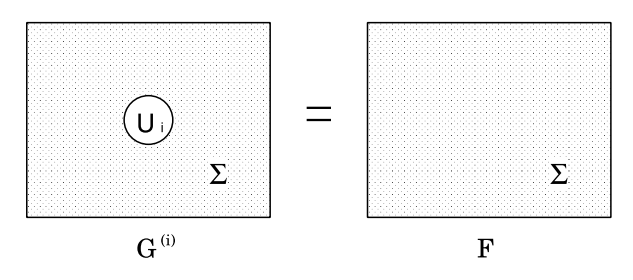
$$F_{i\sigma}(\tau - \tau') = \left[ \left( g^{-1} - \Sigma \right)^{-1} \right]_{i\tau\sigma i\tau'\sigma}.$$
 (3.178)

Here  $g_{ij\sigma}(\tau - \tau')$  is the Green function for the noninteracting Hamiltonian  $H_0$ .

To find the best coherent potential, we consider an impurity Hamiltonian embedded in the effective medium as follows.

$$H^{(i)}(\tau) = \tilde{H}(\tau) - \int_0^\beta d\tau' \sum_{\sigma} a_{i\sigma}^{\dagger}(\tau) \Sigma_{i\sigma}(\tau - \tau') a_{i\sigma}(\tau') + U n_{i\uparrow}(\tau) n_{i\downarrow}(\tau).$$
(3.179)

Fig. 3.9 Schematic picture showing the many-body CPA. The *left-hand side* shows an impurity with a real Coulomb interaction  $U_i$  on site i and the surrounding effective potential  $\Sigma_{\sigma}$ . The *right-hand side* shows a uniform system with the effective potential only



Here the coherent potential on site i has been replaced by the real Coulomb interaction  $Un_{i\uparrow}(\tau)n_{i\downarrow}(\tau)$ . Note that (3.179) corresponds to (3.117) in the dynamical CPA, but the time-dependent random potential  $v_{i\sigma}(\tau)$  has been replaced by the real interaction  $H_{\rm I}(\tau)$  in the MB-CPA (see Fig. 3.9). The on-site Green function for the impurity system is given by

$$\mathcal{G}_{i\sigma}^{(i)}(\tau - \tau') = -Z_i^{-1} \operatorname{Tr} \left[ \mathcal{T} a_{i\sigma}(\tau) a_{i\sigma}^{\dagger}(\tau') e^{-\int_0^{\beta} H^{(i)}(\tau'') d\tau''} \right]. \tag{3.180}$$

Here  $Z_i$  denotes the partition function of the system.

The coherent potential in the many-body CPA is determined so that the diagonal impurity Green function agrees with the coherent Green function (see Fig. 3.9).

$$\mathscr{G}_{i\sigma}^{(i)}(\tau - \tau') = F_{i\sigma}(\tau - \tau'). \tag{3.181}$$

Note that the impurity Green function  $\mathcal{G}_{i\sigma}^{(i)}(\tau - \tau')$  has to be obtained separately by using one of the many-body techniques.

In order to clarify the equivalence of the MB-CPA to the dynamical CPA, we discretize the integral of  $H^{(i)}(\tau'')$  in (3.180) as in (3.32), and apply the Hubbard–Stratonovich transformation (3.24) directly to the impurity Green function (3.180). We obtain then the following relation.

$$\mathscr{G}_{i\sigma}^{(i)}(\tau - \tau') = \langle G_{i\sigma}^{(i)}(\xi, \eta, \tau, \tau') \rangle. \tag{3.182}$$

Here  $G_{i\sigma}^{(i)}(\xi,\eta,\tau,\tau')$  is identical with the diagonal part of the time-dependent Green function (3.119) in the dynamical CPA. The above relation indicates that the CPA equation (3.181) in the many-body CPA is identical with the CPA equation (3.122) in the dynamical CPA. Thus the many-body CPA is equivalent to the dynamical CPA.

# 3.6.2 The DMFT and Its Equivalence to the Dynamical CPA

The dynamical mean field theory (DMFT) was developed to clarify the metal-insulator transition in infinite dimensions, and has extensively been applied to various problems in strongly correlated electron systems [62, 63]. It is equivalent to the

MB-CPA thus to the dynamical CPA as well. In order to introduce the DMFT and to prove its equivalence to the MB-CPA, we employ the temperature Green function which is expressed by the path integral method as follows [65].

$$\mathscr{G}_{i\sigma}(\tau - \tau') = -Z^{-1} \int \left[ \prod_{i\sigma} \mathscr{D} a_{j\sigma}^* \mathscr{D} a_{j\sigma} \right] e^{-S} a_{i\sigma}(\tau) a_{i\sigma}^*(\tau), \tag{3.183}$$

$$S = \int_0^\beta d\tau \left[ \sum_{i\sigma} a_{i\sigma}^*(\tau) \left( \frac{\partial}{\partial \tau} - \mu \right) a_{i\sigma}(\tau) + H(\{a^*\}\{a\}) \right]. \tag{3.184}$$

Here Z denotes the partition function to the action S. The Hamiltonian operator  $H(\{a^*\}\{a\})$  in the action S is defined by the same form as the original Hamiltonian in the interaction representation, though  $a^*_{i\sigma}$  and  $a_{i\sigma}$  are now the Grassmann variables being conjugate to the creation and annihilation operators on the same site.  $\mathcal{D}a^*_{i\sigma}\mathcal{D}a_{i\sigma}(=\prod_{n=1}^{N'}da^*_{i\sigma}(\tau_n)da_{i\sigma}(\tau_n))$  denotes the path integrals for these variables

It is well-known that the Feynman diagram rule obtained in the path integral formulation is exactly the same as in the usual Green function technique [65], so that we can derive the same Dyson equation as follows.

$$\mathcal{G}_{ij\sigma}(\tau,\tau') = g_{ij\sigma}(\tau-\tau') + \int_0^\beta d\tau_1 \int_0^\beta d\tau_2 \sum_{kl} g_{ik\sigma}(\tau-\tau_1) \Sigma_{kl\sigma}(\tau_1-\tau_2) \mathcal{G}_{lj\sigma}(\tau_2,\tau').$$
(3.185)

Here  $g_{ij\sigma}(\tau - \tau')$  is the Green function for the noninteracting Hamiltonian  $H_0$ .  $\Sigma_{ij\sigma}(\tau - \tau')$  denotes the self-energy which should be obtained from the Feynman diagrams.

Furthermore, we note that the same Dyson equation (3.185) is also obtained from the following effective action according to the diagrammatic technique.

$$S' = \int_0^\beta d\tau \left[ \sum_{i\sigma} a_{i\sigma}^*(\tau) \left( \frac{\partial}{\partial \tau} - \mu \right) a_{i\sigma}(\tau) + H'(\{a^*\}\{a\}) \right], \tag{3.186}$$

$$H'(\{a^*\}\{a\}) = H_0(\{a^*(\tau)\}\{a(\tau)\})$$

$$+\sum_{ij\sigma}\int_{0}^{\beta}d\tau' a_{i\sigma}^{*}(\tau)\Sigma_{ij\sigma}(\tau-\tau')a_{j\sigma}(\tau'). \tag{3.187}$$

The DMFT has been developed in infinite dimensions [62]. There, the hopping integrals  $|t_{ij}|$  on the hyper-cubic lattice for example are scaled as  $|t|/\sqrt{2d}$ , so that the band width becomes finite for any dimensions d. Accordingly, the off-diagonal Green function in the noninteracting system becomes of order of  $1/\sqrt{2d}$ . Since the Feynman diagrams to the off-diagonal self-energy have at least three electron internal lines between the different sites, the contribution from all the off-diagonal

self-energy diagrams to the Dyson equation becomes of order of  $2d(1/\sqrt{2d})^3 = 1/\sqrt{2d}$ . Therefore the contribution from the off-diagonal self-energy  $\Sigma_{ij\sigma}(i\omega_l)$   $(i \neq j)$  vanishes in the limit  $d = \infty$  [66].

The DMFT determines the site-diagonal self-energy (or the momentum independent self-energy)  $\Sigma_{\sigma}(i\omega_l)$  by using the following diagonal Green function in the path integral representation.

$$\mathcal{G}_{i\sigma}^{(i)}(\tau - \tau') = -Z^{(i)-1} \int \left[ \prod_{\sigma} \mathcal{D} a_{i\sigma}^* \mathcal{D} a_{i\sigma} \right] e^{-S_i} a_{i\sigma}(\tau) a_{i\sigma}^*(\tau'), \qquad (3.188)$$

$$S_i = -\int_0^\beta d\tau \int_0^\beta d\tau' \sum_{\sigma} a_{i\sigma}^*(\tau) (F^{(i)-1})_\sigma (\tau - \tau') a_{i\sigma}(\tau') + \int_0^\beta d\tau \, U n_{i\uparrow}(\tau) n_{i\downarrow}(\tau). \qquad (3.189)$$

Here  $n_{i\sigma}(\tau) = a_{i\sigma}^*(\tau)a_{i\sigma}(\tau)$ .  $S_i$  is an impurity action with an effective field and the local Coulomb interaction.  $Z^{(i)}$  denotes the partition function to the action  $S_i$ .  $\mathcal{D}a_{i\sigma}^*\mathcal{D}a_{i\sigma}$  denotes the path integrals for these variables.  $F_{\sigma}^{(i)}(\tau - \tau')$  in (3.189) is called the Weiss-field function. According to the Dyson equation of the Green function (3.188), it is given in the Fourier representation as follows.

$$F_{\sigma}^{(i)}(i\omega_l)^{-1} = \Sigma_{\sigma}(i\omega_l) + \mathcal{G}_{i\sigma}^{(i)}(i\omega_l)^{-1}. \tag{3.190}$$

Since the site-diagonal Green function  $\mathscr{G}_{i\sigma}^{(i)}(i\omega_l)$  should be equal to the average of the Green function of the momentum representation  $(1/(i\omega_l - \varepsilon_\sigma^0 - \Sigma_\sigma(i\omega_l) - \varepsilon_k))$ , we have the relation,

$$\mathscr{G}_{i\sigma}^{(i)}(i\omega_l) = \int \frac{\rho(\varepsilon) d\varepsilon}{i\omega_l - \varepsilon_{\sigma}^0 - \Sigma_{\sigma}(i\omega_l) - \varepsilon},$$
(3.191)

where  $\rho(\varepsilon)$  is the one-electron density of states for  $t_{ij}$ . This means that

$$i\omega_l - \varepsilon_\sigma^0 - \Sigma_\sigma(i\omega_l) = R[\mathscr{G}_\sigma^{(i)}(i\omega_l)]. \tag{3.192}$$

Here *R* denotes the reciprocal function to the Hilbert transform (i.e., x = R[y] when  $y = \int d\varepsilon \, \rho(\varepsilon)/(x - \varepsilon)$ ). Eliminating  $\Sigma_{\sigma}(i\omega_l)$  from (3.190) and (3.192), we obtain the expression of the Weiss function by means of the impurity Green function as

$$F_{\sigma}^{(i)}(i\omega_l)^{-1} = i\omega_l - \varepsilon_{\sigma}^0 + \mathcal{G}_{\sigma}^{(i)}(i\omega_l)^{-1} - R[\mathcal{G}_{\sigma}^{(i)}(i\omega_l)]. \tag{3.193}$$

Equations (3.188), (3.189), and (3.193) form the self-consistent equations in the DMFT. Note that the Green function (3.188) for an impurity action has to be solved by using one of the many-body theories (e.g., the quantum Monte-Carlo method [62] and the numerical renormalization group method [67]).

In order to clarify the relation between the DMFT and the MB-CPA, we note that the Green function (3.183) and the Hamiltonian  $H(\{a^*\}\{a\})$  in the action S, i.e., (3.184), have the same form as those in the interaction representation in the Fock space (see (3.176)). Thus we can construct the MB-CPA using the path integral method taking the same steps as in the original MB-CPA. To realize it, we approximate the self-energy  $\Sigma_{ij\sigma}(\tau - \tau')$  in (3.187) by the diagonal  $\Sigma_{i\sigma}(\tau - \tau')$ , and consider the following coherent action with the effective Hamiltonian  $\tilde{H}(\{a^*\}\{a\})$ .

$$\tilde{S} = \int_0^\beta d\tau \left[ \sum_{i\sigma} a_{i\sigma}^*(\tau) \left( \frac{\partial}{\partial \tau} - \mu \right) a_{i\sigma}(\tau) + \tilde{H}(\{a^*\}\{a\}) \right], \tag{3.194}$$

$$\tilde{H}(\lbrace a^*\rbrace\lbrace a\rbrace) = H_0(\lbrace a^*(\tau)\rbrace\lbrace a(\tau)\rbrace) + \sum_{i\sigma} \int_0^\beta d\tau' \, a_{i\sigma}^*(\tau) \, \Sigma_{i\sigma}(\tau - \tau') a_{i\sigma}(\tau'). \tag{3.195}$$

Note that the Hamiltonian  $\tilde{H}(\{a^*\}\{a\})$  is the same as (3.177) in which the creation and the annihilation operators have been replaced by their conjugate variables  $a_{i\sigma}^*(\tau)$  and  $a_{i\sigma}(\tau)$ .

The action  $\tilde{S}$  describes the r.h.s. of Fig. 3.9, and its Green function is given by

$$F_{i\sigma}(\tau - \tau') = -\tilde{Z}^{-1} \int \left[ \prod_{i\sigma} \mathcal{D} a_{j\sigma}^* \mathcal{D} a_{j\sigma} \right] e^{-\tilde{S}} a_{i\sigma}(\tau) a_{i\sigma}^*(\tau'), \qquad (3.196)$$

where  $\tilde{Z}$  is the partition function to action  $\tilde{S}$ . The Green function  $F_{i\sigma}(\tau - \tau')$  is identical to the one obtained from the Hamiltonian (3.177) because both satisfy the same Dyson equation (3.178).

The impurity action describing the l.h.s. of Fig. 3.9 is expressed as

$$S^{(i)} = \int_0^\beta d\tau \left[ \sum_{i\sigma} a_{i\sigma}^*(\tau) \left( \frac{\partial}{\partial \tau} - \mu \right) a_{i\sigma}(\tau) + H^{(i)} \left( \{a^*\} \{a\} \right) \right], \tag{3.197}$$

$$H^{(i)}(\lbrace a^*\rbrace\lbrace a\rbrace) = \tilde{H}(\lbrace a^*\rbrace\lbrace a\rbrace) - \int_0^\beta d\tau' \sum_\sigma a_{i\sigma}^*(\tau) \Sigma_{i\sigma}(\tau - \tau') a_{i\sigma}(\tau')$$
  
+  $U_i a_{i\uparrow}^*(\tau) a_{i\downarrow}^*(\tau) a_{i\downarrow}(\tau) a_{i\uparrow}(\tau).$  (3.198)

The impurity Green function of effective action  $S^{(i)}$  is given by

$$\mathscr{G}_{i\sigma}^{(i)}(\tau - \tau') = -Z^{(i)-1} \int \left[ \prod_{i\sigma} \mathscr{D} a_{j\sigma}^* \mathscr{D} a_{j\sigma} \right] e^{-S^{(i)}} a_{i\sigma}(\tau) a_{i\sigma}^*(\tau'), \quad (3.199)$$

where  $Z^{(i)}$  is the partition function to action  $S^{(i)}$ . The impurity Green function satisfies the following Dyson equation.

$$\mathcal{G}_{i\sigma}^{(i)}(\tau - \tau') = F_{i\sigma}^{(i)}(\tau - \tau') 
+ \int_{0}^{\beta} d\tau_{1} \int_{0}^{\beta} d\tau_{2} F_{i\sigma}^{(i)}(\tau - \tau_{1}) \Lambda_{i\sigma}(\tau_{1} - \tau_{2}) \mathcal{G}_{i\sigma}^{(i)}(\tau_{2} - \tau').$$
(3.200)

Here  $\Lambda_{i\sigma}(\tau - \tau')$  is the self-energy for the impurity Hamiltonian (3.198). The cavity Green function  $F_{i\sigma}^{(i)}(\tau - \tau')$  in (3.200) is defined by

$$F_{i\sigma}^{(i)}(\tau - \tau') = -\tilde{Z}^{(i)-1} \int \left[ \prod_{i\sigma} \mathcal{D}a_{j\sigma}^* \mathcal{D}a_{j\sigma} \right] e^{-\tilde{S}^{(i)}} a_{i\sigma}(\tau) a_{i\sigma}^*(\tau'), \qquad (3.201)$$

$$\tilde{S}^{(i)} = \int_0^\beta d\tau \left[ \sum_{i\sigma} a_{i\sigma}^*(\tau) \left( \frac{\partial}{\partial \tau} - \mu \right) a_{i\sigma}(\tau) + \tilde{H}^{(i)} \left( \{a^*\} \{a\} \right) \right]. \tag{3.202}$$

Here  $\tilde{Z}^{(i)}$  is the partition function for action  $\tilde{S}^{(i)}$ , and  $\tilde{H}^{(i)}(\{a^*\}\{a\})$  is the cavity Hamiltonian defined by the first two terms at the r.h.s. of (3.198). The Green function satisfies the Dyson equation.

$$F_{i\sigma}^{(i)}(\tau - \tau') = F_{i\sigma}(\tau - \tau')$$

$$- \int_0^\beta d\tau_1 \int_0^\beta d\tau_2 F_{i\sigma}(\tau - \tau_1) \Sigma_{i\sigma}(\tau_1 - \tau_2) F_{i\sigma}^{(i)}(\tau_2 - \tau').$$
(3.203)

In the Fourier representation it is expressed as

$$F_{i\sigma}^{(i)}(i\omega_l)^{-1} = F_{i\sigma}(i\omega_l)^{-1} + \Sigma_{i\sigma}(i\omega_l). \tag{3.204}$$

The CPA equation corresponding to Fig. 3.9 is then given by

$$\mathcal{G}_{i\sigma}^{(i)}(\tau - \tau') = F_{i\sigma}(\tau - \tau'). \tag{3.205}$$

The impurity Green function in (3.199) is identical with that of the original MB-CPA, i.e., (3.180), because the path integral method to the Green function leads to the same Feynman diagram scheme as in the usual Green function method, and the same unperturbed Green function and the same Coulomb matrix elements appear there. This means that the CPA equation (3.205) derived by the path integral formulation is identical with the CPA equation (3.181) in the MB-CPA.

Let us rewrite the self-consistent equations for the MB-CPA based on the path integral method. The impurity Green function  $\mathscr{G}_{i\sigma}^{(i)}(\tau-\tau')$  given by (3.199) can also

be expressed by an effective local action  $S_i$  as follows.

$$\mathcal{G}_{i\sigma}^{(i)}(\tau - \tau') = -Z^{(i)-1} \int \left[ \prod_{\sigma} \mathcal{D} a_{i\sigma}^* \mathcal{D} a_{i\sigma} \right] e^{-S_i} a_{i\sigma}(\tau) a_{i\sigma'}^*(\tau'), \qquad (3.206)$$

$$Z^{(i)} = \int \left[ \prod_{\sigma} \mathscr{D} a_{i\sigma}^* \mathscr{D} a_{i\sigma} \right] e^{-S_i}. \tag{3.207}$$

Here  $S_i$  is defined by

$$e^{-S_i} = \int \left[ \prod_{j \neq i} \prod_{\sigma} \mathcal{D} a_{j\sigma}^* \mathcal{D} a_{j\sigma} \right] e^{-S^{(i)}}.$$
 (3.208)

Alternatively,

$$S_{i} = \tilde{S}^{(i)} - \int_{0}^{\beta} d\tau' \sum_{\sigma} a_{i\sigma}^{*}(\tau) \Sigma_{i\sigma} (\tau - \tau') a_{i\sigma} (\tau') + \int_{0}^{\beta} d\tau \, U_{i} n_{i\uparrow}(\tau) n_{i\downarrow}(\tau),$$
(3.209)

$$e^{-\tilde{S}^{(i)}} = \int \left[ \prod_{i \neq i} \prod_{\sigma} \mathcal{D} a_{j\sigma}^* \mathcal{D} a_{j\sigma} \right] e^{-\tilde{S}}.$$
 (3.210)

The path integral at the r.h.s. of (3.210) can be performed exactly by using the Gaussian formula after the Fourier transform of the Grassmann variables, so that we obtain an explicit form of the local effective action  $S_i$  as

$$S_{i} = -\frac{1}{\beta} \sum_{l\sigma} a_{i\sigma}^{*}(i\omega_{l}) \left[ F_{i\sigma}(i\omega_{l})^{-1} + \Sigma_{i\sigma}(i\omega_{l}) \right] a_{i\sigma}(i\omega_{l})$$

$$+ \int_{0}^{\beta} d\tau \, U_{i} n_{i\uparrow}(\tau) n_{i\downarrow}(\tau).$$
(3.211)

Here we have omitted the constant term, which is canceled by the same factor in  $Z^{(i)}$  in (3.206).

Using the Dyson equation (3.204), the action (3.211) reduces to the following form.

$$S_{i} = -\int_{0}^{\beta} d\tau \int_{0}^{\beta} d\tau' \sum_{\sigma} a_{i\sigma}^{*}(\tau) \left(F_{i}^{(i)-1}\right)_{\sigma\sigma} (\tau - \tau') a_{i\sigma}(\tau')$$

$$+ \int_{0}^{\beta} d\tau \, U_{i} n_{i\uparrow}(\tau) n_{i\downarrow}(\tau). \tag{3.212}$$

Here  $(F_i^{(i)-1})_{\sigma\sigma}(\tau-\tau')$  is defined by

$$(F_i^{(i)-1})_{\sigma\sigma}(\tau - \tau') = \frac{1}{\beta} \sum_{l} F_{i\sigma}^{(i)}(i\omega_l)^{-1} e^{-i\omega_l(\tau - \tau')}.$$
 (3.213)

When the coherent potential is site-independent and all the sites are crystallographically equivalent, the frequency representation of the CPA equation (3.205) can be simplified as

$$\mathcal{G}_{\sigma}^{(i)}(i\omega_l) = F_{\sigma}(i\omega_l). \tag{3.214}$$

Here the subscript i has been omitted for simplicity. The r.h.s. of (3.214) is given by

$$F_{\sigma}(i\omega_l) = \int \frac{\rho(\varepsilon) d\varepsilon}{i\omega_l - \varepsilon_{\sigma}^0 - \Sigma_{\sigma}(i\omega_l) - \varepsilon}.$$
 (3.215)

Introducing the reciprocal function R[F] of the Hilbert transform, we can rewrite (3.215) as

$$\Sigma_{\sigma}(i\omega_{l}) = i\omega_{l} - \varepsilon_{\sigma}^{0} - R[\mathcal{G}_{\sigma}^{(i)}(i\omega_{l})]. \tag{3.216}$$

From (3.204), (3.214), and (3.216), we can express the cavity Green function by means of the impurity Green function  $\mathcal{G}_{\sigma}^{(i)}(i\omega_l)$  as follows.

$$F_{i\sigma}^{(i)}(i\omega_l)^{-1} = i\omega_l - \varepsilon_{\sigma}^0 + \mathcal{G}_{\sigma}^{(i)}(i\omega_l)^{-1} - R[\mathcal{G}_{\sigma}^{(i)}(i\omega_l)]. \tag{3.217}$$

Equations (3.206), (3.212), and (3.217) form the self-consistent equations in the MB-CPA, and are identical with (3.188), (3.189), and (3.193) in the DMFT. Thus we have verified the equivalence between the DMFT and the MB-CPA.

# 3.6.3 The Projection Operator Method CPA and Summary of Relations

The MB-CPA and DMFT are based on the temperature Green function. These approaches often require the numerical analytic continuation on the complex energy plane for the calculation of the single-particle excitation spectra. The projection operator method CPA (PM-CPA) [64] is a single-site theory based on the retarded Green function, and is equivalent to the theories mentioned above.

The retarded Green function  $G_{i\sigma i\sigma'}^{R}(t-t')$  is defined by

$$G_{i\sigma j\sigma'}^{R}(t-t') = -i\theta(t-t')\langle \left[a_{Hi\sigma}(t), a_{Hj\sigma'}^{\dagger}(t')\right]_{+}\rangle. \tag{3.218}$$

Here  $\theta(t)$  is the step function,  $a_{\mathrm{H}i\sigma}^{\dagger}(t)$  ( $a_{\mathrm{H}i\sigma}(t)$ ) is the creation (annihilation) operator in the Heisenberg representation which is defined by  $a_{\mathrm{H}i\sigma}^{\dagger}(t) = \mathrm{e}^{iHt}a_{i\sigma}^{\dagger}\,\mathrm{e}^{-iHt}$  ( $a_{\mathrm{H}i\sigma}(t) = \mathrm{e}^{iHt}a_{i\sigma}^{\dagger}\mathrm{e}^{-iHt}$ ), and  $[\ ,\ ]_+$  denotes the anticomutator between the Fermion operators. The average  $\langle \sim \rangle$  is taken over the grand canonical ensemble. Note that the Heisenberg representation of operator A is expressed by means of the Liouville operator L as  $A(t) = \exp(iLt)A$ . The Liouville operator L is a super-operator defined by  $LA = [H,A]_-$ , where  $[\ ,\ ]_-$  is the commutator between operators.

The PM-CPA starts from the Fourier transform of the retarded Green function with the projection technique [68]. By making use of a Laplace transform, the Fourier transform of (3.218) is expressed by an inner-product in the operator space as follows.

$$G_{ij\sigma}^{\mathbf{R}}(z) = \left(a_{i\sigma}^{\dagger} \middle| \frac{1}{z - L} a_{j\sigma}^{\dagger}\right). \tag{3.219}$$

Here  $z = \omega + i\delta$  with  $\delta$  being an infinitesimal positive number. The inner product between the operators A and B is defined by  $(A|B) = \langle [A^+, B]_+ \rangle$ .

A basic idea of the PM-CPA is to approximate the Liouville operator by means of an energy dependent effective Liouville operator  $\tilde{L}(z)$ . It is defined for an operator A as

$$\tilde{L}(z)A = \left[\tilde{H}(z), A\right]_{-},\tag{3.220}$$

$$\tilde{H}(z) = H_0 + \sum_{i\sigma} \Sigma_{\sigma}(z) n_{i\sigma}. \tag{3.221}$$

Here  $\Sigma_{\sigma}(z)$  is a coherent potential or a single-site self-energy.

The coherent potential is determined as follows. We introduce a Liouville operator  $L^{(i)}(z)$  for an impurity system such that

$$L^{(i)}(z)A = [H^{(i)}(z), A]_{-}, (3.222)$$

$$H^{(i)}(z) = \tilde{H}(z) - \sum_{\sigma} \Sigma_{\sigma}(z) n_{i\sigma} + U n_{i\uparrow} n_{i\downarrow}. \tag{3.223}$$

According to the equation of motion we obtain the diagonal Green function for the Liouville operator  $L^{(i)}(z)$  as

$$\mathscr{G}_{\sigma}^{(i)}(z) = \left(F_{\sigma}(z)^{-1} - \Lambda_{\sigma}^{(i)}(z) + \Sigma_{\sigma}(z)\right)^{-1}.$$
 (3.224)

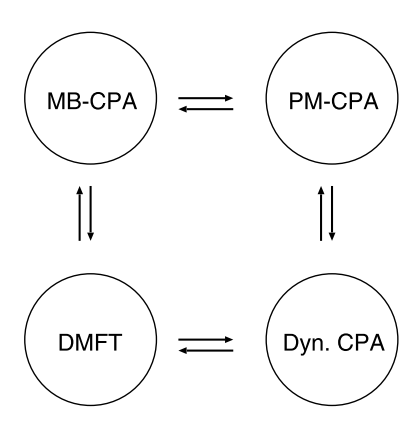
Here  $F_{\sigma}(z)$  is the diagonal coherent Green function defined by (3.215) in which  $i\omega_l$  has been replaced by z.  $\Lambda_{\sigma}^{(i)}(z)$  is the self-energy for the impurity system, consisting of the Hartree–Fock potential and the reduced memory function  $\overline{G}_{\sigma}^{(i)}(z)$ .

$$\Lambda_{\sigma}^{(i)}(z) = U\langle n_{i-\sigma}\rangle + U^2 \overline{G}_{\sigma}^{(i)}(z), \tag{3.225}$$

$$\overline{G}_{\sigma}^{(i)}(z) = \left(A_{i\sigma}^{\dagger} \mid \left(z - \overline{L}^{(i)}(z)\right)^{-1} A_{i\sigma}^{\dagger}\right). \tag{3.226}$$

Note that the operator space of the memory function has been expanded from  $\{|a_{j\sigma}^{\dagger})\}$  to  $\{|A_{j\sigma}^{\dagger})=|a_{j\sigma}^{\dagger}\delta n_{j-\sigma})\}$ , where  $\delta n_{j-\sigma}=n_{j-\sigma}-\langle n_{j-\sigma}\rangle$ . The Liouville operator  $\overline{L}^{(i)}(z)$  is defined by  $\overline{L}^{(i)}(z)=QL^{(i)}(z)Q$  with use of the projection operator Q=1-P and  $P=\sum_{j}|a_{j\sigma}^{\dagger}\rangle(a_{j\sigma}^{\dagger})$ .  $\overline{L}^{(i)}(z)$  operates on the operator space orthogonal to the original space  $\{|a_{j\sigma}^{\dagger}\rangle\}$ .

Fig. 3.10 Schematic diagram showing the equivalence among the many-body CPA (MB-CPA), the dynamical CPA (Dyn. CPA), the dynamical mean-field theory (DMFT), and the projection operator method CPA (PM-CPA)



The coherent potential or the energy dependent Liouville operator is determined from the CPA equation (see Fig. 3.9)

$$\mathscr{G}_{\sigma}^{(i)}(z) = F_{\sigma}(z), \tag{3.227}$$

or equivalently  $\Lambda_{\sigma}^{(i)}(z) = \Sigma_{\sigma}(z)$ . The CPA equation (3.227) in the PM-CPA has the same form as the one obtained from an analytic continuation of the temperature Green function in the MB-CPA (see (3.214)). Thus it is essentially the same as the MB-CPA when a suitable single-site approximation has been made for the static averages in the self-energy (3.225). (Note that the projection method treats the dynamics and the static averages independently.) The PM-CPA is extended to the nonlocal case [69].

Figure 3.10 summarizes the relation among various single-site theories. The dynamical CPA, the MB-CPA in disordered alloys, and the DMFT in the metal-insulator transition are equivalent. The single-site spin fluctuation theory (SSF) [45–49] is obtained from the dynamical CPA as a high-temperature approximation, and the variational approach (VA) [52], which makes use of an effective potential obtained by a variational energy at low temperatures, is an adiabatic approximation to the dynamical CPA. The three equivalent theories are based on the temperature Green function. The PM-CPA in the excitation problem is based on the retarded Green function, and also equivalent to them. These relations imply that the single-site theories developed in the magnetism and those developed in the strongly correlated electron system are unified.

## 3.7 First-Principles Dynamical CPA and Metallic Magnetism

The dynamical CPA theory presented in Sects. 3.4 and 3.5 is based on the single-band Hubbard model. We have to take into account the realistic band structure and associated inter-orbital Coulomb interactions in order to compare theoretical results with experimental data and to discuss quantitative aspects of the theory. In the case

of transition metals and their alloys, electrons on the five d orbitals are responsible for the magnetism. The orbital degeneracy increases the degree of freedom on electron motion and causes different types of Coulomb interactions. Especially, the intraatomic exchange interaction parallels the spins on an atom and tends to form an atomic magnetic moment as well as associated magnetic entropy. The transverse spin fluctuations as shown in Fig. 3.1 are also realized. We introduce in this section a realistic model Hamiltonian obtained by the first-principles local density approximation (LDA) band theory [70], and outline the dynamical CPA applied to the realistic Hamiltonian [71, 72]. We will also discuss the ferromagnetism of Fe, Co, and Ni at finite temperatures on the basis of the realistic theory.

We apply here the following tight-binding model Hamiltonian.

$$H = H_0 + H_{\rm I}. (3.228)$$

The Hamiltonian for noninteracting system  $H_0$  is given by

$$H_0 = \sum_{iL\sigma} \varepsilon_{iL}^0 \hat{n}_{iL\sigma} + \sum_{iLjL'\sigma} t_{iLjL'}^0 a_{iL\sigma}^{\dagger} a_{jL'\sigma}. \tag{3.229}$$

Here  $\varepsilon_{iL}^0$  is the atomic level on site i and orbital L(=lm) for the noninteracting system.  $t_{iLjL'}^0$  is the transfer integral between iL and jL'.  $a_{iL\sigma}^{\dagger}$  ( $a_{iL\sigma}$ ) is the creation (annihilation) operator for an electron with orbital L and spin  $\sigma$  on site i, and  $\hat{n}_{iL\sigma} = a_{iL\sigma}^{\dagger} a_{iL\sigma}$  is a charge density operator. We added the hat sign on the charge and spin density operators in this section in order to distinguish these operators with those in the density functional theory (DFT).

In the transition metal system, for example, the 3d electrons form narrow bands as compared with the 4s and 4p electron bands. The 4s–4p electrons behave like free electrons, and may screen the Coulomb interactions between 3d electrons. Therefore we may apply the following interaction  $H_{\rm I}$  consisting of the intra-atomic Coulomb interactions between d electrons.

$$H_{I} = \sum_{i} \left[ \sum_{m} U_{0} \hat{n}_{ilm} \hat{n}_{ilm} + \sum_{m>m'} \left( U_{1} - \frac{1}{2} J \right) \hat{n}_{ilm} \hat{n}_{ilm'} - \sum_{m>m'} J \hat{s}_{ilm} \cdot \hat{s}_{ilm'} \right].$$
(3.230)

Here  $U_0$  ( $U_1$ ) and J are the intra-orbital (inter-orbital) Coulomb interaction and the exchange interaction, respectively.  $\hat{n}_{ilm}$  ( $\hat{s}_{ilm}$ ) with l=2 is the charge (spin) density operator for d electrons on site i and orbital m, which is defined by  $\hat{n}_{ilm} = \sum_{\sigma} \hat{n}_{ilm\sigma}$  ( $\hat{s}_{ilm} = \sum_{\alpha\gamma} a^{\dagger}_{iL\alpha}(\sigma/2)_{\alpha\gamma} a_{iL\gamma}$ ),  $\sigma$  being the Pauli spin matrices.

As shown earlier in Sect. 2.3.3, we can derive the first-principles tight-binding (TB) Hamiltonian on the basis of the LDA to the DFT and the tight-binding linear

muffin-tin orbital (TB-LMTO) method. The Hamiltonian is written as (see (2.167))

$$H_{\rm LDA} = \sum_{iLiL'\sigma} H_{iLjL'} a_{iL\sigma}^{\dagger} a_{jL'\sigma}, \qquad (3.231)$$

$$H_{iLjL'} = \left\langle \chi_{iL} \left| \left( -\frac{1}{2} \nabla^2 + v(\mathbf{r}) \right) \right| \chi_{jL} \right\rangle = \varepsilon_{iL} \delta_{ij} \delta_{LL'} + t_{iLjL'}. \tag{3.232}$$

Here  $\chi_{iL}$ 's are the nearly orthogonal basis functions for orbital L on site i. v(r) is a LDA potential,  $\varepsilon_{iL}$  is an atomic level, and  $t_{iLjL'}$  is a transfer integral between orbitals  $\chi_{iL}$  and  $\chi_{iL'}$ .

When we construct the tight-binding parameters for noninteracting system from the TB-LMTO LDA Hamiltonian, we have to take into account the fact that the one-electron Hamiltonian (3.232), especially the atomic level  $\varepsilon_{iL}$ , contains the effects of strong intraatomic Coulomb interactions. We therefore subtract the contribution of electron–electron interactions from the LDA Hamiltonian (3.232) via the relation  $\langle H_0 \rangle = E_{\rm LDA} - E_{\rm LDA}^{\rm U}$ . Here  $E_{\rm LDA}$  is the ground-state energy in the LDA, and  $E_{\rm LDA}^{\rm U}$  is a LDA functional to the intra-atomic Coulomb interactions. The atomic level  $\varepsilon_{iL}^0$  for the noninteracting system is then obtained from the relation [63],

$$\varepsilon_{iL}^{0} = \frac{\partial E_{\text{LDA}}}{\partial n_{iL\sigma}} - \frac{\partial E_{\text{LDA}}^{\text{U}}}{\partial n_{iL\sigma}}.$$
(3.233)

Here  $n_{iL\sigma}$  is the charge density at the ground state. For the transfer integral, we adopt the approximation  $t^0_{iLjL'} = t_{iLjL'}$  expecting small corrections.

Several forms of  $E_{\rm LDA}^{\rm U}$  have been proposed. Among them, we adopt here the Hartree–Fock type form [70], since we are considering an itinerant electron system where the ratio of the Coulomb interaction to the d band width is not larger than one.

$$E_{\text{LDA}}^{\text{U}} = \frac{1}{2} \sum_{j} \sum_{mm'\sigma} \overline{U} n_{jd} n_{jd} + \frac{1}{2} \sum_{j} \sum_{mm'} \sum_{\sigma} (\overline{U} - \overline{J}) n_{jd} n_{jd}. \quad (3.234)$$

Here  $n_{jd} = \sum_{m\sigma} n_{jlm\sigma}/2(2l+1)$  with l=2.  $\overline{U}$  and  $\overline{J}$  are the orbital-averaged Coulomb and exchange interactions defined by

$$\overline{U} = \frac{1}{(2l+1)^2} \sum_{mm'} U_{mm'}, \tag{3.235}$$

$$(\overline{U} - \overline{J}) = \frac{1}{2l(2l+1)} \sum_{mm'} (U_{mm'} - J_{mm'}), \tag{3.236}$$

where  $U_{mm'}$  and  $J_{mm'}$  are orbital dependent intra-atomic Coulomb and exchange integrals for d electrons. From (3.233) and (3.234), we obtain the atomic level  $\varepsilon_{iL}^0$ 

for the noninteracting system as

$$\varepsilon_{iL}^{0} = \varepsilon_{iL} - \left[ \left( 1 - \frac{1}{2(2l+1)} \right) \overline{U} - \frac{1}{2} \left( 1 - \frac{1}{(2l+1)} \right) \overline{J} \right] n_d \delta_{l2}. \quad (3.237)$$

Note that  $n_d$  denotes the total d electron number per atom.

The Coulomb and exchange energy parameters,  $\overline{U}$  and  $\overline{J}$ , may be obtained by the following steps. We introduce an orbital dependent energy functional  $E_{\text{LDA+U}}$  as follows.

$$E_{\rm LDA+U} = E_{\rm LDA} + E_{\rm U} - E_{\rm LDA}^{\rm U}$$
 (3.238)

Here  $E_{\rm LDA}$  is the LDA total energy,  $E_{\rm LDA}^{\rm U}$  is the Hartree–Fock type LDA contribution given by (3.234), and  $E_{\rm U}$  is the orbital-dependent contribution due to d electrons, which is given by

$$E_{\mathrm{U}} = \frac{1}{2} \sum_{i} \sum_{mm'\sigma} \overline{U} n_{jdm\sigma} n_{jdm'\sigma'} + \frac{1}{2} \sum_{i} \sum_{mm'} \sum_{\sigma} (\overline{U} - \overline{J}) n_{jdm\sigma} n_{jdm'\sigma}. \quad (3.239)$$

Note that  $E_{\text{LDA+U}}$  reduces to the original LDA energy when  $n_{jdm\sigma} = n_{jd}$ .

The variational principle  $\delta E_{\rm LDA+U} - \mu \delta N = 0$  yields the Kohn–Sham potential as

$$v_{dm\sigma}(\mathbf{r}) = v_{\text{LDA}}(\mathbf{r}) - \mu + \sum_{m'} \overline{U}(n_{jdm'-\sigma} - n_j)$$

$$+ \sum_{m'} (\overline{U} - \overline{J})(n_{jdm'\sigma} - n_j). \tag{3.240}$$

Here  $v_{\text{LDA}}(r)$  is the LDA potential given by (2.116). A method to take into account the orbital dependence of the LDA potential with use of the intra-atomic Coulomb interactions is called the LDA + U method [63]. The above potential suggests that the following atomic levels in the TB-LMTO (see (2.167)) are orbital dependent,

$$\varepsilon_{jL\sigma} = \left\langle \chi_{jL\sigma} \left| \left( -\frac{1}{2} \nabla^2 + v_{L\sigma}(\mathbf{r}) \right) \right| \chi_{jL\sigma} \right\rangle, \tag{3.241}$$

and  $\partial \varepsilon_{jL\uparrow}/\partial n_{jL'\downarrow} = \partial \varepsilon_{jL\downarrow}/\partial n_{jL'\uparrow} = \overline{U}$ ,  $\partial \varepsilon_{jL\uparrow}/\partial n_{jL'\uparrow} = \partial \varepsilon_{jL\downarrow}/\partial n_{jL'\downarrow} = (\overline{U} - \overline{J})(1 - \delta_{mm'})$  for l = 2.

For the evaluation of  $\overline{U}$  and  $\overline{J}$ , we remove the charge transfer between the d orbitals and the other orbitals, and change the d electron number  $n_{jdm\sigma}$  or the spin density  $m_{jdm} = n_{jm\uparrow} - n_{jm\downarrow}$  as  $\delta n_{jdm\sigma'}$  or  $\delta m_{jdm}$ . Then we can calculate the self-consistent change of the LDA atomic level as  $\{\delta \varepsilon_{jdm\sigma}\}$ . The  $\overline{U}$  and  $\overline{J}$ , which are screened by the other electrons, may be obtained as

$$\overline{U} = \frac{\delta \varepsilon_{jdm\uparrow}}{\delta n_{jdm'\downarrow}},\tag{3.242}$$

$$\overline{J} = \frac{\delta(\varepsilon_{jdm\uparrow} - \varepsilon_{jdm\downarrow})}{\delta m_{idm'}}.$$
(3.243)

The method mentioned above to obtain  $\overline{U}$  and  $\overline{J}$  is known as the constraint LDA [70]. The intraatomic Coulomb and exchange interaction energy parameters  $U_0, U_1$ , and J in the Hamiltonian (3.228) are obtained from  $\overline{U}$  and  $\overline{J}$  in the LDA+U via the relations:  $U_0 = \overline{U} + 8\overline{J}/5$ ,  $U_1 = \overline{U} - 2\overline{J}/5$  and  $J = \overline{J}$ , where we adopted the relation  $U_0 = U_1 + 2J$  obtained from the rotational invariance.

We can apply the dynamical CPA to the first-principles model Hamiltonian (3.228). The Hubbard–Stratonovich transformation (3.24) is then extended as follows.

$$e^{\sum_{mm'} a_m A_{mm'} a_{m'}} = \sqrt{\frac{\det A}{\pi^M}} \int \left[ \prod_m dx_m \right] e^{-\sum_{mm'} (x_m A_{mm'} x_{m'} - 2a_m A_{mm'} x_{m'})}. \quad (3.244)$$

Here  $\{a_{\mu}\}$  are the Bose-type operators which commute each other.  $A_{mm'}$  is a  $M \times M$  matrix, and  $\{x_m\}$  are auxiliary field variables.

Discretizing the time in the free energy in the interaction representation (see (3.31)) and applying the Hubbard–Stratonovich transformation (3.244) to the Bose-type operators at each time under the T-product, one can obtain the functional integral form of the free energy to the Hamiltonian (3.228) as follows.

$$e^{-\beta \mathscr{F}} = \int \left[ \prod_{i=1}^{N} \prod_{m=1}^{2l+1} \delta \xi_{im}(\tau) \delta \zeta_{im}(\tau) \right] Z^{0}(\xi(\tau), \zeta(\tau))$$

$$\times \exp \left[ -\frac{1}{4} \sum_{i} \sum_{mm'} \int_{0}^{\beta} d\tau \left( \zeta_{im}(\tau) A_{imm'} \zeta_{m'}(\tau) + \sum_{\alpha}^{xyz} \xi_{im\alpha}(\tau) B_{imm'}^{\alpha} \xi_{im'\alpha}(\tau) \right) \right]. \quad (3.245)$$

Here  $\zeta_{im}(\tau)$  and  $\xi_{im}(\tau)$  denote the time-dependent charge and exchange fields acting on site i and orbital m.  $Z^0(\xi(\tau), \zeta(\tau))$  is a partition function given by (3.35) in which the Hamiltonian  $H(\tau, \xi(\tau), \eta(\tau))$  has been replaced by

$$H(\tau, \boldsymbol{\xi}(\tau), -i\zeta(\tau)) = \sum_{iL} \left[ \left( \varepsilon_{iL}^{0} - \mu - \frac{1}{2} \sum_{m'} i A_{imm'} \zeta_{im'}(\tau) \delta_{l2} \right) \hat{n}_{iL}(\tau) \right.$$
$$\left. - \sum_{\alpha} \left( \frac{1}{2} \sum_{m'} B_{imm'}^{\alpha} \xi_{im'\alpha}(\tau) + h_{im}^{\alpha} \right) \delta_{l2} \hat{m}_{iL}^{\alpha}(\tau) \right]$$
$$+ \sum_{iLjL'\sigma} t_{iLjL'} a_{iL\sigma}^{\dagger}(\tau) a_{jL'\sigma}(\tau). \tag{3.246}$$

Here  $A_{imm'}$  and  $B_{imm'}^{\alpha}$  ( $\alpha = x, y, z$ ) are the Coulomb and exchange energy matrix elements defined by

$$A_{imm'} = U_0 \delta_{mm'} + (2U_1 - J)(1 - \delta_{mm'}), \tag{3.247}$$

$$B_{imm'}^{\alpha} = J(1 - \delta_{mm'}) \quad (\alpha = x, y),$$
 (3.248)

$$B_{imm'}^{z} = U_0 \delta_{mm'} + J(1 - \delta_{mm'}). \tag{3.249}$$

We express in the next step the free energy with use of the Matsubara frequencies, introduce the coherent potential  $(\Sigma)_{iLn\sigma jL'n'\sigma'} = \Sigma_{L\sigma}(i\omega_n)\delta_{ij}\delta_{LL'}\delta_{nn'}\delta_{\sigma\sigma'}$ , and make the single-site approximation in order to reduce the number of variables. Neglecting the out-of-phase thermal spin fluctuations between different orbitals on a site, we obtain the free energy per site as follows.

$$\mathscr{F}_{\text{CPA}} = \tilde{\mathscr{F}} - \beta^{-1} \ln \int \left[ \prod_{\alpha} \sqrt{\frac{\beta \tilde{J}_{\alpha}}{4\pi}} d\xi_{\alpha} \right] e^{-\beta E_{\text{eff}}(\xi)}. \tag{3.250}$$

Here  $\xi_{\alpha} \equiv \sum_{m} \xi_{lm\alpha}$  is the static exchange field. The effective exchange energy parameters are defined by  $\tilde{J}_{x} = \tilde{J}_{y} = \tilde{J}_{\perp} = [1 - 1/(2l + 1)]J$ ,  $\tilde{J}_{z} = U_{0}/(2l + 1) + \tilde{J}_{\perp}$ . The effective potential consists of the static part and the dynamical part;  $E_{\rm eff}(\xi) = E_{\rm st}(\xi) + E_{\rm dyn}(\xi)$ . The former is given by

$$E_{\text{st}}(\xi) = -\frac{1}{\beta} \sum_{mn} \ln \left[ \left( 1 - \delta v_{L\uparrow}(0) F_{L\uparrow}(i\omega_n) \right) \left( 1 - \delta v_{L\downarrow}(0) F_{L\downarrow}(i\omega_n) \right) - \frac{1}{4} \tilde{J}_{\perp}^2 \xi_{\perp}^2 F_{L\uparrow}(i\omega_n) F_{L\downarrow}(i\omega_n) \right] + \frac{1}{4} \left[ -(U_0 - 2U_1 + J) \sum_{m} \tilde{n}_L(\xi)^2 - (2U_1 - J) \tilde{n}_l(\xi)^2 + \tilde{J}_{\perp} \xi_{\perp}^2 + \tilde{J}_z \xi_z^2 \right].$$
(3.251)

Here  $\delta v_{L\sigma}(0) = v_{L\sigma}(0) - \Sigma_{L\sigma}(i\omega_n)$ , and  $v_{L\sigma}(0)$  is the static potential for electrons with orbital L and spin  $\sigma$ .  $F_{L\sigma}(i\omega_n)$  denotes the coherent Green function for orbital L and spin  $\sigma$ . The charge densities,  $\tilde{n}_L(\xi)$  and  $\tilde{n}_l(\xi)$  are defined by  $\tilde{n}_L(\xi) = \sum_{\sigma} \tilde{n}_{L\sigma}(\xi)$  and  $\tilde{n}_l(\xi) = \sum_m \tilde{n}_L(\xi)$ , respectively. Note that the spin-flip contributions as well as the inter-orbital contributions characterized by the parameters  $2U_1 - J$  and  $\tilde{J}_\perp$  now appear in the energy expression. Equation (3.251) is an extension of the static potential (3.149) to the degenerate case.

The dynamical contribution to the effective potential is given by

$$e^{-\beta E_{\rm dyn}(\xi)}$$

$$= \overline{D} \equiv \int \prod_{n=1}^{\infty} \left[ \left\{ \prod_{\alpha} \frac{\beta^{2l+1} \det B^{\alpha}}{(2\pi)^{2l+1}} \prod_{m} d^{2} \xi_{m\alpha}(i\omega_{n}) \right\} \frac{\beta^{2l+1} \det A}{(2\pi)^{2l+1}} \prod_{m} d^{2} \zeta_{m}(i\omega_{n}) \right]$$

$$\times D \exp \left[ -\frac{\beta}{4} \sum_{n \neq 0} \sum_{mm'} \left( \xi_m^*(i\omega_n) A_{mm'} \xi_{m'}(i\omega_n) + \sum_{\alpha} \xi_{m\alpha}^*(i\omega_n) B_{mm'}^{\alpha} \xi_{m'\alpha}(i\omega_n) \right) \right], \qquad (3.252)$$

and

$$D = \det\left(\delta_{nn'}\delta_{LL'}\delta_{\sigma\sigma'} - \sum_{\sigma''}\tilde{v}_{L\sigma\sigma''}(i\omega_n - i\omega_{n'})\tilde{g}_{L\sigma''L'\sigma'}(i\omega_{n'})\right). \quad (3.253)$$

Here  $\zeta_m(i\omega_n)$  ( $\xi_{m\alpha}(i\omega_n)$ ) denotes the dynamical charge (exchange) field for orbital m. The matrices  $A_{mm'}$  and  $B_{mm'}^{\alpha}$  ( $\alpha=x,y,z$ ) have been defined by (3.247), (3.248), and (3.249).  $\tilde{v}_{L\sigma\sigma'}(i\omega_n-i\omega_{n'})$  is the dynamical potential, and  $\tilde{g}_{L\sigma L'\sigma'}(i\omega_n)$  is the Green function in the static approximation.

The dynamical CPA equation is obtained from the stationary condition of the free energy  $\delta \mathscr{F}_{\text{CPA}}/\delta \Sigma_{iL\sigma}(i\omega_n) = 0$  as follows.

$$\langle G_{L\sigma}^{(i)}(i\omega_n)\rangle = F_{L\sigma}(i\omega_n),$$
 (3.254)

$$\langle G_{L\sigma}^{(i)}(i\omega_n)\rangle = \left\langle \tilde{g}_{L\sigma L\sigma}(i\omega_n) + \frac{\sum_{\nu} \frac{\delta D_{\nu}}{\kappa_{L\sigma}(i\omega_n)\delta \Sigma_{L\sigma}(i\omega_n)}}{1 + \sum_{\nu} (\overline{D}_{\nu} - 1)} \right\rangle_{\text{eff}}.$$
 (3.255)

Here  $\langle G_{L\sigma}^{(i)}(i\omega_n)\rangle$  is the Green function with an impurity dynamical potential embedded in the effective medium.  $D_{\nu}$  is the determinant for the scattering matrix due to dynamical potential  $\tilde{v}_{L\sigma\sigma'}(\pm i\omega_{\nu})$ .  $\kappa_{L\sigma}(i\omega_n) = 1 - F_{L\sigma}(i\omega_n)^{-2}H_{L\sigma}(i\omega_n)$  and  $H_{L\sigma}(i\omega_n) = \delta F_{L\sigma}(i\omega_n)/\delta \Sigma_{L\sigma}(i\omega_n)$ . The average  $\langle \sim \rangle_{\rm eff}$  at the r.h.s. of (3.255) denotes a classical average with respect to the effective potential  $E_{\rm eff}(\xi)$ .

The local charge and magnetic moment are derived from the free energy (3.250) as follows.

$$\langle \hat{n}_L \rangle = \frac{1}{\beta} \sum_{n\sigma} F_{L\sigma}(i\omega_n),$$
 (3.256)

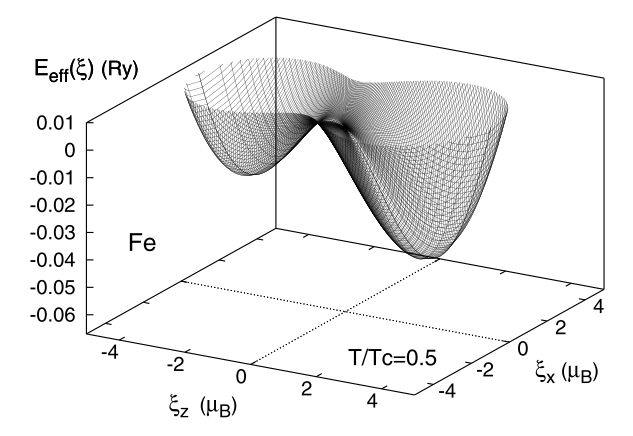
$$\langle \hat{m}_L^z \rangle = \frac{1}{\beta} \sum_{n\sigma} \sigma F_{L\sigma}(i\omega_n). \tag{3.257}$$

In particular, the l=2 components of local charge and magnetic moment (i.e.,  $\langle \hat{n}_l \rangle = \sum_m \langle \hat{n}_L \rangle$  and  $\langle \hat{m}_l \rangle = \sum_m \langle \hat{m}_L \rangle$ ) are expressed as

$$\langle \hat{n}_l \rangle = \langle \tilde{n}_l(\boldsymbol{\xi}) \rangle_{\text{eff}},$$
 (3.258)

$$\langle \hat{\boldsymbol{m}}_l \rangle = \langle \boldsymbol{\xi} \rangle_{\text{eff}}.\tag{3.259}$$

**Fig. 3.11** Effective potential for bcc Fe at the temperature  $T/T_{\rm C} = 0.5$  on the  $\xi_x$ – $\xi_z$  plane [72]



The last expression of magnetic moment indicates a physical picture as shown in Fig. 3.1 that both the longitudinal and transverse components of local moments fluctuate in the metallic system with elevating temperature.

Typical Coulomb and exchange interactions calculated by the LDA + U constraint method are reported to be  $\overline{U}=0.17$  Ry and  $\overline{J}=0.066$  Ry for bcc Fe, and  $\overline{U}=0.22$  Ry and  $\overline{J}=0.066$  Ry for fcc Ni [73]. These values considerably depend on the method of calculations. Recent calculations based on the random phase approximation report that the exchange interaction energy parameters can be reduced by 30 % irrespective of transition metal elements [74]. According to the full Hartree–Fock calculations for solids, on the other hand, the averaged bare Coulomb and exchange interactions are 1.55 Ry and 0.060 Ry (1.66 Ry and 0.065 Ry) for bcc Fe (fcc Ni) [75]. The results imply that the LDA + U Coulomb interaction energy parameters are screened by 4s–4p electrons by a factor of five or ten, while the screening on the exchange interactions is negligible.

Figure 3.11 shows the effective potential of ferromagnetic Fe calculated by the first-principles dynamical CPA. We adopted here the interaction energy parameters,  $\overline{U}=0.17$  Ry and  $\overline{J}=0.066$  Ry. Dynamical corrections are taken into account up to the 4-th orders in Coulomb interaction strength in the calculations. The dynamical potential  $E_{\rm dyn}(\xi)$  acts to reduce the longitudinal amplitude of magnetic moments and enhance the transverse spin fluctuations. The calculated potential for ferromagnetic Fe has a double minimum structure. This implies that the local magnetic moments of Fe show large thermal spin fluctuations which change the magnetic moments in direction. The behavior differs from the case of the single-band model where quantum spin fluctuations are more significant so that the potential shows a single minimum structure (see Fig. 3.7).

The magnetization vs. temperature curves of Fe are presented in Fig. 3.12. Obtained ground-state magnetization 2.58  $\mu_B$  is considerably larger than the experimental value 2.22  $\mu_B$ . Calculated Curie temperatures are summarized in Table 3.2. The Curie temperature in the Hartree–Fock approximation is 12200 K. The static approximation reduces  $T_C$  by a factor of 6. Dynamical corrections in the HA further

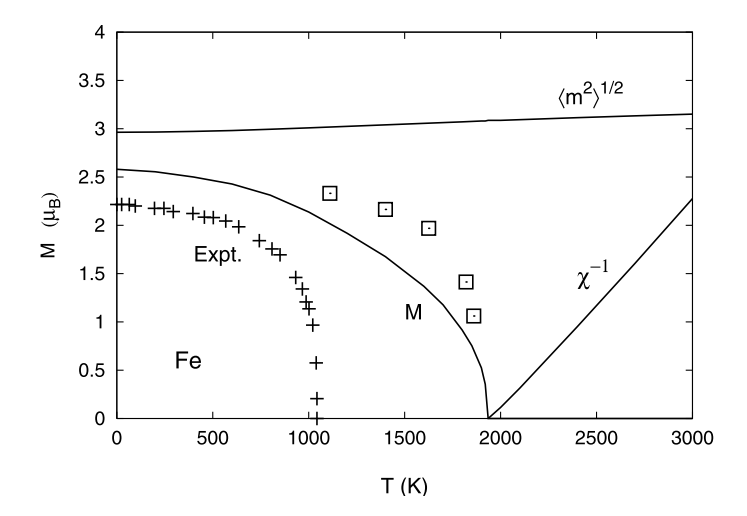


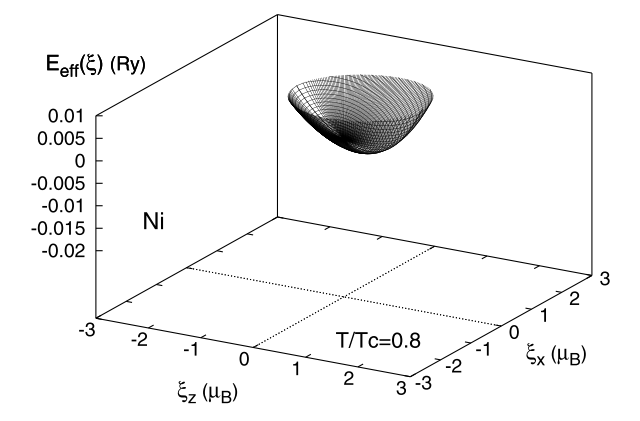
Fig. 3.12 Magnetization vs. temperature curves (M-T), inverse susceptibilities  $(\chi^{-1})$ , and the amplitudes of local magnetic moments  $(\langle m^2 \rangle^{1/2})$  for bcc Fe in the dynamical CPA (*solid curves*) [72]. The magnetizations calculated by the DMFT without transverse spin fluctuations are shown by open squares [73]. Experimental M-T curve is shown by + points [76]

reduce  $T_{\rm C}$  and yield  $T_{\rm C}=1930$  K [72]. The DMFT calculations without transverse spin fluctuations also yield approximately the same value T=1900 K [73]. These values are still higher than the experimental value (1040 K) by a factor of 1.8. The first-principles dynamical CPA also overestimates the Curie temperature of fcc Co by a factor of 1.8 as found on Table 3.2.

The inverse susceptibility above  $T_{\rm C}$  follows the Curie–Weiss law. The dynamical CPA yields the effective Bohr magneton number 3.0  $\mu_{\rm B}$ , which agrees with the experimental value 3.2  $\mu_{\rm B}$  [77]. The amplitudes of local magnetic moments  $\langle {\it m}^2 \rangle^{1/2}$  show a weak temperature dependence and take a value 3.1  $\mu_{\rm B}$  at 2000 K; the calculated effective Bohr magneton number approximately agrees with the amplitude of local moment, so that the Rhodes–Wohlfarth ratio  $(m_{\rm eff}/\langle {\it m}^2 \rangle^{1/2})$  is 1 in agreement with the experimental fact.

An alternative example of ferromagnetic metals is the fcc Ni. The effective potential for Ni shows a single minimum in both the ferro- and para- magnetic states as shown in Fig. 3.13. It indicates small thermal spin fluctuations around the equilibrium point. The dynamical contribution to the effective potential acts as an effective magnetic field which weakens the spin polarization. Calculated ground-state magnetization 0.63  $\mu_B$  is close to the experimental value 0.62  $\mu_B$ . Here the Coulomb and exchange energy parameters are chosen to be  $\overline{U}=0.22$  Ry and  $\overline{J}=0.066$  Ry. The magnetization vs. temperature curve is presented in Fig. 3.14. We find the Curie temperature  $T_C=620$  K. As summarized in Table 3.2, calculated Curie temperatures of Ni in the Hartree–Fock approximation is 4940 K, the static approximation reduces  $T_C$  by a factor of 3 or 4 (1420 K), and the first-principles dynamical CPA with use

**Fig. 3.13** Effective potential of Ni at  $T/T_C = 0.8$  [72]



of the HA yields  $T_{\rm C} = 620$  K [72], being in good agreement with the experimental value 630 K.

The calculated inverse susceptibility for Ni follows the Curie–Weiss law, and shows an upward convexity in the high-temperature region, being in agreement with the experimental data. The effective Bohr magneton number calculated at  $T \sim 2000$  K is 1.6  $\mu_{\rm B}$  in the dynamical CPA. The result is in good agreement with the experimental value 1.6  $\mu_{\rm B}$  [81]. Calculated amplitude of local moment  $\langle m^2 \rangle^{1/2}$  slightly increases with increasing temperature and takes a value 1.97  $\mu_{\rm B}$  at 1000 K, which is larger than 1.27  $\mu_{\rm B}$ , the value in the local moment model. Note that the d electron number in the metallic state is  $n_{\rm d} = 8.7$  because of the hy-

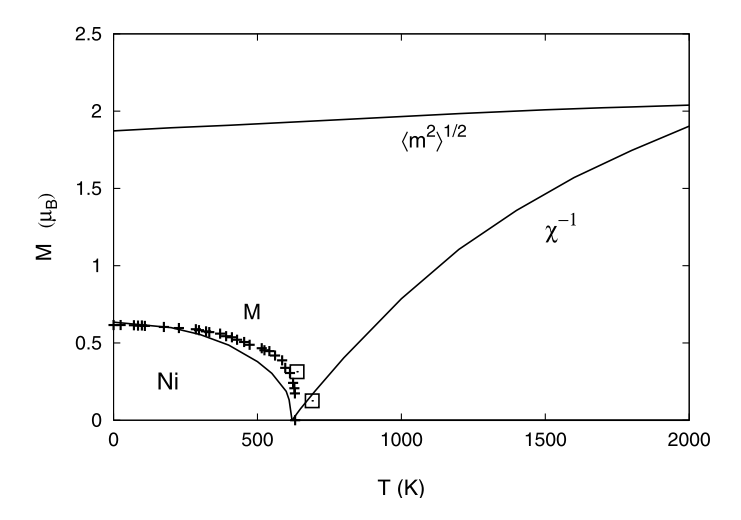


**Fig. 3.14** Magnetization vs. temperature curves (M-T), inverse susceptibilities  $(\chi^{-1})$ , and the amplitude of local magnetic moments  $(\langle m^2 \rangle^{1/2})$  for Ni in the dynamical CPA [72]. Experimental data of magnetization curve are shown by + [82]. The magnetizations calculated by the DMFT without transverse spin fluctuations are shown by open squares [73]

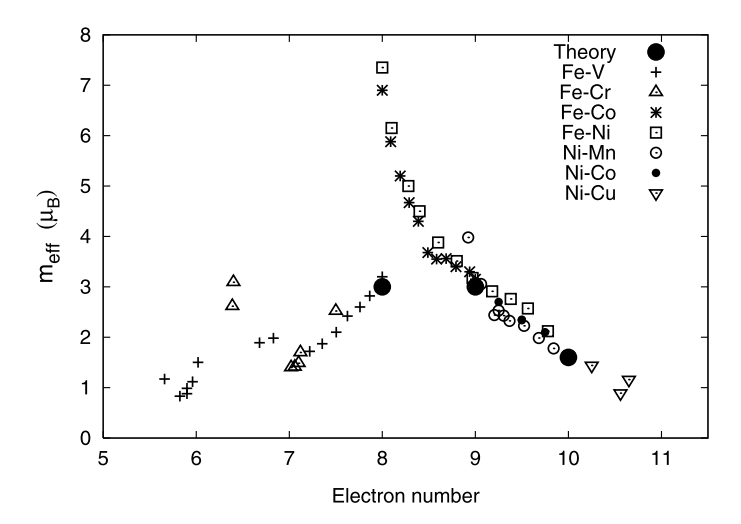


**Fig. 3.15** Effective Bohr magneton numbers in various 3d transition metal alloys as a function of conduction electron number per atom. *Large closed circles* show the theoretical values of Fe, Co, and Ni obtained by the dynamical CPA [72]

**Table 3.2** Curie temperatures  $T_{\rm C}$  for Fe, Co, and Ni calculated by the Hartree–Fock approximation (HF), the dynamical CPA with static approximation (SA), and the dynamical CPA with the harmonic approximation (HA) [72]. The experimental data (Expt.) are shown on the bottom line [78–80]

<i>T</i> <sub>C</sub> (K)	Fe	Co	Ni
HF	12200	12100	4940
SA	2070	3160	1420
HA	1930	2550	620
Expt.	1040	1388	630

bridization of the d bands with the sp bands. It is smaller than  $n_{\rm d}=9.4$  expected from a d-band model with strong ferromagnetism. The amplitude of the local magnetic moment is therefore larger than the value expected from the local moment model,  $1.27\mu_{\rm B}~(=\sqrt{M(0)(M(0)+2)},$  where M(0) is the ground-state magnetization  $0.62~\mu_{\rm B}$ ).

Although the quantitative agreement of  $T_{\rm C}$  is not obtained in the single-site theory, the paramagnetic susceptibilities at high temperatures are quantitatively described by the first-principles dynamical CPA. Experimental data of effective Bohr magneton numbers in 3d transition metal alloys continuously change with the conduction electron number per atom as shown in Fig. 3.15. Calculated effective Bohr magneton numbers, 3.0  $\mu_{\rm B}$  (Fe), 3.0  $\mu_{\rm B}$  (Co), and 1.6  $\mu_{\rm B}$  (Ni) are in the experimental data.

# **Chapter 4 Magnetic Excitations**

The ferromagnetic ground state is excited by applying a time-dependent magnetic field or elevating temperature. These excited states are observed by various experimental methods such as neutron scattering and nuclear magnetic resonance techniques. Here we consider the low-energy excitations from the ferromagnetic ground state in both metals and insulators. We introduce first the spin wave excitations in the local moment system which are instructive for understanding the nature of the excitations. Next, we will show that itinerant electron ferromagnets cause the same type of collective excitations, as well as the spin-flip excitations of each electron called the Stoner excitations. Finally, we introduce the dynamical susceptibility in order to generalize the theory of magnetic excitations, and treat the same topics with use of the susceptibility in the random phase approximation (RPA).

## 4.1 Spin Waves in the Local Moment System

We consider in this section the local moment system described by the Heisenberg model, and clarify the basic concept of spin waves as low-energy excitations.

In the atomic system with n electrons in the unfilled shell, the atomic moment is built up according to the Hund rule (see Sect. 1.3). It consists of the spin magnetic moment with spin S and its z component M, as well as the orbital moment with the angular momentum L and its z component  $M_L$ . In the crystalline system in which the spin-orbit interaction is negligible, the crystal field removes the orbital degeneracy, so that the orbital moments are quenched (see Sect. 1.5). We may then express the magnetic states of the insulator by means of a set of  $\{M_i\}$ , where  $M_i$  denotes the z component of the spin of magnetic ion i. The atomic spin on site i is given by

$$S_{i} = \frac{1}{2} \sum_{m\sigma\sigma'} a^{\dagger}_{im\sigma}(\boldsymbol{\sigma})_{\sigma\sigma'} a_{im\sigma'}, \tag{4.1}$$

where  $a_{im\sigma}^{\dagger}$  ( $a_{im\sigma}$ ) denotes the creation (annihilation) operator for an electron on orbital m in the unfilled shell. The eigen states  $|SM_i\rangle$  of  $S_i^2$  and  $S_{iz}$  are defined by  $S_i|SM_i\rangle = S(S+1)|SM_i\rangle$  and  $S_{iz}|SM_i\rangle = M_i|SM_i\rangle$ .  $M_i$  takes 2S+1 values from -S to S.

We assume that the ferromagnetic state of the insulator is expressed by a Heisenberg model as follows.

$$H = -2J \sum_{(i,j)}^{NN} \mathbf{S}_i \cdot \mathbf{S}_i = -2J \sum_{(i,j)}^{NN} \left[ S_{iz}^2 + \frac{1}{2} \left( S_i^+ S_j^- + S_i^- S_j^+ \right) \right]. \tag{4.2}$$

Here the sum is taken with respect to the nearest-neighbor (NN) pairs for simplicity.  $S_i^{\pm} (= S_{ix} \pm i S_{iy})$  are the raising and lowering operators of spin on atom i, satisfying the relation  $S_i^{\pm} | SM_i \rangle = \sqrt{S(S+1) - M_i(M_i \pm 1)} | SM_i \pm 1 \rangle$ . Note that J > 0 since we assume the ferromagnetic ground state.

As in the case of the Hund-rule coupling, the magnitude of total spin  $S_{\text{tot}} = \sum_{i} S_{i}$  should be maximized at the ground state:  $S_{\text{tot}} = NS$ . Here N is the number of magnetic ions. The ground state wave function is therefore given by

$$\Psi_0 = |\{M_i = S\}\rangle. \tag{4.3}$$

The state  $\Psi_0$  is in fact verified to be the ground state, and its energy is given by  $E_0 = -NJzS^2$  where z is the number of the nearest neighbors.

$$H\Psi_0 = E_0 \Psi_0. \tag{4.4}$$

Note that the ground-state energy  $E_0$  agrees with what is expected from the classical Heisenberg model.

The low-energy excitations from the ground state may be created by the one-spin flipped states defined by

$$|i\rangle = \frac{1}{\sqrt{2S}} S_i^- \Psi_0 = |S, \dots, S, M_i = S - 1, S, \dots\rangle.$$
 (4.5)

Note that these states are orthogonal to the ground state;  $\langle i|\Psi_0\rangle=0$ , and are also orthogonal to each other;  $\langle i|j\rangle=\delta_{ij}$ . The Hamiltonian is diagonalized in the subspace  $\{|i\rangle\}$ . In fact, we can verify that

$$H|i\rangle = \left(-NJzS^2 + 2JzS\right)|i\rangle - 2JS\sum_{l}^{\text{NN of }i}|l\rangle. \tag{4.6}$$

Therefore we have

$$\langle i|H|j\rangle = (E_0 + 2JzS)\delta_{ij} - 2J_{ij}S. \tag{4.7}$$

Here we have defined  $J_{ij}$  as  $J_{ij} = J$  for the NN pair (i, j), and otherwise  $J_{ij} = 0$ .

Since (4.7) is the same type of Hamiltonian matrix as the one-electron tight-binding model (1.53), we can diagonalize it with use of the Bloch wave function  $|k\rangle$  as follows.

$$|\mathbf{k}\rangle = \frac{1}{\sqrt{N}} \sum_{j} e^{-i\mathbf{k}\cdot\mathbf{R}_{j}} |j\rangle,$$
 (4.8)

and

$$H|\mathbf{k}\rangle = (E_0 + \omega_k)|\mathbf{k}\rangle. \tag{4.9}$$

Here  $\omega_k$  is the eigen value for excited states,

$$\omega_k = 2JzS(1 - \gamma(k)), \tag{4.10}$$

and  $\gamma(k) = z^{-1} \sum_{j}^{\text{NN}} \exp(i \mathbf{k} \cdot \mathbf{R}_{j})$ . The excitation energy  $\omega_{k}$  is known as the spin wave energy because the dynamics associated with the excitations form a wave of transverse spin components. Note that  $\omega_{k} \to 0$  as  $\mathbf{k}$  approaches  $\mathbf{0}$ , so that the excitation energy approaches the ground state energy.

The eigen state  $|\mathbf{k}\rangle$  is obtained from the ground state  $\Psi_0$  by applying the spin-flip operator  $S_k^-$  as follows.

$$|\mathbf{k}\rangle = \frac{1}{\sqrt{2S}} S_k^- \Psi_0,\tag{4.11}$$

where

$$S_k^- = \frac{1}{\sqrt{N}} \sum_j e^{-i\mathbf{k} \cdot \mathbf{R}_j} S_j^-.$$
 (4.12)

Let us verify that the dynamics associated with low-energy excitation are spin waves. In the Heisenberg representation, the spin dynamics is determined by the equation of motion as follows.

$$i\frac{dS_k^-}{dt} = [S_k^-, H].$$
 (4.13)

For a low energy state  $\Psi_0$  such as the ground state, we have  $[S_k^-, H]\Psi_0 = -\omega_k S_k^- \Psi_0$ . We have then

$$i\,\frac{dS_k^-}{dt} \approx -\omega_k\,S_k^-. \tag{4.14}$$

Thus,

$$S_k^-(t) = S_k^-(0) e^{i\omega_k t} = \frac{1}{\sqrt{N}} \sum_j S_j^-(0) e^{-i(\mathbf{k} \cdot \mathbf{R}_j - \omega_k t)}.$$
 (4.15)

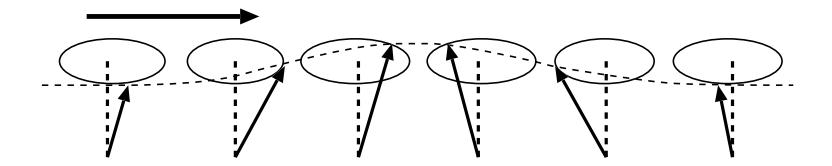


Fig. 4.1 Spin-wave motion associated with the low-energy excitations in the local moment system

In the real space, this means that

$$S_{j}^{-}(t) = \frac{1}{\sqrt{N}} \sum_{k} S_{k}^{-}(0) e^{i(\mathbf{k} \cdot \mathbf{R}_{j} + \omega_{k} t)}.$$
 (4.16)

Since  $S_i^- = S_{jx} - i S_{jy}$ , we obtain

$$S_{jx}(t) = \frac{1}{\sqrt{N}} \sum_{k} S_{k}^{-}(0) \cos(\mathbf{k} \cdot \mathbf{R}_{j} + \omega_{k}t),$$

$$S_{jy}(t) = -\frac{1}{\sqrt{N}} \sum_{k} S_{k}^{-}(0) \sin(\mathbf{k} \cdot \mathbf{R}_{j} + \omega_{k}t).$$

$$(4.17)$$

Thus the motion of spins associated with low-energy excitations in the ferromagnets behaves as a wave of transverse spins (see Fig. 4.1).

## 4.2 Spin Waves in Itinerant Ferromagnets

The spin wave excitations are also possible in the itinerant ferromagnets. We examine in this section the low-energy magnetic excitations in itinerant electron systems. We adopt the Hubbard model (1.51) in the following:

$$H = \sum_{i\sigma} \varepsilon_0 n_{i\sigma} + \sum_{ij\sigma} t_{ij} a_{i\sigma}^{\dagger} a_{j\sigma} + \sum_i U n_{i\uparrow} n_{i\downarrow}. \tag{4.18}$$

We assume that the ground state is ferromagnetic, and that it is approximately described by the Hartree–Fock wave function  $\Psi_0$ , for simplicity.

$$\Psi_0 = \left[\prod_k^{\text{occ}} a_{k\uparrow}^{\dagger}\right] \left[\prod_k^{\text{occ}} a_{k\downarrow}^{\dagger}\right] |0\rangle. \tag{4.19}$$

The Hartree–Fock ground state  $\Psi_0$  and the ground-state energy  $E_0$  then approximately satisfy the following equation as previously discussed in Sect. 2.1.

$$H\Psi_0 \approx E_0 \Psi_0. \tag{4.20}$$

Here

$$E_0 = \sum_{k\sigma}^{\text{occ}} \varepsilon_{k\sigma} - \frac{1}{4} NU \left( \langle n \rangle_0^2 - \langle m \rangle_0^2 \right). \tag{4.21}$$

Here  $\varepsilon_{k\sigma} = \varepsilon_0 + U \langle n \rangle_0 / 2 - U \langle m \rangle_0 \sigma / 2 + \varepsilon_k$  is the Hatree–Fock one-electron energy,  $\varepsilon_k$  being the eigenvalue for the transfer integral matrix  $t_{ij}$ . N denotes the number of lattice points.

As in the local moment case, we may introduce the spin-flip operator  $S_i^- = S_{ix} - i S_{iy} = a_{i\perp}^{\dagger} a_{i\uparrow}$ . In the momentum representation, it is written as

$$S_i^- = \frac{1}{\sqrt{N}} \sum_q e^{i\mathbf{q} \cdot \mathbf{R}_i} S_q^- = \frac{1}{N} \sum_q e^{i\mathbf{q} \cdot \mathbf{R}_i} \sum_k S_{qk}^-.$$
 (4.22)

Here  $S_q^-$  is given by  $S_q^- = \sum_k S_{qk}^- / \sqrt{N}$ , and  $S_{qk}^-$  is the spin-flip operator defined by

$$S_{ak}^{-} = a_{k+a}^{\dagger} a_{k\uparrow}. \tag{4.23}$$

Since  $S_q^-\Psi_0$  described a spin-wave excited state in the case of the insulator model (see (4.11)), we assume here that the low energy excitations in the itinerant system are described by a superposition of the spin-flip states  $\{S_{qk}^-\Psi_0\}$  as follows.

$$\Psi_q = \sum_k c_k \, S_{qk}^- \, \Psi_0. \tag{4.24}$$

The eigen value equation is written as

$$H\Psi_q = (E_0 + \omega_q)\Psi_q. \tag{4.25}$$

Here  $\{c_k\}$  and  $\omega_k$  are coefficients and excitation energy to be determined. Note that  $\langle \Psi_0|S_{qk}^-\Psi_0\rangle=0$  and  $\langle S_{q'k'}^-\Psi_0|S_{qk}^-\Psi_0\rangle=n_{k\uparrow}(1-n_{k+q\downarrow})\delta_{qq'}\delta_{kk'}$ . Here  $n_{k\sigma}$  is the electron occupation number for an electron with momentum k and spin  $\sigma$ .

In order to examine the excited states, we express the Hamiltonian in the momentum representation as follows.

$$H = H_0 + H_{\rm I},\tag{4.26}$$

$$H_0 = \sum_{k\sigma} \varepsilon_k^0 n_{k\sigma}, \tag{4.27}$$

$$H_{\rm I} = \frac{U}{2N} \sum_{k_1 k_2 q \sigma \sigma'} a_{k_1 + q \sigma}^{\dagger} a_{k_2 - q \sigma'}^{\dagger} a_{k_2 \sigma'} a_{k_1 \sigma}. \tag{4.28}$$

Here  $\varepsilon_k^0 = \varepsilon_0 + \varepsilon_k$  is the one-electron energy for the noninteracting Hamiltonian.

In the calculation of  $H \Psi_q$  at the l.h.s. of (4.25), we have

$$H S_{qk}^{-} \Psi_0 = ([H, S_{qk}^{-}] + S_{qk}^{-} H) \Psi_0.$$
 (4.29)

In the second term at the r.h.s. of the above equation, we may adopt (4.20);  $S_{qk}^- H \Psi_0 \approx E_0 S_{qk}^- \Psi_0$ . The commutation relation  $[H, S_{qk}^-]$  in the first term at the r.h.s. is obtained as follows by using (4.27) for  $H_0$  and (4.28) for  $H_1$ , respectively.

$$\begin{bmatrix} H_0, S_{qk}^- \end{bmatrix} = \left( \varepsilon_{k+q}^0 - \varepsilon_k^0 \right) S_{qk}^-, \tag{4.30}$$

$$[H_{\rm I}, S_{qk}^{-}] = \frac{U}{N} \sum_{k'q'\sigma'} \left( a_{k+q+q'\downarrow}^{\dagger} a_{k'-q'\sigma'}^{\dagger} a_{k'\sigma'} a_{k\uparrow} - a_{k+q\downarrow}^{\dagger} a_{k'-q'\sigma'}^{\dagger} a_{k'\sigma'} a_{k-q'\uparrow} \right). \tag{4.31}$$

The interaction part  $[H_I, S_{qk}^-]$  expands the Hilbert space when it is applied to the ground state  $\Psi_0$ . We take the diagonal part among the k' scattering terms, and neglect the other terms that expand the space. This is called the Random Phase Approximation (RPA). For example,

$$\sum_{q'} a_{k+q+q'\downarrow}^{\dagger} \left( \sum_{k'} a_{k'-q'\uparrow}^{\dagger} a_{k'\uparrow} \right) a_{k\uparrow} \Psi_0 \approx \sum_{q'} a_{k+q+q'\downarrow}^{\dagger} a_{k\uparrow}^{\dagger} a_{k+q'\uparrow} a_{k\uparrow} \Psi_0$$

$$= -n_{k\uparrow} \left( \sum_{k'} S_{qk'}^{-} \right) \Psi_0, \tag{4.32}$$

taking only one term k' = k + q' among various k' terms, which is conjugate with  $a_{k\uparrow}$ . Here  $n_{k\sigma}$  is the electron occupation number at the ground state.

Making use of the RPA, we obtain

$$H S_{qk}^{-} \Psi_{0} = \left(\varepsilon_{k+q}^{0} - \varepsilon_{k}^{0}\right) S_{qk}^{-} \Psi_{0}$$

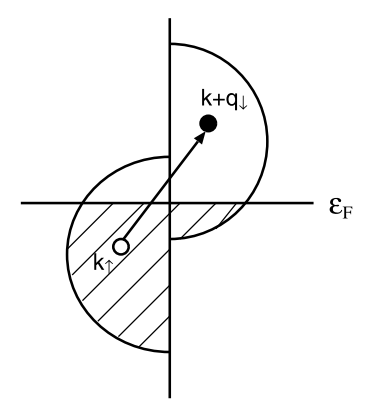
$$+ \frac{U}{N} \sum_{k'} (n_{k'\uparrow} - n_{k'+q\downarrow}) S_{qk}^{-} \Psi_{0}$$

$$- \frac{U}{N} (n_{k\uparrow} - n_{k+q\downarrow}) \sum_{k'} S_{qk'}^{-} \Psi_{0} + E_{0} S_{qk}^{-} \Psi_{0}. \tag{4.33}$$

Substituting the wave function (4.24) into the eigen value equation (4.25) and applying the above relation (4.33) as well as the orthogonality relation  $\langle S_{qk'}^- \Psi_0 | S_{qk}^- \Psi_0 \rangle = n_{k\uparrow} (1 - n_{k+q\downarrow}) \delta_{kk'}$ , we obtain the eigen value equation for  $\{c_k\}$  as follows.

$$\left(\varepsilon_{k+q}^{0} - \varepsilon_{k}^{0} + U\langle m \rangle - \omega_{q}\right)c_{k} = \frac{U}{N} \sum_{k'} (n_{k'\uparrow} - n_{k'+q\downarrow})c_{k'}.$$
 (4.34)

**Fig. 4.2** Stoner excitations  $\omega_{qk} = \varepsilon_{k+q\downarrow} - \varepsilon_{k\uparrow}$  in itinerant electron system



#### (1) Stoner excitations

Equation (4.34) has the simple solutions  $c_k \neq 0$  and  $c_{k'} = 0$  for the other k', which correspond to individual electron excitations. The wave function is given by

$$\Psi_{qk} = S_{qk}^- \Psi_0 = a_{k+q\downarrow}^\dagger a_{k\uparrow} \Psi_0. \tag{4.35}$$

The excitation energy as the eigen value is given by

$$\omega_{qk} = \varepsilon_{k+q}^0 - \varepsilon_k^0 + U\langle m \rangle = \varepsilon_{k+q\downarrow} - \varepsilon_{k\uparrow}, \tag{4.36}$$

where  $\varepsilon_{k\sigma}$  is the Hartree–Fock one-electron energy for  $\sigma$  spin electron.

This is an individual excitation which excites one electron from  $k \uparrow$  to  $k+q \downarrow$ , and is known as the Stoner excitation (see Fig. 4.2). Stoner excitations  $\omega_{qk}$  yield the exchange splitting  $\omega_{q=0} \equiv \Delta = U\langle m \rangle$  at q=0, and form a band for a given  $q \neq 0$ . In the free-electron model band, we have

$$\frac{\hbar}{2m} \left( -2k_{\rm F}q + q^2 \right) + \Delta \le \omega_{qk} \le \frac{\hbar}{2m} \left( 2k_{\rm F}q + q^2 \right) + \Delta. \tag{4.37}$$

The region of the Stoner excitations as a function of q is schematically shown in Fig. 4.3 by hatched lines.

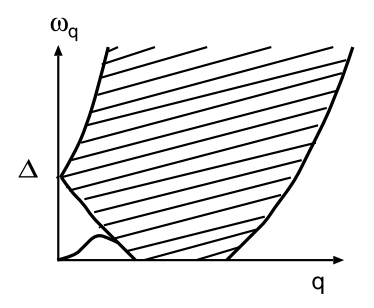
#### (2) Spin wave excitations

There are alternative solutions of low energy excitations with  $\{c_k \neq 0\}$  in the eigen value equation (4.34). After having divided the eigenvalue equation (4.34) by  $(\varepsilon_{k+q}^0 - \varepsilon_k^0 + U\langle m \rangle - \omega_q)$ , we multiply  $n_{k\uparrow} - n_{k+q\downarrow}$  and sum up the equation with respect to k. We then find the equation for excitation energy  $\omega_q$  as follows.

$$1 = \frac{U}{N} \sum_{k} \frac{n_{k\uparrow} - n_{k+q\downarrow}}{\varepsilon_{k+q}^0 - \varepsilon_k^0 + U\langle m \rangle - \omega_q}.$$
 (4.38)

There are many solutions in the case of the strong ferromagnet (large U and  $n_{k\uparrow}=1$ ), because  $\varepsilon_{k+q}^0-\varepsilon_k^0+U\langle m\rangle>0$  and we have each solution between neighboring zero points of the denominator. These solutions correspond to the Stoner

Fig. 4.3 Spin wave excitations (thick line which starts from  $\omega_{q=0}=0$ ) and Stoner excitations (hatched region) as a function of the wave vector  $\mathbf{q}$  in itinerant electron system



excitations. However, we have one more solution below the Stoner continuum solutions as shown in Fig. 4.3. This solution  $\omega_q$  satisfies  $\varepsilon_{k+q}^0 - \varepsilon_k^0 + U\langle m \rangle > \omega_q$ , and  $\omega_q \longrightarrow 0$  as q goes to zero, as verified from (4.38). For small q,  $\varepsilon_{k+q}^0 - \varepsilon_k^0 - \omega_q$  is small as compared with  $\Delta (= U\langle m \rangle)$ . Thus expanding the r.h.s. of (4.38) with respect to  $\varepsilon_{k+q}^0 - \varepsilon_k^0 - \omega_q$ , we obtain the solution for small q as

$$\omega_q = \frac{1}{N\langle m \rangle} \sum_k (n_{k\uparrow} - n_{k+q\downarrow}) \left( \varepsilon_{k+q}^0 - \varepsilon_k^0 \right). \tag{4.39}$$

For the system with cubic symmetry, we obtain

$$\omega_q = Dq^2, \tag{4.40}$$

$$D = \frac{1}{2M} \sum_{k} (n_{k\uparrow} + n_{k\downarrow}) \frac{\partial^2 \varepsilon_k}{\partial k_x^2}.$$
 (4.41)

This is the same dispersion as the one found in the spin wave in the Heisenberg model. The coefficient D is called the spin wave stiffness constant.

The wave function for  $\omega_q=D{\bf q}^2$  is obtained by substituting the eigenvalue into (4.34) and expanding the coefficients  $c_k$  as  $c_k=c_k^{(0)}+c_k^{(1)}+c_k^{(2)}+\cdots$  according to the magnitude of q. Up to the first order, we have  $c_k^{(0)}=0$  and  $c_k^{(1)}=$  const. Thus we obtain

$$\Psi_q = S_q^- \Psi_0. \tag{4.42}$$

This is the same form as the wave function of the spin wave in the Heisenberg model (see (4.11)). In the spin-wave excited state  $\Psi_q$ , total magnetization is reduced by two in unit of the effective Bohr magneton number as compared with that in the ground state.

Taking the same steps as in the spin wave of the Heisenberg model, we can verify that the motions of transverse spins associated with such low energy excitations are given as follows (see (4.17)).

$$S_{jx}(t) = \frac{1}{\sqrt{N}} \sum_{|\boldsymbol{q}| < q_c} S_q^-(0) \cos(\boldsymbol{q} \cdot \boldsymbol{R}_j + \omega_q t),$$

$$S_{jy}(t) = -\frac{1}{\sqrt{N}} \sum_{|\boldsymbol{q}| < q_c} S_q^-(0) \sin(\boldsymbol{q} \cdot \boldsymbol{R}_j + \omega_q t).$$
(4.43)

Here we introduced a cut-off frequency  $q_c$ , below which the spin wave excitation energy  $\omega_q = Dq^2$  is obtained. In conclusion, the spin-wave excitations exist in the long-wave limit even in the itinerant-electron ferromagnet. They correspond to the corrective motion given by (4.43).

It should be noted that the Stoner excitations are included in the eigen states of the Hartree–Fock Hamiltonian (2.7). Associated temperature dependence of the magnetization is obtained from the self-consistent equations (2.11) and (2.12), or (3.1) and (3.2). At low temperatures, one can obtain the temperature dependence of the magnetization per atom as follows solving the self-consistent equations.

$$m(T) = m(0) + \frac{\pi^2}{3} \frac{\rho_{\uparrow}^{(1)} \rho_{\uparrow}^{-1} - \rho_{\downarrow}^{(1)} \rho_{\downarrow}^{-1}}{\rho_{\uparrow}^{-1} + \rho_{\downarrow}^{-1} - U} T^2 + \cdots$$
 (4.44)

Here  $\rho_{\sigma}$  ( $\rho_{\sigma}^{(1)}$ ) denotes the density of states (DOS) at the Fermi level in the ferromagnetic ground state (the first derivative of the DOS at the Fermi level). The above expression indicates that the Stoner excitations yield the temperature variations being proportional to  $T^2$ . The same conclusion is also verified from (3.22) for the weak ferromagnet.

In the spin wave excitations in the strong ferromagnets, we have the eigen-value equation (4.25) with the energy  $\omega_q = D q^2$  and the excited state  $\Psi_q = S_q^- \Psi_0$  for small  $|q| < q_c$ . The equation is written as  $[H, S_q^-] \Psi_0 = \omega_q S_q^- \Psi_0$ . It implies that the following commutation relations are satisfied for low-energy excited states in the strong ferromagnets.

$$\left[H, S_q^-\right] \approx \omega_q S_q^-. \tag{4.45}$$

Then we can find the higher excited states  $\Psi_{nq}=(S_q^-)^n\Psi_0$  such that  $H\Psi_{nq}=(E_0+n\omega_q)\Psi_{nq}$ . These are the higher-order excited states of spin waves called magnon excitations, and the associated magnetization is reduced as  $M_z\Psi_{nq}=(M_0-2n)\Psi_{nq}$ . Here  $M_0$  denotes the ground-state magnetization. We can generalize these results as

$$H\Psi(\lbrace n_q \rbrace) = \left(E_0 + \sum_{q}^{|q| < q_c} n_q \omega_q\right) \Psi(\lbrace n_q \rbrace), \tag{4.46}$$

$$M_z \Psi \left( \{ n_q \} \right) = \left( M_0 - 2 \sum_{q}^{|q| < q_c} n_q \right) \Psi \left( \{ n_q \} \right). \tag{4.47}$$

Here the spin-wave excited states are given by

$$\Psi(\lbrace n_q \rbrace) = \left[\prod_{q}^{|q| < q_c} \left(S_q^-\right)^{n_q}\right] \Psi_0. \tag{4.48}$$

Associated temperature dependence of the magnetization is calculated from (4.47) as

$$\langle M_z \rangle = M_0 - 2 \sum_{q}^{|q| < q_c} \langle n_q \rangle. \tag{4.49}$$

Here the thermal average of the magnon number  $\langle n_q \rangle$  is obtained as  $\langle n_q \rangle = 1/(e^{\beta \omega_q} - 1)$ . Thus we find the magnetization per atom  $m(T) = \langle M_z \rangle / L$  as follows.

$$m(T) = m(0) - \frac{\Omega}{2} \zeta \left(\frac{3}{2}\right) \left(\frac{T}{\pi D}\right)^{3/2} + \cdots$$
 (4.50)

Here  $\Omega$  is the volume of the unit cell and we used the relation  $\omega_q = Dq^2$ .  $\zeta(3/2)$  is Riemann's  $\zeta$  function defined by

$$\int_0^\infty dx \frac{x^2}{e^x - 1} = \frac{\sqrt{\pi}}{2} \sum_{n=1}^\infty \frac{1}{n^{3/2}} = \zeta\left(\frac{3}{2}\right). \tag{4.51}$$

Note that the spin wave excitations are not included in the single-site theory presented in Chap. 3, but govern the temperature dependence of the magnetization in the low temperature limit since the spin wave excitations yield the  $T^{3/2}$  law while the Stoner excitations yield the  $T^2$  law, as seen from (4.50) and (4.44).

## 4.3 Dynamical Susceptibility

Magnetic excitations are described by the dynamical susceptibility. This implies that one can describe the excitations discussed in the last section by means of the susceptibility. In this section we introduce dynamical susceptibility on the basis of the linear response theory and clarify its properties.

Let us assume that the system is perturbed by a time-dependent force F(t), whose interaction is given by

$$H_1(t) = -AF(t).$$
 (4.52)

Here *A* is an operator of a physical quantity. According to the linear response theory [83], the linear change of the physical quantity  $\langle B \rangle(t)$  due to the external time-dependent perturbation  $H_1(t)$  is expressed as follows (see Appendix E).

$$\Delta B(t) = \int_{-\infty}^{t} \chi_{BA}(t - t') F(t') dt'. \tag{4.53}$$

The linear response function  $\chi_{BA}(t)$  is given by a time correlation function at equilibrium state as follows.

$$\chi_{BA}(t) = \frac{i}{\hbar} \langle [B_{H}(t), A] \rangle. \tag{4.54}$$

Here  $B_{\rm H}(t)$  is the Heisenberg representation of the physical quantity B, i.e.,  $B_{\rm H}(t) = \exp(iHt/\hbar) B \exp(-iHt/\hbar)$ .

We consider here the response of the magnetic moments  $m_i$  on site i under the time-dependent magnetic fields  $\{h_i(t)\}$ . The interaction (4.52) is then given by

$$H_1(t) = -\sum_{j} \boldsymbol{m}_{j} \cdot \boldsymbol{h}_{j}(t). \tag{4.55}$$

The response (4.53) of the magnetic moment on site i is given by

$$\Delta m_{i\alpha}(t) = \sum_{i\gamma} \int_{-\infty}^{t} \chi_{ij}^{\alpha\gamma} (t - t') h_{j\gamma}(t') dt'. \tag{4.56}$$

The response function  $\chi_{ij}^{\alpha\gamma}(t)$   $(\alpha, \gamma = x, y, z)$  is given by

$$\chi_{ij}^{\alpha\gamma}(t) = \frac{i}{\hbar} \langle [m_{\text{H}i\alpha}(t), m_{j\gamma}] \rangle. \tag{4.57}$$

When we apply the magnetic field oscillating with a frequency  $\omega$  as

$$\boldsymbol{h}_{j}(t) = \boldsymbol{h}_{j} e^{-i(\omega + is)t}, \tag{4.58}$$

we have the following response from (4.56).

$$\Delta m_{i\alpha}(t) = \sum_{i\gamma} \chi_{ij}^{\alpha\gamma}(\omega + is) h_{j\gamma} e^{-i(\omega + is)t}.$$
 (4.59)

Here s is the positive-definite infinitesimal number. It implies that we apply the infinitesimally small field at  $t = -\infty$ , and increase it continuously up to t = 0. The response function  $\chi_{ij}^{\alpha\gamma}(\omega + is)$  is given as

$$\chi_{ij}^{\alpha\gamma}(\omega + is) = \int_0^\infty \chi_{ij}^{\alpha\gamma}(t) e^{i(\omega + is)t} dt.$$
 (4.60)

The magnetic field and the magnetic moments are expressed by the Fourier lattice series as follows.

$$\boldsymbol{h}_{j} = \sum_{\boldsymbol{q}} \boldsymbol{h}(\boldsymbol{q}, \omega) e^{i\boldsymbol{q} \cdot \boldsymbol{R}_{j}}, \tag{4.61}$$

$$\Delta \mathbf{m}_{i}(t) = \sum_{\mathbf{q}} \Delta \mathbf{m}(\mathbf{q}, \omega) e^{i(\mathbf{q} \cdot \mathbf{R}_{i} - \omega t)}. \tag{4.62}$$

Substituting the above expressions into (4.59), we obtain the linear response in Fourier representation as follows.

$$\Delta m_{\alpha}(\boldsymbol{q},\omega) = \sum_{\gamma} \chi^{\alpha\gamma}(\boldsymbol{q},\omega + is) h_{\gamma}(\boldsymbol{q},\omega). \tag{4.63}$$

Here we assumed the translational symmetry of the system in the equilibrium state. The response function  $\chi^{\alpha\gamma}(q,\omega+is)$  is defined as

$$\chi^{\alpha\gamma}(\boldsymbol{q},\omega+is) = \sum_{i} \chi_{ij}^{\alpha\gamma}(\omega+is) e^{-i\boldsymbol{q}\cdot(\boldsymbol{R}_{i}-\boldsymbol{R}_{j})}.$$
 (4.64)

Substituting (4.60) with (4.57) into (4.64), we obtain

$$\chi^{\alpha\gamma}(\boldsymbol{q},\omega+is) = L \frac{i}{\hbar} \int_0^\infty \langle [m_{\mathrm{H}\alpha}(\boldsymbol{q},t), m_{\gamma}(-\boldsymbol{q})] \rangle e^{i(\omega+is)} dt. \tag{4.65}$$

Here L is the number of lattice points. The operator m(q) is the Fourier component of the local magnetic moment  $m_i$ .

$$m_{\alpha}(\mathbf{q}) = \frac{1}{L} \sum_{i} m_{i\alpha} e^{-i\mathbf{q} \cdot \mathbf{R}_{i}}.$$
 (4.66)

The response function  $\chi^{\alpha\gamma}(q,\omega+is)$  is called the dynamical susceptibility and determines the linear response to the time-dependent perturbation

$$H_1(t) = -L \sum_{\gamma} m_{\gamma}(-\boldsymbol{q}) h_{\gamma}(\boldsymbol{q}, \omega) e^{-i(\omega + is)t}. \tag{4.67}$$

Here  $h_{\gamma}(\boldsymbol{q},\omega)$  is the Fourier transform of the magnetic field  $\boldsymbol{h}_{i}$ .

$$h_{\gamma}(\boldsymbol{q},\omega) = \frac{1}{L} \sum_{i} h_{i\gamma} e^{-i\boldsymbol{q} \cdot \boldsymbol{R}_{i}}.$$
 (4.68)

It should be noted that the interaction  $H_1(t)$  can be written by the spin-flip magnetic moments  $m_i^{\pm} = m_{ix} \pm i m_{iy}$  and conjugate magnetic fields  $h_i^{\pm} = h_{ix} \pm i h_{iy}$  as follows.

$$H_{1}(t) = -L \sum_{q} \left[ \frac{1}{2} \left( m^{+}(-q) h^{-}(q, \omega) + m^{-}(-q) h^{+}(q, \omega) \right) + m_{z}(-q) h_{z}(q, \omega) \right] e^{-i(\omega + is)t}.$$

$$(4.69)$$

Here  $m^{\pm}(\mathbf{q})$  and  $h^{\pm}(\mathbf{q}, \omega)$  are the Fourier transform of  $m_i^{\pm}$  and  $h_i^{\pm}$ , respectively. The interaction (4.69) indicates that we can introduce a transverse response

 $\Delta m^{\pm}(\boldsymbol{q},\omega)$  to the time-dependent magnetic field  $h^{\pm}(\boldsymbol{q},\omega) \exp(-i(\omega+is))$ , instead of  $\Delta m_{\alpha}(\boldsymbol{q},\omega)$  ( $\alpha=x,y$ ). The linear response relation is then written as follows.

$$\Delta m^{\pm}(\boldsymbol{q},\omega) = \sum_{\nu} \chi^{\pm\mp}(\boldsymbol{q},\omega + is)h^{\pm}(\boldsymbol{q},\omega). \tag{4.70}$$

The transverse dynamical susceptibility  $\chi^{\pm \mp}(q, \omega + is)$  is given by

$$\chi^{\pm \mp}(\boldsymbol{q}, \omega + is) = L \frac{i}{\hbar} \int_0^\infty \langle \left[ m_{\rm H}^{\pm}(\boldsymbol{q}, t), m^{\mp}(-\boldsymbol{q}) \right] \rangle e^{i(\omega + is)} dt. \tag{4.71}$$

The dynamical susceptibilities describe magnetic excitations. In order to understand the properties of  $\chi^{-+}(q, \omega + is)$ , for example, we express the time correlation function in (4.71) with use of the eigenstates  $|\alpha\rangle$  and eigenvalues  $E_{\alpha}$  of the Hamiltonian H. The dynamical susceptibility is then given as follows.

$$\chi^{-+}(\boldsymbol{q},\omega+is) = L \sum_{\alpha\gamma} \frac{\mathrm{e}^{-\beta E_{\alpha}}}{Z} \left( \frac{|\langle \gamma | m^{-}(\boldsymbol{q}) | \alpha \rangle|^{2}}{\hbar \omega + is + E_{\gamma} - E_{\alpha}} - \frac{|\langle \gamma | m^{+}(-\boldsymbol{q}) | \alpha \rangle|^{2}}{\hbar \omega + is - E_{\gamma} + E_{\alpha}} \right). \tag{4.72}$$

Here  $\beta$  is the inverse temperature and Z denotes the partition function of the system. The spin-flip magnetic moment  $m^-(q)$  is expressed as

$$m^{-}(q) = \frac{2}{L} \sum_{k} a_{k+q}^{\dagger} a_{k\uparrow} = \frac{2}{L} \sum_{k} S_{qk}^{-}.$$
 (4.73)

In the same way,  $m^+(q)$  is given by

$$m^{+}(\mathbf{q}) = \frac{2}{L} \sum_{k} a_{k+q\uparrow}^{\dagger} a_{k\downarrow} = \frac{2}{L} \sum_{k} S_{qk}^{+}.$$
 (4.74)

Note that the spin-flip operator  $S_{qk}^-$  has been introduced by (4.23), and  $S_{qk}^+$  is defined by  $S_{qk}^+ = a_{k+q\uparrow}^\dagger a_{k\downarrow}$ .

The expression (4.72) indicates that the poles of  $\chi^{-+}(q, -\omega - is)$  give the excitation energies associated with the spin-flip processes  $\{S_{qk}^-\}$ . The imaginary part of dynamical susceptibility describes the excitation spectra. In fact,

$$\operatorname{Im} \chi^{-+}(\boldsymbol{q}, \omega + is) = \frac{\pi L}{\hbar} (\mathcal{M}_{-}^{+}(\boldsymbol{q}, \omega) - \mathcal{M}_{-}(\boldsymbol{q}, -\omega)). \tag{4.75}$$

Here

$$\mathcal{M}_{-}^{+}(\boldsymbol{q},\omega) = \sum_{\alpha\gamma} \frac{e^{-\beta E_{\alpha}}}{Z} \left| \left\langle \gamma \left| m^{-}(\boldsymbol{q})^{\dagger} \right| \alpha \right\rangle \right|^{2} \delta(\omega - \omega_{\gamma\alpha}), \tag{4.76}$$

$$\mathcal{M}_{-}(\boldsymbol{q},\omega) = \sum_{\alpha\gamma} \frac{e^{-\beta E_{\alpha}}}{Z} \left| \left\langle \gamma \left| m^{-}(\boldsymbol{q}) \right| \alpha \right\rangle \right|^{2} \delta(\omega - \omega_{\gamma\alpha}), \tag{4.77}$$

and  $\omega_{\gamma\alpha} = (E_{\gamma} - E_{\alpha})/\hbar$ .

We can verify the following relation by regarding  $\exp(-\beta E_{\alpha})$  as  $\exp(-\beta E_{\gamma} + \beta(E_{\gamma} - E_{\alpha}))$  in (4.77).

$$\mathcal{M}_{-}(\boldsymbol{q},\omega) = e^{\beta\hbar\omega} \mathcal{M}_{-}^{+}(\boldsymbol{q},-\omega). \tag{4.78}$$

Substituting the above relation into (4.75), we find that

$$\operatorname{Im} \chi^{-+}(\boldsymbol{q}, \omega + is) = \frac{\pi L}{\hbar} \left( 1 - e^{-\beta \hbar \omega} \right) \mathcal{M}_{-}^{+}(\boldsymbol{q}, \omega). \tag{4.79}$$

This relation is known as the fluctuation-dissipation theorem. The same relation holds true for the other susceptibilities  $\chi^{\alpha\gamma}(\boldsymbol{q},\omega+is)$  ( $\alpha,\gamma=x,y,z$ ), where the correlation function  $\mathcal{M}_{-}^{+}(\boldsymbol{q},\omega)$  at the r.h.s. of (4.79) should be replaced by

$$\mathcal{M}^{\alpha\gamma}(\boldsymbol{q},\omega) = \sum_{\mu\nu} \frac{e^{-\beta E_{\mu}}}{Z} \langle \mu | m_{\alpha}(\boldsymbol{q}) | \nu \rangle \langle \nu | m_{\gamma}(-\boldsymbol{q}) | \mu \rangle \delta(\omega - \omega_{\nu\mu}). \tag{4.80}$$

The following static spin fluctuation is also expressed by the dynamical susceptibility.

$$\langle \left[ m^{+}(\boldsymbol{q}), m^{-}(-\boldsymbol{q}) \right]_{+} \rangle = \sum_{\alpha \gamma} \frac{e^{-\beta E_{\alpha}}}{Z} \left( \left| \left\langle \gamma \left| m^{-}(-\boldsymbol{q}) \right| \alpha \right\rangle \right|^{2} + \left| \left\langle \gamma \left| m^{-}(-\boldsymbol{q})^{\dagger} \right| \alpha \right\rangle \right|^{2} \right). \tag{4.81}$$

In fact, the r.h.s. is expressed by  $\mathcal{M}_{-}(-q,\omega)$  and  $\mathcal{M}_{-}^{+}(-q,\omega)$  as follows.

$$\left\langle \left[ m^{+}(\boldsymbol{q}), m^{-}(-\boldsymbol{q}) \right]_{+} \right\rangle = \int_{-\infty}^{\infty} d\omega \left( \mathscr{M}_{-}(-\boldsymbol{q}, \omega) + \mathscr{M}_{-}^{+}(-\boldsymbol{q}, \omega) \right). \tag{4.82}$$

Making use of the relation (4.78) and the fluctuation-dissipation theorem (4.79), we obtain the relation between the static spin correlation function and the dynamical susceptibility as follows.

$$\frac{\pi L}{\hbar} \langle \left[ m^{+}(\boldsymbol{q}), m^{-}(-\boldsymbol{q}) \right]_{+} \rangle = \int_{-\infty}^{\infty} d\omega \coth \frac{\beta \hbar \omega}{2} \operatorname{Im} \chi^{-+}(-\boldsymbol{q}, \omega + is). \tag{4.83}$$

Finally, let us examine the static limit of the dynamical susceptibility. The relation (4.70) for q = 0 and  $\omega = 0$  is expressed as follows.

$$\Delta m_x(0,0) - i\Delta m_y(0,0) = \chi^{-+}(0,0)\frac{1}{2}(h_x(0,0) - i(h_y(0,0)). \tag{4.84}$$

In the static limit  $(\omega \to 0)$ ,  $\chi^{-+}(q,0)$  is real according to the fluctuation dissipation theorem (4.79). Moreover in the limit  $q \to 0$ ,  $\Delta m_{\alpha}(q = 0, \omega = 0)$  and

 $h_{\alpha}(\boldsymbol{q}=0,\omega=0)$  are real (see (4.61) and (4.62)). Thus (4.84) yields the following identity.

$$\chi^{xx}(0,0) = \chi^{yy}(0,0) = \frac{1}{2}\chi^{-+}(0,0).$$
 (4.85)

The dynamical susceptibilities are measured directly by means of the neutron magnetic scattering. The neutron has no charge but does have the spin  $s_n=1/2$  and the magnetic moment  $\mu_n=1.913\mu_n\sigma_n$ , where  $\mu_n$  is the nuclear magneton number defined by  $\mu_n=e\hbar/2m_0c$ .  $m_0$  denotes the mass of neutron, and approximately equals that of proton  $m_p$  ( $m_0=1.00138m_p$ ).  $\sigma_n$  denotes the Pauli spin matrix for a neutron. When neutrons enter a solid, they interact with electrons via the magnetic dipole–dipole interaction as an electro-magnetic interaction. A neutron with wave vector  $\mathbf{k}$  is then scattered to the state  $\mathbf{k}'=\mathbf{k}+\mathbf{q}$  with the energy  $\varepsilon=\hbar^2k^2/2m_0$  and energy loss  $\hbar\omega=\hbar^2k^2/2m_0-\hbar^2k'^2/2m_0$ . Here  $\mathbf{q}$  is called the scattering vector. The number of scattered neutrons per energy range  $\Delta\varepsilon$  around energy  $\varepsilon$  and per solid angle fraction  $\Delta\Omega$  in the direction of  $\mathbf{k}'$  is given as follows [14, 15].

$$\frac{d^2\sigma}{d\Omega d\varepsilon} = -\left(1.913 \frac{e^2}{m_e c^2}\right)^2 \left| f(\boldsymbol{q}) \right|^2 \frac{k'}{k} 
\times \sum_{\alpha\gamma} (\delta_{\alpha\gamma} - \hat{q}_{\alpha}\hat{q}_{\gamma}) \frac{\hbar L/\pi}{1 - e^{-\beta\hbar\omega}} \operatorname{Im} \chi^{\alpha\gamma}(\boldsymbol{q}, -\omega + is).$$
(4.86)

Here  $m_e$  is the mass of electron. f(q) is the magnetic form factor defined by  $f(q) = \int d\mathbf{r} \, \rho_i^{(m)}(\mathbf{r}) \exp(-i\mathbf{q}\cdot\mathbf{r})$ , and  $\rho_i^{(m)}(\mathbf{r})$  is the normalized spin density defined by the spin density on atom i as  $\mathbf{m}_i(\mathbf{r}) = \rho_i^{(m)}(\mathbf{r}) \, \mathbf{m}_i$ ,  $\mathbf{m}_i$  being the total spin magnetic moment on atom i. Furthermore  $\hat{\mathbf{q}}$  is the normalized scattering vector. Energy loss of a neutron by  $\hbar\omega$  implies that magnetic excitations with energy  $\hbar\omega$  exist in the solid. They are connected with spin fluctuations of solids via the fluctuation-dissipation theorem.

## 4.4 Dynamical Susceptibility in the RPA and Spin Wave Excitations

We have shown in the last section that the dynamical susceptibility describes the magnetic excitations. We calculate here the dynamical susceptibility of the Hubbard model (4.26) using the equation of motion method combined with the Random Phase Approximation (RPA) [84]. We demonstrate that the spin-wave excitation spectra and the Stoner excitations are obtained from the poles of  $\chi^{-+}(q, -\omega - is)$ . We also discuss the numerical results of the spin wave stiffness constants in Fe and Ni in comparison with the experimental data.

In the equation of motion method, we express the dynamical susceptibility  $\chi^{-+}(q, \omega + is)$ , i.e., (4.71) by means of its retarded Green function  $\chi^{-+}(q, t)$  as

$$\chi^{-+}(q, \omega + is) = \int_{-\infty}^{\infty} \chi^{-+}(q, t) e^{i(\omega + is)t} dt.$$
 (4.87)

The retarded Green function is defined by

$$\chi^{-+}(\boldsymbol{q},t) = L \frac{i}{\hbar} \theta(t) \langle [m_{\rm H}^{-}(\boldsymbol{q},t), m^{+}(-\boldsymbol{q})] \rangle. \tag{4.88}$$

Because of the relations  $m^-(q) = (2/L) \sum_k S_{qk}^-$  and  $S_{qk}^- = a_{k+q}^\dagger \downarrow a_{k\uparrow}$ , we can express  $\chi^{-+}(q,t)$  as a sum of the individual components  $\chi_{qk}(t)$  as follows.

$$\chi^{-+}(\mathbf{q},t) = 2\sum_{k} \chi_{qk}(t). \tag{4.89}$$

Here

$$\chi_{qk}(t) = \frac{i}{\hbar} \theta(t) \langle [S_{qkH}^{-}(t), m^{+}(-\boldsymbol{q})] \rangle. \tag{4.90}$$

The Fourier transform of (4.89) is given by

$$\chi^{-+}(q, \omega + is) = 2\sum_{k} \chi_{qk}(\omega + is),$$
 (4.91)

and

$$\chi_{qk}(\omega + is) = \int_{-\infty}^{\infty} \chi_{qk}(t) e^{i(\omega + is)t} dt.$$
 (4.92)

By differentiating (4.90) with respect to t, we obtain the equation of motion for  $\chi_{qk}(t)$  as follows.

$$i\hbar \frac{\partial \chi_{qk}(t)}{\partial t} = -\delta(t) \langle [S_{qk}^-, m^+(-\boldsymbol{q})] \rangle$$
  
 
$$+ \frac{i}{\hbar} \theta(t) \langle [e^{\frac{i}{\hbar}Ht}[S_{qk}^-, H] e^{-\frac{i}{\hbar}Ht}, m^+(-\boldsymbol{q})] \rangle.$$
 (4.93)

The commutation relation of the first term at the r.h.s. is given as follows.

$$\left[S_{qk}^{-}, m^{+}(-q)\right] = \frac{2}{L}(n_{k+q\downarrow} - n_{k\uparrow}). \tag{4.94}$$

We have obtained in Sect. 4.2 the commutation relation in the second term at the r.h.s. of (4.93) (see (4.30) and (4.31)).

$$\begin{split} \left[S_{qk}^{-}, H\right] &= -\left(\varepsilon_{k+q}^{0} - \varepsilon_{k}^{0}\right) S_{qk}^{-} \\ &- \frac{U}{L} \sum_{k'q'\sigma'} \left(a_{k+q+q'\downarrow}^{\dagger} a_{k'-q'\sigma'}^{\dagger} a_{k'\sigma'} a_{k\uparrow} - a_{k+q\downarrow}^{\dagger} a_{k'-q'\sigma'}^{\dagger} a_{k'\sigma'} a_{k-q'\uparrow}\right). \end{split} \tag{4.95}$$

A difficulty arises from the interaction terms at the r.h.s. of the above equation because they are not expressed by the operators  $\{S_{qk}^-\}$ . As we have mentioned in Sect. 4.2, the RPA simplifies these terms taking the diagonal part among various k' scattering terms and neglecting the other terms. For example, in the second term at the r.h.s. of (4.95), we make the RPA as follows.

$$\sum_{q'} a_{k+q+q'\downarrow}^{\dagger} \left( \sum_{k'} a_{k'-q'\uparrow}^{\dagger} a_{k'\uparrow} \right) a_{k\uparrow} \approx \sum_{q'} a_{k+q+q'\downarrow}^{\dagger} a_{k\uparrow}^{\dagger} a_{k+q'\uparrow} a_{k\uparrow}$$

$$= -n_{k\uparrow} \left( \sum_{k'} S_{qk'}^{-} \right). \tag{4.96}$$

Making the same approximation to the other terms, we obtain the approximate form as

$$\begin{split} \left[ S_{qk}^{-}, H \right] &= -\left( \varepsilon_{k+q}^{0} - \varepsilon_{k}^{0} \right) S_{qk}^{-} \\ &- \frac{U}{L} \sum_{k'} \left( \langle n_{k'\uparrow} \rangle - \langle n_{k'+q\downarrow} \rangle \right) S_{qk}^{-} + \frac{U}{L} \left( \langle n_{k\uparrow} \rangle - \langle n_{k+q\downarrow} \rangle \right) \sum_{k'} S_{qk'}^{-}. \end{split}$$

$$(4.97)$$

Here we have replaced the number operators which appeared after the RPA with their average.

Substituting (4.94) and (4.97) into (4.93), we obtain the equation of motion for  $S_{ak}^-$  in a closed form.

$$i\hbar \frac{\partial \chi_{qk}(t)}{\partial t} = -\delta(t) \frac{2}{L} \left( \langle n_{k+q} \rangle - \langle n_{k\uparrow} \rangle \right) - \left( \varepsilon_{k+q}^{0} - \varepsilon_{k}^{0} \right) \chi_{qk}(t)$$

$$- \frac{U}{L} \sum_{k'} \left( \langle n_{k'\uparrow} \rangle - \langle n_{k'+q} \rangle \right) \chi_{qk}(t)$$

$$+ \frac{U}{L} \left( \langle n_{k\uparrow} \rangle - \langle n_{k+q} \rangle \right) \sum_{k'} \chi_{qk'}(t). \tag{4.98}$$

The above equation can be solved by the Fourier transform as follows. Multiplying  $\exp(i(\omega + is)t)$  in the above equation and integrating both sides with respect to t,

we find that

$$\left[\hbar\omega + is + \varepsilon_{k+q}^{0} - \varepsilon_{k}^{0} + \frac{U}{L} \left( \langle n_{\uparrow} \rangle - \langle n_{\downarrow} \rangle \right) \right] \chi_{qk}(\omega + is) 
= \frac{2}{L} \left( \langle n_{k\uparrow} \rangle - \langle n_{k+q\downarrow} \rangle \right) + \frac{U}{L} \left( \langle n_{k\uparrow} \rangle - \langle n_{k+q\downarrow} \rangle \right) \sum_{k'} \chi_{qk'}(\omega + is).$$
(4.99)

Dividing both sides by the coefficient of the l.h.s. and taking the sum with respect to k, we obtain  $\sum_{k} \chi_{qk}(\omega + is)$ . Substituting the expression into (4.91), we obtain the dynamical susceptibility in the RPA.

$$\chi^{-+}(\mathbf{q}, \omega + is) = \frac{\chi_0^{-+}(\mathbf{q}, \omega + is)}{1 - \frac{U}{4}\chi_0^{-+}(\mathbf{q}, \omega + is)}.$$
 (4.100)

Here  $\chi_0^{-+}(q, \omega + is)$  is the dynamical susceptibility for the noninteracting system given by

$$\chi_0^{-+}(\boldsymbol{q},\omega+is) = \frac{4}{L} \sum_{k} \frac{\langle n_{k\uparrow} \rangle - \langle n_{k+q\downarrow} \rangle}{\hbar\omega + is + \varepsilon_{k+q\downarrow} - \varepsilon_{k\uparrow}}.$$
 (4.101)

As mentioned in the last section (see (4.72)), the poles of the dynamical susceptibility  $\chi^{-+}(q, -\omega - is)$  give the excitation energies  $\hbar\omega_q$  associated with the spin-flip excitations  $a_{k+q\downarrow}^{\dagger}a_{k\uparrow}$ . According to the RPA susceptibility (4.100), the excitation spectra are obtained from the condition

$$\chi_0^{-+}(\boldsymbol{q}, -\omega - is) = \infty, \tag{4.102}$$

or

$$1 - \frac{U}{4} \chi_0^{-+}(q, -\omega - is) = 0. \tag{4.103}$$

The first equation (4.102) yields excitations due to the spin-flip processes of individual electrons, which are known as the Stoner excitations (see (4.36)).

$$\omega_{qk} = \varepsilon_{k+q\downarrow} - \varepsilon_{k\uparrow} = \varepsilon_{k+q}^0 - \varepsilon_k^0 + U\langle m \rangle. \tag{4.104}$$

Another type of excitations is given by (4.103). As we analyzed in Sect. 4.2, (4.103) yields the spin wave excitation energies as well as the energies of the Stoner excitations in the strong ferromagnetic state at zero temperature (see (4.40)).

$$\omega_q = Dq^2. \tag{4.105}$$

Here D is the spin wave stiffness constant defined by (4.41). The wave functions of the excited states are not obtained in this method. The dynamical susceptibility is also useful for obtaining the free energy due to spin fluctuations as will be seen in the next chapter.

Detailed calculations of the spin wave stiffness constant D have been made on the level of the LDA + RPA. The results are rather sensitive to the details of the bands and the exchange splitting  $\Delta$ . For bcc Fe, D=280 meV Å<sup>2</sup> was obtained for  $\Delta=1.94$  eV [85] and is consistent with the value D=280 meV Å<sup>2</sup> obtained by the neutron scatterings [86] and 314 meV Å<sup>2</sup> obtained by the low temperature behavior of the magnetization [87]. In the case of Ni, Wako et al. [88] obtained 285 meV Å<sup>2</sup> for  $\Delta=0.47$  eV, while the neutron experiments [89] show  $D=395\pm20$  meV Å<sup>2</sup>. The latter value is obtained theoretically when  $\Delta=0.40$  eV is adopted [90].

### Chapter 5

## **Spin Fluctuation Theory in Weak Ferromagnets**

The single-site theory of magnetism allows us to understand the finite temperature magnetism qualitatively or semiquantitatively, starting from the microscopic Hamiltonian. We can analyze the magnetic properties from metals to insulators on the basis of the theory. The first-principles dynamical CPA can explain quantitatively high-temperature properties such as the Curie constant in the paramagnetic susceptibility. The single-site theory, however, neglects inter-site spin correlations. The latter influences the Curie temperature and the other quantities related with magnetic short range order. In particular, long-wave spin fluctuations are indispensable for understanding the weak ferromagnetism in  $ZrZn_2$ ,  $Sc_3In$ , and  $Ni_3Al$ , which is characterized by a small Curie temperature ( $\sim 10 \text{ K}$ ) and a large Rhodes–Wohlfarth ratio ( $\gg 1$ ). Here the Rhodes–Wohlfarth ratio is defined by the ratio of the observed Curie constant to the one based on the local moment model. In this chapter, we present a method which takes into account long-range intersite spin correlations at finite temperatures in the weak ferromagnets [91–96].

## 5.1 Free-Energy Formulation of the Stoner Theory

We have described in Sect. 3.1 the Stoner theory in the weak Coulomb interaction region on the basis of the Hartree–Fock self-consistent equations, as well as the single-site spin fluctuation theories which go beyond the Stoner theory. In this section, we rederive the Stoner theory using the free energy at finite temperatures.

We have constructed the dynamical CPA on the basis of the grand canonical ensemble in Chap. 3. There we treated the free energy  $F(\mu, H, T)$  for given chemical potential  $\mu$ , external magnetic field H, and temperature T. Magnetization is then obtained from the thermodynamic relation as

$$M = -\frac{\partial F(\mu, H, T)}{\partial H}. (5.1)$$

The uniform susceptibility is therefore obtained from the relation,

$$\chi = -\frac{\partial^2 F(\mu, H, T)}{\partial H^2}.$$
 (5.2)

We can also make use of the free energy F(N, M, T) for given electron number N, magnetization M, and temperature T when we discuss the thermodynamics of the system. In fact, the free energy  $F(\mu, H, T)$  is written as follows.

$$e^{-\beta F(\mu, H, T)} = \sum_{\alpha NM} e^{-\beta (E_{\alpha}(M, N) - \mu N - MH)} = \sum_{N} e^{-\beta F(N, H, T) + \beta \mu N}.$$
 (5.3)

Here we assumed that magnetization  $\hat{M}$  commutes with the Hamiltonian  $\hat{H}$ .  $E_{\alpha}(M,N)$  is the energy eigen value when the electron number N and magnetization M are given. The free energy F(N,H,T) is defined by

$$e^{-\beta F(N, H, T)} = \sum_{\alpha M} e^{-\beta (E_{\alpha}(M, N) - MH)} = \sum_{M} e^{-\beta F(N, M, T) + \beta MH}.$$
 (5.4)

In the same way, the free energy F(N, M, T) is given by

$$e^{-\beta F(N,M,T)} = \sum_{\alpha} e^{-\beta E_{\alpha}(M,N)}.$$
 (5.5)

We can omit fluctuations of the macroscopic variables N and M, so that we obtain from (5.3) and (5.4) the relations  $F(\mu, H, T) = F(N, H, T) - \mu N$  and F(N, H, T) = F(N, M, T) - MH as well as the associated thermodynamic relations due to stationary conditions. Therefore we find that

$$F(N, M, T) = F(\mu, H, T) + \mu N + MH. \tag{5.6}$$

This is a Legendre transformation from  $F(\mu, H, T)$  to F(N, M, T). When we adopt the free energy F(N, M, T) we can derive from (5.6) the following thermodynamic relation.

$$H = \frac{\partial F(N, M, T)}{\partial M}. (5.7)$$

The uniform susceptibility is therefore obtained by

$$\chi^{-1} = \frac{\partial^2 F(N, M, T)}{\partial M^2}.$$
 (5.8)

The Stoner theory, i.e., the Hartree–Fock theory can be reformulated with use of the free energy F(N, M, T). In the following, we make use the notation m and h instead of M and H for convenience. The Hartree–Fock Hamiltonian to the Hubbard model has been obtained in (2.7). In the momentum representation, it is written as

follows.

$$\tilde{H} = \sum_{k\sigma} \left( \varepsilon_0 + \frac{1}{2} U \langle n \rangle - \Delta \cdot \sigma + \varepsilon_k \right) n_{k\sigma} - \frac{1}{4} U \sum_i \left( \langle n \rangle^2 - \langle m \rangle^2 \right). \tag{5.9}$$

Here  $\varepsilon_k$  is the Fourier transform of the transfer matrix  $t_{ij}$ .  $\Delta = U\langle m \rangle/2 + h$  denotes an exchange splitting of the electron,  $\langle n \rangle$  and  $\langle m \rangle$  are the average electron number and the average magnetization per atom, respectively. The Hartree–Fock free energy  $F_0(\mu, h, T)$  per atom is then given by

$$F_0(\mu, h, T) = -\frac{1}{\beta L} \sum_{k, \sigma} \ln(1 + e^{-\beta(\tilde{\epsilon_0} + \varepsilon_k - \Delta\mu - \Delta \cdot \sigma)}) - \frac{1}{4} U(\langle n \rangle^2 - \langle m \rangle^2). \quad (5.10)$$

Here  $\tilde{\epsilon_0} = \epsilon_0 + U \langle n \rangle / 2 - \epsilon_F$  and  $\Delta \mu = \mu - \epsilon_F$ ,  $\epsilon_F$  being the Fermi level in the nonmagnetic state.

Introducing the density of states per atom per spin in the nonmagnetic state by

$$\rho(\varepsilon) = \frac{1}{L} \sum_{k} \delta(\varepsilon - \tilde{\varepsilon}_0 - \varepsilon_k), \tag{5.11}$$

the free energy  $F_0(\mu, h, T)$  is expressed as

$$F_0(\mu, h, T) = \Phi_0(\mu, h, T) - \frac{1}{4}U(n^2 - m^2), \tag{5.12}$$

$$\Phi_0(\mu, h, T) = -\beta^{-1} \sum_{\sigma} \int d\varepsilon \, \rho(\varepsilon) \ln \left( 1 + \mathrm{e}^{-\beta(\varepsilon - \Delta\mu - \Delta \cdot \sigma)} \right). \tag{5.13}$$

Here the electron number per site  $\langle n \rangle$  and magnetization per site  $\langle m \rangle$  have been written by n and m for convenience, so that  $\tilde{\varepsilon_0}$  and  $\Delta$  stand for  $\varepsilon_0 + Un/2 - \varepsilon_F$  and Um/2 + h, respectively.

The stable configuration of electron number n and magnetization m under given  $\mu$  and h is obtained by minimizing the free energy  $F_0(\mu,h,T)$ ;  $\partial F_0(\mu,h,T)/\partial n=0$  and  $\partial F_0(\mu,h,T)/\partial m=0$ . These equations reproduce the Hartree–Fock equations (3.1) and (3.2);  $n=\langle n\rangle$  and  $m=\langle m\rangle$ . Here the average at the r.h.s. means the Hartree–Fock average.

The Hartree–Fock free energy for given n, m, and T is obtained from the following Legendre transformation (see (5.6)).

$$F_0(n, m, T) = F_0(\mu, h, T) + \mu n + mh. \tag{5.14}$$

We can then verify the thermodynamic relations such as

$$\frac{\partial F_0(n, m, T)}{\partial n} = \mu,\tag{5.15}$$

$$\frac{\partial F_0(n, m, T)}{\partial m} = h. \tag{5.16}$$

The explicit form of the free energy  $F_0(n, m, T)$  is calculated as follows. One electron part of the free energy (5.13), i.e.,  $\Phi_0(\mu, h, T)$  is expressed by  $\Delta\mu$  and  $\Delta$ .  $\Delta\mu$  is expanded by  $\Delta$  according to the Hartree–Fock equation  $n = \langle n \rangle$  (see (3.5)).

$$\Delta \mu = a_0 \Delta^2 \left[ 1 + \left( a^2 + 3b + \frac{c}{a} \right) \Delta^2 + \dots \right].$$
 (5.17)

Here  $a_0$ , a, and b are defined by (3.7) and (3.6). Therefore we can expand  $\Phi_0(\mu, h, T)$  given by (5.13) with respect to  $\Delta$  as follows.

$$\Phi_0(\mu, h, T) = \left[\Phi_0(\mu, h, T)\right]_{m=0} - n\Delta\mu - a_0\Delta^2 + a_0\left(a^2 + \frac{1}{2}b\right)\Delta^4 + \cdots$$
(5.18)

Thus we obtain

$$\Phi_0(n, m, T) \equiv \Phi_0(\mu, h, T) + \mu n + mh$$

$$= \left[\Phi_0(n, m, T)\right]_{m=0} + m\Delta - \frac{1}{2}Um^2 - a_0\Delta^2$$

$$+ a_0\left(a^2 + \frac{1}{2}b\right)\Delta^4 + \cdots$$
(5.19)

On the other hand, with use of the Hartree–Fock equation  $m = \langle m \rangle$ , we can expand m with respect to  $\Delta$  as follows, as has been shown in (3.9).

$$m = 2a_0 \Delta [1 - (2a^2 + b)\Delta^2 + \cdots].$$
 (5.20)

Solving (5.20) with respect to  $\Delta$ , we find

$$\Delta = \frac{1}{2a_0}m + \frac{2a^2 + b}{8a_0^3}m^3 + \cdots$$
 (5.21)

From (5.12), (5.14), (5.19), and (5.21) we obtain the free energy  $F_0(n, m, T)$  expanded by m as follows.

$$F_0(n, m, T) = F_0(n, 0, T) + \frac{1}{2\chi_{\text{HF}}} m^2 + \frac{1}{64} g(T) m^4 + \cdots$$
 (5.22)

Here  $F_0(n, 0, T)$  is the Hartree–Fock free energy in the nonmagnetic state given by

$$F_0(n, 0, T) = n\varepsilon_{\rm F} - \frac{2}{\beta} \int d\varepsilon \, \rho(\varepsilon) \ln(1 + e^{-\beta \varepsilon}) - \frac{1}{4} U n^2. \tag{5.23}$$

The coefficient  $\chi_{HF}$  in the 2nd order term in (5.22) is given by

$$\frac{1}{\chi_{\rm HF}} = \frac{1}{2} \left( \frac{1}{a_0} - U \right) = \frac{1}{\chi_0} - \frac{U}{2}.$$
 (5.24)

The coefficient g(T) in the 4th-order term of (5.22) is given by

$$g(T) = \frac{2(2a^2 + b)}{a_0^3}. (5.25)$$

Note that the coefficient  $a_0$  in (5.24) and (5.25) depends on temperature T via the Fermi distribution function and the Fermi level  $\varepsilon_F$ . It has been obtained before, as shown in (3.14),

$$a_0(T) = \rho \left[ 1 - \frac{\pi^2}{6} R T^2 + \dots \right],$$
 (5.26)

and R is defined by (3.15);  $R = (\rho^{(1)}/\rho)^2 - \rho^{(2)}/\rho$ . Here  $\rho$ ,  $\rho^{(1)}$ , and  $\rho^{(2)}$  denote  $\rho(0)$ ,  $\rho^{(1)}(0)$ , and  $\rho^{(2)}(0)$ , respectively. The coefficient g(T) in the 4th-order term is obtained in the same way as

$$g(T) = \frac{F_1}{\rho} \left( 1 + \frac{\pi^2}{6} R T^2 + \dots \right),$$
 (5.27)

and 
$$F_1 = (\rho^{(1)}/\rho)^2 - \rho^{(2)}/3\rho$$
.

Equation (5.22) is the Hartree–Fock free energy for given n, m, and T in weak ferromagnets. From the thermodynamical relation (5.8), we find that  $\chi_{HF}$  given by (5.24) is the uniform susceptibility in the Hartree–Fock approximation. It agrees with (3.11). The parameter  $\chi_0$  denotes the susceptibility for a noninteracting system. We obtain from the susceptibility (5.24) the Curie temperature in the Stoner theory as follows.

$$T_{\rm C} = \sqrt{\frac{6(\rho U - 1)}{\pi^2 R \rho U}},$$
 (5.28)

which agrees with the expression (3.16).

The spontaneous magnetization m is obtained from the thermodynamical relation (5.7) with h = 0.

$$\frac{\partial F_0(n, m, T)}{\partial m} = \frac{1}{\chi_{\text{HF}}(T)} m + \frac{1}{16} g(T) m^3 + \dots = 0.$$
 (5.29)

For small magnetization we obtain

$$m(T) = \sqrt{-\frac{16}{\chi_{\rm HF}(T)g(T)}}.$$
 (5.30)

This is equivalent to (3.21). Therefore we can derive (3.22) again:

$$m(T) = m(0)\sqrt{1 - \left(\frac{T}{T_{\rm C}}\right)^2}$$
 (5.31)

Here the ground-state magnetization m(0) is given by (3.10);  $m(0) = \sqrt{8(\rho U - 1)} / \sqrt{\rho U F_1 U^2}$ .

We have rederived from the Hartree–Fock free energy (5.22) all the results of the Stoner theory obtained in Sect. 3.1. The free energy (5.22) provides us with a starting point to take into account the nonlocal spin fluctuations on the basis of the free energy.

#### **5.2** Self-Consistent Renormalization Theory

The Hartree–Fock free energy which we derived in the last section is valid only for a small U limit. It overestimates the Curie temperature and does not lead to the Curie–Weiss law in the paramagnetic susceptibility as we have mentioned in Sects. 3.1 and 5.1. In this section, we express the free energy with use of the dynamical susceptibility, and take into account the higher-order contribution in U which yields the nonlocal spin fluctuations [91, 92].

We adopt the Hubbard model in the momentum representation as follows (see (4.26)-(4.28)).

$$H = H_0 + H_{\rm I},$$
 (5.32)

$$H_0 = \sum_{k\sigma} \varepsilon_k^0 n_{k\sigma},\tag{5.33}$$

$$H_{\rm I} = \frac{U}{2L} \sum_{k_1 k_2 q \sigma} a^{\dagger}_{k_1 + q \sigma} a^{\dagger}_{k_2 - q - \sigma} a_{k_2 - \sigma} a_{k_1 \sigma}. \tag{5.34}$$

Here  $\varepsilon_k^0 = \varepsilon_0 + \varepsilon_k$  is the one-electron energy for noninteracting Hamiltonian. *L* denotes the number of the lattice points.

The free energy  $F(\mu, h, T)$  for the grand canonical ensemble is given by

$$F(\mu, h, T) = -\beta^{-1} \text{Tr} \left( e^{-\beta(H - \mu N)} \right). \tag{5.35}$$

Taking the derivative of F with respect to the interaction parameter U, we have  $\partial F(\mu, h, T)/\partial U = \langle H_{\rm I}/U \rangle$ . Integration of both sides with respect to parameter U leads to the following relation.

$$F(\mu, h, T) = -\beta^{-1} \text{Tr} \left( e^{-\beta (H_0 - \mu N)} \right) + \int_0^U dU' \left\langle \frac{H_I}{U'} \right\rangle_{U'}.$$
 (5.36)

Here  $\langle \sim \rangle_{U'}$  denotes the thermal average for the Hamiltonian with coupling parameter U'.

In the Hartree–Fock approximation, we replace the thermal average  $\langle \sim \rangle_{U'}$  with that of a Hamiltonian for independent particle system  $\langle \sim \rangle_0$ , so that  $\int_0^U dU'$ .

 $\langle H_{\rm I}/U'\rangle_{U'}\approx LU\langle n_{\uparrow}\rangle_0\langle n_{\downarrow}\rangle_0$ . Therefore we can express the free energy (5.36) as

$$F(\mu, h, T) = F_0(\mu, h, T) + \frac{1}{L} \int_0^U dU' \left( \left\langle \frac{H_{\rm I}}{U'} \right\rangle_{U'} - \left\langle \frac{H_{\rm I}}{U'} \right\rangle_0 \right).$$
 (5.37)

Here we redefined  $F(\mu, h, T)$  as the free energy per site.  $F_0(\mu, h, T)$  is the free energy per site in the Hartree–Fock approximation and was given by (5.10) in the last section.

$$F_0(\mu, h, T) = -\frac{1}{\beta L} \sum_{k\sigma} \ln\left(1 + e^{-\beta(\tilde{\epsilon_0} + \epsilon_k - \Delta\mu - \Delta \cdot \sigma)}\right) - \frac{1}{4} U(n^2 - m^2). \tag{5.38}$$

The free energy for given electron number per site n, magnetization per site m, and the temperature T is then obtained by the Legendre transformation (5.6):

$$F(n, m, T) = F(\mu, h, T) + \mu n + mh. \tag{5.39}$$

Substituting (5.37) into (5.39), we obtain

$$F(n, m, T) = F_0(n, m, T) + \Delta F.$$
 (5.40)

Here  $F_0(n, m, T)$  is the free energy in the Hartree–Fock approximation defined by (5.14),

$$F_0(n, m, T) = F_0(\mu, h, T) + \mu n + mh, \tag{5.41}$$

and  $\Delta F$  is the correlation correction to the Hartree–Fock free energy.

$$\Delta F = \frac{1}{L} \int_0^U dU' \left( \left\langle \frac{H_{\rm I}}{U'} \right\rangle_{U'} - \left\langle \frac{H_{\rm I}}{U'} \right\rangle_0 \right). \tag{5.42}$$

To calculate the interaction part  $\Delta F$  in (5.40), we express the interaction  $H_{\rm I}$  by means of the spin-fluctuation operators  $m^+(\boldsymbol{q}) = (2/L) \sum_k a_{k+q\uparrow}^\dagger a_{k\downarrow}$  and  $m^-(\boldsymbol{q}) = (2/L) \sum_k a_{k+q\downarrow}^\dagger a_{k\uparrow}$  as follows.

$$H_{\rm I} = \frac{1}{2}UN - \frac{1}{8}LU\sum_{q} \left[ m^{+}(q), m^{-}(-q) \right]_{+}. \tag{5.43}$$

Substituting (5.43) into (5.42), we obtain

$$\Delta F = -\frac{1}{8} \int_0^U dU' \sum_{\mathbf{q}} \left( \left\langle \left[ m^+(\mathbf{q}), m^-(-\mathbf{q}) \right]_+ \right\rangle - \left\langle \left[ m^+(\mathbf{q}), m^-(-\mathbf{q}) \right]_+ \right\rangle_0 \right). \tag{5.44}$$

The spin fluctuation terms are given by dynamical susceptibility according to the relation (4.83).

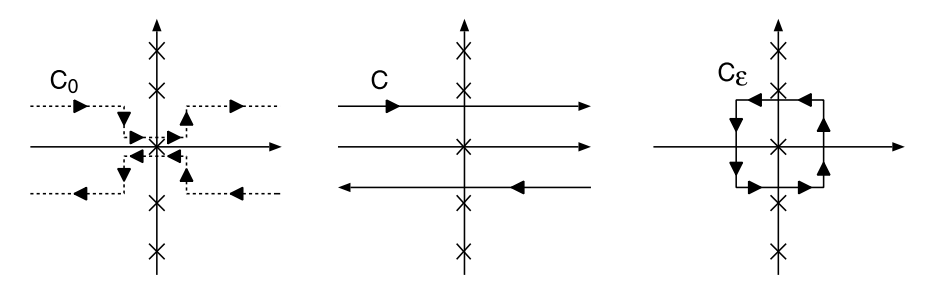


Fig. 5.1 The contour  $C_0$  (*left*), contour C (*center*), and contour  $C_{\varepsilon}$  on the complex plane. Note that the contour  $C_0$  is chosen to pass just on the origin of the complex plane

$$\langle \left[ m^{+}(\boldsymbol{q}), m^{-}(-\boldsymbol{q}) \right]_{+} \rangle = \frac{\hbar}{\pi L} \int_{-\infty}^{\infty} d\omega \coth \frac{\beta \hbar \omega}{2} \operatorname{Im} \chi^{-+}(-\boldsymbol{q}, \omega + is).$$
 (5.45)

Thus, we can express the interaction part by means of the dynamical susceptibility as follows.

$$\Delta F = -\frac{\hbar}{8\pi L} \int_0^U dU' \int_{-\infty}^{\infty} d\omega \coth \frac{\beta \hbar \omega}{2}$$

$$\times \sum_{q} \operatorname{Im} \left( \chi^{-+}(\boldsymbol{q}, -\omega - is) - \chi_0^{-+}(\boldsymbol{q}, -\omega - is) \right). \tag{5.46}$$

Here we made the transformation  $q \to -q$ ,  $\omega \to -\omega$  and used the relation  $\text{Im}\chi^{-+}(q, -\omega + is) = -\text{Im}\chi^{-+}(q, -\omega - is)$  for convenience.

The integral of the dynamical susceptibility with respect to  $\omega$  in the interaction (5.46) is expressed by a sum of Matsubara frequencies on the imaginary axis as follows.

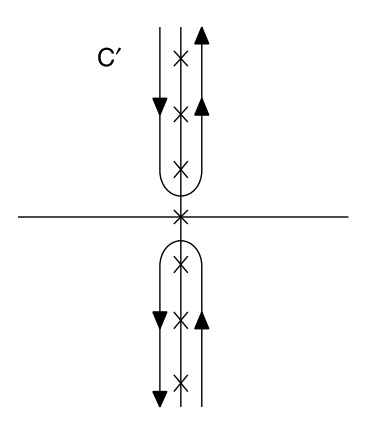
$$I = \frac{\hbar}{2\pi} \int_{-\infty}^{\infty} d\omega \coth \frac{\beta \hbar \omega}{2} \operatorname{Im} \chi^{-+}(\boldsymbol{q}, \omega + is) = \frac{1}{\beta} \sum_{n=-\infty}^{\infty} \chi^{-+}(\boldsymbol{q}, i\omega_n). \quad (5.47)$$

Here  $\omega_n = 2\pi n/\beta \hbar$ . In order to verify the above relation we rewrite the integral at the l.h.s. as

$$I = \frac{\hbar}{4\pi i} \left[ \int_{-\infty}^{\infty} d\omega \coth \frac{\beta \hbar \omega}{2} \chi^{-+}(\mathbf{q}, \omega + is) + \int_{-\infty}^{-\infty} d\omega \coth \frac{\beta \hbar \omega}{2} \chi^{-+}(\mathbf{q}, \omega - is) \right].$$
 (5.48)

These are expressed as an integral along the contour  $C_0$  around the real axis as shown in Fig. 5.1. Note that the integral should pass the origin because the function  $\coth \beta \hbar \omega/2$  is singular there. We can consider the contour  $C_0$  as the superposition of the contours C and  $C_{\varepsilon}$ . The contour C can be changed to C', the sum of the contour around the upper imaginary axis and that around the lower imaginary axis as shown

Fig. 5.2 The contour C' on the complex plane and singular points  $z_n = i\omega_n$  on the imaginary axis leading to the residues



in Fig. 5.2. Because the susceptibility is analytic on the upper and lower complex planes, the contributions from C' and  $C_{\varepsilon}$  are calculated by summing up all residues of  $\coth \beta \hbar \omega/2$  at  $z_n = i\omega_n$  along the imaginary axis, so that we reach the relation (5.47). Making use of the formula (5.47), we obtain alternative expression of  $\Delta F$ .

$$\Delta F = -\frac{1}{4\beta L} \int_0^U dU' \sum_{qn} \left( \chi^{-+}(\boldsymbol{q}, -i\omega_n) - \chi_0^{-+}(\boldsymbol{q}, -i\omega_n) \right).$$
 (5.49)

For the calculation of  $\Delta F$ , we need an explicit form of the dynamical susceptibility. The general form of the dynamical susceptibility is written as follows.

$$\chi^{-+}(\mathbf{q}, \omega + is) = \frac{\chi_0^{-+}(\mathbf{q}, \omega + is)}{1 - \frac{U}{4}\chi_0^{-+}(\mathbf{q}, \omega + is) + \lambda(\mathbf{q}, \omega + is)}.$$
 (5.50)

 $\chi_0^{-+}(\boldsymbol{q},\omega+is)$  is the dynamical susceptibility in the Hartree–Fock approximation given by (4.101). The second term in the denominator is the RPA correction (see (4.100)), and the last term  $\lambda(\boldsymbol{q},\omega+is)$  describes corrections beyond the RPA.

The RPA susceptibility is insufficient to describe finite temperature properties, though it explained the spin wave excitations at zero temperature as discussed in Sect. 4.4. We assume here that  $\lambda(q, \omega + is) = 0$  at zero temperature, but that  $\lambda(q, \omega + is) \approx \lambda(0, 0) = \lambda(T)$  at finite temperatures, expecting low energy excitations and fluctuations around q = 0 to be important for the weak ferromagnetism. We also assume  $\lambda(T) \ll 1$ . Finally, we adopt the following dynamical susceptibility.

$$\chi^{-+}(\mathbf{q}, \omega + is) = \frac{\chi_0^{-+}(\mathbf{q}, \omega + is)}{1 - \frac{U}{4}\chi_0^{-+}(\mathbf{q}, \omega + is) + \lambda(T)}.$$
 (5.51)

The Hartree–Fock dynamical susceptibility is given as follows as we have obtained in (4.101).

$$\chi_0^{-+}(\boldsymbol{q},\omega+is) = \frac{4}{L} \sum_{k} \frac{f(\varepsilon_k - \Delta) - f(\varepsilon_{k+q} + \Delta)}{\hbar\omega + is + \varepsilon_{k+q} - \varepsilon_k + 2\Delta}.$$
 (5.52)

Here  $f(\omega)$  is the Fermi distribution function,  $\Delta = Um/2 + h$ , and we redefined  $\varepsilon_k$  as  $\varepsilon_k = \varepsilon_k^0 - \mu + Un/2$ .  $\varepsilon_k^0$  is the one-electron energy eigen value for noninteracting electrons

Substituting (5.51) into (5.49) and performing the integral on parameter U', we obtain

$$\Delta F = \frac{1}{\beta L} \sum_{qn} \left[ \ln \left( 1 - \frac{U}{4} \chi_0^{-+} (\mathbf{q}, -i\omega_n) + \lambda \right) - \frac{U}{4} \chi_0^{-+} (\mathbf{q}, -i\omega_n) \right]. \quad (5.53)$$

Here we have neglected an additional term  $ln(1 + \lambda)$ , assuming that  $|\lambda| \ll 1$ .

The final form of the free energy for given n, m, and T is expressed by (5.40), (5.41), and (5.53). We have obtained in the last section an explicit form of  $F_0(n, m, T)$  (see (5.22)). The free energy correction (5.53) is given as a function of  $\Delta$ , therefore we can regard  $\Delta F$  as a function of m. The correction  $\lambda(T)$  due to thermal spin fluctuations has not yet been determined. In order to determine  $\lambda(T)$  we make use of a sum rule in the static limit.

In the paramagnetic state, the system is magnetically uniform. Therefore  $\chi^{xx} = \chi^{yy} = \chi^{zz} = \chi$ . According to the relation (4.85), this implies that

$$\chi = \frac{1}{2}\chi^{-+}(\mathbf{q} = 0, \omega = 0). \tag{5.54}$$

For a noninteracting limit (i.e., the Hartree-Fock limit), we have

$$\chi_0 = \frac{1}{2}\chi_0^{-+}(\mathbf{q} = 0, \omega = 0).$$
 (5.55)

Below  $T_{\rm C}$ , the relation  $\chi^{xx} = \chi^{yy} = \chi^{zz}$  is no longer satisfied because the z direction is not magnetically equivalent to the other directions. Instead,  $\chi^{xx} = \chi^{yy} = \chi^{-+}(\boldsymbol{q} = 0, \omega = 0)/2$  should diverge below  $T_{\rm C}$  because the Hamiltonian is rotationally invariant. For the susceptibility (5.51), this implies that

$$1 - \frac{1}{4}U\chi_{m0}^{-+}(\mathbf{q} = 0, \omega = 0) + \lambda_m = 0.$$
 (5.56)

Here the subscript m means that the magnetization m is finite, and it is assumed to be given in the above equation.

In the following, we consider the paramagnetic state for simplicity. Substituting (5.51) and (5.55) into (5.54), we obtain

$$\chi = \frac{\chi_0}{1 - \frac{1}{2}U\,\chi_0 + \lambda},\tag{5.57}$$

i.e.,

$$\frac{1}{\chi} = \frac{1}{\chi_0} - \frac{1}{2}U + \frac{\lambda}{\chi_0}.$$
 (5.58)

On the other hand, the uniform susceptibility is obtained from the thermodynamic relation of the free energy via (5.8) independently of the sum rule (5.58).

$$\frac{1}{\chi} = \left(\frac{\partial^2 F(n, m, T)}{\partial m^2}\right)_{m=0} = \left(\frac{\partial^2 F_0(n, m, T)}{\partial m^2}\right)_{m=0} + \left(\frac{\partial^2 \Delta F(n, m, T)}{\partial m^2}\right)_{m=0}.$$
(5.59)

Here we added the subscript m = 0 because of being in the paramagnetic state. The Hartree–Fock part at the r.h.s. is obtained from the expression of the free energy (5.22) as

$$\left(\frac{\partial^2 F_0(n, m, T)}{\partial m^2}\right)_{m=0} = \frac{1}{\chi_{HF}} = \frac{1}{\chi_0} - \frac{1}{2}U.$$
 (5.60)

Therefore the susceptibility (5.59) is expressed as

$$\frac{1}{\chi} = \frac{1}{\chi_0} - \frac{1}{2}U + \left(\frac{\partial^2 \Delta F(n, m, T)}{\partial m^2}\right)_{m=0}.$$
 (5.61)

From the sum rule (5.58) and the thermodynamic susceptibility (5.61), we obtain the self-consistent equation to determine the spin fluctuation parameter  $\lambda(T)$  as

$$\lambda(T) = \chi_0 \left( \frac{\partial^2 \Delta F(n, m, T)}{\partial m^2} \right)_{m=0}.$$
 (5.62)

The r.h.s. is obtained from (5.53) as

$$\frac{\partial^{2} \Delta F(n, m, T)}{\partial m^{2}} = -\frac{U^{2}}{16\beta L} \sum_{qn} \left[ \frac{\chi_{0}^{-+}(\boldsymbol{q}, -i\omega_{n}) - \frac{4\lambda}{U}}{1 - \frac{U}{4}\chi_{0}^{-+}(\boldsymbol{q}, -i\omega_{n}) + \lambda} \frac{\partial^{2} \chi_{0}^{-+}(\boldsymbol{q}, -i\omega_{n})}{\partial m^{2}} + \frac{1}{(1 - \frac{U}{4}\chi_{0}^{-+}(\boldsymbol{q}, -i\omega_{n}) + \lambda)^{2}} \left( \frac{\partial \chi_{0}^{-+}(\boldsymbol{q}, -i\omega_{n})}{\partial m} \right)^{2} \right].$$
(5.63)

Solving the self-consistent equation (5.62), we obtain  $\lambda(T)$  at each temperature T, thus obtain the susceptibility  $\chi$  via (5.57) or (5.58). This self-consistent scheme based on the RPA is known as the self-consistent renormalization theory (SCR) [93].

The Curie temperature  $T_{\rm C}$  is obtained from (5.57) with the condition  $1/\chi = 0$ .

$$1 - \frac{1}{2}U\chi_0(T_{\rm C}) + \lambda(T_{\rm C}) = 0. \tag{5.64}$$

The above equation shows that the RPA ( $\lambda = 0$ ) does not improve the Curie temperature of the Hartree–Fock approximation. In the SCR,  $\lambda > 0$  at finite temperatures,

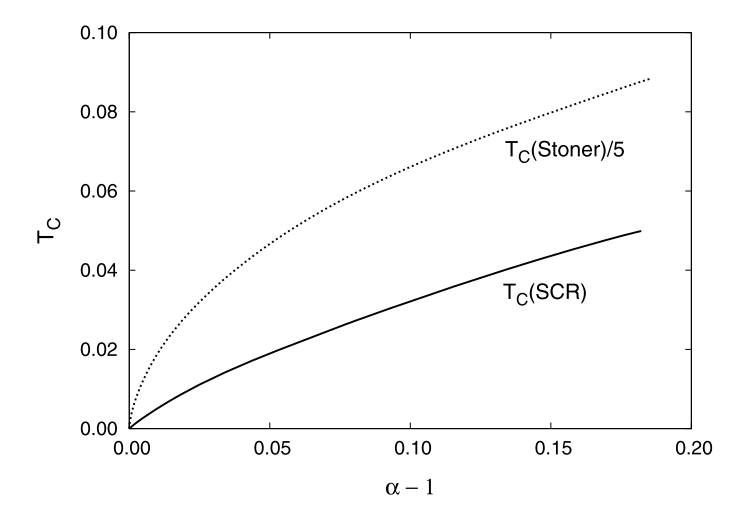


Fig. 5.3 The Curie temperature in the SCR theory (*solid line*) and the Hartree–Fock theory (*dashed line*) as a function of the Stoner parameter  $\alpha = U \chi_0(T=0)/2$  [91, 92]

therefore the renormalization  $\lambda$  can reduce  $T_{\rm C}$ . According to the numerical calculations based on the free electron gas model, the Curie temperature obtained by (5.64) reduces the Hartree–Fock (Stoner)  $T_{\rm C}$  by a factor of 10 (see Fig. 5.3). Since the single-site spin and charge fluctuations reduce the Hartree–Fock  $T_{\rm C}$  by a factor of 5 according to Table 3.2 in the last section, the results suggest that the nonlocal spin fluctuations can reduce  $T_{\rm C}$  by a factor of 2. But the theory based on the realistic Hamiltonian which allows us to make quantitative calculations of  $T_{\rm C}$  has not yet been developed.

Equation (5.64) is equivalent to (5.58) with  $\chi^{-1} = 0$ .

$$0 = \frac{1}{\chi_0(T_C)} - \frac{1}{2}U + \frac{\lambda(T_C)}{\chi_0(T_C)}.$$
 (5.65)

Taking the difference between (5.58) and (5.65) near  $T_{\rm C}$ , we find

$$\frac{1}{\chi} = \frac{\lambda(T) - \lambda(T_{\rm C})}{\chi_0(T_{\rm C})}.\tag{5.66}$$

Expanding  $\lambda(T)$  with respect to T near  $T_{\rm C}$ , we find the Curie–Weiss law.

$$\frac{1}{\chi} = \frac{\lambda (T_{\rm C})'}{\chi_0(T_{\rm C})} (T - T_{\rm C}). \tag{5.67}$$

The expression above indicates that the Curie–Weiss law is caused by the self-consistent renormalization of spin fluctuations beyond the Hartree–Fock approximation. The numerical calculations verify that the susceptibilities approximately follow the Curie–Weiss law as shown in Fig. 5.4. It should be noted that the Curie

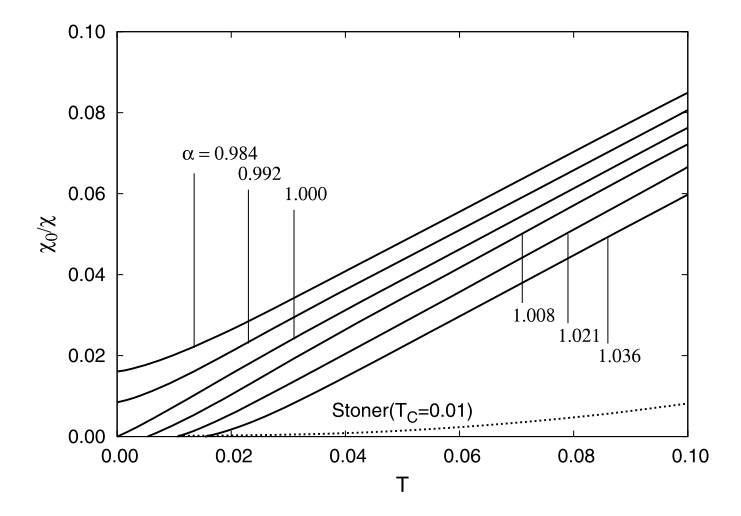


**Fig. 5.4** Inverse susceptibility vs. temperature curves for various Stoner parameters  $\alpha = U \chi_0(T=0)/2$ . Note that  $T_{\rm C} = 0.005, 0.010, 0.015$  for  $\alpha = 1.008, 1.021$ , and 1.036, respectively. The curve in the Stoner theory is also presented for  $T_{\rm C} = 0.01$  [91, 92]

constant is determined by the spin fluctuations in the long-wave regime as seen from (5.67). The theory explains the small  $T_{\rm C}$  and the large Rhodes–Wohlfarth ratio in the weak ferromagnets such as  ${\rm ZrZn_2}$  and  ${\rm Sc_3In}$ .

The same type of theory was also developed by Cyrot [94], and Hertz and Klenin [95, 96]. Cyrot took into account Onsager's reaction field in the calculation of the susceptibility. The spin correlation function was calculated with use of the fluctuation-dissipation theorem. In the theory by Hertz and Klenin, they started from the variational principle for the free energy in the functional integral method, and adopted the RPA type trial functional. Making use of the self-consistent phonon approximation, they obtained the free energy. Both theories yield essentially the same results as those obtained by the self-consistent renormalization theory of the weak ferromagnetism in metals.

# **Chapter 6 Antiferromagnetism and Spin Density Waves**

As we have mentioned in Sect. 1.7, magnetic metals and compounds show a variety of magnetic structures. These include the ferromagnetic structure, the antiferromagnetic (AF) structure, the spin density waves (SDW), and more complex magnetic structures. In this chapter we clarify the microscopic mechanism for the formation of the antiferromagnetism as well as the SDW, and describe theoretical approaches to the complex magnetic structures in metals. We treat in Sect. 6.1 the antiferromagnetism at half filling with use of the Hartree–Fock approximation and the dynamical CPA, and argue the stability of the AF on the U-n plane. In Sect. 6.2, we derive the generalized static susceptibility, and explain the stability of the antiferromagnetism as well as the SDW in 3d transition metals. The susceptibility is not useful for understanding more complex magnetic structures in the itinerant electron system. We present in Sect. 6.3 the molecular dynamics approach which automatically finds the stable magnetic structure at finite temperatures. In the last section, we present a phenomenological theory which is useful for understanding complex magnetic structures in weak itinerant electron magnets, and discuss the multiple spin density waves (MSDW).

### **6.1** Antiferromagnetism in Metals

The 3d transition metals in the vicinity of the middle on the periodic table and their alloys show various antiferromagnetic states. The bcc-base Cr alloys with a few percent of Mn, for example, show the antiferromagnetic state with a simple cubic sublattice as shown in Fig. 6.1. The fcc-base Mn alloys also show the antiferromagnetic structure of the first-kind in which the (001) ferromagnetic plane alternatively changes the magnetization in direction along the c-axis (see Fig. 1.10(c)). The  $\alpha$ -Mn shows more complex noncollinear antiferromagnetic structure in which 29 Mn atoms in the primitive unit cell have magnetic moments different in size and direction [97]. We present in this section the Hartree–Fock theory of the antiferromagnetism at half filling on the basis of the Hubbard model, and clarify the so-called nesting mechanism for the formation of the antiferromagnetism.

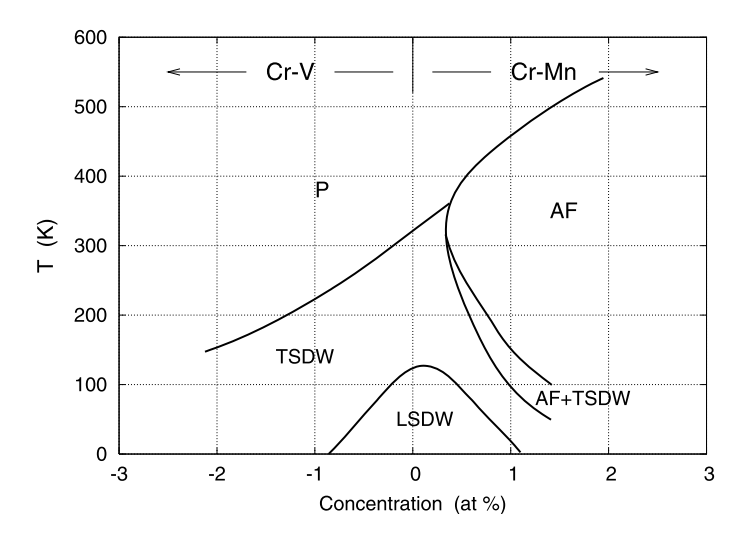


**Fig. 6.1** Magnetic phase diagram of Cr–V and Cr–Mn alloys showing the longitudinal spin density wave state (LSDW), the transverse spin density wave state (TSDW), the antiferromagnetic state (AF), and the paramagnetic state (P) [97]

The Hubbard Hamiltonian in the Hartree–Fock approximation is written as (see (2.7))

$$H = \sum_{ij\sigma} (\boldsymbol{H}_{\sigma})_{ij} a_{i\sigma}^{\dagger} a_{j\sigma} - \sum_{i} U \langle n_{i\uparrow} \rangle \langle n_{i\downarrow} \rangle. \tag{6.1}$$

Here  $(\boldsymbol{H}_{\sigma})_{ij} = \varepsilon_{i\sigma}\delta_{ij} + t_{ij}(1 - \delta_{ij})$  and  $\varepsilon_{i\sigma} = \varepsilon_0 + U\langle n_i \rangle/2 - U\langle m_i \rangle\sigma/2$ . The self-consistent local charge and magnetic moment on site *i* are then given by

$$\langle n_i \rangle = \int d\omega \, f(\omega - \mu) \sum_{\sigma} \rho_{i\sigma}(\omega),$$
 (6.2)

$$\langle m_i \rangle = \int d\omega f(\omega - \mu) \sum_{\sigma} \sigma \rho_{i\sigma}(\omega).$$
 (6.3)

Here  $f(\omega)$  is the Fermi distribution function,  $\mu$  is the chemical potential, and  $\rho_{i\sigma}(\omega)$  is the density of states on site i and spin  $\sigma$  in the Hartree–Fock approximation. The latter is given by the Green function  $G_{ii\sigma}(z)$  as follows.

$$\rho_{i\sigma}(\omega) = -\frac{1}{\pi} \operatorname{Im} G_{ii\sigma}(z), \tag{6.4}$$

$$G_{ii\sigma}(z) = \sum_{\kappa} \frac{\langle i | \kappa \rangle_{\sigma} \langle \kappa | i \rangle_{\sigma}}{z - \varepsilon_{\kappa\sigma}} = \left[ (z - \boldsymbol{H}_{\sigma})^{-1} \right]_{ii}.$$
 (6.5)

Here  $z = \omega + i\delta$  with  $\delta$  being the infinitesimal positive number,  $\varepsilon_{\kappa\sigma}$  is the Hartree–Fock one-electron energy eigen value, and the eigen state is assumed to be given by  $\phi_{\kappa\sigma} = \sum_i \phi_{i\sigma} \langle i | \kappa \rangle_{\sigma}$ .

We consider here the antiferromagnetic (AF) state with two sublattices  $\eta=\pm$  on the simple cubic (sc) lattice with the lattice constant a (see Fig. 1.10(a)) for simplicity. The following arguments are also applicable to the AF structure on the bcc lattice (see Fig. 1.10(b)). Note that each sublattice forms the fcc lattice in the case of the sc structure. We adopt the unit cell with 2 atoms, one with an up magnetic moment belonging to the sublattice (+), and another with a down magnetic moment belonging to the (-) sublattice. The primitive translational vectors are given by a=a(1,1,0), b=a(0,1,1), and c=a(1,0,1). The volume of the unit cell is  $2a^3$ . These vectors form the fcc lattice with lattice constant 2a. The Bloch functions  $|k\eta\rangle$  are given by

$$|k\pm\rangle = \frac{1}{\sqrt{L/2}} \sum_{l}^{\text{fcc}} \phi(\mathbf{r} - \mathbf{R}_l - \mathbf{\eta}_{\pm}) e^{-ik \cdot (R_l + \eta_{\pm})}. \tag{6.6}$$

Here k denotes a wave vector in the first Brillouin zone of the fcc lattice. L denotes the number of simple-cubic lattice points. The atomic position vectors  $\eta_{\pm}$  are given by  $\eta_{+} = \mathbf{0}$  and  $\eta_{-} = a(1,1,1)$ , respectively. The atomic levels belonging to the sublattice  $\eta(=\pm 1)$  are given by  $\varepsilon_{\eta\sigma} = \varepsilon_0 + U\langle n \rangle/2 - U|\langle m \rangle|\eta\sigma/2$ .

When there is no electron hopping between the atoms in the same sublattice and only the nearest-neighbor electron hoppings exist between different sublattices, we have the following  $2 \times 2$  Hamiltonian matrix.

$$\langle \boldsymbol{k}\eta | H_{\sigma} | \boldsymbol{k}\eta' \rangle = \begin{pmatrix} \varepsilon_{+\sigma} & \varepsilon_{k} \\ \varepsilon_{k} & \varepsilon_{-\sigma} \end{pmatrix}. \tag{6.7}$$

Here  $\varepsilon_k$  reduces to the energy eigenvalue for simple cubic lattice;  $\varepsilon_k = t \sum_i^{\text{sc}} \exp(i \mathbf{k} \cdot \mathbf{k}_i) = -2|t|(\cos k_x a + \cos k_y a + \cos k_z a)$ , t being the nearest neighbor hopping matrix element. The eigenfunction is expanded by  $|\mathbf{k}\eta\rangle$  as

$$\psi_{k\nu\sigma} = \sum_{n} |k\eta\rangle u_{\eta\nu\sigma}(k). \tag{6.8}$$

Solving the 2 × 2 eigenvalue problem for  $u_{\eta\nu\sigma}(\mathbf{k})$  we have the eigen values  $\varepsilon_{\nu\sigma}(\mathbf{k})$  as follows.

$$\varepsilon_{\nu\sigma}(\mathbf{k}) = \overline{\varepsilon}_0 + \nu \sqrt{\Delta^2 + \varepsilon_k^2}.$$
 (6.9)

Here  $\nu$  takes  $\pm$ .  $\overline{\varepsilon}_0 = (\varepsilon_{+\sigma} + \varepsilon_{-\sigma})/2 = \varepsilon_0 + U \langle n \rangle/2$  and  $\Delta = U |\langle m \rangle|/2$ . Note that k is a point in the Brillouin zone (BZ) of the fcc sublattice. The eigen vectors  $u_{\eta\nu\sigma}(k)$  are given by

$$u_{\eta\nu\sigma}(\mathbf{k})^2 = \frac{1}{2} \left( 1 - \eta\nu\sigma \frac{\Delta}{\sqrt{\Delta^2 + \varepsilon_k^2}} \right). \tag{6.10}$$

Note that the Brillouin zone (BZ) of the sc lattice with lattice constant a is twice as large as that of the fcc. We can express the eigen values using all the k points in the BZ of the sc lattice. In fact, any k' point of the BZ for the sc lattice which is outside the BZ of the fcc lattice is expressed as k' = k + Q by using a k point in the fcc sublattice and a k' vector such that k' equal to k' expression k' expression k' expression k' expression k' expression k' expression by k' expression by k' expression k' expression k' expression as k' expression expression k' expression eigenvalue on the same k' point is given as k' expression energy eigenvalue is expressed by using the k' points of the BZ of the sc lattice as

$$\varepsilon_{\sigma}(\mathbf{k}) = \overline{\varepsilon}_0 + \frac{\varepsilon_k}{|\varepsilon_k|} \sqrt{\Delta^2 + \varepsilon_k^2}.$$
 (6.11)

Its eigenfunction is expressed by (6.8) in which  $u_{\eta\nu\sigma}(\mathbf{k})$  has been replaced by  $u_{\eta\sigma}(\mathbf{k})$  such that

$$u_{\eta\sigma}(\mathbf{k})^2 = \frac{1}{2} \left( 1 - \eta\sigma \frac{\varepsilon_k}{|\varepsilon_k|} \frac{\Delta}{\sqrt{\Delta^2 + \varepsilon_k^2}} \right). \tag{6.12}$$

The Green function on the (+) sublattice is given by

$$G_{ii\sigma}^{(+)}(z) = \frac{2}{L} \sum_{k}^{\text{sc}} \frac{u_{+\sigma}(\mathbf{k})^2}{z - \varepsilon_{\sigma}(\mathbf{k})} = \int d\varepsilon \, \rho(\varepsilon) \frac{1 - \text{sgn}(\varepsilon)\sigma \frac{\Delta}{\sqrt{\Delta^2 + \varepsilon^2}}}{z - \overline{\varepsilon}_0 - \text{sgn}(\varepsilon)\sqrt{\Delta^2 + \varepsilon^2}}. \quad (6.13)$$

Here  $\rho(\varepsilon)$  is the density of states per atom per spin for the noninteracting sc system. It is worth mentioning that the Green function is alternatively written as

$$G_{ii\sigma}^{(+)}(z) = \sqrt{\frac{z - \varepsilon_{-\sigma}}{z - \varepsilon_{\sigma}}} \int \frac{\rho(\varepsilon) d\varepsilon}{\sqrt{(z - \varepsilon_{\sigma})(z - \varepsilon_{-\sigma})} - \varepsilon},$$
(6.14)

where  $\varepsilon_{-\sigma} = \overline{\varepsilon}_0 + \Delta \varepsilon_{\sigma}$  is the Hartree–Fock potential on the (+) sublattice.

The density of states  $\rho_{\sigma}^{(+)}(\varepsilon)$  on a (+) sublattice site is given by  $\rho_{\sigma}^{(+)}(\varepsilon) = -\pi^{-1} \text{Im} G_{ii\sigma}^{(+)}(z)$  according to the formula (6.4). With use of (6.2), (6.3), and (6.13), we obtain the local charge and local magnetic moment on the (+) sublattice as follows.

$$\langle n \rangle = 2 \int d\varepsilon \, \rho(\varepsilon) f\left(\overline{\varepsilon}_0 - \mu + \operatorname{sgn}(\varepsilon) \sqrt{\Delta^2 + \varepsilon^2}\right),$$
 (6.15)

$$\langle m \rangle = 2\Delta \int d\varepsilon \, \rho(\varepsilon) \frac{\operatorname{sgn}(\varepsilon)}{\sqrt{\Delta^2 + \varepsilon^2}} f\left(\overline{\varepsilon}_0 - \mu + \operatorname{sgn}(\varepsilon) \sqrt{\Delta^2 + \varepsilon^2}\right). \tag{6.16}$$

It should be noted that the self-consistent equations (6.15) and (6.16) can be derived for any antiferromagnets with two sublattices in which there is no electron hopping between atoms belonging to the same sublattice. For example, in the

case of the AF on the bcc lattice as shown in Fig. 1.10(b), each sublattice forms a simple cubic lattice, so that the lattice sum in the Bloch function (6.6) is taken over the sc lattice instead of the fcc one. The atomic position vectors in this case are defined by  $\eta_+ = \mathbf{0}$  and  $\eta_- = (a/2)(1, 1, 1)$ . The energy eigen value  $\varepsilon_k$  in (6.7) should be read as  $\varepsilon_k = t \sum_i^{\text{bcc}} \exp(i\mathbf{k} \cdot R_i) = -8|t|\cos k_x a/2\cos k_y a/2\cos k_z a/2$ . The BZ of the sc sublattice is expanded to that of the bcc lattice by  $\mathbf{Q}$  vectors  $(2\pi/a)(\pm 1, 0, 0)$ ,  $(2\pi/a)(0, \pm 1, 0)$ , and  $(2\pi/a)(0, 0, \pm 1)$ . Thus, taking the same steps, we reach (6.15) and (6.16).

At half-filling and T = 0, the chemical potential satisfying (6.15) is given by  $\mu = \overline{\epsilon}_0$ . The self-consistent equation (6.16) reduces to the following one.

$$\frac{1}{U} = \int_0^{W/2} \frac{\rho(\varepsilon) d\varepsilon}{\sqrt{\Delta^2 + \varepsilon^2}}.$$
 (6.17)

Here W denotes the band width and we made use of the relation  $\rho(\varepsilon) = \rho(-\varepsilon)$ . Note that the function  $1/\sqrt{\Delta^2 + \varepsilon^2}$  is positive and monotonically increases with decreasing  $\Delta = U\langle m \rangle/2$ . Consequently, the r.h.s. of (6.17) also monotonically increases, and diverges at  $\Delta = 0$  because  $\int_0^\infty d\varepsilon \, \rho(\varepsilon)/|\varepsilon| \sim -\rho(0) \ln |0|$ . Thus the self-consistent equation (6.17) has a nonzero solution irrespective of the Coulomb interaction energy strength U; the antiferromagnetic state exists at half-filling for any finite value of U(>0).

Equation (6.17) has the same form as the BCS gap equation for the super conducting state. There the band width W/2 is replaced by the Debye cut-off frequency, the Coulomb interaction parameter U is replaced by the electron–electron attractive interaction V caused by the electron–phonon interaction, and  $\Delta$  corresponds to the super-conducting order parameter.

When  $U \ll W/2$ , we have  $\Delta \ll W/2$ . Thus the integral of the r.h.s. of (6.17) is evaluated as

$$\int_{0}^{W/2} \frac{\rho(\varepsilon) d\varepsilon}{\sqrt{\Delta^{2} + \varepsilon_{k}^{2}}} \approx \int_{0}^{\Delta} \frac{\rho(\varepsilon) d\varepsilon}{\Delta} + \int_{\Delta}^{W/2} \frac{\rho(\varepsilon) d\varepsilon}{|\varepsilon|} \approx \rho(0) + \rho(0) \ln \frac{W/2}{\Delta}.$$
(6.18)

We then obtain the ground-state sublattice magnetization as

$$\langle m \rangle = \frac{W}{U} e^{-\frac{1}{\rho(0)U}}. \tag{6.19}$$

In the case of the completely flat band  $\rho = 1/W$ , one can directly perform the integral in (6.17) and obtain the sublattice magnetization as

$$\langle m \rangle = \frac{W/U}{\sinh W/U}.\tag{6.20}$$

For large W/U, we obtain  $\langle m \rangle = (2W/U) \exp(-1/\rho(0)U)$ , which is essentially the same as (6.19) though the prefactor differs from that of (6.19) by a factor of two.

It should be noted that the antiferromagnetism at half-filling mentioned above is accompanied by a gap  $2\Delta$  on the Fermi surface according to (6.11). The kinetic energy gain due to the formation of the gap is the origin of the antiferromagnetism. This type of the AF is known as the gap-type antiferromagnetism or the nesting-type antiferromagnetism because the gap is caused by a nesting of the energy eigen values which are connected each other via Q vectors.

At finite temperatures, the chemical potential  $\mu = \overline{\epsilon}_0$  satisfies (6.15). Using the relation  $f(-\varepsilon) - f(\varepsilon) = \tanh(\beta \varepsilon/2)$ , the self-consistent equation (6.16) is written as

$$\frac{1}{U} = \int_0^{W/2} \frac{\rho(\varepsilon) d\varepsilon}{\sqrt{\Delta^2 + \varepsilon^2}} \tanh \frac{\beta \sqrt{\Delta^2 + \varepsilon^2}}{2}.$$
 (6.21)

The Néel temperature  $T_N$  at which the antiferromagnetism disappears is obtained from the condition  $\Delta = 0$  in the above equation.

$$\frac{1}{U} = \int_0^{W/2} d\varepsilon \, \frac{\rho(\varepsilon)}{\varepsilon} \tanh \frac{\varepsilon}{2T_{\rm N}}.$$
 (6.22)

Here the r.h.s. is approximately obtained by replacing the DOS with its value at the Fermi level and making integration by parts as follows.

$$\rho(0) \int_0^{W/4T_{\rm N}} dx \, \frac{\tanh x}{x} \approx \rho(0) \bigg( [\ln x \tanh x]_0^{W/4T_{\rm N}} - \int_0^{W/4T_{\rm N}} \ln x \, {\rm sech}^2 x \bigg). \tag{6.23}$$

When  $W/4T_{\rm N}\gg 1$  (i.e., the case of weak antiferromagnet), we can replace the upper bound of the integral in the second term with the infinity and make use of the formula  $-\int_0^\infty \ln x \, {\rm sech}^2 x \, dx = \ln 4 \gamma/\pi$ . Here  $\ln \gamma$  is Euler's constant  $\ln \gamma \approx 0.5772$ . Therefore (6.22) is written as  $1/U = \rho(0) \ln \gamma \, W/\pi \, T_{\rm N}$ . Solving the equation with respect to  $T_{\rm N}$  we obtain

$$T_{\rm N} = \frac{\gamma W}{\pi} e^{-\frac{1}{\rho(0)U}} \approx 1.13 \frac{W}{2} e^{-\frac{1}{\rho(0)U}}.$$
 (6.24)

The ground-state magnetization (6.19) and the Néel temperature (6.24) are applicable in the small U limit because the Hartree–Fock approximation is exact in the limit. The situation is quite different from the ferromagnetic case. There the Hartree–Fock approximation predicted that the magnetic state appears in the region  $\rho(0)U > 1$  where the approximation is not justified in general.

When the Coulomb interaction becomes large, the expression (6.24) of  $T_N$  is no longer applicable. For larger values of U, we can apply the single-site theory at finite temperatures presented in Chap. 3. Let us adopt the static approximation to the functional integral method for simplicity. Introducing the site-dependent coherent potential  $\Sigma_{i\sigma}(z) = \Sigma_{\sigma}^{(\pm)}(z)$ , where (+) or (-) denotes the type of sublattice on site i, into the potential part of the free energy (3.67), we expand the correction terms

with respect to the site. We reach again the free energy (3.82) in the SSA as well as the CPA equation (3.85).

In the antiferromagnetic (AF) state with two sublattices, we have a symmetric relation  $\Sigma_{\sigma}^{(-)}(z) = \Sigma_{-\sigma}^{(+)}(z)$  for the coherent potential. Accordingly we have the relations  $F_{\sigma}^{(-)}(z) = F_{-\sigma}^{(+)}(z)$  for the coherent Green function  $F_{i\sigma}(z) = F_{\sigma}^{(\pm)}(z)$  and  $E^{(-)}(\xi) = E^{(+)}(-\xi)$  for the impurity energy  $E_i(\xi) = E^{(\pm)}(\xi)$ . Thus, the free energy (3.67) as well as the other physical quantities can be expressed by those on the (+) sublattice. The free energy per site is finally written as

$$\mathscr{F}_{\text{CPA}} = \tilde{\mathscr{F}} - \beta^{-1} \ln \int \sqrt{\frac{\beta U}{4\pi}} d\xi \, e^{-\beta E^{(+)}(\xi)}, \tag{6.25}$$

and the CPA equation (3.85) for the AF state is expressed as

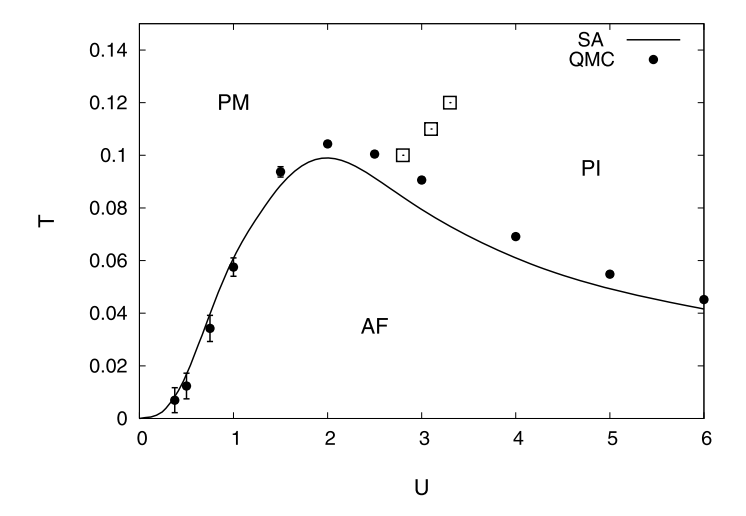
$$\langle G_{\sigma}^{(+)}(z,\xi)\rangle = F_{\sigma}^{(+)}(z).$$
 (6.26)

Here  $G_{\sigma}^{(+)}(z,\xi)$  is the impurity Green function (3.86) on the (+) sublattice. As seen from (6.14), the coherent Green function is expressed by

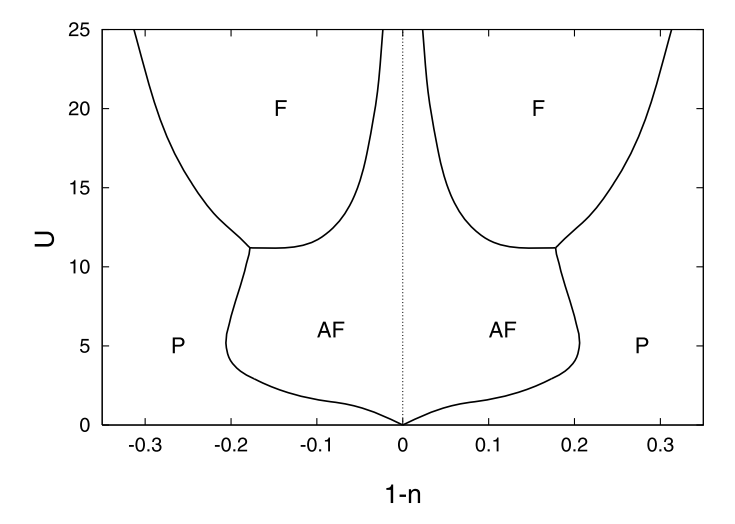
$$F_{\sigma}^{(+)}(z) = \sqrt{\frac{z - \Sigma_{-\sigma}^{(+)}(z)}{z - \Sigma_{\sigma}^{(+)}(z)}} \int \frac{\rho(\varepsilon) d\varepsilon}{\sqrt{(z - \Sigma_{+}^{(+)}(z))(z - \Sigma_{-}^{(+)}(z))} - \varepsilon}.$$
 (6.27)

Figure 6.2 shows the calculated Néel temperatures as a function of the Coulomb interaction parameter U for the half-filled band Hubbard model [53]. The results of the quantum Monte-Carlo method are also shown there. The density of states for the noninteracting state is assumed to be semielliptical:  $\rho(\varepsilon) = (2/\pi W^2)\sqrt{W^2 - \varepsilon^2}$ , which is known to be realized on the Bethe lattice in infinite dimensions. In the weak interaction regime, the Néel temperature  $(T_N)$  exponentially increases with increasing U in accordance with the Hartree–Fock formula (6.24). It shows the maximum around U/W = 2. When U becomes stronger, the Néel temperature approaches to the result of the molecular-field approximation in the Heisenberg model with the super exchange interaction, i.e.,  $H = -\sum_{(i,j)} J_{ij} S_i \cdot S_j$  with  $J_{ij} = -4|t_{ij}|^2/U$  (see (1.86)). In the case of the Bethe lattice in infinite dimensions it is given by  $T_N = W^2/4U$  assuming the nearest-neighbor electron hopping. In finite dimensions, this should be reduced by the magnetic short-range order. It is obtained accurately by the high-temperature expansion. Note that there is the metal–insulator crossover above  $T_N$  in general, so that the paramagnetic metal (PM) changes to the paramagnetic insulator (PI) with increasing Coulomb interaction (see Fig. 6.2).

When the electron number is deviated from the half-filling, one has to solve both equations (6.15) and (6.16) self-consistently. In general the kinetic energy gain due to the gap formation becomes smaller as the electron number deviates from n = 1, and the antiferromagnetism becomes unstable. Figure 6.3 shows a typical magnetic phase diagram obtained by the Gutzwiller approximation to the Hubbard model [98]. For small Coulomb interactions, there is the transition from the AF to the para-



**Fig. 6.2** Néel temperature  $(T_N)$  vs. Coulomb interaction curves in the half-filled Hubbard model on the Bethe lattice in infinite dimensions [53]. The *solid curve* is based on the static approximation (SA) to the dynamical CPA. The *closed circles* are the results of the Quantum Monte-Carlo method (QMC). The energy unit is chosen to be W=1. Below  $T_N$  the antiferromagnetic state (AF) is stabilized. Above  $T_N$  there are the paramagnetic metal (PM) and the paramagnetic insulator (PI) regimes. The *open squares* indicate a crossover line between the two states



**Fig. 6.3** Typical magnetic phase diagram on the U-n plane. The result is calculated with use of the Gutzwiller approximation for the Hubbard model on the hyper-cubic lattice in infinite dimension [98]

magnetic state (P) with increasing electron number from n=1. When the Coulomb interaction is large enough, the transition from the AF to the ferromagnetic state (F) occurs with increasing electron number. It should be noted that the phase diagram

is symmetric around the n = 1 axis when the electron-hole particle symmetry is present.

In the above theoretical treatment of the AF state, we assumed that there is no electron hopping between two sublattices. Furthermore we used a symmetric property of the DOS in the nonmagnetic state. These assumptions are not satisfied in general. For example, in the case of the first-kind AF state on the fcc lattice as shown in Fig. 1.10(c), the transfer integrals between atoms belonging to the same sublattice are not negligible because of the same interatomic distance. Moreover the DOS is not symmetric in the case of the fcc lattice. In this case, the energy gap on the Fermi level is not expected to appear, and the kinetic energy gain due to alternative exchange splitting is not so effective; we do not expect the appearance of the gap-type AF ordered state. The antiferromagnetic metals which are not accompanied by the band gap are referred as the band-type antiferromagnets. The critical Coulomb interaction for the appearance of the AF state is expected to be finite even at half filling in this case.

#### 6.2 Generalized Static Susceptibility and Antiferromagnetism

An alternative way to understand the stability of magnetic structure is to analyze the generalized susceptibility. Let us assume that a metal is in the paramagnetic state when there is no external field. We then consider a linear polarization due to site-dependent magnetic fields  $\{h_i\}$ . The linear polarization of magnetic moment on site i is given by

$$\langle m_i \rangle = \sum_j \chi_{ij} h_j. \tag{6.28}$$

The above expression defines the nonlocal static susceptibility  $\chi_{ij}$ . The susceptibilities in the real space give us the magnetic couplings between the local magnetic moments in metals, and are useful for understanding the complex magnetic structure.

In order to obtain the susceptibility in the Hartree–Fock approximation, we add the Zeeman energy to the atomic level of the Hamiltonian (6.1) as  $\varepsilon_{i\sigma} = \varepsilon_0 + U\langle n_i \rangle/2 - (U\langle m_i \rangle/2 + h_j)\sigma$ , and express the Green function (6.5) by means of the locator matrix  $L_{ij\sigma}$  such that  $(L_{\sigma}^{-1})_{ij} = (z - \varepsilon_0 + \mu - U\langle n_i \rangle/2 + (U\langle m_i \rangle/2 + h_i)\sigma)\delta_{ij}$  as

$$G_{ii\sigma}(z) = [(L_{\sigma} - t)^{-1}]_{ii}.$$
 (6.29)

Here t denotes the transfer integral matrix  $t_{ij}$ . Note that the energy is measured from the Fermi level here.

The linear change of the locator due to spin polarization is given by  $\delta L_{i\sigma}^{-1} = (U \sum_{j} \chi_{ij} h_j / 2 + h_i) \sigma$ , and that of the Green function is given by  $-[G_{\sigma} \delta L_{\sigma}^{-1} G_{\sigma}]_{ii}$ . Substituting the Green function and the linear change of magnetic moment (6.28)

into the self-consistent equation (6.3), we find the equation for nonlocal susceptibility as follows.

$$\chi_{ij} = \chi_{ij}^0 + \sum_{l} \frac{1}{2} U \chi_{il}^0 \chi_{lj}. \tag{6.30}$$

Here  $\chi^0_{ij}$  is the susceptibility for the noninteracting system given by

$$\chi_{ij}^{0} = \int d\omega f(\omega) \frac{(-)}{\pi} \text{Im} \sum_{\sigma} G_{ij\sigma}(z) G_{ji\sigma}(z).$$
 (6.31)

The Green function for the noninteracting system is given by

$$G_{ij\sigma} = \frac{1}{L} \sum_{k} \frac{1}{z - \tilde{\varepsilon}_k} e^{-ik \cdot (R_i - R_j)}.$$
 (6.32)

Here  $\tilde{\varepsilon}_k = \varepsilon_0 - \mu + U \langle n \rangle / 2 + \varepsilon_k$ .

The magnetic coupling in metals and alloys are generally long range, so that their Fourier representations are often useful. The Fourier transform of the linear response (6.28) is given by

$$m(q) = \chi(q)h(q). \tag{6.33}$$

Here m(q) (h(q)) is defined by  $\langle m_i \rangle = \sum_q m(q) \exp(iq \cdot R_i)$   $(h_i = \sum_q h(q) \exp(iq \cdot R_i))$ . The susceptibility  $\chi(q)$  for the wave vector q is defined by

$$\chi_{ij} = \frac{1}{L} \sum_{q} \chi(\mathbf{q}) e^{iq \cdot (R_i - R_j)}. \tag{6.34}$$

Substituting (6.34) into (6.30), we find the Fourier representation of the Hartree–Fock susceptibility.

$$\chi(\mathbf{q}) = \frac{\chi_0(\mathbf{q})}{1 - \frac{1}{2}U\chi_0(\mathbf{q})}.$$
(6.35)

The susceptibility for the noninteracting system is obtained from (6.31) as

$$\chi_0(\mathbf{q}) = \frac{2}{L} \sum_{k} \frac{f(\tilde{\varepsilon}_{k+q}) - f(\tilde{\varepsilon}_k)}{\varepsilon_k - \varepsilon_{k+q}}.$$
 (6.36)

The result agrees with  $\chi_0^{zz}(\boldsymbol{q},\omega=0)=\chi_0^{-+}(\boldsymbol{q},\omega=0)/2$  of (4.101) as it should be. At half-filling  $(\mu=\varepsilon_0+U\langle n\rangle/2)$  and for  $\boldsymbol{Q}$  such that  $\varepsilon_{k+Q}=-\varepsilon_k$  (e.g.,  $\boldsymbol{Q}=(\pi/a)(\pm 1,\pm 1,\pm 1)$  for the sc lattice and  $\boldsymbol{Q}=\pm(2\pi/a)(0,0,1)$  for the bcc lattice), we obtain

$$\chi_0(\mathbf{Q}) = \int d\varepsilon \, \rho(\varepsilon) \frac{\tanh(\beta \varepsilon/2)}{\varepsilon}. \tag{6.37}$$

Here  $\rho(\varepsilon)$  is the noninteracting DOS per atom per spin. The r.h.s. has the same form as that of (6.22). Making the approximation (6.23), we find

$$\chi_0(\mathbf{Q}) = 2\rho(0) \ln \frac{\beta \gamma W}{\pi}. \tag{6.38}$$

The above expression shows that the susceptibility for the noninteracting system diverges as T goes to zero, thus according to (6.35) the susceptibility  $\chi(Q)$  also diverges at a certain temperature  $T_N$  with decreasing temperature. This means that the antiferromagnetic state with a sublattice magnetization m(Q) should be stabilized below  $T_N$ . The Néel temperature  $T_N$  in the Hartree–Fock approximation is obtained from the condition  $1 = U \chi_0(Q)/2$ . Using (6.38), we obtain the following gap-type Néel temperature.

$$T_{\rm N} = \frac{\gamma W}{\pi} e^{-\frac{1}{\rho(0)U}} \approx 1.13 \frac{W}{2} e^{-\frac{1}{\rho(0)U}}.$$
 (6.39)

The result agrees with (6.24).

The generalized susceptibility  $\chi(q)$  is extended to the multi-band case. Let us adopt the nearly orthogonal basis set  $\{\chi_{iL}\}$  for tight-binding linear muffin-tin orbitals (TB-LMTO) (see (2.154)), and assume a system with one atom per unit cell for simplicity. The eigen state  $\psi_{nk}(r)$  to the Hamiltonian (2.167) is given by

$$\psi_{nk}(\mathbf{r}) = \sum_{i,l} \chi_{iL}(\mathbf{r}) \langle iL|n\mathbf{k} \rangle, \tag{6.40}$$

$$\langle iL|n\mathbf{k}\rangle = \hat{u}_{Ln}(\mathbf{k})\frac{1}{\sqrt{N}}e^{-i\mathbf{k}\cdot\mathbf{R}_i}.$$
 (6.41)

Here i(L) denotes site (orbital), and N is the number of unit cells.  $\hat{u}_{Ln}(k)$  is the eigen vector for a given momentum k.

When we insert infinitesimal magnetic field  $h_{jL'}$  on each site j and orbital L' into the TB-LMTO Hamiltonian (2.167), we have a linear polarization of the magnetic moment on site i and orbital L as

$$\langle m_{iL} \rangle = \sum_{jL'} \chi_{iLjL'}^{(0)} h_{jL'}.$$
 (6.42)

Here  $\chi_{iLjL'}^{(0)}$  is the nonlocal susceptibility for the noninteracting system. In order to obtain the nonlocal susceptibility as shown in (6.28), we have to apply the magnetic field  $h_{jL'} = h_j$ . We have then

$$\chi_{ij}^{(0)} = \sum_{II'} \chi_{iLjL'}^{(0)}.$$
(6.43)

Taking the same steps as in the single band model, we find the unenhanced susceptibility at zero temperature as follows.

$$\chi_0(\boldsymbol{q}) = \frac{2}{N} \sum_{n'} \sum_{nk} \left( f\left(\tilde{\varepsilon}_n(\boldsymbol{k})\right) - f\left(\tilde{\varepsilon}_{n'}(\boldsymbol{k} + \boldsymbol{q})\right) \right) \frac{|\sum_L \hat{u}_{Ln}^*(\boldsymbol{k}) \hat{u}_{Ln'}(\boldsymbol{k} + \boldsymbol{q})|^2}{\varepsilon_{n'}(\boldsymbol{k} + \boldsymbol{q}) - \varepsilon_n(\boldsymbol{k})}.$$
(6.44)

Here  $\tilde{\varepsilon}_n(\mathbf{k}) = \varepsilon_n(\mathbf{k}) - \mu$ . The full susceptibility  $\chi(\mathbf{q})$  is enhanced by the exchange potential  $(-I \langle m_i \rangle \sigma/2)$  as follows.

$$\chi(\mathbf{q}) = \frac{\chi_0(\mathbf{q})}{1 - \frac{1}{2}I\chi_0(\mathbf{q})}.$$
 (6.45)

Here I is the Stoner parameter defined by (2.176).

The ferromagnetic structure (F) may be realized when

$$\chi_0(\mathbf{0}) = 2\rho(0) > \frac{2}{I},$$
(6.46)

where  $\rho(0)$  is the total density of states per atom per spin at the Fermi level in the nonmagnetic state. This is the Stoner criterion (2.181) discussed in Sect. 2.3.4. The antiferromagnetic state (AF) is realized when

$$\chi_0(\mathbf{Q}) > \frac{2}{I}.\tag{6.47}$$

Here  $Q = (0, 0, 1)2\pi/a$  in the case of the bcc and fcc structures, a being the lattice constant.  $\chi_0(\mathbf{0})$  ( $\chi_0(\mathbf{Q})$ ) is called the uniform (staggered) susceptibility. Whether the AF or F is stable might be determined by comparing the uniform susceptibility  $\chi_0(\mathbf{0})$  with the staggered  $\chi_0(\mathbf{Q})$ .

Figure 6.4 shows the susceptibilities  $\chi_0(\mathbf{0})$  and  $\chi_0(\mathbf{Q})$  as a function of the conduction electron number (n) [99, 100]. In the case of the bcc Cr (n=6), we find a huge  $\chi_0(\mathbf{Q})$ , indicating the appearance of a gap-type AF. The uniform susceptibilities of bcc Fe (n=8) and fcc Ni (n=10) show a large value, which indicates the ferromagnetism in these systems in agreement with the experimental fact. The ferromagnetism of fcc Co is not clear from the figure because  $\chi_0(\mathbf{0})$  of fcc Co is not so high. Note that Co shows the hcp structure at T=0, though it shows the fcc structure above 700 K. It is interesting that  $\chi_0(\mathbf{Q}) > \chi_0(\mathbf{0})$  in the case of the fcc Fe, while  $\chi_0(\mathbf{0}) \gg \chi_0(\mathbf{Q})$  in the case of bcc Fe. The result suggests the AF in fcc Fe.

Experimentally, the pure bcc Cr shows the spin density waves (SDW) structure with the wave vector  $\mathbf{Q} = (0, 0, 0.95)2\pi/a$  [101], though Cr with a few atomic percent of Mn does show the AF structure (see Fig. 6.1). The fcc Fe is reported to show the SDW with  $\mathbf{Q} = (1, 0, 0.15)2\pi/a$  [102], though it shows the first-kind AF when Mn is added by several percent [103].

A large enhancement of  $\chi_0(\mathbf{Q})$  at Cr in Fig. 6.4 is considered to be a Fermi-surface nesting effect. According to the expression (6.44), the susceptibility  $\chi_0(\mathbf{Q})$ 

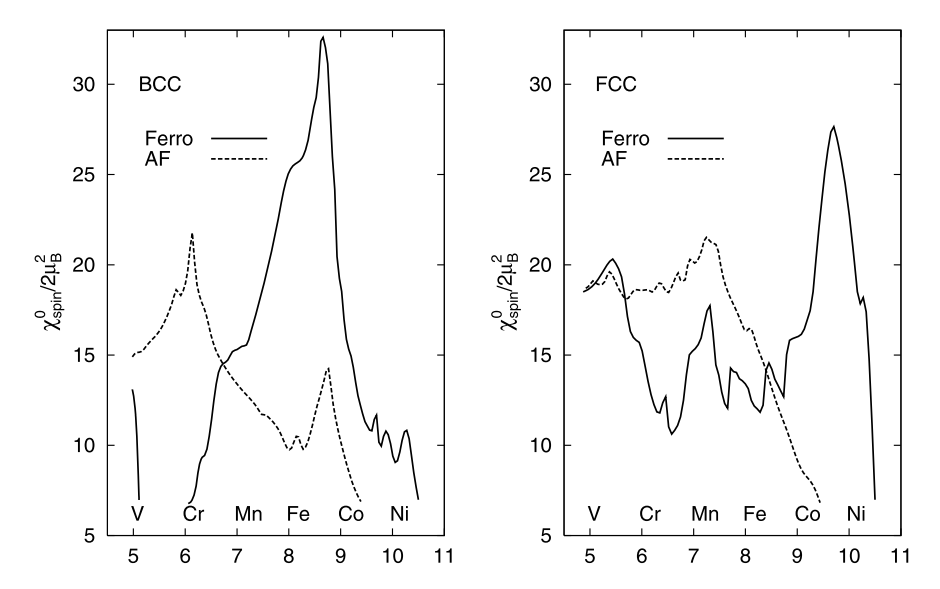
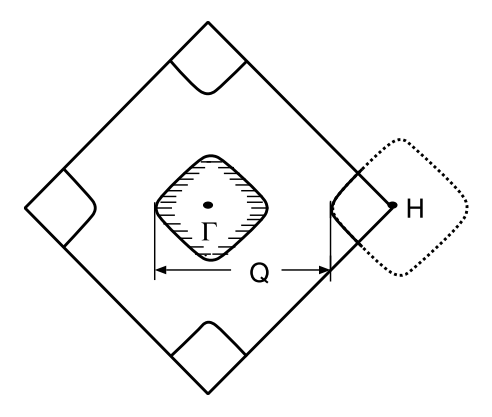


Fig. 6.4 Non-interacting spin susceptibilities  $\chi_0(\mathbf{0})$  (solid curves) and  $\chi_0(\mathbf{Q})$  (dashed curves) as a function of the conduction electron number for bcc transition metals (left) and fcc transition metals (right) [99, 100]. The wave vector is given by  $\mathbf{Q} = (0, 0, 1)2\pi/a$  for both structures, a being the lattice constant

is enhanced when there are many electron k points in the vicinity of Fermi surface and at the same time the k+Q hole points are also in the vicinity of the Fermi surface, because the denominator  $\varepsilon_{n'}(k+Q) - \varepsilon_n(k)$  almost vanishes for such k points. Such an enhancement is expected when there are a large electron Fermi surface and a hole Fermi surface with the same shape which are distant from each other by Q. In this case the Fermi surfaces are called 'being nested', and the enhancement of the susceptibility due to the nesting mechanism is called the Fermi surface nesting effect. Note that the divergence of the susceptibility in (6.38) at T=0 for the single-band Hubbard model at half-filling is also due to the complete nesting because  $\varepsilon_{k_{\rm F}} + 0 = \varepsilon_{k_{\rm F}} = 0$  for the Fermi wave vector  $k_{\rm F}$ .

Figure 6.5 shows a schematic Fermi surface of Cr on the (001) intersection of the Brillouin zone [104]. According to the electronic structure calculations, there is an electron Fermi surface of a nearly octahedral shape around the  $\Gamma$  point (0,0,0), and there is a hole Fermi surface around the H point  $(1,0,0)2\pi/a$  which is also octahedral in shape, though slightly larger than the former around the  $\Gamma$  point. These Fermi surfaces are approximately nested with the wave vector  $\mathbf{Q} = (0,0,1)2\pi/a$ . This is the reason why  $\chi_0(\mathbf{Q})$  is high for Cr in Fig. 6.4. However, we may expect that 50 percent of complete nesting of the Fermi surface using the wave vector  $\mathbf{Q} = (0,0,0.95)2\pi/a$  may be more favorable for the enhancement of  $\chi_0(\mathbf{Q})$ , because the hole Fermi surface is slightly larger than the electron one as shown in Fig. 6.5. This is why the SDW state with  $\mathbf{Q} = (0,0,0.95)2\pi/a$ , instead of the AF structure, is realized in Cr.

**Fig. 6.5** Schematic (001) intersection of chromium Fermi surface



When we add Mn atoms to Cr, the average electron number is increased, so that the octahedral electron Fermi surface grows up in size, while the hole Fermi surface around H point becomes smaller. This implies that the nesting wave vector increases in magnitude, and the AF state is realized as found in the phase diagram, Fig. 6.1. On the other hand, if the neighboring element V is added to Cr, the average electron number decreases, so that the electron Fermi surface shrinks and the hole Fermi surface expands. As the result the enhancement of  $\chi_0(\mathbf{Q})$  due to the nesting is weakened and the paramagnetic state is realized in agreement with the experimental data (see Fig. 6.1).

In the case of the first-kind AF structure in fcc Mn, the Fermi surface nesting is not found. For the fcc structure, neither the gap type of AF as mentioned in Sect. 6.1 nor equivalently the nesting type of AF as have been explained in this section are expected because the hole-particle symmetry of the band is not expected even at half-filling. One has to consider the stability based on the total energy calculation for such a system. Instead of uniform polarization in the ferromagnetism, the local spin polarization as expressed by (6.3), thus the local densities of states (6.4) are essential there. When the Coulomb energy gain due to the local polarization overcomes the band energy loss, the AF is stabilized [105]. The antiferromagnets based on this mechanism are called the band-type AF.

# **6.3** Molecular Dynamics Theory for Complex Magnetic Structures

As we have seen in Fig. 6.3, the ferromagnetic state (F) is stabilized in the region of few electrons or nearly filled shell, while the antiferromagnetic state (AF) is stabilized in the half-filled region. Near the boundary between the F and the AF regions, we can expect competition between the ferro- and the antiferro-magnetic interactions, and thus the appearance of various complex magnetic structures. It is not easy however to find intuitively the complex magnetic structures which yield

the global minimum of the free energy. In this section, we present a molecular dynamics method which automatically determines the complex magnetic structure [108, 109].

We adopt the tight-binding LMTO Hamiltonian (3.228) and the functional integral method. The free energy  $\mathscr{F}$  is then given by (3.245), and the time-dependent Hamiltonian  $H(\tau, \xi(\tau), -i\zeta(\tau))$  in the free energy is given by (3.246). Since we are considering the complex magnetic structure due to the competition between the long-range ferro- and antiferromagnetic couplings, we should take into account intersite correlations. Instead, we adopt in this section the static approximation which neglects the dynamical spin and charge fluctuations. As shown in Sect. 3.2, we approximate the time-dependent Hamiltonian  $H(\tau, \xi(\tau), -i\zeta(\tau))$  given by (3.246) with the static one  $H(\tau, \xi, -i\zeta)$ , where  $\xi_{im}(\zeta_{im})$  are the static exchange (charge) field variables defined by  $\xi_{im} = \int_0^\beta \xi_{im}(\tau) d\tau$  ( $\zeta_{im} = \int_0^\beta \zeta_{im}(\tau) d\tau$ ). Then the partition function  $Z^0(\xi(\tau), \zeta(\tau))$  is given by

$$Z^{0}(\boldsymbol{\xi},\zeta) = \text{Tr}\left(e^{-\beta H(0,\boldsymbol{\xi},-i\zeta)}\right). \tag{6.48}$$

The remaining Gaussian integrals in the free energy can be performed in the same way as in Sect. 3.2 (see (3.57) and (3.58)). Applying the saddle point approximation to the charge fields, we obtain the free energy as follows.

$$\mathscr{F} = -\beta^{-1} \ln \int \left[ \prod_{i\alpha} \sqrt{\frac{\beta^{2l+1} \det B^{\alpha}}{(4\pi)^{2l+1}}} \prod_{m} d\xi_{im\alpha} \right] e^{-\beta E(\xi)}. \tag{6.49}$$

Here and in the following l stands for l=2 assuming the 3d electron system. The effective potential in the static approximation is given by

$$E(\boldsymbol{\xi}) = -\beta^{-1} \ln \operatorname{tr} \left( e^{-\beta H(\boldsymbol{\xi})} \right)$$

$$-\frac{1}{4} \sum_{i} \sum_{mm'} \left( \tilde{n}_{ilm}(\boldsymbol{\xi}) A_{imm'} \tilde{n}_{ilm'}(\boldsymbol{\xi}) - \sum_{\alpha} \xi_{im\alpha} B_{imm'}^{\alpha} \xi_{im'\alpha} \right). \tag{6.50}$$

The Hamiltonian  $H(\xi)$  is given by

$$H(\boldsymbol{\xi}) = \sum_{iL} \left[ \left( \varepsilon_{iL}^{0} - \mu + \frac{1}{2} \sum_{m'} A_{mm'} \tilde{n}_{ilm'}(\boldsymbol{\xi}) \delta_{ld} \right) n_{iL} - \frac{1}{2} \sum_{\alpha} \sum_{m'} B_{imm'}^{\alpha} \xi_{im'\alpha} m_{ilm}^{\alpha} \delta_{ld} \right], \tag{6.51}$$

and  $\tilde{n}_{ilm}(\xi)$  denotes the charge density on site i and orbital lm in the static approximation when the exchange fields  $\{\xi_{im}\}$  are given.  $\mu$  denotes the chemical potential. The Coulomb and exchange interaction matrices  $A_{mm'}$  and  $B_{imm'}^{\alpha}$  are defined by (3.247), (3.248), and (3.249), respectively.

In order to reduce the number of variables, we replace the orbital-dependent charge densities  $\{\tilde{n}_{ilm}(\boldsymbol{\xi})\}$  (exchange field  $\xi_{im\alpha}$ ) in the free energy with an averaged  $\tilde{n}_{il}(\boldsymbol{\xi})/(2l+1)$  ( $\xi_{i\alpha}/(2l+1)$ ). Here  $\tilde{n}_{il}(\boldsymbol{\xi})$  and  $\xi_{i\alpha}$  denote the d-electron charge density on site i and the total exchange field on the same site, respectively;  $\tilde{n}_{il}(\boldsymbol{\xi}) = \sum_{m} \tilde{n}_{ilm}(\boldsymbol{\xi})$  and  $\xi_{i\alpha} = \sum_{m} \xi_{im\alpha}$ . The simplified free energy is then expressed as

$$\mathscr{F} = -\beta^{-1} \ln \int \left[ \prod_{i\alpha} \sqrt{\frac{\beta \tilde{J}_{\alpha}}{4\pi}} d\xi_{i\alpha} \right] e^{-\beta E(\xi)}, \tag{6.52}$$

$$E(\boldsymbol{\xi}) = -\beta^{-1} \ln \operatorname{tr} \left( e^{-\beta H(\boldsymbol{\xi})} \right) - \frac{1}{4} \sum_{i} \left( \tilde{U} \tilde{n}_{il}(\boldsymbol{\xi})^{2} - \sum_{\alpha} \tilde{J}_{\alpha} \xi_{i\alpha}^{2} \right), \tag{6.53}$$

$$H(\boldsymbol{\xi}) = \sum_{iL} \left[ \left( \varepsilon_{iL}^{0} - \mu \right) n_{iL} + \left( \frac{1}{2} \tilde{U} \tilde{n}_{il} (\boldsymbol{\xi}) n_{ilm} - \frac{1}{2} \sum_{\alpha} \tilde{J}_{\alpha} \xi_{i\alpha} m_{ilm}^{\alpha} \right) \delta_{ld} \right] + \sum_{iLiL'\sigma} t_{iLjL'} a_{iL\sigma}^{\dagger} a_{jL'\sigma}.$$

$$(6.54)$$

Here 
$$\tilde{U} = U_0/(2l+1) + [1-1/(2l+1)](2U_1-J)$$
 and  $\tilde{J}_{\alpha} = U_0\delta_{\alpha z}/(2l+1) + [1-1/(2l+1)]J$ .

The free energy (6.52) does not satisfy the rotational invariance in spin space because of the anisotropic exchange interaction  $\tilde{J}_{\alpha}$  inherent in the Hartree–Fock type static approximation. In order to avoid the problem within the static approximation, we introduce the locally rotated coordinates at each site. The interaction term of the Hamiltonian in the locally rotated coordinates has the same form as the original (3.230) due to the rotational invariance. But the operators have been replaced by those on the rotated coordinates;  $\check{n}_{ilm} = \sum_{\sigma} \check{n}_{ilm\sigma}$  and  $\check{s}_{ilm} = \sum_{\alpha\gamma} \check{a}^{\dagger}_{ilm\alpha} (\sigma/2)_{\alpha\gamma} \check{a}_{ilm\gamma}$ . Here  $\check{a}^{\dagger}_{iL\alpha}$  and  $\check{a}_{iL\alpha}$  are the creation and annihilation operators on the rotated coordinates, which are given by  $\check{a}^{\dagger}_{iL\alpha} = \sum_{\gamma} a^{\dagger}_{iL\gamma} D_{\gamma\alpha}(R_i)$  and  $\check{a}_{iL\alpha} = \sum_{\gamma} a_{iL\gamma} D^*_{\gamma\alpha}(R_i)$  with use of the rotation matrix  $D_{\alpha\gamma}(R_i)$  for a spin on site i. Here  $R_i$  denotes a rotation of the z axis.

We apply the functional integral technique to the Hamiltonian on locally rotated coordinates. Taking the same steps as before we obtain the counterpart of the free energy (6.52). We then neglect the transverse static spin fluctuations on the rotated coordinates and take the average of the free energy over the z direction of the locally rotated coordinates, so that we obtain the free energy as follows.

$$\mathscr{F} = -\beta^{-1} \ln \int \left[ \prod_{i} \sqrt{\frac{\beta \tilde{J}}{4\pi}} \, d\xi_{i} \, d\boldsymbol{e}_{i} \right] e^{-\beta E(\xi)}, \tag{6.55}$$

$$E(\xi) = -\beta^{-1} \ln \text{tr} \left( e^{-\beta H(\xi)} \right) - \frac{1}{4} \sum_{i} \left( \tilde{U} \tilde{n}_{il}(\xi)^{2} - \tilde{J} \xi_{i}^{2} \right), \tag{6.56}$$

$$H(\boldsymbol{\xi}) = \sum_{iL} \left[ \varepsilon_{iL}^{0} - \mu + \left( \frac{1}{2} \tilde{U} \tilde{n}_{il} (\boldsymbol{\xi}) n_{il} - \frac{1}{2} \tilde{J} \boldsymbol{\xi}_{i} \cdot \boldsymbol{m}_{il} \right) \delta_{ld} \right]$$

$$+ \sum_{iLjL'\sigma} t_{iLjL'} a_{iL\sigma}^{\dagger} a_{jL'\sigma}.$$
(6.57)

Here  $\tilde{J} = U_0/(2l+1) + [1-1/(2l+1)]J$ ,  $\boldsymbol{e}_i$  is the unit vector on site i showing the direction of rotated z axis, and  $\xi_i$  is the z component of the exchange fields on the rotated coordinates. Furthermore  $\boldsymbol{\xi}_i = \xi_i \boldsymbol{e}_i$  and  $d\boldsymbol{e}_i = (4\pi)^{-1} \sin \theta_i \, d\theta_i \, d\phi_i \, d\phi_i \, \theta_i$  and  $\phi_i$  denote the zenith and azimuth angles of vector  $\boldsymbol{e}_i$ .

Since  $\tilde{n}_{ilm}(\xi)$  is a saddle point value of the charge field  $\zeta_{ilm}$  (see (3.66)), it is given by

$$\tilde{n}_{ilm}(\xi) = \langle n_{ilm} \rangle_0 = \frac{\operatorname{tr}(n_{ilm} e^{-\beta H(\xi)})}{\operatorname{tr}(e^{-\beta H(\xi)})}.$$
(6.58)

The local charge and magnetic moment are obtained by taking the derivative of  $\mathscr{F}$  with respect to the atomic level  $\varepsilon_{iL}^0$  and the local magnetic field  $h_i$  acting on site i.

$$\langle \tilde{n}_i \rangle = \sum_{I} \langle \tilde{n}_{iL}(\xi) \rangle,$$
 (6.59)

$$\langle \mathbf{m}_i \rangle = \left\langle \left( 1 + \frac{4}{\beta \tilde{J} \xi_i^2} \right) \boldsymbol{\xi}_i \right\rangle. \tag{6.60}$$

Here the average  $\langle \sim \rangle$  at the r.h.s. of the equations is defined by

$$\langle \sim \rangle = \frac{\int \left[ \prod_{i} d\xi_{i} \right] (\sim) e^{-\beta \Psi(\xi)}}{\int \left[ \prod_{i} d\xi_{i} \right] e^{-\beta \Psi(\xi)}},$$
(6.61)

$$\Psi(\xi) = E(\xi) + 2\beta^{-1} \sum_{i} \ln \xi_{i}. \tag{6.62}$$

Note that we have adopted the spherical coordinates in the above average, and thus  $d\xi_i = \xi_i^2 \sin \theta_i d\xi_i d\theta_i d\phi_i$ .

An alternative way to recover the rotational invariance of the free energy within the static approximation is to take the limit  $l \to \infty$  (see (6.52)). We obtain in this case  $\tilde{J}_{\alpha} = J$  and the free energy (6.55) in which  $d\xi_i \, de_i$  has been replaced by  $d\xi_i$ . The magnetic moment  $\langle \boldsymbol{m}_i \rangle$  is given by (6.60) in which the prefactor  $(1+4/\beta \tilde{J}\xi_i^2)$  has been replaced by 1, and the potential  $\Psi(\boldsymbol{\xi})$  (i.e., (6.62)) reduces to  $E(\boldsymbol{\xi})$ . In any case, the Coulomb and exchange energies,  $\tilde{U}$  and  $\tilde{J}$ , have to be regarded as effective ones since we adopted the static approximation which neglects the electron correlations at low temperatures.

Equation (6.60) indicates that the thermal average of local magnetic moment (LM) is given by a semiclassical average with respect to the potential energy  $\Psi(\xi)$ . In this case, we can apply the isothermal molecular-dynamics method (MD) [106, 107] in order to treat a large number of atomic magnetic moments  $\{\langle m_i \rangle\}$ .

In the MD method we express the magnetic moment (6.60) by means of the time average assuming the ergodicity of the system as follows.

$$\langle \mathbf{m}_i \rangle = \lim_{t_0 \to \infty} \frac{1}{t_0} \int_0^{t_0} \left( 1 + \frac{4}{\beta \tilde{J} \xi_i^2(t)} \right) \boldsymbol{\xi}_i(t) dt.$$
 (6.63)

The dynamics of the 'time-dependent magnetic moment'  $\{\xi_i(t)\}$  which yields the thermal average (6.60) are given by the following equations of motion (see Appendix F) [108].

$$\dot{\xi_{i\alpha}} = \frac{p_{i\alpha}}{\mu_{IM}},\tag{6.64}$$

$$\dot{p}_{i\alpha} = -\frac{\partial \Psi(\xi)}{\partial \xi_{i\alpha}} - \eta_{\alpha} \cdot p_{i\alpha}, \tag{6.65}$$

$$\dot{\eta}_{\alpha} = \frac{1}{Q} \left( \sum_{i} \frac{p_{i\alpha}^{2}}{\mu_{\rm LM}} - NT \right). \tag{6.66}$$

Here  $p_{i\alpha}$  is a fictitious momentum conjugate to the exchange field variable  $\xi_{i\alpha}$ .  $\mu_{\rm LM}$  is an effective mass for the LM on site i. The first term at the right-hand-side of (6.65) is a magnetic force, and the second term is the friction force which keeps temperature T constant according to (6.66). Q in (6.66) denotes a constant parameter, and N is the number of atoms in the system. Note that we have introduced the anisotropic friction variables  $\eta_{\alpha}(\alpha=x,y,z)$  to guarantee the ergodicity of the system even if N=1.

The magnetic force in (6.65) is obtained from (6.56) and (6.62) as

$$-\frac{\partial \Psi(\xi)}{\partial \xi_{i\alpha}} = \frac{1}{2}\tilde{J}(\langle m_{i\alpha}\rangle_0 - \xi_{i\alpha}) - \frac{2T\xi_{i\alpha}}{\xi_i^2}.$$
 (6.67)

Here  $\langle m_{i\alpha} \rangle_0$  is the average magnetic moment with respect to the Hamiltonian (6.57) in the random exchange fields. It is given by the Green function G(z) for the Hamiltonian as

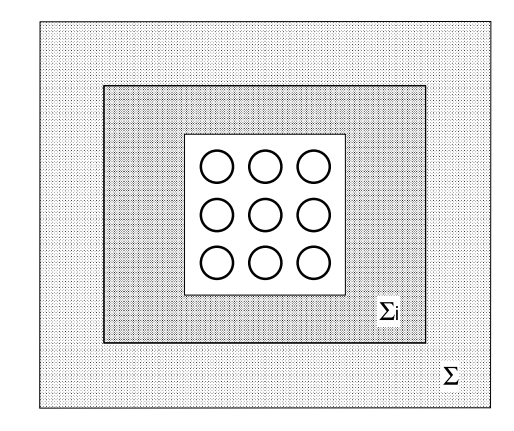
$$\langle m_{i\alpha}\rangle_0 = \int d\omega f(\omega) \frac{(-)}{\pi} \text{Im} \sum_{m\sigma} (\sigma_\alpha G(\omega + i\delta))_{ilm\sigma ilm\sigma},$$
 (6.68)

$$G_{ilm\sigma jl'm'\sigma'}(z) = \left[ \left( z - \boldsymbol{H}(\boldsymbol{\xi}) \right)^{-1} \right]_{ilm\sigma jl'm'\sigma'}.$$
 (6.69)

Here l = 2, and  $H(\xi)$  is the one-electron Hamiltonian matrix of (6.57). The Green functions coupled with the Pauli spin matrices in (6.68) are expressed as follows with use of the new basis functions which diagonalize the Pauli spin matrices  $\sigma_{\alpha}$  ( $\alpha = x, y, z$ ).

$$\sum_{i} (\sigma_x G)_{iL\sigma iL\sigma} = G_{iL1iL1} - G_{iL2iL2}, \tag{6.70}$$

Fig. 6.6 The MD unit cell embedded by the site-dependent effective medium  $\Sigma_{iL\sigma\sigma'}$  and site-independent effective medium  $\Sigma_{L\sigma}$ 



$$\sum_{\sigma} (\sigma_y G)_{iL\sigma iL\sigma} = G_{iL3iL3} - G_{iL4iL4}, \tag{6.71}$$

$$\sum_{\sigma} (\sigma_{z}G)_{iL\sigma iL\sigma} = G_{iL\uparrow iL\uparrow} - G_{iL\downarrow iL\downarrow}. \tag{6.72}$$

Here the local basis functions at the r.h.s. are defined by

$$|iL1\rangle = \frac{1}{\sqrt{2}} (|iL\uparrow\rangle + |iL\downarrow\rangle),$$
 (6.73)

$$|iL2\rangle = \frac{1}{\sqrt{2}} (|iL\uparrow\rangle - |iL\downarrow\rangle),$$
 (6.74)

$$|iL3\rangle = \frac{1}{\sqrt{2}} (|iL\uparrow\rangle + i|iL\downarrow\rangle),$$
 (6.75)

$$|iL4\rangle = \frac{1}{\sqrt{2}} (|iL\uparrow\rangle - i|iL\downarrow\rangle).$$
 (6.76)

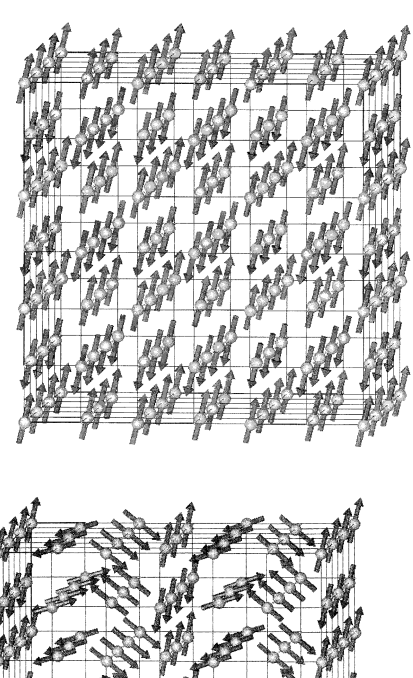
It should be noted that the exchange fields  $\{\xi_i\}$  randomly change in space and time in the MD method, so that the system does not satisfy in general the translational symmetry at each time step in the MD. Therefore, the recursion method is used for the calculation of the Green functions in (6.70), (6.71), and (6.72) (see Appendix G).

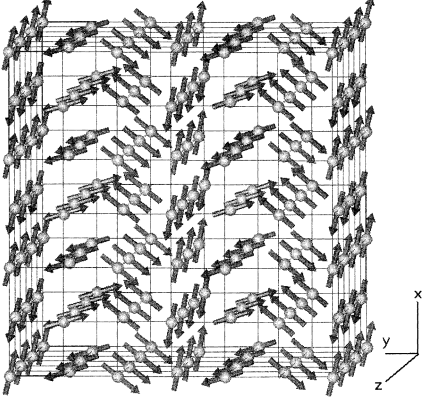
In numerical calculations, we have to consider the MD unit cell with the finite number of atoms N. The 'magnetic moment'  $\xi_i$  is centered in the MD unit cell. In order to simulate the system with  $N=\infty$ , the MD unit cell is usually embedded in a site-dependent effective medium  $\Sigma_{iL\sigma\sigma'}$ . It is further surrounded by a site-independent medium as shown in Fig. 6.6. They are determined self-consistently by the CPA equations (3.254) in which the dynamical correction has been omitted and  $i\omega_l$  has been replaced by z.

The fcc transition metals are expected to form complex magnetic structures around the d electron numbers  $n_d$  between 6.0 and 7.0 due to competing interactions. Some numerical results of the model calculations are presented in Figs. 6.7,

Fig. 6.7 Magnetic structures of the fcc transition metals at 50 K obtained by the MD with 108 atoms per unit cell: case of the d electron number n = 6.2 [109]

Fig. 6.8 Magnetic structures of the fcc transition metals obtained by the MD with 108 atoms per unit cell: case of the d electron number n = 6.4 [109]



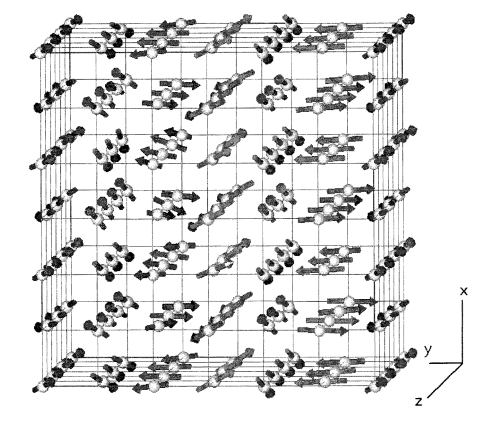


6.8, and 6.9 [108, 109]. The Slater–Koster d band model [31] and N=108 atoms per MD unit cell (3 × 3 × 3 fcc lattice) are adopted there. The band width and effective exchange energy parameter were fixed to be the values of  $\gamma$ -Mn: W=0.443 Ry and  $\tilde{J}=0.060$  Ry. Starting from a random configuration of LM's  $\{\xi_i(0)\}$ , we solve (6.64)–(6.66) and obtain the magnetic moments  $\langle m_i \rangle$  by taking the time average in the equilibrium state.

The calculated magnetic structure for  $n_{\rm d}=6.2$  shows the AF structure of the first kind in accordance with the magnetic structure of  $\gamma$ -Mn as shown in Fig. 6.7. The calculated magnetic moment  $|\langle m_i \rangle| = 2.5~\mu_{\rm B}$  is also consistent with the experimental value 2.3  $\mu_{\rm B}$  and the theoretical one 2.32  $\mu_{\rm B}$  [105]. The MD method yields the Néel temperature  $T_{\rm N}=510~{\rm K}$  for  $\gamma$ -Mn [110] which is in good agreement with the experimental result  $T_{\rm N}=500~{\rm K}$ .

When the d electron number  $n_{\rm d}$  is increased, the AF structure changes to the helical structures due to competition between the ferro- and antiferro-magnetic interactions. For n=6.4, the LM's in an antiferromagnetic plane rotate by  $240^{\circ}$  with a translation by the lattice constant a along the axis perpendicular to the

Fig. 6.9 Magnetic structures of the fcc transition metals obtained by the MD with 108 atoms per unit cell: case of the d electron number n = 6.6 [109]



plane as shown in Figs. 6.8. The wave vector of the helical structure is given by  $Q = (0, 1/3, 1)2\pi/a$  and  $|\langle m_i \rangle| = 2.0~\mu_{\rm B}$ . A further increase in d electron number reduces the average magnetic moments and leads to the helical structure with amplitude modulations as shown in Fig. 6.9; the wave vector Q is the same as in n = 6.4, but the magnitudes of LM  $|\langle m_i \rangle|$  are spatially modulated from 0.75  $\mu_{\rm B}$  to 1.30  $\mu_{\rm B}$ . The modulated structure is characteristic of itinerant electron systems because such a modulation should be suppressed by a large energy loss of Coulomb interactions in the insulator system. It is stabilized by the energy gain due to the break of a frustrated magnetic structure with equal amplitudes of LM's.

The MD approach is useful for theoretical study of the magnetic structure in competing magnetic interaction system. The size of the MD unit cell is however limited to be finite and thus the SDW with wave length larger than the lattice constant of the MD unit cell are not described.

# 6.4 Phenomenological Theory of Magnetic Structure

Competing magnetic interactions often form the complex magnetic structures whose unit cells are huge or which are described by incommensurate wave vectors. Microscopic theories of magnetic structure are often faced with the difficulty in description for such systems because the system size which one can treat is limited to rather small number ( $\lesssim 10^4$ ). Furthermore the accuracy of the microscopic theories is often not enough to describe the stability of magnetic structures when the energy difference between structures is too small. In such cases we have to rely on the phenomenological theory to understand the structure. We present in this section the Ginzburg–Landau phenomenological theory, and discuss possible multiple spin density waves (MSDW) in  $\gamma$ -Fe [111, 112]. The theory is also useful for finding general properties of the magnetic structure determined by crystal symmetry.

Let us consider a system with a magnetic atom per unit cell and assume that it shows a cubic crystal symmetry for simplicity. Assuming small size of magnetic moments, we expand the free energy  $\mathscr{F}$  with respect to the local magnetic moments. Because of the time reversal symmetry in the absence of the external magnetic field, the free energy consists of even-order terms of the magnetic moments. We consider here the terms up to the fourth order. Because of cubic symmetry the free energy should be invariant with respect to the symmetry operations for magnetic moments: rotation  $m_{R_l} \to \mathscr{R}(m_{R_l})$ , inversion  $m_{R_l} \to m_{-R_l}$ , and translations  $m_{R_l} \to m_{R_l+T}$ . Here  $R_l$  is the position vector of site l, and  $m_{R_l} \equiv m_l$  is the thermal average of the local magnetic moment on site l.  $\mathscr{R}$  denotes either the rotation  $C_4$ [100] or  $C_3$ [111], and T denotes an arbitrary lattice translation vector. The free energy of the system per lattice site is then expressed as follows.

$$\mathscr{F} = \frac{1}{N^{2}} \sum_{l,l'} A(l,l') \, \boldsymbol{m}_{l} \cdot \boldsymbol{m}_{l'} + \frac{1}{N^{4}} \sum_{l,l',l'',l'''} \left[ B(l,l',l'',l''') \{ \boldsymbol{m}_{l} \cdot \boldsymbol{m}_{l'} \} \{ \boldsymbol{m}_{l''} \cdot \boldsymbol{m}_{l'''} \} \right]$$

$$+ C(l,l',l'',l''') (m_{ly} m_{l'y} m_{l''z} m_{l'''z} + m_{lz} m_{l'z} m_{l''y} m_{l'''y} + m_{lz} m_{l'z} m_{l''z} m_{l'''x} m_{l'''x} + m_{lx} m_{l'x} m_{l''z} m_{l'''z} + m_{lx} m_{l'x} m_{l''x} m_{l'''y} m_{l'''y} + m_{ly} m_{l'y} m_{l''x} m_{l'''x} \right].$$

$$(6.77)$$

Here N is the number of lattice sites. A(l,l'), B(l,l',l'',l'''), and C(l,l',l'',l''') are expansion coefficients. The second-order terms and the fourth-order terms with B(l,l',l'',l''') in the free energy (6.77) are isotropic since they are expressed in terms of the scalar products of magnetic moment vectors. On the other hand, the fourth-order terms with coefficients C(l,l',l'',l''') are anisotropic. Such an anisotropy is caused by the spin–orbit interactions. Here we restrict ourselves to the transition metals where the spin–orbit coupling effects are negligibly small, and neglect the anisotropic terms; C(l,l',l'',l''')=0.

It is convenient to use the Fourier representation of the local magnetic moment in order to describe the spin density wave (SDW).

$$m_l = \sum_{q}^{\text{EBZ}} m(q) e^{iq \cdot R_l}. \tag{6.78}$$

Here  $\sum_{q}^{\mathrm{EBZ}}$  means a summation with respect to q over the extended first Brillouin zone (EBZ), which is defined to include all zone boundary points. This form has the merit that one can argue the structures in both commensurate and incommensurate cases on the same footing.

The Fourier representation of the isotropic free energy is then given by

$$\mathscr{F} = \sum_{q}^{\text{EBZ}} A(q) \left[ \left| m(q) \right|^{2} + \sum_{K \neq 0} \delta_{q,K/2} m^{2}(q) \right]$$

$$+ \sum_{K} \sum_{q+q'+q''+q'''=K} B(q, q', q'', q''') \left\{ m(q) \cdot m(q') \right\} \left\{ m(q'') \cdot m(q''') \right\}.$$
(6.79)

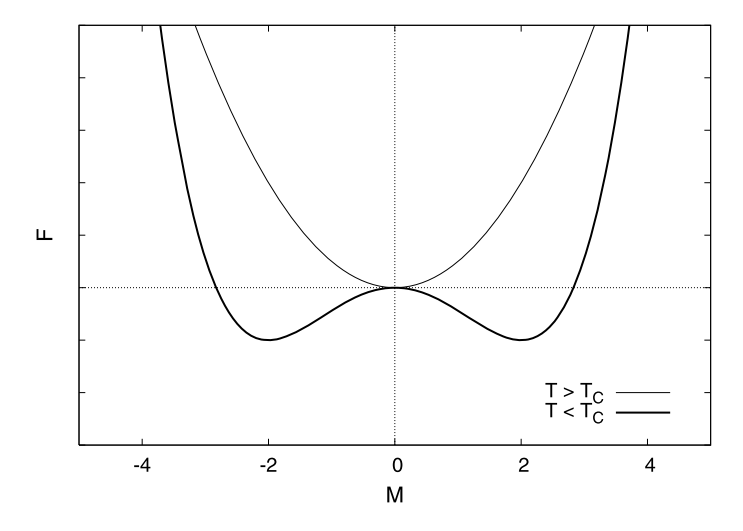


**Fig. 6.10** Phenomenological Landau free energy F of ferromagnet as a function of the magnetization M below and above the Curie temperature ( $T_{\rm C}$ )

Here K is the reciprocal lattice vector. A(q) and B(q, q', q'', q''') are coefficients of the free energy expansion in the Fourier representation.

In the ferromagnetic state, only  $m \equiv |m(q = 0)|$  component remains. We have then the free energy,

$$\mathscr{F}_{\mathrm{F}} = Am^2 + Bm^4 - mh. \tag{6.80}$$

Here  $A \equiv A(\mathbf{0})$ ,  $B \equiv B(\mathbf{0}, \mathbf{0}, \mathbf{0}, \mathbf{0})$ , and the term of uniform magnetic field h is added. The free energies below and above the Curie temperature are depicted for h = 0 in Fig. 6.10. Equilibrium magnetization is obtained from the stationary condition.

$$m(2A + 4Bm^3) = h. (6.81)$$

Above the Curie temperature  $T_C$  and for small h, we have m = h/2A. Thus  $A = 1/2\chi$ ,  $\chi$  being the paramagnetic susceptibility. At  $T_C$  the susceptibility  $\chi$  diverges. When we expand A as  $A = (T - T_C)/2C$  above  $T_C$ , we obtain the Curie–Weiss law  $\chi = C/(T - T_C)$ . Below  $T_C$  and for h = 0, (6.81) is identical with (3.18). We have the magnetization (3.21);  $m = \sqrt{-A/2B}$  under the condition -A/2B > 0. The stability condition for the ferromagnetic solution is given by  $\partial^2 \mathscr{F}_F/\partial^2 m < 0$  at the equilibrium m, and yields A < 0. From the conditions -A/2B > 0 and A < 0, we obtain B > 0. Expanding A with respect to  $T - T_C$  below  $T_C$ , we find  $T_C = 1$ 0. The free energy in the equilibrium state is given by  $T_C = 1$ 1. This is the phenomenological theory of ferromagnetism known as the Landau theory.

The same argument is applicable to the antiferromagnetic structure (AF) which is given by

$$\mathbf{m}_{l} = m(\mathbf{Q})\mathbf{k} \left( e^{i\mathbf{Q} \cdot \mathbf{R}_{l}} + e^{-i\mathbf{Q} \cdot \mathbf{R}_{l}} \right). \tag{6.82}$$

Here Q is a wave vector leading to the AF structure (see Sect. 1.7). k is a unit vector along the z axis. The free energy of the AF is given by

$$\mathscr{F}_{AF} = A(\mathbf{Q})m(\mathbf{Q})^2 + B(\mathbf{Q})m(\mathbf{Q})^4 - m(\mathbf{Q})h(\mathbf{Q}). \tag{6.83}$$

Here A(Q) and B(Q) are coefficients, and h(Q) is the staggard field. Minimizing the free energy, the sublattice magnetization is obtained as  $m(Q) = \sqrt{-A(Q)/2B(Q)}$  when A(Q) < 0 and B(Q) > 0. The free energy in the equilibrium state is given by  $\mathscr{F}_{AF} = -A(Q)^2/4B(Q)$ .

It is also worthwhile to mention the long-wavelength limit of the free energy (6.79). There only the q components around |q| = 0 are important there, so that one can replace B(q, q', q'', q''') with a constant  $\gamma/4 (= B(0, 0, 0, 0))$ .

$$\mathscr{F} = \sum_{q}^{\text{EBZ}} \frac{1}{2\chi(q)} |m(q)|^2 + \frac{1}{4} \gamma \sum_{q+q'+q''+q'''=0} \{m(q) \cdot m(q')\} \{m(q'') \cdot m(q''')\}.$$
(6.84)

Here  $\chi(q)$  is the generalized susceptibility defined by (6.33):  $m(q) = \chi(q)h(q)$ . The form (6.84) is used in the phenomenological spin-fluctuation theory for the weak ferromagnets [113].

## 6.4.1 Multiple SDW with Commensurate Wave Vectors

In the itinerant electron system with high crystalline symmetry, the multiple spin density wave (MSDW) structure becomes possible. We consider in this subsection the commensurate multiple MSDW structures (see Fig. 1.15). We consider the fcc lattice here as an example. The magnetic moments for the MSDW are expressed by

$$\boldsymbol{m}_{l} = \sum_{n=1}^{3} \left[ \boldsymbol{m}(\hat{\boldsymbol{Q}}_{n}) e^{i\hat{\boldsymbol{Q}}_{n} \cdot \boldsymbol{R}_{l}} + \boldsymbol{m}(\hat{\boldsymbol{Q}}_{n}) e^{-i\hat{\boldsymbol{Q}}_{n} \cdot \boldsymbol{R}_{l}} \right].$$
(6.85)

Here the wave vectors are given by  $\hat{\boldsymbol{Q}}_1 = (1,0,0)(2\pi/a)$ ,  $\hat{\boldsymbol{Q}}_2 = (0,1,0)(2\pi/a)$ , and  $\hat{\boldsymbol{Q}}_3 = (0,0,1)(2\pi/a)$ . Each wave vector forms the antiferromagnetic structure of the first kind (AF-I) on the fcc lattice.  $\boldsymbol{m}(\hat{\boldsymbol{Q}}_1)$ ,  $\boldsymbol{m}(\hat{\boldsymbol{Q}}_2)$ , and  $\boldsymbol{m}(\hat{\boldsymbol{Q}}_3)$  are real and assumed to be orthogonal to each other:  $\boldsymbol{m}(\hat{\boldsymbol{Q}}_2) \cdot \boldsymbol{m}(\hat{\boldsymbol{Q}}_3) = \boldsymbol{m}(\hat{\boldsymbol{Q}}_3) \cdot \boldsymbol{m}(\hat{\boldsymbol{Q}}_1) = \boldsymbol{m}(\hat{\boldsymbol{Q}}_1) \cdot \boldsymbol{m}(\hat{\boldsymbol{Q}}_2) = 0$ .

Taking the terms related with  $\{\hat{Q}_i\}$  in the free energy (6.79), we obtain

$$\mathscr{F} = \sum_{i=1}^{3} \left[ \tilde{A}_{Q} | \boldsymbol{m}(\hat{\boldsymbol{Q}}_{i}) |^{2} + (B_{1Q} + \tilde{B}_{2Q}) | \boldsymbol{m}(\hat{\boldsymbol{Q}}_{i}) |^{4} \right] + \sum_{(i,j)}^{(2,3)(3,1)(1,2)} \tilde{B}_{1QQ} | \boldsymbol{m}(\hat{\boldsymbol{Q}}_{i}) |^{2} | \boldsymbol{m}(\hat{\boldsymbol{Q}}_{j}) |^{2}.$$
(6.86)

The coefficients  $\tilde{A}_Q$ ,  $B_{1Q}$ ,  $\tilde{B}_{2Q}$ , and  $\tilde{B}_{1QQ}$  are expressed in terms of linear combinations of the coefficients  $\{A(q)\}$  and  $\{B(q, q', q'', q''')\}$ , where q, q', q'', and q''' are chosen to be one of  $\pm \hat{Q}_1$ ,  $\pm \hat{Q}_2$ , and  $\pm \hat{Q}_3$ .

As mentioned before, the AF-I structure  $(m(\hat{Q}_1) \neq 0, m(\hat{Q}_2) = m(\hat{Q}_3) = 0)$  is stable in the region

$$\tilde{A}_O < 0, \tag{6.87}$$

$$B_{1Q} + \tilde{B}_{2Q} > 0. ag{6.88}$$

We obtain the magnetic moment

$$\left| \boldsymbol{m}(\boldsymbol{Q}_1) \right| = \left[ -\frac{\tilde{A}_{\boldsymbol{Q}}}{2(B_{1\boldsymbol{Q}} + \tilde{B}_{2\boldsymbol{Q}})} \right]^{1/2},$$
 (6.89)

as well as the free energy

$$\mathcal{F}_{1\hat{Q}} = -\frac{\tilde{A}_{Q}^{2}}{4(B_{1Q} + \tilde{B}_{2Q})}.$$
(6.90)

The double Q MSDW  $(2\hat{Q})$  state is characterized by  $m(\hat{Q}_1)$ ,  $m(\hat{Q}_2) \neq 0$  and  $m(\hat{Q}_3) = 0$  (see Fig. 1.14). The stationary condition of the free energy yields the equations for magnetic moments as

$$\tilde{A}_{O} + 2(B_{1O} + \tilde{B}_{2O}) |\boldsymbol{m}(\hat{\boldsymbol{Q}}_{1})|^{2} + \tilde{B}_{1OO} |\boldsymbol{m}(\hat{\boldsymbol{Q}}_{2})|^{2} = 0, \tag{6.91}$$

$$\tilde{A}_{Q} + 2(B_{1Q} + \tilde{B}_{2Q}) |\mathbf{m}(\hat{\mathbf{Q}}_{2})|^{2} + \tilde{B}_{1QQ} |\mathbf{m}(\hat{\mathbf{Q}}_{1})|^{2} = 0.$$
 (6.92)

When

$$D_{2\hat{Q}} \equiv 4(B_{1Q} + \tilde{B}_{2Q})^2 - \tilde{B}_{1QQ}^2 \neq 0, \tag{6.93}$$

equations (6.91) and (6.92) are solved as

$$|\boldsymbol{m}(\hat{\boldsymbol{Q}}_1)| = |\boldsymbol{m}(\hat{\boldsymbol{Q}}_2)| = \left[ -\frac{\tilde{A}_Q}{2(B_{1Q} + \tilde{B}_{2Q}) + \tilde{B}_{1QQ}} \right]^{1/2},$$
 (6.94)

under the condition

$$-\frac{\tilde{A}_{Q}}{2(B_{1Q} + \tilde{B}_{2Q}) + \tilde{B}_{1QQ}} > 0. \tag{6.95}$$

The stability condition to the solution (6.94) is given by

$$\delta^{2} \mathscr{F} = \frac{1}{2} \sum_{i=1}^{2} \sum_{j=1}^{2} \frac{\partial^{2} \mathscr{F}}{\partial \{ |\boldsymbol{m}(\hat{\boldsymbol{Q}}_{i})|^{2} \} \partial \{ |\boldsymbol{m}(\hat{\boldsymbol{Q}}_{j})|^{2} \}} \delta |\boldsymbol{m}(\hat{\boldsymbol{Q}}_{i})|^{2} \delta |\boldsymbol{m}(\hat{\boldsymbol{Q}}_{j})|^{2} > 0. \quad (6.96)$$

It is equivalent to

$$f_{11} > 0, \quad \begin{vmatrix} f_{11} & f_{12} \\ f_{21} & f_{22} \end{vmatrix} > 0,$$
 (6.97)

where  $f_{ij}$  is defined by  $f_{ij} \equiv \partial^2 \mathscr{F}/\partial \{|\boldsymbol{m}(\hat{\boldsymbol{Q}}_i)|^2\}\partial \{|\boldsymbol{m}(\hat{\boldsymbol{Q}}_j)|^2\}$  (i, j = 1, 2). The condition (6.97) yields the inequalities,

$$2(B_{1O} + \tilde{B}_{2O}) > 0, (6.98)$$

$$4(B_{1Q} + \tilde{B}_{2Q})^2 - \tilde{B}_{1QQ}^2 > 0. {(6.99)}$$

Conditions (6.93), (6.95), (6.98), and (6.99) reduce to

$$\tilde{A}_Q < 0, \tag{6.100}$$

$$B_{1Q} + \tilde{B}_{2Q} > \frac{|\tilde{B}_{1QQ}|}{2}.$$
 (6.101)

Inequalities (6.100) and (6.101) yield the stability condition for the  $2\hat{Q}$  structure. The equilibrium free energy is obtained by substituting (6.94) and  $m(\hat{Q}_3) = 0$  into (6.86):

$$\mathcal{F}_{2\hat{Q}} = -\frac{\tilde{A}_{Q}^{2}}{2(B_{1Q} + \tilde{B}_{2Q}) + \tilde{B}_{1QQ}}.$$
(6.102)

In the same way, we obtain magnetic moments of the triple Q MSDW  $(3\hat{Q})$  structure by minimizing free energy (6.86) with respect to  $|\boldsymbol{m}(\hat{Q}_1)|^2$ ,  $|\boldsymbol{m}(\hat{Q}_2)|^2$ , and  $|\boldsymbol{m}(\hat{Q}_3)|^2$ .

$$|\boldsymbol{m}(\hat{\boldsymbol{Q}}_1)| = |\boldsymbol{m}(\hat{\boldsymbol{Q}}_2)| = |\boldsymbol{m}(\hat{\boldsymbol{Q}}_3)| = \left[ -\frac{\tilde{A}_Q}{2(B_{1Q} + \tilde{B}_{2Q} + \tilde{B}_{1QQ})} \right]^{1/2},$$
 (6.103)

under the condition

$$-\frac{\tilde{A}_Q}{2(B_{1Q} + \tilde{B}_{2Q} + \tilde{B}_{1QQ})} > 0. \tag{6.104}$$

The thermodynamical stability condition for the 3  $\hat{Q}$  structure and inequality (6.104) lead to the following condition:

$$\tilde{A}_Q < 0, \tag{6.105}$$

$$B_{1Q} + \tilde{B}_{2Q} > \frac{\tilde{B}_{1QQ}}{2} \quad \text{for } \tilde{B}_{1QQ} > 0,$$
 (6.106)

$$B_{1Q} + \tilde{B}_{2Q} > -\tilde{B}_{1QQ}$$
 for  $\tilde{B}_{1QQ} < 0$ . (6.107)

The equilibrium free energy is obtained by substituting (6.103) into (6.86):

$$\mathscr{F}_{3\hat{Q}} = -\frac{3\tilde{A}_{Q}^{2}}{4(B_{1Q} + \tilde{B}_{2Q} + \tilde{B}_{1QQ})}.$$
(6.108)

It is characteristic of the itinerant electron system that the amplitudes of the magnetic moments are variable. The amplitude M per site is given by

$$M^{2} \equiv \frac{1}{N} \sum_{l} \boldsymbol{m}_{l} \cdot \boldsymbol{m}_{l} = \sum_{\boldsymbol{q}, \boldsymbol{q}'}^{\text{EBZ}} \boldsymbol{m}(\boldsymbol{q}) \cdot \boldsymbol{m}(\boldsymbol{q}') \sum_{\boldsymbol{K}} \delta_{\boldsymbol{q} + \boldsymbol{q}', \boldsymbol{K}}.$$
 (6.109)

In the commensurate case, this becomes

$$M^{2} = 4(|m(\hat{Q}_{1})|^{2} + |m(\hat{Q}_{2})|^{2} + |m(\hat{Q}_{3})|^{2}), \tag{6.110}$$

and we have the amplitude  $M_{1\hat{Q}}$  for the  $1\hat{Q}$ ,  $M_{2\hat{Q}}$  for the  $2\hat{Q}$ , and  $M_{3\hat{Q}}$  for  $3\hat{Q}$  as follows.

$$M_{1\hat{Q}}^2 = -\frac{2\tilde{A}_Q}{B_{1Q} + \tilde{B}_{2Q}},\tag{6.111}$$

$$M_{2\hat{Q}}^{2} = -\frac{8\tilde{A}_{Q}}{2(B_{1Q} + \tilde{B}_{2Q}) + \tilde{B}_{1QQ}},$$
(6.112)

$$M_{3\hat{Q}}^2 = -\frac{6\tilde{A}_Q}{B_{1Q} + \tilde{B}_{2Q} + \tilde{B}_{1QQ}}. (6.113)$$

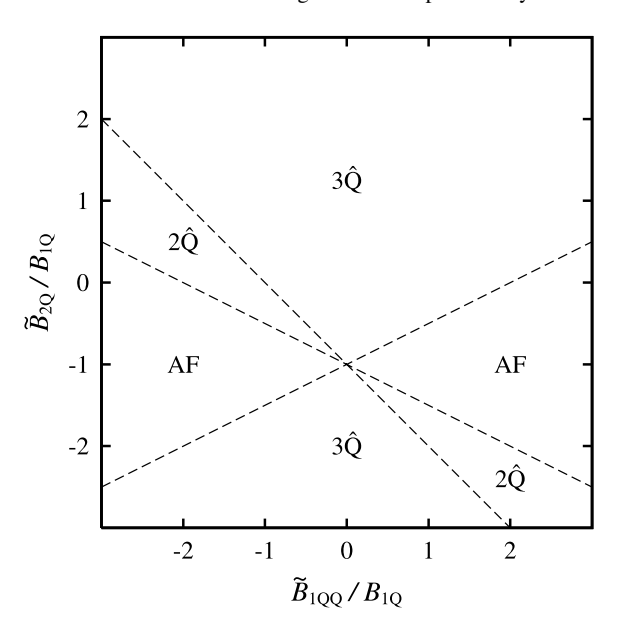
From these expressions, we find that

$$M_{1\hat{O}} < M_{2\hat{O}} < M_{3\hat{O}}, \tag{6.114}$$

when the  $3\hat{\boldsymbol{\varrho}}$  state is stable.

It is common for the three structures that the condition  $\tilde{A}_Q < 0$  is required. By comparing stability conditions (6.88), (6.101), and (6.106)–(6.107), and equilibrium free energies (6.90), (6.102), and (6.108), we obtain the magnetic phase diagram as shown in Fig. 6.11. In the AF phase  $(0 < B_{1Q} + \tilde{B}_{2Q} < |\tilde{B}_{1QQ}|/2)$ , the AF state is

Fig. 6.11 Magnetic phase diagram for commensurate structures with  $|\hat{Q}| = 2\pi/a$  for  $\tilde{A}_Q < 0$  [111]. The first-kind antiferromagnetic (AF), the  $2\hat{Q}$ , and the  $3\hat{Q}$  phases are shown in the space of expansion coefficients  $\tilde{B}_{1QQ}/B_{1Q}$  and  $\tilde{B}_{2Q}/B_{1Q}$ , where  $B_{1Q} > 0$  for  $\tilde{B}_{2Q}/B_{1Q} > -1$  and  $B_{1Q} < 0$  for  $\tilde{B}_{2Q}/B_{1Q} < -1$ 



the only stable structure. In the  $2\hat{Q}$  phase  $(0 < -\tilde{B}_{1QQ}/2 < B_{1Q} + \tilde{B}_{2Q} < -\tilde{B}_{1QQ})$ , the AF and  $2\hat{Q}$  structures are stable, and

$$\mathscr{F}_{1\hat{Q}} > \mathscr{F}_{2\hat{Q}}.\tag{6.115}$$

In the 3  $\hat{Q}$  phase  $(0 < \tilde{B}_{1QQ}/2 < B_{1Q} + \tilde{B}_{2Q}, 0 < -\tilde{B}_{1QQ} < B_{1Q} + \tilde{B}_{2Q})$ , all three commensurate structures are stable, and we find that

$$\mathcal{F}_{1\hat{O}} > \mathcal{F}_{2\hat{O}} > \mathcal{F}_{3\hat{O}}. \tag{6.116}$$

We observe that the MSDW states with higher multiplicity are always more stable than the other states with lower multiplicity. The physical reason for this fact is as follows. First consider the free energy for the MSDW states (6.86) without the mode–mode coupling term (the term with  $B_{1QQ}$ ). The free energy for the 3 $\hat{Q}$  state is three times smaller than that for the 1 $\hat{Q}$  state, as seen from (6.90) and (6.108). This free energy gain is caused by the increase in amplitudes of local magnetic moments as seen from (6.111) and (6.113), and is characteristic of the itinerant electron system. In the localized model such a mechanism of energy gain is forbidden because of the constraint of the constant amplitudes of local magnetic moments, so that only the 1 $\hat{Q}$  state is realized.

When the mode–mode coupling term  $\tilde{B}_{1QQ}$  is positive, it suppresses the increase in amplitudes of local moments of the  $3\hat{Q}$  state (see (6.111) and (6.113)). As a result, the  $3\hat{Q}$  MSDW is stable only when  $\tilde{B}_{1QQ}$  is smaller than a critical value.

In the band theory [114], three possible ground states are found for  $\gamma$ -Fe using the LMTO method and the von Barth–Hedin LDA potential: the first-kind AF, and the  $2\hat{Q}$  and  $3\hat{Q}$  structures. It is found numerically that the  $3\hat{Q}$  structure is the most

 $(1\hat{Q}, 2\hat{Q}, \text{ and } 3\hat{Q})$  MSDW states which are calculated by the LDA-DFT theory [114].  $E(E(3\hat{Q}))$ denotes the ground state energy for each structure (3  $\hat{\boldsymbol{o}}$  structure)

**Table 6.1** Energy differences  $E - E(3\hat{Q})$  and amplitudes M of magnetic moments of fcc Fe for

======================================					
	1 <b>Q</b>	$2\hat{m{Q}}$	3 <b>Q</b>		
$E - E(3\hat{\boldsymbol{Q}}) \text{ (mRy)}$	3.3	0.8	0.0		
$M(\mu_{\rm B})$	1.18	1.24	1.24		

stable among the three at the equilibrium lattice constant a = 6.8 a.u. As shown in Table 6.1, their results of the energy at T=0 follow the inequality (6.116) obtained by the phenomenological theory. It is interesting to note that the amplitudes of their magnetic moments for the  $3\hat{\boldsymbol{\varrho}}$  and  $2\hat{\boldsymbol{\varrho}}$  structures were found to be the same and larger than that for the AF structure:  $M_{3\hat{Q}} = M_{2\hat{Q}} > M_{1\hat{Q}}$ . According to (6.112) and (6.113), this implies that  $B_{1Q} + \tilde{B}_{2Q} = \tilde{B}_{1QQ}/2$ ;  $\gamma$ -Fe calculated by the band theory is located in the vicinity of the AF-3 $\hat{\boldsymbol{Q}}$  boundary in the 3 $\hat{\boldsymbol{Q}}$  phase of Fig. 6.11.

### 6.4.2 Multiple SDW with Incommensurate Wave Vectors

We consider next the multiple spin density waves (MSDW) with three incommensurate wave vectors  $Q_1$ ,  $Q_2$ , and  $Q_3$ . These wave vectors satisfy the condition  $q + q' + q'' + q''' \neq K$  for q, q', q'', and q''' being one of  $\{Q_n\}$  (see (6.79)). The linearly polarized MSDW is one of the possible MSDWs. It is described by

$$\boldsymbol{m}_{l} = \sum_{n=1}^{3} \left[ \boldsymbol{m}(\boldsymbol{Q}_{n}) e^{i\boldsymbol{Q}_{n} \cdot \boldsymbol{R}_{l}} + \boldsymbol{m}^{*}(\boldsymbol{Q}_{n}) e^{-i\boldsymbol{Q}_{n} \cdot \boldsymbol{R}_{l}} \right], \tag{6.117}$$

with

$$\boldsymbol{m}(\boldsymbol{Q}_n) = (m_x(\boldsymbol{Q}_n), m_y(\boldsymbol{Q}_n), m_z(\boldsymbol{Q}_n)) e^{i\alpha_n} \quad (n = 1, 2, 3).$$
 (6.118)

Here  $m_x(\mathbf{Q}_n)$ ,  $m_y(\mathbf{Q}_n)$ , and  $m_z(\mathbf{Q}_n)$  (n = 1, 2, 3) are assumed to be real.  $\alpha_1$ ,  $\alpha_2$ , and  $\alpha_3$  are phase factors. Additionally we consider the case in which  $m(Q_1)$ ,  $m(Q_2)$ , and  $m(Q_3)$  are orthogonal to each other.

The free energy for the linear MSDW has the same form as the commensurate case, i.e., (6.86).

$$\mathcal{F}_{L} = \sum_{i=1}^{3} \left[ A_{\mathcal{Q}} | \boldsymbol{m}(\boldsymbol{Q}_{i}) |^{2} + (B_{1\mathcal{Q}} + B_{2\mathcal{Q}}) | \boldsymbol{m}(\boldsymbol{Q}_{i}) |^{4} \right] + \sum_{(i,j)}^{(2,3)(3,1)(1,2)} B_{1\mathcal{Q}\mathcal{Q}} | \boldsymbol{m}(\boldsymbol{Q}_{i}) |^{2} | \boldsymbol{m}(\boldsymbol{Q}_{j}) |^{2}.$$
(6.119)

We therefore obtain the same results in which  $\tilde{A}_Q$ ,  $\tilde{B}_{2Q}$ , and  $\tilde{B}_{1QQ}$  have been replaced by  $A_Q$ ,  $B_{2Q}$ , and  $B_{1QQ}$ , respectively. The phase diagram is the same as Fig. 6.11 in which  $\tilde{B}_{2Q}$  and  $\tilde{B}_{1QQ}$  have been replaced by  $B_{2Q}$  and  $B_{1QQ}$ , and AF,  $2\hat{Q}$ , and  $3\hat{Q}$  have been replaced by 1Q, 2Q, and 3Q, respectively. Thus we find the 3Q state in a wide range in the magnetic phase diagram.

It is found in the band calculations that there is the incommensurate  $3 \, Q$  MSDW solution with  $\, Q = (0.6, 0, 0)(2\pi/a)$ ,  $(0, 0.6, 0)(2\pi/a)$ , and  $(0, 0, 0.6)(2\pi/a)$  in the fcc Fe at lattice constant  $6.8 \lesssim a \lesssim 7.0$  [115]. Furthermore it is verified to be stable as compared with the  $1 \, Q$  SDW state irrespective of the lattice constant, and the amplitude of the magnetic moment for the  $3 \, Q$  state is larger than that for the  $1 \, Q$  state. These results are consistent with those of the phenomenological theory obtained in the last and present subsections; the  $3 \, Q$  MSDW is always stabilized when the  $3 \, Q$  solution exists, and has a larger amplitude of the magnetic moment as compared with the  $1 \, Q$  and  $2 \, Q$  SDW.

Alternative MSDW are the helically polarized SDWs whose magnetic moments are described by (6.117) with

$$\boldsymbol{m}(\boldsymbol{Q}_{j}) = \frac{|\boldsymbol{m}(\boldsymbol{Q}_{j})|}{\sqrt{2}} (\boldsymbol{e}_{jk} - i\boldsymbol{e}_{jm}) \quad ((j, k, m) = (1, 2, 3)(2, 3, 1)(3, 1, 2)). \tag{6.120}$$

Here  $e_{jk}$  and  $e_{jm}$  are unit vectors being perpendicular to the wave vector  $Q_j$ , and orthogonal to each other (see (1.94) and (1.96)).

The free energy for the helical MSDW is given as follows.

$$\mathcal{F}_{H} = \sum_{i=1}^{3} \left[ A_{\mathcal{Q}} | \boldsymbol{m}(\boldsymbol{Q}_{i}) |^{2} + B_{1\mathcal{Q}} | \boldsymbol{m}(\boldsymbol{Q}_{i}) |^{4} \right] + \sum_{(i,j)}^{(2,3)(3,1)(1,2)} (B_{1\mathcal{Q}\mathcal{Q}} + B_{2\mathcal{Q}\mathcal{Q}H}) | \boldsymbol{m}(\boldsymbol{Q}_{i}) |^{2} | \boldsymbol{m}(\boldsymbol{Q}_{j}) |^{2}.$$
(6.121)

Note that the coefficient  $B_{2Q}$  of the linear MSDW in (6.119) disappears and an additional coefficient  $B_{2QQH}$  appears in the mode–mode coupling term in the case of the helical MSDW. However, the free energy (6.121) is again identical to (6.86) in which  $\tilde{A}_Q$ ,  $B_{1Q} + \tilde{B}_{2Q}$ , and  $\tilde{B}_{1QQ}$  have been replaced by  $A_Q$ ,  $B_{1Q}$ , and  $B_{1QQ} + B_{2QQH}$ , so that we can easily obtain the results for the helical MSDW by exchanging the coefficients in the results of the last subsection.

By comparing the free energy among the incommensurate linear 1Q, 2Q, 3Q MSDW, and the helical 1Q, 2Q, 3Q MSDW, we obtain the phase diagram for the incommensurate MSDW. An example is shown in Fig. 6.12. Note that the condition that both the linear and helical SDWs are stable is  $A_Q < 0$  and  $B_{1Q} > 0$ . We find that the 3Q linear (3Q) and 3Q helical (3QH) MSDWs occupy most of the region  $-2 < B_{1QQ}/B_{1Q} < 1$ . This arises from the fact that the 3Q states are stable when the mode–mode coupling term  $B_{1QQ}$  or  $B_{1QQ} + B_{2QQH}$  is relatively small. Since the stability of the helical 3Q is accompanied by the increase in amplitude

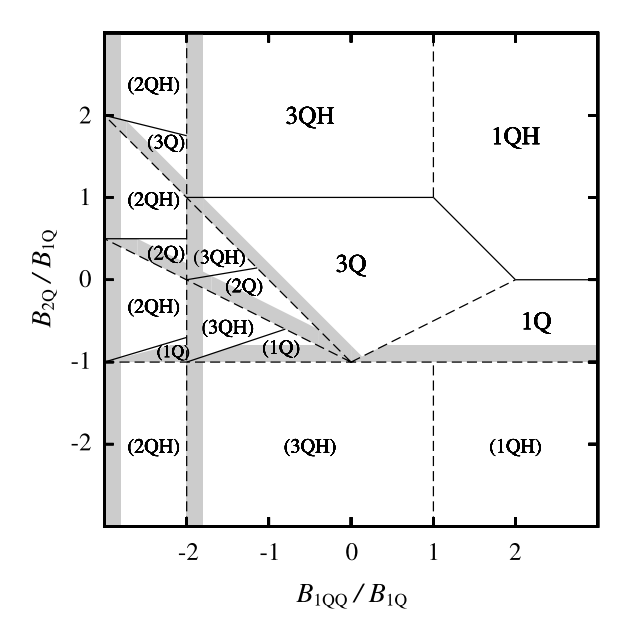


**Fig. 6.12** Magnetic phase diagram for the incommensurate SDWs for the expansion coefficients  $A_Q < 0$ ,  $B_{1Q} > 0$  and  $B_{2QQH}/B_{1Q} = 1$  [112]. The phases of the 1Q linear SDW (1Q), the 2Q linear MSDW (2Q), the 3Q linear MSDW (3Q), the 1Q helical SDW (1QH), the 2Q helical MSDW (2QH), and the 3Q helical MSDW (3QH) are shown in the space of expansion coefficients  $B_{1QQ}/B_{1Q}$  and  $B_{2Q}/B_{1Q}$ . Coexistence lines between the linear and helical SDWs are indicated by *solid lines*. The phases shown with parenthesis are metastable states in which the ground state cannot be determined within the fourth-order Ginzburg–Landau theory. The *gray regions* indicate that the magnetic moment amplitude in the phase becomes so large that the fourth-order theory is not applicable

of the magnetic moment as shown in (6.114), it is characteristic of the itinerant electron magnetism. In the Heisenberg model, only the 1Q helical structure is stabilized by the competition between intersite exchange interactions. Experimentally, the 3Q MSDW is considered to be realized in  $\gamma$ -Fe<sub>x</sub>Mn<sub>1-x</sub> (0.4 < x < 0.8) alloys [103].

Neutron diffraction experiments on the cubic  $\gamma$ -Fe $_{100-x}$ Co $_x$  (x < 4) alloy precipitates in Cu show a magnetic satellite peak at wave vector  $\mathbf{Q} = (0.1, 0, 1)2\pi/a$  [102]. The magnetic structure was suggested to be a helical SDW, but has not yet been determined precisely. This is because the neutron diffraction analysis cannot distinguish between  $1\mathbf{Q}$  and  $3\mathbf{Q}$  states when the crystal structure of the  $\gamma$ -Fe precipitates is properly cubic and the distribution of domains is isotropic. The present result based on the Ginzburg–Landau phenomenological theory tells us that the  $3\mathbf{Q}$  helical MSDW is always stable as compared with the  $1\mathbf{Q}$  and  $2\mathbf{Q}$  SDWs when the  $3\mathbf{Q}$  solution exists. It is desirable to investigate the relative stability be-

tween 3  ${\it Q}$  linear and helical MSDWs in the first-principles ground-state calculations of  $\gamma$ -Fe.

The same type of the helical  $3\,Q$  MSDW has been found to be possible in MnSi system [116]. There we must take into account the spin-orbit coupling called the Dzyaloshinskii-Moriya interaction which appears in the noncentrosymmetric crystal structure.

# **Chapter 7 Magnetism in Dilute Alloys**

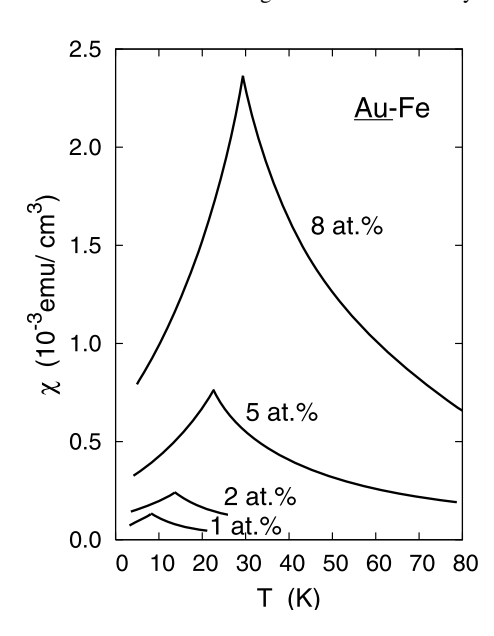
Dilute magnetic alloys such as the transition metals dissolved in a simple metal show a unique magnetic property. In these alloys the oscillating long-range interactions appear via the conduction electrons, and the spin glass state in which the local magnetic moments are randomly oriented forms due to the competition between long-range ferro- and antiferro-magnetic interactions. We present the theoretical aspects of these properties in Sect. 7.1. In Sect. 7.2, we deal with the impurity limit. There the impurity magnetic moment disappears at low temperatures due to the formation of the singlet state. Because of the crossover from the local moment behavior to the Fermi liquid behavior with decreasing temperature, various anomalies called the Kondo effects appear. We briefly describe the formation of the singlet state known as the Kondo singlet.

## 7.1 Magnetic Interactions and Spin Glasses in Dilute Alloys

The noble metal based alloys containing less than several percent of magnetic transition metals such as Cu–Mn and Au–Fe alloys form the substitutional disordered alloys. Susceptibilities of these alloys show a cusp at a temperature  $T_{\rm g}$  indicating a magnetic phase transition as shown in Fig. 7.1. A remarkable point is that  $T_{\rm g}$  showing a phase transition continues up to 0.005 at% impurity concentration in many cases [117]. The average inter-site distance between magnetic impurities at 0.005 at% is about 30 times that of the nearest-neighbor. Such a long-range magnetic interaction is explained neither by the super-exchange interaction nor by the direct exchange interaction as discussed in Sect. 1.6 because both interactions are caused by the overlap between neighboring atomic orbitals. In this section, we derive such a long-range magnetic interaction and briefly discuss the magnetism of dilute alloys.

Let us consider the Cu–Mn dilute alloys as an example to derive the model Hamiltonian. The electronic structures of constituent Cu and Mn atoms are given by 3d<sup>10</sup>4s and 3d<sup>5</sup>4s<sup>2</sup>, respectively. When these atoms form dilute alloys, electron

**Fig. 7.1** Susceptibilities of <u>Au</u>–Fe dilute alloys as a function of temperature [118]



hoppings to the 3d orbitals of Cu atoms are suppressed because these orbitals form almost closed shells even in alloys. Electron hoppings between 4s orbitals must be fast since these atomic wave functions are extended in space. Since 3d orbitals on Mn atoms form unfilled shells, electron hoppings from the 3d orbitals to the 4s orbitals on the surrounding Cu atoms and the hopping backs to the Mn 3d orbitals are possible. We can neglect the direct electron hoppings between 3d orbitals on different Mn atoms because we are considering the dilute alloys less than 10 at% Mn. The Hamiltonian of the system is therefore described by the following two-band model.

$$H = H_{\rm s} + H_{\rm sd} + H_{\rm d},$$
 (7.1)

$$H_{\rm S} = \sum_{i\sigma} \varepsilon_{\rm S} n_{i\sigma} + \sum_{ij\sigma} t_{ij} c_{i\sigma}^{\dagger} c_{j\sigma}, \qquad (7.2)$$

$$H_{\rm sd} = \sum_{ij\sigma} \left( t_{ij}^{\rm (sd)} c_{i\sigma}^{\dagger} a_{j\sigma} + t_{ij}^{\rm (ds)} a_{i\sigma}^{\dagger} c_{j\sigma} \right), \tag{7.3}$$

$$H_{\rm d} = \sum_{i\sigma} \varepsilon_{\rm d} n_{{\rm d}i\sigma} + \sum_{i} U n_{{\rm d}i\uparrow} n_{{\rm d}i\downarrow}. \tag{7.4}$$

Here  $\varepsilon_s$  ( $\varepsilon_d$ ) is the atomic level of the s (d) orbital.  $t_{ij}$  ( $t_{ij}^{(sd)}$ ) is the transfer integral between the s orbital on site i and s (d) orbital on site j. We assumed a single d orbital instead of five d orbitals on each magnetic atom for simplicity. Moreover we have introduced the on-site Coulomb interaction U between d electrons because the d electrons are localized as compared with the 4s electrons.

Since 4s electrons form a wide band, the momentum representation may be more suitable. We can construct the Bloch wave function  $\varphi_k$  from the atomic 4s wave functions  $\phi_i$  as  $\varphi_k = \sum_j \phi_j \langle j | k \rangle = \sum_j \phi_j \exp(-i \mathbf{k} \cdot \mathbf{R}_j)/\sqrt{L}$ . Making use of the Bloch functions  $\{\varphi_k\}$ , we can diagonalize the Hamiltonian matrix  $(\mathbf{H}_s)_{ij} = \varepsilon_s \delta_{ij} + t_{ij} (1 - \delta_{ij})$  as  $\sum_{ij} \langle k | i \rangle (\mathbf{H})_{ij} \langle j | k' \rangle = \varepsilon_k \delta_{kk'}$ . Accordingly we can define the creation (annihilation) operator  $c_{k\sigma}^{\dagger}$   $(c_{k\sigma})$  in the momentum representation, as  $c_{k\sigma}^{\dagger} = \sum_i c_{i\sigma}^{\dagger} \langle i | k \rangle$   $(c_{k\sigma} = \sum_i c_{i\sigma} \langle k | i \rangle)$ . The 4s conduction band Hamiltonian  $H_s$  is then expressed as  $H_s = \sum_{k\sigma} \varepsilon_k n_{k\sigma}$ . Here  $n_{k\sigma} = c_{k\sigma}^{\dagger} c_{k\sigma}$  is the number operator for 4s electrons with momentum k and spin  $\sigma$ . The hybridization term  $H_{sd}$  is also written by the creation and annihilation operators of conduction electrons in the momentum representation, so that the total Hamiltonian (7.1) is expressed as follows.

$$H = \sum_{k\sigma} \varepsilon_{k} n_{k\sigma} + \sum_{jk\sigma} \left( e^{ik \cdot R_{j}} V_{kd} c_{k\sigma}^{\dagger} a_{j\sigma} + e^{-ik \cdot R_{j}} V_{dk} a_{j\sigma}^{\dagger} c_{k\sigma} \right)$$

$$+ \sum_{i\sigma} \varepsilon_{d} n_{di\sigma} + \sum_{i} U n_{di\uparrow} n_{di\downarrow}.$$

$$(7.5)$$

Here  $V_{kd} (= V_{dk}^*)$  is the hybridization matrix element defined by

$$V_{kd} = \int \varphi_k^*(\mathbf{r}) V(\mathbf{r}) \phi_d(\mathbf{r}) d\mathbf{r}, \qquad (7.6)$$

and V(r) is the atomic potential for an electron on the impurity site.

The Hamiltonian (7.5) for dilute alloys is referred as the Anderson lattice Hamiltonian. Note that the Hamiltonian is derived without using the translational symmetry of magnetic impurities, so that it is applicable to disordered alloys.

The Hamiltonian for the system with only one impurity at the origin is a special case of (7.5) and is given by

$$H = \sum_{k\sigma} \varepsilon_k n_{k\sigma} + \sum_{k\sigma} \left( V_{dk} a_{d\sigma}^{\dagger} c_{k\sigma} + V_{kd} c_{k\sigma}^{\dagger} a_{d\sigma} \right) + \sum_{\sigma} \varepsilon_{d} n_{d\sigma} + U n_{d\uparrow} n_{d\downarrow}. \quad (7.7)$$

Here we omitted the site index 0 in the subscripts for simplicity and expressed the creation (annihilation) operator for d electron as  $a_{d\sigma}^{\dagger}$  ( $a_{d\sigma}$ ) to make the d character clearer. The Hamiltonian is called the Anderson model for the magnetic impurity in conduction band [119].

The Anderson lattice Hamiltonian has the eigen states {| $\{n_{k\sigma}\}$ ,  $\{n_{dj} = 1, s_{jz}\}$ } in the zero-mixing limit (i.e.,  $V_{kd} = 0$ ) and at half-filling. Here  $\{n_{k\sigma}\}$  denotes a configuration of the Fermi sea states for conduction electrons, while  $\{n_{dj} = 1, s_{jz}\}$  denotes the atomic states of magnetic impurities with the d electron number  $n_{dj} = 1$  and 'local magnetic moment'  $s_{jz} (= \pm 1/2)$ . Even for the system with a finite hybridization, the local magnetic moments on the impurity atoms should remain and may couple with the conduction electrons via the hybridization  $V_{dk}$  and  $V_{kd}$ . In order to obtain such a picture, we derive an effective Hamiltonian assuming a small hybridization.

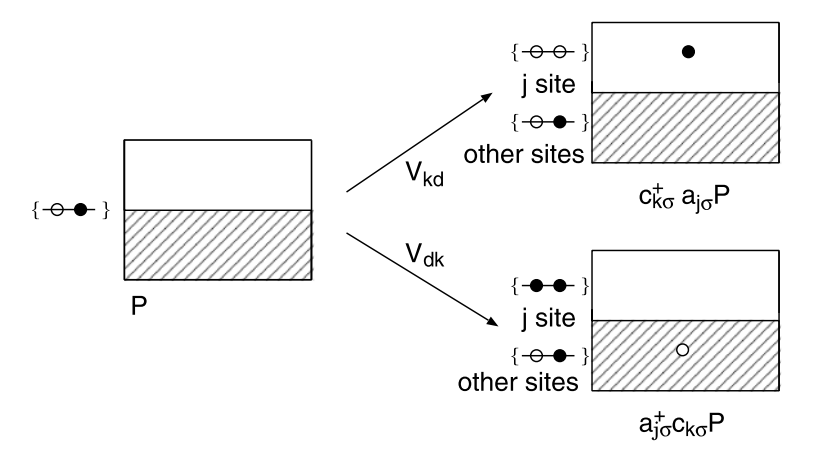


Fig. 7.2 Two possible virtual excitations via hybridization parameters  $V_{kd}$  and  $V_{dk}$ 

We apply the second-order perturbation formula based the projection technique, i.e., (1.80) to obtain the effective Hamiltonian:

$$H_{\rm p} = PHP - PH_{\rm I}Q(E_O^0 - E_P^0)^{-1}QH_{\rm I}P. \tag{7.8}$$

Here we adopt the Hamiltonian in the zero-mixing limit as the noninteracting Hamiltonian  $H_0$ , and treat the hybridization term as an interaction  $H_I$  assuming small parameters:

$$H_{\rm I} = \sum_{jk\sigma} \left( e^{ik \cdot R_j} V_{kd} c_{k\sigma}^{\dagger} a_{j\sigma} + e^{-ik \cdot R_j} V_{dk} a_{j\sigma}^{\dagger} c_{k\sigma} \right). \tag{7.9}$$

The eigen values of  $H_0$  are given by  $E_{\lambda}^0 = \sum_{k\sigma} \varepsilon_k n_{k\sigma} + \sum_{i\sigma} \varepsilon_d n_{di\sigma} + \sum_i U n_{di\uparrow} n_{di\downarrow}$ . Corresponding eigen states are given by  $\{|\{n_{k\sigma}\}, \{n_{dj}, s_{jz}\}\rangle\}$ .

We choose the  $\{n_{\rm dj}=1\}$  states as subspace  $\mathscr P$  on which the effective Hamiltonian  $H_{\rm p}$  operates, and define the projection operator P such that  $P=\sum_{\{n_{k\sigma}\}\{s_{jz}\}}|\{n_{k\sigma}\},\{n_{\rm dj}=1,s_{jz}\}\rangle\langle\{n_{k\sigma}\},\{n_{\rm dj}=1,s_{jz}\}|$ . Then we have  $PHP=P(\sum_{k\sigma}\varepsilon_kn_{k\sigma}+\sum_{j}\varepsilon_{\rm d})P$ . When we apply  $H_{\rm I}$  in subspace  $\mathscr P$ , we have two kinds of excited states as shown in Fig. 7.2, the states with an empty d site and a particle above the Fermi level in the conduction band which is caused via  $V_{k\rm d}$ , and the states with a doubly-occupied d site and a hole below the Fermi level in the conduction band, which is caused via  $V_{dk}$ . Associated excitation energies  $E_Q^0-E_P^0$  are  $\varepsilon_k-\varepsilon_{\rm d}$  for the former and  $\varepsilon_{\rm d}+U-\varepsilon_k$  for the latter, respectively. After the virtual excitations, the system returns to the original state via operator  $PH_{\rm I}$ . Thus the second term of (7.8) is written as

$$PH_{I}Q(E_{Q}^{0} - E_{P}^{0})^{-1}QH_{I}P$$

$$= P\left(\sum_{jlkk'\sigma\sigma'} \frac{e^{ik\cdot R_{j} - ik'\cdot R_{j}}V_{dk'}V_{kd}}{\varepsilon_{k} - \varepsilon_{d}}a_{l\sigma'}^{\dagger}c_{k'\sigma'}c_{k\sigma}^{\dagger}a_{j\sigma}\right)$$

$$+ \sum_{jlkk'\sigma\sigma'} \frac{e^{ik'\cdot R_{l} - ik\cdot R_{j}}V_{k'd}V_{dk}}{\varepsilon_{d} + U - \varepsilon_{k}}c_{k'\sigma'}a_{l\sigma'}^{\dagger}a_{j\sigma}c_{k\sigma}^{\dagger}P.$$

$$(7.10)$$

Arranging the expressions, we finally obtain the effective Hamiltonian as follows.

$$H_{KL} = \sum_{k\sigma} \varepsilon_k n_{k\sigma} + \sum_{j} \left( \varepsilon_{d} + \sum_{k} \frac{V_{dk} V_{kd}}{\varepsilon_{d} - \varepsilon_{k}} \right) + \sum_{jkk'} e^{i(k'-k) \cdot R_{j}} W_{k'k} c_{k'\sigma}^{\dagger} c_{k\sigma}$$

$$- \sum_{jkk'} e^{i(k'-k) \cdot R_{j}} J_{k'k} \sum_{\alpha\gamma} S_{j} \cdot c_{k'\alpha}^{\dagger}(\boldsymbol{\sigma})_{\alpha\gamma} c_{k\gamma}.$$

$$(7.11)$$

Here we have omitted the projector P for simplicity assuming that the Hamiltonian operates on the subspace  $\mathscr{P}$ . The potential scattering parameter  $W_{k'k}$  and effective exchange energy parameter  $J_{k'k}$  between the local magnetic moment  $S_j$  and conduction electron spins  $\sigma$  are defined by

$$W_{k'k} = \frac{1}{2} V_{k'd} V_{dk} \left( \frac{1}{\varepsilon_k - \varepsilon_d - U} - \frac{1}{\varepsilon_d - \varepsilon_{k'}} \right), \tag{7.12}$$

$$J_{k'k} = V_{k'd} V_{dk} \left( \frac{1}{\varepsilon_k - \varepsilon_d - U} + \frac{1}{\varepsilon_d - \varepsilon_{k'}} \right). \tag{7.13}$$

The effective Hamiltonian  $H_{KL}$  consisting of the conduction band and the local magnetic moments is called the Kondo lattice Hamiltonian, and the exchange coupling between the local magnetic moment  $S_j$  and conduction electrons is known as the Kondo exchange coupling.

We can omit the potential scattering term and the constant term of d levels for magnetic phenomena. Moreover we neglect the momentum dependence of the Kondo coupling by assuming the constant hybridization parameter  $V_{\rm dk} \approx V$  and by taking the average of the coupling  $J_{k'k}$  with respect to the conduction band energy. We obtain then a simplified Kondo lattice Hamiltonian as follows.

$$H_{\text{KL}} = \sum_{k\sigma} \varepsilon_k n_{k\sigma} - \frac{J_{\text{K}}}{L} \sum_{ikk'} e^{i(k'-k) \cdot R_j} \sum_{\alpha\gamma} S_j \cdot c_{k'\alpha}^{\dagger}(\sigma)_{\alpha\gamma} c_{k\gamma}. \tag{7.14}$$

Here  $S_j$  is the local magnetic moment on the magnetic impurity site j, which is given by  $S_j = \sum_{\alpha\gamma} a^{\dagger}_{j\alpha}(\sigma)_{\alpha\gamma} a_{j\gamma}/2$ . The Kondo coupling constant  $J_{\rm K}(=\langle J_{k'k}\rangle)$  is expressed as follows.

$$J_{K} = |V|^{2} \sum_{k} \left( \frac{f(\varepsilon_{k} - \mu)}{\varepsilon_{k} - \varepsilon_{d} - U} + \frac{1 - f(\varepsilon_{k} - \mu)}{\varepsilon_{d} - \varepsilon_{k}} \right).$$
(7.15)

Here  $f(\varepsilon_k - \mu)$  is the Fermi distribution function, and  $\mu$  is the chemical potential. Note that  $J_K < 0$  for  $\varepsilon_d \ll \varepsilon_k \sim \mu \ll \varepsilon_d + U$  (case of the strong U and the half filling).

Using the local-orbital representation of the conduction electrons, we obtain the Kondo lattice Hamiltonian in the real space as follows.

$$H_{KL} = \sum_{k\sigma} \varepsilon_k n_{k\sigma} - 2J_K \sum_j S_j \cdot S_j.$$
 (7.16)

Here  $s_j$  is the spin density of conduction electrons on site j, given by  $s_j = \sum_{\alpha\gamma} c_{j\alpha}^{\dagger}(\sigma)_{\alpha\gamma} c_{j\gamma}/2$ . The Kondo lattice Hamiltonian manifests the interaction between the conduction electrons and magnetic impurities. It is useful for analyzing the transport properties and the spin polarization phenomena of dilute magnetic alloys.

In the dilute limit, the Hamiltonians (7.14) and (7.16) reduce to the following Hamiltonian, which is called the Kondo Hamiltonian or the sd Hamiltonian.

$$H_{K} = \sum_{k\sigma} \varepsilon_{k} n_{k\sigma} - \frac{J_{K}}{L} \sum_{kk'} \sum_{\alpha \gamma} S \cdot c_{k'\alpha}^{\dagger}(\sigma)_{\alpha \gamma} c_{k\gamma}. \tag{7.17}$$

The sd Hamiltonian was often used to clarify thermal and transport properties of magnetic alloys in the dilute limit [120].

In the Kondo lattice Hamiltonian, the degree of freedom for conduction electrons remains so that the nature of magnetic interactions between magnetic impurities is not clear in this form. In the following, we consider the sub-subspace in which conduction electrons are in the ground state and only the degree of freedom on the local magnetic moments  $\{S_j\}$  remains. To avoid confusion, we redefine the subspace  $\mathscr{P}_0$  for the Kondo lattice Hamiltonian by  $\{|\{n_{k\sigma}\}, \{n_{dj} = 1, s_{jz}\}\rangle\}$  and the projector  $P_0$  by  $P_0 = \sum_{\{n_{k\sigma}\}\{s_{jz}\}}|\{n_{k\sigma}\}, \{n_{dj} = 1, s_{jz}\}\rangle\}$  and the projector P by we define the sub-subspace  $\mathscr{P}$  by  $\{|\{n_{k\sigma}\}_G, \{n_{dj} = 1, s_{jz}\}\rangle\}\}$  and the projector P by  $P = \sum_{\{s_{jz}\}}|\{n_{k\sigma}\}_G, \{n_{dj} = 1, s_{jz}\}\rangle\}$  ( $\{n_{k\sigma}\}_G, \{n_{dj} = 1, s_{jz}\}\}$ ). Here  $\{n_{k\sigma}\}_G$  denotes the ground-state Fermi-sea configuration. We again make use of the projection technique for the second order perturbation, i.e., (7.8) to obtain the effective Hamiltonian in sub-subspace  $\mathscr{P}$  where only the degree of freedom for magnetic impurity spins remains.

We adopt the Kondo coupling term in (7.14) as the interaction part  $H_{\rm I}$ , and express it as follows.

$$H_{\rm I} = -\frac{J_{\rm K}}{L} \sum_{jkk'} e^{i(k'-k)\cdot R_j} \left( S_{j-} c_{k'\uparrow}^{\dagger} c_{k\downarrow} + S_{j+} c_{k'\downarrow}^{\dagger} c_{k\uparrow} + S_{jz} \sum_{\sigma} \sigma c_{k'\sigma}^{\dagger} c_{k\sigma} \right).$$
(7.18)

Here  $S_{j\pm}$  are the spin-flip operators defined by  $S_{j\pm} = S_{jx} \pm i \, S_{jy}$ . We have then  $PH_{\mathrm{KL}}P = \sum_{k\sigma}^{\mathrm{occ}} \varepsilon_k$ . When we apply  $H_{\mathrm{I}}$  to P in sub-subspace  $\mathscr{P}$ , we have three kinds of excited states: spin-flipped state  $s_{jz}+1$  accompanied by the particle—hole pair excitations in conduction band via the Kondo coupling  $J_{\mathrm{K}}$  as shown in Fig. 7.3,

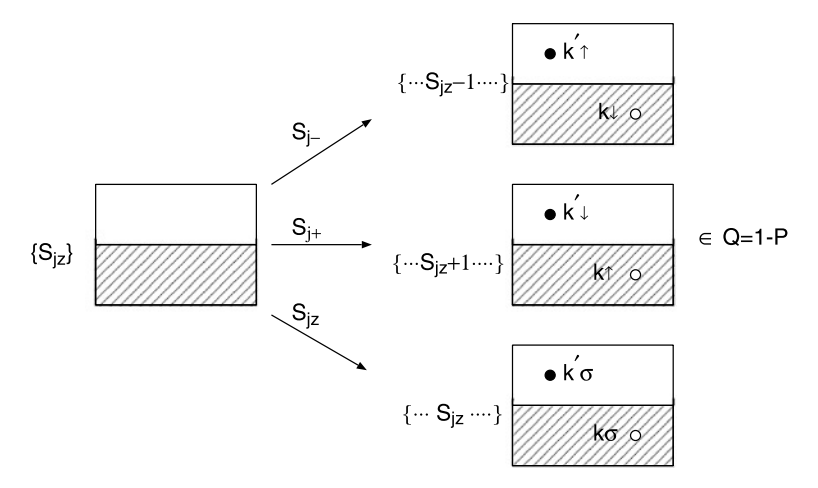


Fig. 7.3 Three possible virtual excitations via the Kondo coupling  $J_{\rm K}$ 

a spin-flipped state  $s_{jz}-1$  accompanied by the particle-hole pair excitations in conduction band, and the non spin-flipped state  $s_{jz}$  accompanied by the particle-hole pair excitations in conduction band. Associated excitation energies are now  $\varepsilon_{k'}-\varepsilon_k$ . Taking into account the possible paths via  $PH_1$ , we obtain the effective Hamiltonian in which the degree of freedom of conduction electrons has been eliminated as follows.

$$H_{\text{RKKY}} = P \left[ 2 \sum_{k}^{\text{occ}} \varepsilon_k - \sum_{j} \frac{1}{2} J(\mathbf{0}) S(S+1) - \sum_{(i,j)} J(\mathbf{R}_i - \mathbf{R}_j) \mathbf{S}_i \cdot \mathbf{S}_j \right] P. \quad (7.19)$$

Here  $J(\mathbf{R}_i - \mathbf{R}_i)$  is defined by

$$J(\mathbf{R}_i - \mathbf{R}_j) = 2\left(\frac{J_K}{L}\right)^2 \sum_{kk'} \frac{n_k - n_{k'}}{\varepsilon_{k'} - \varepsilon_k} \cos\left[\left(\mathbf{k} - \mathbf{k'}\right) \cdot (\mathbf{R}_i - \mathbf{R}_j)\right], \quad (7.20)$$

and  $n_k$  denotes the electron occupation number per spin of conduction electrons with momentum k (i.e., the Fermi distribution function at T = 0 for electrons with momentum k).

The effective Hamiltonian (7.19) has a form of the Heisenberg model as follows when we omit the constant terms.

$$H_{\text{RKKY}} = -\sum_{(i,j)} J(\mathbf{R}_i - \mathbf{R}_j) \mathbf{S}_i \cdot \mathbf{S}_j.$$
 (7.21)

Here the projector P has been omitted by promising that the Hamiltonian is applied on the subspace of the magnetic moments. Equation (7.21) is called the RKKY (Ruderman–Kittel–Kasuya–Yosida) interaction, and the coupling constant J(R) is known as the RKKY interaction coupling constant [121–123].

The RKKY interaction between the magnetic moments of impurity atoms is caused by a polarization of conduction electrons due to the local magnetic moments via the Kondo coupling. In fact, the RKKY interaction is expressed by the susceptibility of conduction electrons as follows.

$$J(\mathbf{R}_i - \mathbf{R}_j) = \frac{J_{K}^2}{L} \sum_{q} \chi(\mathbf{q}) \cos \mathbf{q} \cdot (\mathbf{R}_i - \mathbf{R}_j). \tag{7.22}$$

Here  $\chi(q)$  is the generalized static susceptibility defined by (6.33), i.e.,  $m(q) = \chi(q)h(q)$ , and has been given as follows (see (6.36)).

$$\chi(\mathbf{q}) = \frac{2}{L} \sum_{k} \frac{n_{k+q} - n_k}{\varepsilon_k - \varepsilon_{k+q}}.$$
 (7.23)

The RKKY interaction is obtained by a simple interpretation of the Kondo lattice Hamiltonian. According to the real-space representation of the Kondo lattice Hamiltonian (7.16), the conduction electrons feel a 'magnetic field'  $h_j = J_K S_j$  on site j. The field causes a conduction electron spin polarization  $m_i = \chi_{ij} h_j$  on site i according to the linear response. The local moment  $S_i$  has the Kondo interaction  $-J_K S_i \cdot m_i = -J_K^2 \chi_{ij} S_i \cdot S_j$  according to the Hamiltonian (7.16). Summing up the interactions with respect to all the pairs, we obtain the Hamiltonian (7.21) with a coupling constant

$$J(\mathbf{R}_i - \mathbf{R}_j) = J_{\mathbf{K}}^2 \chi_{ij}. \tag{7.24}$$

Substituting the Fourier transform  $\chi_{ij} = \sum_{q} \chi(q) \exp i q \cdot (\mathbf{R}_i - \mathbf{R}_j)$  into the above expression, we find that the coupling constant (7.24) is identical with (7.22).

The RKKY interaction is long-range since it is based on the interaction between the local magnetic moments via conduction electron polarization. In order to understand its long-range nature, let us consider the free electron model. In this case, the susceptibility (7.23) is expressed as

$$\chi(\mathbf{q}) = \frac{4\Omega}{(2\pi)^3} \int_{|\mathbf{k}| < k_{\rm F}} d\mathbf{k} \left( \frac{1}{(\mathbf{k} - \mathbf{q})^2 - k^2} + \frac{1}{(\mathbf{k} + \mathbf{q})^2 - k^2} \right). \tag{7.25}$$

Here  $\Omega$  is the volume of the unit cell, and  $k_F$  denotes the Fermi wave vector.

For each integral at the r.h.s. of (7.25), we can perform the integral with respect to the azimuthal and polar angles after introducing the polar coordinates. Furthermore, with use of the integration by parts, we obtain

$$\int_{|\mathbf{k}| < k_{\rm F}} d\mathbf{k} \left( \frac{1}{(\mathbf{k} \pm \mathbf{q})^2 - k^2} \right) = \frac{\pi k_{\rm F}}{2} F\left( \frac{q}{2k_{\rm F}} \right). \tag{7.26}$$

The function F(x) is defined by

$$F(x) = 1 + \frac{1 - x^2}{2x} \ln \left| \frac{1 + x}{1 - x} \right|. \tag{7.27}$$

Note that F(x) is an even function, F(0) = 2, and  $F(x) \to 2/3x^2$   $(x \to \infty)$ . Using the integral (7.26), we obtain

$$\chi(\mathbf{q}) = \chi_{\text{Pauli}} \frac{1}{2} F\left(\frac{q}{2k_{\text{F}}}\right). \tag{7.28}$$

Here  $\chi_{Pauli} = 2\rho(\varepsilon_F)$  is the Pauli uniform susceptibility in the free electron model, and  $\rho(\varepsilon_F)$  is the density of states at the Fermi level  $\varepsilon_F$ .

Substituting the expression (7.28) into (7.22) and extending the integration range from the first Brillouin zone to the whole region for convenience, we obtain

$$J(\mathbf{R}) = \frac{J_{\rm K}^2 \Omega}{(2\pi)^2} \frac{\chi_{\rm Pauli}}{R} \int_0^\infty dq \, q \, F\left(\frac{q}{2k_{\rm F}}\right) \sin q \, R. \tag{7.29}$$

Since F(x) is an even function, the above expression is written as follows.

$$J(\mathbf{R}) = \frac{J_{K}^{2} \Omega}{(2\pi)^{2}} \frac{\chi_{\text{Pauli}}}{2iR} I(R), \tag{7.30}$$

and the integral I(R) is given by

$$I(R) = \int_{-\infty}^{\infty} dq \, q \, F\left(\frac{q}{2k_{\rm F}}\right) e^{iqR}.\tag{7.31}$$

As shown in Appendix H, the integral I(R) is obtained as follows.

$$I(R) = \frac{\pi i}{k_{\rm F} R^3} (-2k_{\rm F} R \cos 2k_{\rm F} R + \sin 2k_{\rm F} R). \tag{7.32}$$

Substituting (7.32) into (7.30), we obtain the RKKY interaction in the free electron model.

$$J(\mathbf{R}) = 6\pi n_e J_{\rm K}^2 \chi_{\rm Pauli} \frac{-2k_{\rm F}R\cos 2k_{\rm F}R + \sin 2k_{\rm F}R}{(2k_{\rm F}R)^4}.$$
 (7.33)

Here  $n_{\rm e}$  is the electron number per unit cell given by  $n_{\rm e} = k_{\rm F}^3 \Omega/\pi$ ,  $\Omega$  being the volume of the unit cell. Thus, the RKKY interaction oscillates with the wave length  $\pi/k_{\rm F}$  as a function of R and decays as  $1/R^3$  as shown in Fig. 7.4. Note that the nearest-neighbor distance and the second nearest-neighbor distance correspond to  $2k_{\rm F}R=6.95$  and 9.82, respectively, when we assume  $n_{\rm e}=1$  and the fcc lattice bearing in mind the Cu–Mn dilute alloys. The RKKY interaction is of long range because of the  $1/R^3$  dependence.

Oscillatory long-range interactions are expected to cause a complex magnetism in the dilute alloys. We consider here the RKKY interactions  $J_{ij}$  between the Ising-type spins with S=1/2 for simplicity. The molecular field Hamiltonian acting on a spin on site i is given by  $H_i = -\sum_i J_{ij} \langle S_{jz} \rangle S_{iz}$ . Therefore the thermal average

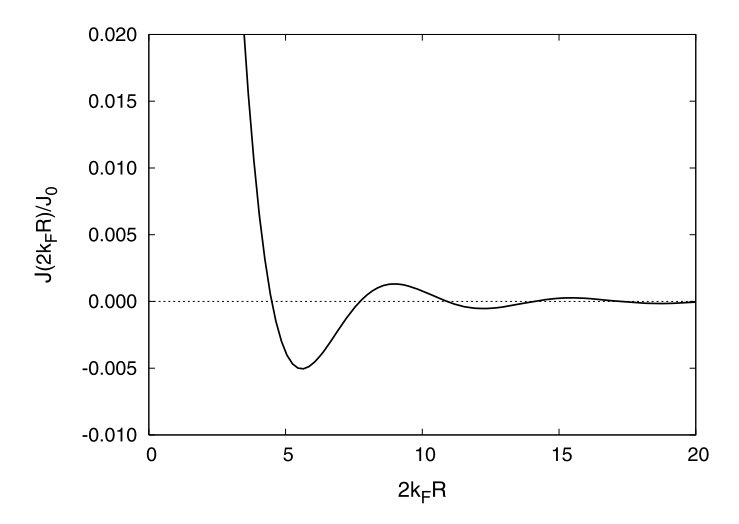


Fig. 7.4 The RKKY interaction  $J/J_0$  as a function of  $2k_FR$ . Here  $J_0 = 6\pi n_e J_K^2 \chi_{\text{Pauli}}$ 

of the magnetic moment on site i ( $\langle m_i \rangle = 2 \langle S_{iz} \rangle$ ) is given in the molecular-field approximation as

$$\langle m_i \rangle = \tanh\left(\frac{\beta}{4} \sum_j J_{ij} \langle m_j \rangle\right).$$
 (7.34)

For small magnetic moments near the critical temperature, we can expand the r.h.s. of the above self-consistent equation as follows.

$$\langle m_i \rangle = \frac{\beta}{4} \sum_j J_{ij} \langle m_j \rangle + \cdots.$$
 (7.35)

Taking the configurational average, we obtain

$$\overline{\langle m_i \rangle} \approx \frac{\beta}{4} \overline{\sum_i J_{ij}} \overline{\langle m_j \rangle} + \cdots$$
(7.36)

Here the upper bar denotes the configurational average on magnetic impurities, and we have decoupled the correlation between the interaction constant and the surrounding magnetic moment for simplicity. From (7.36), we may obtain the Curie temperature  $T_{\rm C}$ .

$$T_{\rm C} = \frac{1}{4} \overline{\sum_{i} J_{ij}}.$$
 (7.37)

In the disordered system, we have another transition temperature. Taking first square of both sides in (7.35) and next taking the configurational average, we find

$$\overline{\langle m_i \rangle^2} \approx \left(\frac{\beta}{4}\right)^2 \overline{\sum_{lj} J_{ij} J_{il}} \overline{\langle m_j \rangle \langle m_l \rangle} + \cdots$$
 (7.38)

When  $\overline{\langle m_i \rangle} = 0$  and we neglect the correlation between local magnetic moments on different sites, we have  $\overline{\langle m_i \rangle \langle m_l \rangle} = \overline{\langle m_i \rangle^2} \delta_{il}$ . Then (7.38) reduces to

$$\overline{\langle m_i \rangle^2} \approx \left(\frac{\beta}{4}\right)^2 \overline{\sum_i J_{ij}^2 \langle m_j \rangle^2} + \cdots$$
(7.39)

Therefore we have one more transition temperature  $T_{\rm g}$  at which  $\overline{\langle m_i \rangle^2}$  vanishes.

$$T_{\rm g} = \frac{1}{4} \overline{\sum_{i} J_{ij}^2}.$$
 (7.40)

From the simple analysis mentioned above, we find at least two order parameters in dilute magnetic alloys:  $\overline{\langle m_i \rangle}$  and  $\overline{\langle m_i \rangle^2}$ . The system is in the ferromagnetic state (F) when  $\overline{\langle m_i \rangle} \neq 0$  and  $\overline{\langle m_i \rangle^2} \neq 0$ . It is in the paramagnetic state (P) when  $\overline{\langle m_i \rangle} = 0$  and  $\overline{\langle m_i \rangle^2} = 0$ . In addition to these cases we can also consider the case

$$\overline{\langle m_i \rangle} = 0$$
 and  $\overline{\langle m_i \rangle^2} \neq 0$ . (7.41)

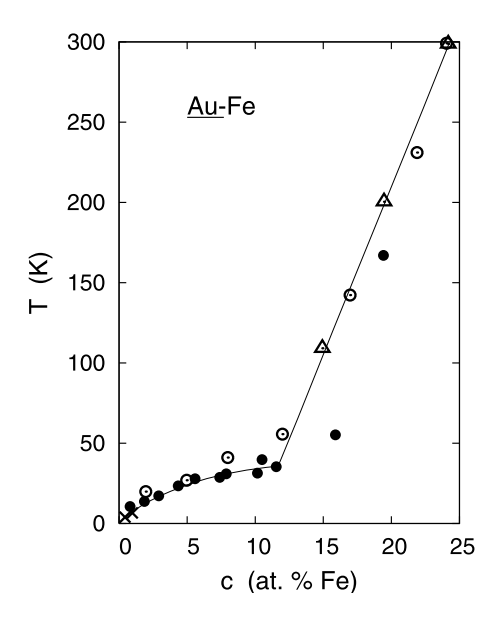
This case may correspond to a state such that there is no magnetization but the randomly oriented spins remain (see Fig. 1.16). It is called the spin-glass state (SG). The SG may be realized when magnetic interactions compete each other in the disordered alloys and there is no long-range order being found as the magnetic Laue spots. The transition temperature  $T_g$  is called the SG temperature. The cusps in the susceptibilities found in Au–Fe dilute alloys as shown in Fig. 7.1 are considered to show the spin glass transition [124].

The coupling constants  $\overline{\sum_j J_{ij}}$  and  $\overline{\sum_j J_{ij}^2}$  in  $T_C$  and  $T_g$  are expressed by the parameters for atomic configuration. Note that the summations at the r.h.s. in (7.37) and (7.40) are taken with respect to the magnetic impurity sites. In order to express these summations as the sum over all the lattice sites, we introduce an occupation number  $\alpha_i$  of the impurity atom A on site i which takes 1 when site i is occupied by the atom A and takes 0 otherwise. In order to distinguish the two kinds of summations, we write them in (7.37) and (7.40) as  $\sum_{i \in A}$ . Then

$$\overline{\sum_{j \in A} J_{ij}} = \overline{\sum_{j} \alpha_i \alpha_j J_{ij}} = \sum_{j} \overline{\alpha_i \alpha_j} J_{ij}. \tag{7.42}$$

Here  $p_{ij}^{AA} \equiv \overline{\alpha_i \alpha_j}$  is the probability of finding the type of atom A on site j when site i is occupied by the same atom A. Using the probability  $p_{ij}^{AA}$ , we can express

Fig. 7.5 Magnetic ordering temperature vs. concentration curves for Au–Fe alloys obtained by various methods [118]



 $\frac{\sum_{j} J_{ij}}{\sum_{j} J_{ij}}$  in (7.37) and  $\frac{\sum_{j} J_{ij}^{2}}{\sum_{j} J_{ij}^{2}}$  in (7.40) as  $\sum_{j} p_{ij}^{AA} J_{ij}$  and  $\sum_{j} p_{ij}^{AA} J_{ij}^{2}$ , respectively. Thus we have

$$T_{\rm C} = \frac{1}{4} \sum_{j} p_{ij}^{\rm AA} J_{ij}, \tag{7.43}$$

$$T_{\rm g} = \frac{1}{4} \sum_{i} p_{ij}^{\rm AA} J_{ij}^2. \tag{7.44}$$

When there is no short-range atomic order, we have  $p_{ij}^{AA} = c_A$ ,  $c_A$  being the impurity concentration. Thus,

$$T_{\rm C} = c_{\rm A} \tilde{J}_0, \tag{7.45}$$

$$T_{\rm g} = \sqrt{c_{\rm A}}\tilde{J}. \tag{7.46}$$

Here  $\tilde{J}_0 = (\sum_i J_{ij})/4$  and  $\tilde{J} = (\sum_i J_{ii}^2)^{1/2}/4$ .

Figure 7.5 shows the ordering temperature vs. concentration curve in Au–Fe alloys. The linear concentration dependence of  $T_{\rm C}$  at  $c_{\rm Fe} > 12$  at% Fe and the concentration dependence of  $T_{\rm g}$  at  $c_{\rm Fe} < 12$  at% Fe are explained by (7.45) and (7.46), respectively.

The theory of spin glasses (SG) in the dilute alloys has been developed as a part of the disordered spin systems in the insulators because their Hamiltonian can be mapped into the RKKY spin Hamiltonian (7.21). Details of the advanced SG theory as a model of statistical mechanics can be found in the books by Parisi et al. [125] and by Fisher and Hertz [126].

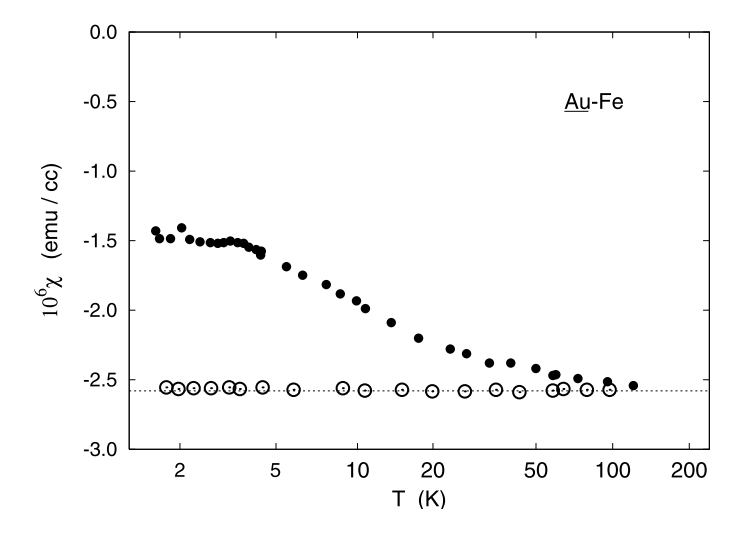


**Fig. 7.6** Susceptibility of pure Au (⊙) and a Au 0.0054 at.% Fe dilute alloy (•) as a function of temperature [129]

### 7.2 Magnetic Impurity in Noble Metals

In the dilute limit, the RKKY interaction is infinitesimally weak, and a magnetic impurity system is realized in the nonmagnetic metal. Such a small system shows a unique property which is quite different from the other systems. Figure 7.6 shows the temperature dependence of the susceptibility in Au–Mn dilute alloys as an example. The impurity contribution follows the Curie law at high temperatures indicating the existence of a local magnetic moment on Mn atom. With decreasing temperature, the susceptibility tends to saturate around a few Kelvin, indicating the disappearance of local magnetic moment of the impurity atom. The low temperature behavior and the related ground state cannot be understood by a simple picture of local magnetic moment. In this section we will briefly explain the basic properties of magnetic impurity dissolved in a simple metal.

The magnetic impurity is described by the Anderson Hamiltonian as derived in the last section.

$$H = \sum_{k\sigma} \varepsilon_k n_{k\sigma} + \sum_{k\sigma} \left( V_{dk} a_{d\sigma}^{\dagger} c_{k\sigma} + V_{kd} c_{k\sigma}^{\dagger} a_{d\sigma} \right) + \sum_{\sigma} \varepsilon_{d} n_{d\sigma} + U n_{d\uparrow} n_{d\downarrow}. \quad (7.47)$$

In order to obtain a physical insight to the magnetic impurity in the noble metals, we consider first a simplified model in which the number of sites in the conduction band has been reduced from infinity to one. This is called the ligand model or the zero-band-width model [127, 128]. The Hamiltonian is written as

$$H = \sum_{\sigma} \varepsilon_{l} n_{l\sigma} + \sum_{\sigma} V \left( a_{\sigma}^{\dagger} c_{\sigma} + c_{\sigma}^{\dagger} a_{\sigma} \right) + \sum_{\sigma} \varepsilon_{d} n_{d\sigma} + U n_{d\uparrow} n_{d\downarrow}. \tag{7.48}$$

Here  $\varepsilon_1$  denotes a ligand level,  $n_{1\sigma}$  is the number operator of the ligand electrons with spin  $\sigma$ . We have omitted the subscripts d and l of the creation and annihilation operators for simplicity.

We assume that the ligand level  $\varepsilon_1$  is higher than the d level  $\varepsilon_d$ , and the Coulomb energy U is large enough as compared with the difference  $\Delta_0 \equiv \varepsilon_1 - \varepsilon_d$ ;  $U \gg \Delta_0$ . Moreover we consider the case that the hybridization |V| is small as compared with the difference, so that  $|V| \ll \varepsilon_1 - \varepsilon_d \ll U$ . When we put two electrons in this system, the doubly occupied state on the impurity site is suppressed due to the strong Coulomb repulsion U, so that the magnetic impurity with one electron is realized and the d electron hybridizes with the ligand electron via V.

In the case that V=0, we have a ligand electron  $(n_1=1)$  and a d electron  $(n_{\rm d}=1)$ , so that the ground-state energy is given by  $E=\varepsilon_1+\varepsilon_{\rm d}$  and associated 4 states are degenerate;  $|n_{1\uparrow}n_{1\downarrow}n_{\rm d\uparrow}n_{\rm d\downarrow}\rangle=|1010\rangle, |1001\rangle, |0110\rangle, |0101\rangle$ . Alternatively, degenerate 4 states are chosen to be the eigen states of the total spin  $S=s_{\rm d}+s_{\rm l}$ .

$$\begin{aligned} \left| \Phi^{(s)} \right\rangle &= \frac{1}{\sqrt{2}} \left( a_{\uparrow}^{\dagger} c_{\downarrow}^{\dagger} - a_{\downarrow}^{\dagger} c_{\uparrow}^{\dagger} \right) |0\rangle, \\ \left| \Phi_{1}^{(t)} \right\rangle &= a_{\uparrow}^{\dagger} c_{\uparrow}^{\dagger} |0\rangle, \\ \left| \Phi_{0}^{(t)} \right\rangle &= \frac{1}{\sqrt{2}} \left( a_{\uparrow}^{\dagger} c_{\downarrow}^{\dagger} + a_{\downarrow}^{\dagger} c_{\uparrow}^{\dagger} \right) |0\rangle, \\ \left| \Phi_{-1}^{(t)} \right\rangle &= a_{\downarrow}^{\dagger} c_{\downarrow}^{\dagger} |0\rangle. \end{aligned}$$
(7.49)

Here  $|\Phi^{(s)}\rangle$  ( $|\Phi_{\alpha}^{(t)}\rangle$ ) denotes the singlet (triplet) state with total spin S=0 (S=1). When  $V \neq 0$ , we have additional configuration with no d electron.

$$\left|\Phi^{(0)}\right\rangle = c_{\uparrow}^{\dagger} c_{\downarrow}^{\dagger} \left|0\right\rangle. \tag{7.50}$$

The Hamiltonian matrix for the 5 states  $(\Phi^{(0)}, \Phi^{(s)}, \Phi_{-1}^{(t)}, \Phi_0^{(t)}, \Phi_1^{(t)})$  is given as follows.

$$H = \begin{pmatrix} 2\varepsilon_{1} & \sqrt{2}V & 0 & 0 & 0\\ \sqrt{2}V & \varepsilon_{1} + \varepsilon_{d} & 0 & 0 & 0\\ 0 & 0 & \varepsilon_{1} + \varepsilon_{d} & 0 & 0\\ 0 & 0 & 0 & \varepsilon_{1} + \varepsilon_{d} & 0\\ 0 & 0 & 0 & 0 & \varepsilon_{1} + \varepsilon_{d} \end{pmatrix}$$
(7.51)

Note that the  $d^0$  state  $|\Phi^{(0)}\rangle$  is not coupled to the triplet states  $|\Phi^{(t)}\rangle$  because the hybridization  $\sum_{\sigma} a^{\dagger}_{\sigma} c_{\sigma}$  which is operated on the  $d^0$  state creates the singlet state. The singlet state is coupled to the  $d^0$  state because of the same reason. Diagonalizing the  $\{\Phi^{(0)}, \Phi^{(s)}\}$  sub-block, we find the eigenvalues

$$E = \varepsilon_{\rm l} + \varepsilon_{\rm d} + \frac{1}{2} \left( \Delta_0 \pm \sqrt{\Delta_0^2 + 8|V|^2} \right), \tag{7.52}$$

$$2\varepsilon_{l} + 2|V|^{2}/\Delta$$

$$\varepsilon_{l} + \varepsilon_{d} = \varepsilon_{l} + \varepsilon_{d}$$

**Fig. 7.7** The energy spectra of the ligand model for V = 0 (*left*) and for  $V \neq 0$  (*right*)

where  $\Delta_0 \equiv \varepsilon_1 - \varepsilon_d$ . For small  $|V|^2/\Delta_0$ , we have  $E = 2\varepsilon_1 + 2|V|^2/\Delta_0$  and  $\varepsilon_1 + \varepsilon_d - 2|V|^2/\Delta_0$ .

In summary, we have (i) the ligand electron state

$$|\Psi^{(0)}\rangle = \left(1 - \frac{|V|^2}{\Delta_0^2}\right) |\Phi^{(0)}\rangle + \sqrt{2} \frac{V}{\Delta_0} |\Phi^{(s)}\rangle,$$
 (7.53)

with the energy  $E_0 = 2\varepsilon_1 + 2|V|^2/\Delta_0$  and the total spin S = 0, (ii) the singlet state

$$\left|\Psi^{(s)}\right\rangle = -\sqrt{2}\frac{V}{\Delta_0}\left|\Phi^{(0)}\right\rangle + \left(1 - \frac{|V|^2}{\Delta_0^2}\right)\left|\Phi^{(s)}\right\rangle,\tag{7.54}$$

with the energy  $E_s = \varepsilon_1 + \varepsilon_d - 2|V|^2/\Delta_0$  and the spin S = 0, and (iii) the triplet states  $|\Phi_{-1}^{(t)}\rangle$ ,  $|\Phi_0^{(t)}\rangle$ ,  $|\Phi_1^{(t)}\rangle$  with energy  $E_t = \varepsilon_1 + \varepsilon_d$  and spin S = 1. The eigenvalues of the ligand model with V = 0 and  $V \neq 0$  are summarized in Fig. 7.7.

The ligand model suggests that the ground state of the Anderson model with strong U is a singlet at half filling. This means that the magnetic dilute alloys lose the magnetic moment at the ground state even in the strong U limit. The second point is that there is a characteristic temperature  $T^* = 2|V|^2/\Delta_0$  above which the magnetic moment of the impurity state recovers and thus the susceptibility follows the Curie law, because the triplet states are located above the singlet ground state and the former is higher than the latter by  $2|V|^2/\Delta_0$ .

Let us now return to the Anderson model, and obtain the singlet ground state in large U limit. According to the singlet ground state (7.54), we assume the following ground state wave function of electrons [130].

$$|\Psi\rangle = A \left[ |\Phi_0\rangle + \sum_{k}^{\text{occ}} B_k \left( a_{\text{d}\uparrow}^{\dagger} c_{k\uparrow} + a_{\text{d}\downarrow}^{\dagger} c_{k\downarrow} \right) |\Phi_0\rangle \right]. \tag{7.55}$$

Here A is a normalization factor, and  $\{B_k\}$  are the amplitudes to be determined variationally. The first term at the r.h.s. of (7.55),  $|\Phi_0\rangle$  is the Fermi sea state with no d electron, which is defined by

$$|\Phi_0\rangle = \prod_{k}^{\text{occ}} \left[c_{k\uparrow}^{\dagger} c_{k\downarrow}^{\dagger}\right] |0\rangle. \tag{7.56}$$

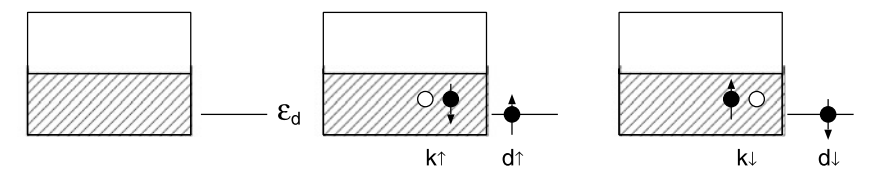


**Fig. 7.8** Three states  $|\Phi_0\rangle$  (*left*),  $a_{\mathrm{d}\uparrow}^{\dagger}c_{k\uparrow}|\Phi_0\rangle$  (*middle*), and  $a_{\mathrm{d}\downarrow}^{\dagger}c_{k\downarrow}|\Phi_0\rangle$  (*right*) in the variational wave function

It corresponds to the ligand electron state  $|\Phi^{(0)}\rangle$  with no d electron in the ligand model. On the other hand, each state in the second term of (7.55) has one d electron and forms a singlet state consisting of a d electron and a conduction electron with momentum k.

$$|\Phi_{k}\rangle \equiv \frac{1}{\sqrt{2}} \left( a_{\mathsf{d}\uparrow}^{\dagger} c_{k\uparrow} + a_{\mathsf{d}\downarrow}^{\dagger} c_{k\downarrow} \right) |\Phi_{0}\rangle = \frac{1}{\sqrt{2}} \left( a_{\mathsf{d}\uparrow}^{\dagger} c_{k\downarrow}^{\dagger} - a_{\mathsf{d}\downarrow}^{\dagger} c_{k\uparrow}^{\dagger} \right) \prod_{k'\neq k}^{\mathrm{occ}} \left[ c_{k'\uparrow}^{\dagger} c_{k'\downarrow}^{\dagger} \right] |0\rangle. \tag{7.57}$$

These states are depicted in Fig. 7.8.

The wavefunction (7.55) with A = 1 is written with use of  $\{|\Phi_k\rangle\}$  as follows.

$$|\Psi\rangle = |\Phi_0\rangle + \sqrt{2} \sum_{k}^{\text{occ}} B_k |\Phi_k\rangle.$$
 (7.58)

Note that  $\{|\Phi_0\rangle, |\Phi_k\rangle\}$  are orthonormal. The amplitudes  $B_k$  are determined from the variational principle of the energy,

$$E = \frac{\langle \Psi | H | \Psi \rangle}{\langle \Psi | \Psi \rangle}.$$
 (7.59)

Here

$$\langle \Psi | \Psi \rangle = 1 + 2 \sum_{k}^{\text{occ}} B_k^* B_k, \tag{7.60}$$

$$\langle \Psi | H | \Psi \rangle = E_0 + 2 \sum_{k}^{\text{occ}} (V_{dk} B_k^* + V_{kd} B_k)$$

$$+2\sum_{k}^{\text{occ}}(E_0+\varepsilon_{d}-\varepsilon_{k})B_k^*B_k, \qquad (7.61)$$

and  $E_0 = 2\sum_{k}^{\text{occ}} \varepsilon_k$  is the energy for the conduction band.

Taking the variation of the energy, we have

$$(\delta \langle \Psi | H | \Psi \rangle) \langle \Psi | \Psi \rangle - \langle \Psi | H | \Psi \rangle \delta \langle \Psi | \Psi \rangle = 0. \tag{7.62}$$

Calculating the variations  $\delta\langle\Psi|\Psi\rangle$  and  $\delta\langle\Psi|H|\Psi\rangle$ , and substituting them into (7.62), we find the self-consistent equation for  $B_k$  as follows.

$$(\Delta E + \varepsilon_k)B_k = V_{dk}. (7.63)$$

Here  $\Delta E = E - E_0 - \varepsilon_d$ , and the energy  $E - E_0$  is obtained from (7.59), (7.60), and (7.61) as follows.

$$E - E_0 = \frac{2\sum_{k}^{\text{occ}} V_{kd} B_k + 2\sum_{k}^{\text{occ}} B_k^* [V_{dk} + (\varepsilon_d - \varepsilon_k) B_k]}{1 + 2\sum_{k}^{\text{occ}} B_k^* B_k}.$$
 (7.64)

Substituting  $V_{dk}$  of (7.63) into the second term of the numerator in (7.64) and multiplying  $1 + 2 \sum_{k}^{\text{occ}} B_{k}^{*} B_{k}$  to both sides, we find the following equation.

$$\Delta E = -\varepsilon_{\rm d} + 2\sum_{k}^{\rm occ} V_{k\rm d} B_k. \tag{7.65}$$

Substitution of  $B_k$  from (7.63) into the above equation yields the self-consistent equation for  $\Delta E$  as follows.

$$\Delta E = -\varepsilon_{\rm d} + 2\sum_{k}^{\rm occ} \frac{|V_{k\rm d}|^2}{\Delta E + \varepsilon_k}.$$
 (7.66)

Note that the above equation reduces to the solution (7.52) in the ligand model limit  $(\varepsilon_k \to \varepsilon_1)$ .

Assuming the flat band with the band edge -D at the bottom for conduction electrons, (7.66) is expressed as follows.

$$\Delta E = -\varepsilon_{\rm d} + 2\rho(0)|V|^2 \ln \frac{|\Delta E|}{D}.$$
 (7.67)

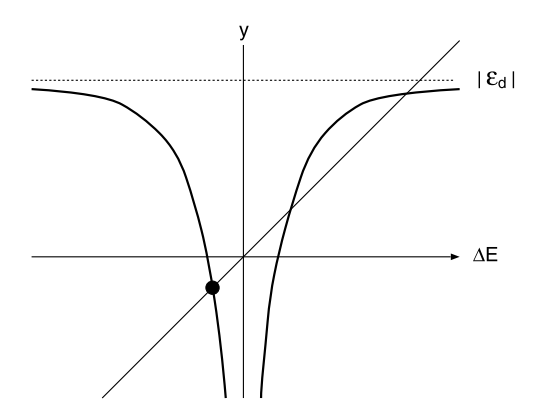
Here  $\rho(\varepsilon)$  is the density of states per spin for conduction electrons which is defined by  $\rho(\varepsilon) = \sum_k \delta(\varepsilon - \varepsilon_k)$ . Moreover we assumed that the band width D is large as compared with  $|\Delta E|$ . We have a solution of (7.67) at  $\Delta E < 0$  as seen from Fig. 7.9 in which the curves of both sides of (7.67) are depicted. Since  $|\Delta E| \to 0$  when  $|V| \to 0$ , we obtain an approximate solution for a small |V| as

$$|\Delta E| = D \exp\left(-\frac{|\varepsilon_{\rm d}|}{2\rho(0)|V|^2}\right). \tag{7.68}$$

The characteristic temperature associated with the formation of the singlet ground state is called the Kondo temperature;  $T_{\rm K} \equiv |\Delta E|$ . In the present case, it is given by

$$T_{\rm K} = D \exp\left(-\frac{|\varepsilon_{\rm d}|}{2\rho(0)|V|^2}\right). \tag{7.69}$$

**Fig. 7.9** Graphical analysis of the self-consistent equation (7.67) for  $\Delta E$ 



Note that the Kondo exchange coupling constant in the Kondo Hamiltonian is given by (7.13):

$$J_{kk'} = V_{k'd} V_{dk} \left( \frac{1}{\varepsilon_k - \varepsilon_d - U} + \frac{1}{\varepsilon_d - \varepsilon_{k'}} \right). \tag{7.70}$$

For large U and the symmetric case ( $\varepsilon_d = -U/2$ ), we have a simplified expression of the Kondo exchange coupling  $J_K$  (=  $\langle J_{k'k} \rangle < 0$ ) as follows.

$$J_{K} = -\frac{2|V|^{2}}{|\varepsilon_{d}|}. (7.71)$$

Here we have omitted the momentum dependence of the hybridization parameter. The Kondo temperature (7.69) is expressed in terms of the Kondo exchange coupling as follows.

$$T_{\rm K} = D \exp\left(\frac{1}{\rho(0)J_{\rm K}}\right). \tag{7.72}$$

In the same way, we can calculate the d electron number as

$$\langle n_{\rm d} \rangle = 1 - \frac{\pi T_{\rm K}}{\Delta}.\tag{7.73}$$

Here  $\Delta = 2\pi\rho(0)|V|^2$ . The expression indicates that  $\langle n_{\rm d}\rangle$  approaches 1 as  $T_{\rm K}\to 0$ . When the magnetic field h is applied on the impurity atom, the impurity d level is modified from  $\varepsilon_{\rm d}$  to  $\varepsilon_{\rm d\sigma} = \varepsilon_{\rm d} - h\sigma$ , so that the variational parameter  $B_k$  is expected to be spin-dependent. The wave function is then modified as

$$|\Psi\rangle = A \left[ |\Phi_0\rangle + \sum_{k}^{\text{occ}} \left( B_{k\uparrow} a_{d\uparrow}^{\dagger} c_{k\uparrow} + B_{k\downarrow} a_{d\downarrow}^{\dagger} c_{k\downarrow} \right) |\Phi_0\rangle \right]. \tag{7.74}$$

**Table 7.1** The Kondo temperatures in the typical dilute alloys [133]

Alloys	Cu–Cr	Cu–Mn	Cu–Fe	Au–Fe	Al–Mn
$T_{\mathrm{K}}\left(\mathrm{K}\right)$	2	0.01	30	0.8	500

Taking the same steps as before we reach the self-consistent equation for the ground state energy.

$$\Delta E(h) = -\varepsilon_{\rm d} + 2\sum_{k}^{\rm occ} \frac{|V_{k\rm d}|^2}{\Delta E(h) + h\sigma + \varepsilon_k}.$$
 (7.75)

The impurity susceptibility  $\chi_{\text{imp}}$  is obtained from  $-(\partial^2 \Delta E(h)/\partial h^2)_{h=0}$  by using the above self-consistent equation as follows.

$$\chi_{\rm imp} = \frac{1}{T_{\rm K}}.\tag{7.76}$$

The results shows that the susceptibility is finite even in the strong Coulomb interaction limit because of the formation of the singlet state. The magnitude is scaled by the inverse Kondo temperature. As expected from the arguments so far, all the related physical quantities are scaled by the Kondo temperature  $T_K$ . The Kondo temperatures for typical dilute magnetic alloys which are determined experimentally are given in Table 7.1.

The finite-temperature properties of the susceptibility in the Anderson model have been obtained accurately by using the numerical renormalization group technique [131, 132]. Figure 7.10 shows the temperature dependence of the susceptibilities of the Anderson model for strong (case A) and weak (case B) Coulomb interactions. In the strong Coulomb interaction regime, the Curie constant defined by  $C = T\chi_{\text{imp}}$  vanishes at T = 0 because the ground state is the singlet. With increasing temperature, the local magnetic moment recovers above  $T_{\rm K}$ , and the Curie constant C approaches to a constant value which is close to the atomic value 1/4 (i.e., S(S+1)/3 with S=1/2). When the temperature is further elevated, the Curie constant starts to decrease around a temperature U and approaches to the free orbital value 1/8 where the empty and doubly occupied states as well as the spin-up and spin-down states are excited equally on the impurity site. In the case of B where the Coulomb interaction is close to the value of the Hartree-Fock magnetic instability point  $U/\pi \Delta = 1$ , the ground state is again singlet, so that the Curie constant again vanishes at the ground state. However the Kondo temperature is very large  $(T_{\rm K} \sim D)$  in this case and the local moment regime does not appear any more as seen in Fig. 7.10.

It should be noted that the Hartree–Fock approximation does not lead to the singlet ground state. The approximation tells us that the local magnetic moment is stabilized when  $\rho_{\rm d}(0)U>1$  [119]. Here  $\rho_{\rm d}(\epsilon)$  is the d density of states per spin on the impurity site. Figure 7.10 suggests that this condition is qualitatively applicable only when the temperature is in the regime  $T_{\rm K}\ll T\ll U$ .

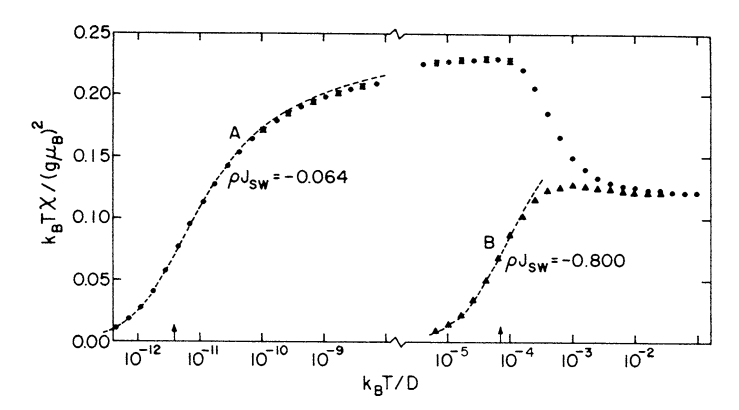


**Fig. 7.10** The impurity susceptibility of the symmetric Anderson model for U/D=0.001;  $U/\pi \Delta=12.66$  (A) and  $U/\pi \Delta=1.013$  (B) [131]

The stability of the Kondo singlet is often influenced by the other degrees of freedom such as the inter-site interactions. For example, the RKKY interaction  $|J_{RKKY}|$  becomes stronger with increasing impurity concentration. When the formation energy of the spin glass per magnetic atom exceeds the Kondo temperature  $T_{\rm K}$ , the spin glass state is stabilized with the appearance of local magnetic moments.

The many-body problem in the dilute magnetic alloys is called the Kondo problem, and associated anomalies are called the Kondo effects. Historically the Kondo effect was first found in the resistivity [120]. Resistivity usually decreases as the temperature decreases as is well known as Matthiessen's law. In fact it consists of the impurity scattering term and the phonon term. The former is independent of temperature, while the latter monotonically decreases with decreasing temperature. In the dilute magnetic alloys such as Cu–Mn and Au–Fe alloys, it was found that the resistivity shows a minimum at low temperatures. Kondo explained first the anomaly on the basis of the sd model (7.17) [120]. He showed that the second-order Born approximation to the resistivity R due to magnetic impurities contains the logarithmic term.

$$R = R_{\rm B} \left( 1 + \frac{4J_{\rm K}\rho(0)}{L} \ln \frac{T}{D} \right). \tag{7.77}$$

Here  $R_{\rm B}$  is the resistivity in the first Born approximation. D is the band width of conduction electrons. Although the logarithmic term explains the resistance minimum, it leads to the divergence of the resistivity at zero temperature, which is unphysical. Higher order perturbation expansions at finite temperatures again led to the divergence of the resistivity at  $T \sim T_{\rm K}$  [134]. The same behaviors were also found in the susceptibility and specific heat.

Yosida investigated the ground-state properties of the magnetic impurity, and found that the singlet state consisting of the localized electron and a conduction electron is stabilized at the ground state [135]. The binding energy was found to be  $T_K$ . Low temperature properties of the sd model were examined by Wilson on the

basis of the renormalization group theory [136]. He found that the ratio of the impurity susceptibility  $\chi_{\text{imp}}$  to the Sommerfeld coefficient due to impurity  $C_{\text{imp}}/T$ ,  $C_{\text{imp}}$  being the impurity contribution to the specific heat, is a temperature-independent constant  $R_{\text{W}}(=2)$ :

$$\frac{T_{\text{Ximp}}}{C_{\text{imp}}} = R_{\text{W}}.$$
(7.78)

The same result was obtained by Nozières on the basis of a phenomenological Fermi liquid theory [137]. Yamada and Yosida derived the relation exactly by means of the perturbation expansion approach to the symmetric Anderson model [138, 139]. Later the exact solution to the sd model was obtained by Andrei with use of the Bethe ansatz method [140]. The exact solution to the Anderson model was also obtained by Wiegmann [141], and Kawakami and Okiji [142] with use of the same method. The readers who are interested in the details of the Kondo problems are recommended to refer to the books by Yosida [143], and by Fulde [127].

The Kondo anomalies as the bulk properties are also found in rare-earth compounds containing Ce and U compounds. Low temperature specific heats of these compounds, for example, show a huge value which is typically 100–1000 times those of the usual metals, indicating the existence of electrons with heavy effective mass. These materials are called the heavy fermion system. Details on the topic are found in the books by Hewson [128] and by Fulde [144, 145].

# **Chapter 8 Magnetism of Disordered Alloys**

Substitutional disordered alloys show a variety of magnetic properties with changes in composition and temperature, which clarify the formation of magnetic moments in metals. In this chapter, we present the theories of itinerant magnetism in disordered alloys, and clarify the magnetic properties of 3d transition metal alloys. We first overview in Sect. 8.1 the magnetization vs. concentration curves in transition metal alloys which are known as the Slater-Pauling curves, and present a simple picture based on the rigid band model and Friedel's virtual bound state. In Sect. 8.2, we introduce the coherent potential approximation (CPA) to treat the configurational disorder within the single-site approximation (SSA). We then present the Hartree– Fock (HF) CPA theory at the ground state and extend the finite-temperature theory presented in Sect. 3.3 to disordered alloys. Since the SSA does not consider the inter-site correlations of the magnetic moments due to configurational disorder, we present in Sect. 8.3 the ground-state theory of the local environment effects (LEE) which goes beyond the HF-CPA. Next we present the theory of the LEE at finite temperatures. In the last Sect. 8.4, we extend the molecular dynamics theory presented in Sect. 6.3 to the disordered alloys to describe more complex system, and argue the magnetism of Fe-Cr alloys showing the ferromagnetism, the antiferromagnetism, and the spin glass.

## 8.1 Slater-Pauling Curves

The substitutional disordered alloys containing 3d transition metals have been much investigated to understand the formation of metallic magnetism and to clarify the effects of disorder on their magnetism. Experimentally the ground-state magnetization vs. concentration curves in 3d transition metal alloys are well-known as the Slater–Pauling curves [146]. Understanding of the systematic change of their magnetizations has been one of the central issues of magnetism in disordered alloys. We briefly explain in this section a global behavior of the magnetism.

Figure 8.1 shows the Slater–Pauling curves in various transition metal alloys. The curves consist of the line with the slope  $-45^{\circ}$  from Cu to Fe which includes Ni–Cu,

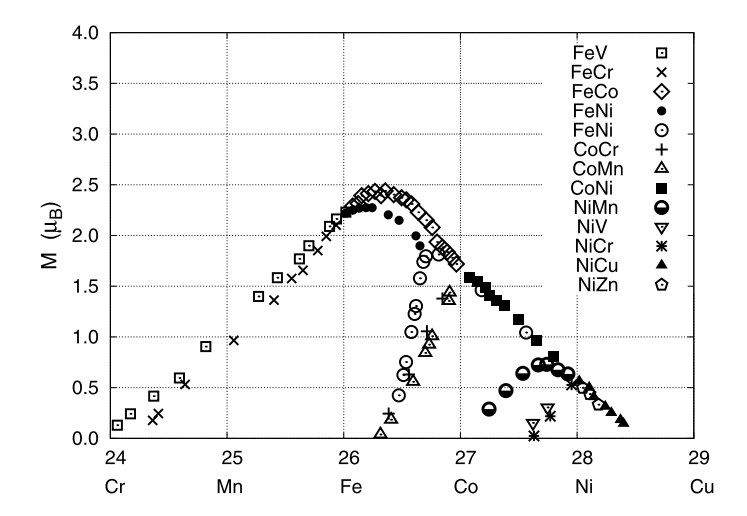


Fig. 8.1 Slater–Pauling curves in transition metal alloys as a function of atomic number [146]

Ni–Co, Co–Fe, and Fe–Ni alloys, the 45° line from Fe to Cr which includes Fe–V and Fe–Cr, and the other branches showing a rapid decrease of magnetization with adding the second elements.

The ground-state magnetization M per atom is given by the up-spin valence electron number  $N_{\uparrow}$  minus the down-spin valence electron number  $N_{\downarrow}$ :  $M = N_{\uparrow} - N_{\downarrow}$ . Since the total valence electron number Z is given by  $Z = N_{\uparrow} + N_{\downarrow}$ , the magnetization is expressed as

$$M = 2N_{\uparrow} - Z. \tag{8.1}$$

The zeroth approximation is to assume that electrons feel a common potential so that they occupy a common band as in the case of the pure metal. This is referred as the rigid-band model. In the rigid band model, Ni and Co alloys are considered to be strong ferromagnets in which the up spin band is filled as shown in the left of Fig. 8.2. In this case,  $N_{\uparrow}$  is constant and the magnetization increases with decreasing Z according to (8.1). This explains the  $-45^{\circ}$  line in the Slater-Pauling curves. It is interpreted that the Fermi level touches the top of the up-spin band around Z=8.25 and the atomic level for down spin electron  $\varepsilon_{\downarrow}$  starts to decrease due to the Hartree-Fock type potential  $\varepsilon_{\downarrow}=\varepsilon_0+UN_{\uparrow}$ , so that  $N_{\downarrow}$  is kept constant with decreasing Z (see the right of Fig. 8.2). Then the magnetization decreases with decreasing Z along the 45° line according to the expression  $M=Z-2N_{\downarrow}$  as found in the Slater-Pauling curves of Fe-Cr and Fe-V alloys (see Fig. 8.1).

For a more detailed explanation, we can take into account explicitly the concentration dependence of  $N_{\uparrow}$  and Z as  $N_{\uparrow} = N_{d\uparrow} + N_{sp\uparrow}$ ,  $N_{d\uparrow} = cN_{d\uparrow}^A + (1-c)N_{d\uparrow}^B$ , and  $Z = cZ_A + (1-c)Z_B$ . Here  $N_{d\uparrow}$  ( $N_{sp\uparrow}$ ) is the d (sp) electron number per atom,  $N_{d\uparrow}^A$  ( $N_{d\uparrow}^B$ ) is the d electron number for atom A (B),  $Z_A$  ( $Z_B$ ) is the valence electron number of atom A (B), and c denotes the concentration of atom A. Substituting

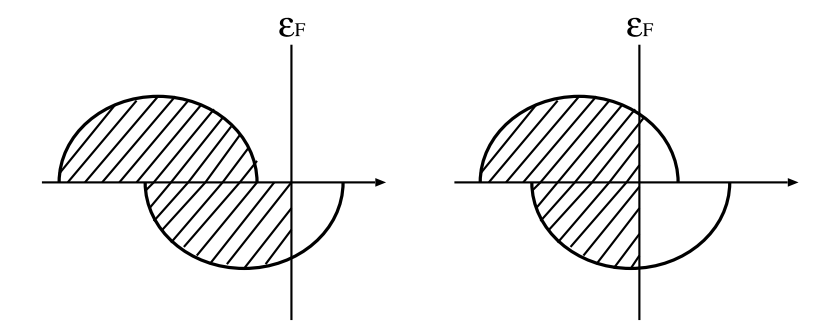


**Fig. 8.2** Schematic densities of states for the strong ferromagnet (*left*) and the weak ferromagnet (*right*)

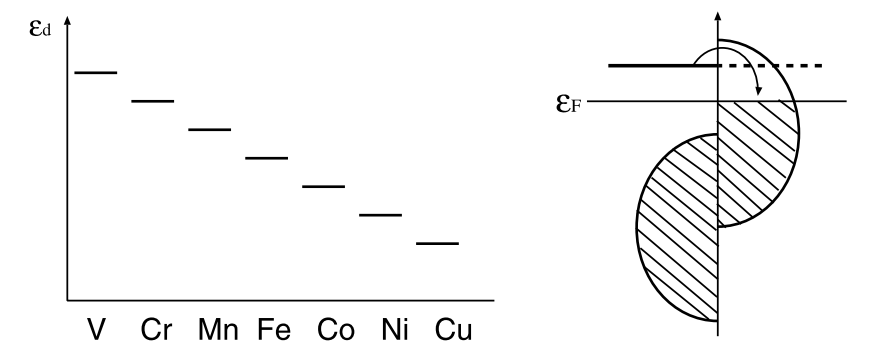


**Fig. 8.3** Systematic change in atomic d levels of 3d transition metals (*left*) and the virtual bound states above the Fermi level  $\varepsilon_F$  (*right*)

these relations into (8.1) and using the magnetization  $M_B$  of the matrix B, we obtain the following expression.

$$M = M_{\rm B} - c \left[ Z_{\rm A} - Z_{\rm B} - 2 \left( N_{\rm d\uparrow}^{\rm A} - N_{\rm d\uparrow}^{\rm B} \right) \right]. \tag{8.2}$$

The Ni–Cu, Ni–Co, and Ni<sub>1-c</sub>Fe<sub>c</sub> (c < 0.75) alloys are strong ferromagnets so that  $N_{\rm d\uparrow}^{\rm A} = N_{\rm d\uparrow}^{\rm B} = 5$ . Equation (8.2) then reduces to  $M = M_{\rm Ni} - c(Z_{\rm A} - 10)$ . Thus we again obtain the curve with the  $-45^{\circ}$  slope in agreement with the experimental data shown in Fig. 8.1. The same argument is applicable to the Co–Ni and Co–Fe alloys.

The concentration dependence of the magnetization in Ni–Cr alloys is quite different from those following the  $-45^{\circ}$  line. Note that the atomic d level  $\varepsilon_{d}$  decreases with increasing the atomic number because the attractive interaction between electron and nucleus becomes stronger (see the l.h.s. of Fig. 8.3). Thus the difference in atomic level  $\Delta\varepsilon_{d}$  between Cr and Ni is expected to be large as compared with the d band width, so that an impurity bound state called the virtual bound state [147] may appear above the Fermi level as shown in the r.h.s. of Fig. 8.3. We have then

 $N_{\rm d\uparrow}^{\rm A}=0$  and  $N_{\rm d\uparrow}^{\rm B}=5$ . The magnetization (8.2) is then expressed as

$$M = M_{\rm B} - c(Z_{\rm A} - Z_{\rm B} + 10). \tag{8.3}$$

Thus we have  $M - M_{\rm B} = -6c$  for Ni–Cr, and  $M - M_{\rm B} = -5c$  for Ni–V. These results explain the branches at Ni in the Slater–Pauling curves (Fig. 8.1). In the same way we obtain  $M - M_{\rm B} = -7c$  for Co–Cr, and  $M - M_{\rm B} = -8c$  for Co–Mn. The results explain the branches at Co in the Slater–Pauling curves [148].

### 8.2 Single-Site Theory of Disordered Alloys

Although a simple interpretation of the Slater–Pauling curves is presented in the last section and it is easy to understand the global behavior of the curves on the basis of a simple interpretation, the role of the electronic structure of disordered alloys behind the phenomena is not clear. In order to understand the magnetic properties of the alloys one must know their electronic structure from a microscopic point of view. Electronic structure calculations in disordered alloys, however, is not easy. The difficulty is that there is no translational symmetry in the system so that we cannot apply the Bloch theory. We present in this section the coherent potential approximation (CPA) [51] to calculate the electronic structure of alloys in the single-site approximation, and demonstrate how the Hartree–Fock CPA theory can explain the Slater–Pauling curves [149, 150]. Furthermore we extend the finite-temperature theory presented in Sect. 3.3 to the disordered alloys.

Let us consider the A–B substitutional binary alloys showing the ferromagnetism, which is described by the Hubbard model in the Hartree–Fock approximation as follows (see (2.7)).

$$H = \sum_{i\sigma} \varepsilon_{i\sigma} n_{i\sigma} + \sum_{ij\sigma} t_{ij} a_{i\sigma}^{\dagger} a_{j\sigma}. \tag{8.4}$$

Here  $\varepsilon_{i\sigma} = \varepsilon_i^0 + U \langle n_i \rangle / 2 - U \langle m_i \rangle \sigma / 2$  is the Hartree–Fock atomic potential on site *i*.  $t_{ij}$  is the transfer integral between sites *i* and *j*. Note that the atomic level  $\varepsilon_i^0$  as well as the charge and spin densities  $(\langle n_i \rangle)$  and  $\langle m_i \rangle$  are now site-dependent.

The local charge and magnetic moment on site i are given by

$$\langle n_i \rangle = \int d\omega f(\omega - \mu) \sum_{\sigma} \rho_{i\sigma}(\omega),$$
 (8.5)

$$\langle m_i \rangle = \int d\omega \, f(\omega - \mu) \sum_{\sigma} \sigma \rho_{i\sigma}(\omega).$$
 (8.6)

Here  $f(\omega)$  is the Fermi distribution function, and  $\mu$  denotes the chemical potential.  $\rho_{i\sigma}(\omega)$  is the density of states on site i for an electron with spin  $\sigma$  in the Hartree–Fock approximation. It is given by the Green function  $G_{ii\sigma}(z)$  with  $z = \omega + i\delta$  as

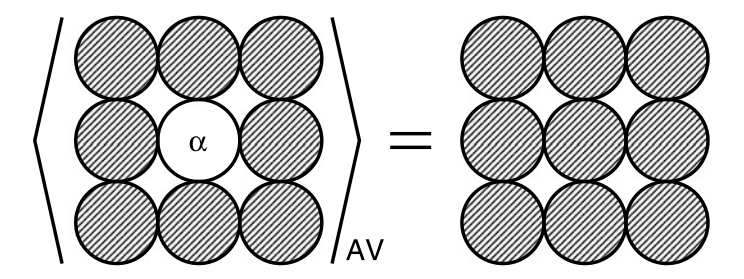


**Fig. 8.4** Schematic representation of the coherent potential approximation [151]. The central site is occupied by an atom  $\alpha$  (= A or B). The hatched sites are occupied by a coherent potential  $\Sigma_{\sigma}(z)$ .  $\langle \ \rangle_{AV}$  at the l.h.s. means a configurational average on the central site

follows.

$$\rho_{i\sigma}(\omega) = -\frac{1}{\pi} \operatorname{Im} G_{ii\sigma}(z), \tag{8.7}$$

$$G_{ii\sigma}(z) = \left[ (z - \boldsymbol{H}_{\sigma})^{-1} \right]_{ii}.$$
 (8.8)

Here  $\boldsymbol{H}_{\sigma}$  is the Hartree–Fock one-electron Hamiltonian matrix defined by  $(\boldsymbol{H}_{\sigma})_{ij} = \varepsilon_{i\sigma}\delta_{ij} + t_{ij}(1 - \delta_{ij})$ .

In the binary alloys, the atomic levels  $\varepsilon_{i\sigma}$  take a value:  $\varepsilon_{A\sigma}$  ( $\varepsilon_{B\sigma}$ ) when site i is occupied by atom A (B). We neglect the disorder of transfer integrals called the off-diagonal disorder. Because the atomic levels  $\varepsilon_{i\sigma}$  are random variables, the Bloch theory is not applicable for the calculation of the Green function. We make use of the coherent potential approximation (CPA) here to obtain the Green function with use of the locator expansion [151]. Introducing the locator matrix L by means of  $(L)_{ij} = L_i \delta_{ij} = (z - \varepsilon_i)^{-1} \delta_{ij}$ , we express the Green function matrix as  $G = (L^{-1} - t)^{-1} = (1 - Lt)^{-1}L$  where t denotes the transfer integral matrix  $t_{ij}$ . Expanding the Green function with respect to t, we obtain

$$G_{ii}(z) = L_i + \sum_{j \neq i} L_i t_{ij} L_j t_{ji} L_i + \sum_{j \neq i} \sum_{k \neq j, i} L_i t_{ij} L_j t_{jk} L_k t_{ki} L_i + \cdots . \quad (8.9)$$

Here we have omitted the spin suffix for simplicity. The r.h.s. of (8.9) consists of the contribution from all the paths which start from site i and end at the same site i. They are expressed as follows by using the sum of all the paths  $S_i$  which start from site i end at site i without returning to site i on the way.

$$G_{ii}(z) = L_i + L_i S_i L_i + L_i S_i L_i S_i L_i + \dots = (L_i^{-1} - S_i)^{-1}.$$
 (8.10)

In the above expression, all the information outside the central atom i is in the self-energy  $S_i$ . To obtain the Green function  $G_{ii}(z)$  in a single-site approximation, we approximate the random potentials on the surrounding sites with an energy-dependent coherent potential  $\Sigma(z)$  (see the l.h.s. of Fig. 8.4). Note that the same idea was used in the metal-insulator transition [9, 10] and the single-site theory of

spin fluctuations (see Sects. 3.3 and 3.4). We have then an impurity Green function for atom  $\alpha$  on site i from (8.10) as follows.

$$G_{\alpha\sigma}(z) = \left(L_{\alpha\sigma}^{-1} - \mathcal{S}_{\sigma}\right)^{-1}.$$
 (8.11)

Here  $L_{\alpha\sigma}^{-1} = z - \varepsilon_{\alpha\sigma}$  is the inverse locator on the central site with a type of atom  $\alpha$ .  $\mathcal{S}_{\sigma}$  is the self energy in which all the atomic levels have been replaced by the coherent potential  $\Sigma_{\sigma}(z)$ . Note that we have omitted the site indices for simplicity and have recovered the spin suffix.

The self-energy  $\mathscr{S}_{\sigma}$  is obtained from the coherent Green function  $F_{\sigma}(z)$  in which all the sites are occupied by the coherent potential (see the r.h.s. of Fig. 8.4).

$$F_{\sigma}(z) = \left(\mathcal{L}_{\sigma}^{-1} - \mathcal{S}_{\sigma}\right)^{-1}.\tag{8.12}$$

Here  $\mathcal{L}_{\sigma}^{-1}(z) = z - \Sigma_{\sigma}(z)$ . Substituting  $\mathcal{L}_{\sigma}$  obtained from (8.12) into (8.11), we obtain the impurity Green function as follows.

$$G_{\alpha\sigma}(z) = \left(L_{\alpha\sigma}^{-1}(z) - \mathcal{L}_{\sigma}^{-1}(z) + F_{\sigma}^{-1}(z)\right)^{-1}.$$
 (8.13)

Since the coherent Green function  $F_{\sigma}(z)$  is defined by  $F_{\sigma}(z) = [(z - \Sigma_{\sigma}(z) - t)^{-1}]_{ii}$ , it is obtained from the following formula.

$$F_{\sigma}(z) = \int \frac{\rho(\varepsilon) d\varepsilon}{\mathcal{L}_{\sigma}^{-1}(z) - \varepsilon}.$$
 (8.14)

Here  $\rho(\varepsilon)$  is the density of states (DOS) for the energy eigen values of transfer matrix  $t_{ij}$ .

The coherent potential  $\Sigma_{\sigma}(z)$  (or coherent locator  $\mathcal{L}_{\sigma}(z)$ ) is obtained from the condition that the configurational average of the impurity Green function (8.13) should be identical with the coherent Green function (see Fig. 8.4).

$$\sum_{\alpha} c_{\alpha} G_{\alpha\sigma}(z) = F_{\sigma}(z). \tag{8.15}$$

Here  $c_{\alpha}$  denotes the concentration of atom  $\alpha$ . The above equation is known as the CPA equation. The same type of self-consistent equation was obtained in (3.85). There the random potential was produced by thermal spin fluctuations, and the thermal average was taken at the l.h.s. of the CPA equation.

When the off-diagonal disorder in transfer integrals is significant, we can take into account the effects assuming that the transfer integral  $t_{AB}$  between atoms A and B is given by the geometrical mean of  $t_{AA}$  and  $t_{BB}$ . This means that the transfer integrals are expressed with use of the parameters  $r_i$  and  $r_j$  as

$$t_{ij} = r_i^* t_{\text{BB}} r_j. \tag{8.16}$$

Here  $|r_i| = \sqrt{|t_{AA}|/|t_{BB}|}$  for i = A and 1 for i = B. In this case the off-diagonal disorder reduces to the diagonal disorder by considering  $r_i^* G_{ii}(z) r_i$ ;  $r_i^* G_{ii}(z) r_i$  reduces to (8.9) in which  $\{L_i\}$  have been replaced by  $\{L_i = |r_i|^2/(z - \varepsilon_{i\sigma})\}$ . Equation

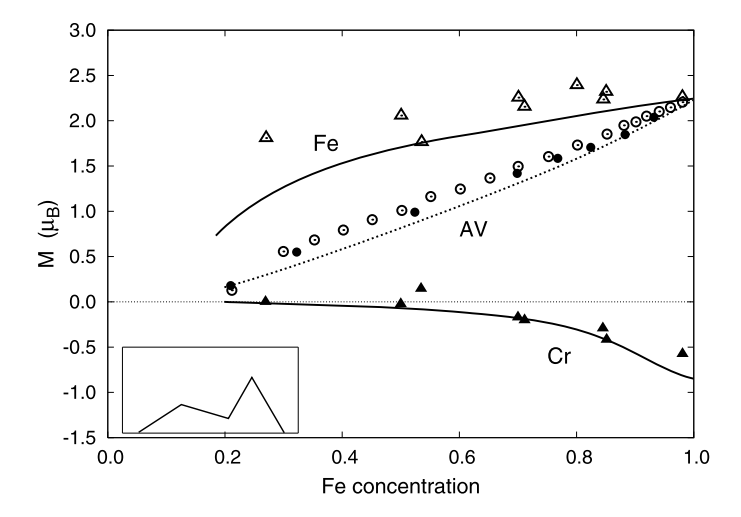


Fig. 8.5 Concentration dependences of average magnetic moment (AV:  $\langle m \rangle$ ), and the local moments of Fe and Cr atoms,  $\langle m_{\rm Fe} \rangle$  and  $\langle m_{\rm Cr} \rangle$  of Fe<sub>x</sub>Cr<sub>1-x</sub> alloys [152]. The *solid lines* show the result calculated by the Hartree–Fock CPA theory with use of the model density of state depicted in the lower-left corner. Experimental data are shown by  $\bullet$ ,  $\circ$  [153–155],  $\triangle$ ,  $\blacktriangle$  [156–158]

#### (8.13) is then replaced by

$$G_{\alpha\sigma}(z) = |r_{\alpha}|^{-2} \left( L_{\alpha\sigma}^{-1}(z) - \mathcal{L}_{\sigma}^{-1}(z) - F_{\sigma}^{-1}(z) \right)^{-1}, \tag{8.17}$$

where  $L_{\alpha\sigma}^{-1} = (z - \varepsilon_{\alpha\sigma})/|r_{\alpha}|^2$ . The CPA equation (8.15) should be replaced by

$$\sum_{\alpha} c_{\alpha} |r_{\alpha}|^2 G_{\alpha\sigma}(z) = F_{\sigma}(z). \tag{8.18}$$

The atomic level  $\varepsilon_{\alpha\sigma}$  in the impurity Green function  $G_{\alpha\sigma}(z)$  is given by  $\varepsilon_{\alpha\sigma} = \varepsilon_{\alpha}^{0} + U\langle n_{\alpha}\rangle/2 - U\langle m_{\alpha}\rangle\sigma/2$ . The impurity charge  $\langle n_{\alpha}\rangle$  and magnetic moment  $\langle m_{\alpha}\rangle$  are calculated from  $G_{\alpha\sigma}(z)$  via the Hartree–Fock equations (8.5) and (8.6) self-consistently. In actual applications the Coulomb interaction U in the Hartree–Fock CPA theory has to be regarded as an effective interaction parameter which is renormalized due to electron correlations (see Sect. 2.2). In the self-consistent calculations, the noninteracting model DOS  $\rho(\varepsilon)$  in the coherent Green function (8.14) is usually taken from band calculations.

The Hartree–Fock CPA theory explains the basic properties of the Slater–Pauling curves presented in Fig. 8.1. Figure 8.5 shows the magnetic moments vs. concentration curves of  $Fe_{1-x}Cr_x$  alloys calculated by the theory [152]. Because of the single band model, we multiplied the results by a factor of 5, and compared them with the experimental data. The averaged magnetic moment monotonically decreases with increasing Cr concentration in agreement with the experimental data. The Fe magnetic moments are parallel to the bulk magnetization and build up the ferromagnetism. The atomic level of Cr is above the Fermi level, and the down-spin

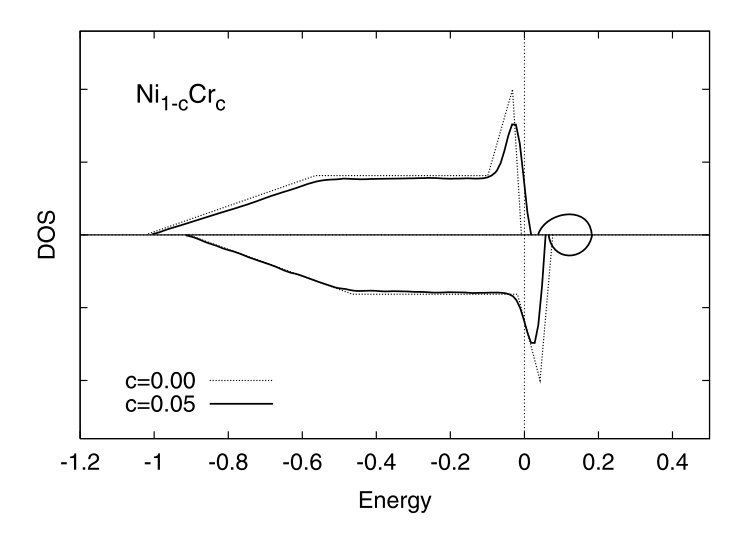


**Fig. 8.6** Calculated densities of states of  $Ni_{1-c}Cr_c$  [149, 150]

bands of Cr sites more hybridize with those of Fe sites. This increases the down-spin states of Cr sites below the Fermi level. Thus, the average Cr magnetic moment is antiparallel to the bulk magnetization. The Cr atoms lose the magnetic moment around 70 at% Cr. These results explain the neutron data for the magnetic moments [154–157].

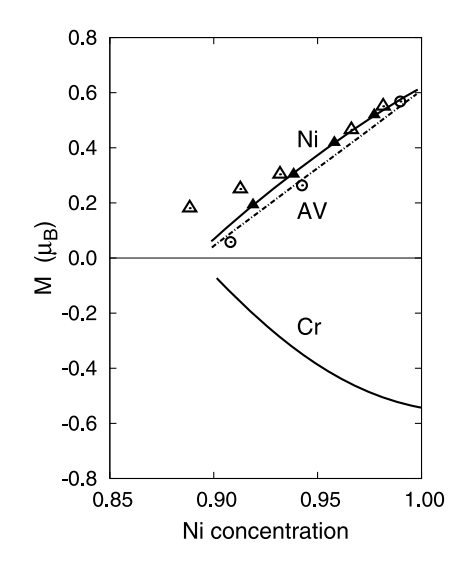
Figure 8.6 shows the calculated DOS in  $Ni_{1-x}Cr_x$  alloys [149, 150]. In the small Cr concentrations, we find the virtual bound state above the Fermi level which was assumed in the last section. It develops with increasing Cr concentration. The strong ferromagnetism collapses around 5 at% Cr, and the alloy loses the average magnetic moment around 10 at% Cr in agreement with the experimental data as shown in Fig. 8.7.

At finite temperatures we need to extend the single-site theory presented in Sects. 3.3 and 3.7 to the disordered alloys. Since the disordered alloys are complex system, we apply a simplified model; we adopt the 5-fold equivalent band model (i.e., 5 times the single band model). Furthermore we adopt the static approximation (i.e., the high-temperature approximation) and omit the transverse spin fluctuations. The free energy (6.52) is then written as

$$\mathscr{F} = -\beta^{-1} \ln \int \left[ \prod_{i} \sqrt{\frac{\beta \tilde{J}_{i}}{4\pi}} d\xi_{i} \right] e^{-\beta E(\xi)}. \tag{8.19}$$

In the above expression,  $\tilde{J}_i$  is the effective exchange energy defined by  $\tilde{J}_i = U_0/D + (1-1/D)J$ , D being the orbital degeneracy (D=5). The effective potential  $E(\xi)$ 

Fig. 8.7 Calculated magnetic moments of Ni and Cr as well as the average in Ni<sub>1-c</sub>Cr<sub>c</sub> alloys [149, 150]. The experimental average moments are shown by  $\triangle$  [159],  $\bigcirc$  [160], and  $\blacktriangle$  [161]



is obtained from (6.53) as

$$E(\xi) = -\beta^{-1} \ln \operatorname{tr} \left( e^{-\beta H(\xi)} \right) - \frac{1}{4} \sum_{i} \left( \tilde{U}_{i} \, \tilde{n}_{i}(\xi)^{2} - \tilde{J}_{i} \, \xi_{i}^{2} \right). \tag{8.20}$$

Here the effective Coulomb interaction  $\tilde{U}_i$  is defined by  $\tilde{U}_i = U_0/D + (1 - 1/D)(2U_1 - J)$ .  $\tilde{n}_i(\xi)$  is the Hartree–Fock charge on site i when the 'magnetic moments'  $\{\xi_i\}$  are given (see (6.58)).

$$\tilde{n}_i(\xi) = \sum_m \langle n_{im} \rangle_0 = \frac{\operatorname{tr}(\sum_m n_{im} e^{-\beta H(\xi)})}{\operatorname{tr}(e^{-\beta H(\xi)})}.$$
(8.21)

The Hamiltonian  $H(\xi)$  is given as follows (see (6.57)).

$$H(\xi) = \sum_{m} \left[ \sum_{i\sigma} \left( \varepsilon_{i}^{0} - \mu + \frac{1}{2} \tilde{U}_{i} \tilde{n}_{i}(\xi) - \frac{1}{2} \tilde{J}_{i} \xi_{i} \sigma \right) n_{im\sigma} + \sum_{ij\sigma} t_{ij} a_{im\sigma}^{\dagger} a_{jm\sigma} \right]. \tag{8.22}$$

In order to treat the disorder of alloys, we rewrite the energy potential  $E(\xi)$  as

$$E(\xi) = \int d\omega f(\omega) \frac{D}{\pi} \operatorname{Im} \operatorname{tr} \left[ \ln(z - \boldsymbol{H}) \right] - \frac{1}{4} \sum_{i} \left( \tilde{U}_{i} \, \tilde{n}_{i}(\xi)^{2} - \tilde{J}_{i} \, \xi_{i}^{2} \right). \quad (8.23)$$

Here the Hamiltonian matrix  $\mathbf{H}$  is defined by

$$(\boldsymbol{H})_{i\sigma j\sigma'} = \left[ \left( \varepsilon_i^0 - \mu + \frac{1}{2} \, \tilde{U}_i \, \tilde{n}_i(\xi) - \frac{1}{2} \, \tilde{J}_i \, \xi_i \, \sigma \right) \delta_{ij} + t_{ij} \right] \delta_{\sigma\sigma'}. \tag{8.24}$$

We assume again the geometrical mean for the transfer integral;  $t_{ij} = r_i^* t_{ij}^0 r_j$ . Introducing the r matrix by means of  $(r)_{i\sigma j\sigma'} = r_i \delta_{ij} \delta_{\sigma\sigma'}$ , we can express the integrand of the first term in (8.23) as

$$\operatorname{Im}\operatorname{tr}\left[\ln(z-\boldsymbol{H})\right] = \operatorname{Im}\operatorname{tr}\left[\ln(r^{\dagger}L^{-1}r - r^{\dagger}t^{0}r)\right] = \operatorname{Im}\operatorname{tr}\left[\ln(L^{-1} - t^{0})\right]. \tag{8.25}$$

Here the locator is defined by

$$(L^{-1})_{i\sigma j\sigma'} = L_{i\sigma}^{-1} \delta_{ij} \delta_{\sigma\sigma'} = \frac{z - \varepsilon_i^0 + \mu - \frac{1}{2} \tilde{U}_i \tilde{n}_i(\xi) + \frac{1}{2} \tilde{J}_i \xi_i \sigma}{|r_i|^2} \delta_{ij} \delta_{\sigma\sigma'}. \quad (8.26)$$

Introducing an effective locator  $\mathcal{L}_{\sigma}(z)$  into the r.h.s. of (8.25), we expand it with respect to the site as

$$\operatorname{tr}\left[\ln(L^{-1} - t^{0})\right] = \operatorname{tr}\ln(\mathcal{L}^{-1} - t^{0}) + \operatorname{tr}\ln\left[1 + (L^{-1} - \mathcal{L}^{-1})F\right] + \operatorname{tr}\ln\left(1 - \tilde{t}F'\right). \tag{8.27}$$

Here F and F' are the diagonal and the off-diagonal coherent Green functions defined by  $F_{ij\sigma} = [(\mathcal{L}^{-1} - t^0)^{-1}]_{ii\sigma} \delta_{ij}$  and  $(F')_{ij\sigma} = [(\mathcal{L}^{-1} - t^0)^{-1}]_{ij\sigma} (1 - \delta_{ij})$ , respectively.  $\tilde{t}$  is the single-site t matrix defined by

$$\tilde{t} = -\left[1 + (L^{-1} - \mathcal{L}^{-1})F\right]^{-1} (L^{-1} - \mathcal{L}^{-1}). \tag{8.28}$$

Substituting (8.27) into (8.23) and neglecting the nonlocal term (i.e., F' term), we obtain the free energy per site in the single-site approximation as follows.

$$\mathcal{F}_{\text{CPA}} = \int d\omega f(\omega) \frac{1}{N} \frac{D}{\pi} \text{Im tr ln} \left( \mathcal{L}^{-1}(z) - t^0 \right)$$
$$-\beta^{-1} \sum_{\alpha} c_{\alpha} \ln \int \sqrt{\frac{\beta \tilde{J}_{\alpha}}{4\pi}} d\xi \, e^{-\beta E_{\alpha}(\xi)}, \tag{8.29}$$

$$E_{\alpha}(\xi) = \int d\omega f(\omega) \frac{D}{\pi} \operatorname{Im} \sum_{\sigma} \ln \left[ 1 + \left( L_{\alpha\sigma}^{-1}(z, \xi) - \mathcal{L}_{\sigma}^{-1}(z) \right) F_{\sigma}(z) \right]$$
$$- \frac{1}{4} \tilde{U}_{\alpha} \tilde{n}_{\alpha}(\xi)^{2} + \frac{1}{4} \tilde{J}_{\alpha} \xi^{2}.$$
 (8.30)

Here  $F_{\sigma}(z)$  is the coherent Green function given by (8.14).  $L_{\alpha\sigma}^{-1}(z,\xi)$  is defined by the diagonal part of (8.26) in which site *i* is occupied by atom  $\alpha$ .

$$L_{\alpha\sigma}(z,\xi)^{-1} = \frac{z - \varepsilon_{\alpha}^{0} + \mu - \frac{1}{2}\tilde{U}_{\alpha}\tilde{n}_{\alpha}(\xi) + \frac{1}{2}\tilde{J}_{\alpha}\xi\sigma}{|r_{\alpha}|^{2}}.$$
 (8.31)

The local charge on atom  $\alpha$ ,  $\tilde{n}_{\alpha}(\xi)$  at the r.h.s. of (8.30) and (8.31) is given by

$$\tilde{n}_{\alpha}(\xi) = \int d\omega f(\omega) \sum_{\sigma} \rho_{\alpha\sigma}(\omega, \xi), \qquad (8.32)$$

and the density of states  $\rho_{\alpha\sigma}(\omega,\xi)$  is obtained from the Green function as

$$\rho_{\alpha\sigma}(\omega) = -\frac{D}{\pi} \operatorname{Im} G_{\alpha\sigma}(z,\xi). \tag{8.33}$$

The Green function  $G_{\alpha\sigma}(z,\xi)$  is given by (8.17) in which  $L_{\alpha\sigma}(z)^{-1}$  has been replaced by (8.31).

The effective medium  $\mathcal{L}_{\sigma}^{-1}(z)$  is determined by the condition that the t matrix vanishes in average so that the nonlocal correlations at the r.h.s. of (8.27) become minimum.

$$\langle \tilde{t}(z,\xi) \rangle \equiv \sum_{\alpha} c_{\alpha} \int d\xi \ p_{\alpha}(\xi) \, \tilde{t}_{\alpha}(z,\xi) = 0.$$
 (8.34)

Here  $p_{\alpha}(\xi)$  is the probability of finding a 'magnetic moment'  $\xi$  on atom  $\alpha$ , and is given by

$$p_{\alpha}(\xi) = \frac{e^{-\beta E_{\alpha}(\xi)}}{\int d\xi \, e^{-\beta E_{\alpha}(\xi)}}.$$
(8.35)

Note that (8.34) is equivalent to the following equation, which is known as the CPA equation.

$$\sum_{\alpha} c_{\alpha} \int d\xi \ p_{\alpha}(\xi) |r_{\alpha}|^2 G_{\alpha\sigma}(z,\xi) = F_{\sigma}(z). \tag{8.36}$$

This is the extension of the Hartree–Fock CPA equation (8.18) to the finite temperature [162], and it reduces to the Hartree–Fock CPA equation (8.18) when  $T \to 0$ . Equations (8.32) and (8.36) form the self-consistent equations for  $\tilde{n}_{\alpha}(\xi)$  and  $\mathcal{L}_{\sigma}^{-1}(z)$ .

The local charge and magnetic moment of atom  $\alpha$  are obtained as (see (3.258) and (3.259))

$$\langle n_{\alpha} \rangle = \langle \tilde{n}_{\alpha}(\xi) \rangle = \int d\xi \ p_{\alpha}(\xi) \tilde{n}_{\alpha}(\xi),$$
 (8.37)

$$\langle m_{\alpha} \rangle = \langle \xi_{\alpha} \rangle = \int d\xi \ p_{\alpha}(\xi) \, \xi.$$
 (8.38)

In the actual calculations, it is convenient to introduce a charge neutrality potential  $\{w_i(\xi)\}\$ . The potential due to the spin polarization is defined by

$$w_i(\xi) = \frac{1}{2} \tilde{U}_i (\tilde{n}_i(\xi) - \tilde{n}_i(0)).$$
 (8.39)

With use of the relation  $\tilde{n}_i(\xi) = 2w_i(\xi)/\tilde{U}_i + \tilde{n}_i(0)$ , we can rewrite the effective potential as

$$E(\xi) = -\beta^{-1} \ln \operatorname{tr} \left( e^{-\beta H(\xi)} \right)$$

$$- \sum_{i} \left( \frac{1}{4} \tilde{U}_{i} \tilde{n}_{i}(0)^{2} + w_{i}(\xi) \, \tilde{n}_{i}(0) + \frac{1}{\tilde{U}_{i}} w_{i}(\xi)^{2} - \frac{1}{4} \tilde{J}_{i} \, \xi_{i}^{2} \right), \qquad (8.40)$$

$$H(\xi) = \sum_{m} \left[ \sum_{i\sigma} \left( \tilde{\varepsilon}_{i} + w_{i}(\xi) - \frac{1}{2} \tilde{J}_{i} \, \xi_{i} \, \sigma \right) n_{im\sigma} + \sum_{ij\sigma} t_{ij} \, a_{im\sigma}^{\dagger} a_{jm\sigma} \right]. \tag{8.41}$$

Here the atomic level in the nonmagnetic state is defined by  $\tilde{\varepsilon}_i = \varepsilon_i^0 - \mu + \tilde{U}_i \tilde{n}_i(0)/2$ .

Eliminating the constant term  $\tilde{U}_i \tilde{n}_i(0)^2/4$  from (8.40), and taking the large Coulomb interaction limit  $(\tilde{U}_i \to \infty)$ , we obtain the effective potential as

$$E(\xi) = -\beta^{-1} \ln \operatorname{tr} \left( e^{-\beta H(\xi)} \right) - \sum_{i} \left( w_i(\xi) \, n_i - \frac{1}{4} \, \tilde{J}_i \, \xi_i^2 \right). \tag{8.42}$$

Here  $n_i = \tilde{n}_i(0)$  is the d electron number of each atom which is usually taken to be the value of the constituent metal in the pure limit because of the charge neutrality on each atom.

The self-consistent equation to determine  $w_i(\xi)$  is obtained from (8.39) with  $\tilde{U}_i \to \infty$  as follows.

$$n_i = \tilde{n}_i \left( \left\{ \tilde{\varepsilon}_i + w_i(\xi) - \frac{1}{2} \tilde{J}_i \xi_i \sigma \right\} \right). \tag{8.43}$$

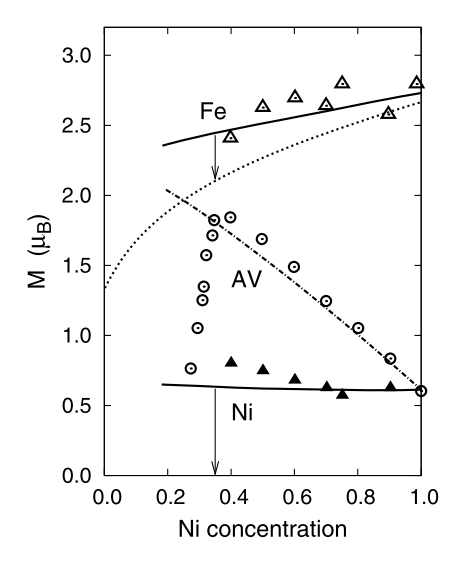
The above equation implies that we can determine the charge potential  $\varepsilon_i + w_i(\xi)$  from the charge neutrality condition on each site. Equation (8.43) reduces the number of adjustable parameters such as the atomic levels and the effective Coulomb interaction parameters  $\tilde{U}_{\alpha}$ , and allow us to determine automatically the chemical potential.

When we adopt the charge neutrality potential, the energy potential (8.30) should be replaced by

$$E_{\alpha}(\xi) = \int d\omega f(\omega) \frac{D}{\pi} \operatorname{Im} \sum_{\sigma} \ln \left[ 1 + \left( L_{\alpha\sigma}^{-1}(z, \xi) - \mathcal{L}_{\sigma}^{-1}(z) \right) F_{\sigma}(z) \right]$$
$$- w_{\alpha}(\xi) n_{\alpha} + \frac{1}{4} \tilde{J}_{\alpha} \xi_{\alpha}^{2}.$$
(8.44)

The effective inverse locator  $L_{\alpha}^{-1}(z,\xi)$  in (8.36) and (8.44) should be replaced by  $L_{\alpha\sigma}^{-1}(z,\xi)=(z-\tilde{\varepsilon}_{\alpha}-w_{\alpha}(\xi)+\tilde{J}_{\alpha}\,\xi\,\sigma/2)/|r_{\alpha}|^2$ . The charge potentials  $w_{\alpha}(\xi)$  are determined by the charge neutrality condition (8.43) in which the suffix for site i has been replaced by the atom  $\alpha$ .

Fig. 8.8 Concentration dependence of magnetic moments at T = 0 K in  $Fe_c Ni_{1-c}$  alloys [162]. The solid curves are the local moments for each atom. The dot-dashed curve is the total magnetization. The dashed curve shows the magnitude of the local moment on Fe site in the paramagnetic state. The arrows means the transition to the paramagnetic state. Experimental data are shown by o (average magnetization),  $\triangle$  (Fe magnetic moment). and ▲ (Ni magnetic moment) [163, 164]



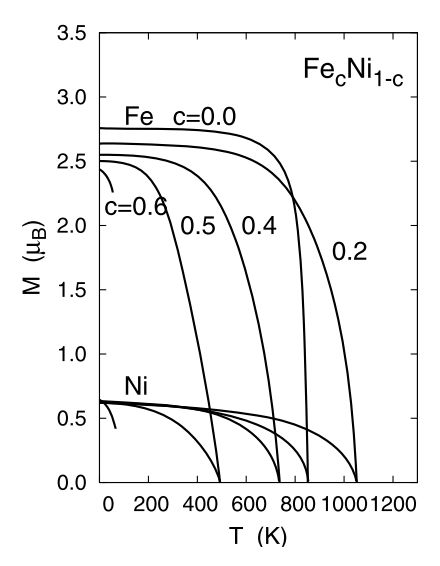
The Fe<sub>c</sub>Ni<sub>1-c</sub> alloys form the fcc lattice in the range  $0 \le c < 0.7$ , and show the ferromagnetic instability around 65 at% Fe where various anomalies called the Invar effects occur. We show in Fig. 8.8 the concentration dependence of magnetic moments calculated by the single-site theory of disordered alloys as an example [162]. With increasing Fe concentration, the Ni local moment (LM) hardly changes due to strong ferromagnetism, while the Fe LM gradually decreases. Calculated results explain the experimental data obtained by the neutron scattering up to 65 at% Fe. Around c = 0.6, the Fermi level reaches the top of the up-spin d band so that the instability of the ferromagnetism is induced. The single-site theory predicts the first-order transition from the ferromagnetic state to the paramagnetic state at  $c^* = 0.65$ , while the experimental data indicate the second-order transition. It is remarkable that the Fe LM remains even beyond  $c^*$  as shown in the figure. It suggests the existence of an ordered state after collapse of the ferromagnetism. Experimentally, the spin glass state is found beyond  $c^*$  [163], which will be discussed in the next section.

Figure 8.9 shows the concentration dependence of the Curie temperature calculated by the single-site theory of disordered alloys. The Curie temperature first increases with increasing Fe concentration, and shows the maximum around 20 at% Fe. It implies a strong ferromagnetic coupling between Fe and Ni LM as compared with Ni–Ni and Fe–Fe couplings. The result explains the experimental curve of  $T_{\rm C}$  qualitatively. The temperature dependences of Fe and Ni LM are shown in Fig. 8.10. The Fe LM in pure Ni (i.e., c=0) hardly changes with increasing temperature and rapidly decreases near  $T_{\rm C}$ , indicating a strong magnetic coupling between Fe and Ni LMs. On the other hand, both curves for Fe<sub>0.5</sub>Ni<sub>0.5</sub> alloys almost linearly decrease near  $T_{\rm C}$ . The result is consistent with the downward deviation from the S=1/2 Brillouin curve near  $c^*$  found in the experimental data.

Fig. 8.9 Concentration dependence of the Curie temperature in  $Fe_cNi_{1-c}$  alloys [162]. The *solid* (*dashed*) *curve* is the calculated result (observed one [146])

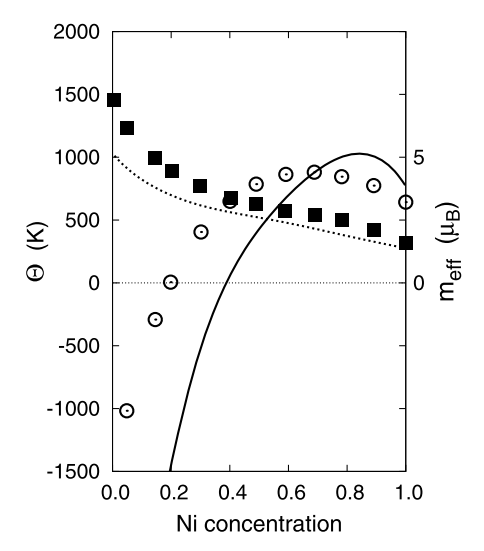
1400 1200 1000 1000 200 400 Expt. 200 0.0 0.2 0.4 0.6 0.8 1.0 Ni concentration

**Fig. 8.10** Temperature dependences of the local magnetic moments of each atom [162]. The Fe concentration is denoted by *c* 



Calculated paramagnetic spin susceptibility follows the Curie–Weiss law except in the case of pure Ni in which the inverse susceptibility shows upward convexity. Calculated effective Bohr magneton number monotonically increases with increasing Fe concentration as shown in Fig. 8.11, and the Weiss constant becomes negative beyond c=0.65 in agreement with the experimental data.

Fig. 8.11 Calculated effective Bohr magneton number  $m_{\rm eff}$  (dashed curve) and the Weiss constant  $\Theta$  (solid curve) [165]. Experimental values are shown by  $\blacksquare$  [166] and  $\bigcirc$  [167], respectively



## 8.3 Theory of Local Environment Effects in Magnetic Alloys

The magnetic properties of disordered alloys are often influenced strongly by the local electronic and magnetic configurations. In particular magnetic moments in the system with holes in the up-spin electron band change their magnitudes and directions depending on their local environments. The behaviors associated with the change of local electronic and magnetic states due to surrounding atomic configurations are known as the local environment effects (LEE). Since the effects are related with the intersite correlations, they are not described by the single-site theories presented in the last section. One needs a theory beyond the CPA. In this section we will present the theories of the LEE at zero temperature [168, 169] as well as at finite temperatures [170–172], and elucidate the LEE in the magnetism of Ni–Cu, Ni–Mn, and Fe–Ni alloys. Finally we summarize the numerical results on the Curie temperature Slater–Pauling curves as well as the Slater–Pauling curves in 3d transition metal alloys.

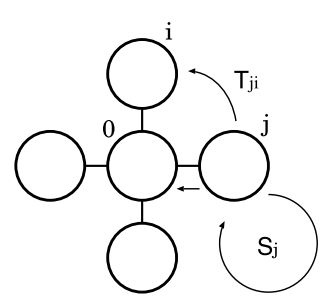
Let us start again from the local magnetic moment in the Hartree Fock approximation (8.6):

$$\langle m_i \rangle = \int d\omega f(\omega - \mu) \sum_{\sigma} \sigma \rho_{i\sigma}(\omega).$$
 (8.45)

The density of state  $\rho_{i\sigma}(\omega)$  is given by the Green function  $G_{ii\sigma}(z)$  as follows in the D-fold equivalent band model.

$$\rho_{i\sigma}(\omega) = -\frac{D}{\pi} \operatorname{Im} G_{ii\sigma}(z). \tag{8.46}$$

Fig. 8.12 A cluster embedded on a lattice. The central atom is connected with z neighboring atoms via transfer integral t.  $S_j$  ( $T_{ji}$ ) denotes the contribution of all the paths which start from j and end at j (i) without returning to the cluster on the way



In the Hartree–Fock approximation, the Green function is given by (8.8):

$$G_{ij\sigma}(z) = \left[ (z - \boldsymbol{H}_{\sigma})^{-1} \right]_{ii}. \tag{8.47}$$

Here  $(\boldsymbol{H}_{\sigma})_{ij} = \varepsilon_{i\sigma}\delta_{ij} + t_{ij}(1 - \delta_{ij})$  is the one-electron matrix element for the Hartree–Fock Hamiltonian (8.4) and  $\varepsilon_{i\sigma}$  is the Hartree–Fock atomic potential on site i given by  $\varepsilon_{i\sigma} = \varepsilon_i^0 + \tilde{U}_i \langle n_i \rangle / 2 - \tilde{J}_i \langle m_i \rangle \sigma / 2$ .

We consider the binary alloys and adopt the geometrical-mean model for the transfer integrals;  $t_{ij} = r_i^* t^0 r_j$ . Here  $|r_i| = (|t_{AA}|/|t_{ij}^0|)^{1/2}$   $(|r_i| = (|t_{BB}|/|t_{ij}^0|)^{1/2})$  when site i is occupied by atom A (B). The Green function  $r_i^* G_{ij}(z) r_j$  is then expressed as

$$r_i^* G_{ij}(z) r_j = \left[ \left( L^{-1} - t^0 \right)^{-1} \right]_{ij}.$$
 (8.48)

Here we have omitted the spin suffix for simplicity. The locator matrix L is defined by  $(L)_{ij} = |r_i|^2/(z - \varepsilon_{i\sigma})\delta_{ij}$ . Equation (8.48) indicates that the Green function with the off-diagonal disorder is obtained from that of the diagonal disorder by replacing  $G_{ij}(z)$  with  $r_i^*G_{ij}(z)r_j$  and  $(L)_{ij} = \delta_{ij}/(z - \varepsilon_{i\sigma})$  with the locator  $(L)_{ij} = |r_i|^2/(z - \varepsilon_{i\sigma})\delta_{ij}$ , respectively. Because of this we assume in the following the system with the diagonal disorder and use t instead of  $t^0$  for simplicity.

The Green function operator is expanded as  $G = (L^{-1} - t)^{-1} = L + LtG = L + LtL + LtLtG$ . Thus it is expressed as follows.

$$G_{ij}(z) = L_i \delta_{ij} + L_i t_{ij} L_j + \sum_{k \neq i} L_i t_{ik} L_k t_{kj} L_j$$
$$+ \sum_{k \neq i} \sum_{l \neq k, j} L_i t_{ik} L_k t_{kl} L_l t_{lj} L_j + \cdots$$
(8.49)

This means that the Green function in the site representation is given by the contributions associated with all the paths which start from site i and end at site j.

We consider a cluster consisting of the central atom on site 0 and the z neighboring atoms which are connected with the central site 0 via the nearest-neighbor transfer integral t. The cluster is embedded on a lattice as shown in Fig. 8.12. Using

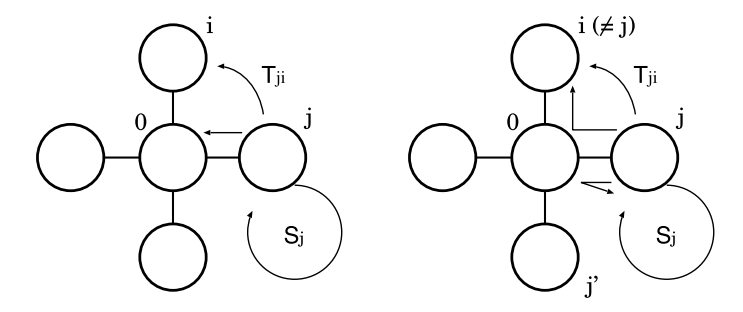


**Fig. 8.13** The paths which start from j and end at 0 (*left*), and the paths which start from j and end at j' (*right*). The former corresponds to (8.51), the latter corresponds to (8.52)

the relation G = L + LtG, we obtain the Dyson equation as

$$G_{00} = L_0 + L_0 \sum_{j} t_{0j} G_{j0}. (8.50)$$

Classifying the terms in the locator expansion (8.49) according to the paths to the inside and outside of the cluster as shown in the left and the right of Fig. 8.13, we obtain the following equations

$$G_{j0} = L_j t_{j0} G_{00} + L_j S_j G_{j0} + L_j \sum_{i \neq 0, j} T_{ji} G_{i0},$$
 (8.51)

$$G_{jj'} = L_j \delta_{jj'} + L_j t_{j0} L_0 t_{0j} G_{jj'} + L_j \sum_{i \neq j} t_{j0} L_0 t_{0i} G_{ij'} + L_j S_j G_{jj'}$$

$$+ L_j \sum_{i \neq j} T_{ji} G_{ij'}. \tag{8.52}$$

Here  $S_j$  ( $T_{ji}$ ) denotes all the paths which start from j and end at j (i) without returning to the cluster on the way.

Now we consider the disordered alloys and replace the random potentials outside the cluster by a uniform effective potential  $\Sigma(z)$  called the coherent potential. This implies that the locators  $\{L_j\}$  outside the cluster have been replaced by an effective locator  $\mathcal{L}(z)$ . Accordingly, the self-energy  $S_j$  and the effective transfer integral  $T_{ji}$  are replaced by  $\mathscr{S}$  and  $\mathscr{T}$ , respectively. The Dyson equations (8.51) and (8.52) then reduce to the following ones.

$$G_{j0} = L_j t G_{00} + L_j \mathcal{S} G_{j0} + L_j \mathcal{T} \sum_{i \neq 0, j} G_{i0}, \tag{8.53}$$

$$G_{jj'} = L_j \delta_{jj'} + L_j (L_0 t^2 + \mathcal{S}) G_{jj'} + L_j (L_0 t^2 + \mathcal{T}) \sum_{i \neq j} G_{ij'}.$$
 (8.54)

In the simplest approximation called the Bethe approximation, we neglect the effective transfer integral  $\mathcal{T}$  assuming the Bethe lattice outside the cluster. We then

obtain the off-diagonal Green function  $G_{j0}$  from (8.53). Substituting the expression into (8.50), we obtain the diagonal Green function as

$$G_{00} = \left(L_0^{-1} - \sum_{j} \frac{t^2}{L_j^{-1} - \mathscr{S}}\right)^{-1}.$$
 (8.55)

In the same way, we obtain the diagonal Green function  $G_{jj}$  on the boundary site from (8.54) without  $\mathcal{T}$  as

$$G_{jj} = \frac{1}{L_j^{-1} - \mathcal{S}} + \frac{1}{(L_j^{-1} - \mathcal{S})^2} t^2 G_{00}.$$
 (8.56)

Here we used the relation (8.53).

The effective self-energy  $\mathscr S$  is obtained from (8.55) in which the random potentials on all the sites have been replaced by the coherent potential:

$$F = \left(\mathcal{L}^{-1} - \frac{zt^2}{\mathcal{L}^{-1} - \mathcal{L}}\right)^{-1}.$$
(8.57)

Here z denotes the number of the nearest neighbors (NN). The coherent Green function F is given by (8.14). In the following equations, we express the energy variable on the complex energy plane as  $\omega + i\delta$  when the number of the NN cannot be distinguished with the energy ' $z = \omega + i\delta$ '. Solving the above equation with respect to the effective self-energy  $\mathcal S$ , we obtain

$$\mathcal{S} = \mathcal{L}^{-1} - \frac{zt^2}{\mathcal{L}^{-1} - F^{-1}}.$$
 (8.58)

The diagonal Green function (8.55) in the Bethe approximation is useful for taking into account the LEE on the magnetic moments because of its simplicity. But it does not include the effects of electron hoppings making a loop via outside of the cluster.

The second approximation [168] takes into account both  $\mathscr{S}$  and  $\mathscr{T}$ . Solving (8.50) and (8.53) with respect to the diagonal Green function, we obtain

$$G_{00} = \left(L_0^{-1} - \frac{t^2}{M^{-1} - \mathcal{T}}\right)^{-1}. (8.59)$$

Here M is defined by

$$M = \sum_{n} \left( L_n^{-1} - \mathcal{S} + \mathcal{T} \right)^{-1}. \tag{8.60}$$

The boundary-site Green function is obtained from (8.54) as

$$G_{jj} = \frac{1}{L_j^{-1} - \mathcal{S} + \mathcal{T}} - \frac{1}{(L_j^{-1} - \mathcal{S} + \mathcal{T})^2} \frac{1}{M - \frac{1}{L_0 t^2 + \mathcal{T}}}.$$
 (8.61)

Note that (8.59) and (8.61) reduce to (8.55) and (8.56), respectively when  $\mathcal{T}$  is omitted.

The effective self-energy  $\mathscr S$  and the transfer integral  $\mathscr T$  are obtained as functions of  $\mathscr L$  from (8.59) and (8.61) in which all random potentials have been replaced by the coherent ones, i.e., from those in which  $G_{00}$ ,  $G_{jj}$ , and  $L_j$  have been replaced by  $F(\mathscr L)$ ,  $F(\mathscr L)$ , and  $\mathscr L$ , respectively. The coherent potential or the effective locator  $\mathscr L(\omega+i\delta)$  is determined by the self-consistent condition

$$\langle G_{00} \rangle = F, \tag{8.62}$$

or

$$\langle G_{ij} \rangle = F. \tag{8.63}$$

Here  $\langle \sim \rangle$  at the l.h.s. of the above equations means the configurational average. It is numerically shown that the self-consistent condition (8.63) at the shell boundary has better analytic property than the condition (8.62) at the central site [169].

The configuration of the cluster is specified by the number of surrounding atoms n of type  $\alpha$  in the case of binary alloys. Here  $\alpha$  denotes the type of the central atoms (i.e., A or B). The probability of finding n atoms of type  $\alpha$  on the surrounding sites are given by the binomial distribution function.

$$\Gamma(n, z, p^{\alpha \alpha}) = \left[z!/n!(z-n)!\right] \left(p^{\alpha \alpha}\right)^n \left(1 - p^{\alpha \alpha}\right)^{z-n}.$$
 (8.64)

Here  $p^{\alpha\alpha}$  is the probability of finding an atom  $\alpha$  at a neighboring site of an atom  $\alpha$ , and is given by Cowley's atomic short-range order parameter  $\tau$  as

$$p^{\alpha\alpha} = c_{\alpha} + (1 - c_{\alpha})\tau, \tag{8.65}$$

 $c_{\alpha}$  being the concentration of atom  $\alpha$ . (Note that the parameter  $\tau$  can vary from  $-c_{\alpha}/(1-c_{\alpha})$  to 1). With use of the binomial distribution (8.64), the configurational average of the Green function  $G_{00}$  in (8.62) is given by

$$\langle G_{00} \rangle = \sum_{n=0}^{z} \Gamma(n, z, p^{\alpha \alpha}) G_{00}(\omega + i\delta, n). \tag{8.66}$$

In the Hartree–Fock self-consistent scheme, the potential  $\varepsilon_{i\sigma}$  changes as  $\varepsilon_{i\sigma} = \varepsilon_i^0 + \tilde{U}_i \langle n_i \rangle / 2 - \tilde{J}_i \langle m_i \rangle \sigma / 2$  depending on their environments. Thus, we have to solve self-consistently (8.45) and (8.63), as well as the equation of the charge potential  $\langle n_i \rangle = \int d\omega \, f(\omega - \mu) \sum_{\sigma} \rho_{i\sigma}(\omega)$  for each environment. This is the Hartree–Fock cluster CPA theory. The theory can describe the LEE on the local magnetic moment self-consistently.

We discuss in the following the LEE in Ni–Cu alloys as an example. Experimentally, the magnetization in Ni–Cu alloys monotonically decreases along the Slater–Pauling curve as shown in Fig. 8.1. The magnetic diffuse-scattering data of polarized neutron experiments however indicate a strong disturbance of Ni local

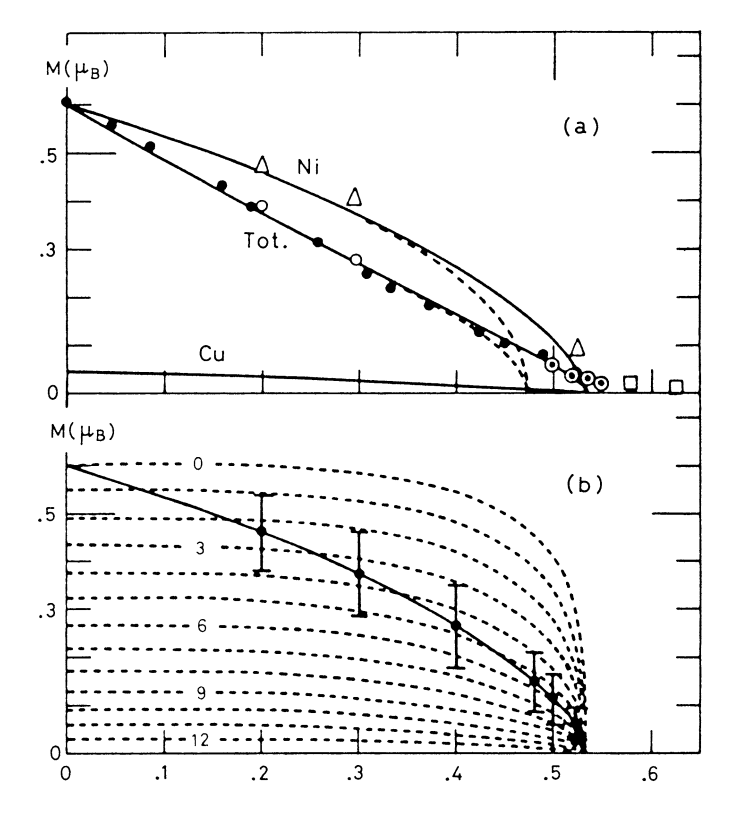


Fig. 8.14 Magnetic moments as a function of Cu concentration in Ni–Cu alloys [173]. (a) The total magnetization and average Ni and Cu moments in the Hartree–Fock cluster CPA (*solid lines*) and in the Hartree–Fock CPA (*dashed lines*). The experimental values are represented by • [174],  $\odot$  [175],  $\Box$  [174], and  $\bigcirc$  [176] for the total magnetization, and by  $\triangle$  [176] for the average Ni moment. The average Cu moment is essentially zero. (b) The Ni atomic moments in various local environments (*dashed lines*) and the average Ni moment (*solid line*). *Vertical bars* represent the root-mean square deviations of the Ni moments from the average values. The local environment is specified by the number of Cu atoms on the NN shell

magnetic moments around 50 at% Cu [176]. Figure 8.14 shows the magnetization vs. concentration curves in Ni–Cu alloys and the local magnetic moment for Ni atom in various environments, which are calculated by the Hartree–Fock cluster CPA based on (8.59) and (8.61) [173]. In the case of Ni–Cu alloys, one has to take into account the hybridization of d electrons with sp electrons, whose effects are phenomenologically taken into account in the model.

The critical concentration of the disappearance of the ferromagnetism is increased by the self-consistent local environment calculations as shown in Fig. 8.14(a); the LEE increase the ferromagnetic region. Figure 8.14(b) indicates that the Ni local moments (LM) are subject to strong local environment effects; the Ni LM surrounded by 12 Cu atoms almost lose the magnetic moment, while the Ni LM surrounded by 12 Ni atoms shows the full moment (see Fig. 8.15). These behav-

Fig. 8.15 Schematic pictures showing the local magnetic moments (LM) of Ni in the environment n = 0 and n = 12 where n is the number of Ni nearest neighbors. In the former, the central LM of Ni disappears, while the LM recovers in the latter

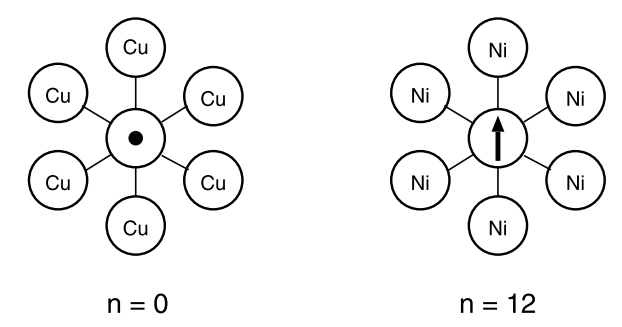
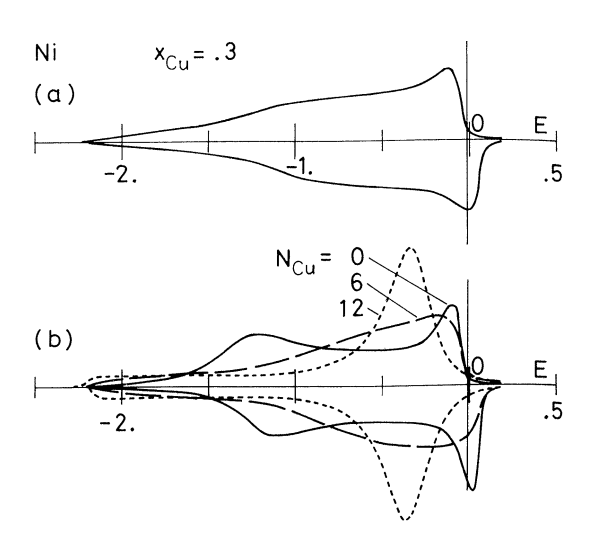


Fig. 8.16 (a) The average DOS of Ni atom and (b) the local DOS of Ni atom in three local environments, which are specified by the number of Cu atoms on the nearest-neighbor shell at 30 at% Cu [173]. Long vertical lines are the Fermi level



iors are verified from the local densities of states (DOS) as shown in Fig. 8.16. The average DOS in Fig. 8.16(a) shows that the Ni<sub>70</sub>Cu<sub>30</sub> alloys are near the boundary between strong and weak ferromagnetism because the top of the up-spin DOS just touches on the Fermi level. The local DOS of a Ni atom with 12 Ni atoms on the NN shell has a sharp peak for both spins showing the strong magnetic moment augmented by surrounding Ni atoms. The DOS of a Ni atom with 12 Cu atoms on the NN shell has a Lorentzian type broad peak below the Fermi level so that Ni loses the magnetic moment.

In Ni–Cu alloys all the local magnetic moments are in the same direction so that we can solve the Hartree–Fock self-consistent equations under a given direction of LMs. On the other hand, the Mn LMs in the Ni–Mn alloys are expected to change their direction depending on their environment because the coupling between Mn LMs is antiferromagnetic while the coupling between Mn and Ni LMs is ferromagnetic. It is not easy in this case to determine the direction of the LMs with use of the Hartree–Fock cluster CPA.

The finite-temperature theory of the local environment effects [170–172] allows us to automatically determine the LM configuration, and describe the magnetic

properties of alloys at finite temperatures. We start from the free energy (8.19) and the effective potential (8.23). Inserting the local magnetic field on site 0 and taking the derivative of the free energy  $\mathscr{F}$  with respect to the field, we can derive the magnetic moment on the central site 0 (see (3.55)):

$$\langle m_0 \rangle = \langle \xi \rangle. \tag{8.67}$$

Here  $\xi$  denotes the exchange field variable on site 0.

In the same way, we obtain the local charge on the central site 0 taking the derivative of  $\mathscr{F}$  with respect to the atomic level on the same site as follows.

$$\langle n_0 \rangle = \langle \tilde{n}_0(\xi, \xi_1, \xi_2, \ldots) \rangle. \tag{8.68}$$

Here we defined the field variables  $\xi_1, \xi_2, \ldots$  acting on the surrounding site  $1, 2, \ldots$ , respectively, bearing in mind that a cluster is centered at the site 0. The local charge  $\tilde{n}_0(\xi, \xi_1, \xi_2, \ldots)$  at the central site 0 is defined by (8.21):

$$\tilde{n}_0(\xi, \xi_1, \xi_2, \dots) = \int d\omega \, f(\omega) \sum_{\sigma} \rho_{i\sigma}(\omega, \xi, \xi_1, \xi_2, \dots). \tag{8.69}$$

The local densities of states  $\rho_{i\sigma}(\omega, \xi, \xi_1, \xi_2, ...)$  are calculated from the Green function for the Hamiltonian (8.24). Note that the average  $\langle \sim \rangle$  at the r.h.s. of (8.67) and (8.68) is a classical average with respect to the effective potential  $E(\xi, \xi_1, \xi_2, ...)$ . For any quantity  $A(\xi, \xi_1, \xi_2, ...)$ , it is defined by

$$\langle A(\xi, \xi_1, \xi_2, \dots) \rangle = \frac{\int d\xi \int \left[ \prod_{i}^{N} d\xi_i \right] A(\xi, \xi_1, \xi_2, \dots) e^{-\beta E(\xi, \xi_1, \xi_2, \dots)}}{\int d\xi \int \left[ \prod_{i}^{N} d\xi_i \right] e^{-\beta E(\xi, \xi_1, \xi_2, \dots)}}. (8.70)$$

We introduce here the effective medium  $\mathcal{L}_{\sigma}$  into the energy (8.23) and express it using the relation (8.27) as

$$E(\xi, \xi_1, \xi_2, ...) = \int d\omega f(\omega) \frac{D}{\pi} \operatorname{Im} \operatorname{tr} \left[ \ln(\mathcal{L} - t) \right] + E_0(\xi, \xi_1, \xi_2, ...)$$

$$+ \sum_{i=1}^{N} E_i(\xi_i) + \Delta E(\xi, \xi_1, \xi_2, ...).$$
(8.71)

Here  $E_i(\xi_i)$  are the single-site effective potentials (see (8.30)).

$$E_{i}(\xi_{i}) = \int d\omega f(\omega) \frac{D}{\pi} \operatorname{Im} \sum_{\sigma} \ln \left[ 1 + \left( L_{i\sigma}^{-1}(z, \xi) - \mathcal{L}_{\sigma}^{-1}(z) \right) F_{\sigma}(z) \right] - \frac{1}{4} \tilde{U}_{i} \, \tilde{n}_{i}(\xi_{i})^{2} + \frac{1}{4} \tilde{J}_{i} \, \xi_{i}^{2}.$$
(8.72)

Here  $\tilde{n}_i(\xi_i)$  is assumed to depend only on  $\xi_i$ .  $E_0(\xi, \xi_1, \xi_2, ...)$  is defined by (8.72) in which the subscript i has been replaced by 0. Note that the second term  $E_0(\xi, \xi_1, \xi_2, ...)$  at the r.h.s. of (8.71) may depend on the surrounding variable

 $\xi_1, \xi_2, \dots$  via the charge potential  $\tilde{U}_0 \tilde{n}_0(\xi, \xi_1, \xi_2, \dots)/2$  which is determined self-consistently.

The last term of the r.h.s. of (8.71) is the nonlocal term defined by

$$\Delta E(\xi, \xi_1, \xi_2, \ldots) = \int d\omega f(\omega) \frac{D}{\pi} \operatorname{Im} \operatorname{tr} \left[ \ln \left( 1 - \tilde{t} F' \right) \right]. \tag{8.73}$$

Expanding  $\Delta E$  with respect to the sites, we obtain the following expression in the lowest order.

$$\Delta E(\xi, \xi_1, \xi_2, \ldots) = \sum_{(i,j)} \Phi_{ij}(\xi_i, \xi_j). \tag{8.74}$$

Here  $\Phi_{ij}(\xi_i, \xi_j)$  is the pair energy defined by

$$\Phi_{ij}(\xi_i, \xi_j) = \int d\omega \, f(\omega) \frac{D}{\pi} \times \operatorname{Im} \sum_{\sigma} \ln \left[ 1 - F_{ij\sigma}(z) F_{ji\sigma}(z) \, \tilde{t}_{i\sigma}(z) \, \tilde{t}_{j\sigma}(z) \right], \tag{8.75}$$

and  $F_{ij\sigma}$  is the off-diagonal component of the coherent Green function given by

$$F_{ij\sigma} = \left[ (\mathcal{L} - t)^{-1} \right]_{ij\sigma}, \tag{8.76}$$

 $\tilde{t}_{i\sigma}$  is the diagonal component of the single-site t matrix (8.28):

$$\tilde{t}_{i\sigma} = -\frac{(L_{i\sigma}^{-1} - \mathcal{L}_{\sigma}^{-1})}{1 + (L_{i\sigma}^{-1} - \mathcal{L}_{\sigma}^{-1})F_{\sigma}}.$$
(8.77)

Substituting (8.71) into (8.70), we obtain an alternative form of the average as follows.

$$\langle A(\xi, \xi_1, \xi_2, \ldots) \rangle = \frac{\int d\xi \int \left[ \prod_{i}^{N} p_i(\xi_i) d\xi_i \right] A(\xi, \xi_1, \xi_2, \ldots) e^{-\beta [E_0(\xi, \xi_1, \xi_2, \ldots) + \Delta E(\xi, \xi_1, \xi_2, \ldots)]}}{\int d\xi \int \left[ \prod_{i}^{N} p_i(\xi_i) d\xi_i \right] e^{-\beta [E_0(\xi, \xi_1, \xi_2, \ldots) + \Delta E(\xi, \xi_1, \xi_2, \ldots)]}}.$$

(8.78)

Here  $p_i(\xi_i) = \exp(-\beta E_i(\xi_i)) / \int d\xi_i \exp(-\beta E_i(\xi_i))$  is the single-site probability of finding the field  $\xi_i$  on site i.

A simple way to reduce the integrals of the surrounding sites in (8.78) is to adopt the decoupling approximation which is correct up to the second moment in the moment expansion;  $\int d\xi_i \ p_i(\xi_i) \xi_i^{2n+k} \approx x_i^{2n} \langle \xi_i \rangle_0^k$  where  $x_i = \langle \xi_i^2 \rangle_0^{1/2}$ . Then for any function  $y(\xi_i)$ , we have

$$\langle y(\xi_i)\rangle_0 = \int p_i(\xi_i)y(\xi_i)\,d\xi_i \approx \sum_{i=1} p_{i\nu}y(\nu x_i). \tag{8.79}$$

Here  $p_{i\nu} = (1 + \nu \langle \xi_i \rangle_0 / x_i)/2$ . It is interpreted as a probability that a local moment with an amplitude  $x_i$  points up.

Applying the decoupling approximation (8.79) successively in (8.78) and adopting the pair approximation (8.74), we obtain [177]

$$\langle A(\xi, \xi_{1}, \xi_{2}, \ldots) \rangle = \frac{\int d\xi \left( \sum_{s_{1} = \pm s_{1} = \pm} \cdots \right) A(\xi, s_{1}x_{1}, s_{2}x_{2}, \ldots) e^{-\beta \Psi(\xi, s_{1}x_{1}, s_{2}x_{2}, \ldots)}}{\int d\xi \left( \sum_{s_{1} = \pm} \sum_{s_{1} = \pm} \cdots \right) e^{-\beta \Psi(\xi, s_{1}x_{1}, s_{2}x_{2}, \ldots)}}.$$
 (8.80)

The effective potential  $\Psi(\xi, s_1x_1, s_2x_2, ...)$  is expressed as

$$\Psi(\xi, s_1 x_1, s_2 x_2, \ldots) = E_0(\xi, s_1 x_1, s_2 x_2, \ldots) + \sum_j \Phi_{0j}^{(a)}(\xi) 
- \sum_{i \neq 0} \left[ \Phi_{0i}^{(e)}(\xi) + \beta^{-1} \tanh^{-1} \frac{\langle \xi \rangle_0}{x_i} + \sum_{j \neq 0, i} \mathcal{K}_{ij} \right] s_i 
- \sum_{(i, j)} \mathcal{J}_{ij} s_i s_j.$$
(8.81)

Here the pair interactions  $\Phi_{0j}^{(a)}(\xi)$ ,  $\Phi_{0i}^{(e)}(\xi)$ ,  $\mathcal{K}_{ij}$ , and  $\mathcal{J}_{ij}$  are defined as

$$\Phi_{0j}^{(a)}(\xi) = \frac{1}{2} \sum_{\nu=+} \Phi_{ij}(\xi, \nu x_j), \qquad \Phi_{0i}^{(e)}(\xi) = -\frac{1}{2} \sum_{\nu=+} \nu \Phi_{ij}(\xi, \nu x_j), \qquad (8.82)$$

$$\mathcal{K}_{ij} = -\frac{1}{4} \sum_{\lambda = \pm} \sum_{\nu = \pm} \lambda \Phi_{ij}(\lambda x_i, \nu x_j), \qquad \mathcal{J}_{ij} = -\frac{1}{4} \sum_{\lambda = \pm} \sum_{\nu = \pm} \lambda \nu \Phi_{ij}(\lambda x_i, \nu x_j).$$
(8.83)

As seen from (8.81),  $\mathcal{J}_{ij}$  is the exchange interaction between local magnetic moments (LM's) in the decoupling approximation and reduces to the super-exchange interaction in the strong Coulomb interaction limit (see (1.86) and note that  $J_{ij} = 4 \mathcal{J}_{ij}$  by definition when D=1).  $\Phi_{0i}^{(e)}(\xi)$  defined by (8.82) is the exchange energy potential for the flexible central LM  $\xi$ .  $\Phi_{0j}^{(a)}(\xi)$  is an atomic potential which changes the amplitude of LM  $\xi$  according to the surrounding atomic configuration.  $\mathcal{K}_{ij}$  is an effective nonlocal magnetic field induced by the polarization of the medium. Note that the latter vanishes in the paramagnetic state.

It should be emphasized that the exchange couplings  $\mathcal{J}_{ij}$  provide us with the magnitude and sign of the couplings between the LMs in the itinerant electron system, thus they are useful for understanding the magnetic couplings between constituent magnetic atoms. The exchange couplings  $\mathcal{J}_{ij}$  are essentially the same as the Alexander–Anderson–Moriya interaction [178, 179], though the latter is based on the Anderson model (7.5).

Equation (8.80) indicates that we can approximate the surrounding spins  $\{\xi_i\}$  with the Ising type of effective spins  $\{s_ix_i\}$  with the amplitude  $\{x_i\}$ . We consider

now a cluster consisting of the central atom and the surrounding nearest-neighbor (NN) atoms, and calculate the central LM (8.67) on the basis of (8.80). The simplest approximation to the effective potential  $\Psi(\xi, s_1x_1, s_2x_2, ...)$  is a molecular-field type in which the surrounding spins  $\{s_i\}$  are replaced by their averages  $\langle m_j \rangle / x_j$ . In this case the effective potential is given by

$$\Psi(\xi) = E_0(\xi) + \sum_{i} \Phi_{0j}^{(a)}(\xi) - \sum_{i \neq 0} \Phi_{0j}^{(e)}(\xi) \frac{\langle m_j \rangle}{x_j}.$$
 (8.84)

In the disordered alloys, the intersite interactions are expected to be rather short range because of the damping effects due to random potentials. Equations (8.84) and (8.67) indicate that the central LM  $\langle m_0 \rangle$  is specified by the type of the central atom  $(\alpha)$ , the number of the NN (z), the types of the surrounding atoms  $(\{\gamma_j\})$ , and the surrounding LM  $(\{\langle m_j \rangle\})$ .

$$\langle m_0 \rangle = \langle m_\alpha \rangle (\{ \gamma_j \}, \{ \langle m_j \rangle \}) = \frac{\int d\xi \, \xi e^{-\beta \Psi(\xi)}}{\int d\xi \, e^{-\beta \Psi(\xi)}}.$$
 (8.85)

In order to determine the LMs in the cluster self-consistently, we introduce a distribution function  $g_{\alpha}(m)$  such that the probability of finding the LM of type  $\alpha$  between m and m+dm is given by  $g_{\alpha}(m)dm$ . Then the probability that the surrounding atomic configuration  $\{\gamma_j\}$  is realized and each LM on site j with a type of atom  $\gamma_j$  has a value between  $m_j$  and  $m_j+dm_j$  is given by  $[\prod_{j=1}^z p^{\alpha\gamma_j}][\prod_{j=1}^z g_{\gamma_j}(m_j)dm_j]$ . Here  $p^{\alpha\gamma}$  is the probability of finding atom  $\gamma$  at the neighboring site of atom  $\alpha$ . It is given by (8.65) for  $\gamma=\alpha$  and  $\gamma=1-\gamma=1$  for  $\gamma=\overline{\alpha}$ . The LM on the central atom  $\gamma=1$  is the given by  $\gamma=1$  that the probability that the central LM of the type of atom  $\gamma=1$  is between  $\gamma=1$  and  $\gamma=1$ . Thus the probability that the central LM of the type of atom  $\gamma=1$  is between  $\gamma=1$  and  $\gamma=1$ .

$$g_{\alpha}(M)\Delta M = \sum_{\{\gamma_j\}} \int_{M \le \langle m_{\alpha} \rangle \le M + \Delta M} \left[ \prod_{j=1}^{z} p^{\alpha \gamma_j} \right] \left[ \prod_{j=1}^{z} g_{\gamma_j}(m_j) dm_j \right]. \quad (8.86)$$

Inserting the identity  $\int dM' \, \delta(M' - \langle m_{\alpha} \rangle)$  and making use of the binomial distribution function (8.64), the above equation is written as follows.

$$g_{\alpha}(M) = \sum_{n=0}^{z} \Gamma(n, z, p^{\alpha \alpha}) \int \delta(M - \langle m_{\alpha} \rangle)$$

$$\times \left[ \prod_{i=1}^{n} g_{\alpha}(m_{i}) dm_{i} \right] \left[ \prod_{i=n+1}^{z} g_{\overline{\alpha}}(m_{j}) dm_{j} \right]. \tag{8.87}$$

This is known as the distribution function method [180, 181].

The self-consistent integral equation (8.87) for  $g_{\alpha}(M)$  is not easy to solve for large z (e.g., 8 for the bcc, 12 for the fcc alloys). A way to solve the equation

is to apply the decoupling approximation of the type of (8.79) to the distribution functions  $\{g_{\nu}(m_i)\}$  at the r.h.s. of (8.87).

$$\int m^{2n+k} g_{\gamma}(m) dm \approx \left[ \langle m_{\gamma} \rangle^2 \right]_{\rm c}^n \left[ \langle m_{\gamma} \rangle \right]_{\rm c}^k \quad (k = 0, 1), \tag{8.88}$$

where  $[\sim]_c$  denotes the configurational average. This implies that we can make the following approximation for any function f(m) at the r.h.s. of (8.87).

$$\int f(m)g_{\gamma}(m) dm \approx \sum_{\nu=+} \frac{1}{2} \left( 1 + \nu \frac{[\langle m_{\gamma} \rangle]_{c}}{[\langle m_{\nu} \rangle^{2}]_{c}^{1/2}} \right) f\left(\nu [\langle m_{\gamma} \rangle^{2}]_{c}^{1/2}\right). \quad (8.89)$$

After making the decoupling approximation, we substitute the approximate distribution  $g_{\alpha}(M)$  (i.e., (8.87)) into the equations  $[\langle m_{\alpha} \rangle]_{c} = \int M g_{\alpha}(M) dM$  and  $[\langle m_{\alpha} \rangle^{2}]_{c} = \int M^{2} g_{\alpha}(M) dM$ , and obtain the self-consistent equations for  $[\langle m_{\alpha} \rangle]_{c}$  and  $[\langle m_{\alpha} \rangle^{2}]_{c}$  as follows.

$$\begin{bmatrix} [\langle m_{\alpha} \rangle]_{c} \\ [\langle m_{\alpha} \rangle^{2}]_{c} \end{bmatrix} = \sum_{n=0}^{z} \Gamma(n, z, p^{\alpha \alpha}) \begin{bmatrix} [\langle m_{\alpha} \rangle_{n}]_{c} \\ [\langle m_{\alpha} \rangle_{n}^{2}]_{c} \end{bmatrix}. \tag{8.90}$$

The magnetic moments  $[\langle m_{\alpha} \rangle_n^k]_c$  (k = 1, 2) at the r.h.s. of the above equations are the LM's for a given environment n. They are given by

$$\left[\langle m_{\alpha}\rangle_{n}^{k}\right]_{c} = \sum_{l=0}^{n} \sum_{m=0}^{z-n} \Gamma(l, n, q_{\alpha+}) \Gamma(m, z - n, q_{\overline{\alpha}+}) \langle \xi_{\alpha}\rangle_{nlm}^{k}. \tag{8.91}$$

Here  $q_{\alpha\pm}=(1\pm[\langle m_{\alpha}\rangle]_{\rm c}/([\langle m_{\alpha}\rangle^2]_{\rm c})^{1/2})/2$  is the probability that the LM of type  $\alpha$  points up or down.  $\langle \xi_{\alpha}\rangle_{nlm}$  is the LM of an atom of type  $\alpha$  at the central site when l of the LMs among the surrounding n atoms of type  $\alpha$  point up, and in addition, m LMs of the remaining z-n atoms of type  $\overline{\alpha}$  also point up:

$$\langle \xi_{\alpha} \rangle_{nlm} = \int p_{\alpha nkl}(\xi) \xi \, d\xi, \tag{8.92}$$

$$p_{\alpha n l m}(\xi) = \frac{e^{-\beta \Psi_{\alpha n l m}(\xi)}}{\int d\xi \, e^{-\beta \Psi_{\alpha n l m}(\xi)}},\tag{8.93}$$

$$\Psi_{\alpha n l m}(\xi) = E_{\alpha}(\xi) + n \, \Phi_{\alpha \alpha}^{(a)}(\xi) + (z - n) \, \Phi_{\alpha \overline{\alpha}}^{(a)}(\xi) - (2l - n) \, \Phi_{\alpha \alpha}^{(e)}(\xi) \, \frac{\left[\langle m_{\alpha} \rangle^{2}\right]_{c}^{1/2}}{x_{\alpha}} - (2m - z + n) \, \Phi_{\alpha \overline{\alpha}}^{(e)}(\xi) \, \frac{\left[\langle m_{\overline{\alpha}} \rangle^{2}\right]_{c}^{1/2}}{x_{\overline{\alpha}}}. \tag{8.94}$$

Equation (8.90) determines  $[\langle m_{\alpha} \rangle]_c$  and  $[\langle m_{\alpha} \rangle^2]_c$  self-consistently when the medium  $\mathcal{L}_{\sigma}^{-1}$  is given, because  $E_{\alpha}(\xi)$ ,  $\Phi_{\alpha\gamma}^{(a)}(\xi)$ , and  $\Phi_{\alpha\gamma}^{(e)}(\xi)$  are the functionals

of the medium  $\mathcal{L}_{\sigma}^{-1}$ . We determine in principle the latter from the CPA equation (8.34) or (8.36). However, in the present case, the thermal average of the single-site Green function depends on the surrounding environment  $\{\gamma_j\}$  and  $\{\langle m_j \rangle\}$  via the effective potential (8.84), so that the CPA equation is expressed as

$$\sum_{\alpha} c_{\alpha} \left[ \langle \left[ L_{\alpha\sigma}^{-1}(z,\xi) - \mathcal{L}_{\sigma}^{-1}(z) + F_{\sigma}^{-1}(z) \right]^{-1} \rangle \right]_{c} = F_{\sigma}(z). \tag{8.95}$$

Here the average  $\langle \sim \rangle$  should be taken with respect to the effective potential (8.84). Applying again the decoupling approximation of the type (8.79) for the average  $[\langle \sim \rangle]_c$ , we obtain a simplified CPA equation as follows.

$$\sum_{\alpha} c_{\alpha} \sum_{\nu=\pm} \frac{1}{2} \left( 1 + \nu \frac{\left[ \langle \xi_{\alpha} \rangle \right]_{c}}{\left[ \langle \xi_{\alpha}^{2} \rangle \right]_{c}^{1/2}} \right) \left[ L_{\alpha\sigma}^{-1} \left( z, \nu \left[ \langle \xi_{\alpha}^{2} \rangle \right]_{c}^{1/2} \right) - \mathcal{L}_{\sigma}^{-1}(z) + F_{\sigma}^{-1}(z) \right]^{-1}$$

$$= F_{\sigma}(z). \tag{8.96}$$

Here  $[\langle \xi_{\alpha}^k \rangle]_c$  (k = 1, 2) is defined by

$$\left[\langle \xi_{\alpha}^{k} \rangle\right]_{c} = \sum_{n=0}^{z} \Gamma(n, z, p^{\alpha \alpha}) \sum_{l=0}^{n} \sum_{m=0}^{z-n} \Gamma(l, n, q_{\alpha+}) \Gamma(m, z-n, q_{\overline{\alpha}+}) \langle \xi_{\alpha}^{k} \rangle_{nlm}, \quad (8.97)$$

$$\langle \xi_{\alpha}^{k} \rangle_{nlm} = \int \xi^{k} p_{\alpha nlm}(\xi) \, d\xi. \tag{8.98}$$

Equations (8.90) and (8.96) determine  $[\langle m_{\alpha} \rangle]_c$ ,  $[\langle m_{\alpha} \rangle^2]_c$ , and  $\mathcal{L}_{\sigma}^{-1}$  self-consistently. It is worth to mention that the self-consistent equations (8.90) contain the spin-glass solution,  $[\langle m_{\alpha} \rangle]_c = 0$  and  $[\langle m_{\alpha} \rangle^2]_c \neq 0$  (see (1.104)). To see the fact, we consider the case  $[\langle m_{\alpha} \rangle]_c = 0$ , and write the second equation of (8.90) for  $v_{\alpha} = [\langle m_{\alpha} \rangle^2]_c^{1/2}/x_{\alpha}$  as follows after making the decoupling approximation (8.79) for the central-site variable  $\xi$ .

$$v_{\alpha}^{2} = \sum_{n=0}^{z} \sum_{l=0}^{n} \sum_{m=0}^{z-n} \Gamma(n, z, c_{\alpha}) \Gamma(l, n, 1/2) \Gamma(m, z - n, 1/2)$$

$$\times \tanh^{2} \left[ \beta(2k - n) \mathcal{J}_{\alpha\alpha} v_{\alpha} + \beta(2l - z + n) \mathcal{J}_{\alpha\overline{\alpha}} v_{\overline{\alpha}} \right]. \tag{8.99}$$

Here we assumed the complete disorder  $p^{\alpha\alpha}=c_{\alpha}$ . Expanding the r.h.s. of (8.99) with respect to  $v_{\alpha}$  and assuming that  $\mathscr{J}_{\alpha\gamma}$  is independent of temperature, we obtain the transition temperature  $T_{\rm g}$  at which  $v_{\alpha}$  vanishes.

$$T_{\rm g}^2 = \frac{1}{2} z \left[ c_{\rm A} \mathcal{J}_{\rm AA}^2 + c_{\rm B} \mathcal{J}_{\rm BB}^2 + \sqrt{\left( c_{\rm A} \mathcal{J}_{\rm AA}^2 - c_{\rm B} \mathcal{J}_{\rm BB}^2 \right)^2 + 4 c_{\rm A} c_{\rm B} \mathcal{J}_{\rm AB}^4} \right]. \quad (8.100)$$

The above expression of  $T_{\rm g}$  reduces to the spin-glass temperature (7.46) for the insulator system in the dilute limit.

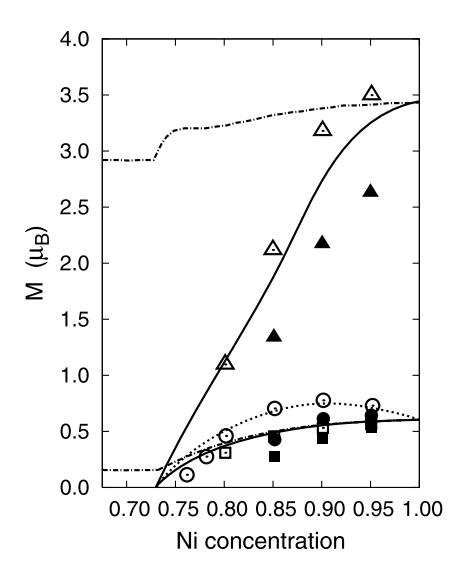
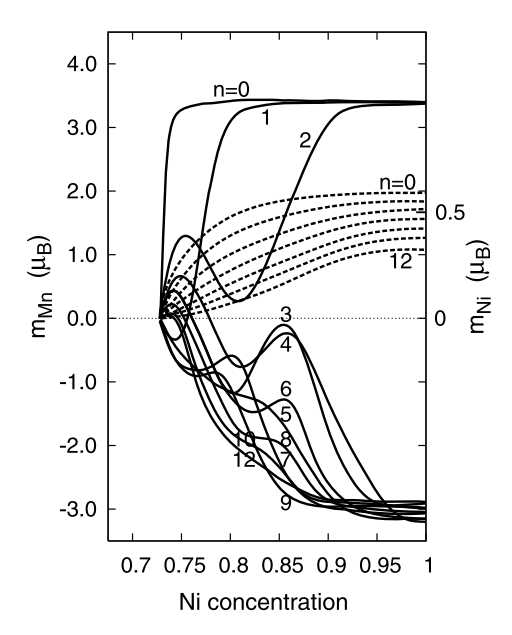


Fig. 8.17 Various local magnetic moments (LM) in Ni–Mn alloys as a function of Ni concentration at 150 K [172]. Solid curves are calculated results of  $[\langle m_{\text{Mn}} \rangle]_c$  (upper curve) and  $[\langle m_{\text{Ni}} \rangle]_c$  (lower curve). Corresponding experimental values at T=4.2 K (room temperatures) are denoted by  $\triangle$  and  $\square$  ( $\blacktriangle$  and  $\blacksquare$ ) [187], respectively. The dotted curve represents the calculated magnetization. The experimental values are shown by  $\circ$  (4.2 K) and  $\bullet$  (room temperatures) [187, 188]. The root mean square values of the thermal average of Mn and Ni LM's  $[\langle m_{\alpha} \rangle^2]_c^{1/2}$  are shown by dot-dashed curves

The magnetic properties of Ni–Mn alloys cannot be explained by the single-site approximation as mentioned before. The magnetization vs. concentration curve shows a deviation from the Slater–Pauling curve as shown in Fig. 8.1. The system is characterized by the strong atomic short range effects on magnetic moment [182–184], and the existence of spin glasses [185, 186]. Finite temperature calculations based on the LEE theory mentioned above allows us to explain these properties of Ni–Mn alloys. Calculated magnetic moments vs. concentration curves are presented in Fig. 8.17. The magnetization curve shows a maximum at 10 at% Mn in agreement with the experimental data. The deviation from the linear Slater–Pauling curve is caused by the rapid decrease of average Mn local magnetic moment (LM) with increasing Mn concentration. The Mn atoms have well-defined LM with a large amplitude more than  $3\mu_{\rm B}$ , and the magnetic couplings in Ni–Mn alloys are verified to be  $J_{\rm MnMn} < 0$ ,  $|J_{\rm MnMn}| \gg J_{\rm NiNi} > 0$ , and  $J_{\rm NiMn} > 0$ . Thus it is expected that the rapid decrease of average Mn LM is accompanied by the reversal of the Mn LM with the increase in Mn concentration.

Figure 8.18 shows the calculated concentration dependences of Mn and Ni LMs in various local environments. At low Mn concentrations, Mn LM are parallel to the magnetization when the number of surrounding Mn LM n is less than n = 3, while they are antiparallel when n are equal to or larger than 3. Such behavior explains the concentration dependence of the magnetization by taking into account the binomial

**Fig. 8.18** Concentration dependences of the LM in various environments,  $[\langle m_{\alpha} \rangle_n]_c$  [172]. The *solid* (*dashed*) *curves* show the Mn (Ni) LM. Integers n in the figure show the coordination number of Mn



distribution via (8.90). Beyond 10 at% Mn, the Mn LM with critical environments n = 2, 3, 4 rapidly reduce their magnitudes with decreasing average polarization. This is because the Mn LM with critical environments feel a weak molecular field. Due to the same reason, they lose rapidly their magnetic moment with increasing temperature.

The Ni LM, on the other hand, do not change their directions irrespective of their local environments as seen in Fig. 8.18, so that the average Ni LM monotonically decreases with increasing concentration as shown in Fig. 8.17. Note that  $[(m_{\alpha})^2]_c$  remain beyond 27 at% Mn after the disappearance of the ferromagnetism, indicating the existence of the spin glass state in agreement with the experimental data [185, 186].

The Ni–Mn alloy forms the Cu<sub>3</sub>Au ordered alloy at 25 at% Mn. Experimentally the degree of order is controlled by quenching. The degree of atomic order is specified by the atomic short-range order (ASRO) parameter  $\tau$  defined by (8.65); the Cu<sub>3</sub>Au ordered state is characterized by  $\tau = -c_{Mn}/c_{Ni} = -0.33$ , while the complete disorder is characterized by  $\tau = 0$ . It is found that the magnetization is strongly influenced by the ASRO at 25 at% Mn; it increases from  $0.1\mu_B$  to  $1.0\mu_B$  when the ASRO decreases from  $\tau = 0$  to  $\tau = -0.33$  [184].

Figure 8.19 shows the local densities of states (LDOS) in various environments at 25 at% Mn for complete disorder. The up-spin electrons on Mn atoms with no Mn NN hybridize with surrounding electrons on Ni atoms with the same spin, while the down-spin electrons on Mn atoms are localized above the Fermi level. The Mn LMs with 12 Mn NN are subject to the ferro- and antiferro-magnetic molecular fields depending on the surrounding Mn configurations in direction, so that the LDOS hardly depend on the spin component. On the other hand, the Ni LDOS with no Mn

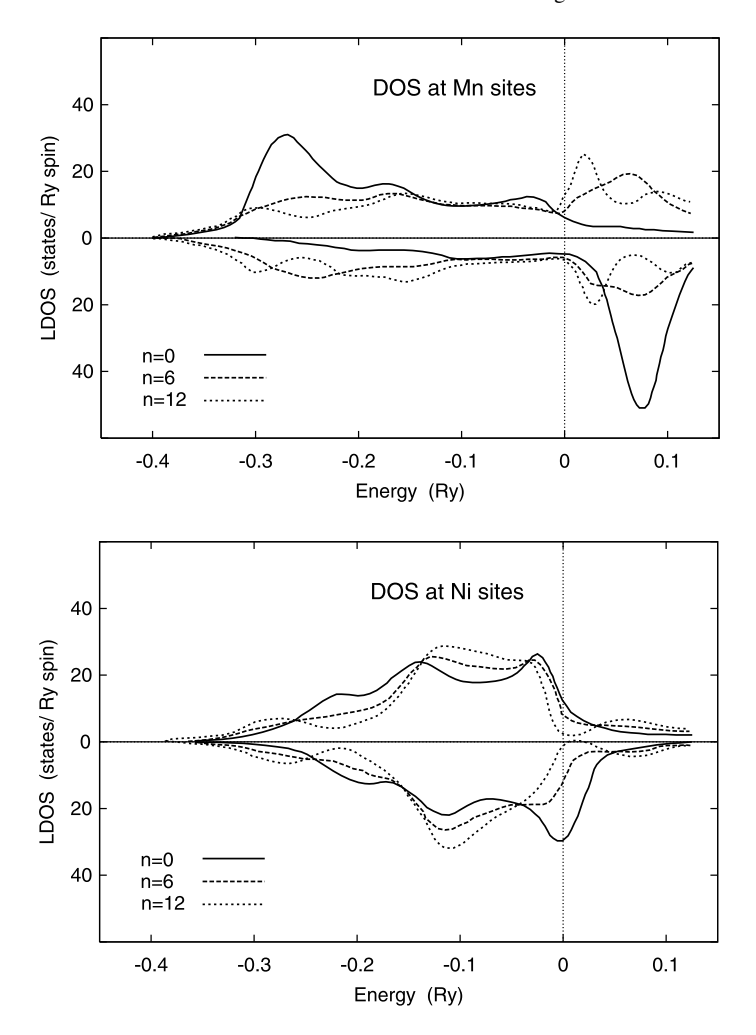
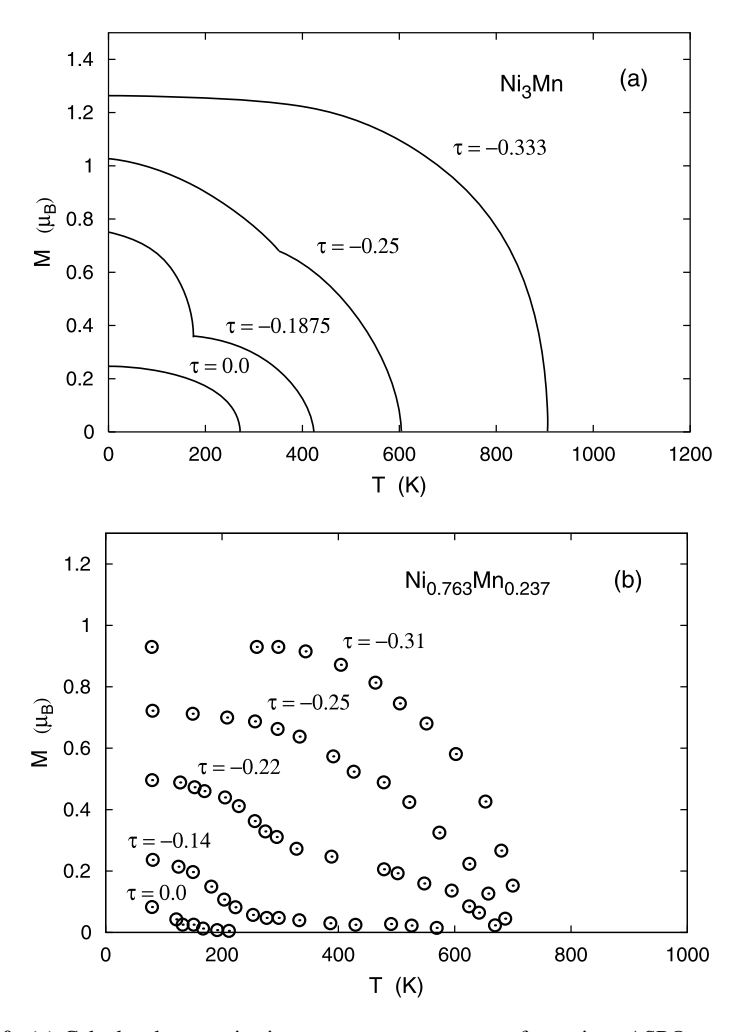


Fig. 8.19 Local densities of states (LDOS) in various environment at 25 at% Mn and 150 K [172]. Solid curves show the LDOS in the environment with no nearest neighbor (NN) Mn atoms. Dashed curves, LDOS with n = 6 Mn NN. Dotted curves, LDOS with n = 12 Mn NN

NN is well polarized due to the Ni cluster. With increasing Mn NN, the polarization of Ni LM decreases and the peak of the DOS sinks below the Fermi level. In the Ni LDOS with 12 Mn NN, we find considerable DOS above the Fermi level due to the hybridization with the electrons on Mn sites.

Calculated magnetization vs. temperature curves at 25 at% Mn are presented in Fig. 8.20 for various ASRO. At low temperatures, it is verified that there are the low-spin state and high-spin state depending on the ASRO, and the first-order transition from the former to the latter takes place between  $\tau = -0.18$  and  $\tau = -0.0195$  due to the change in magnetic couplings with decreasing the number of surrounding Mn LM. The high LM states rapidly decrease with increasing temperature because

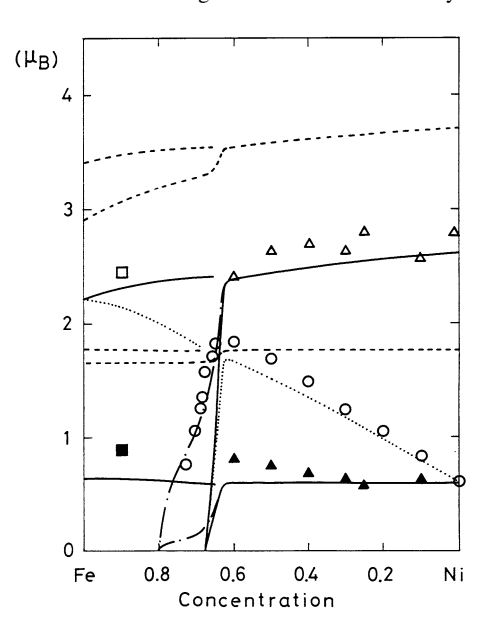


**Fig. 8.20** (a) Calculated magnetization vs. temperature curves for various ASRO parameters  $\tau$  at 25 at% Mn [172]. (b) Experimental magnetization vs. temperature curves for various ASRO parameters  $\tau$  at 23.7 at% Mn [184]

of larger magnetic entropy. When the number of Mn NN decreases with decreasing  $\tau$ , the Ni–Mn ferromagnetic couplings  $\mathcal{J}_{\text{NiMn}}$  become dominant, so that high magnetization and high  $T_{\text{C}}$  are realized at  $\tau = -0.33$ .

As a second example showing strong LEE, we consider the Fe–Ni alloys. The alloys show a rapid deviation from the Slater–Pauling curve at  $c^* = 66$  at% Fe as shown in Fig. 8.1. The ferromagnetic instability takes place when the up-spin band touches the Fermi level, as discussed in the last section. The ferromagnetic instability with strong LEE causes various anomalies such as the broad internal-field distribution in Möbauer experiment [189], the downward deviation of the magnetization vs. temperature curve from the Brillouin curve [190], the large magneto-volume ef-

Fig. 8.21 Concentration dependence of various local moments (LM) in Fe<sub>c</sub>Ni<sub>1-c</sub> alloys calculated for the bcc  $(c \ge 0.65)$  and fcc  $(0 \le c \le 1)$ structures at T = 150 K[192]. Dotted curves: average magnetizations, solid curves: partial magnetization  $[\langle m_{\alpha} \rangle]_{c}$ , dashed curves: amplitudes of LM  $[\langle m_{\alpha}^2 \rangle]_c^{1/2}$ , dot-dashed curves:  $[\langle m_{\alpha} \rangle^2]_{\rm c}^{1/2}$ . Experimental magnetizations are shown by o [190, 193, 194]. Experimental LM  $[\langle m_{\alpha} \rangle]_c$  at 4.2 K are shown by  $\triangle$  ( $\alpha$  = fcc Fe),  $\triangle$  ( $\alpha$  = fcc Ni) [155, 156, 193],  $\square$  ( $\alpha = bcc$ Fe), and  $\blacksquare$  ( $\alpha = bcc Ni$ ) [193]



fects called the Invar effects [191], and the appearance of spin glasses (SG) after the disappearance of ferromagnetism [163]. The finite-temperature theory of the LEE explains these characteristics of Fe–Ni alloys.

Figure 8.21 shows the concentration dependence of various magnetic moments calculated by the theory of LEE [192]. Calculated magnetization linearly increases with increasing Fe concentration and starts to decrease rapidly at 66 at% Fe, where the top of the up-spin band touches the Fermi level. Calculated magnetic moments  $[\langle m_{\alpha} \rangle^2]_c^{1/2}$  remain even after the disappearance of ferromagnetism, showing the existence of the SG. Experimentally, the SG are found in the fcc (Fe<sub>c</sub>Ni<sub>1-c</sub>)<sub>92</sub>C<sub>8</sub> alloys, because the Fe–Ni alloys cause the structural phase transition to the bcc after the disappearance of ferromagnetism beyond 70 at% Fe [163].

The strong LEE found in Fe–Ni alloys originate in a nonlinear magnetic coupling between Fe LMs. Figure 8.22(a) shows various atomic and exchange pair energies of the central LM of type  $\alpha$  when the neighboring LM of type  $\gamma$  with amplitude  $x_{\gamma}$  points up. If the exchange interaction  $\Phi(\xi_i, \xi_j)$  follows the bilinear form like the Heisenberg model  $(-\mathcal{J}_{ij}\xi_i\cdot\xi_j)$ , exchange energy potential  $-\Phi_{\alpha\gamma}^{(e)}(\xi)$  should be linear with respect to  $\xi$  and there is no anomaly in the vicinity of ferromagnetic instability. However, the exchange potential  $-\Phi_{\text{FeFe}}^{(e)}(\xi)$  in the fcc structure shows an S-shape curve. It implies that Fe LMs with the average amplitude  $(\langle \xi^2 \rangle^{1/2})$  less than about  $1.7\mu_{\text{B}}$  couple antiferromagnetically to the neighboring Fe LMs, while the Fe LMs with the amplitude more than  $1.7\mu_{\text{B}}$  couple ferromagnetically to the surrounding Fe LMs. Since the pair-energy functionals  $\Phi_{\text{FeFe}}^{(a)}(\xi)$  and  $\Phi_{\text{FeNi}}^{(a)}(\xi)$  show downward and upward convex curves, respectively, the amplitude of the central LM varies from  $2.6\mu_{\text{B}}$  to  $1.5\mu_{\text{B}}$  with the increasing number of Fe NN. This means that the Fe LMs with a small number of Fe NN show ferromagnetic coupling to

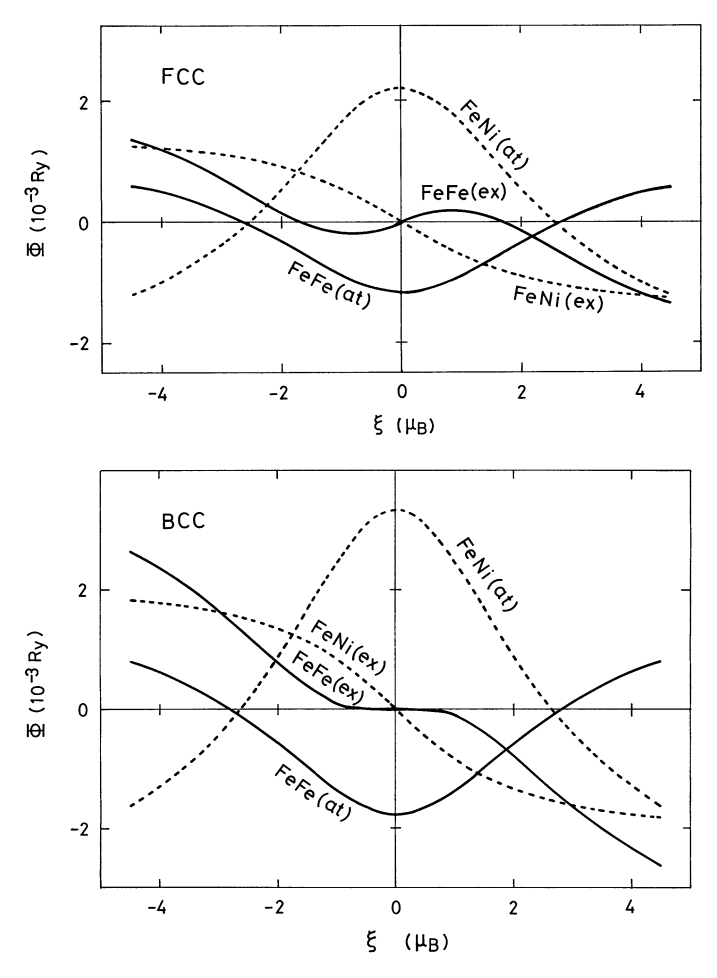


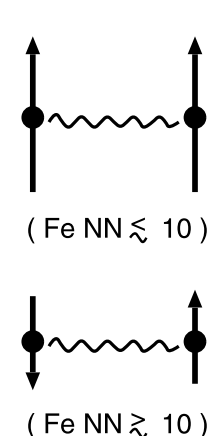
**Fig. 8.22** Pair-energy potentials  $\Phi_{\alpha\gamma}^{(a)}(\xi)$  and  $-\Phi_{\alpha\gamma}^{(e)}(\xi)$  for fcc (*upper*) and bcc (*lower*) Fe<sub>65</sub>Ni<sub>35</sub> alloys calculated at 900 K [192]. The notation  $\alpha\gamma$  (at) ( $\alpha\gamma$  (ex)) indicates the atomic (exchange) coupling between atom  $\alpha$  and atom  $\gamma$ 

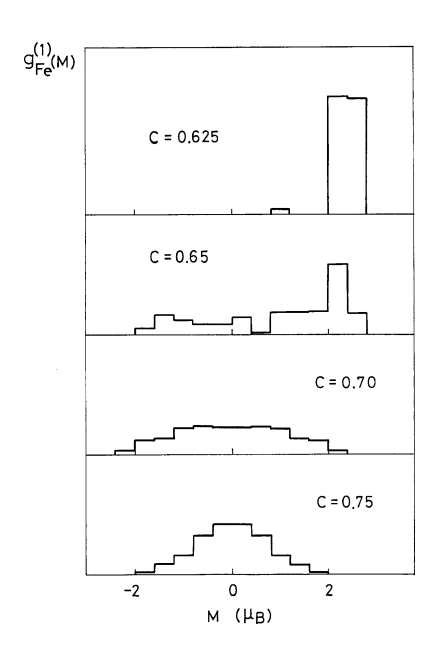
the neighboring Fe LM, while the Fe LMs with a large number of Fe NN show the antiferromagnetic coupling to the neighboring Fe LM's (see Fig. 8.23). The antiferromagnetic coupling of  $\Phi_{\text{FeFe}}^{(e)}(\xi)$  does not appear for any value of  $\xi$  in the bcc lattice as shown in Fig. 8.22(b).

The Fe LMs in Fe–Ni alloys decrease their amplitudes  $(\langle \xi^2 \rangle^{1/2})$  with increasing Fe concentration due to the downward-convex coupling  $\Phi_{\text{FeFe}}^{(a)}(\xi)$  and the upward-convex coupling  $\Phi_{\text{FeNi}}^{(a)}(\xi)$ . Near the critical concentration of ferromagnetic instability, amplitudes of LM with more than 10 Fe NN become less than  $1.7\mu_{\text{B}}$  and the Fe atoms with such local environments reverse their LM, leading to the ferromagnetic instability.

Fig. 8.23 Nonlinear coupling between Fe LM's in the fcc Fe–Ni alloys. Fe LM's with less than ten Fe NN have large amplitudes  $(\xi^2)^{1/2}$  more than  $1.7\mu_B$  and therefore show the ferromagnetic coupling, but Fe LM's with more than ten Fe NN have small amplitudes less than  $1.7\mu_B$ , thus the antiferromagnetic coupling

Fig. 8.24 Distribution functions  $g_{Fe}(M)$  of Fe LM in Fe–Ni alloys at 150 K for various Fe concentrations [192]

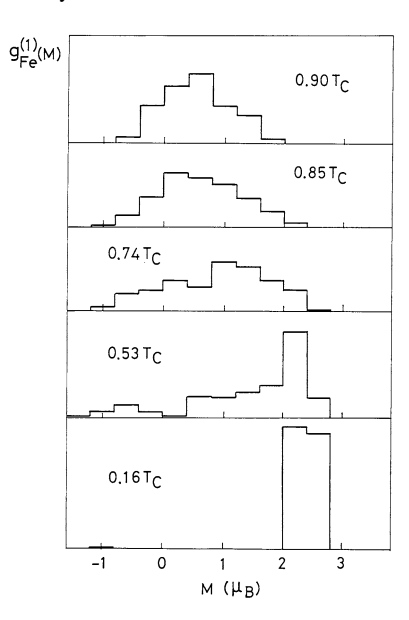




The nonlinear coupling between Fe LMs and its LEE yield a broad distribution of Fe LM near the critical concentration as shown in Fig. 8.24. Note that even after the disappearance of ferromagnetism, a broad LM distribution remains. It implies the existence of the SG specified by  $[\langle m_{\alpha} \rangle]_c = 0$  and  $[\langle m_{\alpha} \rangle^2]_c \neq 0$ .

Strong disturbance of Fe LM due to the LEE is also caused by thermal excitations. As shown in Fig. 8.23, the Fe LMs with more than 10 Fe NN decrease their amplitudes with increasing temperature near the critical concentration, and thus cause the reversal of their LM. Figure 8.25 shows this behavior (see the distribution at  $0.53\ T_{\rm C}$ ). With further increase of temperature, the distribution shrinks and merges into zero value at  $T_{\rm C}$ .

Fig. 8.25 Temperature dependence of the distribution functions for Fe LM at 62.5 at% Fe in Fe–Ni alloys [192]



We can calculate the internal field distribution of <sup>57</sup>Fe in Mössbauer experiments with use of an empirical expression  $H_i = a_i \langle m_i \rangle + \sum_{j=1}^{z} b_{ij} \langle m_j \rangle$  [196]. Here  $a_i$  and  $b_{ij}$  are constants. By making use of the distribution functions  $g_{\alpha}(M)$ , we obtain the distribution of the internal field on atom  $\alpha$  as follows.

$$P_{\alpha}(H) = \sum_{n=0}^{z} \Gamma(n, z, p^{\alpha \alpha}) \int \delta(H - H_{\alpha}(n, z, \{m_i\})) \times \left[ \prod_{i=1}^{n} g_{\alpha}(m_i) dm_i \right] \left[ \prod_{j=n+1}^{z} g_{\overline{\alpha}}(m_j) dm_j \right].$$

$$(8.101)$$

Here  $H_{\alpha}(n, z, \{m_i\})$  is the internal field under a given configuration, and is expressed by

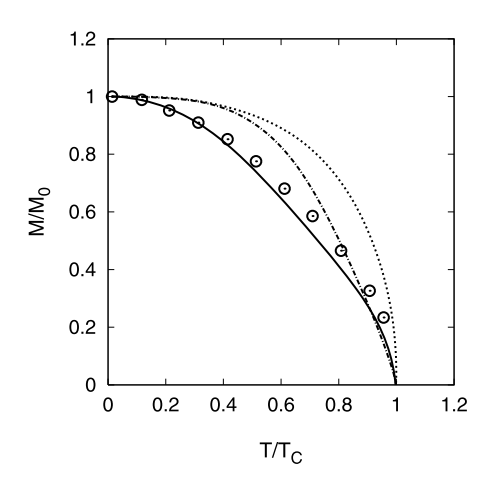
$$H_{\alpha}(n, z, \{m_i\}) = a_{\alpha} \langle \xi_{\alpha} \rangle (n, z, \{m_i\}) + b_{\alpha \alpha} \sum_{i=1}^{n} m_i + b_{\alpha \overline{\alpha}} \sum_{j=n+1}^{z} m_j.$$
 (8.102)

Figure 8.26 shows the calculated temperature dependence of the internal-field distribution function  $P_{\rm Fe}(H)$  at 62.5 at% Fe. With increasing temperature, the distribution rapidly broadens in accordance with the broadening of  $g_{\rm Fe}(M)$  at the same temperature. The results agree with the experimental data depicted in the inset [189]. A peak at  $H \approx 0.7 \mu_{\rm B}$  in the distribution functions for 0.53  $T_{\rm C}$  and 0.74  $T_{\rm C}$  originates in the Fe LM with 9 or 10 Fe NN.

Near the critical concentration of ferromagnetic instability, the magnetization vs. temperature curves deviate downward from the Brillouin curve experimentally [190]. Both the single-site theory and the theory of LEE can explain the fact

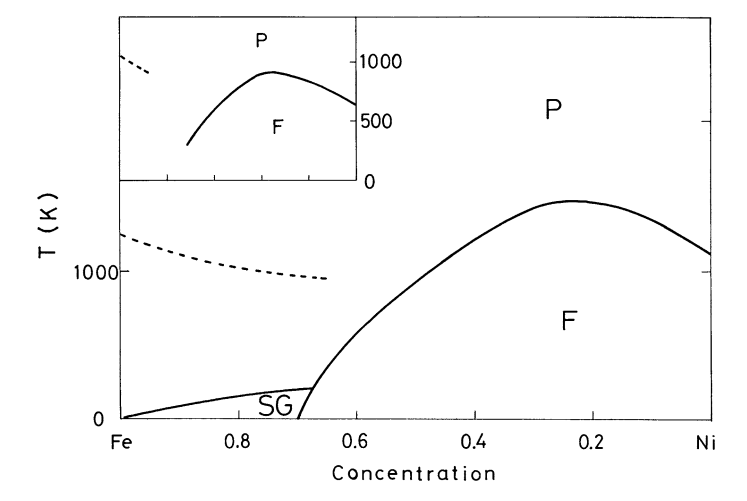
**Fig. 8.26** Temperature dependence of the internal-field distribution functions for <sup>57</sup>Fe at 62.5 at% Fe [192]. The *inset* shows the experimental results at 65 at% Fe [189]

Fig. 8.27 Reduced magnetization curves near the critical concentration of the ferromagnetic instability [171]. The *solid* (*dot-dashed*) *curve* is the result of the finite-temperature theory of the LEE (the SSA) at 50 at% Fe. The *dashed curve* is the S = 1/2 Brillouin curve. The *open circles* are the experimental data at 67 at% Fe



as shown in Fig. 8.27. The theory of LEE yields the smoother curve being close to the experimental data because the fluctuations of the surrounding configurations are favorable to the second order transition. Note that the other type of excitations also becomes important near the critical concentration of ferromagnetic instability. The low-energy spin wave excitations and the electron excitations coupled to the spin waves may also contribute to the smooth magnetization vs. temperature curve at low temperatures.

The calculated magnetic phase diagram of Fe-Ni alloys is summarized in Fig. 8.28. The result explains the experimental data semi-quantitatively as shown



**Fig. 8.28** Calculated magnetic phase diagram showing the ferromagnetic (F), spin-glass (SG), and paramagnetic (P) states [192]. The Curie temperatures for the bcc structure are shown by the *dashed curve*. The *inset* shows the experimental result [146]

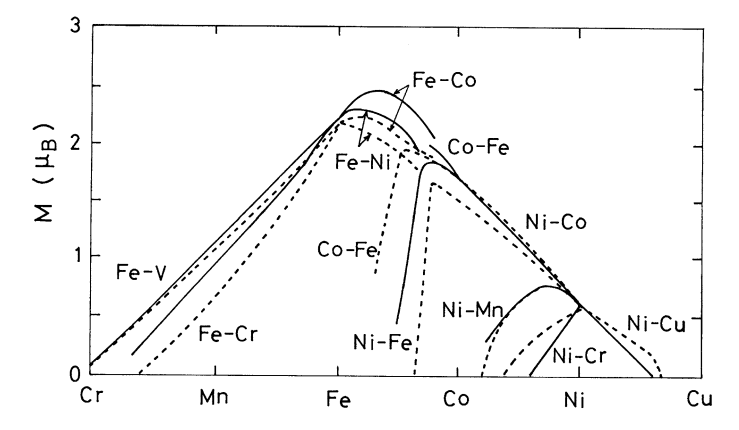


Fig. 8.29 Theory (dashed curves) vs. experiment (solid curves) for the Slater–Pauling curves. The calculations are performed at 150 K [195]

in the inset. The Curie temperature of Fe–Ni alloys shows a maximum with increasing Fe concentration because the ferromagnetic coupling  $\mathscr{J}_{FeNi}$  is stronger than  $\mathscr{J}_{NiNi}$  and the antiferromagnetic coupling  $\mathscr{J}_{FeFe}(<0)$  is weaker than the others in magnitude.

Magnetization vs. concentration curves in 3d transition metal alloys, which are calculated by the theory of LEE and the d band model, are summarized in Fig. 8.29. As discussed in Sect. 8.1, the straight line with  $-45^{\circ}$  slope at the r.h.s. of the Slater–Pauling curves is explained by the increase of holes in the down-spin band of the strong ferromagnet with decreasing average d electron number n. The Fermi level

reaches the top of the up-spin band around n = 7.5. When the d electron number becomes smaller than around 7.5, holes are created in the up-spin band. In Fe–V alloys the V local moments are antiparallel to the magnetization. The magnitudes of both Fe and V LMs decrease with increasing V concentration.

Although the concentration dependence of the magnetization curve in Fe–V alloys is explained by a simple dilution picture, it does not necessarily mean that the LEE are not important. Since the number of holes in the d bands increases with adding V atoms, Fe LMs become more flexible, so that they show the broad distribution of LMs. The distribution is caused by the LEE, i.e., the strong fluctuations in amplitudes due to the fluctuation of the surrounding atomic configuration. These LEE explain the broad distribution of the internal field seen by <sup>57</sup>Fe in Mössbauer experiments [197].

The Fe–Cr alloys show the behaviors similar to that of the Fe–V alloys with strong LEE. The theory explains the concentration dependence of magnetization. It also explains the concentration and temperature dependences of the distribution of the internal field in Mössbauer experiments. The Cr-rich Fe–Cr alloys show the antiferromagnetic state at less than 19 at% Fe. The theory of LEE is extended to the antiferromagnetic case under the assumption of the two sublattices [198]. In this case, we introduce two kinds of effective media,  $\mathcal{L}_{\sigma}^{(+)}$  on the (+) sublattice and  $\mathcal{L}_{\sigma}^{(-)}$  on the (-) sublattice. Accordingly, we have the distribution functions  $g_{\alpha}^{(+)}(M)$  and  $g_{\alpha}^{(-)}(M)$  on the (+) and (-) sublattices, respectively. Because of the symmetric relations  $\mathcal{L}_{\sigma}^{(-)} = \mathcal{L}_{-\sigma}^{(+)}$  and  $g_{\alpha}^{(-)}(M) = g_{\alpha}^{(+)}(-M)$ , we have the same type of integral equation (8.87) in which the distribution functions  $\{g_{\gamma_i}(m_i)\}$  at the r.h.s. of the equation have been replaced by  $\{g_{\gamma_i}(-m_i)\}$ .

The upward deviation of the calculated curve in Ni–Cu alloys originates in the neglect of the sd hybridization. The hybridization delocalizes Ni LMs therefore yields smaller magnetization in Cu-rich Ni alloys, so that the linear-concentration dependence is realized (see Fig. 8.14). The branch in Ni–Cr alloys has been explained by the formation of the virtual-bound state in the up-spin band above the Fermi level when the Cr atoms are dissolved in the host Ni (see Fig. 8.7).

The deviation from the straight line in Ni–Mn alloys has been shown to be caused by the reversal of Mn LMs with more than 3 Mn NN atoms with increasing Mn concentration (see Fig. 8.17). It is also worth to remind that the SG state appears after the disappearance of ferromagnetism, in agreement with the experiment [185], since the ferromagnetic exchange couplings between Ni LMs and between Ni and Mn LMs compete with the antiferromagnetic couplings between Mn LMs.

Rapid but continuous decrease of the curve in Fe–Ni alloys is not described by the single-site theory. The second-order transition with increasing Fe concentration is caused by nonlinear magnetic couplings between Fe LMs and the LEE on both the magnetic moments and their amplitudes of Fe LMs, as we have discussed before (see Fig. 8.21). The nonlinear couplings and the LEE on Fe LMs also describe the SG in Fe–Ni alloys [163] after the disappearance of ferromagnetism. The same type of strong LEE is found in fcc Co–Fe alloys [199], though the alloys change the structure from the fcc to the bcc at 30 at% Fe. According to the theoretical calculations, the fcc Co–Fe alloys show the ferromagnetic instability around 78 at% Fe and

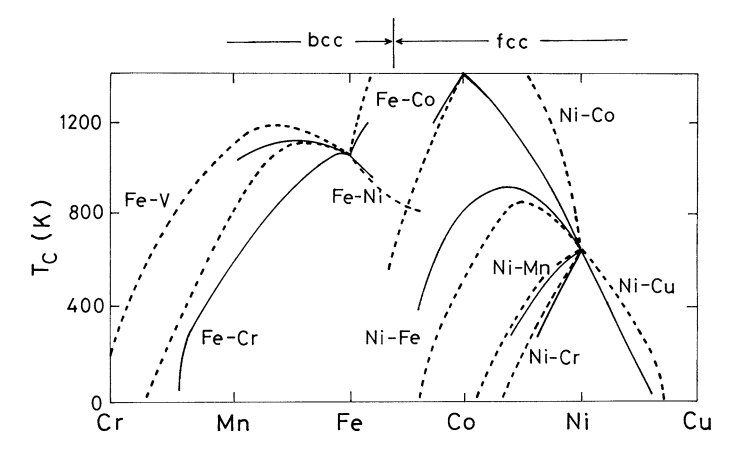


**Fig. 8.30** Theory (*dashed curves*) vs. experiment (*solid curves*) for the Curie-temperature Slater–Pauling curves [195]. Calculated results are renormalized at the pure metals

the SG behavior after the disappearance of ferromagnetism due to the same reason as in the case of Fe–Ni alloys. These behaviors are verified in the fcc Fe–Co particle system precipitated in a Cu matrix [200].

It is well-known that the Curie temperatures ( $T_{\rm C}$ ) in 3d transition metals show the curves being similar to the Slater–Pauling curves. The Curie-temperature Slater–Pauling curves calculated by the theory of the LEE are presented in Fig. 8.30 with the experimental data. Since  $T_{\rm C}$  are determined by thermal excitations, the curves are not directly related to the ground-state magnetizations. It should be noted that theoretical values of  $T_{\rm C}$  remain qualitative or semi-quantitative due to various approximations, so the curves in Fig. 8.30 are renormalized by  $T_{\rm C}$  for one of the constituent metals.

Calculated Curie-temperature Slater-Pauling curves explain overall features of the experimental data. In qualitative discussions on the concentration dependence of  $T_{\rm C}$ , the effective exchange interactions  $\{\mathcal{J}_{\alpha\gamma}\}$  defined by (8.83) are useful. In the case of Fe-V alloys, T<sub>C</sub> shows a maximum with increasing V concentration. In this system, calculated exchange interactions show that  $\mathcal{J}_{\text{FeFe}} \sim |\mathcal{J}_{\text{FeV}}| \gg |\mathcal{J}_{\text{VV}}| > 0$ , and  $\mathcal{J}_{\text{FeV}}$ ,  $\mathcal{J}_{\text{VV}} < 0$  in the bcc pure Fe. With increasing V concentration,  $\mathcal{J}_{\text{FeFe}}$ rapidly increases due to alloying and shows a maximum at 25 at% V, while  $|\mathcal{J}_{\text{FeV}}|$ monotonically decreases. These concentration dependences of magnetic couplings cause a maximum in T<sub>C</sub> around 20 at% V in agreement with the experiment. The same type of alloying effect on T<sub>C</sub> is seen in the bcc Fe–Ni alloys. There the exchange coupling  $\mathcal{J}_{FeFe}$  rapidly decreases up to 10 at% Ni with increasing Ni concentration. The effects decrease  $T_{\rm C}$  in spite of the fact that  $\mathcal{J}_{\rm FeNi} > \mathcal{J}_{\rm FeFe} > 0$ . On the other hand this alloying effect is not found in the bcc Fe-Co alloys. There the magnetic couplings satisfy an inequality  $\mathcal{J}_{CoCo} > \mathcal{J}_{FeCo} > \mathcal{J}_{FeFe} > 0$  and  $\mathcal{J}_{FeFe}$ gradually increases with increasing Co concentration, so that  $T_{\rm C}$  in the bcc Fe–Co alloys monotonically increases.

The maximum in the curve for fcc Fe–Ni alloys and the curves in Fe–Co–Ni alloys are explained basically by a rigid band theory with thermal spin fluctuations. More detailed analyses indicate that the Fe–Ni pairs  $\mathcal{J}_{\text{FeNi}}$  (>  $\mathcal{J}_{\text{NiNi}}$ ) increase  $T_{\text{C}}$  first and the Fe–Fe pairs  $\mathcal{J}_{\text{FeFe}}$ (< 0) decrease  $T_{\text{C}}$  next with increasing Fe concentration.

The Curie temperature in Ni–Mn alloys monotonically decreases with increasing Mn concentration, while the magnetization vs. concentration curve shows a maximum. The former is explained by the fact that  $\mathcal{J}_{\text{NiNi}} > \mathcal{J}_{\text{NiMn}} > 0$  up to 10 at% Mn. The latter is explained by the fact that the small Ni LMs are replaced first by the large Mn LMs parallel to the magnetization, but the Mn LMs become antiparallel to the magnetization when the number of neighboring Mn atoms become larger than 3, as discussed before.

## 8.4 Computer Simulations for Disordered Magnetic Alloys

The finite-temperature theory of local environment effects (LEE) self-consistently determines the distribution of the local moments (LM) of constituent atoms in disordered alloys going beyond the single-site approximation, and allows us to calculate their temperature dependences. The method however relies on the distribution of LM, and therefore does not provide us with details on the magnetic structure in real space. In addition, it is not easy to take into account the effects of inter-site correlations going beyond the nearest-neighbor approximation because the number of integrals rapidly increases with increasing the correlation length in the integral equation for distribution functions. The molecular dynamics (MD) approach presented in Sect. 6.3 allows us to clarify the spatial structure of magnetic moments and to take into account the second, third, and further distant neighbor correlations in disordered alloys. In this section we describe the MD approach to the disordered alloys in greater details and present its application to the Fe–Cr alloys [108, 109, 201].

In the MD approach, we calculate the thermal average of LMs  $\langle \boldsymbol{m}_i \rangle$  by means of the time average given by (6.63). The spin dynamics leading to the thermal average (6.60) is obtained by solving the equations of motion (6.64)–(6.66). At each time step, we calculate the magnetic forces  $-\partial \Psi(\boldsymbol{\xi})/\partial \xi_{i\alpha}$ . The latter is obtained from (6.67) via the temporal LM  $\langle \boldsymbol{m}_i \rangle_0$  as  $-\partial \Psi(\boldsymbol{\xi})/\partial \xi_{i\alpha} = (\tilde{J}/2)(\langle m_{i\alpha} \rangle_0 - \xi_{i\alpha}) - 2T\xi_{i\alpha}/\xi_i^2$ , where the average  $\langle (\sim) \rangle_0$  is taken with respect to the Hamiltonian (6.57).

For simplicity we consider here the d band model Hamiltonian obtained from (6.57), and assume the alloys with off-diagonal disorders described by the geometrical mean model:

$$t_{imjm'} = r_{\alpha}^* t_{imjm'}^0 r_{\gamma}, \tag{8.103}$$

where  $\alpha$  ( $\gamma$ ) denotes the type of atom A or B on sites i (j) (see (8.16)).

The random atomic configuration for a given concentration  $c_{\alpha}$  and the ASRO parameter  $\tau_{\alpha}$  is made on the computer as follows. Let us consider a cubic unit cell consisting of a large number of N atoms with periodic boundary condition. The

ASRO parameter is connected with the probability of finding an atom  $\alpha$  on the nearest-neighbor of atom  $\alpha$  as  $p^{\alpha\alpha}=c_{\alpha}+(1-c_{\alpha})\tau_{\alpha}$  (see (8.65)). We first create an A or B atom on each site of the MD unit cell with the probability  $c_{\rm A}$  or  $c_{\rm B}$  using random numbers. Next, we replace an A atom with a B atom (or a B atom with an A atom) at randomly chosen sites until the given concentration  $c_{\rm A}$  is realized. We then calculate the probability  $\tilde{p}^{\rm AA}=\sum_{i\in A}N_{\rm AA}(i)/N_{\rm A}z$ , i.e., the probability of finding another A atom at the neighboring site of an A atom. Here  $N_{\rm AA}(i)$  denotes the number of A atoms at the nearest-neighbor sites of the A atom at site i,z is the number of nearest-neighbor sites, and  $N_{\rm A}$  is the total number of A atoms in the MD unit cell. If the probability  $\tilde{p}^{\rm AA}$  is smaller (larger) than  $p^{\rm AA}$ , we exchange the A atom with the B atom in a randomly chosen A–B NN pair, and accept the exchange if the new  $\tilde{p}^{\rm AA}$  is larger (smaller) than the old one. We obtain the requested alloy by repeating the procedure until  $|\tilde{p}^{\rm AA}-p^{\rm AA}| \leq \varepsilon (=2/N_{\rm A}z)$  is satisfied.

The magnetic moment on site i in the magnetic force is expressed by means of the Green function G(z) as follows.

$$\langle m_{i\alpha} \rangle_0 = \int d\omega f(\omega) \frac{(-)}{\pi} \text{Im} \sum_{m\sigma} (\sigma_{\alpha} G(z))_{im\sigma im\sigma},$$
 (8.104)

$$G_{im\sigma jm'\sigma'}(z) = \left[ \left( z - \boldsymbol{H}(\boldsymbol{\xi}) \right)^{-1} \right]_{im\sigma jm'\sigma'}.$$
 (8.105)

Here  $H(\xi)$  is the one-electron Hamiltonian matrix of (6.57) in which the matrix elements for the sp electrons have been dropped.

When we calculate the Green function on site i in (8.104), we consider a MD unit cell in which site i is centered. We surround the MD unit cell with 27 MD unit cells in which all atomic levels or locators have been replaced by an effective medium (see Fig. 6.6). As we have discussed in Sect. 6.3, the Green functions in (8.104) are expressed as follows by using the new basis representations which diagonalize the Pauli spin matrices  $\sigma_{\alpha}$  ( $\alpha = x, y, z$ ).

$$\sum_{\sigma} (\sigma_x G)_{im\sigma im\sigma} = G_{im1im1} - G_{im2im2}, \tag{8.106}$$

$$\sum_{\sigma} (\sigma_y G)_{im\sigma im\sigma} = G_{im3im3} - G_{im4im4}, \tag{8.107}$$

$$\sum_{\sigma} (\sigma_z G)_{im\sigma im\sigma} = G_{im\uparrow im\uparrow} - G_{im\downarrow im\downarrow}. \tag{8.108}$$

Here the local basis functions at the r.h.s. are defined by  $|im1\rangle = (|im\uparrow\rangle + |im\downarrow\rangle)/\sqrt{2}$ ,  $|im2\rangle = (|im\uparrow\rangle - |im\downarrow\rangle)/\sqrt{2}$ ,  $|im3\rangle = (|im\uparrow\rangle + i|im\downarrow\rangle)/\sqrt{2}$ , and  $|im4\rangle = (|im\uparrow\rangle - i|im\downarrow\rangle)/\sqrt{2}$ .

The diagonal Green function  $G_{im\alpha im\alpha}$  ( $\alpha = 1-4, \uparrow, \downarrow$ ) can be calculated by using the recursion method as follows (Appendix G).

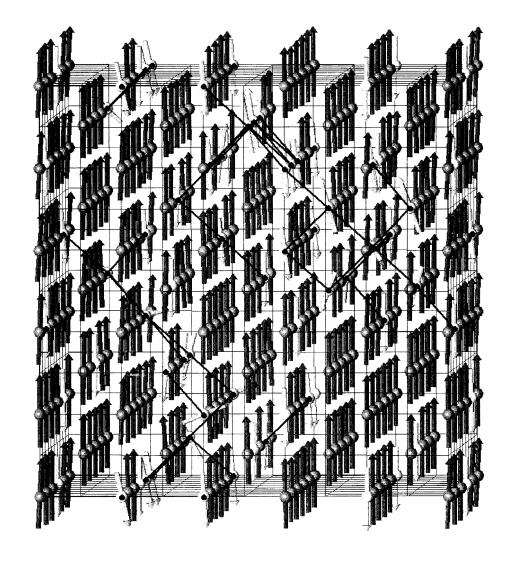
$$G_{im\alpha im\alpha}(z, \xi) = \frac{1}{z - a_{1im\alpha}(\xi) - \frac{|b_{1im\alpha}(\xi)|^2}{z - a_{2im\alpha}(\xi) - \frac{|b_{2im\alpha}(\xi)|^2}{\cdots - \frac{|b_{l-1im\alpha}(\xi)|^2}{z - a_{lim\alpha}(\xi) - T_{lim\alpha}(z, \xi)}}}.$$

Here  $a_{nim\alpha}(\xi)$  and  $b_{nim\alpha}(\xi)$  are the recursion coefficients of the *n*-th order.  $T_{lim\alpha}(z,\xi)$  is called the terminator. When the recursion coefficients begin to contain the matrix elements outside the MD unit cell at the *l*-th level, we approximate the terminator  $T_{liv\alpha}(z,\xi)$  with an effective terminator for the coherent Green function  $[(\mathcal{L}^{-1}-t)^{-1}]_{im\alpha\,im\alpha}/|r_i|^2$ :  $T_{lim\alpha}(z,\xi)\approx |r_\alpha|^2\mathcal{T}_{lm\alpha}$ . Here  $\mathcal{T}_{lm\alpha}$  is the terminator of the *l*th level obtained from the coherent Green function.

100) in the ferromagnetic region within the single-site approximation, and in the last section we briefly discussed the LEE of Fe-Cr alloys in the same region. The Fe-Cr alloys are reported to show the antiferromagnetism (AF) in the Cr-rich region  $(x \lesssim 5 \text{ at\% Fe})$ , while in the Fe-rich region (90 at% Fe  $\lesssim x$ ), they show a simple ferromagnetism (F) with Cr local magnetic moments (LM) being antiparallel to the bulk magnetization. The actual Fe-Cr alloys however show more complex features due to long-range competing magnetic interactions. In fact, the system shows in the concentrated regions complex magnetic structures and its phase diagram has not been established yet. In particular, in the range 10 at% Fe  $\lesssim x \lesssim 30$  at% Fe where the phase boundary of the F in Fe-rich region encounters with that of the Cr-rich AF, two kinds of phase diagrams are proposed experimentally: the phase diagram proposed by Loegel [202] and Rode et al. [203] in which the F and the AF overlap (coexistence of F and AF) at zero temperature, and the phase diagram proposed by Burke et al. [204, 205] which shows up the existence of the spin-glass (SG) like phases between the F and the AF. Also, in the region above the F phase boundary (20 at% Fe  $\leq x \leq$  25 at% Fe), temperature dependent complex magnetic structures are suggested in neutron [206] and Mössbauer experiments [207, 208]. Furthermore, the real microscopic magnetic structures of Fe-Cr alloys in the range 30 at% Fe  $\lesssim x \lesssim 70$  at% Fe are expected to be rather complex because of the competition between the ferro- and antiferro-magnetic couplings, although the composition dependence of the average magnetic moment in the Fe-rich region was explained by a constant number of holes in the down spin band in the rigid band picture (see Sect. 8.1). In what follows, we elucidate the complex magnetic structure obtained by the MD method [201] to see how much information one can obtain from a computer simulation.

The magnetic structures based on the molecular dynamics method are presented in Figs. 8.31-8.36. In the computer simulations, N = 250 atoms are put in a MD

Fig. 8.31 Magnetic structure of Fe<sub>80</sub>Cr<sub>20</sub> alloy obtained by the MD calculations at 25 K [201]. The *bright (dark) spheres* represent the Cr (Fe) atoms. The Cr clusters are shown by the nearest-neighbor Cr networks which are represented by lines and dots on the Cr atoms



unit cell which corresponds to the  $5 \times 5 \times 5$  bcc lattice, and the temperature has been kept at 25 K. When the Cr atoms are added to the ferromagnetic Fe, the calculated Cr LMs are aligned to be antiparallel to the bulk magnetization; the number of the down spin states on Cr atoms below the Fermi level becomes larger than that of the up spin states due to more hybridization of former electrons with the same spin bands of the host Fe. The impurity states of Cr atoms continue to exist until 90 at% Fe, where small clusters consisting of the nearest-neighbor (NN) Cr bonds begin to appear in the ferromagnetic Fe matrix. At 80 at% Fe, about two thirds of all Cr atoms belong to small clusters and the others are still isolated as shown in Fig. 8.31. The isolated Cr LMs are antiparallel to the bulk magnetization, while the Cr LMs in the clusters are declined due to the AF couplings between NN Cr LMs.

The Cr clusters develop with increasing Cr concentration; most Cr atoms belong to a big cluster and only a small number of Cr atoms are isolated at 70 at% Fe. The Cr LMs of the cluster are disordered in directions due to the frustration caused by the competition between the AF Cr-Cr NN couplings and the AF Cr-Fe NN couplings, although the Fe LMs still show the ferromagnetic alignment. The developed Cr clusters form a network consisting of the NN Cr bonds around 60 at% Fe, which spreads throughout the MD unit cell as shown in Fig. 8.32. There the Cr LMs of the network are highly disordered in directions. The Fe LMs, on the other hand, are aligned ferromagnetically, though they are slightly fluctuated in directions by the coupling to the disordered Cr LMs. The disorder of Cr LMs in both direction and amplitude continues until 50 at% Fe as shown in Fig. 8.33. The distribution of LMs becomes wider with increasing Cr concentration due to more competition between the F and AF magnetic interactions. At 50 at% Fe, the partial distribution of the Cr LMs is spread from  $-1.5\mu_B$  to  $1.5\mu_B$ , and the distribution of the Fe LMs (around  $2.0\mu_{\rm B}$ ) is also spread, though less broad as compared with the Cr LMs' at this concentration. These distributions originate mainly in the local-environment effects (LEE), since it is observed from Fig. 8.33 that Cr LMs surrounded by a few Cr

Fig. 8.32 Magnetic structure of Fe<sub>60</sub>Cr<sub>40</sub> alloy obtained by the MD calculations at 25 K [201]. The *bright (dark) spheres* represent the Cr (Fe) atoms

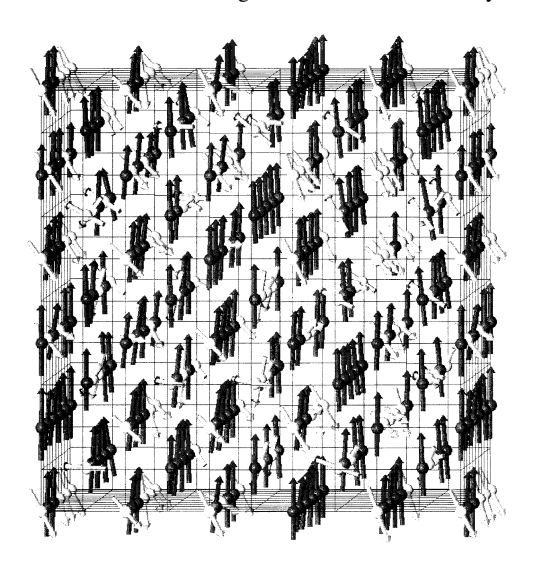
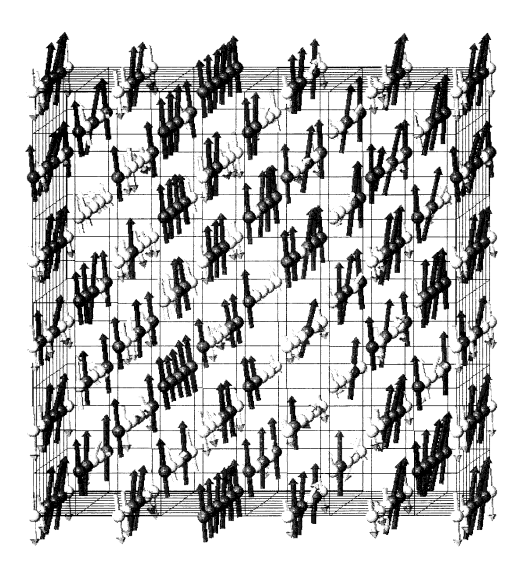


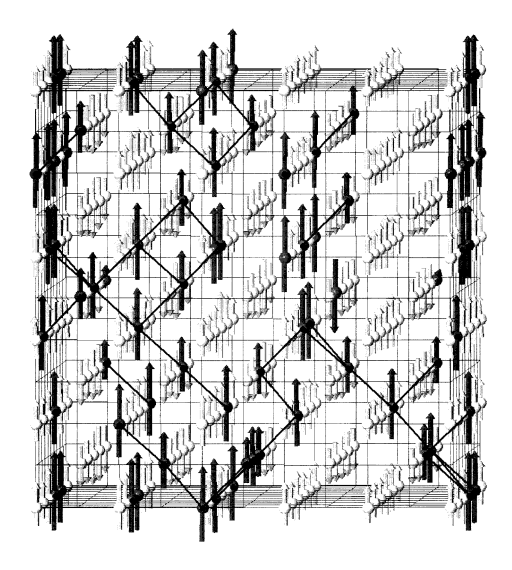
Fig. 8.33 Magnetic structure of Fe<sub>50</sub>Cr<sub>50</sub> alloy obtained by the MD calculations at 25 K [201]. The *bright (dark)* spheres represent the Cr (Fe) atoms



LMs have large amplitudes, while those surrounded by a few Fe LMs tend to have small amplitudes. The broad distribution of the ferromagnetic Fe LMs continues until 20 at% Fe, where the ferromagnetic order of Fe atoms terminates.

At 40 at% Fe, the Cr magnetic moments start to develop the long-range AF order, although some LMs are still fluctuated in directions (broken AF). The ferromagnetic long-range order (LRO) of the Fe coexists with the broken AF of the Cr there. Below 40 at% Fe, the large ferromagnetic Fe NN network which spreads throughout the unit cell starts to split into finite clusters. We find that Fe atoms still form the ferromagnetic LRO at 30 at% Fe. At this concentration, the distribution of Cr LMs

Fig. 8.34 Magnetic structure of Fe<sub>20</sub>Cr<sub>80</sub> alloy obtained by the MD calculations at 25 K [201]. The *bright (dark)* spheres represent the Cr (Fe) atoms. The Fe clusters are shown by the nearest-neighbor (NN) Fe networks drawn by *lines* and *dots* on the Fe atoms



are separated into those of up-spin and down-spin sublattices due to the long-range AF order.

At 20 at% Fe, the coexistence of the collinear F of Fe and the AF of Cr are observed as shown in Fig. 8.34, where the Cr LMs of up-spin and down-spin sublattices are distributed rather symmetrically. All the magnetizations of separated Fe clusters are oriented in the same direction, due to the long-range ferromagnetic interactions between the Fe LMs. Therefore the effective interaction between the Fe clusters is also ferromagnetic at this concentration. The coexistence of the two long-range orders around 20 at% Fe is consistent with the phase diagram proposed by Loegel [202] and Rode et al. [203].

The AF LRO of the Cr is developed with further increase in Cr concentration. At 15 at% Fe, about one third of the Fe atoms are isolated while the others form ferromagnetic clusters. However, the effective ferromagnetic interactions between the Fe clusters seem weak, because some magnetizations of Fe clusters are opposite to those of the other clusters, as shown in Fig. 8.35. It should be noted that the MD simulations lead to different magnetizations in direction for some Fe clusters when we start with different initial configurations at this concentration. This means that the cluster spin glass (SG) state is possible due to the existence of many degenerate quasi-stable states around this concentration. Moreover, the cluster SG in this concentration region is collinear due to the existence of AF LRO in the present calculations. With increasing further the Cr concentration, the ferromagnetic Fe clusters shrink and most Fe atoms become isolated. At 10 at% Fe, the isolated Fe LMs are mostly aligned not to violate the AF LRO of the Cr matrix, though the Fe LMs are modulated in direction due to long-range Fe–Fe magnetic interactions, as shown in Fig. 8.36.

In the range between 5 and 20 at% Fe, every isolated NN Fe pair in the AF Cr sublattices stays in a quasi-stable state in which Fe LMs with different amplitudes

Fig. 8.35 Magnetic structure of Fe<sub>15</sub>Cr<sub>85</sub> alloy obtained by the MD calculations at 25 K [201]. The *bright (dark)* spheres represent the Cr (Fe) atoms. The Fe clusters are shown by the NN Fe networks drawn by *lines* and *dots* on the Fe atoms

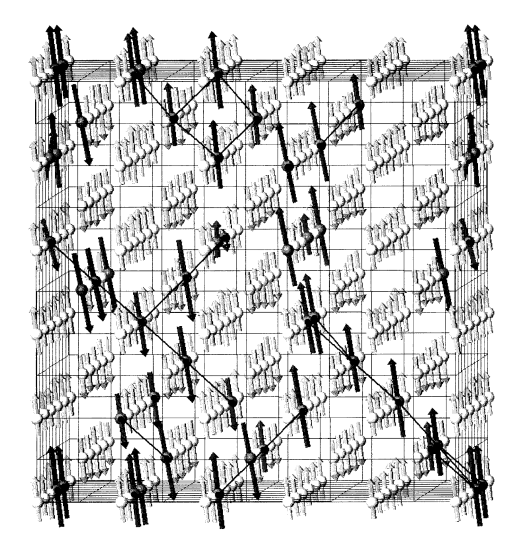
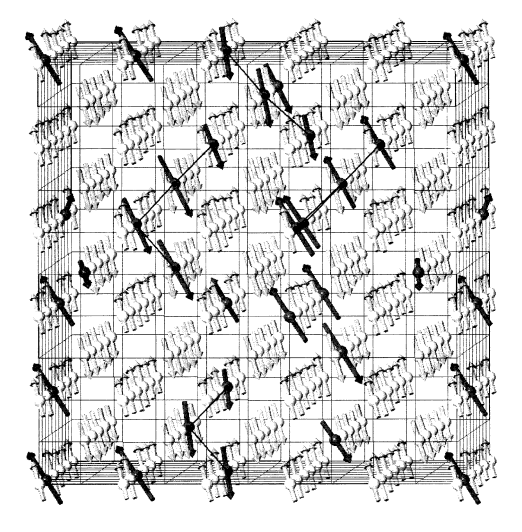
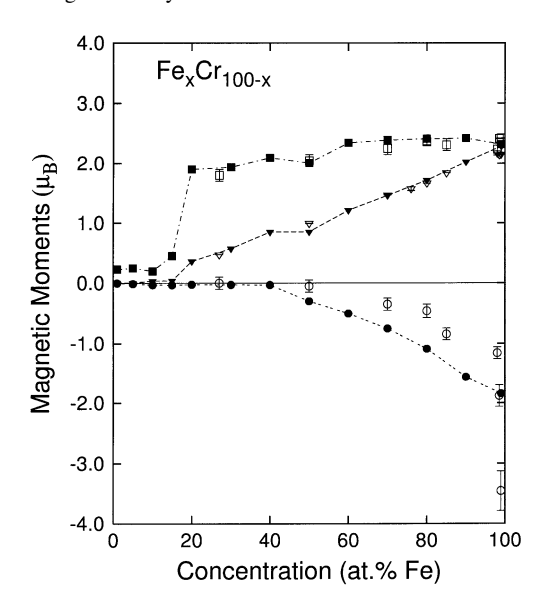


Fig. 8.36 Magnetic structure of Fe<sub>10</sub>Cr<sub>90</sub> alloy obtained by the MD calculations at 25 K [201]. The *bright (dark) spheres* represent the Cr (Fe) atoms. The Fe clusters are shown by the NN Fe networks drawn by *lines* and *dots* on the Fe atoms



are ferromagnetically coupled. One of the LMs of the Fe pair points in the same direction with that of the corresponding sublattice LM and has a larger amplitude, while another LM points in the opposite direction and has a smaller amplitude, as shown in Figs. 8.35 and 8.36. These isolated NN Fe pairs may correspond to the free spin-pairs with equal amplitudes proposed by Friedel and Hedman [209] to explain the Mössbauer line spectra of free rotating iron moments reported at low temperatures. Each isolated Fe pair state with non-equal amplitudes must have a degenerate state whose LMs are exchanged and flipped simultaneously. The potential barrier between these degenerate states in the antiferromagnetic matrix must be low, because no potential barrier arises when we rotate a pair of isolated NN Fe LMs with the same amplitudes, and the energy difference between the isolated NN pairs with

Fig. 8.37 Concentration dependence of various average magnetic moments in Fe-Cr alloys calculated by the MD approach at 25 K [201]. The dashed line with ▼ represents the average magnetization  $[\langle m \rangle]_c$ , and the dash-dotted (dotted) line with ■ (•) represents the average Fe (Cr) magnetic moments  $[\langle m_z Fe \rangle]_c ([\langle m_z Cr \rangle]_c).$ Experimental data of these quantities are shown by  $\nabla$ ,  $\square$ , and () with error bars [157, 158, 210–212]



equal LMs and those with non-equal LMs must be small. The NN Fe pairs with non-equal amplitudes are also found in the Fe clusters consisting of more than three atoms (see Figs. 8.34, 8.35, and 8.36).

Average magnetic moments of Fe–Cr alloys calculated by the MD approach are presented in Fig. 8.37. The calculated magnetization  $[\langle m \rangle]_c$  decreases gradually as the Fe concentration x is decreased and vanishes at  $x \approx 15$  at% Fe in good agreement with the experimental data and the Hartree–Fock CPA results (see Fig. 8.5) in the wide range of concentration ( $30 \lesssim x \le 100$  at% Fe). Average amplitudes of Fe and Cr LMs in the pure Cr limit are  $1.0\mu_B$  and  $0.7\mu_B$ , respectively, while in the pure Fe limit, they are  $2.35\mu_B$  and  $1.9\mu_B$ . As the Fe concentration is reduced, the average moment of Fe atoms  $[\langle m_{Fe} \rangle]_c$  increases slightly until  $2.4\mu_B$  at 90 at% Fe, and decreases very slowly to  $2.3\mu_B$  at 60 at% Fe. Below 60 at% Fe, the Fe LMs are subject to the strong LEE, and  $[\langle m_{Fe} \rangle]_c$  changes to slightly smaller values in the range  $20 \lesssim x \lesssim 60$  at% Fe.

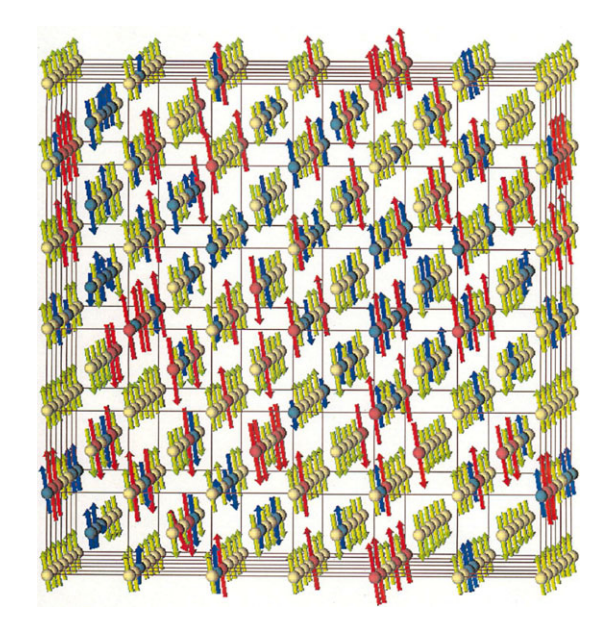
The calculated average moment of Cr atoms  $[\langle m_{\rm Cr} \rangle]_c$ , on the other hand, starts to gradually increase from the value  $-1.8\mu_{\rm B}$  in the pure Fe limit and vanishes at  $x \approx 40$  at% Fe.  $[\langle m_{\rm Cr} \rangle]_c$  agrees semi-quantitatively with the experimental results. It should be noted that the vanishing of  $[\langle m_{\rm Cr} \rangle]_c$  in the range  $0 \lesssim x \lesssim 40$  at% Fe is accompanied by the formation of antiferromagnetic or broken antiferromagnetic states, as mentioned before. The average magnitude of the sublattice moments of Cr atoms, in our MD calculation, is small, but does not vanish in the concentration region around x = 20 at% Fe. In the range  $25 \lesssim x \lesssim 40$  at% Fe, Cr LMs continuously change their configurations from the antiferromagnetically ordered state to less ordered states with increasing Fe concentration.

The phase diagram of Fe-Cr alloys obtained from the MD calculations at low temperatures is summarized in Fig. 8.38. The alloys are characterized by a persis-

0 20		20	40	60	80	100
	AF	<b>AF</b> + <b>F</b>	•	F	,	'
Fe	noncol. cluster		F with LI	EE collin	collinear F	
$\mathbf{Cr}$	AF		broken AF	noncollinear	anti- para	llel

**Fig. 8.38** The magnetic phase diagram of Fe–Cr alloys as a function of Fe concentration obtained from the MD calculations at 25 K [201]. The *upper row* shows the diagram based on the simple category: the Ferromagnetism (F) and the antiferromagnetism (AF). AF + F denotes the coexistence of the AF and the F. The *middle* and *lower rows* are the diagram showing various magnetic structures of each component

Fig. 8.39 The magnetic structure of Fe<sub>20</sub>Cr<sub>65</sub>Mn<sub>15</sub> alloys obtained by the MD calculations at 25 K. The *blue, green,* and *red spheres* represent the Fe, Cr, and Mn atoms, respectively. The *arrows* show their LM's in arbitrary unit



tence of the magnetic LRO of the constituent atoms up to high concentrations; they show the ferromagnetic LRO of Fe atoms up to 80 at% Cr, and the antiferromagnetic LRO of Cr atoms up to 30 at% Fe. In the narrow region around 20 at% Fe, the F LRO due to Fe LMs coexists with the AF LRO of Cr LMs. The result is consistent with the experimental phase diagram proposed by Loegel [202] and Rode et al. [203]. The wide range of the F state is divided into three regimes, i.e., (i) F with isolated antiparallel Cr LMs (80 at% Fe  $\leq x$ ), (ii) F with Cr clusters whose LMs are non-collinearly disordered (50  $\leq x \leq$  75 at% Fe), and (iii) F with broad distributions of Fe LMs and with non-collinear or broken antiferromagnetic Cr LMs (25  $\leq x \leq$  45 at% Fe). Furthermore, in the Cr rich regions, the cluster SG states ex-

ist around 15 at% Fe in the antiferromagnetic LRO of Cr. The SG behaviors around 15 at% Fe are verified experimentally [204, 205].

The MD calculations of ternary alloys are also straightforward. There we construct the random atomic configuration for a given concentration and atomic short range order, and solve the iso-thermal MD equations (6.63). Taking the time average in the equilibrium state, we obtain the average magnetic moment at each site. The magnetic structure of bcc  $Fe_{20}Cr_{80-x}Mn_x$  ( $0 \le x \le 40$ ) ternary alloys for example has been calculated at 25 K with use of 432 atoms in the MD unit cell ( $6 \times 6 \times 6$  bcc lattice) [213]. As we have mentioned,  $Fe_{20}Cr_{80}$  alloys show the coexistence of the Cr AF LRO and the Fe ferromagnetic clusters (see Fig. 8.34 and AF + F in Fig. 8.38). When Cr or Fe atoms are replaced by Mn atoms, the Mn LMs are arranged to enhance the Cr AF LRO, so that the AF structure is stabilized with increasing Mn concentration (see Fig. 8.39). The couplings between the Fe clusters and the Cr–Mn system with the AF LRO are rather weak, so that they form the cluster SG. The MD calculations show that the SG order of Fe ferromagnetic clusters is collinear due to the weak AF coupling between Fe and Cr LMs, and thus the isotropic SG is suppressed in this system.

# **Chapter 9 Magnetism of Amorphous Metals and Alloys**

Amorphous metals and alloys are characterized by the structural disorder which breaks the Bravais lattice. Their magnetic properties are well defined once the quenching method and rate are specified, though their structures are metastable thermodynamically. The amorphous metals and alloys provide us with a fundamental problem of the structure vs. magnetism in the condensed matter physics. In this chapter, we present the theoretical aspects on the magnetism of amorphous metals and alloys. We first give an introduction to the amorphous metallic magnetism in Sect. 9.1. Next we explain how to make the structure model of amorphous metals and alloys, and describe the method to calculate their electronic structure in Sect. 9.2. In Sect. 9.3, we present the finite-temperature theory of magnetism for amorphous metals, and clarify in Sect. 9.4 the basic properties of amorphous transition metals. These properties include the spin glass in amorphous Fe, the enhancement of the Curie temperature of amorphous Co, and the weak ferromagnetism of amorphous Ni. We extend the theory to amorphous alloys in Sect. 9.5, and elucidate in Sect. 9.6 the magnetism of amorphous transition metal alloys as well as the rare-earth transition metal amorphous alloys.

## 9.1 Introduction to the Amorphous Metallic Magnetism

Amorphous alloys are obtained by rapid quenching techniques such as vapor quenching and liquid quenching typically with the cooling rate  $10^6$  K/s. Their X-ray diffraction patterns show a halo, indicating the microscopic structural disorder which violates the Bravais lattice [214, 215]. Historically amorphous transition metal alloys containing considerable amounts of metalloids (typically 20 at.% B or P) were investigated at early stage [216–218]. These alloys show a uniform reduction of the magnetization and Curie temperature ( $T_{\rm C}$ ) as compared with those of the crystalline alloys. Amorphous Fe<sub>80</sub>B<sub>10</sub>P<sub>10</sub> alloy [218], for example, shows the ferromagnetism with the ground-state magnetization  $M = 2.1\mu_{\rm B}$  and  $T_{\rm C} = 640$  K, while the bcc Fe has  $M = 2.2\mu_{\rm B}$  and  $T_{\rm C} = 1040$  K. Amorphous Co<sub>80</sub>B<sub>10</sub>P<sub>10</sub> al-

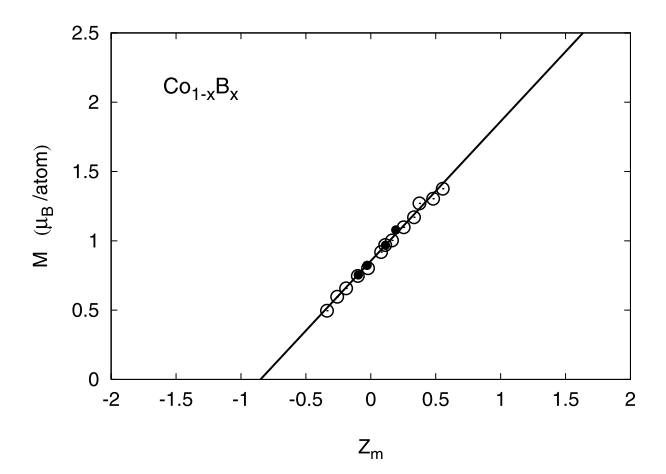


Fig. 9.1 Generalized Slater–Pauling plot of magnetization per atom for amorphous  $Co_{1-x}B_x$  alloys. Experimental data are shown by *open circles* [219] and *closed circles* [220]. The *solid line* shows the curve obtained from (9.1) with  $2N_{sp\uparrow} = 0.85$ 

loy also shows the ferromagnetism with  $M=1.1\mu_{\rm B}$  and  $T_{\rm C}=770$  K, which are compared with  $M=1.7\mu_{\rm B}$  and  $T_{\rm C}=1388$  K in the fcc Co.

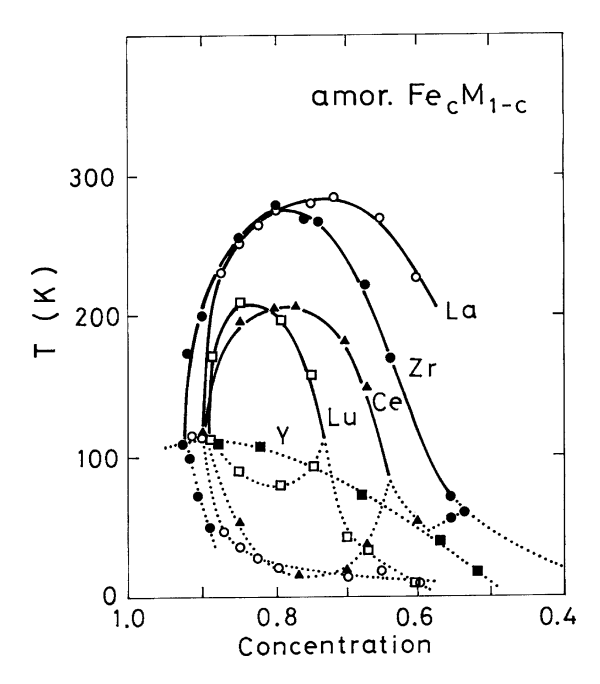
Magnetization vs. concentration curves were analyzed by using a generalized Slater–Pauling curve picture, which was explained in Sect. 8.1. There we expressed the magnetization M by means of the up-spin valence electron number  $N_{\uparrow}$  and the total valence electron number Z as  $M=2N_{\uparrow}-Z$  (see (8.1)). These quantities may be expressed by those of constituent atoms as  $N_{\uparrow}=\sum_{\alpha}c_{\alpha}N_{d\uparrow}^{\alpha}+N_{sp\uparrow}$  and  $Z=\sum_{\alpha}c_{\alpha}Z_{\alpha}$ . Here  $c_{\alpha}$ ,  $N_{d\uparrow}^{\alpha}$ , and  $N_{sp\uparrow}$  are the concentration of atom  $\alpha$ , the d electron number with up spin of atom  $\alpha$ , and the averaged sp electrons with up spin, respectively.  $Z_{\alpha}$  denotes the chemical valence for constituent atom  $\alpha$ . Substituting the expressions of  $N_{\uparrow}$  and Z into  $M=2N_{\uparrow}-Z$ , we obtain

$$M = Z_{\rm m} + 2N_{\rm sp\uparrow}. \tag{9.1}$$

Here  $Z_{\rm m}$  is the averaged magnetic valence defined by  $Z_{\rm m} = \sum_{\alpha} c_{\alpha} (2N_{\rm d}^{\alpha} - Z_{\alpha})$ . Since  $Z_{\rm m}$  has a simple concentration dependence for the transition metal alloys with strong ferromagnetism, we can expect a linear relation between M and  $Z_{\rm m}$ . Figure 9.1 shows the experimental data vs. theoretical curves for amorphous  ${\rm Co}_{1-x}{\rm B}_x$  alloys. We find a linear relation with the slope one between M and  $Z_{\rm m}$  as expected from (9.1). Many amorphous transition metal (TM) metalloid alloys follows a simple generalized Slater–Pauling curve given by (9.1).

On the other hand, amorphous transition metal alloys containing early transition metals (ETM) or rare-earth (RE) metals show a dramatic change in their magnetism. In Fe-rich amorphous alloys, the ferromagnetism collapses with increasing Fe concentration, and the spin glass (SG) appears beyond 90 at% Fe as shown in Fig. 9.2 [221]. It is remarkable that the SG appear irrespective of the second el-

Fig. 9.2 Magnetic phase diagram showing the Curie temperatures (*solid curves*) and spin-glass temperatures (*dotted curves*) of amorphous  $Fe_cM_{1-c}$  alloys (M = La, Zr, Ce, Lu, and Y) [221]



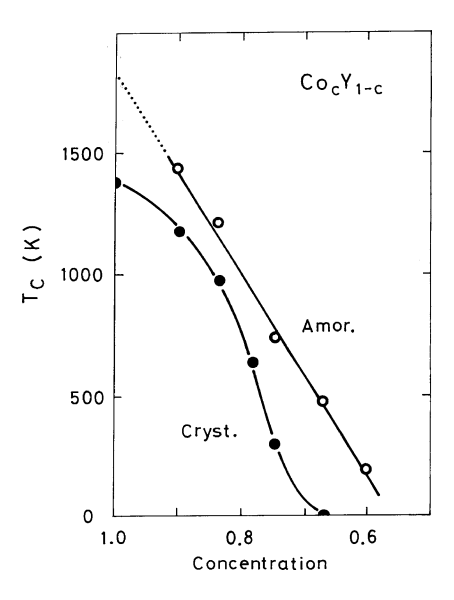
ements, suggesting the SG in amorphous pure iron, which is quite different from the ferromagnetism in bcc Fe. In Co-rich Co-Y amorphous alloys, the Curie temperatures  $T_{\rm C}$  are enhanced as compared with those in crystalline counterparts, and rapidly increase with decreasing Y concentration as shown in Fig. 9.3. Extrapolated value of  $T_{\rm C}$  to amorphous pure Co reaches 1850 K, which is 450 K higher than that of the fcc Co [222]. These drastic changes of magnetism in the vicinity of amorphous pure metals have revealed the significance of the structural disorder in the amorphous metallic magnetism. One needs microscopic theories of amorphous metallic magnetism to understand these anomalies. In the following section, we will briefly clarify the characteristics of amorphous structure and explain the theoretical approach to calculate the electronic structure of amorphous metals and alloys.

## 9.2 Amorphous Structure and Electronic Structure

In crystalline systems, we obtain the crystal structure and lattice constants from the Bragg peaks in X-ray diffraction, and thus we can calculate the electronic structure with use of the Bloch theorem. This procedure is no longer applicable to amorphous metals and alloys due to the lack of the data on amorphous structure. The X-ray experimental techniques give us only the pair distribution function (PDF),  $g_{\alpha\gamma}(R)$ , which is defined by

$$g_{\alpha\gamma}(R) = \frac{\rho_{\alpha\gamma}(R)}{\rho_{\gamma}}. (9.2)$$

**Fig. 9.3** Curie temperatures in crystalline (*solid circles*) and amorphous (*open circles*)  $Co_c Y_{1-c}$  alloys [222]. The *dotted line* is an extrapolation to amorphous pure Co



Here  $\rho_{\alpha\gamma}(R)$  is the density of  $\gamma$  atom at the distance R from an  $\alpha$  atom and  $\rho_{\gamma}$  is the density of  $\gamma$  atom. The distribution function  $g_{\alpha\gamma}(R)$  converges to one as R goes to infinity. Although we can obtain further information on the amorphous structure from EXAFS (extended X-ray absorption fine structure) and neutron measurements, it is not possible to determine experimentally all the atomic positions in the amorphous structure, which are indispensable for electronic-structure calculations of amorphous systems and microscopic understanding of magnetic properties. Thus we have to construct a reasonable model for amorphous structure.

Theoretical determination of the amorphous structure is based on the thermodynamical molecular-dynamics (MD) method [107]. In this method, the constituent atoms are distributed in a box with a periodic boundary condition, and the Newton equations of atomic motion are solved by assuming appropriate short-range interatomic pair potentials. A rapid quenching is simulated by reducing the kinetic energy, which is proportional to the temperature, every constant time length, under the condition that either pressure or volume is constant. In the ab-initio MD method [223], we calculate the interatomic forces directly from electronic and atomic structures without any empirical parameters. The ab-initio MD calculations are accelerated by simultaneously solving the equations of motions for both atoms and electrons. The method is called the Car–Parrinello method, and it is most efficient when combined with the pseudo-potential technique and the plain wave orbitals [224].

A more conventional method to construct the amorphous structure for metals is the static method. There we construct the dense random packing of hard spheres (DRPHS) model using the computer, and calculate the PDF. When the calculated PDF does not agree with the experimental one, we relax successively the structure through the atomic force produced by appropriate pair potentials until the agreement is achieved. This is called the relaxed DRPHS model.

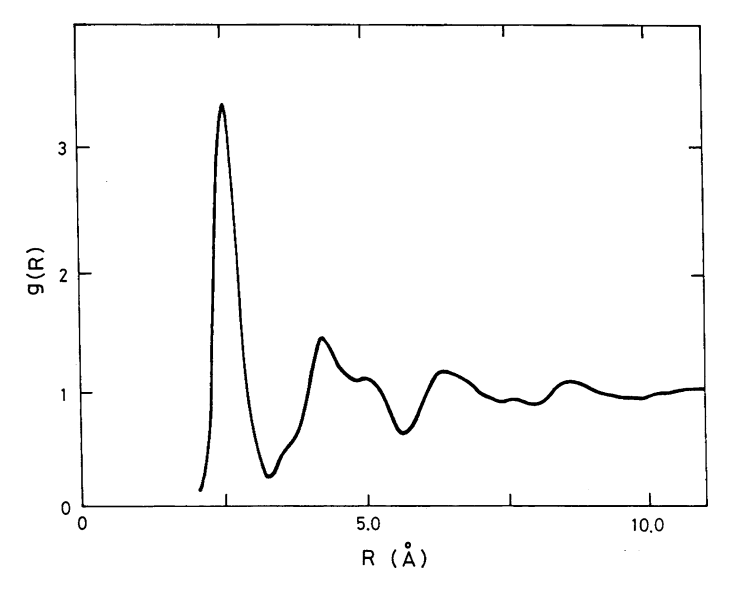


Fig. 9.4 Pair-distribution function of computer-generated amorphous iron [225]

Figure 9.4 shows an example of a pair distribution function for amorphous Fe obtained by the relaxed DRPHS method [225]. We see that the first peak at  $r_1 = 2.54$  Å is sharp, and well separated from the second and third ones. This means that there exists a well-defined nearest-neighbor (NN) shell even in amorphous systems. The ratio of the fluctuation of the NN interatomic distance to the average NN distance is estimated from the width of the first peak to be 0.067, which is in agreement with the experimental data for Fe-rich amorphous alloys. The second peak at  $r_2 = 1.67r_1$  is considered to originate in the local structures of the rhombi which consist of two regular triangles with a side  $r_1$  and the hexahedra which consist of two tetrahedra with the same sides  $r_1$ . The third peak at  $r_3 = 2r_1$  is associated with three contact atoms on a line.

Although the amorphous metals and alloys do not form the Bravais lattice, it is possible to construct the tight-binding linear muffin-tin orbital (TB-LMTO) Hamiltonian (2.167) for a given amorphous structure within the density functional theory (DFT) because it is derived without assuming translational symmetry.

$$H_{iLjL'} = \varepsilon_{iL}\delta_{ij}\delta_{LL'} + t_{iLjL'}(1 - \delta_{ij}\delta_{LL'}). \tag{9.3}$$

Here the atomic level  $\varepsilon_{iL}$  on site *i* and orbital *L* and the transfer integral  $t_{iLjL'}$  between iL and jL' are defined by (2.166).

The first-principles electronic structure calculations were made by combining the TB-LMTO method with the recursion method because the latter does not require any translational symmetry for electronic structure calculations (see Appendix G). Figure 9.5 shows the calculated density of states (DOS) for amorphous iron [226]. Note that the DOS for amorphous Fe shows the two-peak structure, and the valley near

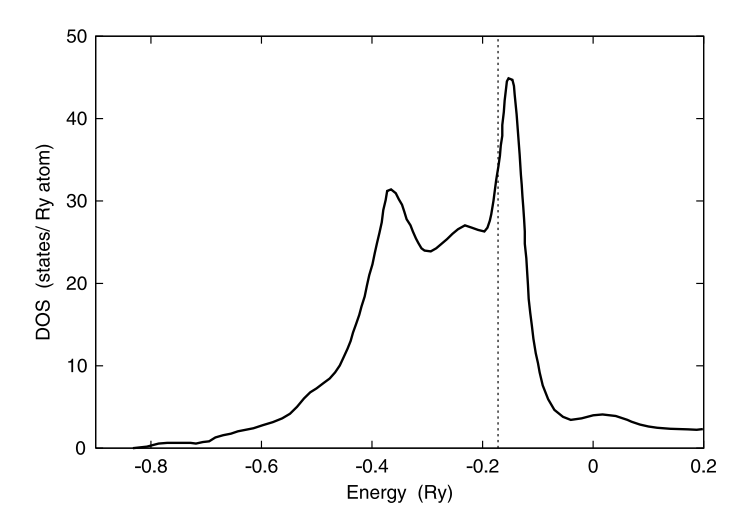


Fig. 9.5 Density of states for amorphous iron [226]

the center of the DOS found in bcc Fe disappears (see the DOS in Fig. 2.6), so that the Fermi level is not on the peak of the DOS. This suggests that the ferromagnetism is not necessarily stable in the amorphous Fe.

#### 9.3 Theory of Amorphous Metallic Magnetism

The finite-temperature theory of the LEE presented in Sect. 8.3 can be extended to the amorphous metals. In this section, we describe the theory of magnetism in amorphous metals on the basis of the functional integral method [227–230].

The amorphous metals form a structure close to the dense random packing one, and have a well-defined nearest-neighbor (NN) shell, as we discussed in the last section. The magnetic interactions between the local moments (LM's) in amorphous metals are expected to be rather short-range because the electron scatterings due to structural disorder cause a strong damping of interaction strength as a function of the interatomic distance. Thus we have a physical picture that the central LM is directly influenced by the LMs on the NN shell, but the effect of more distant atoms and their LMs may be treated as an effective medium.

In order to construct a theory based on the physical picture mentioned above, we start from the tight-binding Hamiltonian (3.228) and adopt the free energy (8.19) in the static approximation:

$$\mathscr{F} = -\beta^{-1} \ln \int \left[ \prod_{i} \sqrt{\frac{\beta \tilde{J}_{i}}{4\pi}} \, d\xi_{i} \right] e^{-\beta E(\xi)}. \tag{9.4}$$

Here we have omitted the transverse spin fluctuations for simplicity, and  $\tilde{J}_i = U_0/D + (1-1/D)J$ , D being the orbital degeneracy (D=5). In the 5-fold equivalent d band model (8.22), the effective potential  $E(\xi)$  is given by (8.23):

$$E(\xi) = \int d\omega f(\omega) \frac{D}{\pi} \operatorname{Im} \operatorname{tr} \left[ \ln \left( L^{-1} - t \right) \right] - \frac{1}{4} \sum_{i} \left( \tilde{U}_{i} \tilde{n}_{i}(\xi)^{2} - \tilde{J}_{i} \xi_{i}^{2} \right). \tag{9.5}$$

In the above expression, the effective Coulomb interaction  $\tilde{U}_i$  is given by  $\tilde{U}_i = U_0/D + (1-1/D)(2U_1-J)$ .  $\tilde{n}_i(\xi)$  is the Hartree–Fock charge on site i given by (8.21). The locator matrix L is defined by

$$(L^{-1})_{i\sigma j\sigma'} = L_{i\sigma}^{-1} \delta_{ij} \delta_{\sigma\sigma'} = \left( z - \varepsilon_i^0 + \mu - \frac{1}{2} \tilde{U}_i \, \tilde{n}_i(\xi) + \frac{1}{2} \tilde{J}_i \, \xi_i \, \sigma \right) \delta_{ij} \delta_{\sigma\sigma'}.$$
 (9.6)

The magnetic moment on site i is obtained by taking the derivative of the free energy  $\mathscr{F}$  with respect to the magnetic field  $h_i$  on the same site.

$$\langle m_i \rangle = \langle \xi_i \rangle = \frac{\int \left[ \prod_j d\xi_j \right] \xi_i \, \mathrm{e}^{-\beta E(\xi)}}{\int \left[ \prod_j d\xi_j \right] \mathrm{e}^{-\beta E(\xi)}}.$$
 (9.7)

The energy potential  $E(\xi)$  in (9.7) determines the local moment (LM) on site i. In the amorphous magnetic metals, the energy contains two types of disorder. One is the spin disorder which is caused by the thermal spin fluctuations via random exchange potentials  $\{\tilde{J}_i\xi_i\sigma/2\}$  in (9.6). Another is the structural disorder being characteristic of amorphous metallic systems. The latter appears via the atomic potentials  $\{\varepsilon_i^0 - \mu + \tilde{U}_i\,\tilde{n}_i(\xi)/2\}$  and transfer integral integrals  $\{(t)_{ij} = t_{ij}\}$ . Consequently, the diagonal disorder in the locator includes both types of disorder, while the off-diagonal disorder in the transfer integral matrix is caused by the structural disorder only.

The diagonal disorder is treated in the same way as in the substitutional disordered alloys, by introducing the inverse effective locator  $\mathcal{L}_{\sigma}^{-1}(z)$  into the first term at the r.h.s. of (9.5). The deviation from the medium is expanded with respect to the sites as has been made in Sect. 8.3 (see (8.71)). The zeroth order in the expansion of the effective potential  $E(\xi)$  is described by the effective medium only. The first-order correction consists of the sum of single-site energy potentials  $E_i(\xi_i)$ , i.e., (8.72):

$$E_{i}(\xi_{i}) = \int d\omega f(\omega) \frac{D}{\pi} \operatorname{Im} \sum_{\sigma} \ln \left[ 1 + \left( L_{i\sigma}^{-1}(z, \xi) - \mathcal{L}_{\sigma}^{-1}(z) \right) F_{ii\sigma}(z) \right]$$

$$- \frac{1}{4} \tilde{U}_{i} \tilde{n}_{i}(\xi_{i})^{2} + \frac{1}{4} \tilde{J}_{i} \xi_{i}^{2}.$$

$$(9.8)$$

Here the coherent Green function  $F_{ij\sigma}$  is defined by (8.76):

$$F_{ij\sigma} = \left[ \left( \mathcal{L}^{-1} - t \right)^{-1} \right]_{ij\sigma}. \tag{9.9}$$

Note that  $F_{ij\sigma}$  is influenced by the structural disorder via the transfer integrals  $\{t_{ij}\}$ . The second-order correction to the effective medium is the pair-interaction terms  $\sum_{(i,j)} \Phi_{ij}(\xi_i, \xi_j)$  (see (8.74)). The pair energy between sites i and j,  $\Phi_{ij}(\xi_i, \xi_j)$  is given by (8.75):

$$\Phi_{ij}(\xi_i, \xi_j) = \int d\omega \, f(\omega) \frac{D}{\pi} \operatorname{Im} \sum_{\sigma} \ln \left[ 1 - F_{ij\sigma} F_{ji\sigma} \tilde{t}_{i\sigma}(\xi_i) \tilde{t}_{j\sigma}(\xi_j) \right]. \tag{9.10}$$

Here  $\tilde{t}_{i\sigma}(\xi_i)$  is the single-site t matrix defined by (8.77):

$$\tilde{t}_{i\sigma}(\xi_i) = -\frac{L_{i\sigma}^{-1} - \mathcal{L}_{\sigma}^{-1}}{1 + (L_{i\sigma}^{-1} - \mathcal{L}_{\sigma}^{-1})F_{ii\sigma}}.$$
(9.11)

The t matrix describes the impurity scattering when the impurity potential  $\varepsilon_i^0 - \mu + \tilde{U}_i \tilde{n}_i(\xi)/2 - \tilde{J}\xi_i\sigma/2$  is embedded in the effective medium  $\mathcal{L}_{\sigma}^{-1}$ .

The higher-order terms in the expansion of  $E(\xi)$  are neglected by assuming a small deviation from the effective medium. The energy potential  $E(\xi)$  is then written as follows.

$$E(\xi) = \sum_{i} E_{i}(\xi_{i}) + \sum_{(i,j)} \Phi_{ij}(\xi_{i}, \xi_{j}). \tag{9.12}$$

Note that the zeroth term has been dropped, since it does not make any contribution to the thermal average (9.7).

Next, one neglects the direct pair interactions between the central LM and the LMs outside the NN shell according to the physical picture discussed at the beginning of this section. By making use of the decoupling approximation as well as the molecular-field approximation for the LMs on the NN shell, the magnetic moment (9.7) is written as follows, as have been made in Sect. 8.3 (see (8.85)).

$$\langle m_0 \rangle = \frac{\int d\xi \, \xi \, \mathrm{e}^{-\beta \Psi(\xi)}}{\int d\xi \, \mathrm{e}^{-\beta \Psi(\xi)}}.$$
 (9.13)

The effective potential  $\Psi(\xi)$  for the central LM is given by (8.84):

$$\Psi(\xi) = E_0(\xi) + \sum_{j=1}^{z} \Phi_{0j}^{(a)}(\xi) - \sum_{j=1}^{z} \Phi_{0j}^{(e)}(\xi) \frac{\langle m_j \rangle}{x_j}.$$
 (9.14)

Here z on the summation denotes the number of atoms on the NN shell. The atomic and exchange pair energies  $\Phi_{0j}^{(a)}(\xi)$  and  $\Phi_{0j}^{(e)}(\xi)$  are defined by (8.82):

$$\begin{bmatrix} \Phi_{0j}^{(a)}(\xi) \\ \Phi_{0j}^{(e)}(\xi) \end{bmatrix} = \frac{1}{2} \sum_{\nu=\pm} \begin{bmatrix} 1 \\ -\nu \end{bmatrix} \Phi_{0j}(\xi, \nu x_j). \tag{9.15}$$

The quantity  $x_j$  in (9.14) and (9.15) is an amplitude in the single-site approximation, which is defined by  $x_j = \langle \xi_j^2 \rangle_0^{1/2}$ , where the average  $\langle \sim \rangle_0$  is taken with respect to  $E_0(\xi)$ .

Equations (9.13) and (9.14) show that a flexible central LM  $\xi$  is directly influenced by the molecular fields from the LMs  $\{\langle m_j \rangle\}$  on the NN shell (the third term in (9.14)) and indirectly by the average molecular field from the LMs outside the NN shell via the spin-dependent effective medium  $\mathcal{L}_{\sigma}^{-1}$  which appears in  $E_0(\xi)$ ,  $\Phi_{0j}^{(a)}(\xi)$ , and  $\Phi_{0j}^{(e)}(\xi)$ .

The effective medium  $\mathcal{L}_{\sigma}^{-1}$  is chosen so that the correction to the single-site energies in  $E(\xi)$  (see (8.73)) becomes as small as possible. This is an extension of the CPA to the structural disorder, and there is a condition that the averaged single-site t matrix should vanish.

$$\left[ \langle \tilde{t}_{i\sigma}(\xi) \rangle \right]_{s} = 0. \tag{9.16}$$

Here the single-site t matrix  $\tilde{t}_{i\sigma}(\xi)$  has been given by (9.11).  $\langle \rangle$  ([ ]<sub>s</sub>) denotes the thermal (structural) average. As we have mentioned in (8.34), the above condition is equivalent to the following CPA equation.

$$\left[ \langle (L_{i\sigma}^{-1} - \mathcal{L}_{\sigma}^{-1} + F_{00\sigma}^{-1})^{-1} \rangle \right]_{s} = F_{\sigma}. \tag{9.17}$$

Here  $F_{\sigma}$  denotes a structural average of the coherent Green function.

The central LM (9.13) depends on the structural disorder outside the NN shell via the coherent Green functions  $F_{00\sigma}$ ,  $F_{0j\sigma} (= F_{j0\sigma})$ , and  $F_{jj\sigma}$  in (9.14) and (9.17). These Green functions are treated within the Bethe approximation presented in Sect. 8.3. Applying (8.50) and (8.51) on the locator expansion of coherent Green functions with structural disorder, we obtain

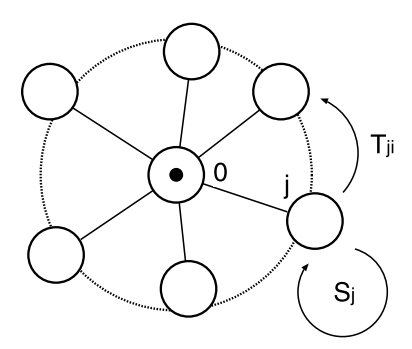
$$F_{00} = \mathcal{L} + \mathcal{L} \sum_{j \neq 0} t_{0j} F_{j0}, \tag{9.18}$$

$$F_{j0} = \mathcal{L}t_{j0}F_{00} + \mathcal{L}S_{j}F_{j0} + \mathcal{L}\sum_{i \neq i,0} T_{ji}F_{i0}.$$
 (9.19)

Here we have omitted the spin suffix  $\sigma$  for brevity and neglected the transfer integrals between the central atom and the atoms outside the NN shell. The self-energy  $S_j$  ( $T_{ji}$ ) expresses the contribution of the sum of all the paths which start from site j and end at site j (i) without returning to the cluster on the way (see Fig. 9.6). It should be noted that all the information outside the cluster is included in  $S_j$  and  $T_{ji}$ .

When we take the structural average outside the cluster, we neglect the last term at the r.h.s. of (9.19) (i.e., the Bethe approximation), and replace  $S_j$  with  $\mathcal{S}$ , i.e., the self-energy of the effective medium for structural disorder. We then obtain (see

**Fig. 9.6** Schematic representation of the irreducible path  $S_i$  and  $T_{ii}$ 



(8.55) and (8.53))

$$F_{00\sigma} = \left(\mathcal{L}_{\sigma}^{-1} + \sum_{j=1}^{z} \frac{t_{j0}^{2}}{\mathcal{L}_{\sigma}^{-1} - \mathcal{L}_{\sigma}}\right)^{-1},\tag{9.20}$$

$$F_{j0\sigma} = \frac{t_{j0}}{\mathscr{L}_{\sigma}^{-1} - \mathscr{I}_{\sigma}} F_{00\sigma}. \tag{9.21}$$

The diagonal Green function  $F_{jj\sigma}$  on the NN shell, on the other hand, is approximated by the averaged one.

$$F_{\sigma} = [F_{jj\sigma}]_{s} = \int \frac{[\rho(\varepsilon)]_{s} d\varepsilon}{\mathcal{L}_{\sigma}^{-1} - \varepsilon}.$$
(9.22)

Note that the averaged DOS  $[\rho(\varepsilon)]_s$  for noninteracting systems can be calculated by using the ground-state theories described in the last section (see, for example, Fig. 9.5).

The effective medium  $\mathcal{S}_{\sigma}$  is determined from the condition that the structural average of the central coherent Green function  $F_{00\sigma}$  should be identical with the neighboring one.

$$[F_{00\sigma}]_{s} = \int \frac{[\rho(\varepsilon)]_{s} d\varepsilon}{\mathscr{L}_{\sigma}^{-1} - \varepsilon}.$$
(9.23)

The central LM in (9.13) is now determined as follows by the number of NN z, the neighboring LM's  $\{\langle m_j \rangle\}$  on the NN shell, the transfer integrals  $y_j = t_{j0}^2$  between the central atom and the neighboring atoms, the effective medium  $\mathcal{L}_{\sigma}^{-1}$  due to the spin fluctuations, and the effective medium  $\mathcal{L}_{\sigma}$  due to the structural disorder outside the NN shell.

$$\langle m_0 \rangle = \langle m_0 \rangle \left( z, \left\{ \langle m_i \rangle \right\}, \left\{ t_{i0}^2 \right\}, \left\{ \mathcal{L}_{\sigma}^{-1} \right\}, \left\{ \mathcal{L}_{\sigma} \right\} \right). \tag{9.24}$$

The structural disorder causes the distribution of LM  $g(\langle m_j \rangle)$  at the neighboring site j, the distribution of the number of NN p(z), and the distribution  $p_s(y_j)$  for the

square of the transfer integral. These distributions determine the LM distribution at the central site via relation (9.13). Since the distribution should be identical with those of the surrounding LMs, we obtain the following integral equation for the LM distribution, taking the same steps as in Sect. 8.3 (see (8.87)).

$$g(M) = \sum_{z} p(z) \int \delta(M - \langle m_0 \rangle) \prod_{i=1}^{z} [p_s(y_i) \, dy_i \, g(m_i) \, dm_i]. \tag{9.25}$$

The effective mediums  $\mathcal{L}_{\sigma}^{-1}$  and  $\mathcal{S}_{\sigma}$  are self-consistently determined from (9.17) and (9.23):

$$\sum_{z} p(z) \int \left( L_{i\sigma}^{-1} - \mathcal{L}_{\sigma}^{-1} + F_{00\sigma}^{-1} \right)^{-1} \prod_{i=1}^{z} \left[ p_{s}(y_{i}) \, dy_{i} \, g(m_{i}) \, dm_{i} \right] = F_{\sigma}, \quad (9.26)$$

$$\sum_{z} p(z) \int F_{00\sigma} \prod_{i=1}^{z} [p_{s}(y_{i}) dy_{i}] = F_{\sigma}.$$
 (9.27)

The LM distribution g(M), and the effective mediums  $\mathcal{L}_{\sigma}^{-1}$  and  $\mathcal{L}_{\sigma}$  are self-consistently determined by solving (9.25), (9.26), and (9.27). This is the finite temperature theory of the local environment effects for amorphous metals.

The average magnetization  $[\langle m \rangle]_s$  and the SG order parameter  $[\langle m \rangle^2]_s$  are obtained from the distribution g(M) as follows.

$$\left[\langle m \rangle\right]_{s} = \int Mg(M) \, dM, \tag{9.28}$$

$$\left[\langle m\rangle^2\right]_s = \int M^2 g(M) \, dM. \tag{9.29}$$

Since self-consistent equations (9.25), (9.26), and (9.27) include 2z-fold integrals, it is not easy to solve the equations. We adopt the following decoupling approximation in the self-consistent equations, which is correct up to the second moment:

$$\int M^{2n+k} g(M) dM \approx \left[ \langle m \rangle^2 \right]_s^n \left[ \langle m \rangle^k \right]_s, \tag{9.30}$$

$$\int (y - [y]_s)^{2n+k} p_s(y) \, dy \approx \left[ (\delta y)^2 \right]_s^n 0^k. \tag{9.31}$$

Here k = 0 or 1. These are the lowest approximations which take into account fluctuations.  $[y]_s$  is a mean square of a transfer integral, and  $[(\delta y)^2]_s$  is the fluctuation around  $[y]_s$ .

After making the decoupling approximations (9.30) and (9.31) at the r.h.s. of (9.25), one can substitute the approximate distribution function g(M) into (9.28) and (9.29). We then obtain the self-consistent equations for  $[\langle m \rangle]_s$  and  $[\langle m \rangle^2]_s$  as

follows.

$$\begin{bmatrix} [\langle m \rangle]_{s} \\ [\langle m \rangle^{2}]_{s} \end{bmatrix} = \sum_{z} p(z) \sum_{n=0}^{z} \Gamma\left(n, z, \frac{1}{2}\right) \begin{bmatrix} [\langle m \rangle_{n}]_{s} \\ [\langle m \rangle_{n}^{2}]_{s} \end{bmatrix}, \tag{9.32}$$

$$\begin{bmatrix} [\langle m \rangle_n]_s \\ [\langle m \rangle_n^2]_s \end{bmatrix} = \sum_{k=0}^n \sum_{l=0}^{z-n} \Gamma(k,n,q) \Gamma(l,z-n,q) \begin{bmatrix} \langle \xi \rangle(z,n,k,l) \\ \langle \xi \rangle^2(z,n,k,l) \end{bmatrix}, \tag{9.33}$$

$$\langle \xi \rangle(z, n, k, l) = \frac{\int d\xi \, \xi \, e^{-\beta \Psi(\xi, z, n, k, l)}}{\int d\xi \, e^{-\beta \Psi(\xi, z, n, k, l)}}, \tag{9.34}$$

$$\Psi(\xi, z, n, k, l) = E(\xi, n) + n\Phi_{+}^{(a)}(\xi, n) + (z - n)\Phi_{-}^{(a)}(\xi, n)$$

$$-\left[(2k-n)\Phi_{+}^{(e)}(\xi,n)+(2l-z+n)\Phi_{-}^{(e)}(\xi,n)\right]\frac{\left[\langle m\rangle^{2}\right]_{s}^{1/2}}{x},$$
(9.35)

$$q = \frac{1}{2} \left( 1 + \frac{[\langle m \rangle]_{s}}{[\langle m \rangle^{2}]_{s}^{1/2}} \right). \tag{9.36}$$

Here  $\Gamma(n, z, p)$  is the binomial distribution function defined by [z!/n!(z-n)!]  $p^n(1-p)^{z-n}$ .

In the present approximation, the local environments inside the NN shell are described via the NN transfer integrals by the contraction  $(-[(\delta R)^2]_s^{1/2})$  of the NN interatomic distance R from average value  $[R]_s$  and the stretch  $([(\delta R)^2]_s^{1/2})$  of distance R. Thus, the local structure for a given z is specified by means of the number of contracted pairs (n) between the central atom and the atoms on the NN shell. Since a local structure is realized with the probability  $\Gamma(n,z,1/2)$ , the averaged LMs are given by (9.32). The magnetic moments in each local structure (n),  $[\langle m \rangle_n]_s$  and  $[\langle m \rangle_n^2]_s$  are given by (9.33). The single-site energy and pair energies are also characterized by n, so that the notations  $E(\xi,n)$ ,  $\Phi_{\pm}^{(a)}(\xi,n)$ , and  $\Phi_{\pm}^{(e)}(\xi,n)$  are used in (9.35). Here the subscript +(-) denotes the contracted (stretched) pair.

The parameter q defined by (9.36) is interpreted as the probability that the fictitious spin  $[\langle m \rangle^2]_{\rm s}^{1/2}$  points up on a site of the NN shell. The probability of finding up spins of k among n contracted atoms on the NN shell is then given by  $\Gamma(k,n,q)$ , and the probability of finding up spins of l among z-n stretched atoms is given by  $\Gamma(l,z-n,q)$ . Therefore, the average LM in the local environment n,  $[\langle m \rangle_n]_{\rm s}$  is obtained by averaging  $\langle \xi \rangle(z,n,k,l)$  over the spin configurations (see (9.33)). Here,  $\langle \xi \rangle(z,n,k,l)$  denotes the central LM in the (z,n,k,l) configuration. Note that the LMs  $\langle \xi \rangle(z,n,k,l)$  are strongly influenced by their local environments (z,n,k,l) in transition metals and alloys. Such effects are referred as local environment effects (LEE) in amorphous metals.

In the same way, one obtains from (9.26) a simplified CPA equation,

$$\sum_{\nu=\pm} \frac{1}{2} \left( 1 + \nu \frac{[\langle \xi \rangle]_{s}}{[\langle \xi \rangle^{2}]_{s}^{1/2}} \right) \left[ L_{\sigma}^{-1} \left( \nu \left[ \langle \xi \rangle^{2} \right]_{s}^{1/2} \right) - \mathcal{L}_{\sigma}^{-1} + F_{\sigma}^{-1} \right]^{-1} = F_{\sigma}, \quad (9.37)$$

and the following equation from (9.27).

$$\sum_{v=\pm} \frac{1}{2} \left[ \mathscr{L}_{\sigma}^{-1} - z^* [y]_s \left( 1 + \nu \frac{[(\delta \theta)^2]_s^{1/2}}{[\theta]_s} \right) \left( \mathscr{L}_{\sigma}^{-1} - \mathscr{S}_{\sigma} \right)^{-1} \right]^{-1} = F_{\sigma}. \quad (9.38)$$

Here  $z^*$  is an effective coordination number,  $\delta\theta=\theta-[\theta]_s$ , and  $\theta=\sum_j^z y_j$ . Adopting a simple form  $p(z)=([z^*]+1-z^*)\delta_{z,[z^*]}+(z^*-[z^*])\delta_{z,[z^*]+1},$  [ ] being Gauss's notation, and Heine's law  $t(R)\equiv t_{j0}\propto R^{-\kappa}$ , we obtain  $[(\delta\theta)^2]_s^{1/2}/[\theta]_s=(z^*-[z^*])([z^*]+1-z^*)/z^*+4\kappa^2\Delta/z^*$  and  $[(\delta y)^2]_s^{1/2}/[y]_s=2\kappa\Delta$ . Here  $\Delta=[(\delta R)^2]_s^{1/2}/[R]_s$ . The average coordination number  $z^*$ , the average interatomic distance  $[R]_s$ , and its fluctuation  $[(\delta R)^2]_s^{1/2}$  are obtained from the theoretical model or the experimental PDF.

The input parameters in the present theory are the d electron number, effective exchange energy parameter  $\tilde{J}$ , the DOS  $[\rho(\varepsilon)]_s$ , average coordination number  $z^*$ , and the fluctuation of the interatomic distance  $[(\delta R)^2]_s^{1/2}/[R]_s$ . The input DOS  $[\rho(\varepsilon)]_s$  are presented in Fig. 9.7.  $[\langle m \rangle]_s$ ,  $[\langle m \rangle^2]_s$ ,  $\mathcal{L}_{\sigma}^{-1}$ , and  $\mathcal{L}_{\sigma}$  are obtained by solving (9.32), (9.37), and (9.38) self-consistently. The theory describes the ferromagnetism  $([\langle m \rangle]_s \neq 0$ ,  $[\langle m \rangle^2]_s^{1/2} \neq 0$ ), the SG  $([\langle m \rangle]_s = 0$ ,  $[\langle m \rangle^2]_s^{1/2} \neq 0$ ), and the paramagnetism  $([\langle m \rangle]_s = 0, [\langle m \rangle^2]_s^{1/2} = 0)$ .

In the theory mentioned above, we assumed the collinear magnetic moments. When we take into account the noncollinear spin arrangements, we start from the magnetic moment (6.60) [231].

$$\langle \mathbf{m}_i \rangle = \frac{\int \left[ \prod_j d\mathbf{\xi}_j \, \boldsymbol{\xi}_j^{-2} \right] \left( 1 + \frac{4}{\beta \tilde{J} \boldsymbol{\xi}_i^2} \right) \boldsymbol{\xi}_i \, \mathrm{e}^{-\beta E(\boldsymbol{\xi})}}{\int \left[ \prod_i d\boldsymbol{\xi}_j \, \boldsymbol{\xi}_j^{-2} \right] \mathrm{e}^{-\beta E(\boldsymbol{\xi})}}.$$
 (9.39)

Here the energy potential  $E(\xi)$  is given by (6.56).

Taking the same steps we obtain the central magnetic moment corresponding to (9.13) as

$$\langle \mathbf{m}_0 \rangle = \frac{\int d\boldsymbol{\xi} \, \boldsymbol{\xi}^{-2} \left( 1 + \frac{4}{\beta \tilde{J} \boldsymbol{\xi}^2} \right) \boldsymbol{\xi} e^{-\beta \Psi(\boldsymbol{\xi})}}{\int d\boldsymbol{\xi} \, \boldsymbol{\xi}^{-2} e^{-\beta \Psi(\boldsymbol{\xi})}}, \tag{9.40}$$

$$\Psi(\xi) = E_{0}(\xi) + \sum_{j=1}^{z} \left[ \Phi_{0j}^{(a)}(\xi) - \sum_{\alpha} \Phi_{0j\alpha}^{(e)}(\xi) \frac{\langle m_{j\alpha} \rangle}{\tilde{a}_{j\alpha}} + \sum_{(\alpha,\gamma)} \Phi_{0j\delta}^{(b)}(\xi) \frac{\langle m_{j\alpha} \rangle \langle m_{j\gamma} \rangle}{\tilde{a}_{j\alpha} \tilde{a}_{j\gamma}} + \Phi_{0j}^{(c)}(\xi) \frac{\langle m_{j\alpha} \rangle \langle m_{j\gamma} \rangle \langle m_{jz} \rangle}{\tilde{a}_{j\alpha} \tilde{a}_{j\gamma} \tilde{a}_{jz}} \right].$$
(9.41)

Here  $E_0(\xi)$  is the single-site energy, and  $\Phi_{0j}^{(a)}(\xi)$  is the atomic type of energy. There are three types of exchange energies,  $\Phi_{0j\alpha}^{(e)}(\xi)$ ,  $\Phi_{0j\delta}^{(b)}(\xi)$ , and  $\Phi_{0j}^{(c)}(\xi)$ . The amplitude  $\tilde{a}_{j\alpha}$  is defined by  $\tilde{a}_{j\alpha} = (1+4/\beta \tilde{J}\langle \xi_j^2\rangle_0)\langle \xi_{j\alpha}^2\rangle_0^{1/2}$ ,  $\langle \sim \rangle_0$  being the average taken with respect to the single-site energy  $E_0(\xi)$ .

Equation (9.40) indicates that the central LM is determined by the coordination number z on the NN shell, neighboring LM's  $\{\langle \boldsymbol{m}_j \rangle\}$ , square of transfer integrals  $\{y_j = t_{j0}^2\}$ , effective medium  $\mathcal{L}_{\sigma}^{-1}$  due to spin fluctuations, and the effective medium  $\mathcal{L}_{\sigma}$  due to structural disorder outside the NN shell:  $\langle \boldsymbol{m}_0 \rangle = \langle \boldsymbol{m}_0 \rangle (z, \{\langle \boldsymbol{m}_j \rangle\}, \{y_j\}, \{\mathcal{L}_{\sigma}^{-1}\})$ . Thus, the self-consistent equation to determine the distribution function (9.25) is extended as

$$g(\mathbf{M}) = \sum_{z} p(z) \int \delta(\mathbf{M} - \langle \mathbf{m}_0 \rangle) \prod_{j=1}^{z} [p_s(y_j) \, dy_j \, g(\mathbf{m}_j) \, d\mathbf{m}_j]. \tag{9.42}$$

Here  $g(\mathbf{m})$  is the distribution function for the vector magnetic moments  $\{\langle \mathbf{m}_i \rangle\}$ .

The average magnetization  $[\langle m_z \rangle]_s$  and the SG order parameters for each direction  $[\langle m_\alpha \rangle^2]_s^{1/2}$  ( $\alpha = x, y, z$ ) are obtained from the distribution  $g(\mathbf{M})$  as follows:

$$\left[ \langle m_z \rangle \right]_{\rm s} = \int M_z g(\mathbf{M}) \, d\mathbf{M},\tag{9.43}$$

$$\left[ \langle m_{\alpha} \rangle^2 \right]_{\rm s} = \int M_{\alpha}^2 g(\mathbf{M}) \, d\mathbf{M}. \tag{9.44}$$

By making use of the decoupling approximation such as (9.30) and (9.31) at the r.h.s. of (9.42) and substituting the approximate expression of g(M) into (9.43) and (9.44), we obtain the self-consistent equations to determine the magnetization  $[\langle m_z \rangle]_s$ , and the SG order parameters  $[\langle m_z \rangle^2]_s^{1/2}$  and  $[\langle m_x \rangle^2]_s^{1/2}$  (=  $[\langle m_y \rangle^2]_s^{1/2}$ ). Since the transverse components of local moments are taken into account, the theory describes the noncollinear ferromagnetism ( $[\langle m_z \rangle]_s \neq 0$ ,  $[\langle m_z \rangle^2]_s^{1/2} \neq 0$  ( $\alpha = x, y, z$ )), the collinear ferromagnetism ( $[\langle m_z \rangle]_s \neq 0$ ,  $[\langle m_z \rangle^2]_s^{1/2} \neq 0$ ,  $[\langle m_\alpha \rangle^2]_s^{1/2} = 0$  ( $\alpha = x, y$ )), the noncollinear SG ( $[\langle m_z \rangle]_s = 0$ ,  $[\langle m_\alpha \rangle^2]_s^{1/2} = 0$  ( $\alpha = x, y$ )), and the paramagnetism ( $[\langle m_z \rangle]_s = 0$ ,  $[\langle m_\alpha \rangle^2]_s^{1/2} = 0$  ( $\alpha = x, y, z$ )). In numerical calculations we apply the Monte-Carlo sampling method because there are too many configurations in the self-consistent equations [231].

## 9.4 Magnetism of Amorphous Transition Metals

Amorphous pure transition metals have not yet been realized in experiments. Nevertheless theoretical results of their magnetism are indispensable for understanding the effects of structural disorder on the metallic magnetism as well as the experimental data of amorphous alloys. In this section, we elucidate the theoretical results

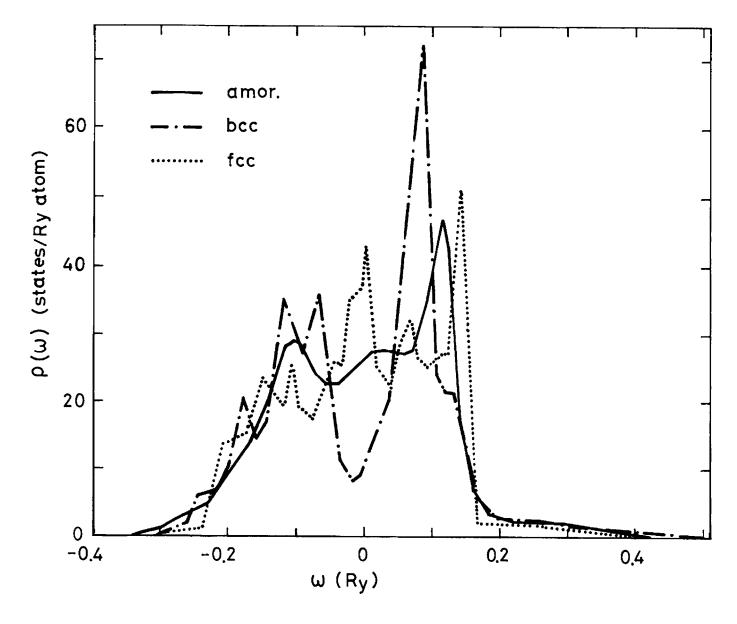


Fig. 9.7 Input DOS per atom for the amorphous (solid curve), bcc (dot-dashed curve), and fcc (dotted curve) structures

obtained by the finite-temperature theory of amorphous metals and discuss on the consistency of the results with experimental data [227, 228, 230, 231].

#### 9.4.1 General Survey

The crystalline Fe, Co, Ni transition metals are well-known to show a simple ferromagnetism with uniform magnetization. There the Stoner condition for the stability of the ferromagnetism provides us with a useful criterion as discussed in Sect. 2.3.4:  $\rho(0)\tilde{J}/2>1$ , where  $\rho(0)$  denotes the noninteracting density of states (DOS) per atom at the Fermi level. Note that we adopted here the DOS per atom instead of the DOS per atom per spin for convenience. Figure 9.7 shows the DOS for the amorphous, bcc, and fcc structures. The ferromagnetism of bcc Fe, for example, is stabilized by the main peak near the Fermi level. The fcc Ni shows the strong ferromagnetism for the same reason.

A characteristic feature of the DOS for amorphous transition metals is that the main peak is located just between the bcc and fcc peaks. The d electron numbers  $N^*$  with the Fermi level at each main peak are  $N^*(bcc) = 7.44$  for the bcc,  $N^*(amor) = 8.35$  for amorphous structure, and  $N^*(fcc) = 9.05$  for the fcc. They indicate the strong ferromagnetic region in each structure. The Stoner criterion for amorphous Fe is estimated to be  $\rho(0)\tilde{J}/2 = 0.96 < 1$  with use of the effective exchange energy parameter  $\tilde{J} = 0.068$  Ry (see Table 2.1) and the first-principles DOS

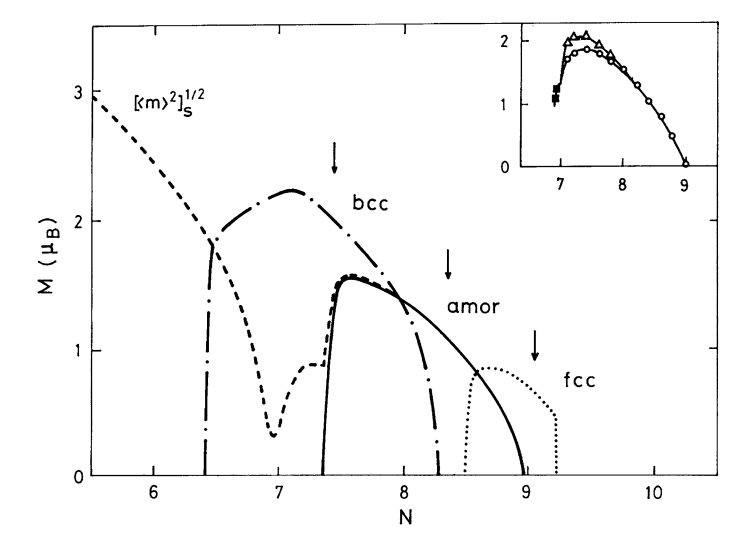


**Fig. 9.8** Calculated magnetization vs. d-electron number curves at 75 K for the amorphous (*solid curve*), bcc (*dot-dashed curves*), and fcc (*dotted curve*) structures [228]. The effective exchange energy parameter is fixed to that of the bcc Fe. The *dashed curve* shows the spin-glass (SG) order parameter. The d-electron numbers  $N^*$  integrated up to the main peak of each DOS in Fig. 9.7 are indicated by the *arrows*. The *inset* shows the experimental data for amorphous (Fe–M) $_{90}$ Zr $_{10}$  alloys. Here, M = Mn ( $\blacksquare$ ), Co ( $\triangle$ ), and Ni ( $\circ$ ) [232]

for amorphous Fe [226]. The result suggests that amorphous Fe does not develop a uniform magnetization. In the same way, the ferromagnetism in amorphous Co is expected to be enhanced because the main peak is near the Fermi level, while amorphous Ni may not maintain strong ferromagnetism because its Fermi level is located above the peak position of the amorphous DOS.

Another characteristic of the DOS for amorphous structure is their similarity to the fcc DOS rather than the bcc ones, particularly near the top of the d bands, because the amorphous structure is close to the close-packed structure. The amorphous transition metals and alloys are therefore expected to show anomalous magnetic properties similar to those found in the fcc ones. For example, we have seen in Sect. 8.3 that the Fe-base fcc alloys have nonlinear magnetic couplings: the ferromagnetic couplings when the amplitudes of Fe LM's are large and the antiferromagnetic couplings when the amplitudes are small. This peculiarity may explain the SG states in Fe-rich amorphous alloys. The Invar anomalies as found in Fe-base amorphous alloys are also expected because of the similarity in electronic structure.

The Stoner model is based on the assumption of the uniform magnetization which is not generally satisfied in the amorphous metallic system. To examine the existence of the ferromagnetism, one needs to perform numerical calculations using the theory presented in the last section. Figure 9.8 shows the calculated magnetization vs. delectron number curves. There the input parameters are set as those of amorphous iron except for the d electron number (N) to see the qualitative feature. We find that the  $N^*$ , which are indicated by arrows, correspond well to the magnetic regions of

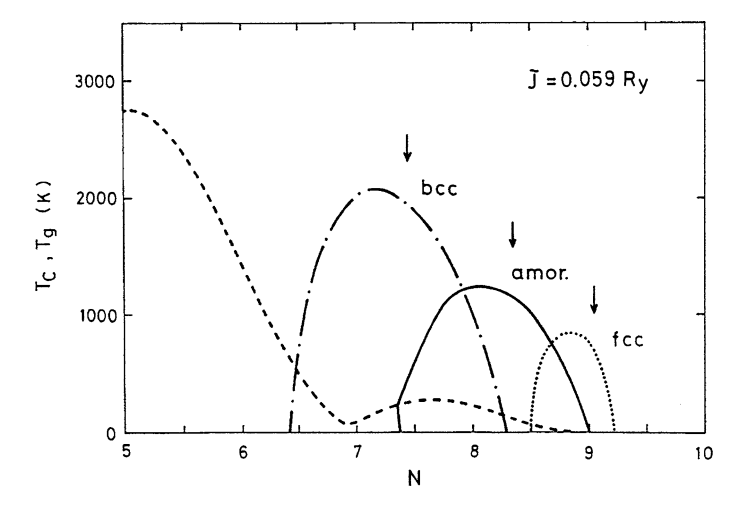


Fig. 9.9 Curie temperature vs. d-electron number curves calculated with use of the same input parameters as in Fig. 9.8 [228]. The SG temperatures are shown by the *dashed curve*. The d-electron numbers  $N^*$  are indicated by *arrows* 

the d electron number for each structure. It verifies that the 3d ferromagnetism is stabilized by the magnetic energy gain associated with the main peak in the DOS for each structure.

The Curie temperature maxima are also characterized by  $N^*$ , as shown in Fig. 9.9. According to thermodynamic considerations, the Curie temperature  $T_{\rm C}$  is roughly given by  $T_{\rm C} \sim E_{\rm mag}/S_{\rm mag}$ . Here  $E_{\rm mag}$  is the magnetic energy defined by the energy difference between the ground state and the paramagnetic state, and  $S_{\rm mag}$  is the magnetic entropy. The result in Fig. 9.9 indicates that the Curie temperatures for transition metals showing strong ferromagnetism are dominated by the magnetic energy gain associated with the main peak for each structure. This explains qualitatively why the Curie temperature of amorphous Co is enhanced. It is found that the paramagnetic susceptibility at high temperatures for each structure also shows the enhancement near the electron number  $N^*({\rm bcc}) = 7.44$ ,  $N^*({\rm amor}) = 8.35$ , and  $N^*({\rm fcc}) = 9.05$ , respectively. It implies that the susceptibility enhancement due to the magnetic energy gain associated with the DOS at the Fermi level remains even above  $T_{\rm C}$ , in spite of large thermal spin fluctuations. The experimental data for liquid transition metal alloys support such a physical picture [233, 234].

One of the important features of the magnetism in amorphous transition metals is that the SG solution ( $[\langle m \rangle^2]_s \neq 0$  and  $[\langle m \rangle]_s = 0$ ) appears, as shown in Figs. 9.8 and 9.9. Although the SG solutions exist even for Co ( $N \approx 8.0$ ), they are not realized because the ferromagnetic state is more stable. The SG state is expected to be stabilized in the region  $N \lesssim 7.35$ , where the ferromagnetism disappears. In the region  $N \lesssim 6.7$  we find antiferromagnetic NN interactions irrespective of the local environment, so that the antiferromagnetism should be stabilized there, though their magnetic structure is not well known.

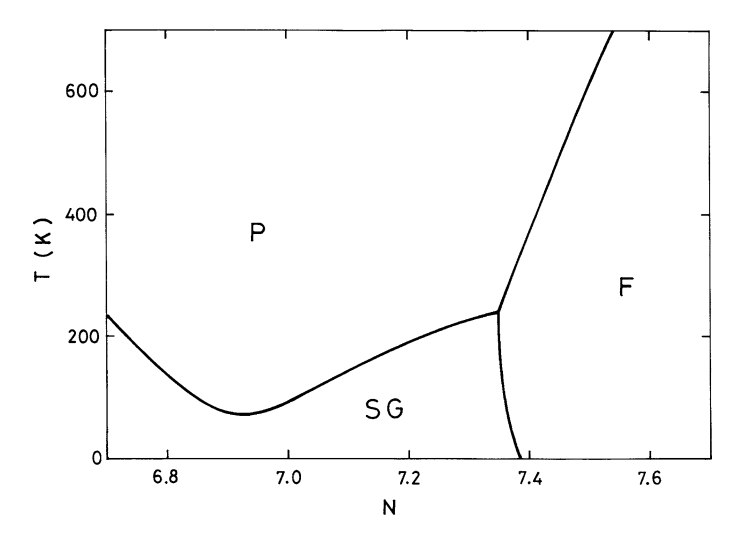
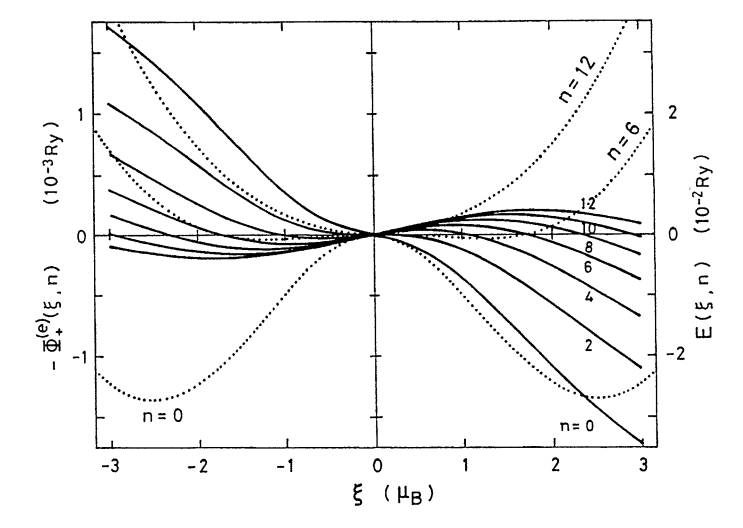


Fig. 9.10 Magnetic phase diagram as a function of the d-electron number N around amorphous Fe showing the ferromagnetic (F), paramagnetic (P), and spin-glass (SG) states [228]. The cluster SG (CSG) phase is expected to fall in the region 7.2 < N < 7.385

#### 9.4.2 Magnetism of Amorphous Fe, Co, and Ni

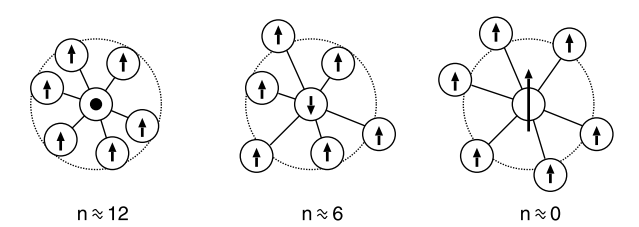
As expected from the general survey of amorphous transition metals, the amorphous Fe shows the SG. Figure 9.10 shows the magnetic phase diagram obtained by the finite-temperature theory (collinear case) presented in Sect. 9.3. The SG states with the transition temperatures  $T_{\rm g}=100$ –200 K are extended to a reasonable range of amorphous Fe (6.7  $\lesssim N \lesssim$  7.35). The transition temperature  $T_{\rm g}=117$  K is obtained for N=7.0 when the experimental value  $[(\delta R)^2]_{\rm s}^{1/2}/[R]_{\rm s}=0.067$  is applied. It is consistent with the observed  $T_{\rm g}=120$  K.

The formation of SG's is understood from the behavior of the exchange pair energy  $-\Phi_{0j}^{(e)}(\xi)$  in  $\Psi(\xi)$  in the nonpolarized medium (see (9.14)). The energy  $-\Phi_{j0}^{(e)}(\xi)$  is interpreted as the magnetic pair-energy gain for the flexible central local moment (LM)  $\xi$  when the neighboring LM with average amplitude  $x_j$  points up, as seen from (9.35). Figure 9.11 shows the exchange pair energies  $-\Phi_{0j}^{(e)}(\xi)$  in various environments in the SG state. In contrast to the bcc Fe (see Fig. 8.22(b)), neighboring Fe LMs show nonlinear magnetic couplings for the environments  $3 \lesssim n \lesssim 12$ ; the Fe LMs with large amplitudes couple ferromagnetically with their neighbors, while the Fe LMs with small amplitudes couple antiferromagnetically with the neighboring ones. This behavior has also been found in fcc Fe crystalline alloys (see Fig. 8.22(a)). Since the amplitudes of LM depend strongly on the surrounding environments via the single-site energy  $E(\xi,n)$  as shown in Fig. 9.11, the sign of the magnetic couplings changes with the local environments. The picture obtained for Fe LMs in various environments is shown in Fig. 9.12. The competition between these ferro- and antiferro-magnetic couplings produces the itinerant-electron



**Fig. 9.11** Single-site energy  $E(\xi, n)$  (dotted curves) and exchange pair energy  $-\Phi_+^{(e)}(\xi, n)$  (solid curves) of amorphous Fe in various environments (n) at T=35 K [228]. Here n denotes the number of contracted pairs

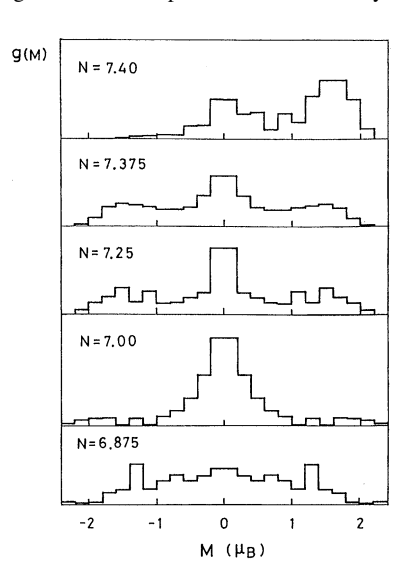
Fig. 9.12 Schematic representation showing the local environment effect on the central local moment (LM) in amorphous Fe. *n* denotes the number of contracted atoms on the NN shell



SG in amorphous iron. The mechanism mentioned above is characteristic of amorphous metallic magnetism, since neither the local environment effects (LEE) on the amplitude of LM nor the non-linearity of the magnetic couplings are seen in the insulators.

Numerical calculations show that anomalous nonlinear magnetic couplings appear in the region  $6.7 \lesssim N \lesssim 7.2$ . When the d electron number N is increased further, the NN couplings do not show any non-linearity irrespective of the local environments at  $7.2 \lesssim N$ . Nevertheless, the SG state is found in the region  $7.2 \lesssim N \lesssim 7.385$ . This is explained as follows. The LM's form local ferromagnetic orders according to the NN ferromagnetic couplings. If these ferromagnetic orders developed a long-range ferromagnetic order, the effective medium would have a polarization consistent with the ferromagnetic clusters. However, the antiferromagnetic couplings between the central LM and the medium occur when the medium is polarized. These couplings reverse the central LM's, so that a long-range ferromagnetic order cannot be developed. This implies that the competition between the short-range ferromagnetic couplings and the long-range antiferromagnetic couplings produces the SG in the region  $7.2 \lesssim N \lesssim 7.35$ . Since the SG is accompanied

**Fig. 9.13** The LM distributions g(M) as a function of the d-electron number at 35 K



by the ferromagnetic clusters, it is referred to as a cluster SG. As the d-electron number is increased, the size of the clusters is expected to increase more and more. Finally, a long-range ferromagnetic order is realized in the region  $7.35 \lesssim N$ . Such a physical picture is consistent with the neutron experiments on reentrant Fe<sub>90</sub>Zr<sub>10</sub> amorphous alloys showing a coexistence of propagating spin-wave excitations and spin-freezing phenomena [235].

Calculated LMs show broad distributions in the vicinity of the ferromagnetic instability and the SG region, as shown in Fig. 9.13. They are caused by the LEE on both the amplitudes and directions of LMs. The results are consistent with the broad distributions of the hyperfine field found in amorphous  $Fe_{93}Zr_7$  [238],  $Fe_{92}La_8$  [239], and  $Fe_{92}Hf_8$  [240] alloys.

The most intriguing feature in the calculated magnetic phase diagram of Fig. 9.10 is the reentrant SG behavior in the narrow region  $7.350 \lesssim N \lesssim 7.385$ . The magnetic states in this region are determined by a detailed balance between the short-range ferromagnetic interactions and the long-range antiferromagnetic interactions. Theoretical calculations showed that the reentrant SG behavior is caused by the temperature-induced enhancement of the short-range ferromagnetic couplings with increasing temperature [228]. The reentrant SG produced by the structural disorder is considered to be realized in Fe-rich amorphous alloys around 90 at.% Fe (see Fig. 9.2).

The noncollinear theory of amorphous metallic magnetism given in the second half of the last section yields similar results [231]. Figure 9.14 shows the calculated magnetic moments as a function of d electron number N. The magnetization  $[\langle m_z \rangle]_s$  shows a maximum at a d electron number around N=7.6 and rapidly decreases with decreasing d electron number towards amorphous Fe  $(N \sim 7.0)$ . The ferromagnetism becomes noncollinear in the region  $7.38 \le N \le 7.43$  as shown in Fig. 9.15. There the transverse SG order parameter  $[\langle m_x \rangle^2]_s^{1/2}$  becomes finite in the

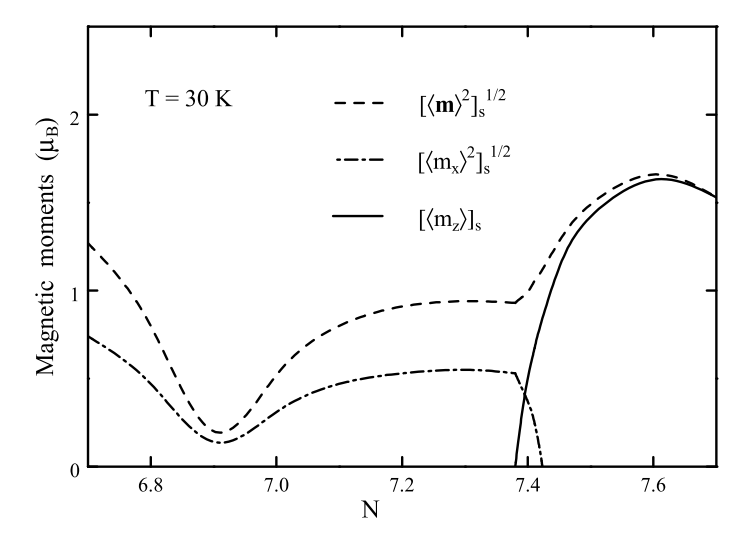
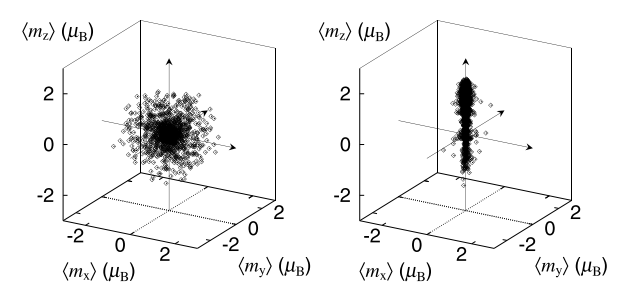


**Fig. 9.14** Total spin glass order parameter  $[\langle \mathbf{m} \rangle^2]_s^{1/2}$ , the transverse spin glass order parameter  $[\langle m_x \rangle^2]_s^{1/2}$ , and the magnetization  $[\langle m_z \rangle]_s$  as functions of d electron number N at 30 K [231]

**Fig. 9.15** Distribution of local moments at 30 K for d electron numbers N = 7.00 (*left*) and N = 7.42 (*right*) [231]. Here 4000 data points among 32000 Monte Carlo samplings are shown



presence of the magnetization  $[\langle m_z \rangle]_s$ . At N=7.38, the magnetization disappears while both total and transverse SG order parameters  $([\langle \boldsymbol{m} \rangle^2]_s^{1/2})$  and  $[\langle m_x \rangle^2]_s^{1/2}$  remain finite, showing the second-order transition from the noncollinear ferromagnetism (F) to the noncollinear SG.

The SG region is divided into two regimes as in the collinear theory. In the region  $7.2 \lesssim N \leq 7.38$ , the cluster SG accompanied by the ferromagnetic clusters is realized, while the SG due to the nonlinear magnetic coupling between NN LMs are realized in the region  $6.9 \lesssim N \lesssim 7.2$ . The SG in amorphous Fe  $(N \sim 7.0)$  is caused by this mechanism. The LM distribution is nearly spherical as shown in Fig. 9.15. It should be noted that the distribution of LMs deviates from the spherical one with decreasing N and shows nearly two-dimensional disc shaped distribution in the vicinity of N = 6.9 where the SG order parameter shows a minimum.

The magnetic phase diagram obtained by the noncollinear theory is presented in Fig. 9.16. The Curie temperature  $T_{\rm C}$  rapidly decreases with decreasing the d electron number and reaches the multicritical point at N=7.38 and T=104 K. Note that

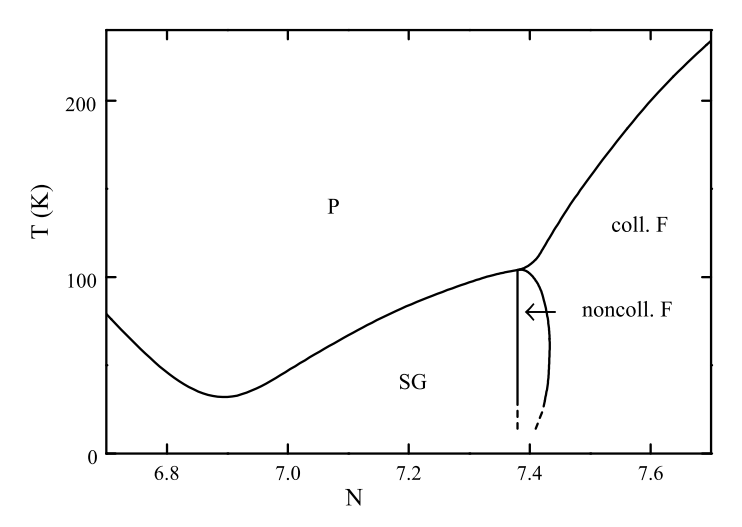


**Fig. 9.16** Magnetic phase diagram as a function of temperature T and d electron number N, showing the paramagnetic (P), the collinear ferromagnetic (coll. F), the noncollinear ferromagnetic (noncoll. F), and the spin glass (SG) states [231]

both  $T_{\rm C}$  and  $T_{\rm g}$  in the noncollinear theory are reduced approximately by a factor of two as compared with the collinear ones because of the semi-classical treatment of spins in the theory. In the noncollinear theory, the re-entrant F–SG transition is not found. Instead in the narrow region around N=7.42, there is a transverse spin freezing temperature  $T_{\rm f}$  at which the transverse SG order parameter  $[\langle m_x \rangle^2]_{\rm s}^{1/2}$  appears. The SG transition temperature  $T_{\rm g}$  shows a minimum as a function of N around N=6.9, where the average NN magnetic interactions change the sign. The noncollinear SG is stable in the region  $6.9 \lesssim N \leq 7.38$  while the collinear and the noncollinear SG are almost degenerate for  $N \lesssim 6.9$ . Experimental phase diagrams seem to be consistent with that of the collinear theory (i.e., Fig. 9.10), suggesting the existence of local anisotropy in the real systems.

The first-principles ground-state calculations for amorphous Co have been performed on the basis of the tight-binding LMTO-recursion method [241]. It is verified that the Fermi level of nonmagnetic amorphous Co is just at the main peak as shown in Fig. 9.17, so that strong ferromagnetism is realized, as discussed before. The calculated ground-state magnetizations are  $1.63\mu_{\rm B}$  for amorphous Co,  $1.58\mu_{\rm B}$  for fcc Co, and  $1.55\mu_{\rm B}$  for hcp Co. The experimental values are reported to be  $1.72\mu_{\rm B}$  for both amorphous and hcp Co. Subtracting the orbital contribution  $0.15\mu_{\rm B}$  from the experimental data, we find the spin contribution  $1.57\mu_{\rm B}$ , being in good agreement with the theoretical results.

As mentioned before, the Curie temperature of amorphous Co obtained by an extrapolation of the data for amorphous Co–Y alloys amounts to 1850 K, which is 450 K higher than that of crystalline Co (see Fig. 9.3). The spin wave stiffness constant is also enhanced by 330 [meV·Å $^2$ ] as compared with that of the hcp Co (510 [meV·Å $^2$ ]), indicating the enhancement of the magnetic coupling due to the

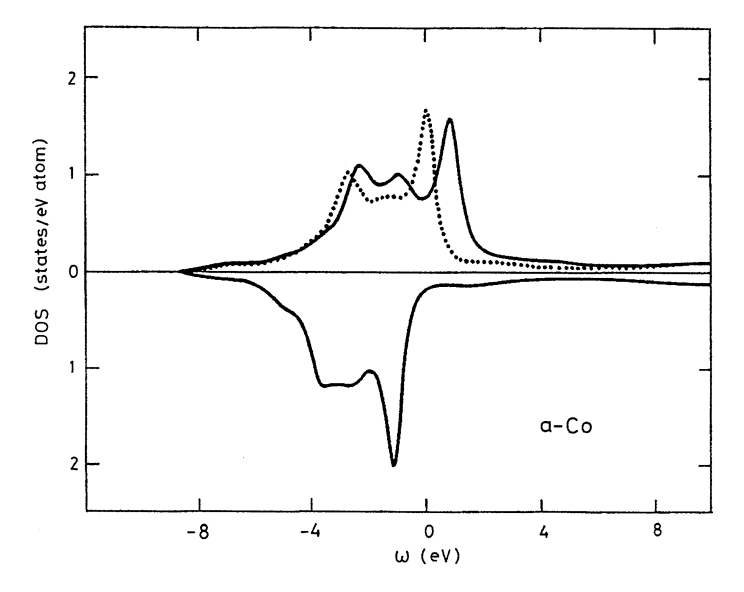


Fig. 9.17 The up and down DOS for amorphous Co at the ground state. The *dotted curve* shows the DOS per spin in the nonmagnetic state [241]

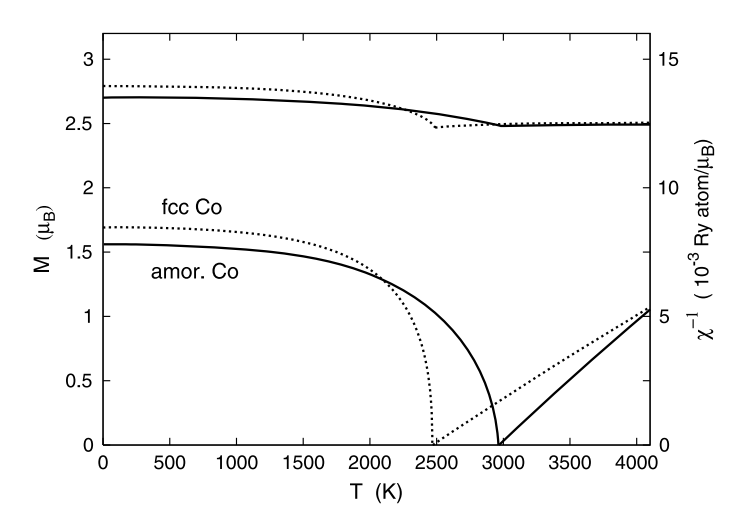
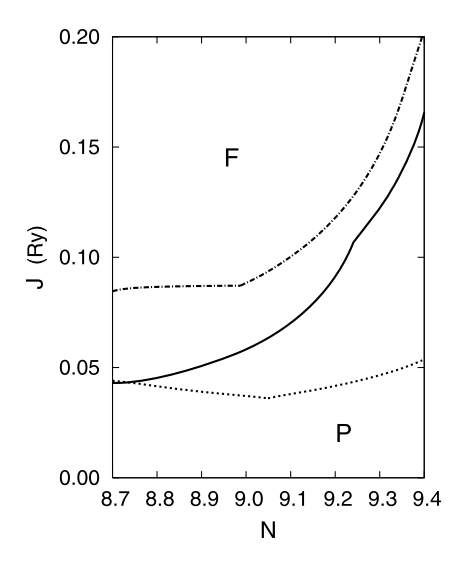


Fig. 9.18 Calculated magnetizations, inverse susceptibilities, and amplitudes of LM's for amorphous (solid curves) and fcc (dotted curves) Co (N=8.1 and  $\tilde{J}=0.100$  Ry) as a function of temperature [228]

structural disorder [222]. The finite-temperature theory of amorphous metallic magnetism allows us to understand the anomaly qualitatively or semiquantitatively as shown in Fig. 9.18. The calculated  $T_{\rm C}$  are overestimated by a factor of 1.8 due to the single-site approximation. Theoretical result of  $T_{\rm C}$  for amorphous Co is 490 K

Fig. 9.19 Ferro- (F) and para-magnetic (P) phase boundaries for the amorphous (solid curve), bcc (dot-dashed curve), and fcc (dotted curve) structures on the  $\tilde{J}-N$  plane, which are obtained by making use of the Stoner theory [229]



higher than that of fcc Co. This is because the magnetic energy gain due to the main peak at the Fermi level enhances  $T_{\rm C}$  in amorphous Co, while the ground-state magnetization is approximately the same for fcc Co because of strong ferromagnetism in both amorphous and fcc Co. The same type of enhancement of  $T_{\rm C}$  is verified to occur in the range  $7.9 \lesssim N \lesssim 8.5$  in accordance with  $N^*({\rm amor}) = 8.35$ .

The strong ferromagnetism in Ni is expected to be weakened with the introduction of structural disorder, since the main peak near the top of the d band is broadened and shifts down to the lower energy region so that the Fermi level is located above the peak. Figure 9.19 shows a diagram for the Stoner ferromagnetism near Ni as a function of the d electron number N, which is obtained with use of the DOS in Fig. 9.5 after a scaling of the band width by a factor of W(Fe)/W(Ni) = 0.393/0.364. A weak ferromagnetism or paramagnetism is obtained around N = 9.0 and the LDA value  $\tilde{J} = 0.074$  Ry (see Table 2.1).

Experimentally, the ground state magnetization,  $0.45\mu_B$ , and  $T_C = 480$  K are obtained by an extrapolation of the data for amorphous  $Ni_x Y_{1-x}(0.75 \lesssim x \lesssim 0.97)$  [236, 237]. The data, however, do not converge to the same value beyond 90 at.% Ni when Y is replaced by La [239]. On the other hand, the negative value of the experimental Weiss constant obtained from the inverse susceptibility in liquid Ni suggests that Ni with the liquid structure would be paramagnetic at zero temperature [233, 234]. These scattered data indicate the importance of the degree of structural disorder which will be discussed in the next subsection.

# 9.4.3 Degree of Structural Disorder and Nonunique Magnetism

It is obvious that different microscopic random structures are possible for the same amorphous metal. Therefore the magnetic properties may change depending on the degree of structural disorder. Experimentally, different structures can be created by the size difference between the transition metal atom and the second elements, the difference in chemical bond with the second elements, and the different preparation techniques. In fact, the magnetization of amorphous Fe obtained by an extrapolation of the magnetization vs. concentration curve is  $2.2\mu_B$  in amorphous Fe  $_cB_{1-c}$  alloys [242, 243], though the Fe-rich amorphous alloys containing early transition metals (ET) show the SG beyond 90 at% Fe (see Fig. 9.2). Amorphous Fe powders containing 2 wt% H, 3 wt% C, and 1 wt% O show the ferromagnetism having the magnetic moment about  $1.4\mu_B$  at the ground state [244].

The same controversial results are also found in amorphous Ni. The Curie temperatures  $T_{\rm C}$  in Ni–Y [236, 237], Ni–La [239], sputtered Ni–Zr [245], and meltquenched Ni–Zr amorphous alloys [246] do not agree with each other even beyond 90 at% Ni, and yield different values when they are extrapolated to amorphous pure Ni. From the analysis of Ni–B amorphous alloys, the pure amorphous Ni is expected to be ferromagnetic with a saturation magnetization of about 60 % of that of the crystalline counterpart and to have the  $T_{\rm C}$  lower by about 60 K [247].

The finite temperature theory of amorphous metallic magnetism presented in the last section allows us to investigate the nonunique magnetism mentioned above as a function of the average coordination number  $z^*$  and the fluctuation of the interatomic distance  $\Delta^{1/2} = [(\delta R)^2]_{\rm s}^{1/2}/[R]_{\rm s}$ . This is understood from the fact that we can obtain the magnetic moments  $[\langle m \rangle]_{\rm s}$  and  $[\langle m \rangle^2]_{\rm s}$  by solving (9.32) and (9.37) self-consistently, once we know the coordination number  $z^*$ , the fluctuation of interatomic distance  $\Delta^{1/2}$ , the average band width  $z^*[y]_{\rm s}$ , and the effective self-energy outside the cluster  $\{\mathscr{S}_{\sigma}\}$ . The latter two quantities are obtained from the average densities of states (DOS)  $[\rho(\varepsilon)]_{\rm s}$  for the noninteracting system via (9.38) and the following relations (see (9.22)).

$$F_{\sigma} = \int \frac{[\rho(\varepsilon)]_{s} d\varepsilon}{\mathcal{L}_{\sigma}^{-1} - \varepsilon},$$
(9.45)

$$z^*[y]_s = \int \varepsilon^2 [\rho(\varepsilon)]_s d\varepsilon. \tag{9.46}$$

A remarkable point of the theory is that it describes the magnetism in both amorphous and crystalline structures. In order to describe the magnetism in the intermediate regime of the degree of structural disorder, we adopt a simple interpolation scheme for  $z^*[y]_s$  and  $\mathcal{S}_{\sigma}$ .

$$z^*[y]_s = A + B(z^* - z_a^*) + C\Delta, \tag{9.47}$$

$$\mathscr{S}_{\sigma} = A_{\sigma} + B_{\sigma} \left( z^* - z_{\mathbf{a}}^* \right) + C_{\sigma} \Delta. \tag{9.48}$$

The coefficients are determined from the values at three points on the  $z^* - \Delta$  plane: the crystalline bcc ( $z_b^* = 8$ ,  $\Delta_b = 0$ ), the fcc ( $z_f^* = 12$ ,  $\Delta_f = 0$ ), and an amorphous structure ( $z_a^* = 11.5$ ,  $\Delta_a^{1/2} = 0.067$ ), for which the DOS [ $\rho(\varepsilon)$ ]<sub>s</sub> are known. These points b (= bcc), f (= fcc), and a (= amor) are shown in Fig. 9.20 by closed circles.

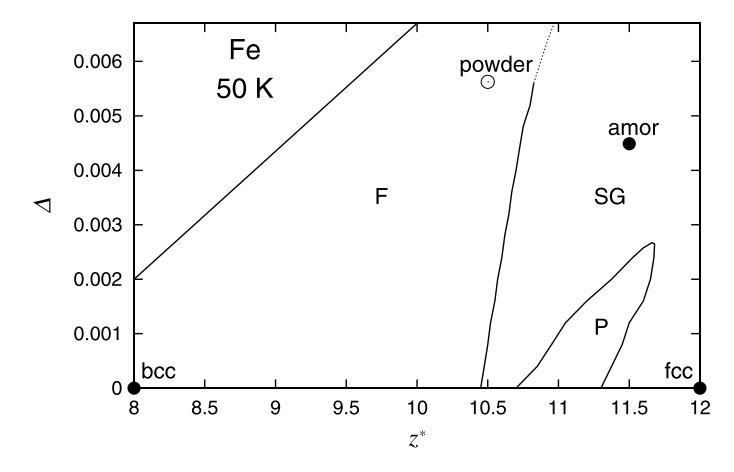


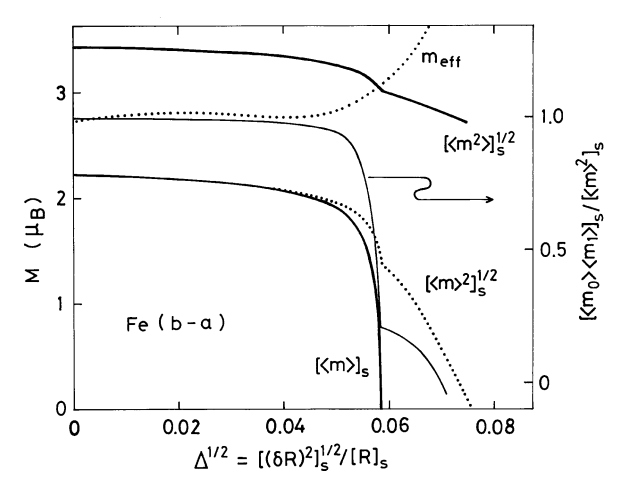
Fig. 9.20 Magnetic phase diagram of Fe on the  $z^* - \Delta$  plane at 50 K [230]. F, SG, and P indicate the ferromagnetism, the spin glass, and the paramagnetism, respectively. The bcc, fcc, sputtered amorphous Fe, and powder amorphous Fe are shown by *closed circles* and *open circles*. Note that calculations are not made in the right-triangle region at the upper left corner, since the region is far from the reference points specified by the *closed circles* 

Figure 9.20 shows the calculated magnetic phase diagram of Fe on the  $z^* - \Delta$  plane at 50 K [230]. Three magnetic phases are possible in the present calculations: the ferromagnetic (F), the SG, and the paramagnetic (P) states depending on the degree of structural disorder. The phase boundary between F and SG may be characterized by a line  $z^* \approx 10.5$ , because the average ferromagnetic couplings are mainly governed by the coordination number  $z^*$ . A paramagnetic region appears around  $z^* \approx 11.0$  and  $\Delta \approx 0$ , because the average magnetic coupling vanishes and fluctuations due to structural disorder are small there. The complex magnetic structures such as spin-density waves are expected near the fcc Fe ( $z^* = 12$ ,  $\Delta = 0$ ) due to long-range competing magnetic interactions, though the present theory does not describe them since the long-range magnetic couplings are not taken into account.

The magnetic phase diagram explains some of the non-unique experimental data of magnetic moment and  $T_{\rm C}$  of amorphous Fe. The Fe-rich early-transition metal (ET) amorphous alloys with more than 90 at.% Fe are reported to have  $z_{\rm a}^*\approx 11.5$  and  $\Delta_{\rm a}^{1/2}\approx 0.067$  [225, 248]. These values lead to the SG of amorphous Fe according to the phase diagram, Fig. 9.20, in agreement with the experimental result. We obtain  $T_{\rm g}=125$  K at this point, which is comparable to the experimental value 110 K (see Fig. 9.2).

Figure 9.21 shows various magnetic moments of amorphous Fe and static spin correlations between the NN LMs at 50 K as a function of  $\Delta$  along the straight line between the bcc point and the amor point (see Fig. 9.20). Calculated magnetization gradually decreases first with introducing structural disorder. It begins to show the ferromagnetic instability beyond  $\Delta^{1/2} \approx 0.05$ , and finally disappears at  $\Delta^{1/2} = 0.058$ . At this point, Fe shows the transition from the ferromagnetism to the SG, since the SG order parameter  $[\langle m \rangle^2]_s^{1/2}$  remains beyond  $\Delta^{1/2} = 0.058$  as seen

**Fig. 9.21** Various magnetic moments of Fe ( $[\langle m \rangle]_s$ : the lower solid curve,  $[\langle m \rangle^2]_s^{1/2}$ : dotted curve,  $[\langle m^2 \rangle]_s^{1/2}$ : the upper solid curve) at 50 K, and the effective Bohr magneton number ( $m_{\rm eff}$ : dotted curve) along the bcc-amor line in Fig. 9.20 [230]. The nearest-neighbor (NN) static spin correlation at 50 K ( $[\langle m_0 \rangle \langle m_1 \rangle]_s / [\langle m \rangle^2]_s^{1/2}$ ) is also presented by the *thin solid curve* 



in Fig. 9.21. These behaviors are explained by the gradual decrease of noninteracting DOS at the Fermi level caused by the shift of the main peak to the higher energy region. Note that the ferromagnetic instability occurs before the Stoner instability point ( $\Delta^{1/2} = 0.0635$ ) where the condition  $[\rho(0)]_s \tilde{J}/2 = 1$  is satisfied. This indicates that the disappearance of the ferromagnetism is realized by the reversal of LMs with increasing  $\Delta$ .

The ferromagnetism with the ground state magnetization  $M=1.4\mu_{\rm B}$  and  $T_{\rm C}/T_{\rm C}({\rm bcc})\gtrsim 0.557$  is reported for amorphous Fe powder containing H, C, and O impurities [244]. Experimental data of the radial distribution function yield the values  $z^*\approx 10.5$  and  $\Delta^{1/2}\approx 0.075$  [244]. These values lead to the ferromagnetism according to the phase diagram (Fig. 9.20). We obtain there  $M=2.02\mu_{\rm B}$  and  $T_{\rm C}/T_{\rm C}$  (bcc) = 0.437, which are consistent with the experimental data mentioned above.

The amorphous Fe expected from Fe-metalloid alloys seems to show the ferromagnetism. Since the metalloid atoms are much smaller than Fe atoms, they tend to occupy the interstitial position between Fe atoms, so that the packing fraction may be smaller than that expected from Fe-ET amorphous alloys. This means that amorphous Fe obtained from the Fe-metalloid alloys are rather close to the bcc structure in coordination number  $z^*$ . The theoretical phase diagram and these structural considerations explain the ferromagnetism of the 'pure' amorphous Fe obtained by an extrapolation from the amorphous Fe-metalloid alloys, though the volume effect and the change of electronic structure due to the metalloid are also significant in this system.

In the case of Ni, the phase diagram consists of the paramagnetic (P) and ferromagnetic (F) states as shown in Fig. 9.22 [249]. The phase boundary is located around  $z^* \approx 11.0$ , though the results are rather sensitive to the d electron number N. Since the average coordination numbers  $z^*$  in typical amorphous Ni are expected to be around 11.0, the magnetism of amorphous Ni is sensitive to the degree of structural disorder as well as the other parameters. Detailed numerical calculations verify that both the ground-state magnetization and  $T_{\rm C}$  in disordered Ni are smaller than those of fcc Ni. The result is consistent with experimental facts.

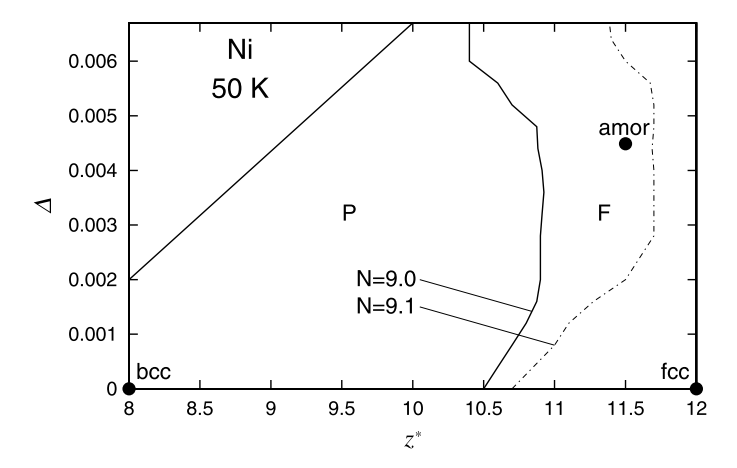


Fig. 9.22 Magnetic phase diagram of Ni on the  $z^* - \Delta$  plane at 50 K for the d electron number N = 9.0 (solid curve) and 9.1 (dot-dashed curve) [249]. Note that the calculations are not made in the right-triangle region at the upper left

The ground-state magnetization  $[\langle m \rangle]_s$  and  $T_C$  of amorphous pure Ni obtained from the Ni–B amorphous alloys are  $[\langle m \rangle]_s \approx 0.37 \mu_B$  and  $T_C \approx 580$  K [247]. With use of the estimated structural parameters,  $z^* \approx 11.75$  and  $\Delta^{1/2} \approx 0.060$  for amorphous Ni, we obtain the theoretical result  $[\langle m \rangle]_s = 0.40 \mu_B$  and  $T_C = 380$  K, being consistent with the experimental data. The Curie temperatures of the melt-quenched amorphous Ni<sub>91</sub>Zr<sub>9</sub> alloy [246] and its counterpart in the bcc phase are practically identical and are much smaller than those obtained by the sputtering method [245]. We can explain the behavior from the phase diagram as a difference in coordination numbers between the two:  $z^*$  (melt-quenched)  $< z^*$  (sputtered), though one has to take into account the other factors such as the effects of second elements, atomic volume and the chemical short-range order. The concentration dependence of the Weiss constants in liquid Fe–Ni alloys suggests that Ni with liquid structure is nonmagnetic at the ground state. As is well-known, the structure of liquid Ni is characterized by  $z^* \approx 10.5$  and  $\Delta^{1/2} \approx 0.083$ . The phase diagram (Fig. 9.2) explains the paramagnetism of liquid Ni if  $\Delta^{1/2} \approx 0.083$  and  $z^* \lesssim 10.5$ .

## 9.5 Theory of Magnetism in Amorphous Alloys

It is remarkable that all the metallic glasses are realized in amorphous alloys where both structural and configurational disorders play an important role on their magnetic properties. In this section, we extend the finite-temperature theory of amorphous metallic magnetism to the amorphous alloys in order to understand the magnetism of amorphous transition metal (TM) alloys.

The structure of amorphous alloys is characterized by structural disorder and random atomic configuration of the constituent atoms. To specify the local structure of

these amorphous alloys, we need more detailed microscopic parameters. The average coordination number on the nearest-neighbor (NN) shell depends on the type of the central atom  $\alpha$  as  $z_{\alpha}^*$ , due to the difference in atomic size of the constituent atoms. We expect that for example  $z_A^* < z_B^*$  when the atomic size of atom A is smaller than that of B. Accordingly the atomic short-range order (ASRO) parameters also depend on the type of atom  $\alpha$  as  $\tau_{\alpha}$ , so that the probability of finding atom  $\alpha$  at the neighboring site of atom  $\alpha$  is given by

$$p^{\alpha\alpha} = c_{\alpha} + (1 - c_{\alpha})\tau_{\alpha}. \tag{9.49}$$

The consistency for the number of neighboring A–B pairs (i.e.,  $c_A z_B^* p^{AB} = c_B z_A^* p^{BA}$ ) yields the following relation among  $\{z_\alpha^*\}$  and  $\{\tau_\alpha\}$ .

$$z_{\rm A}^*(1-\tau_{\rm A}) = z_{\rm B}^*(1-\tau_{\rm B}).$$
 (9.50)

In the DRPHS-like model we have an approximate but simple relation as follows.

$$z_{\alpha}^{*} = z_{\alpha}^{*}(0) + p^{\alpha\alpha} [z_{\alpha}^{*}(1) - z_{\alpha}^{*}(0)]. \tag{9.51}$$

Here  $z_{\alpha}^{*}(1)$   $(z_{\alpha}^{*}(0))$  is the average coordination number for  $p^{\alpha\alpha} = 1$   $(p^{\alpha\alpha} = 0)$ .

When the relations mentioned above are accepted, the independent parameter which controls the degree of atomic short-range order is either  $\tau_A$  or  $\tau_B$ . Note that choice of a random configuration  $\tau_A = \tau_B = 0$  is not allowed because of the relation (9.50). The most random configuration is obtained by minimizing the mean square of deviation taken over all the NN pairs  $\Phi = (N/2) \sum_{\alpha} c_{\alpha} \sum_{\gamma} z_{\alpha}^* p^{\alpha \gamma} (p^{\alpha \gamma} - c_{\gamma})^2$  under the condition (9.50), so that the following condition is obtained [250].

$$c_{\mathcal{A}}\tau_{\mathcal{B}} + c_{\mathcal{B}}\tau_{\mathcal{A}} = 0. \tag{9.52}$$

Equations (9.50), (9.51), and (9.52) determine the parameters  $\{\tau_{\alpha}, z_{\alpha}^*\}$  in the most random configuration.

The Green function theory of electronic structure calculations for substitutional alloys, which was presented in Sect. 8.3, can be extended to the amorphous alloys [250, 251]. We adopt the Hartree–Fock tight-binding Hamiltonian (8.4) and assume the geometrical mean model for the transfer integral model  $t_{ij} = r_{\alpha}^{(c)*} t_{ij}' r_{\gamma}^{(c)}$  (see (8.16)). We then consider the Green function  $G'_{ij} = r_{\alpha}^{(c)} G_{ij} r_{\gamma}^{(c)*} = (L'^{-1} - t')^{-1}$ . Here  $(L'^{-1})_{ij} = L_j'^{-1} \delta_{ij} = \delta_{ij} (\omega + i\delta - \varepsilon_i) / |r_i^{(c)}|^2$  and we have omitted the spin indices for simplicity. By making use of the Dyson equations (8.50) and (8.51) for G', and making the Bethe approximation (see (8.55)), the site-diagonal Green function is obtained as follows.

$$G_{00} = \frac{1}{|r_{\alpha}^{(c)}|^2} \left( L_{\alpha}^{\prime - 1} - \sum_{j \neq 0}^{z} \frac{t_{ij}^{\prime 2}}{L_{j}^{\prime - 1} - S_{j}^{\prime}(L^{\prime})} \right)^{-1}.$$
 (9.53)

Here z is the coordination number on the nearest neighbor shell.  $S'_{j}(L')$  is the sum of all the paths which start from site j and end at the same site without returning to the cluster on the way.

It should be noted that the transfer integral  $t'_{ij}$  still depends on the atomic configuration on sites i and j via the interatomic distance  $R_{ij} = R_{ij}^{\alpha\gamma}$  in the case of amorphous alloys. Experimentally the geometrical-mean relation  $R_{ij}^{\alpha\gamma}=(R_{ij}^{\alpha\alpha}R_{ij}^{\gamma\gamma})^{1/2}$ holds true within a few percent error [251]. Thus, using the relation and assuming the same power law relation  $t'_{ii} \propto R_{ii}^{-\kappa}$ , we find

$$t'_{ij} = r_{\alpha}^{(s)*} \hat{t}_{ij} r_{\gamma}^{(s)}. \tag{9.54}$$

Here  $\hat{t}_{ij}$  is the transfer integral between sites i and j for an amorphous metal as a reference system. When amorphous pure metals A and B have the same structure except for the interatomic distance, the factor  $r_{\alpha}^{(s)}$  does not depend on sites i and j. Adopting (9.54), we obtain the Green function  $G_{00}$  as follows.

$$G_{00} = \frac{1}{|r_{\alpha}|^2} \left( L_{\alpha}^{-1} - \sum_{j \neq 0}^{z} \frac{\hat{t}_{j0}^2}{L_j^{-1} - S_j'(L)/|r_j^{(s)}|^2} \right)^{-1}.$$
 (9.55)

Here  $r_{\alpha}=r_{\alpha}^{(c)}r_{\alpha}^{(s)}$ . It is given by  $r_{\rm A}=\sqrt{\mu_2({\rm A})/\mu_2({\rm B})}$  and  $r_{\rm B}=1$ ,  $\mu_2(\alpha)$  being the second moment for the average DOS for amorphous pure metal  $\alpha$ :  $\mu_2(\alpha)=\int \varepsilon^2 [\rho_{\alpha}^0(\varepsilon)]_{\rm S}\,d\varepsilon$ . Moreover  $L_j^{-1}=(\omega+i\delta-\varepsilon_j)/|r_j|^2$ . When we take the structural and configurational average outside the cluster, we

replace the self-energy  $S_i'(\hat{L})/|r_i^{(s)}|^2$  with an effective  $\mathcal{S}$ , so that we obtain

$$G_{\alpha\alpha} = \frac{1}{|r_{\alpha}|^2} \left( L_{\alpha}^{-1} - \sum_{i \neq 0}^{z} \frac{y_j}{L_i^{-1} - \mathcal{S}} \right)^{-1}.$$
 (9.56)

Here  $y_j = \hat{t}_{i0}^2$ . Introducing the probability  $p_{\alpha}(z)$  of finding z sites on the NN shell of atom  $\alpha$  and the probability  $p_s(y_j) dy_j$  of finding  $\hat{t}_{i0}^2$  between  $y_j$  and  $y_j + dy_j$ , we obtain the averaged Green function for the type of atom  $\alpha$  as follows.

$$\left[ \left[ G_{\alpha\alpha} \right]_{s} \right]_{c} = \sum_{z} p_{\alpha}(z) \sum_{n=0}^{z} \Gamma(n, z, p^{\alpha\alpha}) \int \left[ \prod_{j=1}^{z} p_{s}(y_{j}) dy_{j} \right] G_{\alpha\alpha}. \tag{9.57}$$

Here  $[\ ]_c([\ ]_s)$  means the configurational (structural) average.  $\Gamma(n,z,p)$  is the binomial distribution function  $[z!/n!(z-n)!]p^n(1-p)^{z-n}$ , and  $\Gamma(n,z,p^{\alpha\alpha})$  expresses the probability of finding n atoms of type  $\alpha$  on the NN shell of atom  $\alpha$  with z sites.

By making use of the decoupling approximation (9.31), we obtain

$$[[G_{\alpha\alpha}]_s]_c = \sum_z p_{\alpha}(z) \sum_{n=0}^z \Gamma(n, z, p^{\alpha\alpha})$$

$$\times \sum_{i=0}^n \sum_{i=0}^{z-n} \Gamma(i, n, \frac{1}{2}) \Gamma(j, z - n, \frac{1}{2}) G_{\alpha\alpha}(z, n, i, j), \tag{9.58}$$

$$G_{\alpha\alpha}(z,n,i,j) = \frac{1}{|r_{\alpha}|^2} \left[ L_{\alpha}^{-1} - \left( n + (2i-n) \frac{\left[ (\delta y)^2 \right]_{s}^{1/2}}{[y]_{s}} \right) [y]_{s} K_{\alpha} - \left( z - n + (2i-z+n) \frac{\left[ (\delta y)^2 \right]_{s}^{1/2}}{[y]_{s}} \right) [y]_{s} K_{\tilde{\alpha}} \right]^{-1}.$$
(9.59)

Here  $[y]_s$  is obtained from the second moment and the average coordination number  $z^*$  as  $[y]_s = \mu_2(B)/z^*$ . Moreover  $[(\delta y)^2]_s^{1/2}/[y]_s = 2\kappa \Delta$ ,  $\Delta$  being defined by  $\Delta = [(\delta R)^2]_s^{1/2}/[R]_s$ . The quantity  $K_\alpha$  is defined by  $K_\alpha = (L_\alpha^{-1} - \mathscr{S})^{-1}$ .

To obtain the effective self-energy  $\mathscr S$  outside the cluster, we consider the coherent Green function in which the locators of the Green function  $r_{\alpha}^*G_{00}r_{\alpha}=[(L^{-1}-\hat t)^{-1}]$  have been replaced by the effective one  $\mathscr L$ , i.e.,  $F(\mathscr L^{-1})=[[(\mathscr L^{-1}-\hat t)^{-1}]_{00}]_s$ . In the Bethe approximation it is given as

$$F(\mathcal{L}^{-1}) = \left[ \left( \mathcal{L}^{-1} - \theta K \right)^{-1} \right]_{s}. \tag{9.60}$$

Here  $\theta = \sum_{j=1}^{z} y_{j}$  and  $K = (\mathcal{L}^{-1} - \mathcal{S})^{-1}$ . We thus obtain K and  $\mathcal{S}$  from the above equation because the l.h.s. is given by (9.22).  $K_{\alpha}$  in (9.59) is obtained from K as

$$K_{\alpha} = \left(L_{\alpha}^{-1} - \mathcal{L}^{-1} - K^{-1}\right)^{-1}.\tag{9.61}$$

The effective locator  $\mathcal{L}^{-1}$  should be determined by the self-consistent equations for the shell boundary condition which corresponds to (8.63) for substitutional alloys.

$$\left[\left[r_{j}^{*}G_{jj}r_{j}\right]_{s}\right]_{c} = F(\mathcal{L}^{-1}). \tag{9.62}$$

Here the Green function  $r_i^*G_{jj}r_j$  is given by (8.56):

$$r_j^* G_{jj} r_j = \frac{1}{L_j^{-1} - \mathscr{S}} + \frac{1}{(L_j^{-1} - \mathscr{S})^2} y_j r_\alpha^* G_{00} r_\alpha.$$
 (9.63)

In a more simple version, the medium  $\mathcal{L}^{-1}$  is determined by the CPA equation (8.18):

$$\sum_{\alpha} c_{\alpha} \left[ L_{\alpha}^{-1} - \mathcal{L}^{-1} + F(\mathcal{L}^{-1})^{-1} \right]^{-1} = F(\mathcal{L}^{-1}). \tag{9.64}$$

In order to describe the different shapes of the DOS in both pure amorphous metal limits, it is suitable to adopt a common band model such as  $\hat{t}_{ij} = \lambda \tilde{t}_{ij} = \lambda [c_A t_{ij}(A) + c_B t_{ij}(B)]$ . Here  $t_{ij}(\alpha)$  is the transfer integral for the pure amorphous metals  $\alpha$ . The parameter  $\lambda$  is determined as  $\lambda = \sqrt{\mu_2(B)/\tilde{\mu}_2}$  by taking the second moment at both sides of equation  $\hat{t}_{ij} = \lambda \tilde{t}_{ij}$ .  $\tilde{\mu}_2$  is the second moment of the average DOS for the common band  $\{\tilde{t}_{ij}\}$  and is given by  $\tilde{\mu}_2 = [c_A \mu_2(A)^{1/2} + c_B \mu_2(B)^{1/2}]^2$ . When we adopt the common band model, K in (9.61) is modified as  $K = (\mathcal{L}^{-1} - \lambda \tilde{\mathcal{L}})^{-1}$ ,

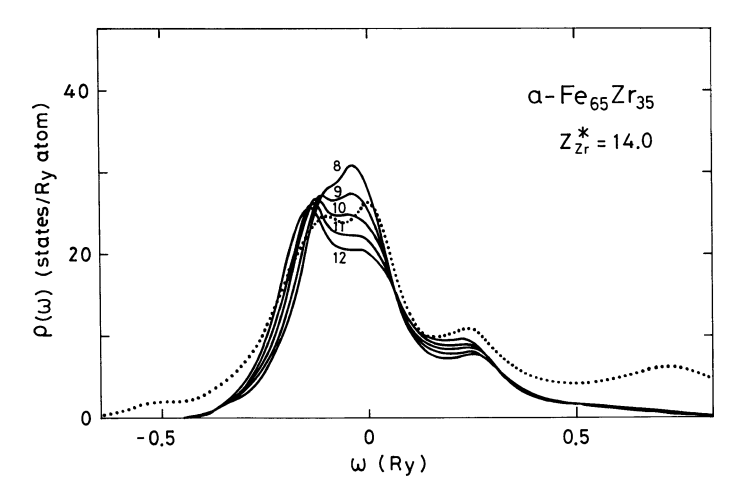


Fig. 9.23 Calculated DOS for amorphous  $Fe_{65}Zr_{35}$  alloys with the use of the Bethe-type approximation (*solid curve*) and the tight-binding LMTO recursion method (*dotted curve*) [251]. The numbers for the *solid curves* denote the average coordination numbers of Fe atoms ( $z_{Fe}^*$ )

and  $\tilde{\mathscr{I}}$  for the transfer integral  $\tilde{t}_{ij}$  is approximated as  $\tilde{\mathscr{I}} = c_{\mathrm{A}}\mathscr{S}(\mathrm{A}) + c_{\mathrm{B}}\mathscr{S}(\mathrm{B})$ . Each  $\mathscr{S}(\alpha)$  or  $K_{\alpha}^{0} = (\mathscr{L}^{-1} - \lambda \mathscr{S}(\alpha))^{-1}$  for amorphous pure metal  $\alpha$  is determined from the following condition corresponding to (9.60).

$$F_{\alpha}(\mathcal{L}^{-1}) = \left[ \left( \mathcal{L}^{-1} - \lambda^2 \theta_{\alpha} K_{\alpha}^0 \right)^{-1} \right]_{c}. \tag{9.65}$$

Thus K in the common band model is obtained from  $K_{\alpha}^{0}$  as

$$K = (c_{\mathcal{A}}(K_{\mathcal{A}}^{0})^{-1} + c_{\mathcal{B}}(K_{\mathcal{B}}^{0})^{-1})^{-1}.$$
 (9.66)

Finally, (9.60), (9.64), and (9.66) form the self-consistent equations to obtain  $\mathcal{L}^{-1}$  and K at each energy  $\omega + i\delta$ . Once we obtain them, we obtain  $K_{\alpha}$  via (9.61). Thus we can calculate the Green function  $[[G_{\alpha\alpha}]_{c}]_{s}$  from (9.58) and (9.59).

The densities of states (DOS) of the amorphous Fe<sub>65</sub>Zr<sub>35</sub> alloy calculated by the above-mentioned Bethe-type theory are shown in Fig. 9.23 [251]. Calculated DOS's show a two-peak structure near the Fermi level. The low energy peak is higher than the high-energy peak when  $z_{\rm Fe}^* = 12$ . The high-energy peak on the Fermi level rapidly develops with decreasing  $z_{\rm Fe}^*$  and becomes dominant at  $z_{\rm Fe}^* = 8.0$ . The calculated DOS agrees well with the first-principles DOS when  $z_{\rm Fe}^* = 9.0$ . The amorphous Fe<sub>65</sub>Zr<sub>35</sub> alloy is known to show the ferromagnetism with the ground state magnetization of  $0.95\mu_{\rm B}$ . Since the high DOS at the Fermi level is important for the appearance of the ferromagnetism according to the Stoner criterion, the results indicate that the ferromagnetism in amorphous Fe<sub>65</sub>Zr<sub>35</sub> alloy originates in the formation of the high-energy peak due to the atomic-size difference, which is not seen in the substitutional alloys.

The finite-temperature theory of amorphous metallic magnetism is extended to the case of amorphous alloys [250]. In the theory for amorphous alloys, we start from the expression of the magnetic moment on site i given by (9.7). The energy potential  $E(\xi)$  is given by (9.5) in which the locator matrix L has been replaced by

$$(L^{-1})_{i\sigma j\sigma'} = L_{i\sigma}^{-1} \delta_{ij} \delta_{\sigma\sigma'}$$

$$= \left(\omega + i\delta - \varepsilon_i^0 + \mu - \frac{1}{2} \tilde{U}_i \tilde{n}_i(\xi) + \frac{1}{2} \tilde{J}_i \xi_i \sigma\right) / |r_j|^2 \delta_{ij} \delta_{\sigma\sigma'}, \quad (9.67)$$

and the transfer integral  $(t)_{ij}$  with  $(\hat{t})_{ij}$ . The latter is defined by  $t_{ij} = r_i^* \hat{t}_{ij} r_j$ .

Taking the same steps as in Sect. 9.3, we introduce the effective medium  $\mathcal{L}_{\sigma}^{-1}$  and expand the energy  $E(\xi)$  with respect to the site in the medium. After making the decoupling approximation for surrounding field variables as well as the molecular-field type approximation, we reach (9.13) for the central local moment (LM):

$$\langle m_0 \rangle = \langle \xi \rangle = \frac{\int d\xi \, \xi \, \mathrm{e}^{-\beta \Psi(\xi)}}{\int d\xi \, \mathrm{e}^{-\beta \Psi(\xi)}}.$$
 (9.68)

Here  $\Psi(\xi)$  is given by (9.14):

$$\Psi(\xi) = E_0(\xi) + \sum_{i=1}^{z} \Phi_{0j}^{(a)}(\xi) - \sum_{i=1}^{z} \Phi_{0j}^{(e)}(\xi) \frac{\langle m_j \rangle}{x_j}.$$
 (9.69)

 $E_0(\xi)$ ,  $\Phi_{0j}^{(a)}(\xi)$ , and  $\Phi_{0j}^{(e)}(\xi)$  are given by (9.8), (9.10), and (9.15) in which the locators L have been replaced by (9.67) and coherent Green functions  $F_{ij\sigma}$  have been replaced by

$$F_{ij\sigma} = \left[ \left( \mathcal{L}_{\sigma}^{-1} - \hat{t} \right)^{-1} \right]_{ij}. \tag{9.70}$$

In the Bethe approximation, they are given by (9.20) and (9.21) in which  $\{t_{ij}\}$  have been replaced by  $\{\hat{t}_{ij}\}$ .

The central LM in (9.68) is regarded as a function of the surrounding LM's  $\{\langle m_j \rangle\}$  on the NN shell, the squares of transfer integrals  $\{y_j = \hat{t}_{j0}^2\}$ , the atomic configuration on the NN shell  $\{\gamma_j\}$ , and the coordination number z. These variables randomly change because of the structural and configurational disorders. Thus we introduce a probability  $g_{\gamma_j}(m_j) dm_j$  of finding LM on the atom of type  $\gamma_j$  between  $m_j$  and  $m_j + dm_j$ , a probability  $p_s(y_j) dy_j$  of finding  $\hat{t}_{j0}^2$  between  $y_j$  and  $y_j + dy_j$ , a probability  $p^{\alpha\alpha}$  of finding an atom of type  $\alpha$  at the neighboring site of the central atom  $\alpha$ , and a probability  $p_{\alpha}(z)$  of finding z sites on the NN shell of the central atom  $\alpha$ . These determine the distribution function of the central LM  $\langle m_{\alpha} \rangle$  via (9.68) and the latter should be identical with those of the neighboring sites. Then the self-consistent equation for the distribution function is obtained as follows (see (9.25)).

$$g_{\alpha}(M) = \sum_{z} p_{\alpha}(z) \sum_{n=0}^{z} \Gamma(n, z, p^{\alpha \alpha}) \int \delta(M - \langle m_{\alpha} \rangle)$$

$$\times \prod_{i=1}^{n} [p_{s}(y_{i}) dy_{i} g_{\alpha}(m_{i}) dm_{i}] \prod_{i=n+1}^{z} [p_{s}(y_{j}) dy_{j} g_{\tilde{\alpha}}(m_{j}) dm_{j}]. \quad (9.71)$$

By making use of the decoupling approximations (9.30) and (9.31) for the distribution functions  $g_{\gamma}(m_j)$  and  $p_s(y_j)$  at the r.h.s. of (9.71) and substituting the approximate expression of  $g_{\alpha}(M)$  into  $[[\langle m_{\alpha} \rangle]_s]_c = \int M g_{\alpha}(M) dM$  and  $[[\langle m_{\alpha} \rangle]_s]_c = \int M^2 g_{\alpha}(M) dM$ , we obtain the self-consistent equations for  $[[\langle m_{\alpha} \rangle]_s]_c$  and  $[[\langle m_{\alpha} \rangle^2]_s]_c$  as follows.

$$\begin{bmatrix}
[[\langle m_{\alpha} \rangle]_{s}]_{c} \\
[[\langle m_{\alpha} \rangle^{2}]_{s}]_{c}
\end{bmatrix} = \sum_{z} p_{\alpha}(z) \sum_{n=0}^{z} \Gamma(n, z, p^{\alpha \alpha}) \sum_{i=0}^{n} \Gamma(i, n, \frac{1}{2}) \\
\times \sum_{i=0}^{z-n} \Gamma(j, z-n, \frac{1}{2}) \left[ [[\langle \xi_{\alpha} \rangle^{2}(z, n, i, j)]_{s}]_{c} \right]. \quad (9.72)$$

In the approximate expression, the central LM of atom, i.e.,  $[[\langle \xi_{\alpha} \rangle^k(z,n,i,j)]_s]_c$  (k=1,2) at the r.h.s. of (9.72) are specified by the coordination number (z), the number of  $\alpha$  atoms on the NN shell (n), the number of contracted atoms among n atoms of type  $\alpha$  on the shell (i), and the number of contracted atoms among the remaining z-n atoms of type  $\bar{\alpha}(j)$ . The distribution function  $p_{\alpha}(z)$  is given in the simplest form as follows.

$$p_{\alpha}(z) = ([z_{\alpha}^{*}] + 1 - z_{\alpha}^{*})\delta_{z[z_{\alpha}^{*}]} + (z_{\alpha}^{*} - [z_{\alpha}^{*}])\delta_{z[z_{\alpha}^{*}]+1}, \tag{9.73}$$

where [] denotes Gauss' notation.

The LMs  $[[\langle \xi_{\alpha} \rangle^k(z, n, i, j)]_s]_c$  (k = 1, 2) are obtained by taking the average over the configurations of fictitious spins  $\{[[\langle m_{\alpha} \rangle^2]_s]_c^{1/2}\}$  on the NN shell with use of the probability  $q_{\alpha}$  of finding an up spin [250]. Here  $q_{\alpha}$  is given by

$$q_{\alpha} = \frac{1}{2} \left( 1 + \frac{[[\langle m_{\alpha} \rangle]_{s}]_{c}}{[[\langle m_{\alpha} \rangle^{2}]_{s}]_{c}^{1/2}} \right). \tag{9.74}$$

The theory covers a wide range of amorphous and liquid magnetic alloys, from metals to insulators within a molecular-field approximation. In the limit of the pure amorphous metal, it reduces to the theory presented in Sect. 9.3. The theory reduces to the finite-temperature theory of the LEE presented in Sect. 8.3 in the case of substitutional alloys. There numerical investigations revealed the following points: (1) the magnetizations at low temperatures are semi-quantitatively described by the effective exchange energy parameters  $\tilde{J}_{\alpha}$ ; (2) the concentration dependences of Curie temperatures are reproduced, but the absolute values are overestimated by a factor of 1.5–2.0 due to the molecular-field approximation and the neglect of transverse spin fluctuations; and (3) the effective Bohr magneton numbers obtained from the Curie–Weiss susceptibilities are generally underestimated by about 25 %

because of the overestimated itinerant character due to the use of reduced  $\tilde{J}_{\alpha}$  and static approximation.

The theory takes into account the fluctuations of the LM's with respect to the structural and configurational disorders. This leads to the spin-glass (SG) solution  $([[\langle m_{\alpha} \rangle]_s]_c = 0 \text{ and } [[\langle m_{\alpha} \rangle^2]_s]_c \neq 0)$ , in addition to the ferromagnetic  $([[\langle m_{\alpha} \rangle]_s]_c \neq 0)$  and  $[[\langle m_{\alpha} \rangle^2]_s]_c \neq 0)$  and paramagnetic  $([[\langle m_{\alpha} \rangle]_s]_c = [[\langle m_{\alpha} \rangle^2]_s]_c = 0)$  solutions.

In the local-moment limit, the SG transition temperature reduces to (8.100) for the case of substitutional alloys:

$$T_{\rm g}^2 = \frac{1}{2} z \left\{ c_{\rm A} \mathcal{J}_{\rm AA}^2 + c_{\rm B} \mathcal{J}_{\rm BB}^2 + \left[ \left( c_{\rm A} \mathcal{J}_{\rm AA}^2 - c_{\rm B} \mathcal{J}_{\rm BB}^2 \right)^2 + 4 c_{\rm A} c_{\rm B} \mathcal{J}_{\rm AB}^4 \right]^{1/2} \right\}. \tag{9.75}$$

For amorphous metals, it is given by

$$T_{\rm g}^2 = \frac{1}{2} z^* (\mathcal{J}_+^2 + \mathcal{J}_-^2).$$
 (9.76)

Here  $z^*$  is the average coordination number,  $\mathcal{J}_{\alpha\gamma}$  is the exchange coupling energy between  $\alpha$  and  $\gamma$  atoms, and  $\mathcal{J}_+(\mathcal{J}_-)$  is the exchange coupling for a contracted (stretched) pair. Equation (9.75) is in agreement with the SG temperature  $T_g$  for an insulator model in the molecular field approximation (see (7.46)). Equation (9.76) reduces to  $T_g$  for the  $\pm \mathcal{J}$  model, i.e.,  $T_g = \sqrt{z^*} |\mathcal{J}|$  when  $\mathcal{J} = \mathcal{J}_+ = -\mathcal{J}_-$ . These facts show that the theory describes both types of SG on the same footing, i.e., the SG due to configurational disorder and the SG due to structural disorder. Needless to say, the latter is essential for amorphous magnetism.

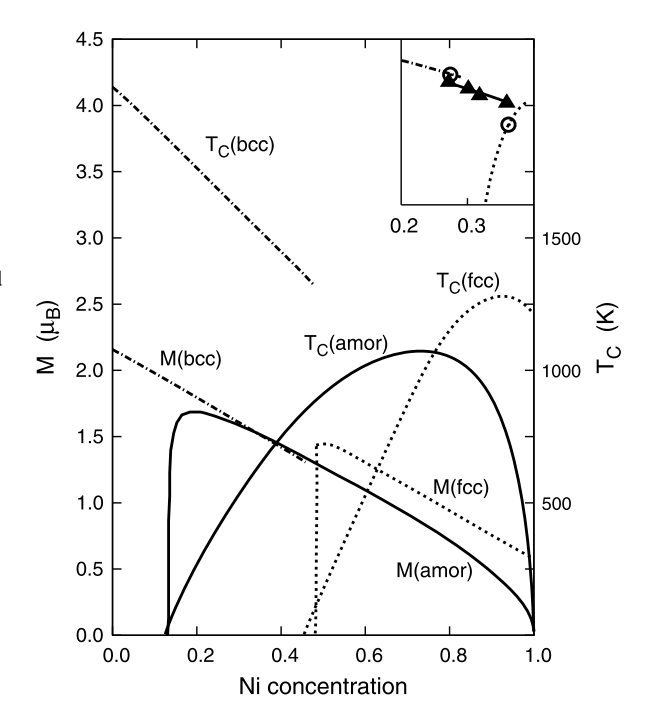
### 9.6 Magnetism of Amorphous Transition Metal Alloys

Amorphous transition metal (TM) alloys show a variety of magnetic properties due to structural and configurational disorders. In this section, we elucidate their properties on the basis of their electronic structure and the finite-temperature theory of magnetism for amorphous alloys.

### 9.6.1 TM-TM Amorphous Alloys

Amorphous TM–TM alloys are significant from the theoretical point of view because they enable us to clarify the effects of structural disorder by comparing their magnetic properties with those of substitutional alloys. We first discuss the magnetism of Fe–Ni amorphous alloys. Experimentally these alloys are found in rather narrow concentration regime  $0.64 \le c_{\text{Fe}} \le 0.72$  [252]. In the crystalline Fe–Ni alloys, the saturation magnetization abruptly decreases around 65 at% Fe (see Sect. 8.3). There the Invar anomalies such as the zero thermal expansion and a broad hyperfine field distribution occurs. In contrast to the crystalline case, the hyperfine field in amorphous Fe–Ni films was found to show no anomaly around

Fig. 9.24 Concentration dependence of the magnetic moment at 150 K and the Curie temperature calculated by a single-site theory for amorphous (*solid lines*), fcc (*dashed lines*), and bcc (*dot-dashed lines*) Fe–Ni alloys [254]. The *inset* is the corresponding hyperfine field observed experimentally [252]

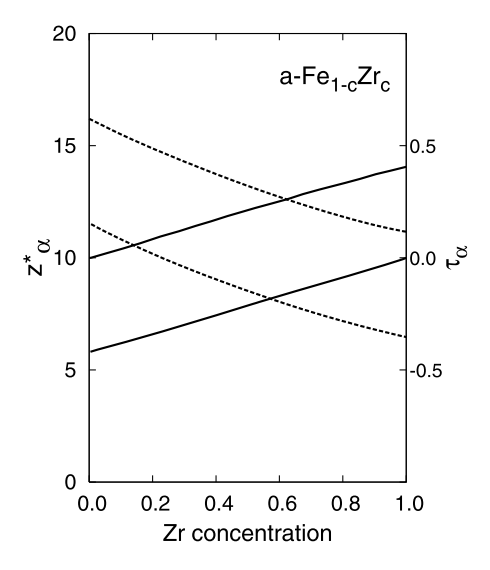


the Invar concentration range in contrast to the crystalline case. Instead it increases along the Slater-Pauling curve with increasing Fe concentration, as shown in the inset of Fig. 9.24.

Magnetic properties of amorphous Fe–Ni alloys have been calculated by means of the single-site theory of amorphous magnetic alloys with use of the geometrical mean model [254]. The results are shown in Fig. 9.24. A remarkable point is that the critical concentration of the ferromagnetic instability shifts to the Fe side by about 30 at% Fe, so that the strong ferromagnetism is realized around 70 at% Fe. It originates from the change of electronic structure. In fact, the shift of the main peak to the lower energy region in the nonmagnetic DOS, which was found in amorphous pure metals (see Fig. 9.7), remains even in amorphous alloys, therefore amorphous Fe–Ni alloys have the Fermi level at the main peak around 70 at% Fe, whereas their crystalline fcc counterparts have the Fermi level below the peak in the same concentration region. The change of the main peak due to structural disorder leads to the strong ferromagnetism in the Invar concentrations in amorphous Fe–Ni alloys. The shift of the Curie temperature maximum to the higher Fe concentration due to structural disorder is also explained by the magnetic energy gain associated with the shift of the main peak in the DOS.

Most of the TM-TM magnetic alloys are formed by adding 4d and 5d early transition metals (ET = Y, Zr, Nb, Mo, La, Hf, Ta, and W) to 3d magnetic transition metals (TM = Fe, Co, and Ni). These alloys are characterized by a large difference in atomic size between the ET and the 3d TM, so that the NN atomic distance depends strongly on the type of the NN pair and that the coordination number depends

Fig. 9.25 Concentration dependencies of ASRO parameters  $\{\tau_{\alpha}\}$  (solid lines) and the average coordination numbers  $\{z_{\alpha}^*\}$  (dashed lines) in amorphous Fe–Zr alloys, which are obtained from the condition of the most random atomic configuration (see (9.52)) and a linear equation for  $\{z_{\alpha}^*\}$  (see (9.51)) [250]



strongly on the type of the central atom as well as the atomic short-range order parameters.

Figure 9.25 shows the average coordination number  $\{z_{\alpha}^*\}$  as well as the atomic short range order (ASRO) parameters for amorphous Fe–Zr alloys in the most random atomic configuration (see (9.52)) [250]. Here the coordination numbers in the pure limits,  $z_{\text{Fe}}^*(0) = 7.0$ ,  $z_{\text{Zr}}^*(0) = 16.0$ , and  $z_{\text{Fe}}^*(1) = z_{\text{Zr}}^*(1) = 11.5$  are estimated on the basis of the DRPHS model. The average coordination numbers  $z_{\alpha}^*$  simply decrease with decreasing Fe concentration.

An example of calculated DOS for the amorphous Fe<sub>75</sub>Zr<sub>25</sub> alloy is presented in Fig. 9.26 [250]. The DOS calculated with use of the finite temperature theory at low temperatures agree well with those of the tight-binding LMTO supercell method [253]. The latter leads to the magnetization  $1.27\mu_B$  at T=0 K and the former to the magnetization  $0.9\mu_B$  at 75 K. These values are compared with the experimental data  $0.96\mu_B$ . Note that Zr atoms are also polarized to be anti-parallel to the magnetization because of the strong hybridization of Zr 4d bands with 3d Fe minority-spin bands. The appearance of the ferromagnetism is explained by a large difference in atomic size between Fe and Zr atoms, as discussed in the last section (see Fig. 9.23).

The atomic short range order is also important for the magnetism of amorphous Fe–Zr alloys. Figure 9.27 shows the calculated phase diagram on the  $p^{\text{FeFe}}$ – $c_{\text{Fe}}$  plane at 75 K. When we decrease the Fe concentration along the line of the most random atomic configuration, we have the spin glass (SG) to the ferromagnetic state (F) and to the paramagnetic state (P) transition. However, we have no ferromagnetic region when  $p^{\text{FeFe}} \gtrsim 0.8$ , and the SG to P transition is expected with decreasing the Fe concentration in the region  $p^{\text{FeFe}} \gtrsim 0.8$ . The disappearance of the ferromagnetism is caused by the formation of amorphous Fe clusters accompanied by the 3d band broadening. Experimentally the Curie temperatures  $T_{\text{C}}$  in the sputtered Fe–Zr

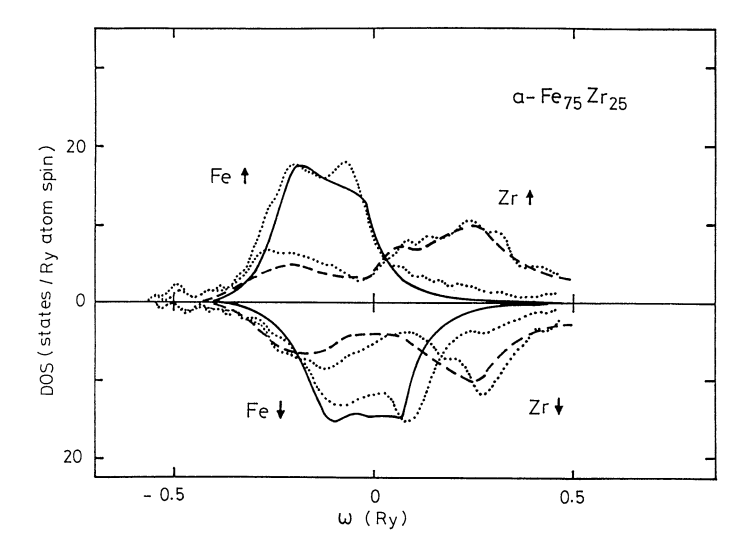


**Fig. 9.26** Calculated average local DOS of amorphous  $Fe_{75}Zr_{25}$  alloy for Fe (*solid curves*) and Zr (*dashed curves*) atoms at 75 K [250]. *Dotted curves* show the local DOS at zero temperature obtained by the tight-binding LMTO supercell method with 64 atoms in a unit cell [253]

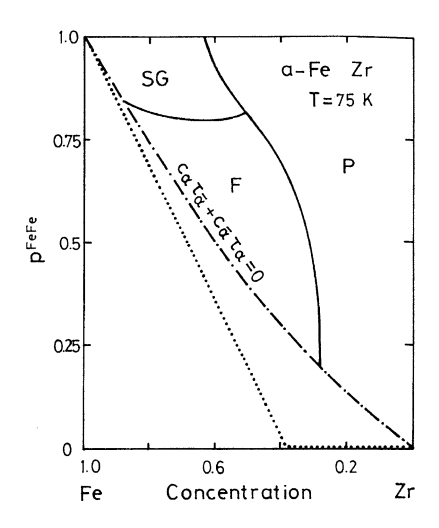
amorphous alloys are larger than those in the melt-span Fe–Zr amorphous alloys. The result is explained by  $p^{\text{FeFe}}(\text{sputtered}) < p^{\text{FeFe}}(\text{melt-spun})$  according to the diagram.

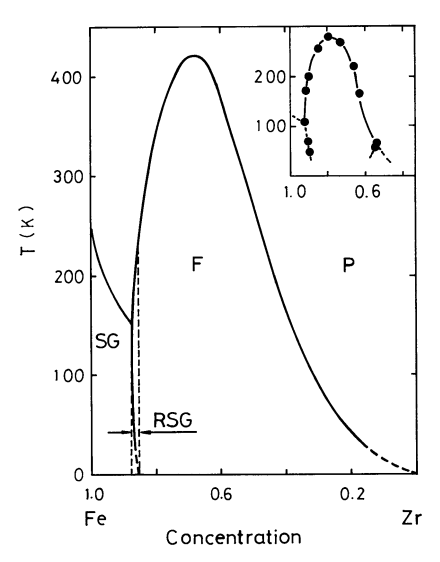
The calculated magnetic phase diagram on the temperature-concentration plane is shown in Fig. 9.28 [250]. The phase diagram is obtained for the most random atomic configuration. It consists of the three different phases: P, F, and SG. In the narrow range of concentration between the F and the SG, the re-entrant SG (RSG) appears. In the amorphous pure Fe limit, the SG is stable as has been discussed in Sect. 9.4. With decreasing Fe concentration, the ferromagnetism appears because of the atomic-size effects as mentioned in the last section. Calculated  $T_{\rm C}$  shows the maximum at 70 at% Fe in agreement with the experimental data (see the inset of Fig. 9.28), and decreases with decreasing Fe concentration. The transition temperatures ( $T_{\rm C}$  and  $T_{\rm g}$ ) are overestimated by a factor of 1.5–2.0 as compared with the experimental ones because of the molecular-field approximation.

The SG in the Fe-rich region are partly caused by the nonlinear magnetic couplings between the NN Fe LM's and partly by the competition between short-range ferromagnetic coupling and long-range antiferromagnetic coupling as discussed in the amorphous pure Fe (see Fig. 9.11). In fact in the former case the central Fe LM with more than 5 contracted Fe NN (l > 5) couples antiferromagnetically with the neighboring Fe LMs via  $-\Phi_{\text{FeFe}+}^{(e)}(\xi,l)$ , but the central Fe LM with l < 5 ferromagnetically couples to the neighboring Fe LMs. On the other hand, the correlation between the central Fe LM  $\langle m_{0\text{Fe}} \rangle$  and the neighboring Fe LM  $\langle m_{1\text{Fe}} \rangle$ , i.e.,  $[[\langle m_{0\text{Fe}} \rangle \langle m_{1\text{Fe}} \rangle]_{\text{c}}]_{\text{s}}$  is 0.15 at 90 at% Fe and 75 K. This means that the NN ferromagnetic interactions are rather strong as compared with the NN antiferromagnetic

Fig. 9.27 The magnetic phase diagram on the  $p^{\text{FeFe}}$ - $c_{\text{Fe}}$  plane at 75 K obtained by the finite-temperature theory [255]. The dot-dashed line denotes the most random atomic configuration (see (9.52)), and the solid curves denote the phase boundaries among the spin glass (SG), the ferromagnetism, and the paramagnetism (P). The dotted line shows the lower bound;  $p^{\text{FeFe}} = 1$  $c_{\mathrm{Zr}}z_{\mathrm{Zr}}^{*}/c_{\mathrm{Fe}}z_{\mathrm{Fe}}^{*}$ 

Fig. 9.28 Calculated magnetic phase diagram of amorphous Fe–Zr alloys showing the paramagnetism (P), ferromagnetism (F), spin glass (SG), and the re-entrant spin glass (RSG) [255]. The phase boundary below 50 K are extrapolated by *dashed lines*. The *inset* shows the experimental result [221, 256]





ones. The SG near the phase boundary therefore should be formed by the competition between short-range ferromagnetic couplings and long-range antiferromagnetic interaction.

The Co–Y amorphous alloys show the ferromagnetism and it is enhanced as compared with their crystalline counterparts in a wide range of Co concentrations, as shown in Fig. 9.3. Enhancement of the ferromagnetism at more than about 80 at% Co is explained by the high DOS of the main peak at the Fermi level as found in amorphous pure Co (see Fig. 9.17). However, the enhancement around 50 to 80 at% Co is attributed to the differences in local atomic structure, especially, the small

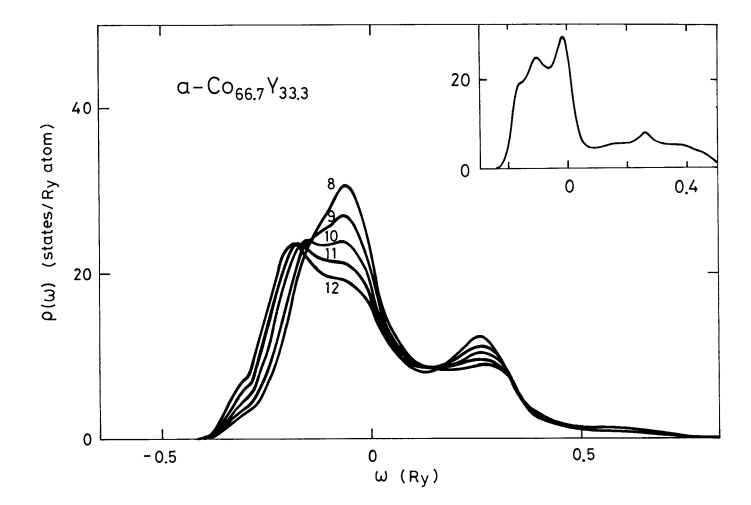


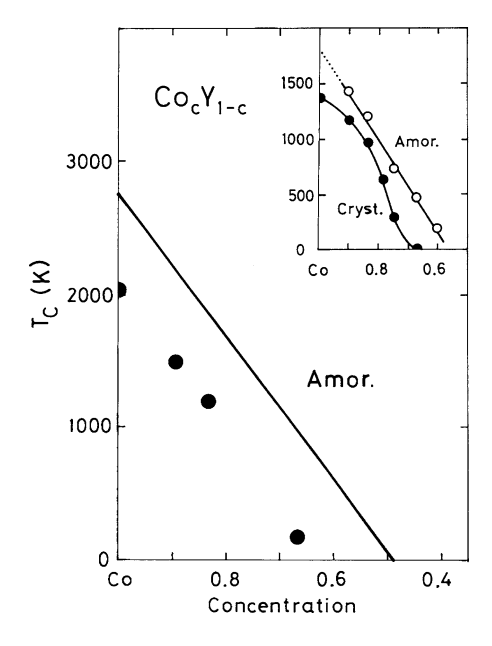
**Fig. 9.29** Change in DOS for amorphous  $Co_{67}Y_{33}$  alloy with varying the coordination number around a Co atom,  $z_{Co}^*$ , from 8 to 12 [251].  $z_Y^*$  is fixed to be 12. The *inset* shows the result based on the tight-binding d orbital model [258]. The DOS at the Fermi level is developed with decreasing  $z_{Co}^*$ 

atomic coordination number of Co due to the difference in the atomic sizes between Co and Y atoms. We discuss here the  $Co_2Y$  alloys as an example.

The amorphous  $Co_2Y$  alloy shows the ferromagnetism with the average magnetization  $0.7\mu_B$  per atom, while the crystalline Laves-phase  $Co_2Y$  shows the paramagnetism (see Fig. 9.3). The first-principles band calculations show that the Fermi level of the Laves-phase  $Co_2Y$  is pinned in a local minimum of the DOS, so that the compound does not satisfy the Stoner criterion [257]. On the other hand, the DOS in amorphous  $Co_2Y$  alloy show the peak at the Fermi level as shown in the inset of Fig. 9.29 [258]. The DOS for various average coordination number of  $Co_2Y$ , which are calculated by means of the theory of the LEE of amorphous alloys presented in the last section are shown in Fig. 9.29 [251]. The peak near the Fermi level strongly depends on  $z_{Co}^*$ . The DOS at the Fermi level increases with decreasing  $z_{Co}^*$ , and satisfies the Stoner criterion between  $z_{Co}^* = 10$  and 9. The coordination number around a  $Co_2Y$  alores the latter satisfies the Stoner criterion, one concludes that the atomic-size difference causes the ferromagnetism in the amorphous  $Co_2Y$  alloy.

Calculated Curie temperature vs. concentration curves of both amorphous and compound Co–Y alloys are given in Fig. 9.30. The Curie temperatures for the crystalline counterparts are calculated as the close-packed Co–Y alloys having the same average local atomic configurations  $\{z_{\alpha}^*\}$  and  $\{\tau_{\alpha}\}$  as those in the crystalline counterparts (i.e., Co<sub>2</sub>Y, Co<sub>3</sub>Y, Co<sub>5</sub>Y, Co<sub>17</sub>Y<sub>2</sub>, and fcc Co) and no fluctuations of  $\Delta = [(\delta R)^2]_s^{1/2}/[R]_s$  (i.e.,  $\Delta = 0$ ). Calculated  $T_C$ 's explain qualitatively the difference between the amorphous structure and its Laves phase crystalline counterpart as well as their concentration dependence, though the calculated  $T_C$  for crystalline Co<sub>2</sub>Y alloy is still finite in this approach.

**Fig. 9.30** Calculated Curie temperature ( $T_{\rm C}$ ) vs. concentration curve [259]. Closed circles show the Curie temperatures for close-packed alloys with the same average local atomic configurations as in the crystalline fcc Co, Co<sub>17</sub>Y<sub>2</sub>, Co<sub>5</sub>Y, Co<sub>3</sub>Y, and Co<sub>2</sub>Y compounds. The *inset* shows the experimental results [222, 260]



The TM–Y alloys form amorphous alloys with all the magnetic TM from Mn to Ni in a wide range of concentration. Their magnetic phase diagrams are obtained experimentally as shown in Fig. 9.31 [261]. Amorphous  $\mathrm{Mn}_c\mathrm{Y}_{1-c}$  (0.18  $\leq c \leq 0.76$ ) alloys show the SG with SG transition temperatures ( $T_g$ ) less than 60 K [262, 263]. Amorphous  $\mathrm{Fe}_c\mathrm{Y}_{1-c}$  (0.32  $\leq c \leq 0.925$ ) alloys are reported to have two different phase diagrams: the sputtered Fe—Y alloys show the SG in the whole concentration [264–266], while the melt-spun Fe–Y alloys show the ferromagnetism with the reentrant SG behavior in the range  $0.5 \lesssim c \lesssim 0.8$  [267–269]. Amorphous  $\mathrm{Co}_c\mathrm{Y}_{1-c}$  (0.38  $\leq c \leq 0.90$ ) alloys show the enhancement of  $T_C$  as compared with their crystalline counterparts as has been mentioned. The Ni $_c\mathrm{Y}_{1-c}$  (0.65  $\leq c \leq 0.97$ ) alloys show a weak ferromagnetism beyond 83 at% Ni [236, 270]. Both alloys cause the F–P (paramagnetism) transition at 50 at% Co and 83 at% Ni, respectively.

The overall feature of the magnetic phase diagrams of TM–Y amorphous alloys is explained by the finite temperature theory of the LEE for amorphous alloys as shown in Fig. 9.32 [261]. There the most random atomic configuration is assumed. Calculated  $T_{\rm C}$  in amorphous Ni–Y alloys is 500 K for amorphous pure Ni, which is smaller than the  $T_{\rm C}$  in fcc Ni (630 K), and monotonically decreases with increasing 3d–4d hybridization. As discussed before, the main peak at the Fermi level in amorphous Co enhances the magnetic coupling, therefore  $T_{\rm C}$ . The atomic-size effects tend to keep this enhancement when Co concentration is decreased. The calculated SG temperature in amorphous Mn–Y alloys, on the other hand, linearly increases with increasing Mn concentration, and show a maximum at 80 at% Mn because of the band broadening with increasing Mn concentration.

Calculated phase diagram in amorphous Fe-Y alloys shows the SG beyond 87 at% Fe and the re-entrant SG behavior in a very small region near the

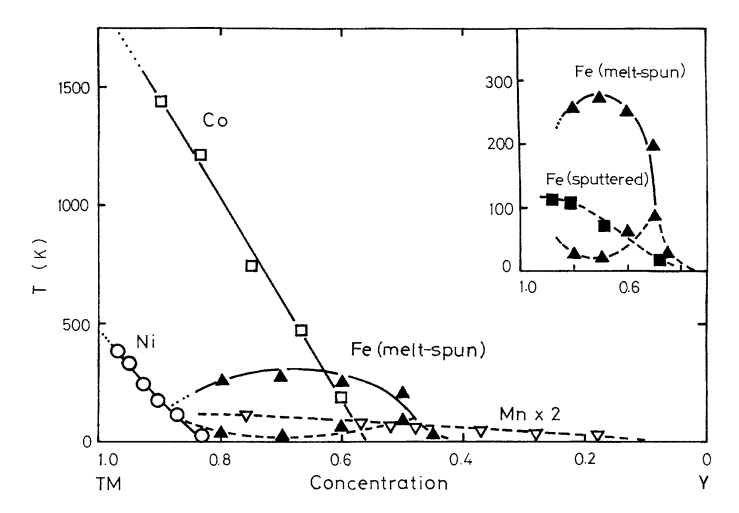


**Fig. 9.31** Experimental magnetic phase diagrams in amorphous TM-Y (TM = Mn, Fe, Co, Ni) alloys [222, 262, 263, 267–270]. *Solid (dashed) curves* denote the Curie (spin-glass) temperature  $T_{\rm C}$  ( $T_{\rm g}$ ). The SG temperatures in Mn-Y alloys are multiplied by a factor of 2. The *inset* shows different phase diagrams for the melt-spun Fe-Y [267–269] and sputtered Fe-Y amorphous alloys [264, 265]

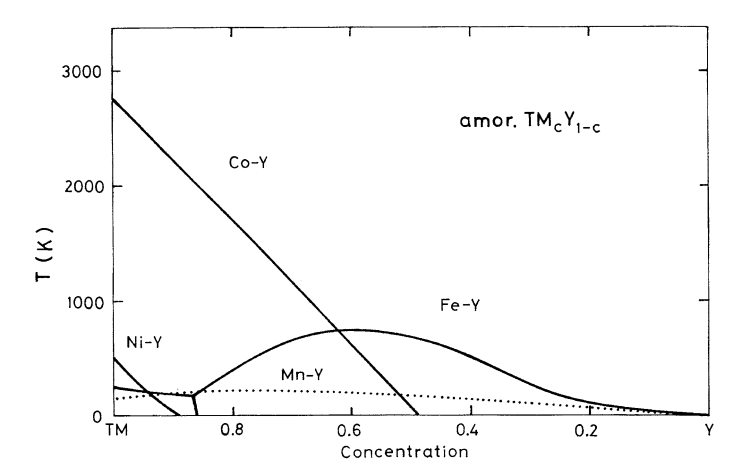


**Fig. 9.32** Calculated magnetic phase diagrams in amorphous TM-Y alloys [230]. The *solid line* in Fe-Y beyond 87 at% Fe and the *dotted line* show the SG temperature. The *other solid curves* show the Curie temperature

F–SG boundary. Calculated  $T_{\rm g}$  changes from 240 K (amorphous Fe) to 165 K (86.5 at% Fe). Below 86 at% Fe, the alloys show the ferromagnetism. The Curie temperature rapidly increases with decreasing Fe concentration, and show a maximum ( $T_{\rm C}=740$  K) around 60 at% Fe. These results qualitatively agree with the

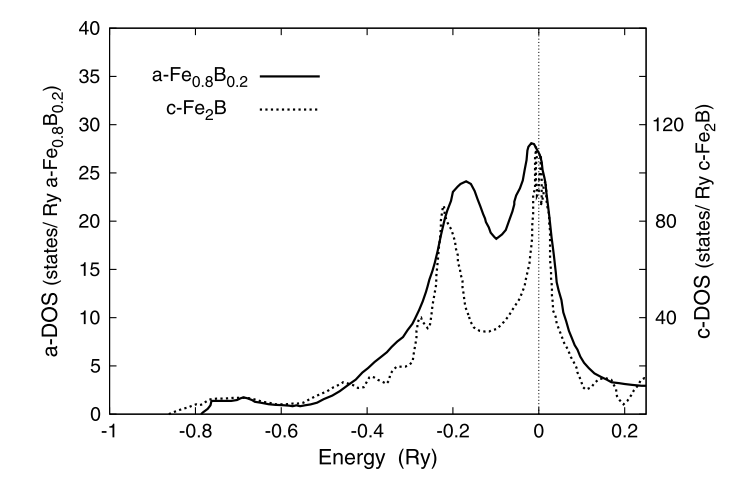


Fig. 9.33 The DOS for amorphous  $Fe_{80}B_{20}$  alloys (*solid curve*), and for crystalline  $Fe_2B$  compound (*dashed curve*) [272]

magnetic phase diagram in melt-spun Fe–Y alloys (see Fig. 9.31), though the reentrant SG behaviors are not found in a wide range of concentration.

The sputtered amorphous Fe–Y alloys do not show the ferromagnetism in whole concentrations according to the experiments. It is explained by the ASRO effects. In fact, theoretical calculations verify that the amorphous Fe–Y alloys show the SG irrespective of concentration when the condition  $p^{\text{FeFe}} \gtrsim 0.8$  is satisfied. Since the experimental values of  $p^{\text{FeFe}}$  seem to satisfy the condition (for example,  $p^{\text{FeFe}} = 0.845$  for the sputtered Fe<sub>85</sub>Y<sub>15</sub> alloys), the SG in sputtered Fe–Y alloys are explained by the formation of small Fe clusters due to strong ASRO.

### 9.6.2 The Other TM Alloys

The transition metal metalloid amorphous alloys have also been intensely investigated from the earliest stage of investigations [216–218]. Their local structures are shown to be similar to those of the crystalline counterparts. For example, there is no direct contact between metalloid P atoms in Co–P amorphous alloys from 0 at% P to about 20 at% P, and metalloid atoms are captured in the interstitial positions called the Bernal holes in the DRPHS model [271]. The local structure is quite similar to that of trigonal-prismatic crystalline Fe<sub>3</sub>P and Fe<sub>2</sub>P compounds.

Figure 9.33 shows the calculated DOS for the amorphous  $Fe_{80}B_{20}$  alloy and the crystalline  $Fe_{2}B$  [272]. The characteristic feature of these DOS is that they are almost the same. Their electronic structure based on the first-principles calculations is summarized as follows. The B sp states hybridize strongly with Fe d states. The hybridization splits B sp states into bonding and antibonding states, and shifts the main peak of DOS for Fe d states toward the low energy side. The Fermi level

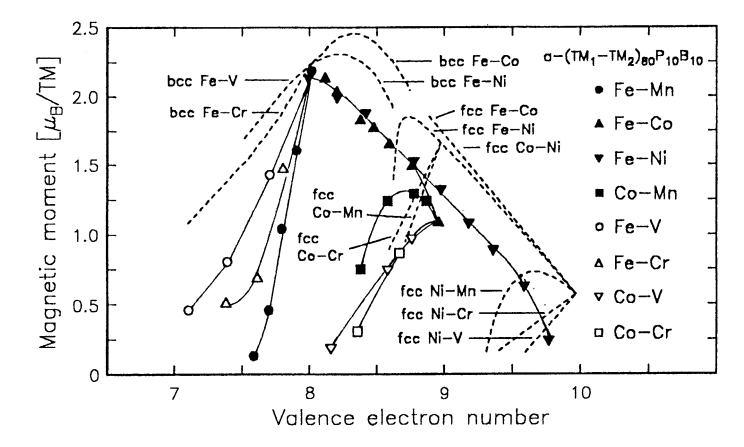


**Fig. 9.34** The average magnetization per TM atom for the pseudo-binary transition metal amorphous alloys as a function of valence electron number [273]. The crystalline Slater–Pauling curves are also plotted by *dashed lines* 

becomes close to the main peak position of the DOS. The Fe–Fe distances increase, and the coordination numbers of Fe–Fe pairs decrease with the addition of B atoms, so that the d band width of Fe narrows. These effects are common for TM-metalloid alloys. In particular, the peak shift of the DOS toward the low energy side enhances the DOS of Fe at the Fermi level, so that the ferromagnetism is stabilized according to the Stoner criterion in the Fe–metalloid amorphous alloys.

The effects of the peak shift of the DOS are also found in the other TM-metalloid amorphous alloys. Figure 9.34 shows the average magnetization vs. d electron number curves for pseudo-binary transition metal metalloid alloys in the form  $(TM_x^1TM_{1-x}^2)_{80}B_{10}P_{10}$  [273]. It is remarkable that the curves for amorphous alloys are obtained simply by shifting the corresponding curves for crystalline alloys by 0.5 electrons to lower d-electron numbers. The shift of the electron number corresponds to that of the peak position of the DOS with the addition of metalloids. We have discussed the same kind of systematic change of the magnetism in amorphous TM metals in Sect. 9.4. The origin of the shift of the DOS here, however, is different from the case of amorphous pure metals; the shift of the DOS in the TM-metalloid system is caused by the change in chemical bondings between TM and metalloid atoms, while the shift in pure TM amorphous metals is caused by structural disorder.

The rare-earth transition metal (RE-TM) amorphous alloys have also extensively been investigated. Their atomic structures are similar to those obtained by the DRPHS model, which are different from the crystalline counterparts. The valence electron configurations and atomic radii of RE atoms are quite similar to those of a Y atom. The itinerant-electron contributions to the magnetic properties are similar to those of Y-TM amorphous alloys. The RE atoms on the other hand have unfilled f-electron shell inside  $6s^2$  filled shell, so that they have well-defined atomic LMs even in solids [16]. The magnetic moment of an RE atom is given by M = L + 2S ( $\mu_B$ ), while the total angular momentum J is given by J = L + S. Here L and S

denote the total atomic orbital and spin angular momenta of f electrons, respectively. These atomic moments are built up by the Hund's rule coupling, i.e., the Coulomb interactions between f electrons, except for Ce showing the valence fluctuations. In the case of RE atoms, the spin–orbit coupling  $\lambda L \cdot S$  is significant, and the coupling constant  $\lambda$  takes plus (minus) sign for the f electron number less (more) than half in filling (see (1.44) in Sect. 1.3). Therefore the atoms form the multiplet ground state with J = L - S for the RE atoms with less than half-filled f electrons (i.e., light RE atoms) and J = L + S for the RE atoms with more than half-filled f electrons (i.e, heavy RE atoms).

Between the 3d TM atomic spin  $S_{\rm TM}$  and the RE atomic spin S, there is an effective interaction of the type  $-J_{\rm RT}S\cdot S_{\rm TM}$ . To derive the interaction, assume that the 3d bands are ferromagnetically polarized. Since the broad 5d up-spin band electrons strongly hybridize with the 3d down-spin band electrons as compared with the hybridization with 3d up-spin bands, the 5d electrons are polarized antiferromagnetically. The latter electrons polarize f electrons in the same direction due to the direct exchange interaction on RE sites. This implies that the effective coupling between TM spin  $S_{\rm TM}$  and RE spin S is antiferromagnetic;  $J_{\rm RT} < 0$ .

The crystalline-field effects on the RE LM are usually assumed to be described by the single-ion anisotropy such as  $-D_i(\mathbf{n}_i \cdot \mathbf{J}_i)^2$  [214, 215]. Here the random unit vector  $\mathbf{n}_i$  denotes a local 'easy axis' on site i and  $D_i$  (> 0) is the anisotropy constant. Since the local easy axis is random, this interaction is favorable for the noncollinear magnetic structure.

Because of the magnetic interactions mentioned above, the RE-TM amorphous alloys are classified into the following three groups.

### Light RE-TM amorphous alloys

The local moment (LM) of TM (TM = Fe, Co, and Ni) atoms couples antiferromagnetically to the spin S of the RE atoms and the latter antiferromagnetically couples with the orbital LM L ( $\lambda > 0$ ). Since the orbital LM exceeds the spin LM in magnitude, it turns out that the total LM of RE atoms ferromagnetically couple to those of the TM atoms. The random single-ion anisotropic interactions cant the RE LM to some extent. Therefore this system shows non-collinear ferromagnetism as shown in Fig. 9.35(left). The Nd–Fe and Nd–Co amorphous alloys belong to this category.

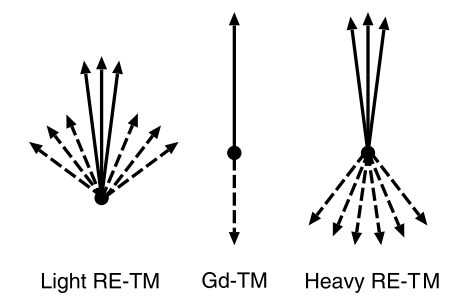
#### Heavy RE-TM amorphous alloys

The LM of TM (TM = Fe, Co, and Ni) atoms couples antiferromagnetically to the spin S of the RE atoms and the latter ferromagnetically couples with the orbital LM L ( $\lambda < 0$ ). Thus the total LM of the RE atoms antiferromagnetically couple to those of the TM atoms. The random single-ion anisotropic interactions cant the RE LM to some extent. Therefore this system shows non-collinear ferrimagnetism as shown in Fig. 9.35(right). Amorphous Dy–Fe and Dy–Co alloys for example belong to this category.

#### Gd-TM amorphous alloys

The LM of TM (TM = Fe, Co, and Ni) atoms couples antiferromagnetically to the spin S of Gd atoms. Since the orbital LM L for Gd atoms disappear, the total LM (i.e, spin S) of the RE atoms antiferromagnetically couple to those of the TM

Fig. 9.35 Three types of magnetic configurations in amorphous RE-TM alloys: light RE-TM alloys (*left*), Gd-TM alloys (*middle*), and heavy RE-TM alloys (*right*). The *solid* (*dashed*) arrows denote the TM (RE) LM



atoms. This system therefore shows the ferrimagnetism as shown in the middle of Fig. 9.35. Amorphous Gd–Fe, Gd–Co, and Gd–Ni alloys show the ferrimagnetism.

The first-principles calculations have been performed for some RE–TM amorphous alloys with the use of the density functional theory (DFT) with the local density approximation (LDA). Figure 9.36 shows the densities of states (DOS) for the amorphous Gd<sub>33</sub>Fe<sub>67</sub> alloy [274]. The Fe 3d states ferromagnetically polarize as in the case of bcc Fe and the projected DOS show the two-peak structure. The two-peak structure originates in the local atomic structure which is rather more similar to the closed packed structure than the crystalline bcc or the Laves structure. The Gd 5d states extend from -3 eV to 8 eV and strongly hybridize with the minority spin 3d band because the latter is energetically closer to the 5d states than the majority 3d states, as seen in Fig. 9.36. Consequently, the 5d electrons polarize to be antiparallel to the 3d LM's. The localized Gd 4f states form the narrow up and down bands. Since the polarized 5d electrons ferromagnetically couple to the 4f electrons via the intraatomic d–f exchange interaction, the 4f electrons antiparallely couple to the 3d Fe LM's as mentioned before. Note that the DFT-LDA theory underestimates the

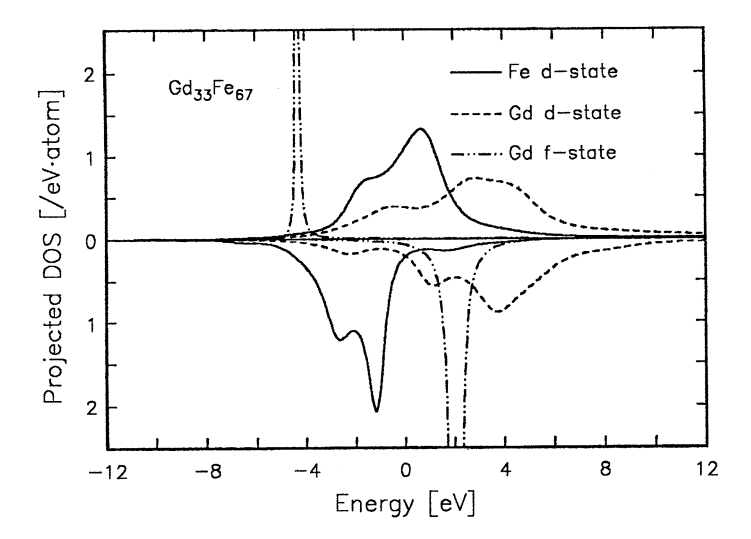


Fig. 9.36 Projected DOS's of amorphous Gd<sub>33</sub>Fe<sub>67</sub> alloy [274]

binding energy of the occupied f states; the calculated value 4.3 eV is much smaller than the experimental value 9.4 eV [275].

The calculated magnetic moments in the amorphous  $Gd_{33}Fe_{67}$  alloy are  $7.2\mu_B$  for the Gd site and  $-2.0\mu_B$  for the Fe site. The average magnetic moment per atom is  $1.1\mu_B$ , which is in good agreement with the experimental value  $1.2\mu_B$ . In the case of the crystalline Laves phase GdFe<sub>2</sub> compound, calculated magnetic moments of the Gd site are  $7.5\mu_B$ , which is larger than in the amorphous alloy, and  $-1.9\mu_B$  for Fe site. The average magnetic moment per atom is  $1.2\mu_B$ , which is also in good agreement with the experimental value  $(0.9-1.2\mu_B)$  [276].

In order to discuss the temperature dependence of magnetic properties of the RE–TM amorphous alloys, one has to rely on the model Hamiltonian. A possible effective Hamiltonian which takes into account the itinerant character of d electrons as well as the localized f electrons may be written as follows [277–279].

$$H = \sum_{i\sigma} \varepsilon_{i} n_{i\sigma} + \sum_{ij} t_{ij} a_{i\sigma}^{\dagger} a_{j\sigma} + \sum_{i} U_{i} n_{i\uparrow} n_{i\downarrow} - \tilde{J}_{RT} \sum_{i} \boldsymbol{J}_{i} \cdot \boldsymbol{s}_{j}$$
$$- \sum_{i} D_{i} (\boldsymbol{n}_{i} \cdot \boldsymbol{J}_{i})^{2}. \tag{9.77}$$

Here the first three terms denote the d-band Hubbard model (see (1.51)).  $\varepsilon_i$ ,  $t_{ij}$ , and  $U_i$  denote the atomic level on site i, the transfer integrals between sites i and j, and the intraatomic Coulomb interaction between d electrons on site i, respectively. The fourth term at the r.h.s. of (9.77) expresses the exchange couplings between the RE moment  $J_i$  and the TM spin  $s_i$ . The last term represents random anisotropy. The spin fluctuation theories of amorphous alloys based on the Hamiltonian (9.77) are left for future investigations.

### Appendix A

# Equivalence of the CPA Equations (3.83), (3.85), and (3.89)

We verify here the equivalence of three equations on the CPA, (3.83), (3.85), and (3.89). We start from the CPA equation (3.83) showing the disappearance of the single-site t matrix in average.

$$\langle \tilde{t}_{i\sigma} \rangle = \left\langle \frac{\delta v_{i\sigma}}{1 - \delta v_{i\sigma} F_{i\sigma}} \right\rangle = 0.$$
 (A.1)

Here  $\delta v_{i\sigma} = v_{i\sigma} - \Sigma_{i\sigma}(z)$ ,  $v_{i\sigma}$  and  $\Sigma_{i\sigma}(z)$  being the impurity potential and the coherent potential, respectively. Note that we have generalized the coherent potential to be site-dependent.  $F_{i\sigma}(z)$  is the coherent Green function defined by

$$F_{i\sigma}(z) = \left[ (z - \Sigma_{\sigma} - t)^{-1} \right]_{ii}. \tag{A.2}$$

The average  $\langle \sim \rangle$  in (A.1) is a classical average defined by (3.84).

Since the t-matrix in (A.1) is written as

$$\tilde{t}_{i\sigma} = \left(\frac{F_{i\sigma}^{-1}}{F_{i\sigma}^{-1} - \delta v_{i\sigma}} - 1\right) F_{i\sigma}^{-1},\tag{A.3}$$

we obtain an alternative expression for the CPA condition as

$$\langle G_{i\sigma}^{(i)}(z)\rangle = F_{i\sigma}(z).$$
 (A.4)

This is identical with the CPA equation (3.85), and the Green function  $G_{i\sigma}^{(i)}(z)$  is defined by

$$G_{i\sigma}^{(i)}(z) = \frac{1}{F_{i\sigma}^{-1}(z) - \delta v_{i\sigma}}.$$
 (A.5)

The Green function  $G_{i\sigma}^{(i)}(z)$  is the on-site Green function for an impurity embedded in the effective medium, of which the Hamiltonian is given by

$$(H_{\sigma}^{(i)}(z))_{il} = \left[v_{i\sigma}(z,\xi)\delta_{ij} + \Sigma_{\sigma}(z)(1-\delta_{ij})\right]\delta_{jl} + t_{jl}(1-\delta_{jl}). \tag{A.6}$$

Y. Kakehashi, *Modern Theory of Magnetism in Metals and Alloys*, Springer Series in Solid-State Sciences 175, DOI 10.1007/978-3-642-33401-6, © Springer-Verlag Berlin Heidelberg 2012 To verify this fact, we rewrite the Hamiltonian as  $H_{\sigma}^{(i)}(z) = \tilde{H}_{\sigma}(z) + \delta v_{i\sigma}$ . Here  $\tilde{H}_{\sigma}(z)$  is the coherent Hamiltonian defined by  $(\tilde{H}_{\sigma}(z))_{jl} = \Sigma_{j\sigma}(z)\delta_{jl} + t_{jl}(1-\delta_{jl})$ .  $\delta v_{i\sigma}$  is defined by  $(\delta v_{i\sigma})_{jl} = (v_{i\sigma} - \Sigma_{i\sigma}(z))\delta_{ij}\delta_{jl}$ . We then expand the Green function on the impurity site as

$$\left[\left(z - H_{\sigma}^{(i)}(z)\right)^{-1}\right]_{ii} = \left[\tilde{G}_{\sigma}(z) + \tilde{G}_{\sigma}(z)v_{i\sigma}(z)\tilde{G}_{\sigma}(z) + \cdots\right]_{ii}.$$
 (A.7)

Here  $\tilde{G}_{\sigma}(z)$  is the resolvent of the Hamiltonian  $\tilde{H}_{\sigma}(z)$ , i.e.,  $\tilde{G}_{\sigma}(z) = (z - \tilde{H}_{\sigma}(z))^{-1}$ . Equation (A.7) means that

$$\left[ \left( z - H_{\sigma}^{(i)}(z) \right)^{-1} \right]_{ii} = \tilde{G}_{ii\sigma} (1 - \delta v_{i\sigma} \tilde{G}_{ii\sigma})^{-1}. \tag{A.8}$$

Since  $F_{i\sigma} = \tilde{G}_{ii\sigma}(z)$ , we find the relation:

$$G_{i\sigma}^{(i)}(z) = \left[ \left( z - H_{\sigma}^{(i)}(z) \right)^{-1} \right]_{ii}. \tag{A.9}$$

The CPA equations (A.1) and (A.4) are expressed as the stationary condition for the free energy (3.82):

$$\mathscr{F}_{SSA} = \tilde{\mathscr{F}} - \beta^{-1} \sum_{i} \ln \int \sqrt{\frac{\beta U}{4\pi}} \, d\xi_i \, e^{-\beta E_i(\xi_i)}. \tag{A.10}$$

Here the coherent part of the free energy  $\tilde{\mathscr{F}}$  is defined by (3.72):

$$\widetilde{\mathscr{F}} = \int d\omega f(\omega) \frac{1}{\pi} \operatorname{Im} \sum_{\sigma} \operatorname{tr} \left[ \ln(z - \Sigma - t) \right]. \tag{A.11}$$

Note that tr at the r.h.s denotes the trace over sites. The single-site energy  $E_i(\xi_i)$  is given by (3.78):

$$E_i(\xi_i) = \int d\omega f(\omega) \frac{1}{\pi} \operatorname{Im} \sum_{\sigma} \ln(z - \delta v_{i\sigma}(z) F_{i\sigma}(z)) + \frac{1}{4} U(\xi_i^2 - \zeta_i^2).$$
 (A.12)

To derive the stationary condition, we rewrite the free energy (A.10) as follows.

$$\mathscr{F}_{SSA} = -\beta^{-1} \ln \int \left[ \prod_{j} \sqrt{\frac{\beta U}{4\pi}} d\xi_{j} \right] e^{-\beta(\tilde{\mathscr{F}} + \sum_{i} E_{i}(\xi_{i}))}. \tag{A.13}$$

Here

$$\tilde{\mathscr{F}} + \sum_{i} E_i(\xi_i) = \int d\omega f(\omega) \frac{1}{\pi} \operatorname{Im} \sum_{\sigma} X_{\sigma}(z) + \frac{1}{4} \sum_{i} U_i (\xi_i^2 - \zeta_i^2), \quad (A.14)$$

and  $X_{\sigma}(z)$  is defined by

$$X_{\sigma}(z) = \operatorname{tr} \ln(z - \Sigma_{\sigma} - t) + \sum_{i} \ln[z - \delta v_{i\sigma}(z, \xi) F_{i\sigma}(z)]. \tag{A.15}$$

Taking the variation of  $\mathscr{F}_{SSA}$  with respect to the coherent potential  $\Sigma_{i\sigma}(z)$ , we have

$$\delta \mathscr{F}_{\text{SSA}} = \left\langle \delta \left( \tilde{\mathscr{F}} + \sum_{i} E_{i}(\xi_{i}) \right) \right\rangle = \int d\omega \, f(\omega) \frac{1}{\pi} \operatorname{Im} \sum_{\sigma} \langle \delta X_{\sigma}(z) \rangle. \quad (A.16)$$

Note that we have used here the stationary condition for  $\zeta_i(\xi)$ ;  $\partial E_i(\xi)/\partial \zeta_i(\xi) = 0$ . The variation of  $X_{\sigma}(z)$  is obtained as

$$\delta X_{\sigma}(z) = -\sum_{i} F_{i\sigma}(z) \delta \Sigma_{i\sigma}(z) + \sum_{i} (z - \delta v_{i\sigma}(z, \xi) F_{i\sigma}(z))^{-1} F_{i\sigma}(z) \delta \Sigma_{i\sigma}(z)$$
$$-\sum_{i} (z - \delta v_{i\sigma}(z, \xi) F_{i\sigma}(z))^{-1} \delta v_{i\sigma}(z, \xi) \delta F_{i\sigma}(z). \tag{A.17}$$

Thus the average is obtained as follows

$$\langle \delta X_{\sigma}(z) \rangle = \sum_{i} \left[ -F_{i\sigma}(z) + \langle G_{i\sigma}^{(i)}(z) \rangle \right] \delta \Sigma_{i\sigma}(z) - \sum_{i} \langle \tilde{t}_{i\sigma}(z) \rangle \delta F_{i\sigma}(z).$$
 (A.18)

By making use of the CPA equations (A.1) and (A.4), we find the stationary condition as follows.

$$\langle \delta X_{\sigma}(z) \rangle = 0. \tag{A.19}$$

From (A.16) and (A.19), we obtain the stationary condition.

$$\frac{\delta \mathscr{F}_{\text{SSA}}}{\delta \Sigma_{i\sigma}(z)} = 0. \tag{A.20}$$

This is identical with (3.89), so that we have verified that (3.83), (3.85), and (3.89) are equivalent to each other.

### Appendix B

# **Dynamical CPA Based on the Multiple Scattering Theory**

The dynamical CPA theory presented in Sect. 3.4 is also obtained by using the multiple scattering theory in the disordered alloys [51]. We derive in this appendix the dynamical CPA equation on the basis of the temperature Green function and the multiple scattering theory.

The temperature Green function  $\mathcal{G}_{ij\sigma}(\tau - \tau')$  is given by an average of the time-dependent Green function  $G_{ij\sigma}(\tau, \tau')$  with respect to the energy functional  $E[\xi, \eta]$  as shown in (3.48):

$$\mathscr{G}_{ij\sigma}(\tau - \tau') = \langle G_{ij\sigma}(\tau, \tau') \rangle = \frac{\int \left[ \prod_{i} \delta \xi_{i} \delta \eta_{i} \right] G_{ij\sigma}(\tau, \tau') e^{-\beta E[\xi, \eta]}}{\int \left[ \prod_{i} \delta \xi_{i} \delta \eta_{i} \right] e^{-\beta E[\xi, \eta]}}.$$
 (B.1)

The time-dependent Green function is determined by solving the Dyson equation (3.43):

$$G_{ij\sigma}(\tau,\tau') = g_{ij\sigma}(\tau-\tau') + \int_0^\beta d\tau'' \sum_k g_{ik\sigma}(\tau-\tau'') v_{k\sigma}(\tau'') G_{kj\sigma}(\tau'',\tau').$$
(B.2)

Here  $g_{ij\sigma}(\tau - \tau')$  is the Green function for noninteracting Hamiltonian  $H_0$ , and  $v_{i\sigma}(\tau)$  is the time-dependent random potential given by (3.37). The Dyson equation is written in matrix form as

$$G = g + gvG = (g^{-1} - v)^{-1}.$$
 (B.3)

The matrices are for example defined as  $(G)_{i\tau\sigma j\tau'\sigma'} = G_{ij\sigma}(\tau,\tau')\delta_{\sigma\sigma'}$ .

Now, we consider a scattering from an effective potential  $\Sigma'$ . Inserting potential  $\Sigma'$  into the potential part in the above expression, we expand the Green function with respect to the scattering potential  $\delta v = v - \Sigma'$  as

$$G = \tilde{G} + \tilde{G}\delta v\tilde{G} + \tilde{G}\delta v\tilde{G}\delta v\tilde{G} + \cdots.$$
(B.4)

Y. Kakehashi, *Modern Theory of Magnetism in Metals and Alloys*, Springer Series in Solid-State Sciences 175, DOI 10.1007/978-3-642-33401-6, © Springer-Verlag Berlin Heidelberg 2012 Here  $\tilde{G}$  is the coherent Green function defined by

$$\tilde{G} = \left(g^{-1} - \Sigma'\right)^{-1}.\tag{B.5}$$

The Green function (B.4) is expressed with use of the  $\mathcal{T}$  matrix as

$$G = \tilde{G} + \tilde{G}\mathcal{T}\tilde{G}. \tag{B.6}$$

Here the  $\mathcal{T}$  matrix is defined by the potential scattering as

$$\mathscr{T} = \delta v + \delta v \tilde{G} \delta v + \dots = \delta v (1 + \tilde{G} \mathscr{T}). \tag{B.7}$$

On the other hand the real self-energy  $\Sigma$  for the temperature Green function (B.1) is defined by

$$\mathscr{G} = \langle G \rangle = \left( g^{-1} - \Sigma \right)^{-1}. \tag{B.8}$$

This is nothing but the Dyson equation for the temperature Green function. To obtain the expression of  $\Sigma$  with use of the  $\mathscr T$  matrix, we solve the above equation as  $\Sigma = g^{-1} - \langle G \rangle^{-1}$ , and substitute the expression  $\langle G \rangle^{-1} = \tilde{G}^{-1}(1 + \tilde{G}\langle \mathscr T \rangle)^{-1}$ , which is obtained from (B.6), into  $\langle G \rangle$  at the r.h.s., so that we obtain

$$\Sigma = g^{-1} - \tilde{G}^{-1} (1 + \tilde{G} \langle \mathcal{T} \rangle)^{-1}. \tag{B.9}$$

According to the definition of the coherent Green function (B.5), we have the relation  $g^{-1} = \Sigma' + \tilde{G}^{-1}$ . Thus we can express the self-energy (B.9) as

$$\Sigma = \Sigma' + \langle \mathcal{T} \rangle \left( 1 + \tilde{G} \langle \mathcal{T} \rangle \right)^{-1}. \tag{B.10}$$

This is the exact self-energy expression when we start from an effective medium  $\Sigma'$ . The correction is given by the  $\mathscr T$  matrix caused by the scattering potential  $\delta v$ .

In order to obtain the averaged  $\mathscr T$  matrix, i.e.,  $\langle \mathscr T \rangle$  at the r.h.s. of (B.9), we solve (B.7) with respect to  $\mathscr T$  as

$$\mathscr{T} = (1 - \delta v \tilde{G})^{-1} \delta v. \tag{B.11}$$

Next, we divide  $\tilde{G}$  into the diagonal part F and the off-diagonal part F';  $\tilde{G} = F + F'$  to make the single-site approximation (SSA). Substituting the expression into (B.11) and expanding  $\mathscr{T}$  with respect to F', we obtain

$$\mathscr{T} = \left(1 - \tilde{t}F'\right)^{-1}\tilde{t},\tag{B.12}$$

and  $\tilde{t}$  is given by

$$\tilde{t} = (1 - \delta v F)^{-1} \delta v = \sum_{i} \tilde{t}_{i}. \tag{B.13}$$

Here  $\tilde{t}_i$  denotes the single-site t matrix on site i, which is given by

$$\tilde{t}_i = (1 - \delta v_i F_i)^{-1} \delta v_i, \tag{B.14}$$

and  $F_i = \tilde{G}_{ii}$ .

Making the SSA we obtain  $\langle \mathcal{T} \rangle$  from (B.12) as

$$\langle \mathcal{T} \rangle \approx \langle \tilde{t} \rangle.$$
 (B.15)

Substituting (B.15) into (B.10) and making the single-site approximation  $\tilde{G} \approx F$  in the denominator, we find the self-energy in the SSA as

$$\Sigma = \Sigma' + (1 + \langle \tilde{t} \rangle F)^{-1} \langle \tilde{t} \rangle, \tag{B.16}$$

or

$$\Sigma = \Sigma' + \sum_{i} (1 + \langle \tilde{t}_i \rangle F_i)^{-1} \langle \tilde{t}_i \rangle. \tag{B.17}$$

Note that the second term depends on the effective medium  $\Sigma'$ . When we choose  $\Sigma' = \langle v \rangle$  (i.e., the Hartree–Fock value), we call (B.17) the average *t*-matrix approximation (ATA). The best choice of the effective medium  $\Sigma'$  should be obtained from the condition:

$$\langle \tilde{t}_i \rangle = \langle (1 - \delta v_i F_i)^{-1} \delta v_i \rangle = 0.$$
 (B.18)

This is identical with the dynamical CPA equation (3.112). The present method indicates that the medium  $\Sigma' = \Sigma$  is the self-energy of the temperature Green function.

Equation (B.17) is often used to obtain the CPA solution. Assuming that we start from the Hartree–Fock value  $\Sigma' = \langle v \rangle$ , we calculate the corrections according to the second term at the r.h.s. of (B.17). If the obtained self-energy  $\Sigma^{(1)}$  does not agree with  $\Sigma'$ , we renew as  $\Sigma' = \Sigma^{(1)}$  and repeat the procedure until the self-consistency  $\Sigma = \Sigma'$  is achieved. Equation (B.17) is identical with (3.97) when  $i\omega_l$  in the frequency representation is replaced by  $z = \omega + i\delta$ .

### Appendix C

## Derivation of the Single-Site Spin Fluctuation Theory from the Dynamical CPA

We verify in this Appendix that the dynamical CPA presented in Sect. 3.4 reduces to the single-site spin fluctuation theory (SSF) given in Sect. 3.3 in the static limit.

The free energy per atom in the dynamical CPA is given by (3.148) in the static approximation:

$$\mathscr{F}_{\text{CPA}} = \tilde{\mathscr{F}} - \beta^{-1} \ln \int \sqrt{\frac{\beta U}{4\pi}} d\xi \, e^{-\beta E_i(\xi)}. \tag{C.1}$$

The static energy potential  $E_i(\xi)$  is given by (3.149).

$$E_i(\xi) = -\beta^{-1} \sum_{l\sigma} \ln\left(1 - \delta v_{i\sigma}(i\omega_l, \xi) F_{i\sigma}(i\omega_l)\right) + \frac{1}{4} U\left(\xi^2 - \zeta_i^2(\xi)\right). \quad (C.2)$$

Here  $\delta v_{i\sigma}(i\omega_l, \xi)$  is defined by (3.79), the coherent Green function  $F_{i\sigma}(i\omega_l)$  is given by (3.88), and  $\zeta_i(\xi)$  by (3.150):

$$\zeta_i(\xi) = \frac{1}{\beta} \sum_{l\sigma} G_{i\sigma}^{(i)}(i\omega_l, \xi). \tag{C.3}$$

The static Green function  $G_{i\sigma}^{(i)}(z,\xi)$  is defined by (3.86);  $G_{i\sigma}^{(i)}(z,\xi) = 1/(F_{i\sigma}(z)^{-1} - \delta v_{i\sigma}(z,\xi))$ . The dynamical CPA equation to determine the coherent potential is given by (3.143):

$$\langle G_{i\sigma}^{(i)}(i\omega_l,\xi)\rangle = F_{i\sigma}(i\omega_l). \tag{C.4}$$

The CPA equation on the real axis is obtained by direct replacement  $i\omega_l \rightarrow z$   $(=\omega + i\delta)$  as follows.

$$\langle G_{i\sigma}^{(i)}(z,\xi)\rangle = F_{i\sigma}(z). \tag{C.5}$$

The frequency sums in (C.2) and (C.3) can also be transformed into the integrals on the real axis of the complex z plane. To prove this we adopt the Lehmann represen-

tation of the Green function.

$$G_{i\sigma}^{(i)}(i\omega_l,\xi) = \int \frac{\rho_{i\sigma}(\omega,\xi) d\omega}{i\omega_l - \omega}.$$
 (C.6)

Here  $\rho_{i\sigma}(\omega,\xi)$  is the single-particle density of states of interacting electrons, and is given by

$$\rho_{i\sigma}(\omega,\xi) = -\frac{1}{\pi} \operatorname{Im} G_{i\sigma}^{(i)}(\omega + i\delta, \xi). \tag{C.7}$$

Substituting (C.6) into (C.3), we find

$$\zeta_i(\xi) = \sum_{\sigma} \int d\omega \, \rho_{i\sigma}(\omega, \xi) \frac{1}{\beta} \sum_{l} \frac{e^{i\omega_l \eta}}{i\omega_l - \omega}.$$
 (C.8)

Here we explicitly wrote a convergence factor with an infinitesimal positive number  $\eta$ . Using the following formula [43] on the Fermi distribution function at the r.h.s. of (C.8),

$$f(\omega) = \frac{1}{e^{\beta\omega} + 1} = \frac{1}{\beta} \sum_{l} \frac{e^{i\omega_{l}\eta}}{i\omega_{l} - \omega},$$
 (C.9)

we find the expression with use of the Green function on the real axis.

$$\zeta_i(\xi) = \int d\omega f(\omega) \sum_{\sigma} \rho_{i\sigma}(\omega, \xi). \tag{C.10}$$

Next, we rewrite the energy potential (C.2). In this case, we consider the following function.

$$\Phi_{\sigma} = \frac{1}{2\pi i} \int_{C} dz \frac{e^{\eta z}}{e^{\beta z} + 1} \ln(1 - \delta v_{i\sigma}(z, \xi) F_{i\sigma}(z)). \tag{C.11}$$

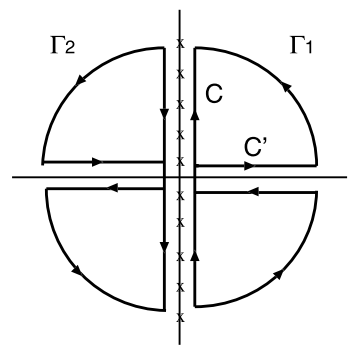
Here contour C is given in Fig. C.1. Note that the same contour was used to prove the formula (C.9) [43]. Counting the residues along the imaginary axis, we find

$$\Phi_{\sigma} = -\frac{1}{\beta} \sum_{l=-\infty}^{\infty} e^{i\omega_l \eta} \ln(1 - \delta v_{i\sigma}(i\omega_l, \xi) F_{i\sigma}(i\omega_l)). \tag{C.12}$$

Next, we change the contour in (C.11) from C to  $C' + \Gamma_1 + \Gamma_2$  in Fig. C.1, assuming that the integrand is analytic except for the real and imaginary axes, and evaluate the contribution from each path. We find that the contribution from the paths  $\Gamma_1$  and  $\Gamma_2$  vanishes, and only the contribution from C' remains, so that we obtain

$$\Phi_{\sigma} = \int_{-\infty}^{\infty} d\omega \, \frac{1}{\pi} \operatorname{Im} \ln \left( 1 - \delta v_{i\sigma}(z, \xi) F_{i\sigma}(z) \right). \tag{C.13}$$

**Fig. C.1** Contour for calculation of frequency sums on the complex plane



Using (C.2), (C.12), and (C.13), we find the expression which is written by the quantities in the real axis.

$$E_i(\xi) = \sum_{\sigma} \int_{-\infty}^{\infty} d\omega \frac{1}{\pi} \operatorname{Im} \ln \left( 1 - \delta v_{i\sigma}(z, \xi) F_{i\sigma}(z) \right) + \frac{1}{4} U \left( \xi^2 - \zeta_i^2(\xi) \right). \quad (C.14)$$

The equations (C.1), (C.14), (C.10), and (C.5) are identical with (3.82), (3.78), (3.91), and (3.85) in the SSF, so that we have verified that the dynamical CPA in the static approximation reduces to the SSF.

### Appendix D

## Expansion of $D_{\nu\sigma}$ with Respect to Dynamical Potential

The determinant  $D_{\nu\sigma}$  in the harmonic approximation is defined by (3.165):

$$D_{\nu\sigma} = \det[\delta_{lm} - (\tilde{v}_{\sigma}(\nu)\delta_{l-m,\nu} + \tilde{v}_{\sigma}(-\nu)\delta_{l-m,-\nu})\tilde{g}_{\sigma}(m)]. \tag{D.1}$$

In this appendix, we derive an alternative expression of the determinant  $D_{\nu\sigma}$  which is expanded with respect to the dynamical potentials  $\tilde{v}_{\sigma}(\pm\nu)$ , i.e., (3.167).

The determinant  $D_{\nu\sigma}$  has the following form.

Application of the Laplace expansion to the first column of Q yields the relation,

$$Q(\{b_i\}\{c_i\}) = Q^{(N-1)} - b_1c_1Q^{(N-2)}.$$
 (D.3)

Here  $Q^{(N-1)}$  ( $Q^{(N-2)}$ ) is the  $(N-1)\times (N-1)$  ( $(N-2)\times (N-2)$ ) matrix with the same structure as Q, assuming that Q is the  $N\times N$  matrix. Repeating the same expansions for  $Q^{(N-1)}$  and  $Q^{(N-2)}$ , we find that Q is the function of  $\{b_ic_i\}$ . Thus we have the relation

$$Q({b_i}{c_i}) = Q({b_ic_i}{1}).$$
 (D.4)

Thus we can consider  $Q(\{b_i\}\{1\})$  as follows.

We move the  $b_1$  row to the 2nd row, the  $b_{\nu+1}$  row to the 3rd row, the  $b_{2\nu+1}$  row to the 4th row, and so on. Next, we move the  $b_{\nu+1}$  column to the 2nd column, the  $b_{2\nu+1}$  column to the 3rd column, the  $b_{3\nu+1}$  column to the 4th column, and so on. We have then

Thus the determinant Q is given by the products of the sub-determinants

Applying the properties of the determinant Q to  $D_{\nu\sigma}$ , we find that  $D_{\nu\sigma}$  is written by the product of tridiagonal matrices as follows.

Here  $D_{\nu\sigma}(k)$  is the determinant of the tridiagonal matrix consisting of the Green functions with frequency remainder k for modulus  $\nu$ , and  $a_{n\sigma}(\nu)$  is defined by

$$a_{n\sigma}(\nu) = \tilde{v}_{\sigma}(\nu)\tilde{v}_{\sigma}(-\nu)\tilde{g}_{\sigma}(n-\nu)\tilde{g}_{\sigma}(n). \tag{D.9}$$

Here we used the notation  $\tilde{v}_{\sigma}(v) = \tilde{v}_{\sigma}(i\omega_{v})$  and  $\tilde{g}_{\sigma}(n) = \tilde{g}_{\sigma}(i\omega_{n})$ , for simplicity.

Note that according to the Laplace expansion theorem  $D_{\nu\sigma}(k)$  is expressed by the determinants of the sub-matrices as

Furthermore the determinant  $D_{\nu\sigma}^{(m)}(\pm\nu,k)$  is expanded as follows.

$$D_{\nu\sigma}^{(m)}(\pm\nu,k) = \sum_{n=0}^{\infty} (-)^n \left(\tilde{v}_{\sigma}(\nu)\tilde{v}_{\sigma}(-\nu)\right)^n A_{n\pm\nu k\sigma}^{(m)}.$$
 (D.12)

Here

$$A_{0 \pm \nu k\sigma}^{(m)} \equiv 1,\tag{D.13}$$

$$A_{0 \pm \nu k \sigma}^{(m)} \equiv 1,$$

$$A_{n \pm \nu k \sigma}^{(m)} = \sum_{l_1 = m+1}^{\infty} \sum_{l_2 = m+1}^{l_1 - 2} \cdots \sum_{l_n = m+1}^{l_{n-1} - 2} \hat{a}_{l_1(\pm \nu) + k \sigma}(\nu) \hat{a}_{l_2(\pm \nu) + k \sigma}(\nu) \cdots \hat{a}_{l_n(\pm \nu) + k \sigma}(\nu),$$
(D.14)

and

$$\hat{a}_{n\sigma}(\nu) = \tilde{g}_{\sigma}(n-\nu)\tilde{g}_{\sigma}(n). \tag{D.15}$$

To prove (D.12), let us consider the determinant of a finite matrix as follows.

To prove (D.12), let us consider the determinant of a finite matrix as follows. 
$$D^{(m,M)} = \begin{vmatrix} 1 & 1 & & 0 \\ a_{(m+1)\nu+k} & 1 & 1 & & \\ & a_{(m+2)\nu+k} & 1 & 1 & \\ & & a_{(m+3)\nu+k} & 1 & 1 \\ & & & \ddots & \\ 0 & & & & a_{M\nu+k} & 1 \end{vmatrix}. \quad (D.16)$$

By applying the Laplace expansion, we have the recursion relation as

$$D^{(m,M)} = D^{(m,M-1)} - a_{M\nu+k}D^{(m,M-2)}.$$
 (D.17)

In the same way, we obtain the following recursion relations in general.

$$D^{(m,n)} = D^{(m,n-1)} - a_{n\nu+k} D^{(m,n-2)}, (D.18)$$

$$D^{(m,m+1)} = 1 - a_{(m+1)\nu+k}, \tag{D.19}$$

$$D^{(m,m)} = 1. (D.20)$$

Now, we start from the following identity.

$$D^{(m,M)} = 1 + \sum_{l_1=m+1}^{M} \left( D^{(m,l_1)} - D^{(m,l_1-1)} \right). \tag{D.21}$$

Substituting (D.18) into (D.21), we obtain

$$D^{(m,M)} = 1 - \sum_{l_1=m+1}^{M} a_{l_1\nu+k} D^{(m,l_1-2)}.$$
 (D.22)

Repeating the same procedure for  $D^{(m,l_1-2)}$ , we have

$$D^{(m,M)} = 1 - \sum_{l_1=m+1}^{M} a_{l_1\nu+k} \left( 1 - \sum_{l_2=m+1}^{l_1-2} a_{l_2\nu+k} D^{(m,l_2-2)} \right), \quad (D.23)$$

and finally we reach the following expansion.

$$D^{(m,M)} = 1 + \sum_{n=1}^{M} (-)^n \sum_{l_2=m+1}^{l_1-2} \cdots \sum_{l_n=m+1}^{l_{n-1}-2} a_{l_1\nu+k} \cdots a_{l_n\nu+k}.$$
 (D.24)

Substituting  $a_n = \tilde{v}_{\sigma}(\nu)\tilde{v}_{\sigma}(-\nu)\tilde{g}_{\sigma}(n-\nu)\tilde{g}_{\sigma}(n)$  into (D.24) and taking the limit  $M \to \infty$ , we obtain (D.12).

Substituting (D.12) for m = 0 and 1 into (D.10), we obtain an expression of  $D_{\nu\sigma}(k)$  which is expanded with respect to the dynamical potential as follows.

$$D_{\nu\sigma}(k) = \sum_{l=0}^{\infty} \frac{1}{l!} \left( \frac{i\beta \tilde{v}_{\sigma}(\nu) \tilde{v}_{\sigma}(-\nu)}{2\pi \nu} \right)^{l} B_{\nu\sigma}^{(l)}(k). \tag{D.25}$$

Here

$$B_{\nu\sigma}^{(0)}(k) \equiv 1,$$
 (D.26)

$$B_{\nu\sigma}^{(l)}(k) = (-)^{l} l! \left(\frac{2\pi\nu}{i\beta}\right)^{l} \times \left[A_{l\nu k\sigma}^{(0)} + \sum_{m=0}^{l-1} \left(A_{m\nu k\sigma}^{(0)} A_{l-m-\nu k\sigma}^{(0)} + \hat{a}_{k\sigma} A_{m\nu k\sigma}^{(1)} A_{l-1-m-\nu k\sigma}^{(1)}\right)\right].$$
(D.27)

From (D.7) and (D.25) we obtain the expansion form of  $D_{\nu\sigma}$  as follows.

$$D_{\nu\sigma} = \sum_{l=0}^{\infty} \frac{1}{l!} \left( 4\beta \tilde{v}_{\sigma}(\nu) \tilde{v}_{\sigma}(-\nu) \right)^{l} \left( \frac{i}{8\pi \nu} \right)^{l} B_{\nu\sigma}^{(l)}, \tag{D.28}$$

$$B_{\nu\sigma}^{(l)} = \sum_{\substack{\sum_{k=0}^{\nu-1} l_k = l}} \frac{l!}{\left[\prod_{k=0}^{\nu-1} l_k!\right]} \left[\prod_{k=0}^{\nu-1} B_{\nu\sigma}^{(l_k)}(k)\right]. \tag{D.29}$$

Equation (D.28) is identical with (3.167); the coefficient  $B_{\nu\sigma}^{(l)}$  is given by (D.29).

### Appendix E

### **Linear Response Theory**

We derive in this appendix the linear response formula (4.53) for the time dependent perturbation [83], which was used in the calculation of the dynamical susceptibility in Sect. 4.3.

$$\Delta B(t) = \int_{-\infty}^{t} \chi_{BA}(t - t') F(t') dt'. \tag{E.1}$$

Here F(t) is a time-dependent external force,  $\Delta B(t)$  denotes the linear change of a physical quantity  $\langle B \rangle$ , and  $\chi_{BA}(t-t')$  is the linear response function.

Let us consider the ensemble in which each system was in the equilibrium state at  $t = -\infty$  and assume that it develops according to the Hamiltonian H of the system, neglecting a small perturbation from the outside during the time development. The average of a physical quantity  $\hat{B}$  is then given by

$$\langle \hat{B} \rangle = \sum_{\alpha} \rho_{\alpha} \langle \Psi_{\alpha}(t) | \hat{B} | \Psi_{\alpha}(t) \rangle.$$
 (E.2)

Here  $\rho_{\alpha}$  is the distribution in the equilibrium state at the beginning. The state  $\Psi_{\alpha}(t)$  develops according to the Schrödinger equation.

The time-dependent average (E.2) is expressed as

$$\langle \hat{B} \rangle = \text{tr}(\rho(t)\hat{B}).$$
 (E.3)

Here  $\rho(t)$  is called the density matrix which is defined by

$$\rho(t) = \sum_{\alpha} |\Psi_{\alpha}(t)\rangle \rho_{\alpha} \langle \Psi_{\alpha}(t)|. \tag{E.4}$$

The time development of the density matrix operator  $\rho(t)$  is obtained from the Schrödinger equation as follows.

$$\frac{d\rho(t)}{dt} = \frac{1}{i\hbar}[H, \rho]. \tag{E.5}$$

Assume now that the system is perturbed by a time-dependent force F(t), whose interaction is given by

$$H_1(t) = -\hat{A}F(t). \tag{E.6}$$

Here  $\hat{A}$  is an operator of a physical quantity and the force F(t) is assumed to be  $F(-\infty) = 0$ . Accordingly we assumed that the Hamiltonian H consists of the original Hamiltonian  $H_0$  and  $H_1(t)$ :  $H = H_0 + H_1(t)$ . The density matrix is written by the distribution in the equilibrium state  $\rho_0$  and the deviation  $\Delta \rho(t)$  as follows.

$$\rho(t) = \rho_0 + \Delta \rho(t). \tag{E.7}$$

With use of  $\Delta \rho(t)$  the change of physical quantity  $\hat{B}$  is given as

$$\Delta B(t) \equiv \langle \hat{B} \rangle(t) - \langle \hat{B} \rangle_0 = \text{tr}(\Delta \rho(t)\hat{B}). \tag{E.8}$$

Here  $\langle \hat{B} \rangle_0$  denotes the thermal average of  $\hat{B}$  in the equilibrium state which is determined by the Hamiltonian  $H_0$ .

The density matrix  $\Delta \rho(t)$  is obtained from the equation of motion (E.5). By making use of the relation  $[H_0, \rho_0] = 0$  and linearizing the equation of motion with respect to the perturbation, we obtain

$$\frac{d\Delta\rho(t)}{dt} = -\frac{1}{i\hbar}[\hat{A}, \rho_0]F(t) + \frac{1}{i\hbar}[H_0, \Delta\rho(t)]. \tag{E.9}$$

Integrating the above equation from  $-\infty$  to t and solving the equation iteratively, we find that

$$\Delta \rho(t) = -\frac{1}{i\hbar} \int_{-\infty}^{t} dt' \, e^{\frac{1}{i\hbar} H_0(t-t')} [\hat{A}, \rho_0] e^{-\frac{1}{i\hbar} H_0(t-t')} F(t'). \tag{E.10}$$

Here we used the following formula for any operators S and T.

$$e^{S}Te^{-S} = T + [S, T] + \frac{1}{2!}[S, [S, T]] + \cdots$$
 (E.11)

Substituting (E.10) into (E.8), we obtain the linear response formula.

$$\Delta B(t) = \int_{-\infty}^{t} \chi_{BA}(t - t') F(t') dt'. \tag{E.12}$$

Here the linear response function  $\chi_{BA}(t)$  is given by a time correlation function at equilibrium state as follows.

$$\chi_{BA}(t) = \frac{i}{\hbar} \langle [\hat{B}_{H}(t), \hat{A}] \rangle. \tag{E.13}$$

Here we have omitted the suffix 0 in the average  $\langle \rangle$  for simplicity promising that the average is taken in the equilibrium state. Accordingly, we have redefined H by

the Hamiltonian  $H_0$  in the equilibrium state.  $\hat{B}_{\rm H}(t)$  is the Heisenberg representation of physical quantity  $\hat{B}$ , i.e.,  $\hat{B}_{\rm H}(t) = \exp(iHt/\hbar)\hat{B}\exp(-iHt/\hbar)$ . Equations (E.1) and (E.13) are identical with (4.53) and (4.54) in Sect. 4.3.

### Appendix F

# **Isothermal Molecular Dynamics and Canonical Distribution**

We adopted in Sect. 6.3 the isothermal molecular dynamics method [106], and solved the following equations of motion (6.64), (6.65), and (6.66) for a given temperature T:

$$\dot{\xi}_{i\alpha} = \frac{p_{i\alpha}}{\mu_{\rm LM}},\tag{F.1}$$

$$\dot{p}_{i\alpha} = -\frac{\partial \Psi(\xi)}{\partial \xi_{i\alpha}} - \eta_{\alpha} \cdot p_{i\alpha}, \tag{F.2}$$

$$\dot{\eta}_{\alpha} = \frac{1}{Q} \left( \sum_{i} \frac{p_{i\alpha}^{2}}{\mu_{\rm LM}} - NT \right). \tag{F.3}$$

Here  $\mu_{\rm LM}$ ,  $\xi_i$ , and  $p_i$  denote the mass, the position vector, and the momentum for a fictitious particle i, respectively.  $\Psi(\xi)$  is the potential energy between particles, so that  $-\partial \Psi(\xi)/\partial \xi_{i\alpha}$  denotes the force acting on the particle i.  $\eta_{\alpha}$  are the friction variables, and Q is a constant. Moreover N is the number of particles of the system.

In this Appendix we will prove that the equations of motion (F.1), (F.2), and (F.3) yield the canonical ensemble whose distribution in the  $\{\xi, p\}$  space is given by

$$f(\boldsymbol{\xi}, \boldsymbol{p}) = Ce^{-\beta H(\boldsymbol{\xi}, \boldsymbol{p})}.$$
 (F.4)

Here  $\beta$  is the inverse temperature and C is a constant.  $H(\xi, p)$  is the Hamiltonian for a classical system with the interaction potential  $\Psi(\xi)$ .

$$H(\xi, p) = \sum_{i} \frac{p_i^2}{2\mu_{\rm LM}} + \Psi(\xi).$$
 (F.5)

Let us consider the ensemble of the system described by (F.1), (F.2), and (F.3) and introduce the probability distribution  $\tilde{f}(\boldsymbol{\xi}, \boldsymbol{p}, \boldsymbol{\eta}, t)$  in the 6N+3 phase space.

The latter satisfies the equation of continuity as follows.

$$\frac{\partial \tilde{f}}{\partial t} + \frac{\partial}{\partial \xi} (\tilde{f}\dot{\xi}) + \frac{\partial}{\partial p} (\tilde{f}\dot{p}) + \frac{\partial}{\partial \eta} (\tilde{f}\dot{\eta}) = 0.$$
 (F.6)

Alternatively,

$$\frac{d\tilde{f}}{dt} = -\left(\frac{\partial}{\partial \xi}\dot{\xi} + \frac{\partial}{\partial p}\dot{p} + \frac{\partial}{\partial \eta}\dot{\eta}\right)\tilde{f}.$$
 (F.7)

Substituting the equations of motion (F.1), (F.2), and (F.3) into (F.7), we find

$$\frac{d\tilde{f}}{dt} = N\left(\sum_{\alpha} \eta_{\alpha}\right) \tilde{f}.$$
 (F.8)

On the other hand, we consider the extended Hamiltonian defined by

$$\tilde{H}(\boldsymbol{\xi}, \boldsymbol{p}, \boldsymbol{\eta}) = H(\boldsymbol{\xi}, \boldsymbol{p}) + \frac{1}{2} \sum_{\alpha} Q \eta_{\alpha}^{2}.$$
 (F.9)

Taking the derivative of  $\tilde{H}(\xi, p, \eta)$  with respect to t and making use of the equations of motion (F.1), (F.2), and (F.3), we obtain

$$\frac{d\tilde{H}(\boldsymbol{\xi},\boldsymbol{p},\boldsymbol{\eta})}{dt} = -NT\left(\sum_{\alpha}\eta_{\alpha}\right). \tag{F.10}$$

From (F.8) and (F.10), we find the relation

$$\frac{d\tilde{f}}{dt} = -\frac{1}{T}\frac{d\tilde{H}}{dt}\tilde{f}.$$
 (F.11)

Solving the equation, we obtain

$$\tilde{f}(\boldsymbol{\xi}, \boldsymbol{p}, \boldsymbol{\eta}) = \tilde{C} e^{-\beta \tilde{H}(\boldsymbol{\xi}, \boldsymbol{p}, \boldsymbol{\eta})}.$$
 (F.12)

Here  $\beta = 1/T$  and  $\tilde{C}$  is a constant. Thus the distribution  $f(\xi, p)$  is given by the canonical distribution as follows.

$$f(\boldsymbol{\xi}, \boldsymbol{p}) = \int \tilde{f}(\boldsymbol{\xi}, \boldsymbol{p}, \boldsymbol{\eta}) d\boldsymbol{\eta} = C e^{-\beta H(\boldsymbol{\xi}, \boldsymbol{p})}.$$
 (F.13)

The ergodic theorem tells us that the average of a physical quantity  $A(\boldsymbol{\xi}(t), \boldsymbol{p}(t))$  is given by

$$\int A(\boldsymbol{\xi}, \boldsymbol{p}) f(\boldsymbol{\xi}, \boldsymbol{p}) d\boldsymbol{\xi} d\boldsymbol{p} = \lim_{t_0 \to \infty} \frac{1}{t_0} \int_0^{t_0} A(\boldsymbol{\xi}(t), \boldsymbol{p}(t)) dt.$$
 (F.14)

Thus we can calculate thermal average by taking the time average of the physical quantity after we solve the equations of motion (F.1), (F.2), and (F.3). In the case of magnetic moment (6.60), we obtain the thermal average from time average (6.63).

#### Appendix G

# **Recursion Method for Electronic Structure Calculations**

The recursion method allows us to calculate the Green function for the tight-binding Hamiltonian without translational symmetry.

Let us assume that the Hamiltonian is given by

$$H_{ij} = \varepsilon_i \delta_{ij} + t_{ij} (1 - \delta_{ij}). \tag{G.1}$$

Here  $\varepsilon_i$  is the atomic level on site i and  $t_{ij}$  is the transfer integral between sites i and j. The Green function  $G_{ij}(z) (= (G(z))_{ij})$  is defined by

$$G_{ij}(z) = [(z - H)^{-1}]_{ij}.$$
 (G.2)

Here  $(H)_{ij} = H_{ij}$  denotes the Hamiltonian matrix.

Now, we make a unitary transformation of the Hamiltonian matrix H to a tridiagonal Hamiltonian matrix H'.

$$H' = U^{\dagger} H U = (\mathbf{u}_i^{\dagger} H \mathbf{u}_i). \tag{G.3}$$

Here  $U = (u_{ij}) = (u_1, u_2, ..., u_N)$  is a unitary matrix such that  $U^{\dagger}U = 1$  (or  $u_i^{\dagger}u_j = \delta_{ij}$ ). The unitary column vectors  $\{u_j\}$  are defined by  $(u_j)_i = u_{ij}$  (i = 1, ..., N). The Green function  $G'(z) = [(z - H')^{-1}]_{ij}$  for the Hamiltonian H' is connected with the original Green function matrix G(z) as

$$\boldsymbol{u}_{i}^{\dagger}G(z)\boldsymbol{u}_{j} = G_{ij}^{\prime}(z). \tag{G.4}$$

In particular, we have the following relation when i = j = 1 and the unit vector  $\mathbf{u}_1$  is chosen such that  $(\mathbf{u}_1)_i = 1$  and  $(\mathbf{u}_1)_m = 0$   $(m \neq i)$ .

$$G_{ii}(z) = G'_{ii}(z). \tag{G.5}$$

The Hamiltonian is tridiagonalized by the Lanczos method. There we produce both the unitary vectors and the tridiagonal matrix elements with use of the recursive relations. We choose the starting vector to be a unit vector, and produce a new orthogonal basis set  $\{u_i\}$  successively with use of the following relations.

$$b_1 \mathbf{u}_2 = H \mathbf{u}_1 - a_1 \mathbf{u}_1, \tag{G.6}$$

$$b_n \mathbf{u}_{n+1} = H \mathbf{u}_n - a_n \mathbf{u}_n - b_{n-1} \mathbf{u}_{n-1}. \tag{G.7}$$

The unit vector  $\boldsymbol{u}_{n+1}$  is obtained by normalization of the r.h.s. of (G.6) or (G.7). The coefficients  $a_n$  and  $b_n$  are also successively obtained by using the orthogonality  $\boldsymbol{u}_i^{\dagger} \boldsymbol{u}_i = \delta_{ij}$ .

$$a_n = \boldsymbol{u}_n^{\dagger} H \boldsymbol{u}_n, \tag{G.8}$$

$$b_n = \mathbf{u}_{n+1} H \mathbf{u}_n. \tag{G.9}$$

Note that  $\mathbf{u}_l^{\dagger}H\mathbf{u}_1 = 0$  for l > 2,  $\mathbf{u}_{n-1}^{\dagger}H\mathbf{u}_n = b_{n-1}^*$ , and  $\mathbf{u}_l^{\dagger}H\mathbf{u}_n = 0$  for l < n-1 and l > n+1; thus the Hamiltonian  $H'_{ij} = \mathbf{u}_l^{\dagger}H\mathbf{u}_j$  is tridiagonalized as follows.

$$H' = \begin{pmatrix} a_1 & b_1 & 0 & \cdots & & 0 \\ b_1^* & a_2 & b_2 & 0 & \cdots & 0 \\ 0 & b_2^* & a_3 & b_3 & 0 & \vdots \\ 0 & \ddots & \ddots & \ddots & \\ \vdots & & 0 & b_{N-2}^* & a_{N-1} & b_{N-1} \\ 0 & \cdots & & 0 & b_{N-1}^* & a_N \end{pmatrix}.$$
 (G.10)

Choosing  $u_1$  so that  $(u_1)_i = 1$  and  $(u_1)_m = 0$   $(m \neq i)$ , we can obtain the diagonal Green function  $G_{ii}(z)$  via (G.5). The Green function  $G'_{ii}(z)$  is expressed by using Cramer's formula and Laplace's expansion as  $G'_{ii}(z) = D_1/D_0 = 1/(z-a_1-|b_1|^2D_2/D_1)$ . Here  $D_0 = \det(z-H')$ ,  $D_1$  is the cofactor of  $(z-H')_{11}$ , and  $D_2$  is the cofactor of  $(z-H')_{22}$  for the submatrix of  $D_1$ . Repeating the same procedure, we find that the Green function  $G_{ii}(z)$  is given by a continued fraction as follows.

$$G_{ii}(z) = G'_{ii}(z) = \frac{1}{z - a_1 - \frac{|b_1|^2}{z - a_2 - \frac{|b_2|^2}{\cdots - \frac{|b_{n-1}|^2}{z - a_n - T_n(z)}}}.$$
 (G.11)

Here  $T_n(z)$  is a terminator at the *n*-th order recursion. The square-root terminator with use of the asymptotic recursion coefficients  $a_{\infty}$  and  $b_{\infty}$  is usually applied.

$$T_n \approx T_\infty = \frac{1}{2} \left( z - a_\infty - \sqrt{(z - a_\infty)^2 - 4|b_\infty|^2} \right).$$
 (G.12)

The projected density of states is obtained as

$$\rho_i(\omega) = -\frac{1}{\pi} \operatorname{Im} G_{ii}(z). \tag{G.13}$$

In some cases, we need the off-diagonal Green function  $G_{ij}(z)$ . In this case we start from the unit vectors  $\boldsymbol{u}_{1\pm}$  such that  $(\boldsymbol{u}_{1\pm})_i=1/\sqrt{2},~(\boldsymbol{u}_{1\pm})_j=\pm 1/\sqrt{2},$  and  $(\boldsymbol{u}_{1\pm})_m=0~(m\neq i,j)$ . We have then the relation  $G_{ij}+G_{ji}=\boldsymbol{u}_{1+}^{\dagger}G\boldsymbol{u}_{1+}-\boldsymbol{u}_{1-}^{\dagger}G\boldsymbol{u}_{1-}$ . When we start from the unit vectors  $\boldsymbol{v}_{1\pm}$  such that  $(\boldsymbol{v}_{1\pm})_i=1/\sqrt{2},$   $(\boldsymbol{v}_{1\pm})_j=\pm i/\sqrt{2},$  and  $(\boldsymbol{v}_{1\pm})_m=0~(m\neq i,j),$  we have the relation  $G_{ij}-G_{ji}=i(\boldsymbol{v}_{1-}^{\dagger}G\boldsymbol{v}_{1-}-\boldsymbol{v}_{1+}^{\dagger}G\boldsymbol{v}_{1+})$ . Thus we obtain the off-diagonal Green function as

$$G_{ij}(z) = \frac{1}{2} \left[ G'_{11}(z) - G'_{22}(z) - i \left( G'_{33}(z) - G'_{44}(z) \right) \right]. \tag{G.14}$$

Here  $G'_{11}(z) = \boldsymbol{u}_{1+}^{\dagger} G \boldsymbol{u}_{1+}$ ,  $G'_{22}(z) = \boldsymbol{u}_{1-}^{\dagger} G \boldsymbol{u}_{1-}$ ,  $G'_{33}(z) = \boldsymbol{v}_{1+}^{\dagger} G \boldsymbol{v}_{1+}$ , and  $G'_{44}(z) = \boldsymbol{v}_{1-}^{\dagger} G \boldsymbol{v}_{1-}$ . These diagonal Green functions are obtained by the recursion method as presented above.

In the MD calculation, we need to obtain the following off-diagonal Green functions to calculate the magnetic forces (see (6.70) and (6.71)).

$$\sum_{\sigma} (\sigma_x G)_{iL\sigma iL\sigma} = G_{iL\uparrow iL\downarrow} + G_{iL\downarrow iL\uparrow}, \tag{G.15}$$

$$\sum_{\sigma} (\sigma_{y} G)_{iL\sigma iL\sigma} = i(G_{iL\uparrow iL\downarrow} - G_{iL\downarrow iL\uparrow}). \tag{G.16}$$

To obtain (G.15), we consider the unit vector  $\mathbf{u}_{1\pm}$  such that  $(\mathbf{u}_{1\pm})_{iL\uparrow}=1/\sqrt{2}$ ,  $(\mathbf{u}_{1\pm})_{iL\downarrow}=\pm 1/\sqrt{2}$ , and  $(\mathbf{u}_{1\pm})_{jL'\sigma}=0$  ( $j\neq i$ ). Then we obtain  $G_{iL\uparrow iL\downarrow}+G_{iL\downarrow iL\uparrow}=\mathbf{u}_{1+}^{\dagger}G\mathbf{u}_{1+}-\mathbf{u}_{1-}^{\dagger}G\mathbf{u}_{1-}$ . Each term of the r.h.s. is given by a continued fraction. In the case of (G.16), we consider the unit vector  $\mathbf{u}_{1\pm}$  such that  $(\mathbf{u}_{1\pm})_{iL\uparrow}=1/\sqrt{2}$ ,  $(\mathbf{u}_{1\pm})_{iL\downarrow}=\pm i/\sqrt{2}$ , and  $(\mathbf{u}_{1\pm})_{jL'\sigma}=0$  ( $j\neq i$ ). We then obtain  $i(G_{iL\uparrow iL\downarrow}-G_{iL\downarrow iL\uparrow})=\mathbf{u}_{1+}^{\dagger}G\mathbf{u}_{1+}-\mathbf{u}_{1-}^{\dagger}G\mathbf{u}_{1-}$ .

#### Appendix H

## An Integral in the RKKY Interaction

When we calculate the RKKY interaction in the free electron model, we employ the formula (7.32) for the integral (7.31) in Sect. 7.1. We derive in this appendix the formula (7.32):

$$I(R) = \frac{i\pi}{k_{\rm F}R^3} (-2k_{\rm F}R\cos 2k_{\rm F}R + \sin 2k_{\rm F}R). \tag{H.1}$$

The integral I(R) is defined by

$$I(R) = \int_{-\infty}^{\infty} dq \, q \, F\left(\frac{q}{2k_{\rm F}}\right) e^{iqR}. \tag{H.2}$$

Here the function F(x) is given by (7.27):

$$F(x) = 1 + \frac{1 - x^2}{2x} \ln \left| \frac{1 + x}{1 - x} \right|.$$
 (H.3)

Note that F(x) is an even function, F(0) = 2, and  $F(x) \to 2/3x^2$   $(x \to \infty)$ . By integration by parts, we can rewrite the integral (H.2) as follows.

$$I(R) = -\frac{1}{iR} \int_{-\infty}^{\infty} dq \, \frac{d[(q/2k_{\rm F})F(q/2k_{\rm F})]}{d(q/2k_{\rm F})} e^{iqR}.$$
 (H.4)

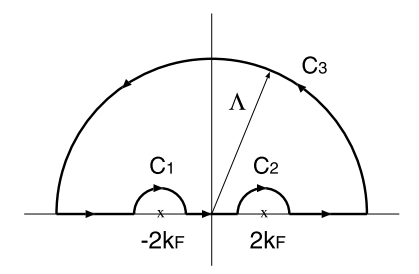
Here  $d[xF(x)]/dx = 2 - x \ln|1 + x|/|1 - x|$ . Making use of the integration by parts again, we obtain

$$I(R) = \frac{1}{2k_{\rm F}R^2} \int_{-\infty}^{\infty} dq \left( \ln \left| \frac{2k_{\rm F} + q}{2k_{\rm F} - q} \right| + \frac{4k_{\rm F}q}{4k_{\rm F}^2 - q^2} \right) e^{iqR}.$$
 (H.5)

The first term at the r.h.s. of (H.5) is expressed by integration by parts as

$$\int_{-\infty}^{\infty} dq \ln \left| \frac{2k_{\rm F} + q}{2k_{\rm F} - q} \right| e^{iqR} = \frac{4k_{\rm F}i}{R} \int_{-\infty}^{\infty} dq \, \frac{e^{iqR}}{4k_{\rm F}^2 - q^2}. \tag{H.6}$$

**Fig. H.1** Contour on the complex plane to calculate the integrals (H.8) and (H.11)



Thus we obtain

$$I(R) = \frac{2}{iR^3} \int_{-\infty}^{\infty} dq \, \frac{e^{iqR}}{q^2 - 4k_{\rm F}^2} - \frac{2}{R^2} \int_{-\infty}^{\infty} dq \, \frac{q e^{iqR}}{q^2 - 4k_{\rm F}^2}.$$
 (H.7)

Let us calculate the first term at the r.h.s. of (H.7):

$$A = \int_{-\infty}^{\infty} dq \, \frac{e^{iqR}}{q^2 - 4k_{\rm F}^2}.\tag{H.8}$$

In order to calculate the integral A, we consider the following integral along the contour on the complex plane as shown in Fig. H.1, which vanishes according to the Cauchy theorem.

$$A + \int_{C_1 + C_2 + C_3} dq \frac{e^{iqR}}{q^2 - 4k_{\scriptscriptstyle E}^2} = 0.$$
 (H.9)

Here the integral along  $C_1$  ( $C_2$ ) is obtained as  $(i\pi/4k_{\rm F})\exp(-i2k_{\rm F}R)$  ( $(-i\pi/4k_{\rm F})\times\exp(-i2k_{\rm F}R)$ ). The integral along  $C_3$  is proven to vanish. Thus we obtain

$$A = -\frac{\pi \sin 2k_{\rm F}R}{2k_{\rm F}}.\tag{H.10}$$

In the same way, we obtain

$$\int_{-\infty}^{\infty} dq \, \frac{q e^{iqR}}{q^2 - 4k_{\rm E}^2} = i\pi \cos 2k_{\rm F}R. \tag{H.11}$$

From (H.7), (H.10), and (H.11), we obtain

$$I(R) = \frac{i\pi}{k_{\rm F}R^3} (-2k_{\rm F}R\cos 2k_{\rm F}R + \sin 2k_{\rm F}R), \tag{H.12}$$

which is identical with (H.1), i.e., (7.32) in Sect. 7.1.

- 1. J.D. Jackson, Classical Electrodynamics (Wiley, New York, 1962)
- 2. J.H. Van Vleck, *The Theory of Electric and Magnetic Susceptibilities* (Oxford University Press, London, 1932), Chap. VI
- 3. L.I. Schiff, Quantum Mechanics (McGraw-Hill, New York, 1968), Chap. 13
- 4. J.C. Slater, The Self-Consistent Field for Molecules and Solids: Quantum Theory of Molecules and Solids, vol. 4 (McGraw-Hill, New York, 1974), Chap. 1
- 5. J.B. Mann, Los Alamos Scientific Laboratory Rep. No. LASL-3690, 1967
- 6. M.C. Gutzwiller, Phys. Rev. Lett. 10, 159 (1963)
- 7. M.C. Gutzwiller, Phys. Rev. **134**, A923 (1964)
- 8. M.C. Gutzwiller, Phys. Rev. 137, A1726 (1965)
- 9. J. Hubbard, Proc. R. Soc. Lond. A 276, 238 (1963)
- 10. J. Hubbard, Proc. R. Soc. Lond. A **281**, 401 (1964)
- 11. N.F. Mott, Metal-Insulator Transitions (Taylor & Francis, London, 1990)
- 12. T. Oguchi, K. Terakura, A.R. Williams, Phys. Rev. B 28, 6443 (1983)
- 13. P. Fulde, Electron Correlations in Molecules and Solids (Springer, Berlin, 1995), Chap. 12
- W. Marshall, S.W. Lovesey, Theory of Thermal Neutron Scattering (Clarendon, Oxford, 1971)
- S.W. Lovesey, Theory of Neutron Scattering from Condensed Matter (Clarendon, Oxford, 1986)
- J. Jensen, A.R. Mackintosh, Rare Earth Magnetism Structures and Excitations (Clarendon, Oxford, 1991)
- V.L. Moruzzi, C.B. Sommers, Calculated Electronic Properties of Ordered Alloys: A Handbook (World Scientific, Singapore, 1995)
- 18. J. Kanamori, Prog. Theor. Phys. 30, 275 (1963)
- 19. W.F. Brinkman, T.M. Rice, Phys. Rev. B 2, 4302 (1970)
- P. Fulde, Y. Kakehashi, G. Stollhoff, in *Metallic Magnetism*, ed. by H. Capellmann (Springer, Berlin, 1987), Chap. 5
- 21. A.M. Oles, G. Stollhoff, Phys. Rev. B **29**, 314 (1984)
- 22. P. Hohenberg, W. Kohn, Phys. Rev. B 136, 864 (1964)
- 23. W. Kohn, L.J. Sham, Phys. Rev. A 140, 1133 (1965)
- 24. M. Levy, Proc. Natl. Acad. Sci. USA 76, 6062 (1979)
- R.G. Parr, W. Yang, Density-Functional Theory of Atoms and Molecules (Oxford University, Oxford, 1989)
- 26. U. von Barth, L. Hedin, J. Phys. C 5, 1625 (1972)
- 27. G.S. Painter, Phys. Rev. B 24, 4264 (1981)
- 28. O.K. Andersen, O. Jepsen, D. Glötzel, in *Highlights of Condensed-Matter Theory*, ed. by F. Bassani, F. Fumi, M. Tosi (North-Holland, Amsterdam, 1985), p. 59

References References

 O.K. Andersen, O. Jepsen, M. Sob, in *Electronic Band Structure and its Applications*, ed. by M. Yussouff. Springer Lecture Notes (1987), p. 1

- 30. O.K. Andersen, O. Jepsen, G. Krier, in *Methods of Electronic Structure Calculations* (World Scientific, Singapore, 1994), p. 63
- 31. J.C. Slater, G.F. Koster, Phys. Rev. 94, 1498 (1954)
- 32. O. Gunnarsson, Physica B **91**, 329 (1977)
- 33. J.F. Janak, Phys. Rev. B 16, 235 (1977)
- V.L. Moruzzi, J.F. Janak, A.R. Williams, Calculated Electronic Properties of Metals (Pergamon, New York, 1978)
- 35. J.P. Perdew, Y. Wang, Phys. Rev. B 33, 8800 (1986)
- 36. J.P. Perdew, Y. Wang, Phys. Rev. B **45**, 13244 (1992)
- J.P. Perdew, J.A. Chevary, S.H. Vosko, K.A. Jackson, M.R. Pederson, D.H. Singh, C. Fiolhais, Phys. Rev. B 46, 6671 (1992)
- 38. R. Wu, in *Band-Ferromagnetism*, ed. by K. Baberschke, M. Donath, W. Nolting (Springer, Berlin, 2001)
- 39. O. Gunnarsson, J. Phys. F, Met. Phys. **6**, 587 (1976)
- 40. J.B. Staunton, B.L. Gyorffy, Phys. Rev. Lett. 69, 371 (1992)
- 41. J.R. Schrieffer, W.E. Evenson, S.Q. Wang, J. Phys. (Paris) 32, C1 (1971)
- 42. G. Morandi, E. Galleani D'Agliano, F. Napoli, C.F. Ratto, Adv. Phys. 23, 867 (1974)
- 43. A.L. Fetter, J.D. Walecka, *Quantum Theory of Many-Particle Systems* (McGraw Hill, New York, 1971)
- 44. A.A. Abrikosov, L.P. Gor'kov, I.E. Dzyaloshinskii, Quantum Field Theoretical Methods in Statistical Physics (Pergamon, Oxford, 1965)
- 45. J. Hubbard, Phys. Rev. B 19, 2626 (1979)
- 46. J. Hubbard, Phys. Rev. B **20**, 4584 (1979)
- 47. J. Hubbard, Phys. Rev. B 23, 5974 (1981)
- 48. H. Hasegawa, J. Phys. Soc. Jpn. 46, 1504 (1979)
- 49. H. Hasegawa, J. Phys. Soc. Jpn. 49, 178 (1980)
- 50. B. Velický, S. Kirkpatrick, H. Ehrenreich, Phys. Rev. 175, 747 (1968)
- H. Ehrenreich, L.M. Schwartz, in *Solid State Physics*, vol. 31, ed. by H. Ehrenreich, F. Seitz,
   D. Turnbull (Academic, New York, 1976)
- 52. Y. Kakehashi, P. Fulde, Phys. Rev. B 32, 1595 (1985)
- 53. T. Tamashiro, S. Nohara, K. Miyagi, Y. Kakehashi, J. Phys. Soc. Jpn. 80, 064702 (2011)
- 54. Y. Kakehashi, Phys. Rev. B **65**, 184420 (2002)
- 55. Y. Kakehashi, Phys. Rev. B 45, 7196 (1992)
- 56. Y. Kakehashi, J. Magn. Magn. Mater. 104-107, 677 (1992)
- 57. Y. Kakehashi, Adv. Phys. **53**, 497 (2004)
- 58. D.J. Amit, C.M. Bender, Phys. Rev. B 4, 3115 (1971)
- 59. D.J. Amit, H.J. Keiter, J. Low Temp. Phys. 11, 603 (1973)
- 60. X. Dai, J. Phys. Condens. Matter **3**, 4389 (1991)
- 61. S. Hirooka, M. Shimizu, J. Phys. Soc. Jpn. 43, 70 (1977)
- 62. A. Georges, G. Kotliar, W. Krauth, M.J. Rosenberg, Rev. Mod. Phys. 68, 13 (1996)
- 63. V.I. Anisimov, Yu.A. Izyumov, *Electronic Structure of Strongly Correlated Materials* (Springer, Berlin, 2010)
- 64. Y. Kakehashi, P. Fulde, Phys. Rev. B 69, 045101 (2004)
- J.W. Negele, H. Orland, Quantum Many Particle Systems (Addison-Wesley, New York, 1998)
- 66. E. Müller-Hartmann, Z. Phys. B **74**, 507 (1989)
- 67. R. Bulla, Phys. Rev. Lett. 83, 136 (1999)
- 68. P. Fulde, Electron Correlations in Molecules and Solids (Springer, Berlin, 1995), Chap. 6
- 69. Y. Kakehashi, T. Nakamura, P. Fulde, J. Phys. Soc. Jpn. **78**, 124710 (2009)
- 70. V.I. Anisimov, J. Zaanen, O.K. Andersen, Phys. Rev. B 44, 943 (1991)
- 71. Y. Kakehashi, J. Phys. Soc. Jpn. 77, 094706 (2008)
- 72. Y. Kakehashi, M. Atiqur, R. Patoary, J. Phys. Soc. Jpn. **80**, 034706 (2011)

- 73. A.I. Lichtenstein, M.I. Katsnelson, G. Kotliar, Phys. Rev. Lett. 87, 067205 (2001)
- 74. T. Miyake, F. Aryasetiawan, Phys. Rev. B 77, 085122 (2008)
- 75. I. Schnell, G. Czycholl, R.C. Albers, Phys. Rev. B 68, 245102 (2003)
- 76. H.H. Potter, Proc. R. Soc. Lond. A **146**, S362 (1934)
- 77. M. Fallot, J. de Phys. Rad. V 153 (1944)
- 78. A. Arrott, J.E. Noakes, Phys. Rev. Lett. 19, 786 (1967)
- 79. R.V. Colvin, S. Arajs, J. Phys. Chem. Solids 26, 435 (1965)
- 80. J.E. Noakes, N.E. Tornberg, A. Arrott, J. Appl. Phys. 37, 1264 (1966)
- 81. W. Sucksmith, R.R. Pearce, Proc. R. Soc. Lond. A 167, 189 (1938)
- 82. P. Weiss, R. Forrer, Ann. Phys. Paris 5, 153 (1926)
- 83. R. Kubo, J. Phys. Soc. Jpn. 12, 570 (1957)
- 84. T. Izuyama, D.J. Kim, R. Kubo, J. Phys. Soc. Jpn. 18, 1025 (1963)
- 85. R.B. Muniz, J.F. Cooke, D.M. Edwards, J. Phys. F, Met. Phys. 15, 2357 (1985)
- 86. H.A. Mook, R.M. Niklow, Phys. Rev. B 7, 336 (1973)
- 87. M.W. Stringfellow, J. Phys. C, Solid State Phys. 1, 950 (1968)
- 88. S. Wako, D.M. Edwards, E.P. Wohlfarth, J. Phys. 32(C1), 1073 (1971)
- 89. P.W. Mitchell, D.M. Paul, Phys. Rev. B 32, 3272 (1985)
- 90. D.M. Edwards, R.B. Muniz, J. Phys. F, Met. Phys. 15, 2339 (1985)
- 91. T. Moriya, A. Kawabata, J. Phys. Soc. Jpn. **34**, 639 (1973)
- 92. T. Moriya, A. Kawabata, J. Phys. Soc. Jpn. 35, 669 (1973)
- 93. T. Moriya, Spin Fluctuations in Itinerant Electron Magnetism (Springer, Berlin, 1985)
- M. Cyrot, in Electron Correlation and Magnetism in Narrow-Band Systems, ed. by T. Moriya (Springer, Berlin, 1981)
- 95. J. Hertz, M. Klenin, Phys. Rev. B 10, 1084 (1974)
- 96. J.A. Hertz, M.A. Klenin, Physica B **91**, 49 (1977)
- 97. H.P.J. Wijn, in *Data in Science and Technology* (Springer, Berlin, 1991)
- 98. P. Fazekas, B. Menge, E. Müller-Hartmann, Z. Phys. B 78, 69 (1990)
- 99. S. Asano, J. Yamashita, J. Phys. Soc. Jpn. 31, 1000 (1971)
- 100. S. Asano, J. Yamashita, Prog. Theor. Phys. 49, 373 (1973)
- 101. S. Komura, N. Kunitomi, J. Phys. Soc. Jpn. 20, 103 (1964)
- 102. Y. Tsunoda, J. Phys. Condens. Matter 1, 10427 (1989)
- 103. Y. Endoh, Y. Ishikawa, J. Phys. Soc. Jpn. 30, 1614 (1971)
- 104. S. Asano, J. Yamashita, J. Phys. Soc. Jpn. 23, 714 (1964)
- 105. T. Oguchi, A.J. Freeman, J. Magn. Magn. Mater. 46, L1 (1984)
- 106. S. Nosé, J. Chem. Phys. 81, 511 (1984)
- 107. W.G. Hoover, Computational Statistical Mechanics (Elsevier, Amsterdam, 1991)
- 108. Y. Kakehashi, S. Akbar, N. Kimura, Phys. Rev. B 57, 8354 (1998)
- Y. Kakehashi, S. Akbar, N. Kimura, in *Itinerant Electron Magnetism: Fluctuation Effects*, ed. by D. Wagner et al. (Kluwer, Amsterdam, 1998)
- 110. Y. Kakehashi, H. Al-Attar, N. Kimura, Phys. Rev. B **59**, 8664 (1999)
- 111. T. Uchida, Y. Kakehashi, J. Phys. Soc. Jpn. **75**, 094703 (2006)
- 112. T. Uchida, Y. Kakehashi, J. Phys. Soc. Jpn. **76**, 087001 (2007)
- 113. A.Z. Solontsov, D. Wagner, Phys. Rev. B 51, 12410 (1995)
- 114. S. Fujii, S. Ishida, S. Asano, J. Phys. Soc. Jpn. 60, 4300 (1991)
- 115. Y. Kakehashi, O. Jepsen, N. Kimura, Phys. Rev. B 65, 134418 (2002)
- 116. B. Binz, A. Vishwanath, V. Aji, Phys. Rev. Lett. 96, 207202 (2006)
- 117. J.A. Mydosh, J. Magn. Magn. Mater. 2, 237 (1978)
- 118. V. Cannella, J.A. Mydosh, Phys. Rev. B 6, 4220 (1972)
- 119. P.W. Anderson, Phys. Rev. 124, 41 (1961)
- 120. J. Kondo, Prog. Theor. Phys. 32, 37 (1964)
- 121. M.A. Ruderman, C. Kittel, Phys. Rev. 96, 99 (1954)
- 122. T. Kasuya, Prog. Theor. Phys. **16**, 45 (1956)
- 123. K. Yosida, Phys. Rev. 106, 893 (1957)
- 124. S.F. Edwards, P.W. Anderson, J. Phys. F, Met. Phys. **5**, 965 (1975)

References References

M. Mezard, G. Parisi, M. Virasoro, Spin Glass Theory and Beyond (World Scientific, Singapore, 1987)

- 126. K.H. Fischer, J.A. Hertz, Spin Glasses (Cambridge Univ. Press, Cambridge, 1999)
- 127. P. Fulde, Electron Correlations in Molecules and Solids (Springer, Berlin, 1995), Chap. 12
- A.C. Hewson, The Kondo Problem to Heavy Fermions (Cambridge Univ. Press, Cambridge, 1993)
- 129. J.W. Loram, A.D.C. Grassie, G.A. Swallow, Phys. Rev. B 2, 2760 (1970)
- 130. C.M. Varma, Y. Yafet, Phys. Rev. B 13, 2950 (1976)
- 131. H.R. Krishna-murthy, J.W. Wilkins, K.G. Wilson, Phys. Rev. B 21, 1003 (1980)
- 132. H.R. Krishna-murthy, J.W. Wilkins, K.G. Wilson, Phys. Rev. B 21, 1044 (1980)
- 133. M.D. Daybell, in *Magnetism V*, ed. by H. Rado, H. Suhl (Academic Press, New York, 1973), Chap. 4
- 134. A.A. Abrikosov, Physics 2, 5 (1965)
- 135. K. Yosida, Phys. Rev. 147, 223 (1966)
- 136. K. Wilson, Rev. Mod. Phys. 47, 773 (1975)
- 137. P. Noziéres, J. Low Temp. Phys. 17, 31 (1974)
- 138. K. Yamada, Prog. Theor. Phys. 53, 970 (1975)
- 139. K. Yosida, K. Yamada, Prog. Theor. Phys. **53**, 1286 (1975)
- 140. N. Andrei, Phys. Rev. Lett. 45, 379 (1980)
- 141. P.B. Wiegmann, Phys. Lett. A 31, 163 (1981)
- 142. N. Kawakami, A. Okiji, Phys. Lett. A 86, 483 (1981)
- 143. K. Yosida, *Theory of Magnetism* (Springer, Berlin, 1996)
- 144. P. Fulde, Electron Correlations in Molecules and Solids (Springer, Berlin, 1995), Chap. 13
- P. Fulde, Correlated Electrons in Quantum Matter (World Scientific, Singapore, 2012), Chap. 13
- 146. R.M. Bozorth, Ferromagnetism (Van Nostrand, Princeton, 1968)
- 147. J. Friedel, Suppl. Nuovo Cim. 7, 287 (1958)
- 148. N.F. Mott, Adv. Phys. 13, 325 (1964)
- 149. H. Hasegawa, J. Kanamori, J. Phys. Soc. Jpn. 33, 1599 (1972)
- 150. H. Hasegawa, J. Kanamori, J. Phys. Soc. Jpn. 33, 1607 (1972)
- 151. H. Shiba, Prog. Theor. Phys. **46**, 77 (1971)
- 152. H. Hasegawa, J. Phys. Soc. Jpn. 50, 802 (1981)
- 153. M. Fallot, Ann. Phys. Paris 6, 305 (1936)
- 154. A.T. Aldred, Phys. Rev. B 14, 219 (1976)
- 155. C.G. Shull, M.K. Wilkinson, Phys. Rev. **97**, 304 (1955)
- 156. M.F. Collins, G.G. Low, Proc. Phys. Soc. **86**, 535 (1965)
- 157. G.H. Lander, L. Heaton, J. Phys. Chem. Solids 32, 427 (1971)
- 158. A.T. Aldred, B.D. Rainford, J.S. Kouvel, T.J. Hicks, Phys. Rev. B 14, 228 (1976)
- 159. C. Sadron, Ann. Phys. (Paris) 371 (1932)
- 160. H.C. Van Elst, B. Lubach, G.J. Van Den Berg, Physica 28, 1297 (1962)
- 161. R. Chiffery, T.J. Hicks, Phys. Lett. A 34, 267 (1971)
- 162. Y. Kakehashi, J. Phys. Soc. Jpn. 50, 2236 (1981)
- 163. S. Ishio, K. Nushiro, M. Takahashi, J. Phys. F, Met. Phys. 16, 1093 (1986)
- 164. M.F. Collins, J.B. Forsyth, Philos. Mag. 8, 401 (1963)
- 165. Y. Kakehashi, J. Phys. Soc. Jpn. 51, 3183 (1982)
- 166. Y. Nakagawa, J. Phys. Soc. Jpn. 12, 700 (1957)
- 167. V.I. Chechernikov, Sov. Phys. JETP **15**, 659 (1962)
- 168. H. Miwa, Prog. Theor. Phys. **52**, 1 (1974)
- 169. N. Hamada, H. Miwa, Prog. Theor. Phys. 59, 1045 (1977)
- 170. Y. Kakehashi, J. Phys. Soc. Jpn. 51, 94 (1982)
- 171. Y. Kakehashi, J. Magn. Magn. Mater. 37, 189 (1983)
- 172. Y. Kakehashi, J. Magn. Magn. Mater. 43, 79 (1984)
- 173. N. Hamada, J. Phys. Soc. Jpn. 50, 77 (1981)
- 174. S.A. Ahern, M.J.C. Martin, W. Sucksmith, Proc. R. Soc. Lond. A 248, 145 (1958)

- 175. C.G. Robbins, H. Claus, P.A. Beck, J. Appl. Phys. 40, 2269
- 176. R.A. Medina, J.W. Cable, Phys. Rev. B 15, 1539 (1977)
- 177. Y. Kakehashi, J. Phys. Soc. Jpn. 50, 1505 (1981)
- 178. S. Alexander, P.W. Anderson, Phys. Rev. A 133, 1954 (1964)
- 179. T. Moriya, Prog. Theor. Phys. **33**, 157 (1965)
- 180. F. Matsubara, M. Sakata, Prog. Theor. Phys. 55, 672 (1972)
- 181. S. Katsura, S. Fujiki, S. Inawashiro, J. Phys. C 12, 2839 (1979)
- 182. S. Kaya, A. Kussman, Z. Phys. 72, 293 (1931)
- 183. S. Kaya, N. Nakayama, Proc. Phys. Math. Soc. Jpn. 22, 126 (1940)
- 184. M.J. Marcinkowski, N. Brown, J. Appl. Phys. 32, 375 (1961)
- 185. W. Abdul-Razzaq, J.S. Kouvel, Phys. Rev. B 35, 1764 (1987)
- 186. A.J. Gyozalyan, J. Contemp. Phys. 42, 248 (2007)
- 187. J.W. Cable, H.R. Child, Phys. Rev. B 10, 605 (1974)
- 188. H. Tange, T. Tokunaga, M. Goto, J. Phys. Soc. Jpn. 45, 105 (1978)
- 189. M. Shiga, Y. Nakamura, J. Magn. Magn. Mater. 40, 319 (1984)
- 190. J. Crangle, G.C. Hallam, Proc. R. Soc. Lond. 272, 119 (1963)
- 191. E.F. Wasserman, in *Ferromagnetic Materials*, vol. 5, ed. by K.H.J. Buschow, E.P. Wohlfarth (North-Holland, Amsterdam, 1990), p. 237
- 192. Y. Kakehashi, Phys. Rev. B 38, 474 (1988)
- 193. M.F. Collins, R.V. Jones, R.D. Lowde, J. Phys. Soc. Jpn. 17, 19 (1962)
- 194. Y. Bando, J. Phys. Soc. Jpn. 19, 237 (1964)
- 195. Y. Kakehashi, Prog. Theor. Phys. Suppl. 101, 105 (1990)
- 196. A.Z. Menshikov, E.E. Yarchikov, Sov. Phys. JETP 36, 100 (1973)
- 197. M. Shiga, Y. Nakamura, J. Phys. F, Met. Phys. 8, 177 (1978)
- 198. Y. Kakehashi, Phys. Rev. B 35, 4973 (1987)
- 199. Y. Kakehashi, O. Hosohata, Phys. Rev. B 40, 9080 (1989)
- 200. Y. Muraoka, T. Fujiwara, M. Shiga, Y. Nakamura, J. Phys. Soc. Jpn. 50, 3284 (1981)
- 201. N. Kimura, Y. Kakehashi, Found. Phys. 30, 2079 (2000)
- 202. B. Loegel, J. Phys. F, Met. Phys. 5, 497 (1975)
- V.E. Rode, S.A. Finkelberg, A.I. Lyalin, J. Magn. Magn. Mater. 31–34, 293 (1983)
- 204. S.K. Burke, B.D. Rainford, J. Phys. F, Met. Phys. 13, 441 (1983)
- 205. S.K. Burke, B.D. Rainford, J. Phys. F, Met. Phys. 8, L239 (1978)
- 206. S.K. Burke, B.D. Rainford, J. Phys. F, Met. Phys. 13, 471 (1983)
- 207. S.M. Dubiel, Ch. Sauer, W. Zinn, Phys. Rev. B 30, 6285 (1984)
- 208. S.M. Dubiel, Ch. Sauer, W. Zinn, Phys. Status Solidi (b) 140, 191 (1987)
- 209. J. Friedel, L.E. Hedman, J. Phys. 39, 1225 (1978)
- 210. F. Kajzar, G. Parette, Phys. Rev. B 22, 5471 (1980)
- 211. F. Kajzar, G. Parette, Phys. Rev. B 20, 2002 (1979)
- 212. G. Frollani, F. Menzinger, F. Sacchetti, Phys. Rev. 175, 747 (1968)
- 213. T. Uchida, Y. Kakehashi, N. Kimura, J. Magn. Magn. Mater. 310, 1809 (2007)
- 214. K. Moorjani, J.M.D. Coey, Magnetic Glasses (Elsevier, Amsterdam, 1984)
- P. Hansen, in *Handbook of Magnetic Materials*, vol. 6, ed. by K.H.J. Bushow (North-Holland, Amsterdam, 1991), p. 289
- T. Mizoguchi, K. Yamaguchi, H. Miyajima, in *Amorphous Magnetism*, ed. by H.O. Hooper, A.M. de Graaf (Plenum, New York, 1973)
- R. Hasegawa, R.C. O'Handley, L. Tanner, R. Ray, S. Kavesh, Appl. Phys. Lett. 29, 219 (1976)
- 218. R.C. O'Handley, R. Hasegawa, R. Ray, C.-P. Chou, J. Appl. Phys. 48, 2095 (1976)
- 219. R. Hasegawa, R. Ray, J. Appl. Phys. 50, 1586 (1979)
- 220. H. Watanabe, H. Morita, H. Yamaguchi, IEEE Trans. Magn. MAG-14, 944 (1978)
- K. Fukamichi, T. Goto, H. Komatsu, H. Wakabayashi, in *Proc. 4 th Int. Conf. on Phys. Magn. Mater*, Poland, ed. by W. Gorkowski, H.K. Lachowics, H. Szymczak (World Scientific, Singapore, 1989), p. 354
- 222. K. Fukamichi, T. Goto, U. Mizutani, IEEE Trans. Magn. MAG-23, 3590 (1987)

References References

223. D. Marx, J. Hutter, *Ab Initio Molecular Dynamics: Basic Theory and Advanced Methods* (Cambridge Univ. Press, Cambridge, 2009)

- 224. T.D. Kühne, M. Krack, F.R. Mohamed, M. Parrinello, Phys. Rev. Lett. 98, 066401 (2007)
- 225. R. Yamamoto, M. Doyama, J. Phys. F, Met. Phys. 9, 617 (1979)
- 226. T. Fujiwara, Nippon Butsuri Gakkaishi 40, 209 (1985)
- 227. Y. Kakehashi, Phys. Rev. B 41, 9207 (1990)
- 228. Y. Kakehashi, Phys. Rev. B 43, 10820 (1991)
- 229. Y. Kakehashi, H. Tanaka, in *Magnetism of Amorphous Metals and Alloys*, ed. by J.A. Fernandez-Baca, W.-Y. Ching (World Scientific, Singapore, 1995), Chap. 1
- 230. Y. Kakehashi, T. Uchida, M. Yu, Phys. Rev. B 56, 8807 (1997)
- 231. T. Uchida, Y. Kakehashi, Phys. Rev. B 64, 054402 (2001)
- T. Masumoto, S. Ohnuma, K. Shirakawa, N. Nose, K. Kobayashi, J. Phys., Colloq. 41, C8-686 (1980)
- 233. Y. Nakagawa, J. Phys. Soc. Jpn. 11, 855 (1956)
- 234. Y. Nakagawa, J. Phys. Soc. Jpn. 12, 700 (1956)
- J.A. Fernandez-Baca, J.J. Rhyne, G.E. Fish, M. Hennion, B. Hennion, J. Appl. Phys. 67, 5223 (1990)
- 236. A. Liénard, J.P. Rebouillat, J. Appl. Phys. 49, 1680 (1978)
- 237. A. Fujita, T.H. Chang, N. Kataoka, K. Fukamichi, J. Phys. Soc. Jpn. 62, 2579 (1993)
- 238. J.M.D. Coey, E. Batalla, Z. Altonian, J.O. Ström-Olsen, Phys. Rev. B 35, 8630 (1987)
- H. Wakabayashi, K. Fukamichi, H. Komatsu, T. Goto, K. Kuroda, in *Proceedings of the International Symposium on Physics of Magnetic Materials*, ed. by W. Gorkowski, H.K. Lachowicz, H. Szymczak (World Scientific, Singapore, 1987), p. 342
- 240. D.H. Ryan, J.M.D. Coey, J.O. Ström-Olsen, J. Magn. Magn. Mater. 67, 148 (1987)
- 241. H. Tanaka, S. Takayama, J. Phys. Condens. Matter 4, 8203 (1992)
- 242. R. Hasegawa, R. Ray, J. Phys. **49**, 4174 (1978)
- 243. Z. Xianyu, Y. Ishikawa, S. Ishio, M. Takahashi, J. Phys. F, Met. Phys. 15, 1787 (1985)
- 244. R. Bellissent, G. Galli, M.W. Grinstaff, P. Migliardo, K.S. Suslick, Phys. Rev. B 48, 15797 (1993)
- 245. R. Morel, L. Abadli, R.W. Cochrane, J. Appl. Phys. 67, 5790 (1990)
- I. Bakonyi, V. Skumryev, R. Reisser, G. Hilscher, L.K. Varga, L.F. Kiss, H. Kronmüller, R. Kirchheim, Z. Met.kd. 88, 117 (1997)
- J.M. Rojo, A. Hernando, M. El Ghannami, A. Garcia-Escorial, M.A. Gonzalez, R. Garcia-Martinez, L. Ricciarelli, Phys. Rev. Lett. 76, 4833 (1996)
- M. Matsuura, H. Wakabayashi, T. Goto, H. Komatsu, K. Fukamichi, J. Phys. Condens. Matter 1, 2077 (1989)
- 249. H. Al-Attar, Y. Kakehashi, J. Appl. Phys. 86, 3265 (1999)
- 250. M. Yu, Y. Kakehashi, H. Tanaka, Phys. Rev. B 49, 352 (1994)
- 251. Y. Kakehashi, H. Tanaka, M. Yu, Phys. Rev. B 47, 7736 (1993)
- 252. J. Arai, J. Appl. Phys. **64**, 3143 (1988)
- 253. I. Turek, Ch. Becker, J. Hafner, J. Phys. Condens. Matter 4, 7257 (1992)
- 254. M. Yu, Y. Kakehashi, J. Appl. Phys. **73**, 3426 (1993)
- 255. M. Yu, Y. Kakehashi, J. Magn. Magn. Mater. 162, 189 (1996)
- 256. G.K. Nicolaides, K.V. Rao, J. Magn. Magn. Mater. 125, 195 (1993)
- 257. S. Asano, S. Ishida, J. Phys. F, Met. Phys. 18, 501 (1988)
- 258. J. Inoue, M. Shimizu, J. Phys. F, Met. Phys. 15, 1525 (1985)
- 259. Y. Kakehashi, M. Yu, Phys. Rev. B 49, 15076 (1994)
- 260. K.H.J. Buschow, Rep. Prog. Phys. 40, 1179 (1977)
- 261. Y. Kakehashi, M. Yu, Z. Phys. B 101, 487 (1996)
- 262. Y. Obi, Y. Kamigaki, H. Morita, H. Fujimori, J. Phys. Soc. Jpn. 56, 1623 (1987)
- 263. Y. Obi, S. Kondo, H. Morita, H. Fujimori, J. Phys. C 8, 1097 (1988)
- 264. J.M.D. Coey, D. Givord, A. Liénard, J.P. Rebouillat, J. Phys. F, Met. Phys. 11, 2707 (1981)
- 265. J. Chappert, J.M.D. Coey, A. Liénard, J.P. Rebouillat, J. Phys. F, Met. Phys. 11, 2727 (1981)
- 266. J.J. Croat, J. Appl. Phys. **53**, 6932 (1982)

- 267. S. Ishio, M. Fujikura, T. Ishii, M. Takahashi, J. Magn. Magn. Mater. **60**, 236 (1986)
- 268. A. Fujita, H. Komatsu, K. Fukamichi, T. Goto, J. Phys. Condens. Matter 5, 3003 (1993)
- H. Tange, T. Ikeda, T. Ono, T. Kamimori, M. Goto, J. Magn. Magn. Mater. 140–144, 287 (1995)
- 270. A. Fujita, T.H. Chiang, N. Kataoka, K. Fukamichi, J. Phys. Soc. Jpn. 62, 2579 (1993)
- 271. J.F. Sadoc, J. Dixmier, Mater. Sci. Eng. 23, 187 (1976)
- 272. H.J. Nowak, O.K. Andersen, T. Fujiwara, O. Jepsen, P. Vargas, Phys. Rev. B 44, 3577 (1991)
- 273. T. Mizoguchi, AIP Conf. Proc. **30**, 286 (1976)
- 274. H. Tanaka, S. Takayama, T. Fujiwara, Phys. Rev. B 46, 7390 (1992)
- 275. G. Güntherrodt, N.J. Shevchik, AIP Conf. Proc. 29, 174 (1976)
- K.H.J. Buschow, in Ferromagnetic Materials, ed. by E.P. Wohlfarth (North-Holland, Amsterdam, 1980), p. 388
- 277. D. Bloch, D.M. Edwards, M. Shimizu, J. Voiron, J. Phys. F, Met. Phys. 5, 1217 (1975)
- 278. A.K. Bhattacharjee, R. Julien, M.J. Zuckermann, J. Phys. F, Met. Phys. 7, 393 (1977)
- 279. A.K. Bhattacharjee, B. Coqblin, R. Julien, M.J. Zuckermann, Physica B 91, 179 (1977)

#### **Index**

**Symbols** 

3d transition metal, 18, 29

#### 5-fold equivalent band model, 210 Azimuthal quantum number, 4 $\alpha$ -Mn, 149 γ-Mn, 24, 168 Band narrowing factor, 45 Band-narrowing, 36 A Ab-initio MD method, 256 Band-type AF, 162 Action, 97 BCS gap equation, 153 Bernal holes, 295 Alexander-Anderson-Moriya interaction, 226 Amorphous Co, 268 Bethe ansatz method, 201 Amorphous $Co_{1-x}B_x$ , 254 Bethe approximation, 219, 261 Amorphous Fe, 267 Bethe lattice, 155 Amorphous metals, 258 Binding energy, 299 Amplitude of local moment, 78 Binomial distribution function, 221 Amplitudes of the magnetic moments, 175 Bloch theory, 206 Analytic continuation, 104 Bohr magneton, 2 Anderson lattice Hamiltonian, 183 Bonding, 54 Anderson model, 183 Bonding state, 11 Anisotropy, 170 Brillouin curve, 215, 237 Anti-bonding state, 11 Brillouin zone, 23, 152 Antibonding, 54 Broken AF, 246 Antiferromagnetic insulators, 18 Broken antiferromagnetic states, 249 Antiferromagnetic states, 149 Antiferromagnetic structure, 24 $\mathbf{C}$ Antiferromagnetism, 18, 244, 269 Canonical distribution, 324 ASRO effects, 295 Canonical structure constant, 55 Atomic magnetic moment, 23 Car-Parrinello method, 256 Atomic orbitals, 4 Cauchy theorem, 330 Atomic potential, 226 Cavity Green function, 100 Atomic short-range order, 231 Atomic short-range order parameters, 281 Charge neutrality potential, 213 Atomic sphere approximation, 57 Chemical bondings, 296 Atomic-size difference, 284, 292 Closed shell, 16 $Au_{1-x}Fe_x$ , 28 Cluster SG, 251, 272 Au<sub>2</sub>Mn, 26 Cluster spin glass, 247 Average coordination number, 281 Co, 23, 29, 60, 67, 112, 160

Average t-matrix approximation, 307

Averaged t-matrix approximation, 79

Co-P, 295	Density correlations, 47
Co-Y amorphous alloys, 291	Density functional theory, 49, 105, 298
Co-rich Co-Y amorphous alloys, 255	Density of states, 15
Co <sub>2</sub> Y alloy, 292	Determines, 163
$Co_c Y_{1-c}$ , 293	Diagonal coherent Green function, 103
Coexistence, 244, 247	Diamagnetism, 4
Coherent action, 99	Direct exchange interaction, 20, 181
Coherent Green function, 75, 83, 85, 262	Distribution, 263
Coherent potential, 75, 76, 109, 154	Distribution function, 227, 285
Coherent potential approximation (CPA), 77,	Distribution function method, 227
206	DMFT, 89, 96, 102
Collinear, 247, 265	Double <b>Q</b> MSDW, 173
Collinear ferromagnetism, 266	Double $Q$ multiple SDW, 27
Collinear SG, 266	Double counting, 7
Commensurate, 25	Double occupancy, 12, 31
Commensurate multiple MSDW, 172	Double occupation number, 36, 45
Common band model, 283	Dy, 26
Complete ferromagnetism, 32	Dy-Co, 297
Complex magnetic structures, 244, 278	Dy-Fe, 297
Configurational average, 27	Dynamical coherent-potential approximation,
Configurational disorders, 280	83
Conical magnetic structure, 26	Dynamical CPA, 305, 309
Constraint LDA, 108	Dynamical CPA equation, 85, 88, 110, 307
CoO, 17	Dynamical mean-field theory, 89, 96
Coulomb integral, 7	Dynamical potential, 90, 313
Coulomb interaction, 4, 34	Dynamical spin fluctuations, 83
Covalent bond, 12	Dynamical susceptibility, 126, 129, 143
Cowley's atomic short-range order parameter,	Dyson equation, 71, 85, 97, 100, 219
221	Dzyaloshinskii–Moriya interaction, 180
CPA, 77, 207, 301	•
CPA equation, 77, 100, 102, 104, 208, 213	$\mathbf{E}$
Cr, 18, 24, 25, 61, 149, 160	Effective action, 97
Cr–Mn, 150	Effective Bohr magneton number, 81, 112, 114
Cr-V, 150	Effective Coulomb interaction, 37, 40, 46
CrBr <sub>2</sub> , 17	Effective exchange interaction, 35
Critical Coulomb interaction, 46	Effective Hamiltonian, 20, 95
CrO <sub>2</sub> , 17, 26	Effective locator, 259
Crystalline-field effects, 297	Effective mass, 46
$Cu_{1-x}Mn_x$ , 28	Effective medium, 224, 262
Cu <sub>3</sub> Au, 231	Effective potential, 91, 109
Cubic harmonics, 5	Electron correlations, 36
Curie constant, 11	Electron gas, 52
Curie law, 11, 195	Electron hopping integral, 12
Curie temperature, 66, 111, 139, 269, 274	Electron-electron attractive interaction, 153
Curie-Weiss law, 66, 112, 113, 146, 171	Electron-electron interaction, 4
Curie-temperature Slater–Pauling curves, 241	Electron-phonon interaction, 153
Cut-off frequency, 123	Electrostatic potential, 7
	Energy, 79
D	Energy dependent effective Liouville operator,
Debye cut-off frequency, 153	103
Decoupling approximation, 225, 263	Energy functional, 70
Degree of structural disorder, 277	Entropy, 79
Dense random packing of hard spheres	Envelope function, 55
(DRPHS), 256	Equation of motion method, 129

Equations of motion, 103, 130, 323 Ergodic theorem, 324 Ergodicity, 166	First-principles dynamical CPA, 104 First-principles TB-LMTO Hamiltonian, 58 First-principles tight-binding, 105
Eu, 26	Fluctuation–dissipation theorem, 128
Exchange correlation energy, 50	Fourier representation, 87
Exchange energy parameter, 59	Free electron model, 329
Exchange energy potential, 226	Free energy, 69, 86, 109, 164
Exchange integral, 7	Free spin-pairs, 248
Exchange interaction, 34, 226	Functional integral method, 68
Exchange potential, 7	
Exchange splitting, 137	G
Exchange-correlation potential, 50	g-value, 2
T.	Gap-type antiferromagnetism, 154
F	Gd, 29
f-electron, 296	Gd-Co, 298
Fcc transition metals, 167	Gd–Fe, 298
Fe, 23, 29, 35, 60, 61, 67, 81, 93, 111, 133, 160	Gd–Ni, 298
Fe powder, 279	Gd <sub>33</sub> Fe <sub>67</sub> , 298
Fe-Co, 241	$GdFe_2$ , 299
Fe-Cr, 240, 244	Generalized gradient approximation, 62
Fe–ET amorphous alloys, 279	Generalized Slater–Pauling curve, 254
Fe-metalloid alloys, 279	Generalized susceptibility, 157, 159
Fe-Ni, 233, 240, 242, 288	Geometrical mean model, 281
Fe-V, 240	Ginzburg-Landau phenomenological theory,
Fe–Zr, 289	169
Fe-rich amorphous alloys, 254	Grassmann variables, 97
$Fe_{1-x}Cr_x$ , 209	Green function, 70
$Fe_{100-x}Co_x$ , 179	Green function theory, 281
$Fe_2B$ , 295	Ground-state energy, 15
Fe <sub>2</sub> P, 295	Ground-state magnetization, 65, 81
Fe <sub>3</sub> P, 295	Ground-state sublattice magnetization, 153
$Fe_{80}B_{20}, 295$	Gutzwiller approximation, 43, 155
$Fe_cB_{1-c}$ , 277	Gutzwiller overlap function, 42
$Fe_cNi_{1-c}$ , 215	Gutzwiller variational method, 40
$Fe_c Y_{1-c}$ , 293	
$Fe_x Cr_{100-x}$ , 244	H
$Fe_xMn_{1-x}$ , 179	Hamiltonian, 105
FeO, 17	Harmonic approximation, 90, 92, 313
Fermi distribution function, 7, 32	Hartree–Fock approximation, 6, 31, 140, 199
Fermi level, 15	Hartree–Fock cluster CPA theory, 221
Fermi liquid theory, 201	Hartree-Fock CPA theory, 206, 209
Fermi surface, 161	Hartree–Fock energy, 32, 74
Ferrimagnetism, 298	Hartree–Fock equations, 137
Ferromagnetic instability, 233, 235	Hartree–Fock ground state, 118
Ferromagnetic insulators, 17	Hartree–Fock susceptibility, 158
Ferromagnetic state, 191	Hartree–Fock theory, 136
Ferromagnetic structure, 23	Hartree–Fock wave function, 47
Ferromagnetism, 29, 244, 265, 268, 278	Hartree–Fock–Slater exchange potential, 48
Feynman diagram, 97	Hartree–Fock–Stoner theory, 67
Field operator, 3	Heavy effective mass, 201
Finite-temperature theory of the LEE, 258	Heavy fermion system, 201
Finite-temperature theory of the local	Heavy rare-earth elements, 11
environment effects, 223	Heavy RE atoms, 297
First-order transition, 215	Heavy transition-metal elements, 11

Heisenberg model, 19, 20, 22, 115, 155	Kondo Hamiltonian, 186
Heitler–London theory, 20	Kondo lattice Hamiltonian, 185
Helical MSDW, 178	Kondo problem, 200
Helical structure, 25, 169, 179	Kondo temperature, 197
Hilbert transform, 98	L
Ho, 26	
Hohenberg–Kohn theorem, 49	Lanczos method, 325
Hohenberg–Kohn–Sham method, 51	Landau theory, 171
Hubbard bands, 16	Landé's g factor, 11
Hubbard model, 13	Laplace expansion, 313
Hubbard–Stratonovich transformation, 68, 96,	Lattice, 151
108	Laves-phase Co <sub>2</sub> Y, 292
Hubbard's alloy analogy picture, 16	LDA + U method, 107
Hund rule, 9	Legendre transformation, 136
Hund-rule coupling, 8, 9, 297	Ligand electron state, 195
Hund's first rule, 8	Ligand model, 193
Hund's second rule, 9	Light rare-earth elements, 11
Hydrogen molecule, 11, 54	Light RE atoms, 297
Hyper-cubic lattice, 97	Light transition-metal elements, 10
Hypergeometric functions, 44	Linear response, 319
	Linear response function, 319
I	Linear response theory, 124
Impurity action, 98, 99	Linearly polarized MSDW, 177
Impurity Green function, 85, 96, 99	Liouville operator, 102
Impurity Hamiltonian, 95	Liquid Ni, 280
Impurity susceptibility, 199	Liquid transition metal, 269
Incommensurate wave, 169, 177	Local anisotropy, 274
Incomplete ferromagnetism, 32	Local ansatz variational method, 46
Infinite dimensions, 97	Local charge, 78
Insulating state, 16	Local density approximation, 52, 105, 298
Insulator, 14	Local environment effects (LEE), 217, 222,
Inter-site Coulomb interaction, 13	264
Internal-field distribution function, 237	Local ferromagnetic orders, 271
Intra-atomic Coulomb interaction energy, 60	Local magnetic moment, 11, 78, 193
Intra-atomic Coulomb interactions, 13	Local moment system, 67, 80
Intraatomic exchange interaction, 105	Local spin density approximation, 52
Invar anomalies, 268	Locally rotated coordinates, 164
Invar effects, 215	Long-range magnetic interaction, 181
Irreducible representation, 5	Long-wave limit, 123
Ising type, 226	Low density limit, 37
Isothermal molecular dynamics method, 165,	Low-energy excitations, 118
323	
Isotropic SG, 251	M
Itinerant electron magnets, 18	Magnetic diffuse-scattering, 221
Itinerant ferromagnets, 118	Magnetic entropy, 79
Itinerant magnetism, 18, 30	Magnetic force, 166
Itinerant-electron ferromagnet, 123	Magnetic form factor, 129
Itinerant-electron SG, 271	Magnetic moment, 1
	Magnetic phase diagram, 155, 175
K	Magnetic quantum number, 5
Kohn–Sham equation, 51	Magnetic structure, 22
Kohn–Sham theory, 51	Magnetization, 66, 124, 171, 239, 268
Kondo effects, 200	Magnon excitations, 123
Kondo exchange coupling, 185	Many-body CPA, 89, 95
	J J J J

Matthiessen's law, 200 MB-CPA, 95, 102 MD approach, 242 Mean-field theory, 67 Medium, 75 Metal, 14, 16 Metalinsulator crossover, 155 Metall-insulator transition, 16, 46 Metallic ferromagnet, 18 Metallic magnetism, 18 Metallic magnets, 18 Metallic magnets, 18 Metallic magnet, 18 Metallic magnet, 253 Mn, 18, 149, 162 Mn <sub>c</sub> Y <sub>1-c</sub> , 293 MnO, 17	NiO, 16, 17  Non-collinear ferrimagnetism, 297  Noncollinear, 265, 272  Noncollinear ferromagnetism, 266, 273, 297  Noncollinear magnetic structure, 297  Noncollinear SG, 266, 273  Noncollinear theory, 272  Nonlinear magnetic coupling, 234, 240, 270  Nonlocal susceptibility, 158  Nonunique magnetism, 277  Nuclear magneton, 3  Nuclear magneton number, 129  Numerical renormalization group method, 98  Numerical renormalization group technique, 199
MnO <sub>2</sub> , 26	
MnSi, 180 Mode-mode coupling, 92, 176, 178 Modulated structure, 169 Molecular dynamics method, 163, 256 Momentum independent self-energy, 98 Most random configuration, 281 Mott insulator, 16	O Off-diagonal disorder, 207, 208, 218 Off-diagonal Green function, 327 Off-diagonal self-energy, 98 Onsager's reaction field, 147 Orbital degeneracy, 93, 105 Orbital magnetic moment, 2, 18
Mott transition, 16	P
Mott transition, 16 MSDW, 172, 177 Muffin-tin, 54 Multicritical point, 273 Multiple scattering theory, 305 Multiple spin density wave, 172, 177 Multiplet, 9  N Nd-Co, 297 Nd-Fe, 297 Nearly orthogonal representation, 56 Néel temperature, 154, 155 Nesting effect, 160 Nesting mechanism, 149 Nesting-type antiferromagnetism, 154 Neutral state, 12 Neutron magnetic scattering, 129 Ni, 23, 29, 35, 60, 61, 67, 81, 111, 112, 133, 160 Ni-B, 277, 280 Ni-Cr, 240 Ni-Cu, 221, 240	P Pair distribution function, 255 Pair energy, 225 Paramagnetic spin susceptibility, 32 Paramagnetic state, 191 Paramagnetic susceptibility, 65, 81, 171 Paramagnetism, 265, 266, 278 Path integral method, 97 Pauli principle, 8, 38, 68 Pauli spin matrices, 3 Pauli uniform susceptibility, 189 Pd, 61 Phenomenological spin-fluctuation theory, 172 PM-CPA, 102 Point group, 5 Polarized state, 12 Potential parameter, 57 Principal quantum number, 4 Projection operator, 20 Projection operator method CPA, 89, 102 Projection technique, 103 Pseudo-potential, 256 Pt, 61
Ni–La, 277 Ni–Mn, 230, 240, 242 Ni–Y, 277 Ni–Zr, 277 Ni <sub>1-x</sub> Cr <sub>x</sub> , 210 Ni <sub>3</sub> Al, 135 Ni <sub>c</sub> Y <sub>1-c</sub> , 293 Nickel, 40	Q Quantum fluctuations, 93 Quantum Monte-Carlo method, 98 Quenching of orbital magnetic moments, 18 Random phase approximation, 111, 120, 129 Rapid quenching, 253 Rare-earth metals, 18

344 Index

Rare-earth transition metal, 296 Spin susceptibility, 61 Re-entrant SG, 272, 290 Spin wave, 115, 118, 132, 238 Recursion method, 167, 243, 257, 325 Spin wave energy, 117 Relaxed DRPHS model, 256 Spin wave excitations, 121, 123, 272 Renormalization group theory, 201 Spin wave stiffness constant, 122, 132, 274 Response function, 125 Spin-orbit coupling, 297 Retarded Green function, 102, 130 Spin-orbit interaction, 4, 18, 170 Spin-flip magnetic moment, 127 Rhodes-Wohlfarth ratio, 112, 135 Riemann's  $\zeta$  function, 124 Spin-flip operator, 117, 119 Rigid band picture, 244 Spin-glass temperature, 229 Rigid-band model, 204 Spontaneous magnetization, 139 RKKY interaction, 187, 200, 329 Stability condition, 174 Rotational invariance, 164, 165 Staggered susceptibility, 160 Static approximation, 69, 73, 163 RPA, 120, 129 Static energy potential, 91 Static field variables, 72 Sc<sub>3</sub>In, 135, 147 Static potential, 109 Scattering vector, 129 Stationary condition, 77, 86, 302 Screened structure constant, 55 Stoner condition, 31, 35, 60, 267 Sd Hamiltonian, 186 Stoner continuum, 122 SDW, 160 Stoner criterion, 160, 292 Second-order Born approximation, 200 Stoner excitations, 121, 123, 132 Second-order transition, 215 Stoner parameter, 58 Self-consistent phonon approximation, 147 Stoner theory, 64, 135 Self-consistent renormalization theory (SCR), Strong ferromagnetism, 32 145 Strong ferromagnets, 204 Self-energy, 261, 307 Structural disorder, 253, 259, 280, 296 SG, 234, 236, 244, 265, 268 Sublattice, 24, 151 SG states, 270 Substitutional disordered alloys, 27 SG temperature, 191 Sum rule, 144 Short-range atomic order, 192 Super-conducting order parameter, 153 Simple cubic, 151 Super-exchange interaction, 22, 155, 181, 226 Simple dilution picture, 240 Susceptibility, 11, 66 Single-site approximation, 77 Symmetry operations, 170 Single-site spin fluctuation theory, 75, 90, 309 Single-site theory, 74 Т Single-site t matrix, 76, 84 Tb, 26 Singlet, 38, 194, 200 TB-LMTO, 106, 257 Singlet state, 195 Temperature Green function, 71, 95 Sinusoidal spin density wave, 24 Terminator, 244, 326 Slater determinant, 8 Ternary alloys, 251 Slater-Pauling curves, 203, 239 Thermal spin fluctuations, 93 Slater's two-center tight-binding Hamiltonian, Ti. 35 Tight-binding linear muffin-tin orbital Sommerfeld coefficients, 29 (TB-LMTO), 54, 106, 159 Spherical harmonics, 5 Tight-binding LMTO, 163 Tight-binding LMTO supercell method, 289 Spin angular momentum, 2 Spin correlations, 47 Time reversal symmetry, 170 Spin density waves, 160, 278 Time-dependent coherent potential, 95 Time-dependent Green function, 96 Spin disorder, 259 Spin fluctuation parameter, 145 Time-dependent Hamiltonian, 70 Spin glass, 28, 234, 278 Time-dependent magnetic moment, 166 Spin glass state, 191, 200, 215, 229, 231, 287 Time-dependent potential, 70 Spin magnetic moment, 2 Time-ordered product, 69

Tm, 29
Total angular momentum, 9
Transition metal metalloid, 295
Transverse dynamical susceptibility, 127
Transverse SG order parameter, 272
Transverse spin freezing temperature, 274
Tridiagonal matrices, 314
Triple *Q* MSDW, 174
Triple *Q* multiple SDW, 27
Triplet, 38, 194
Triplet states, 195
Two-band model, 182

U U, 201 Unenhanced susceptibility, 160 Uniform susceptibility, 139

**V** V, 60 Variational approach, 104 Very weak ferromagnetism, 65 Virtual bound state, 205, 210, 240 Voronoi polyhedra, 23

#### W

Weak ferromagnetism, 32 Weiss-field function, 98 Wigner–Seitz cells, 23

X  $X\alpha$  potential, 48

# **Z**Zeeman interaction, 4 Zero-band-width model, 193 ZrZn<sub>2</sub>, 135, 147